frontiers | Research Topics

Network learning and propagation dynamics analysis

Edited by
Xuzhen Zhu, Fei Xiong, Shirui Pan, Yi Zhang and Ningbo Zhang

Published in
Frontiers in Physics

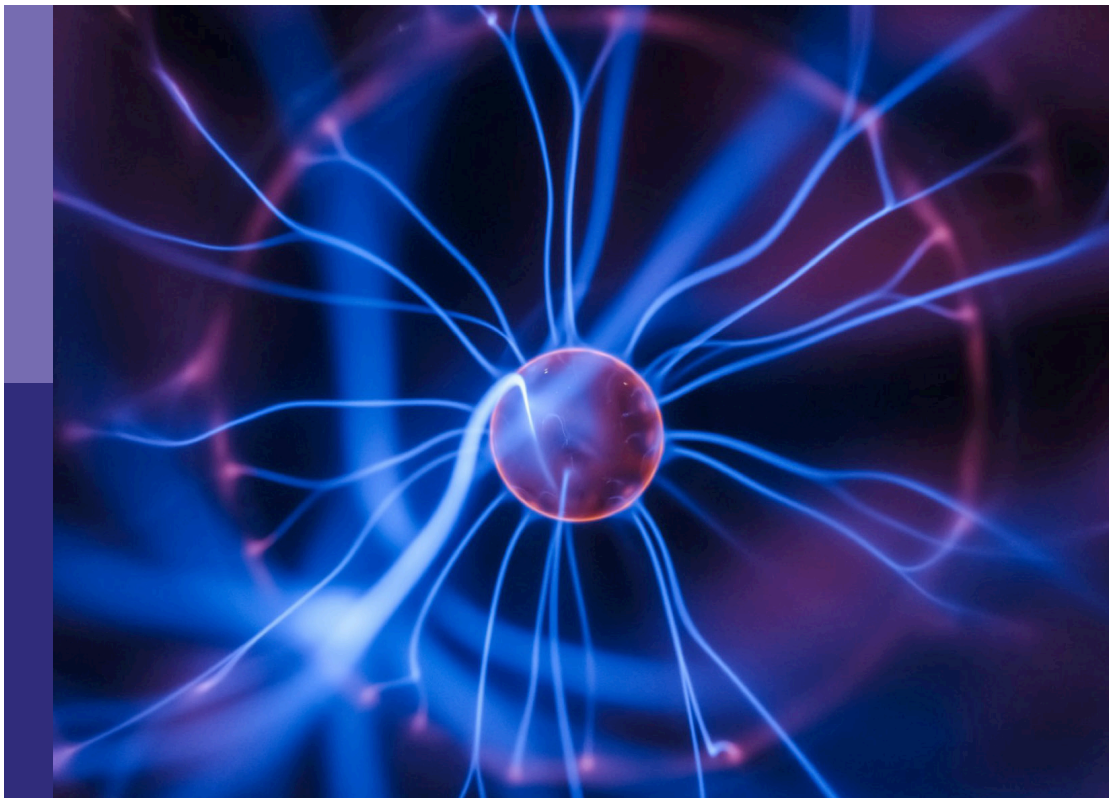

ISSN 1664-8714
ISBN 978-2-8325-6325-0
DOI 10.3389/978-2-8325-6325-0

About Frontiers

Frontiers is more than just an open access publisher of scholarly articles: it is a pioneering approach to the world of academia, radically improving the way scholarly research is managed. The grand vision of Frontiers is a world where all people have an equal opportunity to seek, share and generate knowledge. Frontiers provides immediate and permanent online open access to all its publications, but this alone is not enough to realize our grand goals.

Frontiers journal series

The Frontiers journal series is a multi-tier and interdisciplinary set of open-access, online journals, promising a paradigm shift from the current review, selection and dissemination processes in academic publishing. All Frontiers journals are driven by researchers for researchers; therefore, they constitute a service to the scholarly community. At the same time, the *Frontiers journal series* operates on a revolutionary invention, the tiered publishing system, initially addressing specific communities of scholars, and gradually climbing up to broader public understanding, thus serving the interests of the lay society, too.

Dedication to quality

Each Frontiers article is a landmark of the highest quality, thanks to genuinely collaborative interactions between authors and review editors, who include some of the world's best academicians. Research must be certified by peers before entering a stream of knowledge that may eventually reach the public - and shape society; therefore, Frontiers only applies the most rigorous and unbiased reviews. Frontiers revolutionizes research publishing by freely delivering the most outstanding research, evaluated with no bias from both the academic and social point of view. By applying the most advanced information technologies, Frontiers is catapulting scholarly publishing into a new generation.

What are Frontiers Research Topics?

Frontiers Research Topics are very popular trademarks of the *Frontiers journals series*: they are collections of at least ten articles, all centered on a particular subject. With their unique mix of varied contributions from Original Research to Review Articles, Frontiers Research Topics unify the most influential researchers, the latest key findings and historical advances in a hot research area.

Find out more on how to host your own Frontiers Research Topic or contribute to one as an author by contacting the Frontiers editorial office: frontiersin.org/about/contact

Network learning and propagation dynamics analysis

Topic editors

Xuzhen Zhu — Beijing University of Posts and Telecommunications (BUPT), China
Fei Xiong — Beijing Jiaotong University, China
Shirui Pan — Griffith University, Australia
Yi Zhang — University of Technology Sydney, Australia
Ningbo Zhang — Beijing University of Posts and Telecommunications (BUPT), China

Citation

Zhu, X., Xiong, F., Pan, S., Zhang, Y., Zhang, N., eds. (2025). *Network learning and propagation dynamics analysis*. Lausanne: Frontiers Media SA.
doi: 10.3389/978-2-8325-6325-0

Table of contents

frontiers | Frontiers in Physics

TYPE Editorial
PUBLISHED 24 April 2025
DOI 10.3389/fphy.2025.1609957

OPEN ACCESS

EDITED AND REVIEWED BY
Matjaž Perc,
University of Maribor, Slovenia

*CORRESPONDENCE
Xuzhen Zhu,
zhuxuzhen@bupt.edu.cn

RECEIVED 11 April 2025
ACCEPTED 16 April 2025
PUBLISHED 24 April 2025

CITATION
Nie S, Zhu X, Xiong F and Zhang N (2025) Editorial: Network learning and propagation dynamics analysis.
Front. Phys. 13:1609957.
doi: 10.3389/fphy.2025.1609957

Editorial: Network learning and propagation dynamics analysis

Sushuang Nie[1], Xuzhen Zhu[1]*, Fei Xiong[2] and Ningbo Zhang[1]

[1]Beijing University of Posts and Telecommunications (BUPT), Beijing, China, [2]Beijing Jiaotong University, Beijing, China

KEYWORDS

propagation dynamics, network learning, information diffusion, opinion dynamics, recommendation systems

Editorial on the Research Topic
Network learning and propagation dynamics analysis

1 Introduction

In a rapidly expanding digital interconnectivity era, understanding how information, behaviors, and innovations propagate through complex networks has become a central interdisciplinary challenge. From online social platforms to transportation systems, scientific collaboration, and cybersecurity, network-driven diffusion processes are shaping collective decision-making and system performance. The Topic "Network Learning and Propagation Dynamics Analysis" brings together a diverse set of 13 high-quality studies that explore the mechanisms, structures, and emergent patterns of learning and propagation within multi-agent, multi-layered, and heterogeneous networks.

The articles we gathered range in subject from the diffusion of diseases and behavioral modeling of the epidemic, to public opinion governance, recommender systems, edge caching, and other related fields. These studies show that the theoretical richness and practical significance of propagation dynamics in contemporary complicated systems are reflected by the use of tools such as networks theory, data science, physics, and artificial intelligence.

2 Presentation of the papers

The first paper, titled "*Dynamics analysis of epidemic spreading with individual heterogeneous infection thresholds*" (Li) studies the diffusion of epidemics on single-layer complex networks by analyzing the individual vulnerability of each vertex in relation to infection spread and modeling it with a logarithmic threshold. It develops novel theoretical models for epidemic dynamics. This study paves the way for developing vaccination and containment strategies.

The second paper, titled "*The coupled awareness-epidemic dynamics with individualized self-initiated awareness in multiplex networks*" (Zhang et al.), derives a Microscopic Markov Chain Approach (MMCA) and validates its correctness with Monte Carlo simulations to provide a joint model of awareness and epidemic propagation while considering self-induced awareness at an individual level. The probability of an individual becoming aware is conditional on the number of their aware social links. Individuals'

knowledge increase reduces the epidemic's spread, and a metacritical threshold λc appears as a result of the propagation of this knowledge.

The third paper, titled "*Information propagation characteristic by individual hesitant-common trend on weighted network*" (Jia et al.), proposes a network model with cautious and casual users and studies the spread of information. They find that different behaviors have substantial effects on information spread rate and scale. A transition from first-order and second-order phase transitions is found. The evidence of the edge-partition theory by simulations allows us to observe how individual opinions affect aggregate spreading behaviors of heterogeneous networks.

The fourth paper, titled "*The information propagation mechanism of individual heterogeneous adoption behavior under the heterogeneous network*" (Cui et al.), introduces a two-tiered heterogeneous network framework that integrates unique hesitant and standard adoption mechanisms to investigate information dissemination in intricate networks. Simulations demonstrate that when one layer is dominant, it results in second-order continuous phase shifts, whereas balanced layers trigger first-order discontinuous changes. And elements like hesitation parameters and the diversity of node degrees impact the spread significantly.

The fifth paper, titled "*A novel spreading dynamic based on adoption against the trend*" (Hao et al.), introduces a novel formulation of the process of opinion diffusion under the influence of opposing adoption. The simulations on ER and SF networks indicate that polarized oppositions hinder the diffusion process, while moderate opposition allows for a smooth second-order phase transition and leads to rough first-order phase transition. The non-conformist influence over the patterns of propagation in social systems is mutually determined together with bounded influence and susceptibility.

The sixth paper is titled "*Communication dynamics of congestion warning information considering the attitudes of travelers*" (Yan et al.). In this paper, a social network background is incorporated by a congestion alert system that propagates information spreading using dynamical systems and optimal control theory. Results show that sensitivity to reputation and higher propensity to share contributes to more extensive dissemination and, thus, less congestion.

The seventh paper, titled "*Analysis of differences in fossil fuel consumption in the world based on the fractal time series and complex network*" (Zhang et al.), performs a detailed study of the fossil fuel usage of 38 countries using fractal times series analysis and complex network methodologies. The results show that usage is resilient for a long duration of time, in other words demonstrating high Hurst exponents. The visibility graph methodology also exposes the structure of the data, thus underlining the disparities between countries.

The eighth paper, titled "E*ffect of network structure on the accuracy of resilience dimension reduction*" (Liu et al.), explores the fidelity of resilience dimensionality reduction with the impact of the network structure. In these experiments, real-world and synthetic networks are used; it was shown that high assortativity, clustering, and a large modularity cause improved performance. Enhanced fidelity is observed for both social and small-world networks owing to specific topological properties. Theoretical support from this work suggests that refining network topology can improve robustness evaluation, so to enable more effective strategies to examine complicated systems under disruption.

The ninth paper, titled "*Exploring network dynamics in scientific innovation: collaboration, knowledge combination, and innovative performance*" (Jia et al.), constructs a multilayer framework of institutions, knowledge components, and innovative outputs to examine the impact of collaboration and knowledge attributes on innovation effectiveness and network behavior. Results indicate that the variety, distinctiveness, and centrality of knowledge in collaborative networks substantially enhance innovation results.

The tenth paper, titled "*SABTR: semantic analysis-based tourism recommendation*" (Li et al.), introduces a tourist attraction recommendation framework, SABTR, that combines LDA topic modeling with collaborative filtering to recover latent user preferences and predict missing ratings. Results on our modified datasets show that SABTR outperforms conventional models (such as PLSA or Skip-Gram) when data are sparse. This improves both the accuracy and coverage of the echo chamber effect, resulting in a higher selection of diverse and personalized attraction recommendations to the user.

The eleventh paper, titled "*Evolution and governance of online public opinion during COVID-19: a hybrid approach using communication visualization, SIR modeling, and simulation validation*" (Ren et al.), uses a two-stage SIR model along with communication visualization to discuss the dynamics of public opinion during the COVID-19 pandemic. Their findings reveal the importance of key opinion nodes to accelerate the process of the spread of opinion and average nodes to stabilize the situation. Their simulations reveal that optimal government action should be taken at the beginning and the climax of the spread. This study sheds light on the need for personalized guidance and continuous monitoring to maintain stability in online public discussions.

The twelfth paper, titled "*Dynamic analysis of malicious behavior propagation based on feature selection in software network*" (Xue et al.), introduces an efficient recurrent neural network-based malware detection framework, MBDFE, which extracts feature selection based on different feature lengths, specifically n-gram features from API calls sequences, and ranks them based on the information gain. It then classifies their behaviors using RNNs. Their experimental findings illustrate that MBDFE provides a more accurate and faster-to-train solution than the baselines in high-density data cases. MBDFE provides an accurate and scalable solution for the detection and mitigation of malicious activities in software systems.

The last paper, titled "*Epidemic dynamics edge caching strategy for 6G networks*" (Wang et al.), proposes a 6G edge caching technique named CDSED which employs epidemic dynamics to build models of content delivery. The predict genetic-annealing algorithm is adopted in fine-grained optimizing cache allocation to enhance hit probability. Through simulations, we demonstrate that CDSED outperforms LRU, LFU, and MPC schemes in different scenarios, such as when the cache scale, content number, and user numbers are different. The model is able to provide a robust real-time edge content delivery solution for future 6G networks.

Finally, we want to thank all the authors and reviewers who have participated, worked hard in their efforts to organize this challenge, and support our efforts. Our results are both a theoretical and practical contribution toward the comprehension of dynamic complex systems that may find further applications in real and complex intelligently monitored systems.

Author contributions

SN: Writing – original draft. XZ: Writing – review and editing. FX: Writing – review and editing. NZ: Writing – review and editing.

Funding

The author(s) declare that financial support was received for the research and/or publication of this article. The work was supported in part by the Sub Project of the National Key Research and Development plan in 2020 No. 2020YFC1511704.

Acknowledgments

We are grateful for the contributions to this Research Topic made by Frontiers editorial staff members. We also thank the reviewers who provided valuable input for each manuscript.

Conflict of interest

The authors declare that the research was conducted in the absence of any commercial or financial relationships that could be construed as a potential conflict of interest.

Generative AI statement

The authors declare that no Generative AI was used in the creation of this manuscript.

Publisher's note

frontiers | Frontiers in Physics

TYPE Original Research
PUBLISHED 12 June 2024
DOI 10.3389/fphy.2024.1406403

OPEN ACCESS

EDITED BY
Fei Xiong,
Beijing Jiaotong University, China

REVIEWED BY
Wei Wang,
Chongqing Medical University, China
Run-Ran Liu,
Hangzhou Normal University, China
Yuexia Zhang,
Beijing Information Science and Technology University, China

*CORRESPONDENCE
Jinming Ma,
jmma@bupt.edu.cn

RECEIVED 25 March 2024
ACCEPTED 22 April 2024
PUBLISHED 12 June 2024

CITATION
Hao J, Ma J, Liu S and Tian Y (2024), A novel spreading dynamic based on adoption against the trend.
Front. Phys. 12:1406403.
doi: 10.3389/fphy.2024.1406403

A novel spreading dynamic based on adoption against the trend

Jiaqi Hao[1], Jinming Ma[1]*, Siyuan Liu[2] and Yang Tian[2]

[1]School of Artificial Intelligence, Beijing University of Posts and Telecommunications, Beijing, China, [2]School of Information and Communication Engineering, Beijing University of Posts and Telecommunications, Beijing, China

In the spreading dynamics of previous fashion trends, adoption researchers have neglected to consider that some individuals may behave differently from popular tendencies, which is called opposite-trend adoption behavior. To explore the dissemination mechanisms of the behavior, we first establish the adoption-against-trend model. Additionally, an edge division theory based on the adoption of opposite trends was proposed to quantitatively analyze this unique dissemination mechanism. This study presents three different degrees of opposite trends, each highlighting unique spreading scenarios. In the case of a strong opposite trend, no spreading occurs. In the case of a weak opposite trend, limited contact will accelerate information spreading, but it will not alter the mode of spreading. Nevertheless, in the case of a moderately opposite trend, the degree of the opposite trend alters the mode of spreading. Meanwhile, a cross-phase transition occurs. The findings of this paper can be applied to various areas, including social media and commercial trades.

KEYWORDS

complex networks, information propagation, limited contact network, opposite-trend adoption, spreading dynamics

1 Introduction

The theory of spreading dynamics can be used to analyze many aspects of life, including healthy behaviors [1-3], social recommendations [4-9], advertising and promotion [10-11], and fashion trends. The adoption of popular trends is strengthened by the reinforcement effect, which can lead to further expansion. Furthermore, investigators have found that due to the reinforcement effect, individuals showing a higher adoption trend toward certain behaviors are more likely to adopt those behaviors [12]. Additionally, there appears to be a connection between the reinforcement and memory effects. Upon receiving information, individuals accumulate pieces of information, leading to either a full or partial memory effect, as there are accumulative messages present. Moreover, the memory effect is characterized by being non-Markovian [13-15]. Apart from the features mentioned above, investigators discover a lot of elements that affect the infection region, including group heterogeneity [16], network structure [17], and node preference for connection [18].

To harness information spreading, certain researchers have introduced the threshold model [19-20]. Individuals only accept information once they have received messages exceeding a certain threshold. Subsequent studies have proposed the use of a truncated normal distribution due to the varying adoption probabilities of individuals impacted by factors such as age and education level [21-22]. Leng et al. discovered that the acceptance of information by individuals is not only related to the level of intimacy with their neighbors but also to the degree of nodes in the social network [23]. Similarly, Cui et al. proved that the adoption of behavior is influenced by individual interest and not merely by the behavior

itself [24]. Some studies have demonstrated that the acceptance and adoption of information and behavior are governed by various influential factors in social networks. Ruan et al. examined the process by which nodes provide inverse feedback upon the receipt of messages, influencing vulnerable nodes [25]. Otherwise, group behaviors should also be observed beyond individual actions. Investigators have grouped networks into two categories: positive and negative [26-27]. Researchers have identified imitative behaviors in society and are studying information propagation laws in double-layered networks by establishing gate-like adoption functions [28]. To comprehend the information dissemination process precisely, Zhu et al. suggested that an individual can only obtain limited information from their finite neighbors due to time and energy constraints [29-34].

Hence, it is crucial to establish a network with limited contact. To date, researchers have rarely studied the dissemination of information against the fashionable trend, which is called the adoption of behavior against the trend. People refrain from adopting their neighbors' behavior when they lack sufficient information. However, if a few nodes adopt the behavior, individuals are much more likely to adopt it as well. As the number of individuals displaying the behavior increases, the likelihood of additional individuals adopting the behavior decreases significantly. For example, new clothing brands do not immediately form a trend. Initially, only a few unique individuals will purchase them. As the clothing becomes more popular, more people will buy it. However, some individuals may choose to avoid the trend.

Focusing on the aforementioned situation, this paper studies the spreading mechanism among single-layer network neighbors with limited contact. A comparable adoption threshold model is constructed to characterize the spreading characters since the quasi-right triangle is associated with the adoption qualities against neighbors, which have a rapidly increasing character at first and a slowly decreasing character thereafter. Afterward, we propose a general edge compartmental to quantitatively analyze the mechanism of propagation. In addition, our acceptable model has been confirmed through simulations that coincide with theoretical calculations. We note that there is a phase transition present, regardless of whether the network is random or scale-free. In cases of strong opposition, we observe that information is not transmitted. In the weak scenario, limited contact hastens transmission but does not convert the spreading mode. In both networks, the mode of spreading continuously grows with a second-order transition. In the moderate scenario, the dissemination mode changes due to the influence of the opposite adaptive parameter.

The remainder of this paper is divided into five sections. Section 2 introduces a model of opposite trend acceptance with limited contact ability. Section 3 presents evidence to support the validity of the model. Section 4 examines the process of information dissemination across two distinct networks, using both inference and simulation. Section 5 offers a conclusion about the study as a whole.

2 Model description

To investigate the mechanism of individual information sharing within a single-layer social network under the influence of opposite trend adoption and limited contact heterogeneity, a network containing N nodes was designed. The social network is comparable to platforms such as WeChat, Microblog, and Facebook, and thus, a distribution of node degrees $p(k)$ was obtained.

According to the above description of a single-layer network model, we use the traditional SAR model to research information-spreading mechanisms, as shown in Figure 1. In the SAR model, individuals can be in three different stages. Susceptible individuals have the zest to receive information. Adopted nodes have already received information and subsequently transmit it to their neighbors. On the other hand, recovered nodes have received information but have no interest in the message, so they will not participate in the propagation of information.

We introduced limited contact to represent the contact ability of each node. $f(k_j)$ denotes the limited contact of nodes, and k_j represents the degree of node j. If $f(k_j) \geq k_j$, adopted nodes can transmit information to all of their neighbors. However, when $f(k_j) < k_j$, they can only transmit information to their $f(k_j)$ nodes, resulting in a reduced amount of information that individuals can access. Within a unit of time, the adopted nodes were converted by susceptible nodes with a probability of λ. Additionally, the nodes adopted the practice of spreading messages to all of their neighbors with a probability of $\frac{\lambda f(k_j)}{k_j}$.

We define m as the accumulation of information by nodes. Information is not transmitted initially, but when a susceptible node receives information, m increases by 1. We present an adoption threshold model that exhibits the characteristic of information spread against trends in a similar manner to a right triangle as Eq. 1.

$$\mathrm{h}(x,b) = \begin{cases} 0 & ,0 < x < b \\ \dfrac{1-x}{1-b} & ,b \leq x < 1 \end{cases}. \tag{1}$$

Here, x represents the ratio of received information to the degree of a susceptible node and b denotes the degree parameter of opposite trend adoption.

- The process of information spreading in a single-layer network with limited contact is outlined as follows: prior to transmission, we randomly select the proportion of ρ_0 adopted nodes. The remaining nodes are deemed susceptible.
- Adopted nodes, which are stochastically chosen $f(k_j)$ times from susceptible nodes, transmit messages along edges with a probability of $\frac{\lambda f(k_j)}{k_j}$.
- As susceptible nodes receive messages, the number of susceptible nodes decreases by 1.
- The node will reject duplicate information that has been previously received.
- During a unit of time, the adopted nodes have a probability of transitioning into recovered nodes. However, if there are no adopted nodes left, the process will terminate within that time frame.

3 Theoretical analysis

In accordance with the hole theorem in a single-layer network with limited contact, we assume the random selection of node i as

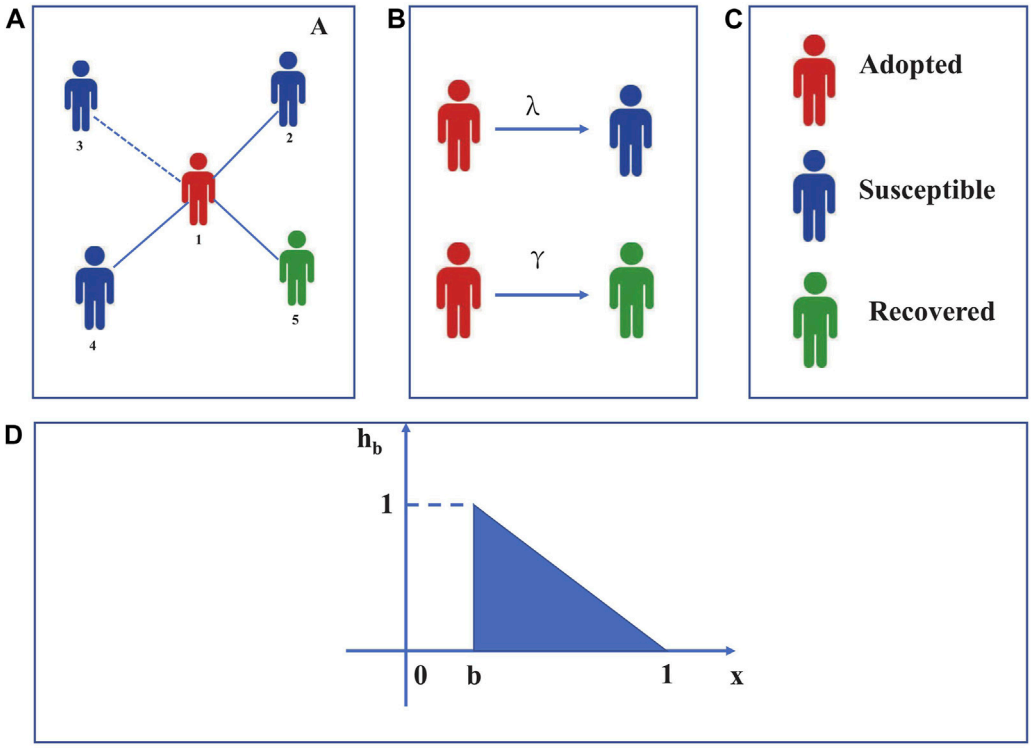

FIGURE 1
(A) Dissemination of information in a complex network comprising a single layer. Individual 1 has embraced the information, while individuals 2, 3, and 4 are still prone to it. Individual 5 has already regained information. Information was effectively disseminated through the blue dashed line, and node 1 that has received the information has conveyed it to its neighbors through this route. To represent the impact of limited contact, the paper sets the parameters of limited contact at 5 and 20. This means that each node can receive either 5 or 20 pieces of information from its neighbors. **(B)** Nodes that have embraced the information disseminate it to susceptible nodes with a likelihood of λ. When state nodes transition from adopted to recovered, the probability is represented by γ. **(C)** Each color represents a dissemination state—red for adopted nodes, blue for susceptible nodes, and green for recovered nodes. **(D)** Probability of neighbors adopting the opposite trend. Adoption probability is 0 when $0 < x < b$, but as soon as $b \leq x < 1$, individuals will adopt behavior with a probability of $\frac{1-x}{1-b}$.

the hole state. In this state, node i can merely receive information from its adopted neighbors. The probability of nodes not delivering information to their neighbors is determined as θ_{k_j}. We subsequently calculate the probability of node i being unable to accept messages from its neighbors at time t as

$$\theta(t) = \sum_{k_j=0}^{k_j\,\max} \frac{k_j p(k_j)}{< k >} \theta_{k_j(t)}. \tag{2}$$

At time t, the likelihood of the hole-state node receiving information from multiple neighbors can be represented by Eq. 3.

$$\Phi_m(k_i, t) = \binom{k_i}{m} \theta(t)^{k_i - m} [1 - \theta(t)]^m. \tag{3}$$

Although node i may receive information, it will not transition immediately to the adopted state upon gaining such information. The probability of node i remaining susceptible is defined as $\Pi_{l=0}^{m}[1 - h(\frac{l}{k}, b)]$. We accumulate the probability of the susceptible state at time t. The degree of node i is also defined as $k = k_i$. Node i is defined to be in one of three states: susceptible, adopted, or recovered. We accumulate the probability of the susceptible state at time t as Eq. 4.

$$\begin{aligned}\tau(k_i, t) &= \sum_{m=0}^{k_i} \Phi_m(k_i, t) \prod_{l=0}^{m} \left[1 - h\left(\frac{l}{k_i}, b\right)\right] \\ &= \sum_{m=0}^{\lfloor bk_i \rfloor} \Phi_m(k_i, t) + \sum_{m=\lceil bk_i \rceil}^{k_i} \Phi_m(k_i, t) \prod_{l=\lceil bk_i \rceil}^{m} \left(1 - \frac{1 - \frac{l}{k_i}}{1 - b}\right).\end{aligned} \tag{4}$$

In addition, the probability of all the susceptible nodes at time t can be represented by Eq. 5.

$$\begin{aligned}s(k_i, t) &= (1 - \rho_0) \sum_{m=0}^{k_i} \Phi_m(k_i, t) \prod_{l=0}^{m} \left[1 - h\left(\frac{l}{k_i}, b\right)\right]. \\ &= (1 - \rho_0)\tau(k_i, t)\end{aligned} \tag{5}$$

The probability of susceptible nodes maintaining their current status is represented by Eq. 6.

$$\eta = \sum_{k_i}^{k_i\,\max} p(k_i)\tau(k_i, t). \tag{6}$$

Until time t, the ratio of susceptible nodes in the single-layer network is observed to be as represented by Eq. 7.

$$S(t) = \sum_k p(k)s(k,t) = (1-\rho_0)\eta. \tag{7}$$

The probability of node j being in one of the three states and not acquiring any information from its neighboring nodes is represented by Eq. 8.

$$\theta_{k_j}(t) = \xi_{S,k_j}(t) + \xi_{A,k_j}(t) + \xi_{R,k_j}(t). \tag{8}$$

However, the probability of node j gaining information as of time t is represented by Eq. 9.

$$\Phi_m\left(k_j - 1, t\right) = \binom{k_j - 1}{m}\theta(t)^{k_j-1-m}\left[1-\theta_{k_j}(t)\right]^m. \tag{9}$$

Susceptible nodes will not transition to adopted state nodes until they receive a certain quantity of messages. Therefore, we define the probability of a node receiving n messages and remaining in the susceptible state as $\varsigma(k_j - 1, t)$. At time t, the probability of a node j with degree k_j remaining in the susceptible state is calculated.

$$\begin{aligned}\zeta_n\left(k_j-1,t\right) &= \sum_{n=0}^{k_j-1}\Phi_n\left(k_j-1,t\right)\prod_{l=0}^{n}\left[1-h\left(\frac{l}{k_j},b\right)\right]\\ &= \sum_{n=0}^{\lfloor bk_j\rfloor}\Phi_n\left(k_j,t\right) + \sum_{n=\lceil bk_j\rceil}^{k_j}\Phi_n\left(k_j,t\right)\prod_{l=\lceil bk_j\rceil}^{n}\left(1-\frac{1-\frac{l}{k_j}}{1-b}\right),\end{aligned} \tag{10}$$

where the likelihood of nodes connecting to neighbors via an edge is determined as $\frac{k_j p(k_j)}{<k_j>}$. At time t, the probability of susceptible nodes remaining in their current state as they have not received any information is

$$\xi_{S,k_j}(t) = (1-\rho_0)\zeta_n\left(k_j-1,t\right). \tag{11}$$

Since the impact is limited by contact, the probabilities of an adopted node j delivering information to its neighbors and transmitting through edges are determined as $\frac{f(k_j)}{k_j}$ and λ, respectively. Therefore, the probability of a node transmitting information to its neighboring nodes via edges is established as $\frac{\lambda f(kj)}{kj}$, and a function can be obtained as Eq. 12:

$$\frac{d\theta_{k_j}(t)}{dt} = -\frac{\lambda f\left(k_j\right)}{k_j}\xi_{A,k_j}. \tag{12}$$

Due to the adopted nodes being converted to a recovered state with a certain probability γ, it is possible to require the function about $\frac{d\xi_{R,k_j}(t)}{dt}$, which can be expressed as Eq. 13

$$\frac{d\xi_{R,k_j}(t)}{dt} = \gamma\xi_{A,k_j}(t)\left(1-\frac{\lambda f\left(k_j\right)}{k_j}\right). \tag{13}$$

By combining Eqs 10, 11, we can derive

$$\xi_{R,k_j}(t) = \gamma\left[1-\theta_{k_j}(t)\right]\left[\frac{k_j}{\lambda f\left(k_j\right)}-1\right]. \tag{14}$$

By applying Eqs 11, 14 along with Eq. 10, we derive the following result: $\xi_{A,k_j(t)}$. Regarding the initial conditions, information has not been transmitted yet. As a consequence, we can calculate the probability of susceptible nodes not receiving any messages using Eq. 15:

$$\theta_{k_j}(0) = 1. \tag{15}$$

At the same time, the network does not have any recovered nodes, providing us with the knowledge that

$$\xi_{R,k_j}(0) = 0. \tag{16}$$

Overwriting function

$$\begin{aligned}\frac{d\theta_{k_j}(t)}{dt} = &-\frac{\lambda f\left(k_j\right)}{k_j}\left[\theta_{k_j}(t) - \xi_{S,k_j}(t)\right] + \gamma\left[1-\theta_{k_j}(t)\right]\\ &\times\left(1-\frac{\lambda f\left(k_j\right)}{k_j}\right).\end{aligned} \tag{17}$$

When $t \to \infty$, on the basis of Eq. 20, we obtain

$$\theta_{k_j}(\infty) = \xi_{S,k_j}(\infty) + \gamma\left[1-\theta_{k_j}(\infty)\right]\left[\frac{k_j}{\lambda f\left(k_j\right)}-1\right]. \tag{18}$$

Substituting Eq. 18 into Eq. 2, we obtain Eq. 19

$$\theta(\infty) = \sum_{k_j=0}\frac{k_j p\left(k_j\right)}{<k>}\theta_{k_j}(\infty) = g(\theta(\infty)). \tag{19}$$

In order to simplify the process, we consider

$$\theta(\infty) = g(\theta(\infty)). \tag{20}$$

When Eq. 16 is in tangency with Eq. 17, it can be observed that a value abruptly changes into another value. The implication is that $R(\infty)$ increases discontinuously with λ. When $\theta(\infty) < 1$, the critical condition for information spreading can be obtained as Eq. 21:

$$\frac{\partial g(\theta(\infty))}{\partial\theta(\infty)} = 1. \tag{21}$$

4 Results and discussion

In this study, the network comprised a set number of total nodes of 2×10^4 and an average degree of 10. To demonstrate the parameter, experiments were conducted on both the random networks (ER) and scale-free networks (SF). The ER network adheres to a Poisson distribution $p(k) = e^{-<k>}\frac{<k>^k}{k!}$ for its node degree, unlike the SF network, which displays a power–law distribution with values of $p(k) = \zeta k^{-\nu}$ and $\zeta = 1/\sum_k k^{-\nu}$. It was observed that the heterogeneity of the node distribution was negatively correlated with the degree exponent ν. To comprehend the complete information transmission process, we establish γ as 1. The specific critical value is denoted by χ, as detailed in Eq. 22.

$$\chi = \frac{<\left(R(\infty) - <R(\infty)>\right)^2>}{<R(\infty)>^2}. \tag{22}$$

4.1 Analysis of opposite adoption against neighbors on the ER network

The limited contact that is heterogeneous in nature is observed to impact the ultimate range of propagation for both

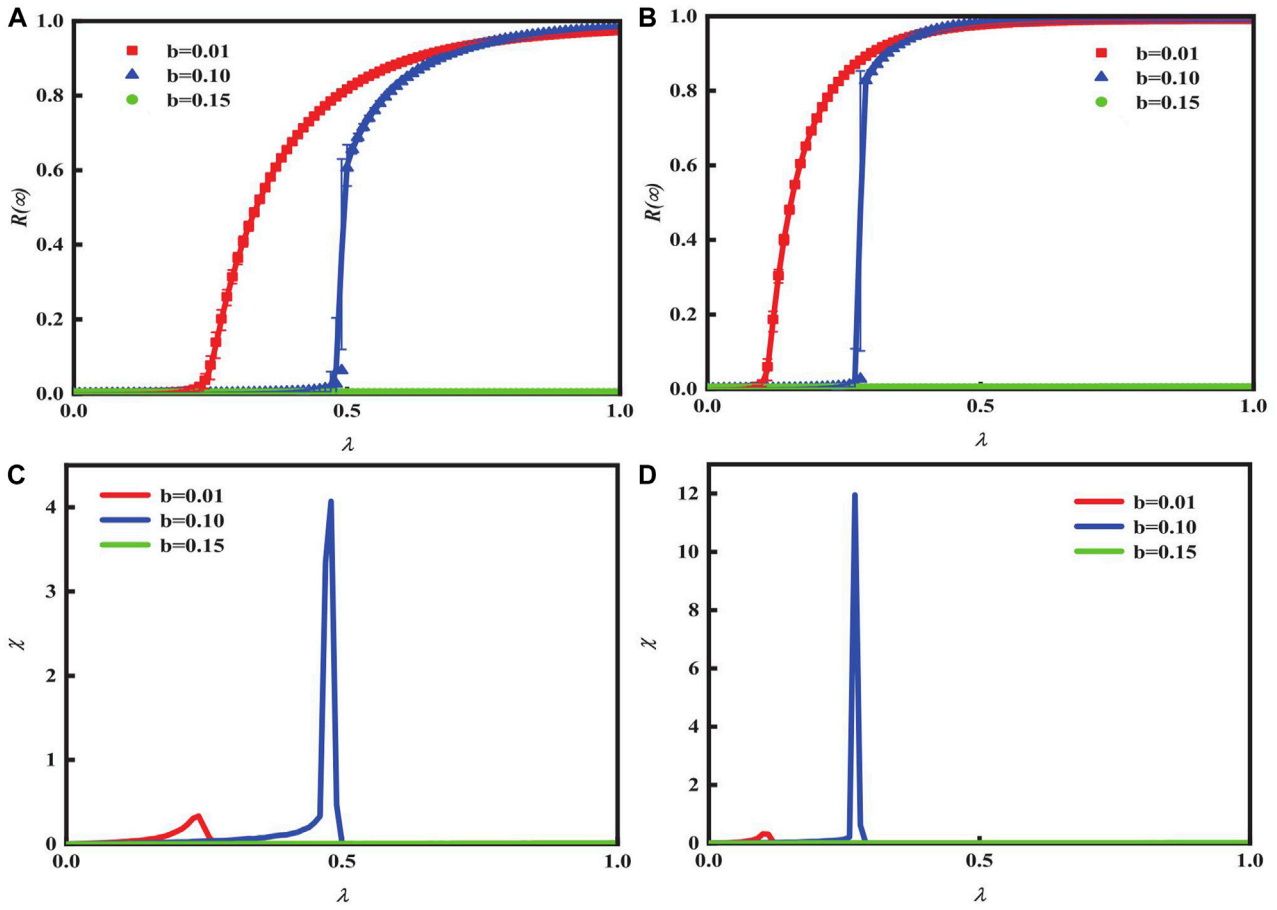

FIGURE 2
Impact of final spreading scope $R(\infty)$ on distinct opposite trend degree parameters b and heterogeneous limited contact with unit transmission rates λ in the ER network. Limited contact values of 5 and 20 are shown in **(A)** and **(B)** respectively. The ratio of initial infected nodes is also presented ρ_0 = 0.00125. Relative mistakes corresponding to **(A)** and **(B)** are depicted in **(C)** and **(D)** respectively.

Figures 2A, B. Additionally, variations in the mode of dissemination are uncovered. The data suggest that the increase in λ eventually leads to universal acceptance $R(\infty)$. If in a weak opposite trend condition $b = 0.01$, the growth mode of $R(\infty)$ continues in a second-order fashion. Notably, $R(\infty)$ remains unchanged, and information is not disseminated under strong opposite conditions $b = 0.15$. Under moderate opposite-trend conditions $b = 0.10$ with limited contact, the transition $R(\infty)$ is second-order and continuous. However, under strong limited contact, the transition $R(\infty)$ is first-order and discontinuous. A comparison of the figures reveals that stronger limited contact has a greater impact on the spread of the network than weaker contact.

Figures 2C, D indicate the ratio of critical dissemination of information, including relative errors. The highest point of relative errors χ, known as the critical point, demonstrates global adoption. The theoretical (lines) and simulated (symbols) results coincide.

The growth mode about $R(\infty)$ depends on λ and b (Figure 3). In region I, as λ increases, there is a second-order phase transition of $R(\infty)$ in continuous forms. In region II, there is a first-order phase transition in discontinuous forms. No information was reported for region III. The condition for the phase transition changes with varying degrees of parameter opposition. It is worth noting that the critical conditions for first- and second-order phase transitions correspond to the continuous and discontinuous growth of propagation, respectively. Additionally, the color temperature chart can elucidate the mechanisms of spreading and analyze the changes in spreading modes.

4.2 Analysis of opposite adoption against neighbors on the SF network

Figures 4A, B demonstrate the relationship between heterogeneous degree distribution and b influence on global adoption $R(\infty)$. With λ growing, $R(\infty)$ increase to globally adoption. The findings from Figures 4C, D indicate the ratio of critical dissemination of information, including relative errors. It becomes clear that heterogeneous degree distribution has no effect on the transmission mode of information. In the condition with an

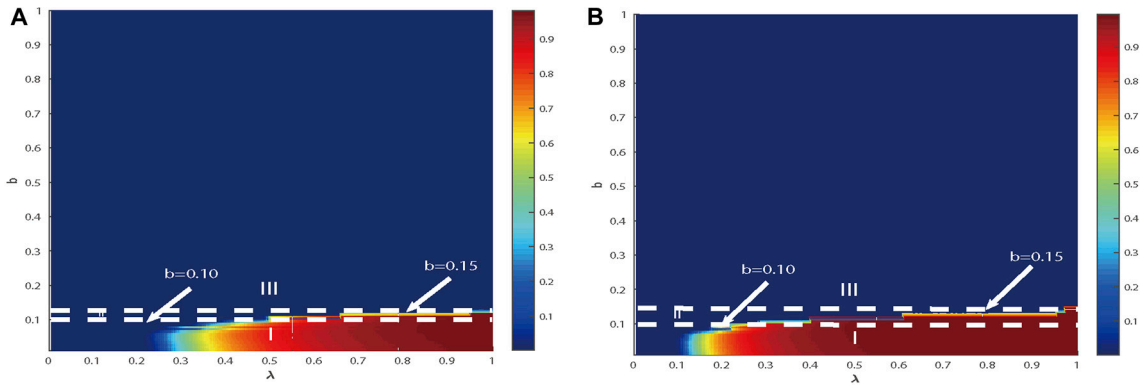

FIGURE 3
It can be inferred that there is a shared impact (λ, b) on $R(\infty)$ in the ER network. Limited contacts are observed at 5 in **(A)** and 20 in **(B)**, with the ratio of initial infected nodes being $\rho_0 = 0.00125$. In region I, the increase in $R(\infty)$ follows a second-order continuous pattern, which distinguishes it from region II, where it increases in a first-order discontinuous pattern. No information propagation is detected in region III.

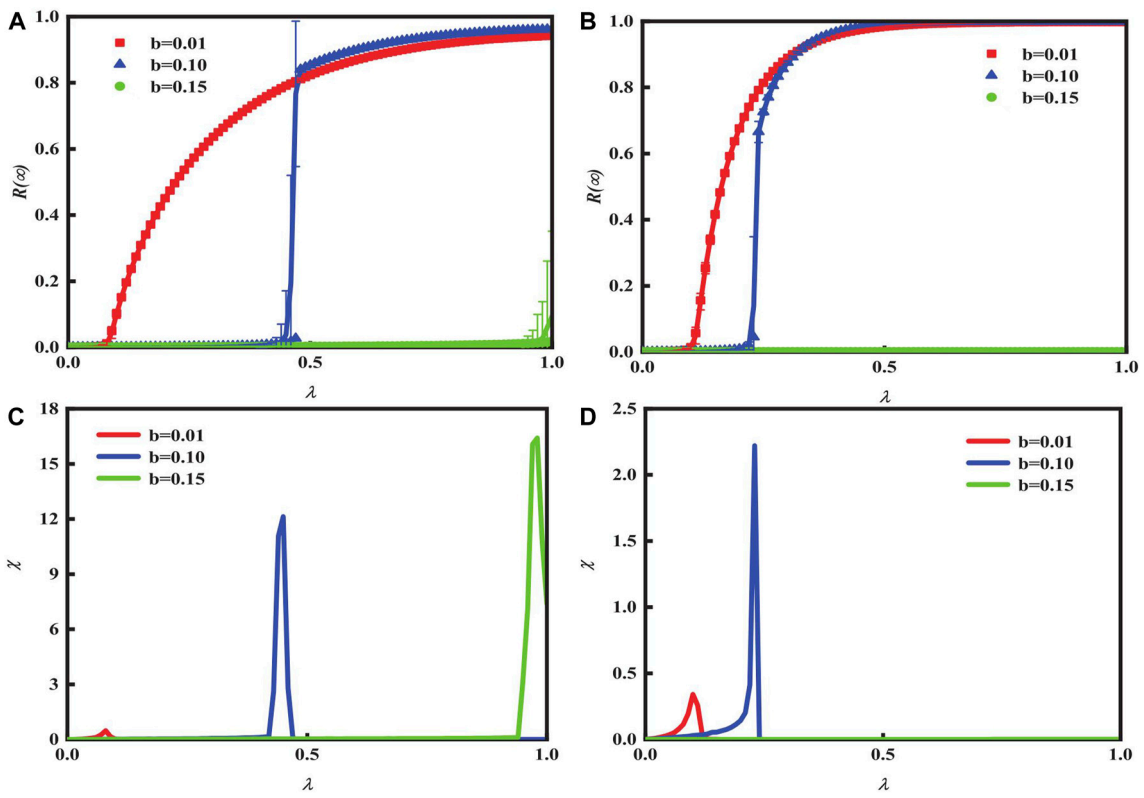

FIGURE 4
Impact b and heterogeneous limited contact on $R(\infty)$ with λ in the SF network. Limited contact is 20, while the heterogeneity of degree v is 2.1 in **(A)** and 4 in **(B)**. The impact of these factors on the phase transition in **(A)** and **(B)** is evidenced by b. And we set initial infected nodes $\rho_0 = 0.00125$. **(C)** and **(F)** represent relative discrepancies that correspond to **(A)** and **(B)**.

opposite middle $b = 0.10$, phase transitions vary. In a strong opposite situation $b = 0.15$, the growth pattern of $R(\infty)$ is first discontinuous. Conversely, in a weak condition $b = 0.01$, the increment mode about $R(\infty)$ is continuously second. The maximum value of relative error can indicate an explosion in information propagation at a certain point. Studying the amplitude of relative error can reflect the scale and pattern of propagation bursts during propagation.

In Figure 5, the combination effect of (λ, b) on the variable $R(\infty)$ is depicted. In region I, as λ increases, the pattern of $R(\infty)$

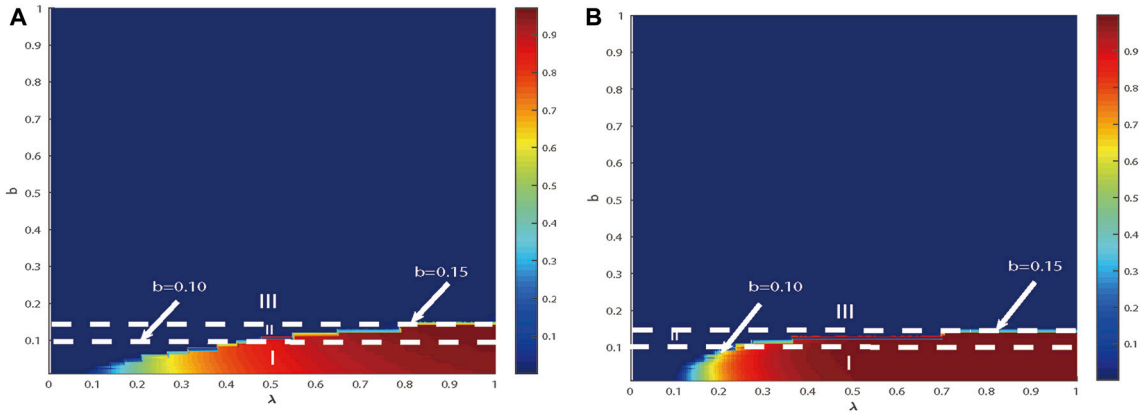

FIGURE 5
It can be inferred that there is a shared impact (λ, b) on $R(\infty)$ in the SF network. It demonstrates that in the scale-free network, there is a common influence about (λ, b) on $R(\infty)$ across different heterogeneity parameters, i.e., 2.1 in **(A)** and 4 in **(B)**, with same limited contact at 20. The ratio of initial infected nodes is specified $\rho_0 = 0.00125$. In region I, the increase in $R(\infty)$ follows a second-order continuous pattern, differing from region II, where the increase follows a first-order discontinuous pattern. No information spreading occurs in region III.

represents a second continuous phase transition. In region II, the mode of increments $R(\infty)$ represents a first discontinuous phase transition. In region III, there is no explosion of information. Regardless of the scenario shown in Figure 3 or Figure 5, a cross-phase transition occurs at the junction of a discontinuous (in region II) or continuous (in region I) phase transition.

5 Conclusion

In this paper, we analyze the mechanism of information spreading in relation to the adoption of opposing views within neighboring communities. We investigate the impact of opposite trend adoption among neighbors in a single-layer network and find that this behavior influences information dissemination to varying degrees. Meanwhile, we propose an adoption threshold function that takes the form of a right triangle with limited contacts.

The results demonstrate that under a strong opposite trend condition ($b = 0.15$), information will not be disseminated. Moreover, limited contact promotes the dissemination process, and with the increase in $R(\infty)$, the dissemination scope is second-order continuous under a weak condition ($b = 0.01$). Interestingly, there is a cross-phase transition in the results of the opposite trend condition in the middle ($b = 0.10$). The growth mode about $R(\infty)$ in the ER network shifts from continuous second-order to discontinuous first-order, whereas in the SF network, it transits quite contrarily. These results reveal the significant importance of opposite-trend adoption.

In future research, researchers could investigate the prevalence of counter-trend adoption in new settings. For instance, investigators can study counter-trend adoption in multi-layer networks and even discover information heterogeneity among individuals.

Data availability statement

The original contributions presented in the study are included in the article/Supplementary Material; further inquiries can be directed to the corresponding author.

Author contributions

JH: Conceptualization, methodology, software, writing–original draft, writing–review and editing. JM: Conceptualization, methodology, software and writing-review and editing. SL: Validation, writing–review and editing. YT: Validation, writing–review and editing.

Funding

The author(s) declare that no financial support was received for the research, authorship, and/or publication of this article.

Conflict of interest

The authors declare that the research was conducted in the absence of any commercial or financial relationships that could be construed as a potential conflict of interest.

Publisher's note

All claims expressed in this article are solely those of the authors and do not necessarily represent those of their affiliated organizations, or those of the publisher, the editors, and the reviewers. Any product that may be evaluated in this article, or claim that may be made by its manufacturer, is not guaranteed or endorsed by the publisher.

References

1. Ji P, Ye J, Mu Y, Lin W, Tian Y, Hens C, et al. Signal propagation in complex networks. *Phys Rep* (2023) 1017:1–96. doi:10.1016/j.physrep.2023.03.005

2. Wang H, Ma C, Chen H-S, Zhang H-F. Effects of asymptomatic infection and self-initiated awareness on the coupled disease-awareness dynamics in multiplex networks. *Appl Math Comput* (2021) 400:126084. doi:10.1016/j.amc.2021.126084

3. Chen X, Gong K, Wang R, Cai S, Wang W. Effects of heterogeneous self-protection awareness on resource-epidemic coevolution dynamics. *Appl Math Comput* (2020) 385: 125428. doi:10.1016/j.amc.2020.125428

4. Ni Q, Guo J, Wu W, Wang H, Wu J. Continuous influence-based community partition for social networks. *IEEE Trans Netw Sci Eng* (2021) 9:1187–97. doi:10.1109/tnse.2021.3137353

5. Liu S, Yu J, Deng X, Wan S. Fedcpf: an efficient-communication federated learning approach for vehicular edge computing in 6g communication networks. *IEEE Trans Intell Transportation Syst* (2021) 23:1616–29. doi:10.1109/tits.2021.3099368

6. Hu Y, Xiong F, Pan S, Xiong X, Wang L, Chen H. Bayesian personalized ranking based on multiple-layer neighborhoods. *Inf Sci* (2021) 542:156–76. doi:10.1016/j.ins.2020.06.067

7. Zhong C, Xiong F, Pan S, Wang L, Xiong X. Hierarchical attention neural network for information cascade prediction. *Inf Sci* (2023) 622:1109–27. doi:10.1016/j.ins.2022.11.163

8. Ni X, Xiong F, Pan S, Wu J, Wang L, Chen H. Community preserving social recommendation with cyclic transfer learning. *ACM Trans Inf Syst* (2023) 42:1–36. doi:10.1145/3631115

9. Zhu H, Xiong F, Chen H, Xiong X, Wang L. Incorporating a triple graph neural network with multiple implicit feedback for social recommendation. *ACM Trans Web* (2024) 18:1–26. doi:10.1145/3580517

10. Ren Z-M, Zeng A, Zhang Y-C. Structure-oriented prediction in complex networks. *Phys Rep* (2018) 750:1–51. doi:10.1016/j.physrep.2018.05.002

11. Yin H, Wang Q, Zheng K, Li Z, Yang J, Zhou X. Social influence-based group representation learning for group recommendation. In: 2019 IEEE 35th International Conference on Data Engineering (ICDE). IEEE (2019). p. 566–77.

12. Zheng M, Lü L, Zhao M. Spreading in online social networks: the role of social reinforcement. *Phys Rev E* (2013) 88:012818. doi:10.1103/physreve.88.012818

13. Wang W, Liu Q-H, Cai S-M, Tang M, Braunstein LA, Stanley HE. Suppressing disease spreading by using information diffusion on multiplex networks. *Scientific Rep* (2016) 6:29259. doi:10.1038/srep29259

14. Wang W, Liu Q-H, Liang J, Hu Y, Zhou T. Coevolution spreading in complex networks. *Phys Rep* (2019) 820:1–51. doi:10.1016/j.physrep.2019.07.001

15. Juul JS, Porter MA. Hipsters on networks: how a minority group of individuals can lead to an antiestablishment majority. *Phys Rev E* (2019) 99:022313. doi:10.1103/physreve.99.022313

16. Tian Y, Tian H, Cui Y, Zhu X, Cui Q. Influence of behavioral adoption preference based on heterogeneous population on multiple weighted networks. *Appl Math Comput* (2023) 446:127880. doi:10.1016/j.amc.2023.127880

17. Yang M, Wu C, Xie T. Information propagation dynamics model based on implicit cluster structure network. In: 2020 IEEE 5th Information Technology and Mechatronics Engineering Conference (ITOEC). IEEE (2020). p. 1253–7.

18. Ren Y, Li L. Sar dynamical mechanism affected by diminishing marginal effect based on personal fashion psychology on multi-layer contacted network. *Physica Scripta* (2024) 99:035252. doi:10.1088/1402-4896/ad295f

19. Kobayashi T. Trend-driven information cascades on random networks. *Phys Rev E* (2015) 92:062823. doi:10.1103/physreve.92.062823

20. Juul JS, Porter MA. Synergistic effects in threshold models on networks. *Chaos: Interdiscip J Nonlinear Sci* (2018) 28:013115. doi:10.1063/1.5017962

21. Tian Z, Zhang G, Yu H, Liu H, Lu D. Negemotion: explore the double-edged sword effect of negative emotion on crowd evacuation. *IEEE Trans Comput Soc Syst* (2024) 1–14. doi:10.1109/tcss.2023.3344172

22. Huo S, Yu Y. The impact of the self-recognition ability and physical quality on coupled negative information-behavior-epidemic dynamics in multiplex networks. *Chaos, Solitons and Fractals* (2023) 169:113229. doi:10.1016/j.chaos.2023.113229

23. Leng H, Zhao Y, Wang D. Message passing approach for social contagions based on the trust probability with multiple influence factors. *Physica A: Stat Mech its Appl* (2022) 587:126510. doi:10.1016/j.physa.2021.126510

24. Cui Y, Wei R, Tian Y, Tian H, Zhu X. Information propagation influenced by individual fashion-passion trend on multi-layer weighted network. *Chaos, Solitons and Fractals* (2022) 160:112200. doi:10.1016/j.chaos.2022.112200

25. Ruan Z, Zhang L, Shu X, Xuan Q. Social contagion with negative feedbacks. *Physica A: Stat Mech its Appl* (2022) 608:128304. doi:10.1016/j.physa.2022.128304

26. Salling MC, Martinez D. Brain stimulation in addiction. *Neuropsychopharmacology* (2016) 41:2798–809. doi:10.1038/npp.2016.80

27. Chen X, Wang N. Rumor spreading model considering rumor credibility, correlation and crowd classification based on personality. *Scientific Rep* (2020) 10: 5887. doi:10.1038/s41598-020-62585-9

28. Ye J, Chen Y. Social contagion influenced by active-passive psychology of college students. *Front Phys* (2022) 10:1019118. doi:10.3389/fphy.2022.1019118

29. Zhu Y-X, Cao Y-Y, Chen T, Qiu X-Y, Wang W, Hou R. Crossover phenomena in growth pattern of social contagions with restricted contact. *Chaos, Solitons and Fractals* (2018) 114:408–14. doi:10.1016/j.chaos.2018.06.010

30. Du J, Zhao D, Issa RR, Singh N. Bim for improved project communication networks: empirical evidence from email logs. *J Comput Civil Eng* (2020) 34:04020027. doi:10.1061/(asce)cp.1943-5487.0000912

31. Yang D, Xian J, Pan L, Wang W, Zhou T. Effective edge-based approach for promoting the spreading of information. *IEEE Access* (2020) 8:83745–53. doi:10.1109/access.2020.2992058

32. Lv C, Yuan Z, Si S, Duan D, Yao S. Cascading failure in networks with dynamical behavior against multi-node removal. *Chaos, Solitons and Fractals* (2022) 160:112270. doi:10.1016/j.chaos.2022.112270

33. Huo S, Chen S. Rumor propagation model with consideration of scientific knowledge level and social reinforcement in heterogeneous network. *Physica A: Stat Mech Its Appl* (2020) 559:125063. doi:10.1016/j.physa.2020.125063

34. Li W, Li J, Nie Y, Lin T, Chen Y, Liu X, et al. Infectious disease spreading modeling and containing strategy in heterogeneous population. *Chaos, Solitons and Fractals* (2024) 181:114590. doi:10.1016/j.chaos.2024.114590

frontiers | Frontiers in Physics

TYPE Original Research
PUBLISHED 14 June 2024
DOI 10.3389/fphy.2024.1404464

OPEN ACCESS

EDITED BY
Chengyi Xia,
Tiangong University, China

REVIEWED BY
Shimin Cai,
University of Electronic Science and Technology of China, China
Hai-Feng Zhang,
Anhui University, China
Xiaoyang Liu,
Chongqing University of Technology, China

*CORRESPONDENCE
Xuzhen Zhu,
zhuxuzhen@bupt.edu.cn

RECEIVED 21 March 2024
ACCEPTED 16 May 2024
PUBLISHED 14 June 2024

CITATION
Cui S and Zhu X (2024), The information propagation mechanism of individual heterogeneous adoption behavior under the heterogeneous network.
Front. Phys. 12:1404464.
doi: 10.3389/fphy.2024.1404464

The information propagation mechanism of individual heterogeneous adoption behavior under the heterogeneous network

Shiru Cui and Xuzhen Zhu*

State Key Laboratory of Networking and Switching Technology, Beijing University of Posts and Telecommunications, Beijing, China

To explore heterogeneous behavior diffusion in the same population under a heterogeneous network, this study establishes a dual-layer heterogeneous network model to simulate the spreading patterns of hesitant individuals and regular individuals in different networks. It analyzes the influence of to investigate heterogeneous behavior diffusion within the same population in a heterogeneous network, this paper establishes a dual-layer heterogeneous network model to simulate the spreading patterns of hesitant individuals and regular individuals in different networks. It analyzes the influence of individuals' hesitation states and different spreading patterns in heterogeneous networks on the information diffusion mechanism. In the propagation of this model, when either layer of the dual-layer network becomes the dominant spreading layer, second-order continuous spreading is observed. However, when the regular adoption behavior serves as the dominant spreading layer, its spreading threshold occurs earlier than the spreading threshold when hesitant adoption behavior is the dominant spreading layer. When there is no dominant spreading layer, first-order discontinuous spreading is observed, and the spreading threshold occurs later than the threshold in the presence of a dominant spreading layer. Additionally, the study discovers the existence of cross-phase transitions during the spreading process. The results of theoretical analysis align with the simulation results.

KEYWORDS

complex network, nonlinear dynamics, behavioral propagation, heterogeneous network layer, heterogeneous adoption functions

1 Introduction

In the field of network science, the study of social communication has garnered widespread attention among researchers [1, 2]. It can be applied to analyze financial behaviors [3, 4], social information diffusion [5], and emotional contagion [6]. Furthermore, it can be utilized for disaster prediction [7] and risk mitigation [8]. Scholars have explored the mechanisms of social communication through both theoretical analysis and extensive experimental validation. Research has revealed that social communication exhibits certain unique reinforcement effects compared to biological propagation [9, 10].

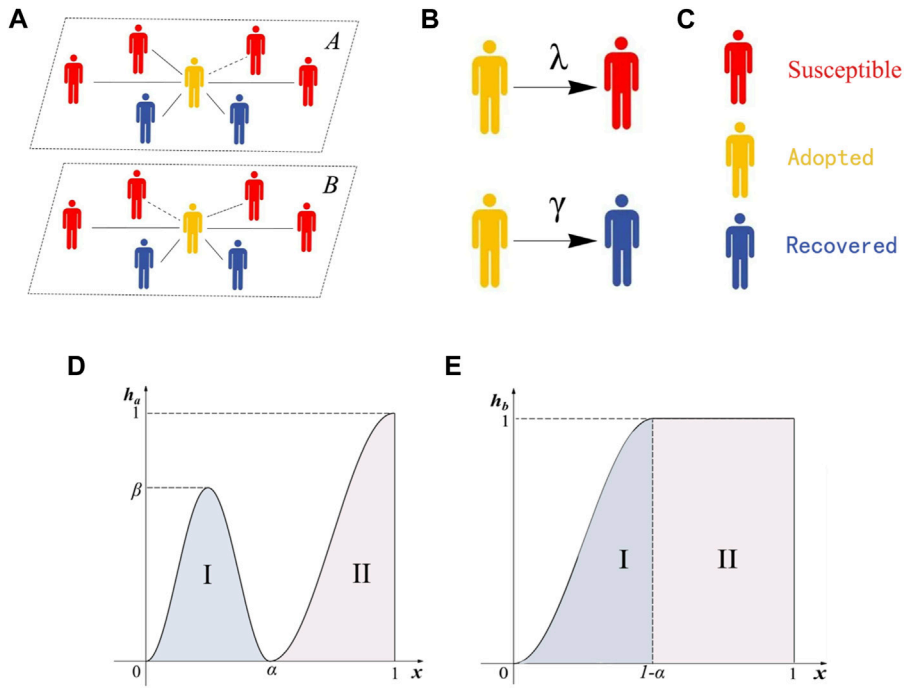

FIGURE 1
(A) shows the connections between individuals and the information dissemination of individuals in a two-layer heterogeneous network. **(B)** The probability of an adoptive individual transferring information to a susceptible individual is λ. The probability of an adoptive individual changing into a recovered individual is γ. **(C)** shows different colors represent different individual states. **(D)** shows the individual adoption behavior function image of an individual at layer *A*, and **(E)** shows the individual adoption behavior function image of an individual at layer *B*.

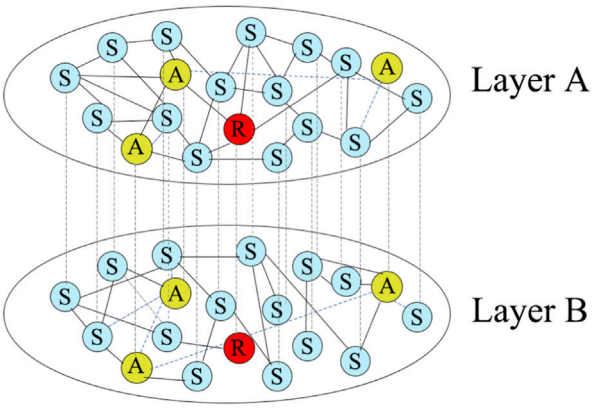

FIGURE 2
Figure illustrates the intricate connections within a complex network comprising multiple nodes. The states of the nodes and their relationships are essentially identical to those described in Figure 1. Layer *A* and Layer *B* represent the social context of the same node within two distinct social communication networks. While the node maintains the same status across different social networks, its connectivity varies. Within each layer, solid lines denote connected nodes that do not propagate information, while dashed lines indicate the transmission of information between two nodes connected by an edge.

In the early stages of research, the most commonly used approach was the threshold model based on memoryless Markov processes [11]. In this threshold model, a behavior is adopted when the number of adopting neighbors exceeds a predetermined threshold [12, 13]. Given the small proportion of initial seeds, the initial infection rate is predicted using percolation principles [14, 15]. Based on the assumption of constant thresholds, because of variations in the average degree, saddle-node bifurcation occurs, leading to a continuous increase and subsequent discontinuous decrease in the final adoption size with increasing network average degree. Research has found that factors such as the initial number of seeds [16, 17], clustering coefficient [18], multilayer networks [19], network temporal dynamics [20] and time-varying [21] significantly affect information propagation in the threshold model.

In the field of complex networks, numerous scholars have conducted extensive research on propagation behaviors in single-layer networks. However, studies have shown that multilayer networks better represent real-world social networks. In the context of bio-information networks [22], individuals can access various information in the information network to execute different strategies in the biological network [23]. For example, during the COVID-19 pandemic, people could obtain preventive measures through the internet, leading to improved habits and reduced chances of contracting the virus in the biological network. In the case of multilayer information networks, individuals often do not rely on a single channel to interact with the external world. Each person has multiple social channels, such as WeChat, Twitter, Instagram, and more. Thus, in a multilayer network, information does not propagate solely within a single layer but rather disseminates through multiple coupled networks. However, individual information acquisition remains singular [24]. For instance, on the YouTube platform, users can upload and share video content, and other users can subscribe to their channels. This

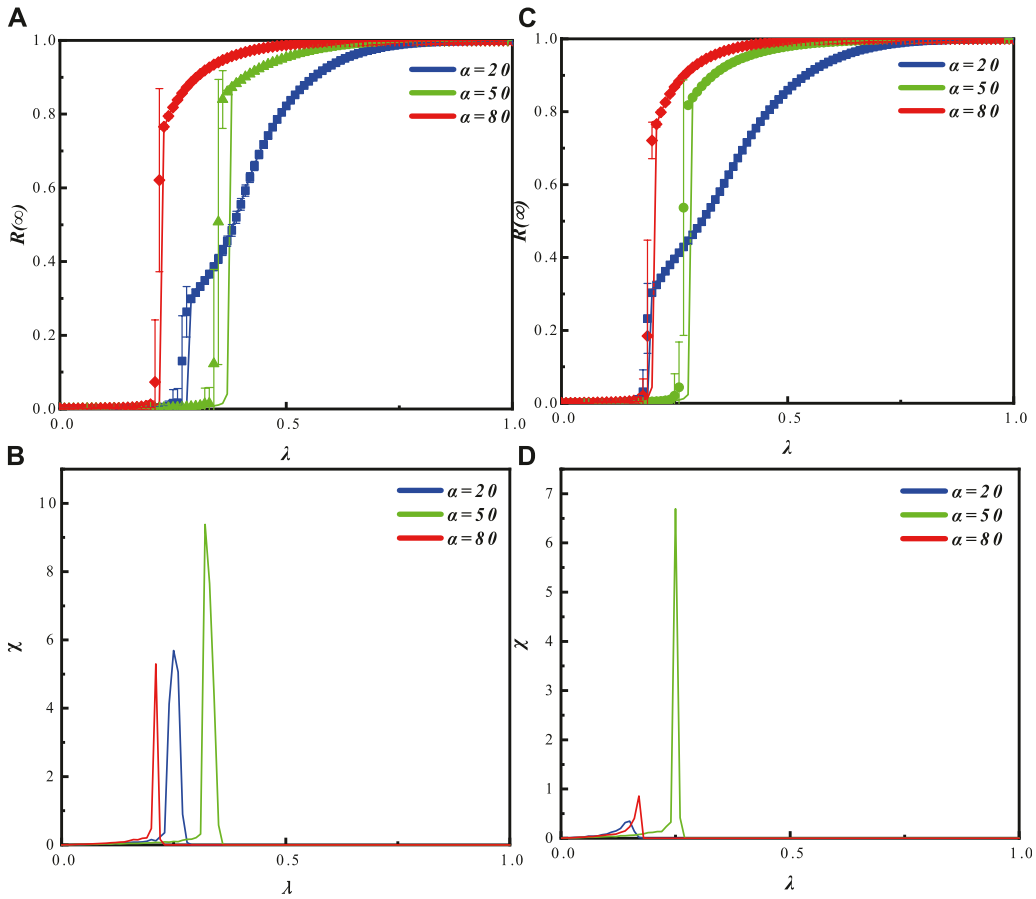

FIGURE 3
The graph illustrates the impact of the hesitation degree parameter α and the propagation probability λ on the information outbreak size R (∞), the final adoption range, and the relative variance in an ER-ER network, with a fixed hesitation amplitude parameter β. In graph **(A)** (β = 0.5) and graph **(C)** (β = 0.8), the influence of α on the information outbreak size is shown as the propagation probability varies. The symbols represent simulation results, while the lines depict theoretical predictions. Different values of α correspond to different propagation patterns of information. In graph **(B)** (β = 0.5) and graph **(D)** (β = 0.8), the peak distribution of the relative variance of the adoption range is shown as the propagation probability varies for different α values. The peaks correspond to the outbreak points in graph **(A)** and graph **(C)**, respectively. The remaining parameters are set as ρ_0 and γ = 1.

forms a user-user connectivity network. Each video can be viewed, commented on, and shared by other users, creating a video-user connectivity network. When a user uploads a video, their subscribers can see it in their subscription feed. If these subscribers find the video appealing or valuable, they can choose to share it with their own audience. Consequently, the video spreads through user-to-user sharing in the network. In this example, the social network among users and the video-user connectivity network constitute a multilayer network. Video content propagates through sharing and viewing behaviors among users, and this multilayer network structure can influence the dissemination path, view counts, and impact of videos. In conclusion, multilayer networks better capture the essence of real-world networks, allowing us to simulate human behavior in real-life situations.

With the diversification of information channels and the complexity of information forms, people are living in an era of fragmented information, and the adoption patterns of information have gradually become differentiated and heterogeneous. This is especially true for differentiating information sources. For information channels with low trustworthiness, people may encounter a mix of correct and incorrect information, leading to skepticism towards the information from these channels. Conversely, for information channels with high trustworthiness, such as those associated with authoritative sources or long-standing trust, people are more likely to trust and adopt information from these channels [25]. Therefore, the two-layer network model [26] takes into account the more complex information transmission, which has significant practical implications. Previous research has not extensively addressed heterogeneous threshold functions. While some studies have explored two-layer networks, they often assume the same threshold function for both layers. However, in real life, due to the heterogeneity between layers, people have different levels of trust and acceptance for information from different sources. Consequently, people behave differently after acquiring information from different platforms. Therefore, adopting heterogeneous functions for different channels better reflects reality. In this study, a heterogeneous threshold function is employed in the two-layer model to capture this phenomenon.

Existing research has shown that individuals exhibit different adoption attitudes towards the same information on different network layers, and their attitudes may change as the amount of information they receive fluctuates [27]. However, there is relatively limited research on considering heterogeneous adoption in

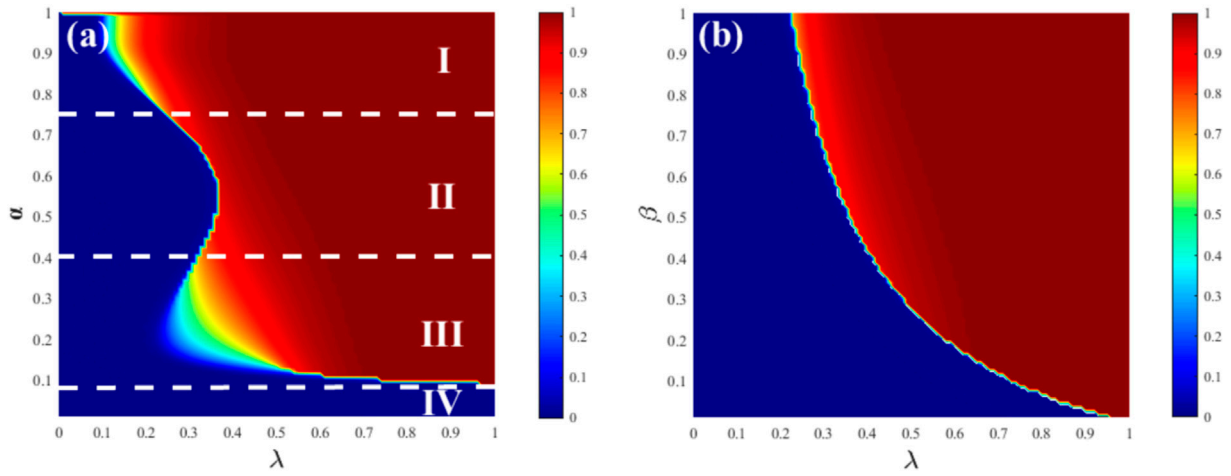

FIGURE 4
Graph **(A)** represents the relationship between the information outbreak size and the hesitation degree parameter α and propagation probability λ in an ER-ER network, with a fixed hesitation amplitude parameter $\beta = 0.5$. Graph **(B)** represents the relationship between the information outbreak size and the hesitation amplitude parameter β and propagation probability λ in an ER-ER network, with a fixed hesitation degree parameter $\alpha = 0.5$. The remaining parameters are set as ρ_0 and $\gamma = 1$.

information propagation within complex networks. In real social networks, individuals vary in their level of adoption across different layers of information. Based on the adoption attitudes towards information on different layers, this study categorizes heterogeneous adoption in social networks into two types: regular adoption and hesitant adoption. Regular adoption refers to a linear increase in the willingness to adopt with the number of received information or behaviors. Hesitant adoption, on the other hand, involves a state of hesitation regarding whether to adopt, requiring repeated verification of information and accumulating more information before developing the willingness to adopt. For instance, when a popular piece of information appears on the internet, an individual is more likely to increase their trust and adopt it on reliable information platforms, leading to a rapid saturation of adoption on such platforms. However, when the same individual encounters this information on an untrustworthy platform, they may exhibit a hesitant adoption stance, repeatedly verifying the information before deciding to adopt. As a result, the propagation speed on such platforms is slower, and it takes some time for the adoption to reach a relative saturation point. Therefore, studying the behavioral division of inter-layer adoption heterogeneity will contribute to a deeper understanding of the propagation mechanisms in multi-layer social networks.

The paper proposes a heterogeneous threshold adoption function on a two-layer model and constructs a heterogeneous adoption behavior network model for the same information on the two layers. It investigates the heterogeneous information propagation in a heterogeneous network of the same population. Through extensive simulation and theoretical analysis, the study reveals that when either layer dominates, the final outbreak of the adoption range manifests a second-order continuous phase transition. In contrast, when there is no clear dominant layer, the outbreak follows a first-order discontinuous phase transition. The timing and extent of the outbreak are influenced by various factors such as hesitant adoption parameter, degree heterogeneity parameter, and propagation probability. In the steady state, the final propagation range reaches global dissemination.

2 Model introduction

2.1 SAR model and information adoption mechanism

To investigate heterogeneous adoption behavior in a heterogeneous network within the same population, this study utilizes the SF network model and ER network model as the physical network structure models for the experiments. In each layer, a bipartite network model with N nodes and a degree distribution of $P(k)$ is constructed. The layers A and B stand for two different social networks, while the edges between nodes stand for their social connections. To explain heterogeneous behavior propagation on the multilayer network, a generalized Susceptible-Adopter-Recovered (SAR) model is used. At any given time, each node can only be in one of the following three states: susceptible (S), adopter (A), or recovered (R). S-state nodes can only obtain behavioral information from their neighboring nodes and adopt that information with a certain probability. A-state nodes have already adopted the behavior and are willing to propagate the behavioral information to their neighbors. R-state nodes are not interested in the behavioral information and do not propagate it to other neighbors.

The variables m_A and m_B are used to accumulate the information received by nodes in layers A and B, respectively. At each time step, when a node successfully gets information from neighbors in layer A or layer B, the corresponding variable m_i^A or m_i^B will be incremented by 1. The adoption probability functions for layer A and layer B are denoted by $h_a(x, \alpha, \beta)$ and $h_b(x, \alpha)$, respectively. During the propagation process, S-state node i adopts information from layer A and layer B with adoption probabilities $h_a(x, \alpha, \beta)$ and $h_b(x, \alpha)$, respectively, converting to the A-state. The states of nodes in the bipartite network are synchronized, meaning that any node in the A-layer and B-layer has the same state. Once the state of a node changes in one layer, it will correspondingly change in the other layer as well.

Figure 2 more intuitively illustrates the relationship between Layers A and B as discussed earlier. Arrows and directional cues emphasize the flow of information or influence from Layer A to

Layer B, indicating the dynamic relationship between them. This illustration aims to enhance understanding by providing a visual aid that complements the textual description, helping to grasp the complex interactions between the layers more visually.

2.2 Heterogeneous adoption functions

For layer A, Eq. 1 is as follows:

$$h_a(x,\alpha,\beta) = \begin{cases} \beta\left(-0.5\cos\dfrac{2\pi x}{\alpha} + 0.5\right), 0 \le x < \alpha \\ -0.5\cos\left(\dfrac{\pi(x-\alpha)}{1-\alpha}\right) + 0.5, \alpha \le x < 1 \end{cases} \tag{1}$$

When $0 \le x < \alpha$ (Region I in Figure 1D), the adoption probability initially increases non-linearly to its maximum value β and then decreases to 0. When $\alpha \le x < 1$ (Region II in Figure 1D), the adoption probability increases non-linearly with x from 0 to 1:

For layer B, Eq. 2 is as follows:

$$h_b(x,\alpha) = \begin{cases} -0.5\cos\left(\dfrac{\pi x}{1-\alpha}\right) + 0.5, 0 \le x < 1-\alpha \\ 1, 1-\alpha \le x < 1 \end{cases} \tag{2}$$

When $0 \le x < 1-\alpha$, as Region I in Figure 1E, the adoption probability increases with the increase of x until it reaches 1. On the other hand, when $1-\alpha \le x < 1$, as Region II in Figure 1E, the adoption probability remains constant at 1. When $x < 1-\alpha$, the increase in x enhances the individual's adoption capability, while when $x < 1-\alpha$, the adoption capability remains stable.

2.3 Propagation process and methods

- The network consists of N individuals, with a portion initially in state A and the remaining in state S, without any behavioral information ($m_X = 0$). The quantity ρ_0 stands for the initial ratio of individuals in state A, defined as the proprtion of the number of individuals in state A to the total number of individuals in the network.
- The probability of an individual in state S receiving behavioral information from an individual in state A is λ. When an individual receives behavioral information from another individual in state A, the information count m of that individual increases by 1. Due to the non-redundancy of information, an individual cannot receive the same neighbor's information repeatedly.
- In layers A and B, individuals in state S adopt behavioral information with probabilities N and M, respectively. If adopted, the individual transitions to state A; otherwise, it remains in state S. Additionally, whenever the state of a node changes in one layer, the state of the other layer also changes accordingly.
- When an individual in state A transmits behavioral information to neighboring individuals, there is a possibility of transitioning to state R with probability γ, ceasing to take part in the subsequent propagation process.
- Repeat the process from Step 2 to Step 4 until the state of individual nodes in the network remains unchanged, with only nodes in states S and R. At this moment, the propagation reaches a steady state, and the behavioral information stops spreading.

3 Formula derivation

Based on Ref. [28], this study employs an edge-based compartmental (EBC) method for theoretical analysis of the model. By analyzing the variation in the number of individuals in different states in a multilayer network, the study provides a theoretical evaluation of the propagation mechanism in a heterogeneous adoption behavior network for the same information in a dual-layer setting.

Inspired by the "Hole Theory" [29], it shows that individual i is in a "hole" state, meaning it cannot transmit information to its neighbors but can receive information from them. Let $\theta^X_{k_j^X}(t)\,(X \in \{A,B\})$ represent the probability that an individual with degree k_j has not transmitted information to i until time t. Then, in different layers, the probability that individual i has not received any information until time t can be expressed as Eqs 3, 4:

$$\theta_A(t) = \sum_{k_j^A=0} \frac{k_j^A P\left(k_j^A\right)}{\langle k^A\rangle} \theta^A_{k_j^A}(t) \tag{3}$$

and

$$\theta_B(t) = \sum_{k_j^B=0} \frac{k_j^B P\left(k_j^B\right)}{\langle k^B\rangle} \theta^B_{k_j^B}(t) \tag{4}$$

Based on the assumption that $\frac{k_j^X P(k_j^X)}{\langle k^X\rangle}\,(X \in \{A,B\})$ represents the probability of node j being connected to node i in layer X, it can be derived that the probability that node i accumulates m_X non-redundant information in layer X at time t as Eq. 5:

$$\phi^X_{m_X}\left(k_i^X, m_X, t\right) = \binom{k_i^X}{m_X} \theta_X(t)^{k_i^X - m_X} \left[1-\theta_X(t)\right]^{m_X} \tag{5}$$

Therefore, the probability that node i does not adopt any behavior in layer A and remains in state S is $\prod_{l=0}^{m_A}\left[1-h_a(x,\alpha,\beta)\right]$, and the probability that node i does not adopt any behavior in layer B and remains in state S is $\prod_{l=0}^{m_B}\left[1-h_b(x,\alpha)\right]$. It can be then calculated that the probability that node i remains in state S after receiving m_X non-redundant information in both layer A and layer B until time t as Eqs 6, 7:

$$\begin{aligned} \tau_A\left(k_i^A, m_A, t, \alpha, \beta\right) &= \sum_{r=0}^{m} \phi^A_{m_A}\left(k_i^A, t\right) \prod_{l=0}^{r}\left[1 - h_a\left(\frac{k_i^A}{l}, \alpha, \beta\right)\right] \\ &= \sum_{r=0}^{\alpha k_i^A} \phi^A_{m_A}\left(k_i^A, t\right) \\ &\quad \times \prod_{l=0}^{r}\left(1 - \beta\left(-0.5\cos\frac{2\pi k_i^A}{\alpha l} + 0.5\right)\right) \\ &\quad + \sum_{n=\alpha k_i^A}^{m} \phi^A_{m_A}\left(k_i^A, t\right) \\ &\quad \times \prod_{l=0}^{\alpha k_i}\left(1 - \beta\left(-0.5\cos\frac{2\pi k_i^A}{\alpha l} + 0.5\right)\right) \\ &\quad \times \prod_{l=\alpha k_i^A}^{n}\left(1 - \left(-0.5\cos\left(\frac{\pi(x-\alpha)}{1-\alpha}\right)\right) + 0.5\right) \end{aligned} \tag{6}$$

$$\tau_B\left(k_i^B, m_B, t, \alpha, \beta\right) = \sum_{r=0}^{m} \phi_{m_B}^B\left(k_i^B, t\right)\Big) \prod_{l=0}^{r}\left[1 - h_b\left(\frac{k_i^B}{l}, \alpha\right)\right]$$
$$= \sum_{r=0}^{(1-\alpha)k_i^B} \phi_{m_B}^B\left(k_i^B, t\right) \times \prod_{l=0}^{r}\left(1 - \left(-0.5\cos\left(\frac{\pi k_i^B}{(1-\alpha)l}\right) + 0.5\right)\right) + \sum_{n=ak_i^B}^{m} \phi_{m_B}^B\left(k_i^B, t\right) \times \prod_{l=0}^{(1-\alpha)k_i^B}\left(1 - \left(-0.5\cos\left(\frac{\pi k_i^B}{(1-\alpha)l}\right) + 0.5\right)\right) \times \prod_{l=ak_i^B}^{n}(1-1)$$
$$= \sum_{r=0}^{(1-\alpha)k_i^B} \phi_{m_B}^B\left(k_i^B, t\right) \prod_{l=0}^{r}\left(0.5 + 0.5\cos\left(\frac{\pi k_i^B}{(1-\alpha)l}\right)\right) \tag{7}$$

So, the probability that node i, with $\vec{k}_i = (k_i^A, k_i^B)$, remains in state S after accumulating m_A and mB messages in networks A and B respectively until time t can be calculated as Eq. 8:

$$s(\vec{k}, t) = (1-\rho_0) \sum_{m_A=0}^{k_i^A} \phi_{m_A}^A\left(k_i^A, t\right) \prod_{l=0}^{m_A}\left[1 - h_a\left(\frac{k_i^A}{l}, \alpha, \beta\right)\right] \times \sum_{m_B=0}^{k_i^B} \phi_{m_B}^B\left(k_i^B, t\right) \prod_{l=0}^{m_B}\left[1 - h_b\left(\frac{k_i^B}{l}, \alpha\right)\right]$$
$$= (1-\rho_0)\tau_A\left(k_i^A, m_A, t, \alpha, \beta\right)\tau_B\left(k_i^B, m_B, t, \alpha, \beta\right) \tag{8}$$

If $S(t)$, $A(t)$, $R(t)$ are used to represent the proportions of nodes in different states, considering nodes with different degrees, the proportion of nodes in the susceptible state at time t can be expressed as Eq. 9:

$$S(t) = \sum_{\vec{k}} P_X\left(\vec{k}\right) s\left(\vec{k}, t\right) \tag{9}$$

Considering that the neighbors of individual i can be in the susceptible, adopter, or recovered state, $\theta_{k_j^X}^X(t)$ can be further expressed as Eq. 10:

$$\theta_{k_j^X}^X(t) = \xi_{S,k_j^X}^X(t) + \xi_{A,k_j^X}^X(t) + \xi_{R,k_j^X}^X(t) \tag{10}$$

In this case, $\xi_{S,k_j^X}^X(t), xi_{A,k_j^X}^X(t), xi_{R,k_j^X}^X(t)$ represent the probabilities of neighbor node j being in the susceptible, adopter, and recovered states, respectively, and not having transmitted information to node i until time t. Since node i is in a "hole" state, it cannot transmit information to node j. Therefore, the probability that node j accumulates n_X non-redundant information in layer X at time t can be expressed as Eqs 11, 12:

$$\zeta_A\left(k_j^A - 1, n_A, t\right) = \sum_{n_A=0}^{k_j^A-1} \phi_{n_A}^A\left(k_j^A - 1, n_A, t\right) \prod_{l=0}^{n_A}\left[1 - h_a(x, \alpha, \beta)\right] \tag{11}$$

$$\zeta_B\left(k_j^B - 1, n_B, t\right) = \sum_{n_X=0}^{k_j^B-1} \phi_{n_B}^B\left(k_j^B - 1, n_B, t\right) \prod_{l=0}^{n_B}\left[1 - h_b(x, \alpha)\right] \tag{12}$$

In layer X, the probability that node j remains in the susceptible state at time t is as Eqs 13, 14:

$$\xi_{S,k_j^X}^A(t) = (1-\rho_0)\left[1 - \left(1 - \zeta_A\left(k_j^A - 1, n_A, t\right)\right)\left(1 - \tau_B\left(k_j^B, n_B, t\right)\right)\right] \tag{13}$$

and

$$\xi_{S,k_j^X}^B(t) = (1-\rho_0)\left[1 - \left(1 - \zeta_B\left(k_j^B - 1, n_B, t\right)\right)\left(1 - \tau_A\left(k_j^A, n_A, t\right)\right)\right] \tag{14}$$

Since the probability of transmitting information through edges is λ, and the recovery probability of adopter nodes is γ, the equation for $\xi_{R,k_j^X}^X(t)$ as Eq. 15:

$$\frac{d\xi_{R,k_j^X}^X(t)}{dt} = \gamma(1-\lambda)\xi_{A,k_j^X}^X(t) \tag{15}$$

At time t, the probability of information being transmitted through an edge is equal to the probability of an adopter node transmitting the information to a susceptible neighbor. Therefore, Eq. 16 is as follows:

$$\frac{d\theta_{k_j^X}^X(t)}{dt} = -\lambda\xi_{A,k_j^X}^X(t) \tag{16}$$

By combining Eqs 12 and 13, Eq. 17 can be obtained:

$$\xi_{R,k_j^X}^X(t) = \frac{\gamma(1-\lambda)\left[1 - \theta_{k_j^X}^X(t)\right]}{\lambda} \tag{17}$$

By substituting Eqs 8 and 14 into Eq. 13, Eq. 18 can be obtained:

$$\frac{d\theta_{k_j^X}^X(t)}{dt} = -\lambda\left[\theta_{k_j^X}^X(t) - \xi_{S,k_j^X}^X(t)\right] + \gamma(1-\lambda)\left[1 - \theta_{k_j^X}^X(t)\right] \tag{18}$$

Given the initial conditions for $\theta_X(0) = 1$ and $\xi_{R,k_j^X}^X(t) = 0$, when $t \to \infty$ the Eq. 15 equals 0, Eq. 19 can be derived the expression for $\theta_{k_j^X}^X(t)$ as:

$$\theta_{k_j^X}^X(t) = \frac{\lambda\xi_{S,k_j^X}^X(t) + \gamma(1-\lambda)}{\gamma(1-\lambda) + \lambda} \tag{19}$$

By substituting the expression for $\theta_{k_j^X}^X(t)$ into Eqs 2 and 3, Eq. 20 can be obtained:

$$\theta_X(\infty) = \sum_{k_j^X=0} \frac{k_j^X P\left(k_j^X\right)}{\langle k^X\rangle} \theta_{k_j^X}^X(\infty) = f_X\left(\theta_A(\infty), \theta_B(\infty)\right) \tag{20}$$

To simplify the notation, let's use the function $f(x)$ to represent $\theta_X(\infty)$.

By substituting the obtained equations into (4)–(7), it can be derived that the proportion of susceptible nodes $S(\infty)$. Since the growth of $\frac{dA(t)}{dt}$ is due to the decrease in $S(t)$, so the equations for the proportions of nodes in different states as Eqs 21, 22:

$$\frac{dA(t)}{dt} = -\frac{dS(t)}{dt} - \gamma A(t) \tag{21}$$

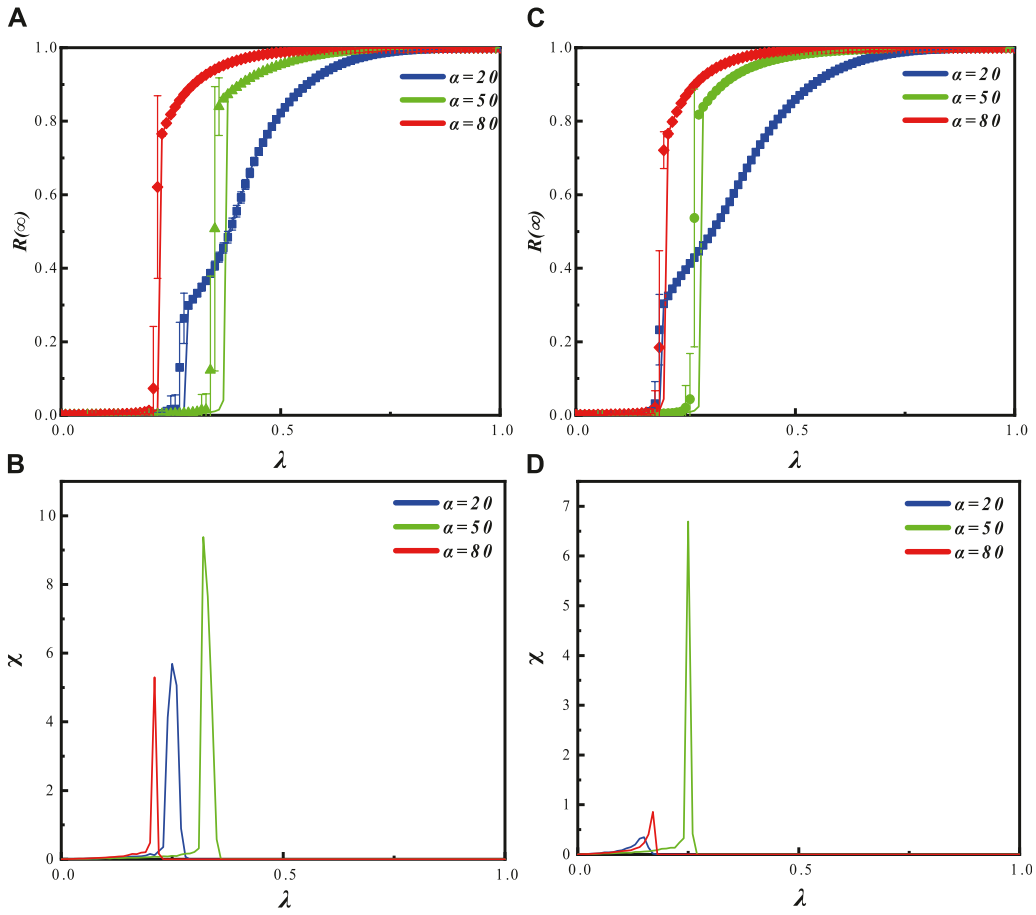

FIGURE 5
The graph shows the effects of the hesitation degree parameter α and the propagation probability λ on the information outbreak size R (∞) and the relative variance of the final adoption range in an SF-SF network with a fixed hesitation amplitude parameter β, where the heterogeneity parameter V is set to 2.1. Graphs **(A)** (β = 0.5) and **(C)** (β = 0.8) illustrate the influence of α on the information outbreak size as the propagation probability varies. The symbols represent simulation results, while the lines depict theoretical predictions. Different propagation patterns of information are observed for different values of α. Graphs **(B)** (β = 0.5) and **(D)** (β = 0.8) display the distribution of the relative variance of the adoption range for different α values as the propagation probability changes. They correspond to the variations observed in graphs **(A, C)**, respectively. The remaining parameters are set as ρ_0 and γ = 1.

and

$$\frac{dR(t)}{dt} = \gamma A(t) \tag{22}$$

Based on S (∞), it can be obtained that R (∞) as a complement to 1, since the proportions of nodes in all states must sum up to 1.

To further investigate the conditions for non-continuous growth of the function, the situation can be determined when Eq. 17 is tangent to θ_X (∞) < 1 by calculating the following Eq. 23:

$$\frac{\partial f_A(\theta_A(\infty),\theta_B(\infty))}{\partial \theta_B(\infty)} \frac{\partial f_B(\theta_A(\infty),\theta_B(\infty))}{\partial \theta_A(\infty)} = 1 \tag{23}$$

4 Parameter settings

To ensure simulation accuracy, a minimum of 10^3 dynamic realizations are recommended in the network for this study. The network size is set to $N = 10^4$, with an average degree of $\langle k_A\rangle = \langle k_B\rangle = \langle k_{10}\rangle = 10$. To investigate the impact of contact capacity on information propagation mechanisms in ER-ER and SF-SF networks, the network layer $XX \in \{A, B\}$ in ER-ER network follows a Poisson degree distribution $p_X(k_X) = e^{-\langle k_X\rangle}\frac{\langle k_X\rangle^{k_X}}{k_X!}$, while in SF-SF network, the network layer follows a power-law degree distribution $p_X(k_X) = \xi_X k_X^{-\nu}$. Here, $\xi_X = \frac{1}{\sum_{k_X} k_X^{-\nu}}$ and ν are parameters representing the degree exponent of layer A and layer B, respectively.

The heterogeneity of the network degree distribution is negatively correlated with the degree distribution exponent ν. When ν is small, the network contains a few high-degree nodes and many low-degree nodes. Additionally, to make the process more convenient, the information transmission probability is set as $\lambda_A = \lambda_B = \lambda$, and the recovery rate is set as γ = 1.0.

The peak of the relative variance χ curve of the final adoption range and the corresponding information transmission probability at the critical points are as Eq. 24:

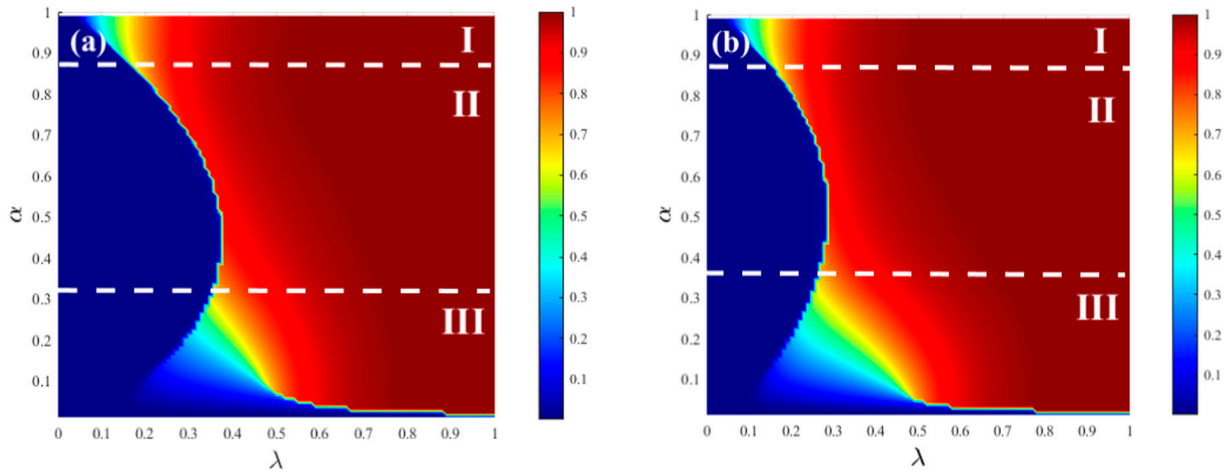

FIGURE 6
The graphs represent the relationship between the information outbreak size and the hesitation degree parameter α and the propagation probability λ in an SF-SF network with $\nu = 2.1$, while the hesitation amplitude parameter β is fixed. In Graph **(A)**, the hesitation amplitude parameter β is set to 0.5, while in graph **(B)**, it is set to 0.8. The remaining parameters are set as ρ_0 and $\gamma = 1$.

$$\chi = N\frac{\left\langle (R(\infty)^2\right\rangle - \langle R(\infty)\rangle^2}{\langle R(\infty)\rangle} \tag{24}$$

The symbol $\langle \ldots \rangle$ here represents the ensemble average.

5 Simulation and discussion

In this paper, the first exploration is about the propagation of information on a weighted ER network, where the nodes in the ER network follow a Poisson distribution, denoted as $[P(k) = e^{-\langle k\rangle}\langle k\rangle^k/k!$. The simulation results represented by symbols and the predicted results represented by lines show consistent trends.

5.1 ER network

From Figure 3A, it can be observed that when the individual hesitation amplitude is relatively small ($\beta = 0.5$), the outbreak of $R(\infty)$ exhibits second-order continuous phase transitions for $\alpha = 0.2$ and $\alpha = 0.8$. The propagation outbreak occurs earlier but with a slower growth rate for $\alpha = 0.2$ compared to $\alpha = 0.8$. However, when $\alpha = 0.5$, the outbreak point occurs later, and the growth pattern is characterized by discontinuous growth with a faster rate. In the steady state, the final propagation size reaches complete spread for all values of α. Figure 3C indicates that when the individual hesitation amplitude is relatively large ($\beta = 0.8$), the propagation patterns are similar to those in Figure 3A, but the outbreak of $R(\infty)$ occurs earlier, and there are cross-over phase transitions in the propagation. Additionally, when $\alpha = 0.2$ and $\alpha = 0.8$, the outbreak point for $\alpha = 0.2$ precedes that of $\alpha = 0.8$, indicating that the impact of the hesitation amplitude β on the propagation differs for different hesitation degrees α.

Figure 3B demonstrates that when $\beta = 0.5$, the relative variance of the adoption range exhibits an earlier outbreak for $\alpha = 0.8$, followed by $\alpha = 0.2$, and finally $\alpha = 0.5$. The saturation order is $\alpha = 0.8$, $\alpha = 0.2$, $\alpha = 0.5$. In Figure 3D, when $\beta = 0.8$, the relative variance of the adoption range exhibits an earlier outbreak for $\alpha = 0.2$, followed by $\alpha = 0.8$, and finally $\alpha = 0.5$. The saturation order is $\alpha = 0.2$, $\alpha = 0.8$, $\alpha = 0.5$.

Figure 4A represents the joint effect of the hesitation amplitude parameter β and the hesitation degree parameter α on the final adoption range $R(\infty)$ in an ER network. Based on different phase transition patterns, Figure 4A can be divided into four regions. In regions I ($0.75 < \alpha \leq 1$) and III ($0.09 < \alpha \leq 0.41$), as λ increases, a second-order continuous phase transition is observed. This is because when α is large (dominance of the ordinary state) or small (dominance of the hesitant state), both layer A (ordinary state adoption) and layer B (hesitant state adoption) exhibit single-layer outbreaks, where the outbreak of one layer leads to the outbreak of the other layers, resulting in continuous propagation. In region II ($0.41 < \alpha \leq 0.75$), a discontinuous first-order phase transition is observed as λ increases. This occurs when both layers simultaneously outbreak, but with a delayed outbreak point, indicating the absence of a dominant propagation layer. In region IV ($0 < \alpha \leq 0.09$), there is no growth, indicating the absence of information outbreak in this region.

Figure 3B represents a continuous single-stage process, exhibiting a continuous second-order phase transition as λ increases. As β decreases, the propagation becomes slower, indicating a positive correlation between the hesitation amplitude parameter and the hesitant population.

5.2 SF network

In a weighted SF network, there is a negative correlation between the heterogeneity of node degree distribution and the degree exponent ν. Node degrees in this network follow a power-law distribution, denoted as $P(k) = \xi k^{-\nu}$, $\xi = 1/\sum_k k^{-\nu}$, where the parameter ν represents the heterogeneity parameter of the SF network.

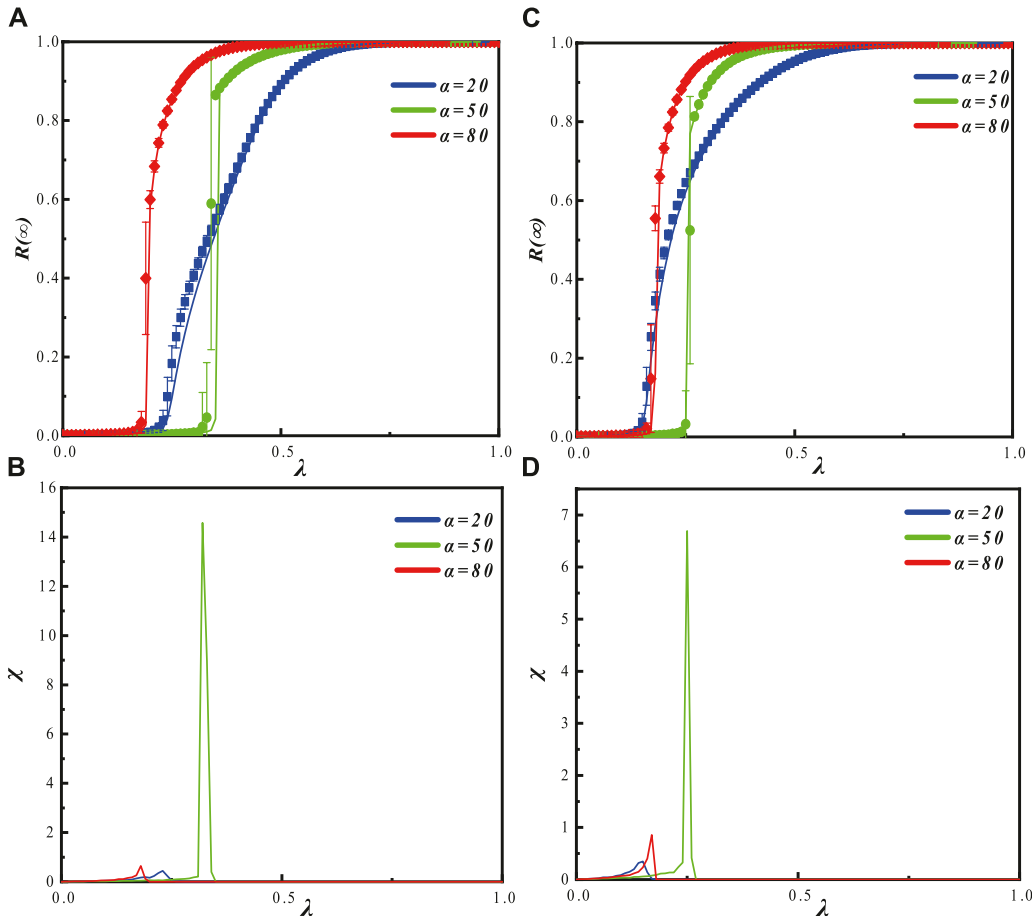

FIGURE 7
$\nu = 4$, with a fixed hesitation amplitude parameter β, the graphs **(A)** ($\beta = 0.5$) and **(C)** ($\beta = 0.8$) illustrate the effects of the hesitation degree parameter α and the propagation probability λ on the information outbreak size $R(\infty)$ and the relative variance of the final adoption range. Graphs **(A)** and **(C)** show the impact of α on the information outbreak size as the propagation probability varies. The symbols represent simulation results, while the lines depict theoretical predictions. Different propagation patterns of information are observed for different values of α. Graphs **(B)** ($\beta = 0.5$) and **(D)** ($\beta = 0.8$) display the distribution of the relative variance of the adoption range for different α values as the propagation probability changes. They correspond to the variations observed in graphs **(A)** and **(C)**, respectively.

- for $\nu = 2.1$

In Figure 5A, it is shown that when the individual hesitation amplitude is relatively low ($\beta = 0.5$), the values of the outbreak threshold for $\alpha = 0.2$, $\alpha = 0.5$, and $\alpha = 0.8$ are all relatively large, indicating a first-order discontinuous phase transition. The outbreaks in these cases are rapid and of short duration. In the steady state, the final propagation size is fully spread. In Figure 5C, it is shown that when the individual hesitation amplitude is relatively high ($\beta = 0.5$), the outbreaks for $\alpha = 0.2$ and $\alpha = 0.8$ exhibit second-order continuous phase transitions. The outbreak point for $\alpha = 0.2$ occurs earlier than that for $\alpha = 0.8$, which is different from the case when $\beta = 0.5$. This indicates that the impact of changes in the hesitation amplitude β on the propagation varies depending on the hesitation degree α. For $\alpha = 0.5$, the outbreak exhibits a first-order discontinuous phase transition. Additionally, when the individual hesitation amplitude is larger, the outbreaks occur earlier, and there is evidence of cross-contagion.

In Figure 5B, when $\beta = 0.5$, the relative variance of the adoption range first reaches its outbreak point for $\alpha = 0.8$, followed by $\alpha = 0.2$, and finally $\alpha = 0.5$. The saturation order of the relative variance is $\alpha = 0.8$, $\alpha = 0.2$, $\alpha = 0.5$. In Figure 5D, when $\beta = 0.8$, the relative variance of the adoption range first reaches its outbreak point for $\alpha = 0.2$, followed by $\alpha = 0.8$, and finally $\alpha = 0.5$. The saturation order of the relative variance is $\alpha = 0.2$, $\alpha = 0.8$, $\alpha = 0.5$.

Figure 6 represents the joint effect of the hesitation amplitude parameter α and the hesitation degree parameter β on the final adoption range $R(\infty)$ in an ER network. Based on different phase transition patterns, Figure 6A can be divided into three regions. In regions I ($0.84 < \alpha \leq 1$) and III ($0 < \alpha \leq 0.32$), as λ increases, there is a continuous second-order phase transition. This is because when α is large (dominance of ordinary state) or small (dominance of hesitant state), in layer A (ordinary state adoption) and layer B (hesitant state adoption), there is a single-layer outbreak triggered by the outbreak of the other layer, resulting in continuous propagation. In region II ($0.32 < \alpha \leq 0.84$), as λ increases, there is a discontinuous first-order phase transition. This is because both layers simultaneously undergo an outbreak, and the outbreak occurs relatively late, indicating that there is no dominant propagating layer. In region III, as λ

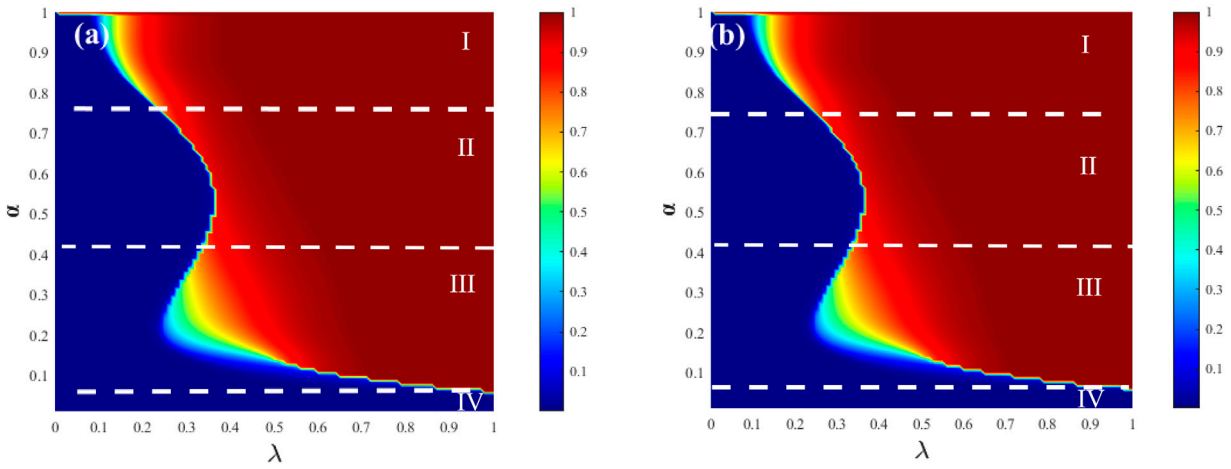

FIGURE 8
The graphs illustrate the relationship between the information outbreak size and the hesitation degree parameter α and the propagation probability λ in an SF-SF network with v = 4, while the hesitation amplitude parameter β is fixed. In graph **(A)**, the hesitation amplitude parameter β is set to 0.5, while in graph **(B)**, it is set to 0.8. The remaining parameters are set as ρ_0 and $\gamma = 1$.

increases, there is a continuous second-order phase transition, similar to region I. Comparing Figures 6A, B, it can be observed that when the hesitation amplitude is higher, a larger λ is required to achieve the same adoption range.

- for $\nu = 4$

Figure 7A indicates that when the individual hesitation amplitude is relatively low ($\beta = 0.5$), the outbreaks for $\alpha = 0.2$ and $\alpha = 0.8$ exhibit second-order continuous phase transitions. The outbreaks occur earlier compared to $\alpha = 0.5$, but the growth rate is slower for $\alpha = 0.2$ compared to $\alpha = 0.8$. For $\alpha = 0.5$, the outbreak shows a first-order discontinuous phase transition. The outbreak occurs later but with a faster growth rate, and in the end, the propagation is fully spread. Figure 7C shows that when the individual hesitation amplitude is relatively high ($\beta = 0.8$), the propagation patterns are similar to those in Figure 7A, but the outbreaks occur earlier. Additionally, there is evidence of cross-contagion in the propagation. Furthermore, for $\alpha = 0.2$ and $\alpha = 0.8$, the outbreak point occurs earlier for $\alpha = 0.2$ compared to $\alpha = 0.8$, indicating that the impact of changes in the hesitation amplitude β on the propagation varies depending on the hesitation degree α.

In Figure 7B, when $\beta = 0.5$, the relative variance of the adoption range first reaches its outbreak point for $\alpha = 0.8$, followed by $\alpha = 0.2$, and finally $\alpha = 0.5$. The saturation order of the relative variance is $\alpha = 0.8$, $\alpha = 0.2$, $\alpha = 0.5$. In Figure 7D, when $\beta = 0.8$, the relative variance of the adoption range first reaches its outbreak point for $\alpha = 0.2$, followed by $\alpha = 0.8$, and finally $\alpha = 0.5$. The saturation order of the relative variance is$\alpha = 0.2$, $\alpha = 0.8$, $\alpha = 0.5$.

Figure 8 represents the process of change in four stages. In regions I ($0.75 < \alpha \leq 1$) and III($0.05 < \alpha \leq 0.41$), as λ increases, there is a continuous second-order phase transition. This is because when α is large (dominance of the ordinary state) or small (dominance of the hesitant state), in layer A (adoption of the ordinary state) and layer B (adoption of the hesitant state), there is a single-layer outbreak triggered by the outbreak of the other layer, resulting in continuous propagation. In region II($0.41 < \alpha \leq 0.75$), as λ increases, there is a discontinuous first-order phase transition. This is because both layers simultaneously undergo an outbreak, and the outbreak occurs relatively late, indicating that there is no dominant propagating layer. In region IV($0 < \alpha \leq 0.05$), there is no growth, indicating the absence of information outbreaks in this region. Additionally, from the Figures 8A, B, it can be observed that as β decreases, the propagation becomes slower, indicating a positive correlation between the hesitation amplitude parameter and the hesitant population.

6 Conclusion

In real-life, individuals exhibit different social behaviors within various social networks. To analyze the propagation mechanisms and investigate heterogeneous adoption behavior in a heterogeneous network of the same population, this study proposes a dual-layer heterogeneous adoption information propagation network model from both simulation and theoretical perspectives. A heterogeneous threshold function based on realistic psychological research is designed, and extensive experiments demonstrate the consistent results between simulations and theory.

This paper focuses on the innovative aspect of heterogeneous adoption behavior within a dual-layer model and explores the propagation of heterogeneous behavior within the same population in a dual-layer heterogeneous network. Through extensive simulation and theoretical analysis in SF and ER networks, it is observed that when either layer dominates, the final adoption range exhibits a second-order continuous phase transition. In the absence of a clear dominant layer, a first-order discontinuous phase transition occurs with the presence of cross-propagation phenomena. The propagation process and modes are influenced by factors such as hesitation parameters, degree heterogeneity parameters, and propagation probabilities, ultimately leading to complete propagation.

The inter-layer adoption heterogeneity in information propagation networks has a crucial impact, yet there is limited research in this area.

This paper rigorously models and analyzes the significant influence of heterogeneous adoption behavior within multi-layer networks on information propagation. The study also provides a new direction for information propagation in multi-layer heterogeneous networks. However, this article has certain limitations. Firstly, it does not use real datasets, lacks standardized data representing human behavioral characteristics, and cannot extensively validate the behavior propagation with real-world data. Secondly, it does not consider several conventional parameters that may influence the research process, such as weights and fluctuation-based adoption. To emphasize the influence of heterogeneous adoption behavior within this model, other parameters were reduced to better highlight the significance of studying heterogeneous adoption behavior. It is hoped that more experts and scholars will pay attention to this field and further expand the research.

Data availability statement

The raw data supporting the conclusion of this article will be made available by the authors, without undue reservation.

Author contributions

SC: Writing–review and editing, Writing–original draft, Visualization, Software, Project administration, Investigation, Formal Analysis, Data curation. XZ: Writing–review and editing, Writing–original draft, Visualization, Validation, Resources, Methodology, Investigation, Formal Analysis, Conceptualization.

Funding

The author(s) declare that no financial support was received for the research, authorship, and/or publication of this article.

Acknowledgments

We would like to thank the reviewers for their insightful comments on the manuscript, as their remarks led to an improvement of the work.

Conflict of interest

The authors declare that the research was conducted in the absence of any commercial or financial relationships that could be construed as a potential conflict of interest.

Publisher's note

All claims expressed in this article are solely those of the authors and do not necessarily represent those of their affiliated organizations, or those of the publisher, the editors and the reviewers. Any product that may be evaluated in this article, or claim that may be made by its manufacturer, is not guaranteed or endorsed by the publisher.

References

1. Kobayashi T, Ogisu Y, Onaga T. Unstable diffusion in social networks. *J Econ Dyn Control* (2022) 146:104561. doi:10.1016/j.jedc.2022.104561

2. Furutani S, Shibahara T, Akiyama M, Aida M. Analysis of homophily effects on information diffusion on social networks. *IEEE Access* (2023) 11:79974–83. doi:10.1109/access.2023.3299854

3. Cai X, Xia W, Huang W, Yang H. Dynamics of momentum in financial markets based on the information diffusion in complex social networks. *J Behav Exp Finance* (2024) 41:100897. doi:10.1016/j.jbef.2024.100897

4. Lin M, Duan L, Li Y, Xiao Q. The roles of information diffusion on financial risk spreading on two-layer networks. *Front Phys* (2022) 10. doi:10.3389/fphy.2022.905205

5. Gaeta R. A model of information diffusion in interconnected online social networks. *ACM Trans Web* (2018) 12:1–21. doi:10.1145/3160000

6. Jiang M, Wang M, Kong J. Prototype equilibrium network with group emotional contagion for few-shot emotion recognition in conversation. *Int J Machine Learn Cybernetics* (2023) 15:2229–46. doi:10.1007/s13042-023-02025-y

7. Yin C, Wang Z, Zhao X. Spatial prediction of highway slope disasters based on convolution neural networks. *Nat Hazards* (2022) 113:813–31. doi:10.1007/s11069-022-05325-8

8. Yu Y, Yin X. Financial risk avoidance based on the sensor network and edge computing. *J Electr Comp Eng* (2022) 2022:1–11. doi:10.1155/2022/2028155

9. Wang F. Research on optimization algorithms for artificial intelligence network security management based on all ip internet of things fusion technology. *Comput Electr Eng* (2024) 115:109105. doi:10.1016/j.compeleceng.2024.109105

10. Tsai K-C, Zhuang Z, Lent R, Wang J, Qi Q, Wang L-C, et al. Tensor-based reinforcement learning for network routing. *IEEE J Selected Top Signal Process* (2021) 15:617–29. doi:10.1109/jstsp.2021.3055957

11. Bryc W, Wang Y, Kuznetsov A, Wesołowski J. Markov processes related to the stationary measure for the open kpz equation. *Probab Theor Relat Fields* (2023) 185:353–89. doi:10.1007/s00440-022-01110-7

12. Moser BA, Lunglmayr M. On quasi-isometry of threshold-based sampling. *IEEE Trans Signal Process* (2019) 67:3832–41. doi:10.1109/tsp.2019.2919415

13. Han JG, Park TH, Moon YH, Eom IK. Efficient markov feature extraction method for image splicing detection using maximization and threshold expansion. *J Electron Imaging* (2016) 25:023031. doi:10.1117/1.jei.25.2.023031

14. Fan J, Meng J, Liu Y, Saberi AA, Kurths J, Nagler J. Universal gap scaling in percolation. *Nat Phys* (2020) 16:455–61. doi:10.1038/s41567-019-0783-2

15. Hermon J, Sousi P. A comparison principle for random walk on dynamical percolation. *Anim Probab* (2020) 48:2952–87. doi:10.1214/20-AOP1441

16. Zhou H, Chen X, He S, Zhu C, Leung VCM. Freshness-aware seed selection for offloading cellular traffic through opportunistic mobile networks. *IEEE Trans Wireless Commun* (2020) 19:2658–69. doi:10.1109/twc.2020.2967658

17. Shekatkar SM, Barve S. Importance of initial conditions in the polarization of complex networks. *EPL* (2018) 122:38002. doi:10.1209/0295-5075/122/38002

18. Masuda N, Sakaki M, Ezaki T, Watanabe T. Clustering coefficients for correlation networks. *Front Neuroinformatics* (2018) 12:7. doi:10.3389/fninf.2018.00007

19. Ding J, Zhang Y, Song K, Li G, Wang W, Liu K. Target controllability of multiplex networks with weighted interlayer edges. *IEEE Trans Netw Sci Eng* (2024) 11:313–25. doi:10.1109/tnse.2023.3296706

20. Xue X, Pan L, Zheng M, Wang W. Network temporality can promote and suppress information spreading. *Chaos Interdiscip J Nonlinear Sci* (2020) 30:113136. doi:10.1063/5.0027758

21. Huang P, Chen X-L, Tang M, Cai S-M. Coupled dynamic model of resource diffusion and epidemic spreading in time-varying multiplex networks. *Complexity* (2021) 2021:1–11. doi:10.1155/2021/6629105

22. Wang J, Cai S, Wang W, Zhou T. Link cooperation effect of cooperative epidemics on complex networks. *Appl Math Comput* (2022) 437:127537. doi:10.1016/j.amc.2022.127537

23. Wang J, Cai S-M, Zhou T. Immunization of cooperative spreading dynamics on complex networks. *Complexity* (2021) 2021:1–7. doi:10.1155/2021/6645113

24. Zhang H, Cao L, Fu C, Cai S, Gao Y. Epidemic spreading on multi-layer networks with active nodes. *Chaos Interdiscip J Nonlinear Sci* (2023) 33:073128. doi:10.1063/5.0151777

25. Ting L, Ahn J. Understanding the roles of interaction and trust in formation of loyalty toward customer-to-customer (c2c) platforms. *Asia Pac J Marketing Logistics* (2023) 35:2565–81. doi:10.1108/APJML-12-2022-1072

26. Lv H, Zhang B, Li T, Hu S. Construction and analysis of multi-relationship bipartite network model. *Complex Intell Syst* (2023) 9:5851–63. doi:10.1007/s40747-023-01038-y

27. Huo L, Yu Y. Impact of individual behavior adoption heterogeneity on epidemic transmission in multiplex networks. *Chin Phys B* (2023) 32:108703. doi:10.1088/1674-1056/acea65

28. Zhang Y-X, Zou L. Research on information dissemination on social networks based on edge-based compartmental theory. *Int J Mod Phys B* (2021) 35. doi:10.1142/s0217979221502490

29. Zheng Y, Gao J, Zhou Y, Cao X, Yang H, Li S, et al. Wideband gain enhancement and rcs reduction of fabry-perot resonator antenna with chessboard arranged metamaterial superstrate. *IEEE Trans Antennas Propagation* (2018) 66:590–9. doi:10.1109/TAP.2017.2780896

frontiers | Frontiers in Physics

TYPE Original Research
PUBLISHED 19 June 2024
DOI 10.3389/fphy.2024.1420556

OPEN ACCESS

EDITED BY
Fei Xiong,
Beijing Jiaotong University, China

REVIEWED BY
Qi Xuan,
Zhejiang University of Technology, China
Xiaoke Xu,
Dalian Nationalities University, China

*CORRESPONDENCE
Jianguo Liu,
liujg004@ustc.edu.cn

RECEIVED 20 April 2024
ACCEPTED 28 May 2024
PUBLISHED 19 June 2024

CITATION
Liu M, Guo Q and Liu J (2024), Effect of network structure on the accuracy of resilience dimension reduction.
Front. Phys. 12:1420556.
doi: 10.3389/fphy.2024.1420556

Effect of network structure on the accuracy of resilience dimension reduction

Min Liu[1], Qiang Guo[1] and Jianguo Liu[2]*

[1]Business School, University of Shanghai for Science and Technology, Shanghai, China, [2]Department of Digital Economics, Shanghai University of Finance and Economics, Shanghai, China

Dimension reduction is an effective method for system's resilience analysis. In this paper, we investigate the effect of network structure on the accuracy of resilience dimension reduction. First, we introduce the resilience dimension reduction method and define the evaluation indicator of the resilience dimension reduction method. Then, by adjusting node connections, preferential connection mechanisms, and connection probabilities, we generate artificial networks, small-world networks and social networks with tunable assortativity coefficients, average clustering coefficients, and modularities, respectively. Experimental results for the gene regulatory dynamics show that the network structures with positive assortativity, large clustering coefficient, and significant community can enhance the accuracy of resilience dimension reduction. The result of this paper indicates that optimizing network structure can enhance the accuracy of resilience dimension reduction, which is of great significance for system resilience analysis and provides a new perspective and theoretical basis for selecting dimension reduction methods in system resilience analysis.

KEYWORDS

system's resilience, dimension reduction, network structure, social network, assortativity, clustering coefficient, modularity

1 Introduction

Resilience describes a system's ability to retain the basic functionality when errors or failures occur, which is a fundamental property for complex systems [1–4]. The loss of resilience in numerous real-world systems could lead to catastrophic consequences, such as large-scale extinctions in ecological networks [5], and cascading failures in infrastructure systems [6]. As such, exploring resilience patterns for complex systems, making systems resilient to environmental changes has been one of the most critical issues in network science.

Resilience is an absolute measure that quantifies the extent to which a system recovers from instability. For instance, in biological systems, resilience may refer to a population's ability to maintain its size and distribution in the face of environmental changes, predation pressures, diseases, or other disturbances. A population with high resilience can adapt to environmental changes by regulating birth rates, death rates, immigration, and emigration, thus maintaining population stability. In some literatures on network analysis, resilience and robustness are used as interchangeable concepts [7]. Resilience is defined on network dynamics [1, 8], measuring the ability of a network to maintain its structure and function in the face of disturbances or attacks, while robustness is related to the static structure of a network, measuring the ability to maintain its connectivity when a fraction of nodes (links) is damaged [9]. However, when dealing with complex networks composed of numerous interconnected components, traditional resilience analysis frameworks may become inadequate. The multi-dimensional and nonlinear characteristics of these networks

poses challenges for analysis. As a result, the dimension reduction method is needed to map a large number of nonlinear dynamic systems to one-dimensional dynamic systems, while keeping systems' key dynamic characteristics. Gao et al. [1] proposed the dimension reduction method that decomposes N-dimensional networks into one-dimensional effective models and uses it to predict the global activity of the original network. Subsequently, based on the theoretical tools for large-scale networks and the advanced data analyzing techniques [10–13], the method has been extended to many aspects such as noise effects [14–16], reduction methods based on spectral dimension [17], sequence mean field [18] and degree weighted average [19], and has been applied to various fields [20–22]. The dynamic characteristics of a system strongly depend on the underlying network structure [17]. Understanding the topology or properties of a network can help us better reveal its inherent behavior from different perspectives [23–25]. Gao et al. [1] found that density, heterogeneity, and symmetry are three key structural factors affecting a system's resilience. Xu et al. [26] established a dynamic model of a multi-dimensional Supplier-Manufacturer network by combining structural information and network parameters. The results show that the resilience of Supplier-Manufacturer networks is highly sensitive to network structural characteristics, namely, nesting, and density. Dong et al. [3] found that community structure can significantly affect the resilience of a system. Meng et al. [27] used link density, algebraic connectivity, and aggregation coefficients to measure the number of links, fault tolerance, and redundancy in a network to evaluate the resilience of the power system. According to the simulation experiments, Costa [28] found that applying growth strategies on pre-existing structures can significantly enhance the resilience of complex networks. Li et al. [29] proposed a network resilience evaluation method that considers both network structure and node load, and then improved the network resilience enhancement strategy based on optimization theory. Laurence et al. [17] used the dominant eigenvalues and eigenvectors of the network adjacency matrix to construct a dimension reduction method based on spectrogram theory. Therefore, network structure plays an important role in the system's resilience analysis. Real networks are usually heterogeneous [30, 31] and may have certain topological structures or attributes. For example, interpersonal networks on social networking platforms such as LinkedIn have high assortativity coefficients, protein-protein interaction networks in biology [32], and collaborative networks of jazz musicians have obvious community structures [33]. The dimension reduction proposed by Gao et al. [1] can be used to accurately predict the system's response to diverse perturbations and correctly locate the critical points, at which the system loses its resilience. So, what role does network structure play in resilience dimension reduction?

In this paper, we investigate the effect of network structure on the accuracy of resilience dimension reduction. First, we introduce the resilience dimension reduction method and define the resilience measurement error. Then, by adjusting node connections, preferential connection mechanisms, and connection probabilities, we construct TAC model, HK model and TQ model, respectively. Based on the TAC model, HK model, and TQ model, we generate artificial networks, small-world networks and social networks with tunable assortativity coefficients, average clustering coefficients, and modularities, respectively. We conduct resilience dimension reduction analysis experiments on gene regulatory dynamics. The experimental results show that network structures with positive assortativity, large clustering coefficient, and significant community can enhance the accuracy of resilience dimension reduction. Finally, through error analysis of resilience dimension reduction on the reconstructed social networks, the results validate our conclusion.

2 Method and models

2.1 Resilience dimension reduction method

In a multi-dimensional system, the dynamics of each component not only depend on the self-dynamics but also relate to the interactions between the components and their interacting partners [34, 35]. The dynamic equation of a multi-dimensional system consisting of N components (nodes) can be formally written as

$$\frac{dx_i}{dt} = F(x_i) + \sum_{j=1}^{N} a_{ij} G\left(x_i, x_j\right). \tag{1}$$

The first term on the right-hand side of Eq. 1 describes the self-dynamics of each component, while the second term describes the interaction between component i and its interacting partners. The matrix element a_{ij} denotes the interactions between node i and j, and $a_{ij} = 1$ when there are an link between node i and j, and $a_{ij} = 0$ otherwise.

The resilience of multi-dimensional systems can be captured by calculating the stable fix point of Eq. 1. However, this point may depend on the changes in any of the parameters of the adjacency matrix. Moreover, there are maybe different forms of perturbations bringing changes to the adjacency matrix, for example, node/link removal, or weight reduction. It means that the resilience of multi-dimensional systems depends on the network topology and the forms of perturbations. For large-scale multi-dimensional models, it is impossible to predict their resilience by direct calculations on Eq. 1. A framework based on dimension reduction addresses this challenge.

In a network, the activity of each node is governed by its nearest neighbors through the interaction term $\sum_{j=1}^{N} a_{ij} G(x_i, x_j)$ of Eq. 1. If the adjacency matrix a_{ij} has little correlation, Gao et al. [1] introduced an operator.

$$L(\mathbf{y}) = \frac{\boldsymbol{I}^{\mathsf{T}} \boldsymbol{A} \mathbf{y}}{\boldsymbol{I}^{\mathsf{T}} \boldsymbol{A} \boldsymbol{I}}, \tag{2}$$

where the unit vector $\mathbf{1} = (1, 1, \ldots, 1)^{\mathsf{T}}$, $\mathbf{y} = (y_1, y_2, \ldots, y_N)^{\mathsf{T}}$, and y_i represents a scalar related to node i, such as the activity of node i. $\boldsymbol{A} = [a_{ij}]_{N\times N}$ is the adjacency matrix. The operator L averages the scalar values of all neighboring nodes of the target node as the output, and $\mathbf{y} = (y_1, y_2, \ldots, y_N)^{\mathsf{T}}$ as the input. Eq. 2 can be written as

$$L(\mathbf{y}) = \frac{\sum_{i=1}^{N}\sum_{j=1}^{N} a_{ij} y_j}{\sum_{i=1}^{N}\sum_{j=1}^{N} a_{ij}} = \frac{\frac{1}{N}\sum_{j=1}^{N} s_j^{\text{out}} y_j}{\frac{1}{N}\sum_{j=1}^{N} s_j^{\text{out}}} = \frac{\langle s_j^{\text{out}} y_j \rangle}{\langle s_j^{\text{out}} \rangle}, \tag{3}$$

where $s_j^{\text{out}} = \sum_{i=1}^{N} a_{ij}$. If $y_j\ (x_i) = G\ (x_i, x_j)$, when the degrees are uncorrelated, then the mean of node j is independent of node i. In other words, assuming that the nearest neighbor mean of i is the same as the nearest neighbor mean of all other nodes, the interaction

term in Eq. 1 composed of the sum of the actions of all neighbors j of i can be written as

$$\sum_{j=1}^{N} a_{ij} G\left(x_i, x_j\right) = s_i^{\text{in}} \langle y_j(x_i) \rangle_{nn} = s_i^{\text{in}} L(G(x_i, \mathbf{x})), \tag{4}$$

where $s_i^{\text{in}} = \sum_{j=1}^{N} a_{ij}$. $\langle y_j(x_i) \rangle_{nn}$ represents the mean value of the neighbor node state $y_j(x_i)$ of node i. Based on the Eq. 4, the Eq. 1 can be written as

$$\frac{dx_i}{dt} = F(x_i) + s_i^{\text{in}} L(G(x_i, \mathbf{x})). \tag{5}$$

Then, based on the mean field approximation theory, $L(G(x_i, \mathbf{x})) \approx G(x_i, L(\mathbf{x}))$, $L(F(\mathbf{x})) \approx F(L(\mathbf{x}))$, $L(\mathbf{s}^{\text{in}} \circ G(\mathbf{x}, L(\mathbf{x}))) \approx L(\mathbf{s}^{\text{in}}) \circ G(L(\mathbf{x}), L(\mathbf{x}))$. Eq. 5 can be written as

$$\frac{dx_i}{dt} = F(x_i) + s_i^{\text{in}} G(x_i, L(\mathbf{x})), \tag{6}$$

$$\frac{d\mathbf{x}}{dt} = F(\mathbf{x}) + \mathbf{s}^{\text{in}} \circ G(\mathbf{x}, L(\mathbf{x})), \tag{7}$$

and then this allows us to write Eq. 6 and Eq. 7 as

$$\frac{dL(\mathbf{x})}{dt} = L\left(F(\mathbf{x}) + \mathbf{s}^{\text{in}} \circ G(\mathbf{x}, L(\mathbf{x}))\right) \approx F(L(\mathbf{x})) + L\left(\mathbf{s}^{\text{in}}\right) \circ G(L(\mathbf{x}), L(\mathbf{x})), \tag{8}$$

where $\circ$ represents Hadamard convolution [36].

Finally, based on the Eq. 3, we obtain the average effective state of the system

$$x_{\text{eff}} = \frac{\boldsymbol{I}^{\mathsf{T}} \boldsymbol{A} \mathbf{x}}{\boldsymbol{I}^{\mathsf{T}} \boldsymbol{A} \boldsymbol{I}} = \frac{\langle \mathbf{s}^{\text{out}} \mathbf{x} \rangle}{\langle \mathbf{s} \rangle}, \tag{9}$$

and the nearest neighbor weighted degree

$$\beta_{\text{eff}} = \frac{\boldsymbol{I}^{\mathsf{T}} \boldsymbol{A} \mathbf{s}^{\text{in}}}{\boldsymbol{I}^{\mathsf{T}} \boldsymbol{A} \boldsymbol{I}} = \frac{\langle \mathbf{s}^{\text{out}} \mathbf{s}^{\text{in}} \rangle}{\langle \mathbf{s} \rangle}, \tag{10}$$

where $\mathbf{s}^{\text{out}} = (s_1^{\text{out}}, s_2^{\text{out}}, \ldots, s_N^{\text{out}})^{\mathsf{T}}$ is the vector of outgoing degrees with $s_j^{\text{out}} = \frac{1}{N} \sum_{i=1}^{N} a_{ij}$. $\mathbf{s}^{\text{in}} = (s_1^{\text{in}}, s_2^{\text{in}}, \ldots, s_N^{\text{in}})^{\mathsf{T}}$ is the vector of incoming degrees with $s_i^{\text{in}} = \frac{1}{N} \sum_{j=1}^{N} a_{ij}$. $\langle \mathbf{s}^{\text{out}} \mathbf{x} \rangle = \frac{1}{N} \sum_{i=1}^{N} s_i^{\text{out}} x_i$, $\langle \mathbf{s}^{\text{out}} \mathbf{s}^{\text{in}} \rangle = \frac{1}{N} \sum_{i=1}^{N} s_i^{\text{out}} s_i^{\text{in}}$. $\langle \mathbf{s} \rangle = \langle \mathbf{s}^{\text{in}} \rangle = \langle \mathbf{s}^{\text{out}} \rangle$ is the average weighted degree.

Based on the Eqs 8–10 and Eq. 1 is simplified into an effective one-dimensional equation

$$\frac{dx_{\text{eff}}}{dt} = F(x_{\text{eff}}) + \beta_{\text{eff}} G(x_{\text{eff}}, x_{\text{eff}}). \tag{11}$$

Although the resilience function is uniquely determined by the dynamical functions $F(x_i)$ and $G(x_i, x_j)$, the actual position of the system along this curve, capturing its momentary state, is determined by the network topology a_{ij}. So we constructed networks with different structures to explore the effect of network structure on the accuracy of the resilience dimension reduction method.

2.2 Models

Networks with different topological structures have different properties. The section mainly introduces three models for generating tunable parameter networks.

1) The assortativity coefficient ρ is an indicator that measures the degree of correlation between adjacent nodes in a network [37]. The Tunable-Assortativity-Coefficient (TAC) model changes the network's assortativity by adjusting the node connectivity, and generates the artificial networks with tunable assortativity coefficient ρ. The program for an artificial network using the TAC model can be divided into three steps.

   a) Initial condition: Randomly generate a connected network consisting of n_0 nodes and m_0 edges.
   b) Network growth: Add one new node i at each time step and connect to m existing nodes, and $m \leq m_0$.
   c) Preferential connection: The probability p_j of a new node being connected to an existing node i and the degree k_i of node i satisfy the relationship $p_j = k_j^{\alpha} / \sum_i k_i^{\alpha}$ (where α is a tunable parameter) [38].

2) The Holme-Kim (HK) model can construct artificial networks with tunable average clustering coefficient C [39]. When generating a network, the HK model will generate a fixed number of closed triangular adjacency relationships as required to adjust the average clustering coefficient C of the network. The program for generating artificial networks using the HK model can be divided into four steps.

   a) Initial condition: Randomly generate a connected network consisting of n_0 nodes and m_0 edges.
   b) Network growth: Add one new node i at each time step. At the same time, node i selects m existing nodes as neighbor nodes through preferential connection or triangulation, and $m \leq m_0$.
   c) Preferential connection: Calculate the probability Π_j ($\Pi_j = k_j / \sum_i k_i$) of node j being selected as a neighbor node by the new node i based on the degree k_j of each existing node j in the network. The new node i selects the neighbor nodes based on probability Π_j, and the first neighbor node of node i is selected according to the preferential connection.
   d) Triangle formation: Triangle formation is generally executed with a probability of $1 - P_t$ after preferential connection. If a new node i has already selected a neighbor j, then the selection range for the next neighbor of node i is all the neighbors of node j, thus forming a closed triangular adjacency relationship.

3) The modularity Q is a parameter used to characterize the strength of community features. The Tunable-Modularity (TM) model can adjust the connection probability as needed to generate the artificial networks with tunable modularity Q. The program for an artificial network using the TM model can be divided into three steps.

   a) Initialize the network: Create an initial network containing a small number of nodes that are interconnected to ensure network connectivity.
   b) Gradually add nodes: Gradually add new nodes and connect them to existing nodes.
   c) Reconnect edges: When connecting new nodes, reconnect some edges according to the required modularity to adjust the network's community structure.

In Addition, by adjusting the reconnection probability, we can generate small-world networks and social networks [40] with different average clustering coefficients, assortativity coefficients, and modularities.

3 Simulation results

3.1 Dynamic equation

The dynamic equation of the gene regulatory network is governed by Michaelis-Menten [1].

$$\frac{dx_i}{dt} = -Bx_i^q + \sum_{j=1}^{N} A_{ij}\frac{x_i^h}{x_i^h + 1}, \tag{12}$$

where the first item on the right-hand side describes the self-dynamic of each cell, and the second item is intercellular activity. The Hill coefficient h describes the level of cooperation in gene regulation [34]. We conduct interference experiments on three types of different tunable parameter networks, and explore the resilience reduction performance of tunable parameter networks. Then we mainly perturb the network in three different ways, including randomly deleting a certain proportion of nodes, deleting a certain proportion of edges, and changing a certain proportion of global weights. The initial state of all nodes is set to $x_0 = 2$, and it depends on the dynamic equation to calculate the node state when the system converges. Conducting 100 removals for each type of perturbation. Based on the mapping process and Eqs 11, 12 is rewritten as

$$\frac{dx_{\text{eff}}}{dt} = -Bx_{\text{eff}}^q + \beta_{\text{eff}}\frac{x_{\text{eff}}^h}{x_{\text{eff}}^h + 1}. \tag{13}$$

Based on this, we define the system's resilience measurement error to quantify the accuracy of the resilience dimension reduction model. The parameter settings for the gene regulatory dynamic equation are $B = 1$, $q = 1$, and $h = 2$.

3.2 Evaluation indicator

In this section, we define the system's resilience measurement error *Err* to quantify the accuracy of the resilience dimension reduction model. The *Err* can be expressed as

$$Err = \sum_{i=1}^{l} |x_{\text{eff}}(i) - x(\beta_{\text{eff}}(i))|, \tag{14}$$

where $x_{\text{eff}}(i) - x(\beta_{\text{eff}}(i))$ denotes the error between the numerical value $x_{\text{eff}}(i)$ of the system state obtained through Eq. 9 and the numerical value $x(\beta_{\text{eff}}(i))$ of the system state obtained through Eqs 10, 13. l represents the total number of perturbations, including randomly removing a certain proportion of nodes, removing a certain proportion of links, and changing a certain proportion of global weights. We conduct 100 experiments on each perturbation. The smaller the *Err* value, the better the performance of the dimension reduction method.

3.3 Result analysis

We analyze the accuracy of the resilience dimension reduction method on empirical networks, as measured by the error *Err* (Eq. 14). Table 1 shows the accuracy results of resilience dimension reduction on empirical networks. We can find that the errors *Err* of resilience dimension reduction on Facebook and Twitter networks are relatively small comparing with other networks (biological and ecological networks) (bold values in Table 1). For the same dynamics, the errors *Err* of resilience dimension reduction on Polbooks and Jazz networks are smaller than that of *E. coli* and *S. cerevisiae* networks (bold values in Table 1), which indicates that comparing with other networks, the accuracy of resilience dimension reduction on social networks is larger, and dynamics do not affect the accuracy of resilience dimension reduction. As shown in Figure 1, the error *Err* of uniform networks is smaller than that of homogeneous networks, random networks, scale-free networks, small-world networks, and community networks, while the error *Err* of scale-free networks is larger than that of uniform networks, homogeneous networks, random networks, small-world networks, and community networks. Hence, we obtain the order of accuracy of resilience dimension reduction as follows: uniform networks, small-world networks, homogeneous networks, community networks, random networks, and scale-free networks. The dimension reduction method analysis by Gao et al. [1], it can be concluded that the accuracy of a uniform network reaches the optimal values, which is shown in Figure 1. In addition, we can also find that the accuracy of small world networks is smaller than the one obtained from the uniform networks and larger than the ones get from other networks. The reason lies in the fact that a uniform network, each node is connected to the same number of other nodes. Comparing with other networks, small-world networks usually have higher homogeneity, meaning that nodes tend to connect to nodes with similar degrees, while in scale-free networks, the connection patterns of nodes exhibit high heterogeneity, meaning that there are a few "hub nodes" with a large number of connections. The above results indicate that the dimension reduction method of the resilience has remarkable performance for social networks.

In Table 1, we find that the error *Err* of resilience dimension reduction on Polbooks network is larger than that of Jazz network. The reason is that the accuracy of the resilience dimension reduction method varies depending on the size and structure of the network. So we investigate the accuracy of resilience dimension reduction on networks with different network sizes. As shown in Figure 2, we find that the error *Err* of network with $N = 200$ is larger than that of 150 and 100, and the error *Err* of network with $N = 150$ is larger than that of 100, which indicates that the network size will affect the accuracy of resilience dimension reduction, and the larger the size, the greater the influence. We can also find in Figure 2 that as the assortativity coefficient ρ increases, the error *Err* decreases. Therefore, one can find that the accuracy of resilience dimension reduction for social networks is large. The question is raised what kind of structure can enhance the accuracy of resilience dimension reduction? We generate artificial networks with different structures (assortativity coefficient, average clustering coefficient and modularity) and analyze the accuracy of the resilience dimension reduction method.

TABLE 1 Network characteristics of empirical networks and accuracy results of resilience dimension reduction.

Networks	N	E	Dynamics	C	ρ	Err
E.coli	1,550	3,244	Gene regulatory	0.0018	−0.3523	0.2764
S.cerevisiae	4,441	12,873	Gene regulatory	0.0001	−0.5580	0.3167
Facebook	539	6,384	SIS [41]	0.2262	0.2227	**0.0198**
Twitter	148	3,942	SIS [41]	0.4262	−0.0632	**0.0254**
Polbooks	105	882	Gene regulatory	0.4875	−0.1279	**0.1642**
Jazz	198	5,484	Gene regulatory	0.2525	0.0196	**0.0983**
Rain forest-Ants	41	468	Mutualistic [42]	0	1	1.4310
Rain forest-Plants	51	488	Mutualistic [42]	0	1	2.4985
Coral Reefs-Fish	26	140	Mutualistic [42]	0	1	0.2595
Coral Reefs-Anemones	10	108	Mutualistic [42]	0	1	0.2319

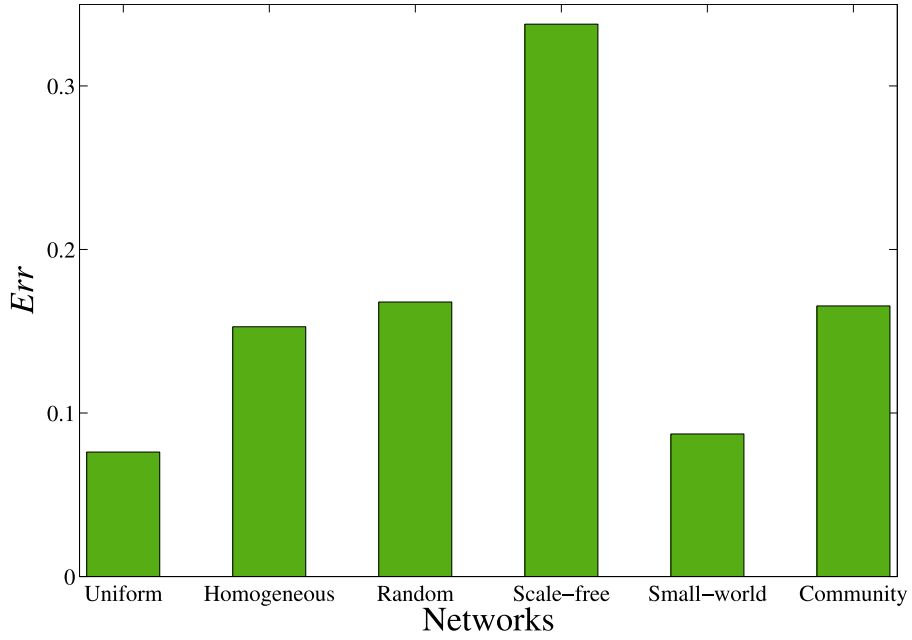

FIGURE 1
The resilience dimension reduction performance of different networks.

Firstly, based on the models in Section 2.2, we generate three sets of networks with 200 nodes and 800 edges, including assortativity coefficient $\rho \in$ [-0.4,0.4], average clustering coefficient $C \in$ [0.1,0.7] and modularity $Q \in$ [0.1,1.0]. Figure 3A shows the accuracy of dimension reduction on networks with different assortativity coefficients ρ. As the assortativity coefficient ρ increases, the error *Err* decreases, indicating that the network structure with high assortativity coefficient has larger accuracy of resilience dimension reduction. The error *Err* of the network resilience dimension reduction method with the assortativity coefficient $\rho > 0$ is smaller than that of the network resilience dimension reduction method with the assortativity coefficient $\rho < 0$, indicating that the accuracy of resilience dimension reduction is larger for the network structure with positive assortativity coefficient. Figure 3B shows the accuracy of resilience dimension reduction under different average clustering coefficients *C*. As the average clustering coefficient *C* increases, the error *Err* decreases. The results indicate that the dimension reduction method could generate larger accuracy for networks with large average clustering coefficient. Figure 3C shows the accuracy of resilience dimension reduction under different modularity *Q*. As the modularity *Q* increases, the error *Err* decreases. The results indicate that the accuracy of resilience dimension reduction is large for networks with high modularity. The clustering coefficient measures the probability that the neighbors of a node are also neighbors of each other, reflecting the local clustering

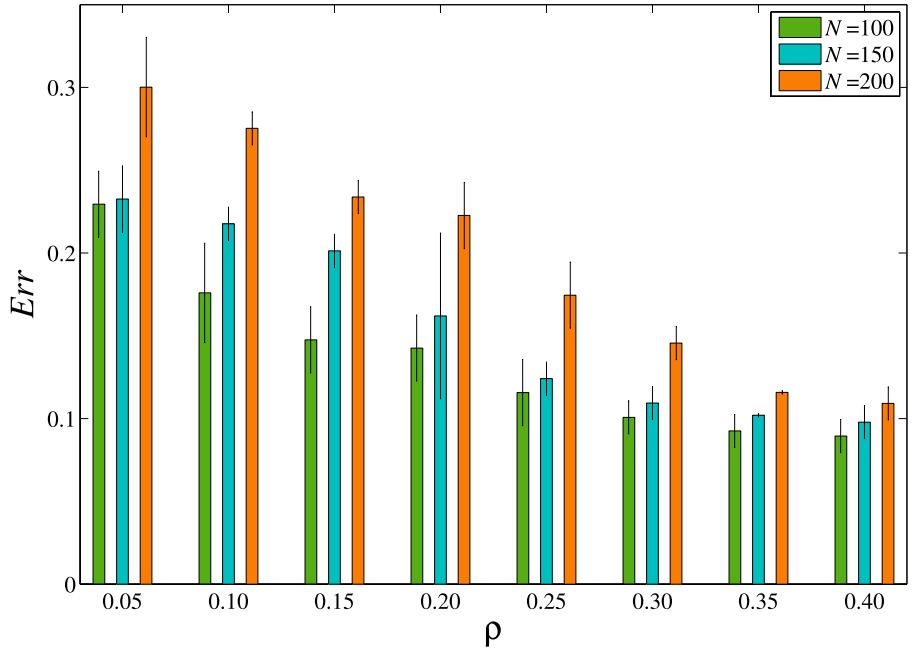

FIGURE 2
The resilience dimension reduction performance of different network sizes.

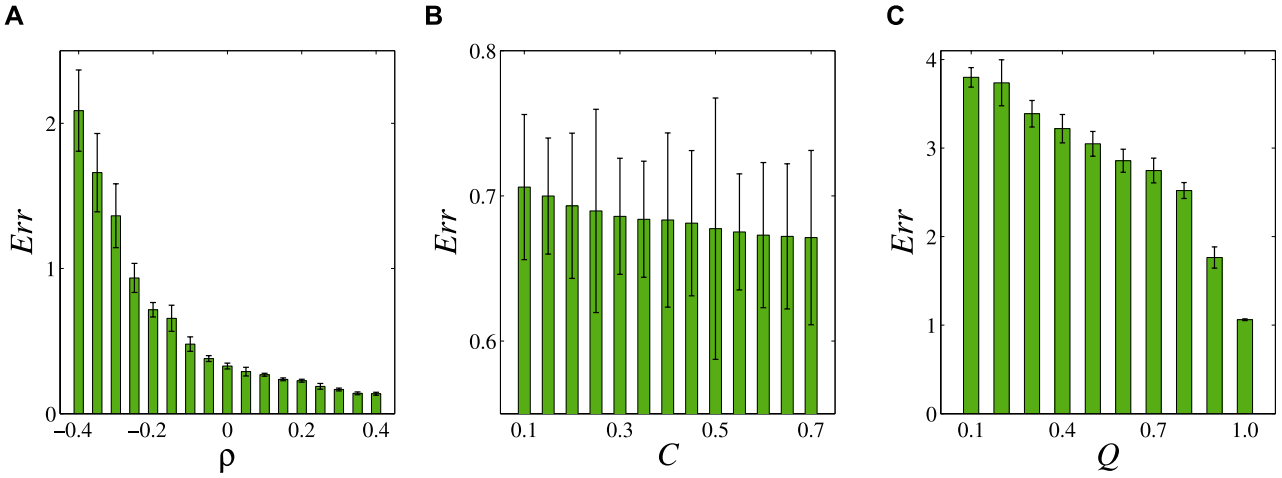

FIGURE 3
The resilience dimension reduction performance of networks with different structures. The subplots **(A–C)** show the correlations between the assortativity coefficient $\rho \in [-0.4,0.4]$, average clustering coefficient $C \in [0.1,0.7]$, modularity $Q \in [0.1,1.0]$, and resilience dimension reduction error *Err* of the network. The network size is all 200. We obtain each data value by averaging 10 independent runs of each network.

property of the network. Assortativity describes the tendency of similar nodes (such as nodes with similar degrees) in the network to connect with each other. The community structure network refers to the clear division of the network into communities, where nodes within a community are densely connected while connections between communities are relatively sparse. Networks with large clustering coefficient often have large modularity, which indicates that networks with clustering coefficient also exhibit large modularity, leading to smaller resilience dimension reduction errors. Networks with large assortativity, similar nodes are more likely to form tightly connected communities, which suggests that networks with large assortativity also large modularity, resulting in smaller resilience dimension reduction errors. Both clustering coefficient and assortativity are related to the local structure of the network. The clustering coefficient focuses on connections between neighboring nodes, while assortativity focuses on connections between similar nodes. In some cases, large clustering coefficient may be associated with large assortativity because a high probability of connections between neighboring nodes may imply that these nodes are similar in some attribute.

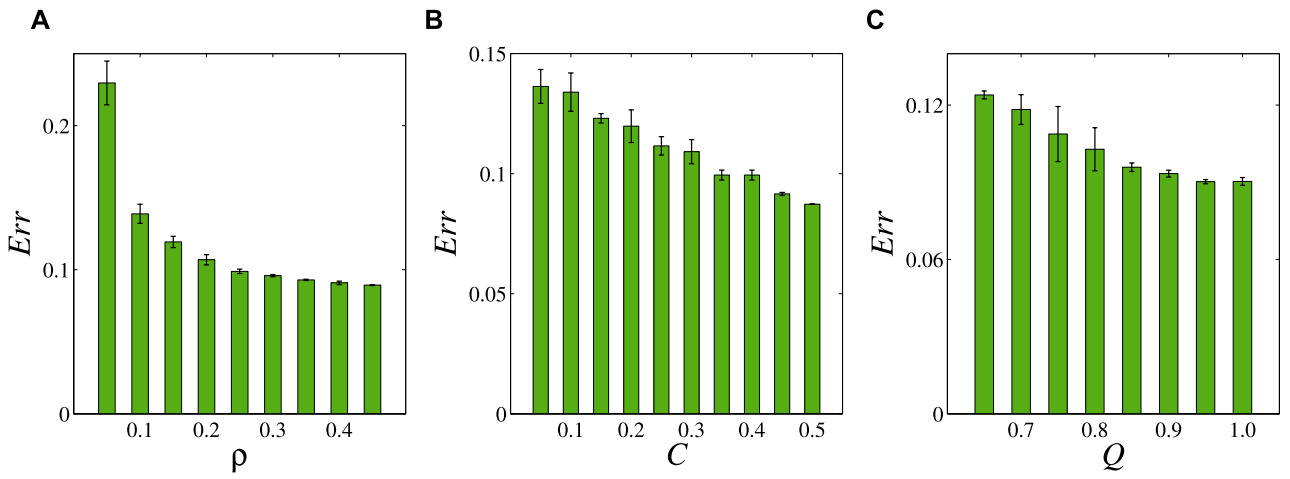

FIGURE 4
The resilience dimension reduction performance of small-world networks with different structures. The subplots **(A–C)** show the correlations between the assortativity coefficient $\rho \in [0.05,0.45]$, average clustering coefficient $C \in [0.05,0.50]$, modularity $Q \in [0.65,1.0]$, and resilience dimension reduction error *Err* of the network. The network size is all 200. We obtain each data value by averaging 10 independent runs of each network.

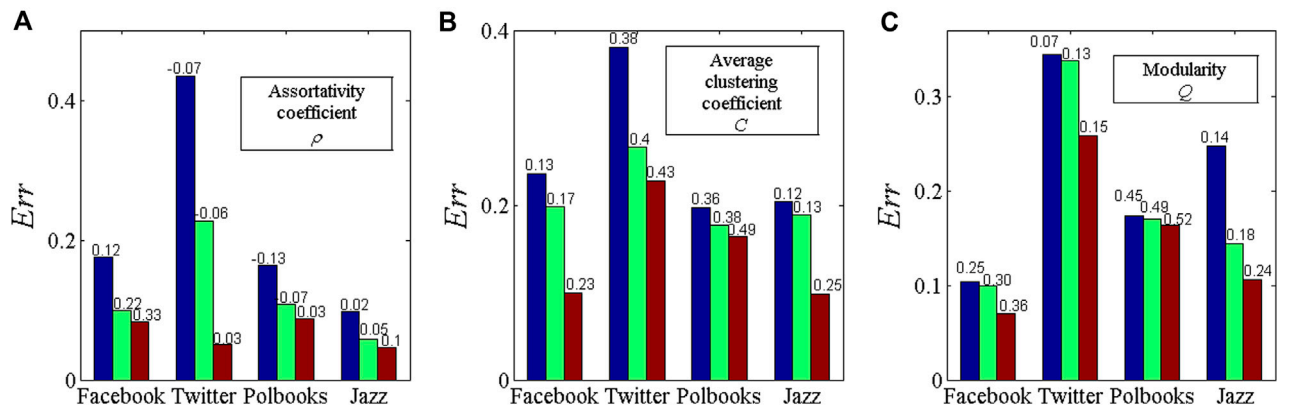

FIGURE 5
The resilience dimension reduction performance of social networks. The subplots **(A–C)** show the correlations between the assortativity coefficient ρ, average clustering coefficient C, modularity Q, and resilience dimension reduction error *Err* of the social network, respectively.

This indicates that the more homogeneous the local structure of the network, the better the performance of resilience dimension reduction. In summary, for networks with large assortativity, large average clustering coefficient, and large modularity, the resilience dimension reduction can result in smaller errors. In other words, large assortativity indicates the presence of similar nodes in the network, large average clustering coefficient indicate high local connectivity between neighboring nodes, and large modularity indicates the presence of closely related subnetworks in the network. In such network structures, resilience dimension reduction can better preserve information about these similar nodes, closely related subnetworks, and connections between neighboring nodes, thereby improving the accuracy of resilience dimension reduction.

Secondly, we investigate the accuracy of resilience dimension reduction on small-world networks with different structures. The small-world network is a network structure that lies between regular networks and random networks, characterized by short average paths, high clustering coefficients, and community structure. We generate three sets of small-world networks with 200 nodes and 800 edges, with assortativity coefficient $\rho \in [0.05,0.45]$, average clustering coefficient $C \in [0.05,0.50]$, and modularity $Q \in [0.65,1.0]$. As shown in Figure 4, with the increase of ρ, C, and Q increase, the *Err* values decrease. The experimental results show that the larger the assortativity coefficient, average clustering coefficient, and modularity of the network, the better the accuracy of resilience dimension reduction.

Social networks have characteristics such as small world phenomena, node degree distributions that follow power-law distributions, high clustering coefficients, assortativity that nodes are more inclined to connect with similar nodes, and community structures. The above results indicate that the network structure

with positive assortativity, large average clustering coefficient, and significant community can enhance the accuracy of resilience dimension reduction.

Finally, we reconstruct the network structures to generate social networks with different assortativity coefficients, average clustering coefficients and modularities. As shown in Figure 5, the error analysis of dimension reduction on social networks indicates that as ρ, C and Q increase, the accuracy of resilience dimension reduction on social networks increases. The empirical results show that the network structure with positive assortativity, large average clustering coefficient, and significant community can enhance the accuracy of resilience dimension reduction.

4 Conclusion and discussions

In this paper, we investigated the effect of network structure on the accuracy of resilience dimension reduction. First, we introduce the resilience dimension reduction method and define the resilience measurement error. Then, by adjusting node connections, preferential connection mechanisms, and connection probabilities, we construct TAC model, HK model and TQ model, respectively. Based on the TAC model, HK model, and TQ model, we generated artificial networks, small-world networks and social networks with tunable assortativity coefficients, average clustering coefficients, and modularities, respectively. We conducted dimension reduction analysis experiments on gene regulatory dynamics using the generated networks, and analyzed the effect of tunable parameters on the accuracy of resilience dimension reduction based on the error analysis. We found that the error *Err* of resilience dimension reduction for social networks is small. The larger the assortativity coefficient $\rho(>0)$, the smaller the error *Err*. The larger the average clustering coefficient C, the smaller the error *Err*. As the modularity Q increases, the error *Err* decreases. The error values *Err* of resilience dimension reduction on small-world networks with large assortativity coefficient, high average clustering coefficient, and high modularity are small, which indicates that the resilience dimension reduction method has remarkable performance for networks with positive assortativity, large average clustering coefficient, and significant community.

In summary, network structure has a significant impact on the accuracy of the resilience dimension reduction, which is of great research importance on practical applications. In this paper, when the HK model generated a tunable clustering coefficient network, due to the limitations of structural properties such as sparsity and average assortativity coefficient, we did not further analyze the accuracy of the dimension reduction for networks with the average clustering coefficient $C > 0.7$. According to preliminary speculation, if the number of nodes, sparsity, and average assortativity coefficient of the network remains unchanged, the average clustering coefficient C will continue to increase from 0.7, and the number of triangles in the network will increase accordingly. When the total number of edges in the network remains constant, an increase in the number of triangles should cause most of the edges of dense nodes to transfer to the adjacency relationships of other non-dense nodes. The accuracy of the resilience dimension reduction should increase with the increase of the average clustering coefficient. In the process of resilience analysis of artificial networks, although we applied it to gene regulation dynamics, we can obtain corresponding results by applying it to SIS propagation dynamics. For example, when Polbooks, Jazz, E. coli, and S. cerevisiae networks are all applied in gene regulation dynamics, we found that the error values of resilience dimension reduction on Polbooks and Jazz networks are smaller than that of E. coli and S. cerevisiae networks. In addition, we only studied the effects of assortativity coefficient, average clustering coefficient, and modularity on the accuracy of the resilience dimension reduction. However, in real networks, there often exist motifs [43, 44] or hypernetworks that describe rich and complex multivariate relationships [45]. So further research is needed to investigate the accuracy of resilience dimension reduction for motifs and hypernetworks.

Data availability statement

The original contributions presented in the study are included in the article/Supplementary material, further inquiries can be directed to the corresponding author.

Author contributions

ML: Methodology, Validation, Writing–original draft, Writing–review and editing. QG: Conceptualization, Methodology, Validation, Writing–original draft, Writing–review and editing. JL: Conceptualization, Methodology, Supervision, Writing–original draft, Writing–review and editing, Validation.

Funding

The author(s) declare that financial support was received for the research, authorship, and/or publication of this article. This work was partially supported by the National Natural Science Foundation of China (Grant Nos 72371150, 72171150), and the Fundamental Research Funds for the Central Universities: High-Quality Development of Digital Economy: An Investigation of Characteristics and Driving Strategies (Grant No. 2023110139).

Conflict of interest

The authors declare that the research was conducted in the absence of any commercial or financial relationships that could be construed as a potential conflict of interest.

Publisher's note

References

1. Gao JX, Barzel B, Barabási AL. Universal resilience patterns in complex networks. *Nature* (2016) 530:307–12. doi:10.1038/nature16948

2. Asllani M, Carletti T. Topological resilience in non-normal networked systems. *Phys Rev E* (2018) 97:042302. doi:10.1103/PhysRevE.97.042302

3. Dong GG, Fan JF, Shekhtman LM, Shai S, Du RJ, Tian LX, et al. Resilience of networks with community structure behaves as if under an external field. *Proc Natl Acad Sci USA* (2018) 115:6911–5. doi:10.1073/pnas.1801588115

4. De Domenico M, Arenas A. Modeling structure and resilience of the dark network. *Phys Rev E* (2017) 95:022313. doi:10.1103/PhysRevE.95.022313

5. Barzel B, Biham O. Quantifying the connectivity of a network: the network correlation function method. *Phys Rev E* (2009) 80:046104. doi:10.1103/PhysRevE.80.046104

6. Duan DL, Lv CC, Si SB, Wang Z, Li DQ, Gao JX, et al. Universal behavior of cascading failures in interdependent networks. *Proc Natl Acad Sci USA* (2019) 116:222452–7. doi:10.1073/pnas.1904421116

7. Cohen R, Erez K, ben-Avraham D, Havlin S. Resilience of the internet to random breakdowns. *Phys Rev L* (2000) 85(21):4626–8. doi:10.1103/PhysRevLett.85.4626

8. Holling CS. Resilience and stability of ecological systems. *Annu Rev Ecol S* (1973) 4(1):1–23. doi:10.1146/annurev.es.04.110173.000245

9. Albert R, Jeong H, Barabasi AL. Error and attack tolerance of complex networks. *Nature* (2000) 406(6794):378–82. doi:10.1038/35019019

10. Chaovalitwongse WA, Yuan Y, ZhangLiu QPJG. Special issue: innovative applications of big data and artificial intelligence. *Front Eng Manag* (2022) 9:517–9. doi:10.1007/s42524-022-0234-0

11. He YJ, Xu XK, Xiao J. Predicting higher order links in social interaction networks. *IEEE Trans Comput Soc Syst* (2024) 11(2):2796–806. doi:10.1109/TCSS.2023.3293075

12. Ni XL, Xiong F, Pan SR, Wu J, Wang L, Chen HS. Community preserving social recommendation with cyclic transfer learning. *ACM Trans Inf Syst* (2023) 42(3):1–36. doi:10.1145/3631115

13. Zhu HR, Xiong F, Chen HS, Xiong X, Wang L. Incorporating a triple graph neural network with multiple implicit feedback for social recommendation. *ACM Trans Web* (2024) 18(2):1–26. doi:10.1145/3580517

14. Liang JH, Hu YQ, Chen GR, Zhou TS. A universal indicator of critical state transitions in noisy complex networked systems. *Sci Rep* (2017) 7:42857. doi:10.1038/srep42857

15. Tu CY, Grilli J, Schuessler F, Suweis S. Collapse of resilience patterns in generalized Lotka-Volterra dynamics and beyond. *Phys Rev E* (2017) 95:062307. doi:10.1103/PhysRevE.95.062307

16. Lv CC, Si SB, Duan DL, Zhan RJ. Dynamical robustness of networks against multi-node attacked. *J Phys A Math Theor* (2017) 471:837–44. doi:10.1016/j.physa.2016.12.066

17. Laurence E, Doyon N, Dube LJ, Desrosiers P. Spectral dimension reduction of complex dynamical networks. *Phys Rev* (2019) 9:011042. doi:10.1103/PhysRevX.9.011042

18. Moutsinas G, Guo WS. Node-level resilience loss in dynamic complex networks. *Sci Rep* (2020) 10:3599. doi:10.1038/s41598-020-60501-9

19. Jiang JJ, Huang ZG, Seager TP, Lin W, Grebogi C, Hastings A, et al. Predicting tipping points in mutualistic networks through dimension reduction. *Proc Natl Acad Sci USA* (2018) 115:E639–E647. doi:10.1073/pnas.1714958115

20. Zhang HX, Liu XM, Wang Q, Zhang WD, Gao JX. Co-adaptation enhances the resilience of mutualistic networks. *J R Soc Interf* (2020) 17(168):20200236. doi:10.1098/rsif.2020.0236

21. Macy MW, Ma MQ, Tabin DR, Gao JX, Szymanski BK. Polarization and tipping points. *Proc Natl Acad Sci USA* (2021) 118(50):e2102144118. doi:10.1073/pnas.2102144118

22. Dong SJ, Gao XY, Mostafavi A, Gao JX, Gangwal U. Characterizing resilience of flood-disrupted dynamic transportation network through the lens of link reliability and stability. *Reliab Eng Syst Saf* (2023) 232:109071. doi:10.1016/j.ress.2022.109071

23. Ahn YY, Bagrow JP, Lehmann S. Link communities reveal multiscale complexity in networks. *Nature* (2010) 466:761–4. doi:10.1038/nature09182

24. Boccaletti S, Bianconi G, Criado R, del Genio CI, Gómez-Gardeñesi J, Romance M, et al. The structure and dynamics of multilayer networks. *Phys Rep* (2014) 544:1–122. doi:10.1016/j.physrep.2014.07.001

25. Peng ST, Shu XC, Ruan ZY, Huang ZG, Xuan Q. Classifying multiclass relationships between ASes using graph convolutional network. *Front Eng Manag* (2022) 9:653–67. doi:10.1007/s42524-022-0217-1

26. Xu MK, Radhakrishnan S, Kamarthi S, Jin XN. Resiliency of mutualistic supplier-manufacturer networks. *Sci Rep* (2019) 9:13559. doi:10.1038/s41598-019-49932-1

27. Meng FL, Fu GT, Farmani R, Sweetapple C, Butler D. Topological attributes of network resilience: a study in water distribution systems. *Water Res* (2018) 143:376–86. doi:10.1016/j.watres.2018.06.048

28. Costa LDF. Reinforcing the resilience of complex networks. *Phys Rev E* (2004) 69(6):066127–7. doi:10.1103/PhysRevE.69.066127

29. Li J, Wang Y, Zhong JL, Sun Y, Guo ZJ, Chen ZW, et al. Network resilience assessment and reinforcement strategy against cascading failure. *Chaos Soliton Fract* (2022) 160(C):112271. doi:10.1016/j.chaos.2022.112271

30. Sun HC, Liu XF, DuWu ZWY, Zhang HF, Xu XK. Heterogeneous influence of individuals' behavior on mask efficacy in gathering environments. *Front Eng Manag* (2022) 9:550–62. doi:10.1007/s42524-022-0193-5

31. Sakib N, Sun X, KongMasterson NC, Meng HD, Smith K, et al. Heterogeneous length-of-stay modeling of post-acute care residents in the nursing home with competing discharge dispositions. *Front Eng Manag* (2022) 9:577–91. doi:10.1007/s42524-022-0203-7

32. Barabási AL, Oltvai ZN. Network biology: understanding the cell's functional organization. *Nat Rev Genet* (2004) 5(2):101–13. doi:10.1038/nrg1272

33. Gleiser PM, Danon L. Community structure in jazz. *Adv Complex Syst* (2003) 06(04):565–73. doi:10.1142/S0219525903001067

34. Barzel B, Barabási AL. Universality in network dynamics. *Nat Phys* (2013) 9(10):673–81. doi:10.1038/NPHYS2741

35. Barzel B, Liu YY, Barabási AL. Constructing minimal models for complex system dynamics. *Nat Commun* (2015) 6:7186. doi:10.1038/ncomms8186

36. Davis C. The norm of the Schur product operation. *Numer Math* (1962) 4(1):343–4. doi:10.1007/BF01386329

37. Zhou B, Yan X, Lv Y, Xuan Q. Adversarial attacks on clustering coefficient in complex networks. *IEEE Trans Circuits Syst Express Briefs* (2024) 71(4):2199–203. doi:10.1109/TCSII.2023.3337896

38. Guo Q, Liang G, Fu JQ, Han JT, Liu JG. Roles of mixing patterns in the network reconstruction. *Phys Rev E* (2016) 94(5):052303–3. doi:10.1103/PhysRevE.94.052303

39. Holme P, Kim BJ. Growing scale-free networks with tunable clustering. *Phys Rev E* (2002) 65(2):026107. doi:10.1103/PhysRevE.65.026107

40. Ou Y, Guo Q, Liu JG. Identifying spreading influence nodes for social networks. *Front Eng Manag* (2022) 9:520–49. doi:10.1007/s42524-022-0190-8

41. Pastor-Satorras R, Castellano C, Van Mieghem P, Vespignani A. Epidemic processes in complex networks. *Rev Mod Phys* (2015) 87:925–79. doi:10.1103/RevModPhys.87.925

42. Holland JN, Deangelis DL, Bronstein JL. Population dynamics and mutualism: functional responses of benefits and costs. *Am Nat* (2002) 159:231–44. doi:10.1086/338510

43. Milo R, Shen-Orr S, Ltzkovitz S, Kashtan N, Chklovskii D, Alon U. Network motifs: simple building blocks of complex networks. *Science* (2002) 298(5594):824–7. doi:10.1126/science.298.5594.824

44. Xu MD, Zhang ZF, Xu XK. Research on spreading mechanism of false information in social networks by motif degree. *J Comput Res Dev* (2021) 58(7):1425–35. doi:10.7544/ISSN1000-1239.2021.20200806

45. Estrada E, Rodriguez-Velazquez JA. Subgraph centrality and clustering in complex hyper-networks. *Physica A* (2006) 364:581–94. doi:10.1016/j.physa.2005.12.002

frontiers | Frontiers in Physics

TYPE Original Research
PUBLISHED 19 June 2024
DOI 10.3389/fphy.2024.1410472

OPEN ACCESS

EDITED BY
Xuzhen Zhu,
Beijing University of Posts and Telecommunications (BUPT), China

REVIEWED BY
Xin Liu,
Google, United States
Wang Fengli,
Chinese Academy of Sciences (CAS), China
Wei Wang,
Chongqing Medical University, China
Shimin Cai,
University of Electronic Science and Technology of China, China

*CORRESPONDENCE
Yuexia Zhang,
zhangyuexia@bistu.edu.cn

RECEIVED 01 April 2024
ACCEPTED 29 May 2024
PUBLISHED 19 June 2024

CITATION
Wang X, Zhang Y and Zhang S (2024), Epidemic dynamics edge caching strategy for 6G networks.
Front. Phys. 12:1410472.
doi: 10.3389/fphy.2024.1410472

Epidemic dynamics edge caching strategy for 6G networks

Xinyi Wang[1], Yuexia Zhang[2]* and Siyu Zhang[2]

[1]Key Laboratory of Information and Communication Systems, Ministry of Information Industry, Beijing Information Science and Technology University, Beijing, China, [2]Key Laboratory of Modern Measurement and Control Technology, Ministry of Education, Beijing Information Science and Technology University, Beijing, China

By caching popular content on edge servers closer to users to respond to users' content requests in 6G networks, the transmission load of backhaul links can be reduced. However, the time-varying characteristics of content prevalence leads to the issue that the cache content may not match the user's needs, resulting in a decrease in cache success ratio. To solve these issues, we proposed a cache distribution strategy based on epidemic dynamics (CDSED) for 6G edge network. First, a 6G edge caching content model (6G ECCM) is constructed to establish the process of cache content propagation among users as an infectious disease propagation process, analyze the distribution of users' interest in cache content and obtain the cache content state probability prediction equation, and use the cache content state probability prediction equation to predict the cache content prevalence. Second, based on the predicted prevalence results, a prevalence predictive genetic-annealing cache content algorithm (PGAC) is proposed with the optimization objective of maximizing the cache success ratio. The algorithm designs the selection function of the traditional genetic algorithm as a simulated annealing selection function based on the cache content success ratio, which avoids the defect of the genetic algorithm that converges to the locally optimum cache strategy too early and enhances the cache success ratio. Finally, the optimum cache content decision is solved by iterative alternation. Simulation results demonstrate that CDSED strategy can enhance cache success ratio than the LRU strategy, the LFU strategy, and the MPC strategy.

KEYWORDS

6G edge caching, epidemic dynamics, content caching, content prevalence, genetic simulated annealing algorithm

1 Introduction

6G mobile communication network will support a variety of applications, for instance immersive cloud augmented reality, autonomous driving, holographic communication, smart manufacturing and other new applications [1–3]. These new applications bring convenience to people's lives, but also inevitably increase mobile data traffic. And when popular services are repeatedly requested in a short period of time, 6G cloud server backhaul is facing tremendous pressure [4–6]. In order to fulfill the application requirements and reduce the pressure on the cloud server, the edge caching technology allows for service content caching on edge servers, enabling users to retrieve content from these edge servers to meet their repetitive requests, so as to cope with the swift expansion of 6G wireless service load and significantly reduce the transmission load of 6G cloud server [7–9]. Therefore, the research of edge caching technology is of paramount importance for 6G.

Compared with the large-scale user request content, the cache resources of the edge network are limited. This means that only a small amount of popular content requested by users can be pre-cached on the edge of the network. However, a plentiful amount of content is generated at every moment in real life. How to find popular content requested by users in a massive content repository is a very challenging problem. At present, most caching strategies adopt rule-based content caching methods, such as Least Recently Used (LRU) [10] and Least Frequently Used (LFU) [11]. Although these strategies achieve real-time updates of cache content at the edge network, they do not fully exploit the content request patterns of users at different time points, leading to an inability to accurately perceive the prevalence patterns of different content at future moments, making it difficult to achieve accurate prediction of content prevalence.

The fundamental purpose of edge caching is to decide what content to cache in edge servers [12,13], and prediction of content prevalence is a major issue in existing caching research. Many researchers have explored the field of content prevalence prediction and proposed various caching strategies. Wu et al.[14] introduced a collaborative caching strategy based on a social-aware graph to minimize content download latency, caching the most popular content based on weighted content prevalence. Sun et al.[15] proposed an intelligent gateway-assisted edge caching strategy, using a predictive algorithm based on heterogeneous information networks to anticipate end-user preferences for new content files. Zhu et al.[16] studied multi-layer collaborative edge caching in integrated space-ground networks, formulating a content placement problem based on content prevalence to minimize users' average content retrieval delay. Wang et al.[17] proposed a vehicle-to-vehicle collaborative caching strategy based on content request prediction, using historical content request information and a reinforcement learning method to obtain optimum caching decisions. Ayenew et al.[18] proposed a collaborative demand-aware caching strategy based on the separable allocation problem, solving the cache success ratio maximization problem using recursive enumeration. Tang et al.[19] modeled user request behavior and user preferences using MDP and Zipf distribution, and proposed a new reinforcement learning-based algorithm to reveal file prevalence and user preferences. Zhu et al.[20] developed an AoI-based time attention graph neural network to maximize the accuracy of user interest prediction. Liu et al.[21] designed a context-aware prevalence learning algorithm to adapt to the changing trend of content prevalence. However, most of the aforementioned caching strategies assume that content prevalence follows a static distribution. In actual scenarios, content prevalence is time-varying and usually not known in advance, as user interest in a cache content can spread through word-of-mouth in social networks, leading to the time-varying nature of content prevalence in the entire network [22]. Therefore, static prevalence distribution models cannot accurately describe the dynamic characteristics of content prevalence.

Users' interests are constantly changing, and new content is constantly being generated [23,24]. Thus, some researchers have proposed learning-based caching algorithms to adapt to the changing prevalence of content. Zhang et al.[25] designed a learning-based edge collaborative caching scheme, using a temporal convolutional network to predict the prevalence of future content. Mehrizi et al.[26] developed a Bayesian dynamic model of content requests, which can accurately predict prevalence using spatiotemporal correlation. Nguyen et al.[27] proposed a caching strategy based on a hierarchical deep learning architecture to maximize cache success ratio by predicting networks and user environments. Tao et al.[28] proposed a prevalence prediction strategy based on a content feature-based content request probability model, in which model parameters are learned through Bayesian learning. Li et al.[29] proposed a similarity-based content popularity prediction method to predict the popularity of new content by introducing a dynamic content directory. Jiang et al.[30] proposed a method to guarantee the accuracy of prevalence prediction by predicting user locations and analyzing request data of specific users in the next time period. Gao et al.[31] designed a probability-based content placement and replacement strategy, aiming to increase cache success ratio under changing instantaneous content prevalence and converge to target content cache probability under constant instantaneous content prevalence. Fan et al.[32] proposed an evolving learning-based content caching strategy, which can adaptively learn the changing prevalence of content over time and determine which content should be replaced when the cache is full. A caching scheme based on private federated learning is proposed [33], which uses a federated learning framework and a pseudo-rating matrix to collect statistical features of user groups by predicting the prevalence of content. Although the above-mentioned research considers the time-varying characteristics of content prevalence, they rarely consider the impact of caching strategies on user content propagation. In the edge network with limited caching resources, caching affects the propagation of content among users, thereby affecting the prevalence of content. Moreover, the above-mentioned learning-based prevalence prediction algorithms rely on large amounts of historical data and trained models, resulting in high training complexity and are not suitable for new popular content.

In summary, although many studies have shown that learning-based edge caching algorithms significantly improve cache performance in predicting content popularity, in practical scenarios, user interests are constantly changing and new content continues to emerge. The above-mentioned algorithms rely heavily on a large amount of historical data, which mainly reflects past user behaviors and interests. However, these data may not capture users' immediate interest changes in new content, making them unsuitable for new popular content. Additionally, the allocation of cache resources can affect the dissemination of content among users, thereby influencing content popularity. Therefore, optimizing cache performance based on popularity prediction in scenarios where content popularity is constantly changing and typically unknown has become a critical issue that needs to be addressed.

In view of the above problems, this paper proposes a cache distribution strategy based on epidemic dynamics for 6G edge network. This strategy studies the influence of cache content propagation process and content prevalence based on the epidemic model in 6G edge network. According to the prevalence prediction results of the content, a genetic simulated annealing cache content algorithm is proposed to provide the optimum cache strategy for the 6G edge caching network to maximize the cache success ratio, thereby improving the cache performance.

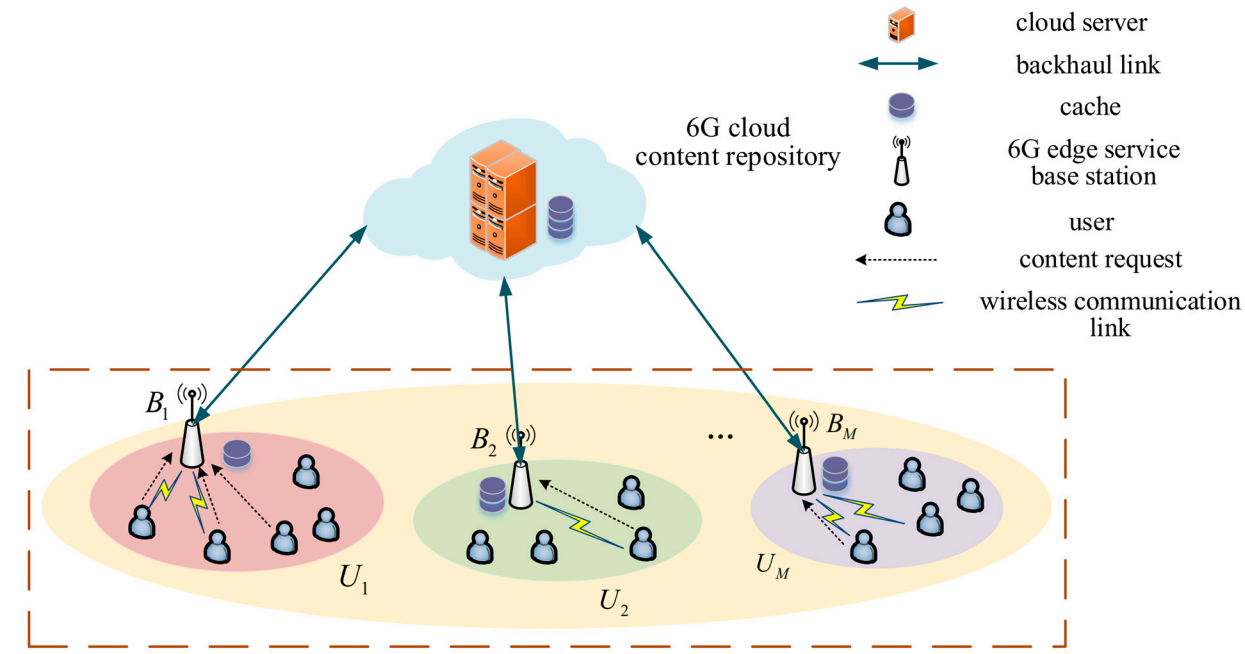

FIGURE 1
6G edge caching network.

The primary contributions of this paper can be outlined as follows:

1) The 6G ECCM is established, and the user's interest state distribution of the cache content is analyzed and the user's cache content state probability prediction equation is obtained, and the content prevalence prediction is realized from the perspective of the user individual.
2) Then this study proposed a prevalence predictive genetic-annealing cache content algorithm, which redesigned the selection function based on the traditional genetic algorithm and incorporated simulated annealing selection, using the cache success ratio, into chromosome selection, thereby improving the cache success ratio.
3) In a scenario involving a single edge service base station network, an experiment was designed to compare the CDSED, LFU, LRU, and MPC strategies, validating the cache optimization effect of the CDSED strategy.

The rest of this paper is organized as follows: In Section 2, the System Model is introduced. In Section 3, Section 4, the optimization problem and PGAC algorithm are proposed. In Section 5, the performance of the CDSED strategy is evaluated, and the simulation results and analysis are given. In Section 6, the conclusion of this paper is proposed.

2 System model

2.1 6G edge caching network

In this paper, we construct a 6G edge caching network, as shown in Figure 1, which is composed of a 6G cloud content repository, M edge service base stations and N users. The 6G cloud content repository consists of cloud servers that store all the cache contents. Assuming that there are K contents to be cached within the edge service base stations, the set of cache contents can be indicated as $f = \{f_1, f_2, \ldots, f_k, \ldots, f_K\}$, f_k is expressed as the kth cache content with size C_k bit. The set of edge service base stations is indicated by set $B = \{B_1, B_2, \ldots, B_m, \ldots, B_M\}$. Each edge service base station has a certain storage capacity. However, it can only store content that satisfies the needs of some users because of the limitation of the cache capacity of the base station. The set of cache resources of the edge service base station is represented by set $C_{base} = \{c^1_{base}, c^2_{base}, \ldots, c^m_{base}, \ldots, c^M_{base}\}$, wherein c^m_{base} represents the cache capacity of the edge service base station B_m. Considering the different prevalence of content by users under the service area of different edge service base stations, edge service base stations adopt different caching strategies. The set of the edge service base station caching strategies is $S = \{S_1, S_2, \ldots, S_m, \ldots, S_M\}$, S_m is the caching strategy of the edge service base station B_m. There are a total of K contents to be cached, which can be denoted as $S_m = \{s_{m,1}, s_{m,2}, \ldots s_{m,k}, \ldots, s_{m,K}\}$, where $s_{m,k}$ indicates the probability that the edge service base station B_m will cache the kth content, $s_{m,k} = 1$ indicates that the cache content f_k is being cached by the edge service base station B_m, and $s_{m,k} = 0$ denotes that the edge service base station B_m does not have the cache content f_k. Therefore, the set of caching strategies S of the edge service base station is a $M \times K$ matrix, i.e., $S = (s_{m,k})_{M \times K}$.

Since the edge service base station has a certain service range, all users in the 6G edge caching network are divided into M user subsets, denoted as $U = \{U_1, U_2, \ldots, U_m, \ldots, U_M\}$. This means that all users under the service range of each edge service base station are categorized into one user set, and each user can only communicate

with the edge service base station within the user set in which it is located, where U_m indicates the set of users who under the service area of the edge service base station B_M, $U_m = \{u_m^1, u_m^2, \ldots, u_m^n, \ldots, u_m^{N_m}\}$, and N_m is the sum total of users under the service area of the edge service base station B_M. The locations of all users and edge service base stations obey a Poisson distribution with distribution density coefficients λ_α and λ_β.

All 6G edge service base stations can serve as edge servers in the 6G edge caching network. These base stations caching content from the cloud server based on prevalence prediction. Users is curious about the cache content, they will first expresses its demand by sending a content request to the 6G edge service base station. If the requested cache content is already cached, it will be transmitted directly to the user through the wireless communication link, completing the download process. If the 6G edge service base station has not cache the requested content, it must communicate with the 6G cloud content repository through the backhaul link and download the requested content from the 6G cloud content repository.

2.2 6G edge caching content model

An edge service base station caching a particular piece of content may affect other users in the neighboring area, leading them to download the same content. This content download can spread among the user community, creating a process similar to the spread of an epidemic over time [34,35]. Therefore, the process of spreading cache content among users can be modeled by the process of spreading epidemics.

Considering that users who receive content do not immediately forward it to other users, but rather need some time to contemplate, understand, or decide whether to forward it, which is closer to the actual propagation process among users, this paper uses the SEIRD model to simulate the content propagation process among users and defines the user's propagation state about the cache content f_k as follows:

S: the user does not have access to information about the cache content f_k.

E: Users are influenced by cache content commended by other users and may be curious about that cache content f_k. At the same time, users send requests to the edge service base station and wait to obtain the cache content. Users may also choose to ignore commendations from other users regarding cache content.

I: users are curious about cache content f_k and have successfully obtained content f_k from the service base station.

D: the user downloads the cache content f_k from the edge service base station B_M and commends it to the neighboring users.

R: the user are not curious about cache content f_k or users lose interest in cache content f_k after acquiring it. They can neither influence nor be influenced by others, and they do not actively commend the cache content f_k to other users.

This study supposed that the user is in state *S* at the initial moment, and they reaches out to the user in state *D* through the social network, it becomes in state *E*. State *E* user does next with the cache content f_k is divided into two scenarios: one is that he is not curious about the cache content f_k and transitions directly from the *E* state to the *R* state, and the other scenario is that it is curious about the cache content f_k and stays in the *E* state. The state is transformed from *E* to *I* when the user acquires f_k. Considering the selfishness of the user, after acquiring the cache content f_k, the user may choose not to commend the content to other users, or it may transform to *D* state to give the cache content to other users by word-of-mouth. Finally, the user may lose their interest in the cache content after acquiring it, and the user state is transformed from *I* or *D* state *R* state.

By analogizing this state transfer process with the infectious disease process, a 6G ECCM is established, as shown in Figure 2. In this paper, we use $S_m^k(t), E_m^k(t), I_m^k(t), D_m^k(t)$, and $R_m^k(t)$ to denote the count of users in the above five states in the service area of edge service base station B_m at time t Assuming that the sum total of users in the entire edge network and the sum total of users in the service area of each edge service base station are kept stable, and the users can only transition from one state to another in each unit of time, the propagation state transfer equation for content f_k can be established as:

$$\frac{dS_m^k(t)}{dt} = -\gamma_{m,k} S_m^k(t) \frac{I_m^k(t)}{N_m} \tag{1}$$

$$\frac{dE_m^k(t)}{dt} = \gamma_{m,k} S_m^k(t) \frac{I_m^k(t)}{N_m} - \left(\chi_{m,k} + \eta_{m,k}\right) E_m^k(t) \tag{2}$$

$$\frac{dI_m^k(t)}{dt} = \eta_{m,k} E_m^k(t) - \left(\delta_{m,k} + \omega_{m,k}\right) I_m^k(t) \tag{3}$$

$$\frac{dD_m^k(t)}{dt} = \delta_{m,k} I_m^k(t) - \xi_{m,k} D_m^k(t) \tag{4}$$

$$\frac{dR_m^k(t)}{dt} = \xi_{m,k} D_m^k(t) + \chi_{m,k} E_m^k(t) + \omega_{m,k} I_m^k(t) \tag{5}$$

$\gamma_{m,k}$ is the influence rate, the probability that user u_m^n successfully receives commendations from other users for cache content f_k through the social network, which can be formulated as:

$$\gamma_{m,k} = \varsigma \phi_m \tag{6}$$

where ς is the probability of establishing a social relationship between user u_m^n and other users under the range of the same edge service base station; $\phi_m = \sum_{n=1}^{N_m} \phi_m^n$, ϕ_m^n is the probability of the existence of other users in the neighboring area of user u_m^n, $\phi_m^n = 1 - e^{-\lambda_\alpha \pi R_{m,n}^2}$, $R_{m,n}$ indicates the physical distance between user u_m^n and other users to establish communication.

$\eta_{m,k}$ is the service rate, the probability that a user in state *E* can successfully acquire the cache content f_k from the edge service base station. The channel capacity [36] between edge serving base station B_m and user u_m^n is calculated as:

$$C_m^n = W_m \log_2\left(1 + \frac{P_m h_m^n}{N_0}\right) \tag{7}$$

where W_m is the channel bandwidth, P_m is the transmission power of the edge service base station B_m, and h_m^n is defined as the channel gain of the wireless link between the edge service base station B_m and the user. $h_m^n = \sigma_0 R_{m,n}^{-\lambda}$, σ_0 is the path loss when the distance is 1 m; λ is the path loss index; and N_0 is the Gaussian channel noise power.

The ability of a user to access the cache content from the edge service base station is affected by the backhaul link capacity between the edge service base station and the cloud content repository, the channel capacity between the user and the edge service base station,

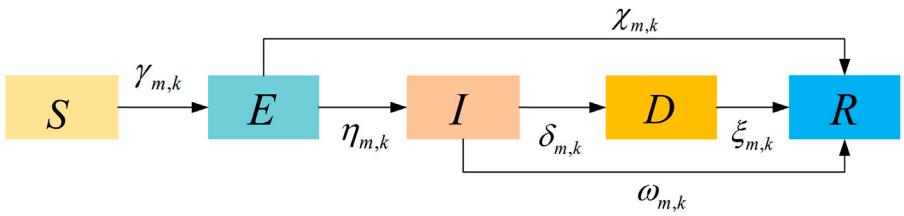

FIGURE 2
6G edge caching content model.

and the magnitude of the cache content, and the total count of users able to access the content from the edge service base station needs to satisfy a certain requirement, and thus the service rate can be calculated as:

$$\eta_{m,k}^{n} = p\left(\tau_{m,k}^{n} \le \tau_{m,n,k}^{'}\right) \tag{8}$$

where $\tau_{m,k}^{n}$ is the magnitude of the content that can be transmitted over the wireless communication link between the user and the base station. It can be expressed as:

$$\tau_{m,k}^{n} = \frac{C_m^n}{C_k} = \frac{W_m \log_2\left(1 + \frac{p_m h_m^n}{N_0}\right)}{C_k} \tag{9}$$

Then we substitute Eq. 9 into Eq. 8 can be derived:

$$p\left(\tau_{m,k}^{n} < \tau_{m,n,k}^{'}\right) = p\left(R_{m,n} \ge \left(\frac{N_0\left(2^{\frac{\tau_{m,k}^{'} C_k}{W_m}} - 1\right)}{P_m \sigma_0}\right)^{\frac{-1}{\lambda}}\right) \tag{10}$$

The location of the user obeys the Poisson distribution, and according to the probability calculation formula of Poisson distribution, Eq. 10 can be formulated as:

$$\eta_{m,k} = p\left(\tau_{m,k} < \tau_{m,k}^{'}\right) = e^{-\lambda_\alpha F} \tag{11}$$

$$F = \frac{N_0^{\frac{-1}{\lambda}}\left(2^{\frac{\tau_{m,k}^{'} C_k}{W_m}} - 1\right)^{\frac{-1}{\lambda}}}{\left(P_m \sigma_0\right)^{\frac{-1}{\lambda}}} \tag{12}$$

$\tau_{m,k}^{'}$ is the maximum amount of content that can be supported for transmission from the user to the base station. This value takes into account the transmission limitations from the user to the base station as well as the limitations of the backhaul link from the base station to the cloud content repository, $\tau_{m,n,k}^{'} = \frac{C_{m,\max}^{n} + C_{core}^{m}}{C_k}$, where $C_{m,\max}^{n}$ denotes the maximum channel capacity for transmission between user u_m^n and edge service base station B_m; C_{core}^{m} is the upper limit of the backhaul link capacity from the edge service base station to the cloud content repository.

Substituting $\tau_{m,k}^{'}$ into Eqs 11, 12, we get:

$$F = \frac{N_0^{\frac{-1}{\lambda}}\left(2^{\frac{C_{m,\max}^{n} + C_{core}^{m}}{W_m}} - 1\right)^{\frac{-1}{\lambda}}}{\left(P_m \sigma_0\right)^{\frac{-1}{\lambda}}} \tag{13}$$

$\delta_{m,k}$ is the commendation rate, the probability that a user will commend the cache content f_k to other users.

$\chi_{m,k}$ is refusal rate, the probability that user is not favor of f_k.

$\omega_{m,k}$ and $\xi_{m,k}$ are loss rate, the probability that user loses interest in f_k after acquiring it.

It is difficult to directly solve the specific expressions for $S_m^k(t)$, $E_m^k(t)$, $I_m^k(t)$, $D_m^k(t)$, and $R_m^k(t)$ in the state transfer differential equations obtained by bringing Eqs 6–13 into Eqs 1–5. Therefore, we defined $p_{m,n,k}^{S}(t)$, $p_{m,n,k}^{E}(t)$, $p_{m,n,k}^{D}(t)$, $p_{m,n,k}^{I}(t)$, and $p_{m,n,k}^{R}(t)$ as the probabilities that user u_m^n is in the states S, E, I, D, R at moment t. We can get the probability that the u_m^n is in each propagation state at the moment $t + 1$ based on the Markov chain method as follow:

$$p_{m,n,k}^{S}(t+1) = \left(1 - \gamma_{m,k}^{n} p_{m,n,k}^{I}(t)\right) p_{m,n,k}^{S}(t) \tag{14}$$

$$p_{m,n,k}^{E}(t+1) = \gamma_{m,k}^{n} p_{m,n,k}^{I}(t) p_{m,n,k}^{S}(t) + \left(1 - \eta_{m,k}^{n} - \chi_{m,k}^{n}\right) p_{m,n,k}^{E}(t) \tag{15}$$

$$p_{m,n,k}^{I}(t+1) = \eta_{m,k}^{n} p_{m,n,k}^{E}(t) + \left(1 - \delta_{m,k}^{n} - \omega_{m,k}^{n}\right) p_{m,n,k}^{I}(t) \tag{16}$$

$$p_{m,n,k}^{D}(t+1) = \delta_{m,k} p_{m,n,k}^{I}(t) + (1 - \xi_{m,k}) p_{m,n,k}^{D}(t) \tag{17}$$

$$p_{m,n,k}^{R}(t+1) = \chi_{m,k}^{n} p_{m,n,k}^{E}(t) + \xi_{m,k}^{n} p_{m,n,k}^{D}(t) + \omega_{m,k}^{n} p_{m,n,k}^{I}(t) + p_{m,n,k}^{R}(t) \tag{18}$$

The right side of Eq. 14 represents the probability that u_m^n will remain in state S at time $t + 1$.

The first part of the right-hand side in Eq. 15 indicates the probability that the user is in the state E at the moment $t + 1$ after accessing the cache content; The second part signifies the probability of the user remaining in state E from moment t to the moment $t + 1$.

Similarly, the first part of Eq. 16 denotes the probability that the user u_m^n is in the state E at the moment t and succeeds in obtaining the content and thus transitions to the state I at the moment $t + 1$; the second term indicates the probability that the user u_m^n exists at the moment t with the probability of $p_{m,n,k}^{I}$, and then remains in this state up to the moment $t + 1$ with the probability $(1 - \delta_{m,k}^{n} - \omega_{m,k}^{n})$.

The first part of Eq. 17 is the probability that the user turns into D state with the probability of $\delta_{m,k}$ and commend the content to the neighboring users; the second term represents that the user keeps the original state unchanged with probability $1 - \xi_{m,k}$ at the moment $t + 1$.

The first three parts on the right-hand side of Eq. 18 are the probabilities that the user is known at moment t to turn into state R by moment $t + 1$; and the fourth term represents the probability that the user keeps the state R unchanged from moment t to moment $t + 1$. $\chi_{m,k}^{n}$ denotes the probability that the user u_m^n will not be interested by the commendation of any of its other users (neighbors or friends) the cache content f_k, which can be articulated as:

$$\chi_{m,k}^{n}=\prod_{j=1}^{N_m}\left[1-\gamma_{m,k}p_{m,j,k}^{D}(t)\left(1-\left(1-\frac{\varpi_{jn}}{\sum_{j}\varpi_{jn}}\right)^{\kappa_j}\right)\right] \tag{19}$$

where ϖ_{jn} denotes the closeness between user u_m^n and u_m^j, κ_j denotes the total count of times user u_m^j forwarded the commended cache content of interest.

Eqs 14–19 are organized into matrix form, which leads to the form of the equation expressed as follows:

$$\begin{bmatrix} p_{m,n,k}^{S}(t+1)\\ p_{m,n,k}^{E}(t+1)\\ p_{m,n,k}^{I}(t+1)\\ p_{m,n,k}^{D}(t+1)\\ p_{m,n,k}^{R}(t+1)\end{bmatrix}=\begin{bmatrix} 1-\gamma_{m,k}^{n}p_{n,k}^{I}(t) & 0 & 0 & 0 & 0\\ \gamma_{m,k}^{n}p_{n,k}^{I}(t) & 1-\eta_{m,k}^{n}-\chi_{m,k}^{n} & 0 & 0 & 0\\ 0 & \eta_{m,k}^{n} & 1-\delta_{m,k}^{n}-\omega_{m,k}^{n} & 0 & 0\\ 0 & 0 & \delta_{m,k}^{n} & 1-\xi_{m,k}^{n} & 0\\ 0 & \chi_{m,k}^{n} & \omega_{m,k}^{n} & \xi_{m,k}^{n} & 1\end{bmatrix}\times\begin{bmatrix} p_{m,n,k}^{S}(t)\\ p_{m,n,k}^{E}(t)\\ p_{m,n,k}^{I}(t)\\ p_{m,n,k}^{D}(t)\\ p_{m,n,k}^{R}(t)\end{bmatrix} \tag{20}$$

The propagation state probability transition matrix $\mathrm{P}_{m,k}^{n}(t)$ in this paper is defined as:

$$\mathrm{P}_{m,k}^{n}(t)=\begin{bmatrix} 1-\gamma_{m,k}^{n}p_{n,k}^{I}(t) & 0 & 0 & 0 & 0\\ \gamma_{m,k}^{n}p_{n,k}^{I}(t) & 1-\eta_{m,k}^{n}-\chi_{m,k}^{n} & 0 & 0 & 0\\ 0 & \eta_{m,k}^{n} & 1-\delta_{m,k}^{n}-\omega_{m,k}^{n} & 0 & 0\\ 0 & 0 & \delta_{m,k}^{n} & 1-\xi_{m,k}^{n} & 0\\ 0 & \chi_{m,k}^{n} & \omega_{m,k}^{n} & \xi_{m,k}^{n} & 1\end{bmatrix} \tag{21}$$

In accordance with the state transition matrix in Eq. 21, the user cache content state probability prediction equation of content f_k can be obtained as follows:

$$p_{m,k}^{S}(t+1)=\sum_{n=1}^{N_m}\mathrm{P}_{m,k}^{n}(t)\times p_{m,n,k}^{S}(t) \tag{22}$$

$$p_{m,k}^{E}(t+1)=\sum_{n=1}^{N_m}\mathrm{P}_{m,k}^{n}(t)\times p_{m,n,k}^{E}(t) \tag{23}$$

$$p_{m,k}^{I}(t+1)=\sum_{n=1}^{N_m}\mathrm{P}_{m,k}^{n}(t)\times p_{m,n,k}^{I}(t) \tag{24}$$

$$p_{m,k}^{D}(t+1)=\sum_{n=1}^{N_m}\mathrm{P}_{m,k}^{n}(t)\times p_{m,n,k}^{D}(t) \tag{25}$$

$$p_{m,k}^{R}(t+1)=\sum_{n=1}^{N_m}\mathrm{P}_{m,k}^{n}(t)\times p_{m,n,k}^{R}(t) \tag{26}$$

Therefore, the total count of users in the *S*, *E*, *I*, *D*, and *R* states at time *t*:

$$S_m^k(t)=N_m\sum_{n=1}^{N_m}p_{m,n,k}^{S}(t) \tag{27}$$

$$E_m^k(t)=N_m\sum_{n=1}^{N_m}p_{m,n,k}^{E}(t) \tag{28}$$

$$I_m^k(t)=N_m\sum_{n=1}^{N_m}p_{m,n,k}^{I}(t) \tag{29}$$

$$D_m^k(t)=N_m\sum_{n=1}^{N_m}p_{m,n,k}^{D}(t) \tag{30}$$

$$R_m^k(t)=N_m\sum_{n=1}^{N_m}p_{m,n,k}^{R}(t) \tag{31}$$

u_m^n in state *E* and *I* can request to download cache content f_k from the edge service base station, i.e., the caching strategy at the edge service base station is influenced by $E_m^k(t)$, $\eta_{m,k}$, $I_m^k(t)$ and $\delta_{m,k}$. Therefore the prevalence for cache content f_k at moment t can be described as:

$$J_{m,k}(t)=E_m^k(t)\times\eta_{m,k}+I_m^k(t)\times\delta_{m,k} \tag{32}$$

3 Optimization objective

In this paper, we concentrate on caching decisions for edge service base stations, without considering the case where the user acquires the cache content directly from the cloud server. The caching strategy needs to maximize the user's demand, i.e., maximize the cache success ratio. However, with the increasing demand for cache content in the 6G edge caching network, the edge service base station faces the challenge that the limited cache capacity cannot meet all users' demand, so this paper takes maximizing the cache success ratio as the optimization objective. Define cache success ratio $P_{cache,hit}^{k}$ as the probability that the demand for content f_k by all users in the entire edge caching network is satisfied, and $P_{cache,hit}^{k}$ can be articulated as:

$$P_{cache,hit}^{k}=\frac{\sum_{m=1}^{M}\left(E_m^k(t)\times\eta_{m,k}+I_m^k(t)\times\delta_{m,k}\right)\times s_{m,k}}{\sum_{m=1}^{M}\left(1-\chi_{m,k}\right)\times E_m^k(t)} \tag{33}$$

where $\sum_{m=1}^{M}(1-\chi_{m,k})\times E_m^k(t)$ indicates the total amount of user demand for cache content f_k in the entire 6G edge caching network, i.e., the sum total of times all users are curious about cache content f_k and issued access requests; $\sum_{m=1}^{M}(E_m^k(t)\times\eta_{m,k}+I_m^k(t)\times\delta_{m,k})\times s_{m,k}$ denotes the caching scheme for content f_k. According to the cache success ratio definition in Eq. 33, the specific optimization problem expression is:

$$\begin{aligned}&\max_{S}\sum_{k=1}^{K}P_{cache,hit}^{k}\\ &s.t.C1:\ c_{base}^{m}\le\sum_{k=1}^{K}C_k,\ \forall m\in M\\ &C2:\ \sum_{k=1}^{K}s_{m,k}C_k\le c_{base}^{m},\ \forall m\in M\\ &C3:\ s_{m,k}\in\{0,1\},\ \forall m\in M\end{aligned} \tag{34}$$

where constraint *C*1 indicates that it is not possible to cache all the cache content in the 6G cloud content repository on the edge service base station; *C*2 satisfies the cache capacity limitation of the edge service base station, and the total magnitude of the cache content cached in the edge service base station must not exceed the magnitude of the caching capacity of the edge service base station; *C*3 represents the caching decision of the cache content by the edge service base station, and $s_{m,k}$ is a Boolean variable taking the value of 0 or 1.

4 Prevalence predictive genetic-annealing cache content algorithm

The search space in the cache optimization problem in Eq. 34 contains discrete variables and it is an integer linear programming (ILP) problem. This type of problem is also an NP-hard problem, which is difficult to solve directly in general. Heuristic algorithms such as genetic algorithms and simulated annealing algorithms have convenient properties in solving optimization problems containing discrete variables [37,38]. Therefore, this paper proposes a PGAC algorithm, which combines the genetic algorithm and simulated annealing algorithm to solve the optimum caching scheme.

4.1 Chromosomal gene coding

Chromosome: a chromosome corresponds to an individual object in a solution in an optimization problem, i.e., a possible solution. In this paper, a chromosome is represented as a possible caching solution. Each chromosome is a solution consisting of genes. In this problem, the length of the chromosome is usually M, because there are M edge service base stations in this paper, and each gene represents the caching decision state of the corresponding edge service base station.

Genes: Each gene in the chromosome represents the caching status of the corresponding edge service base station, i.e., whether or not the content is cached. Each gene is encoded in binary. 0 represents that the edge service base station has not cached the content; 1 represents that the edge service base station has cached the content. In the proposed 6G edge cache propagation model, there are a total of K cache contents, and each edge service base station needs to make a decision on these K cache contents. That is each content can choose whether to be cached within the edge service base station or not.

The chromosomes and genes are expressed in a matrix form, where each row represents a chromosome and each column represents a gene. In the problem of cache allocation using genetic algorithm in edge caching network, define a matrix of $M \times K$, where M is the total count of edge service base stations and K is the total count of cache contents as represented below:

$$I = \begin{bmatrix} s_{1,1} & s_{1,2}, \ldots, & s_{1,k}, \ldots, & s_{1,K} \\ s_{2,1} & s_{2,2}, \ldots, & s_{2,k}, \ldots, & s_{2,K} \\ \vdots & \vdots & \vdots & \vdots \\ s_{M,1} & s_{M,2}, \ldots, & s_{M,k}, \ldots, & s_{M,K} \end{bmatrix} \tag{35}$$

Each element of the matrix Eq. 35 may be 0 or 1 indicating whether the corresponding edge service base station caches the corresponding cache content. Through this matrix representation, a chromosome corresponds to a row of the matrix and each gene corresponds to an element of the matrix. A genetic algorithm is used to generate a new chromosome by performing crossover, mutation, and other operations on this matrix.

4.2 The design of the fitness function

The optimization problem Eq. 34 is a maximization problem. Therefore, for the chromosome in this paper, a larger fitness value indicates a better solution, suggesting that the solution represented by this chromosome is closer to the optimum solution. The fitness function is represented as follows:

$$fit = \sum_{k=1}^{K} P^{k}_{cache,hit} \tag{36}$$

A higher fitness value corresponds to a greater cache success ratio, indicating that the corresponding caching strategy is more optimum.

4.3 Selection, crossover and mutation

Crossover: A single point crossover is used to combine two separate chromosomes to generate a new chromosome in this paper, and the new chromosome is generated by exchanging some genes of the selected chromosome based on randomly generated crossover sites, with an adaptive crossover probability p_c:

$$p_c = \begin{cases} \dfrac{k_1 (fit_{\max} - fit)}{fit_{\max} - fit_{\min}}, & fit < fit_{avg} \\ p_c' & fit \geq fit_{avg} \end{cases} \tag{37}$$

where $fit_{\max}$, $fit_{\min}$ and fit_{avg} are defined as the maximum fitness value, the minimum fitness value and the average fitness value of all chromosomes in the population, respectively; k_1 is a constant in the interval [0,1]; p_c' takes the value of a fixed constant in general.

Mutation: The chromosomes in the population are mutated with an adaptive mutation probability p_e, where p_e can be represented as:

$$p_e = \begin{cases} \dfrac{k_2 (fit_{\max} - fit)}{fit_{\max} - fit_{\min}}, & fit < fit_{avg} \\ p_e' & fit \geq fit_{avg} \end{cases} \tag{38}$$

where k_2 is a constant in the interval [0,1]; p_e' takes the value of a fixed constant in general.

In order to enhance the local search capability of the genetic algorithm, this paper introduces a simulated annealing selection method instead of the roulette algorithm for chromosome selection. The simulated annealing selection algorithm utilizes the Metropolis criterion [39] to select chromosomes by first randomly selecting chromosome I_1 from the initialized chromosome population P_1 generated after the chromosome correction step, which has a fitness value of fit (I_1). Then chromosome I_2 is randomly selected from the newly generated chromosome population P_2 generated after the crossover and mutation step, which has a fitness value of fit (I_2). Setting the temperature of the simulated annealing method as T, the probability of I_2 being selected into the new chromosome result set P_3 with probability P:

$$P = \begin{cases} e^{\frac{fit(I_1) - fit(I_2)}{T}}, & fit(I_1) \geq fit(I_2) \\ 1 & fit(I_1) < fit(I_2) \end{cases} \tag{39}$$

If the fitness of chromosome I_2 in population P_2 is greater than that of chromosome I_1 in population P_1, I_2 will definitely be selected to be placed in the new result set P_3; However, if the fitness of chromosome I_1 is greater than that of chromosome I_2, I_2 still has a probability $e^{\frac{fit(I_1) - fit(I_2)}{T}}$ of being selected to be placed in result set P_3.

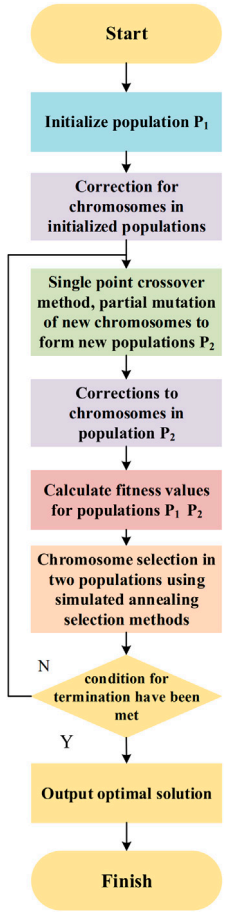

FIGURE 3
Flowchart of the genetic simulated annealing algorithm.

Chromosomes that are not placed in P_3 will be returned to their original chromosome population.

4.4 The Chromosome Check method

The Chromosome Check method is used to check if all the chromosomes are within the constraints and if there are gene points that are not within the constraints, this check method will correct all the relevant chromosome gene points based on the cached parameters of the service base station. This step will be used after all the steps where new chromosomes need to be generated to ensure that the newly generated chromosomes meet the constraints. Chromosome correction is the core of the chromosome test method.

Chromosome correction: the correction of chromosomes that do not meet the constraints. The content of $s_{m,k} = 1$ is sorted from largest to smallest according to the cache value $cac_{m,k}^{value}$ while $\sum_{k=1}^{K} s_{m,k} C_k > c_{base}^{m}$. Then the content is cached sequentially according to the sorting order, and the corresponding chromosome gene is 1, until it approaches but does not exceed the cache capacity c_{base}^{m} of the edge service base station. The remaining content is then changed from state $s_{m,k} = 1$ to $s_{m,k} = 0$, corresponding to the chromosome gene being changed to 0. The cache value is expressed by the following equation:

$$cache_{m,k}^{value} = J_{m,k}(t) \tag{40}$$

Figure 3 shows the general flowchart of the genetic simulated annealing algorithm. First the entire population is generated based on the total count of chromosomes in the population. Then new chromosomes are generated using single-point crossover and mutation, and the chromosome fitness in the population is calculated separately, and finally the simulated annealing selection method is used to select chromosomes for the new population based on the ordering of fitness. In this case, genetic adjustment of all chromosomes is required after the initialization of the population and crossover mutation steps to ensure that they do not fall outside the constraints.

The PGAC algorithm comprises two parts: first, the prevalence of cache content is predicted based on the probabilistic prediction equation of cache content state in Eqs 22–26. Then, the genetic simulated annealing algorithm is used to acquire the optimum caching scheme based on the predicted prevalence results. In summary, the specific flow of the genetic simulated annealing cache content algorithm is shown in Algorithm 1 below.

INPUT: At initial moment $t = 0$, calculate the influence rate, service rate, initialize the population size, the total count of genetic algorithm iterations, initial temperature of simulated annealing, Cooling coefficient, adaptive crossover probabilityand adaptive mutation probability.
  Calculate the proportion of users in each state according to Eqs 20–26, predict the number of users in each state using Eqs 27–31, and obtain the content popularity from Eq. 32.
  Use the chromosome correction method to correct the chromosomes in the initial population;
  for i = 1 to n_{GA} do:
  Mutate and cross all chromosomes in population P_1 according to Eqs 37, 38, generating a new population P_2
  Use the chromosome correction method to correct the chromosomes in population P_2
  Calculate the fitness of each chromosome in the initial population P_1 and the newly generated population P_2 according to Eq. 36.
  Calculate the probability of chromosomes being selected according to Eq. 39 and place the selected chromosomes into population P_3;
  Until the total count of chromosomes in P_3 is equal to num;
  $P_3 = P_1$, $T = \theta T$;
  end for;
  Calculate the fitness for each chromosome in population P_1;
  I^* = the chromosome with the highest fitness;
  return I^*
  $t = t + 1$
  end
  content cache finished.
OUTPUT: optimum caching scheme

Algorithm 1. PGAC.

TABLE 1 Simulation parameters

Parameters	Numerical values
User density, λ_α	0.2 m^2
Physical distance for communication between users, $R_{m,n}$	10 m
Cache content size, C	[50,200]$bits$
Loss rate, ξ_k, ω_k	[0.01, 0.05]
Refusal rate, χ_k	[0.01, 0.05]
Channel bandwidth, W_m	1 MHz
Transmission power of the edge service base station, p_m	1.3 W
Channel gain, h_m^n	10^{-5}
Gaussian white noise,N_0	10^{-13} dm
Population size, num	20
amount of iterations, n_{GA}	200
Initial temperature, T	1000
Cooling coefficient, θ	0.98

5 Simulation and results

In this paper, the CDSED strategy is simulated and verified based on Matlab platform. To simplify the processing, the whole 6G edge caching network consists of a single edge service base station with several users, the service area of the edge service base station is a circular area with a radius of 50 m, the users obey a Poisson distribution with a density of 0.2. The generation and propagation of all contents are randomized for easy comparison, with ξ_k, ω_k and χ_k between 0.01 ~ 0.05 for each cache content [40], and γ_k uniformly distributed between 0.1 ~ 0.5 [41]. The primary simulation parameters are displayed in Table 1:

In the simulation process, the caching performance of CDSED strategy is compared with LRU strategy [10], LFU strategy [11] and MPC strategy [42] respectively.

1. Least Recently Used (LRU) caching strategy: if cache content has been requested in the recent period, then there is a high chance that the cache content will be requested in the future period. When the cache space of the base station is full, the content that has not been requested for the longest time in the recent period is deleted.
2. Least Frequently Used (LFU): The edge service base station records the total count of requests for each cache content. When the total count of requests for an edge service base station's uncache content is greater than the total count of requests for the least cache content, the edge service base station removes the least requested content and caches it.
3. Most Popular Caching (MPC): The edge service base station caches the most popular content within the service area until the cache capacity limit of the edge service base station is reached.

This paper describes the change in the total count of users in each interest propagation state during content dissemination when the sum total of users is 200. The black solid line, pink dotted line, red dashed line, cyan dotted line and blue dotted line shown in Figure 4 represent the changes in the total count of S, E, I, D, and R state users, respectively. From the figure, it can be seen that there are a large amount of S state users in the 6G edge caching network at the initial moment, and they are easily influenced by the commendations of other users to change their state and become E state users. With the passage of time, the total count of E state users increases rapidly, and they become I state users after acquiring the cache content, and the corresponding amount of E state users decreases. I state users commend the interest of cache content on their own terms. However, with the increase of time and the propagation of the cache content, the interest of the user may gradually weaken, resulting in the user changing from the I state and the D state to the R state. The total count of the I state and the D state users are decreasing, and the state of the user remaining unchanged in the R state. Therefore, the trends of S, E, I, D, and R curves are consistent with the results in the theoretical analysis.

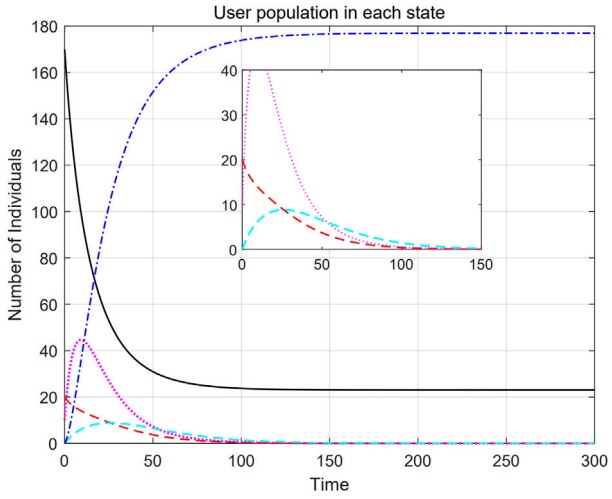

FIGURE 4
Amount of users in each state during content distribution.

Figure 5 illustrates the results of content prevalence for different amount of users. In the figure, the horizontal coordinate is time and the vertical coordinate is the content prevalence. In addition, the curves with blue crosses, red triangles and yellow circles in the figure represent the change in content prevalence for user numbers of 100, 200 and 300, respectively. From the figure, it can be seen that the trend of the curves for all three cases of amount of users is increasing and then decreasing to zero, which is in line with the pattern of cache content in 6G edge caching networks. This is because newly released cache content quickly arouses the interest of neighboring users, leading to a rapid increase in the total count of users curious about the cache content across the 6G edge caching network, and accordingly triggering a significant rise in requests for that cache content as well as an increase in the prevalence of the content. After a period of time, the user interest in the cache content in the 6G edge caching network gradually becomes saturated and users are no longer curious about the cache content. This ultimately leads to a gradual decrease in user interest in the cache content and a corresponding decrease in

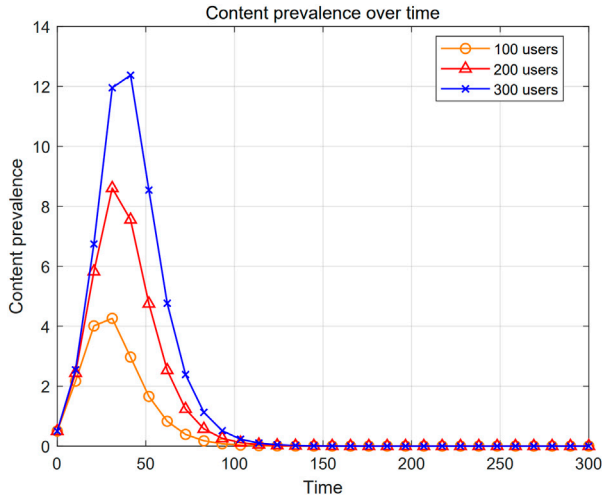

FIGURE 5
Content prevalence prediction results.

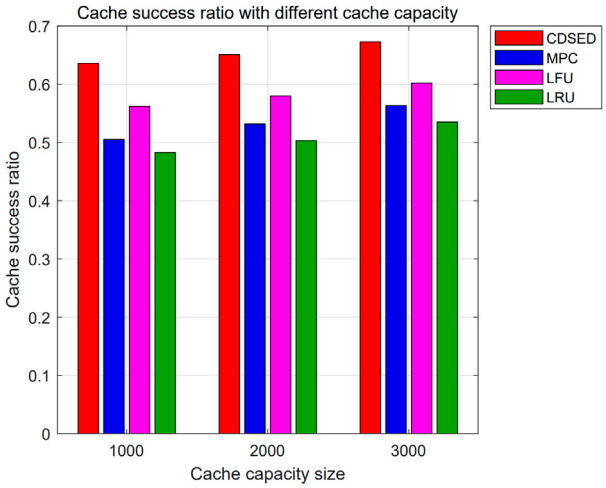

FIGURE 7
Variation of cache success ratio with cache capacities.

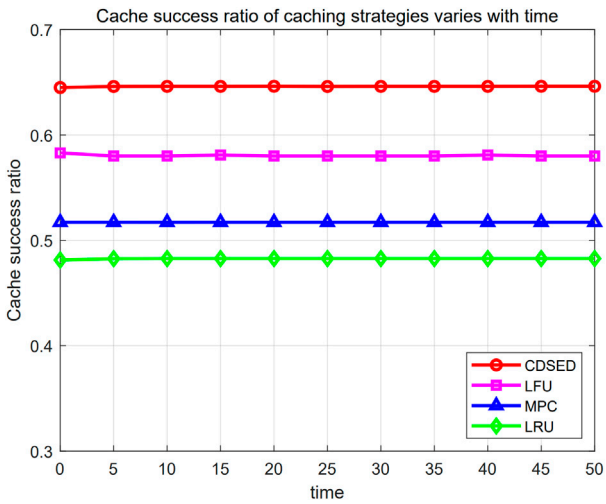

FIGURE 6
Cache success ratio changes over time.

the prevalence of the content. As a result, the total count of new interested users tends to decrease in the next time period and eventually stabilizes until it reaches zero.

The variation of cache success ratio at different times when simulating different caching strategies is shown in Figure 6. In the figure, the horizontal axis represents the time and the vertical axis represents the cache success ratio. In addition, the graph with circle, triangle, rectangle and diamond curves represent CDSED strategy, MPC strategy, LFU strategy and LRU strategy respectively. From the figure, it is evident that average cache success ratio of CDSED strategy is 0.645, while the average cache success ratios of LFU, MPC, and LRU strategies are 0.579, 0.517, and 0.482, indicating that the cache hit rate of the CDSED strategy is higher than the other three strategies. This is because, the LFU, MPC and LRU strategies mainly rely on the user's previous content requests, which consequently leads to the challenge of capturing real-time content prevalence. Specifically, the LFU, MPC and LRU strategies' responses to content requests are limited by the total count of users' previous access history, making it difficult to adapt to dynamically changing content prevalence. In contrast, the CDSED strategy is more flexible in meeting new user interests and needs through a real-time content update mechanism by comprehensively considering the real-time nature of user interests and needs. In addition, the MPC strategy is prone to fall into local optimum solutions, and the introduction of the simulated annealing selection algorithm provides the CDSED strategy with a more global search capability, which enables it to make caching decisions more flexibly in the face of complex dynamic environments, thus improving the overall caching success ratio. Therefore, compared with the other three caching strategies, the CDSED strategy achieves a higher cache success ratio.

The simulation compares the variation of cache success ratio in different caching strategies with different cache capacity sizes, as shown in Figure 7. In the figure, the horizontal coordinate represents the cache capacity magnitude of the edge service base station and the vertical coordinate represents the cache success ratio. In addition, the bar chart shows the CDSED strategy, MPC strategy, LFU strategy, and LRU strategy from left to right, respectively. From the figure, it is observable that when cache capacity increases from 1000 to 3000, the cache success ratio of CDSED strategy, MPC strategy, LFU strategy and LRU strategy increased from [0.636, 0.505, 0.562, 0.482] to [0.673, 0.563, 0.602, 0.535]. This is because the larger cache capacity provides more cache resources for the 6G edge caching network, enabling the edge service base station to accommodate more cache content to better satisfy the increasing content requests from users in the edge caching network. Meanwhile, the CDSED strategy can design the caching strategy according to the cache capacity of the serving base station. Therefore, the cache success ratio of CDSED is higher than that of LFU, MPC and LFU with the same cache capacity.

Figure 8 shows the change of cache success ratio in different cache strategies when the cache capacity of the base station is

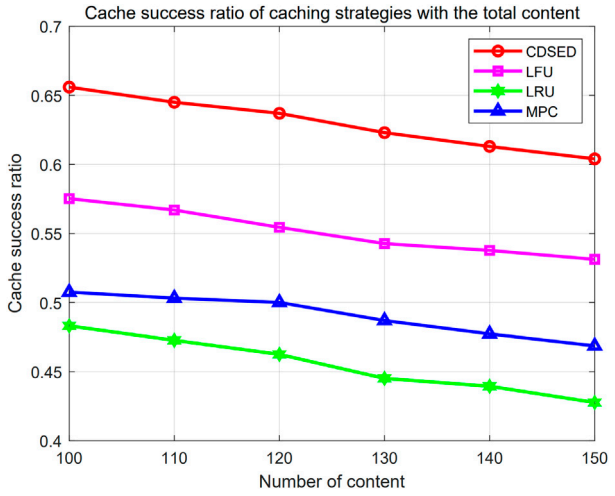

FIGURE 8
Cache success ratio under different content number.

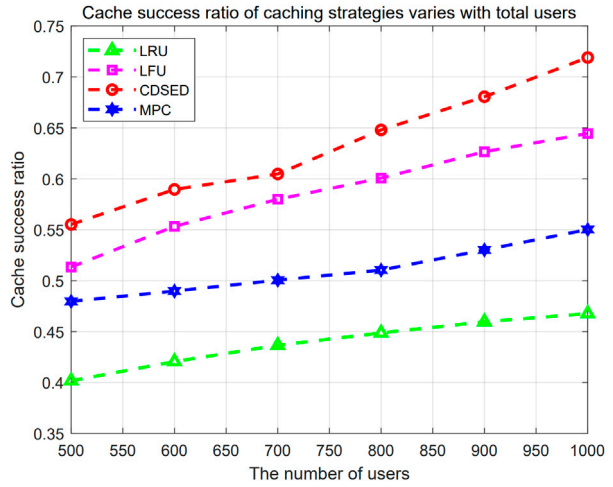

FIGURE 9
Cache success ratio changes under different amount of users.

constant and the total count of content is increasing. In the figure, the abscissa represents the total count of content, and the ordinate indicates the cache success ratio. The circles, triangles, rectangles are represented by CDSED strategy, MPC strategy, LRU strategy and LFU strategy respectively. It is clear from the figure that as the total count of content increases, the cache success ratio decreases accordingly. This is because when the cache content is increasing, the types of content requested by the user will also increase, while the cache space of the edge service base station is unchanged. The edge service base station cannot cache all the requested cache content, so it is necessary for the remote cloud server to respond to the user's content demand, resulting in a decrease in success ratio. In addition, the average cache success ratio of CDSED strategy is 0.629, while the average cache success ratios of MPC strategy, LRU strategy and LFU strategy are 0.491, 0.454 and 0.551, respectively. When the amount of content is 100, the cache success ratios of CDSED, MPC, LRU, and LFU strategies are 0.656, 0.507, 0.483, and 0.575. This is because LRU and LFU strategies mainly make decisions based on historical behavior or simple frequency information, which cannot effectively adapt to the large and diverse cache content set. Although the MPC strategy considers the prevalence of cache content, when the total count of cache content increases, it may not be able to accurately select the content suitable for a specific user group due to only focusing on the global prevalence, which affects the cache success ratio. By simulating the propagation process of content between users, the CDSED strategy can more comprehensively understand the formation and propagation of user interests, and more flexibly and selectively cache content with potential propagation trends, thereby improving the success ratio. Therefore, when the total content number is the same, the CDSED strategy can increase success ratio than LRU, LFU and MPC strategies.

The simulation compares cache success ratio changes of different caching strategies with different total count of users, as displayed in Figure 9. In the figure, the horizontal axis is the total count of users, and the vertical axis is the cache success ratio. In addition, the graphs with red circles, pink rectangles, blue hexagons and green triangular curves represent CDSED strategy, LFU strategy, MPC strategy and LRU strategy, respectively. From the figure, it is evident that as the total count of users increases, the cache success ratio will increase accordingly. This is because LRU and LFU strategies selectively replace inactive or low-frequency cache content by monitoring user behavior, thereby effectively satisfying user interests. The MPC strategy is based on prevalence information to better retain popular cache content. The CDSED strategy considers the content propagation process, makes full use of the interest propagation relationship between users, and improves the caching effect for popular content. In addition, the average cache success ratios of the CDSED strategy, MPC strategy, LRU strategy, and LFU strategy are 0.632, 0.512, 0.451, and 0.573. When the amount of users is 500, the cache success ratios of the CDSED strategy, MPC strategy, LRU strategy, and LFU strategy are 0.552, 0.474, 0.405, and 0.527 respectively. This is because the increase in the total count of users means that the information propagation path becomes more complex. The CDSED strategy captures the heat evolution of content more accurately by simulating the propagation process of information, and can predict future hot content more accurately according to the influence relationship between users. Therefore, the CDSED strategy can enhance success ratio under the same amount of users.

6 Conclusion

This study proposed a cache distribution strategy based on epidemic dynamics for 6G edge network. First, the strategy constructs a 6G ECCM, which investigates the time-varying content prevalence in edge caching networks. The user propagation process of cache content is modeled as an infectious disease propagation process, and the distribution of user interest in cache content is obtained from the content propagation state prediction matrix. In addition, the CDSED strategy includes PGAC algorithm, which introduces a simulated

annealing selection algorithm derived from GA to improve the local search capability and maximize the cache success ratio. Simulation results show that the CDSED can significantly increase the cache success ratio compared with LFU, LRU and MPC. In our future work, we will further optimize the propagation dynamics model based on this work, and consider more factors such as user behaviors, social relationships, etc., to improve the accuracy of popularity prediction. We will also research edge caching strategies based on technologies such as 6G space-air-integrated network (6G SAGIN) and integrated sensing and computation (ISAC).

Data availability statement

The original contributions presented in the study are included in the article/supplementary material, further inquiries can be directed to the corresponding author.

Author contributions

XW: Methodology, Software, Writing–original draft. YZ: Methodology, Software, Writing–original draft. SZ: Methodology, Writing–original draft.

Funding

The author(s) declare that financial support was received for the research, authorship, and/or publication of this article. The work was supported in part by Sub Project of National Key Research and Development plan in 2020. NO. 2020YFC1511704, Beijing Science and Technology Project (Grant No. Z211100004421009), Beijing Information Science and Technology University. NO. 2020KYNH212, NO. 2021CGZH302 and in part by the National Natural Science Younth Foundation of China (Grant No. 62301058).

Acknowledgments

We are grateful for the contributions to this article made by Frontiers editorial staff members. We also thank the reviewers who provided valuable input for this manuscript.

Conflict of interest

The authors declare that the research was conducted in the absence of any commercial or financial relationships that could be construed as a potential conflict of interest.

Publisher's note

References

1. Bagaa M, Dutra DLC, Taleb T, Flinck H Toward enabling network slice mobility to support 6g system. *IEEE Trans Wireless Commun* (2022). 21:10130–44. doi:10.1109/TWC.2022.3182591

2. Mao B, Liu J, Wu Y, Kato N Security and privacy on 6g network edge: a survey. *IEEE Commun Surv Tutorials* (2023). 25:1095–127. doi:10.1109/COMST.2023.3244674

3. Chukhno N, Chukhno O, Pizzi S, Molinaro A, Iera A, Araniti G Approaching 6g use case requirements with multicasting. *IEEE Commun Mag* (2023). 61:144–50. doi:10.1109/MCOM.001.2200659

4. Yang L, Hu H, Li M A distributed caching approach for minimizing average transmission delay in ultra-dense networks. *IEEE Trans Vehicular Technol* (2023). 72:11041–6. doi:10.1109/TVT.2023.3261896

5. Zhao L, Li H, Lin N, Lin M, Fan C, Shi J Intelligent content caching strategy in autonomous driving toward 6g. *IEEE Trans Intell Transportation Syst* (2022). 23:9786–96. doi:10.1109/TITS.2021.3114199

6. Lin Z, Fang Y, Chen P, Chen F, Zhang G Modeling and analysis of edge caching for 6g mmwave vehicular networks. *IEEE Trans Intell Transportation Syst* (2023). 24:7422–34. doi:10.1109/TITS.2022.3147696

7. Yu P, Zhang J, Fang H, Li W, Feng L, Zhou F, et al. Digital twin driven service self-healing with graph neural networks in 6g edge networks. *IEEE J Selected Areas Commun* (2023). 41:3607–23. doi:10.1109/JSAC.2023.3310063

8. Li D, Zhang H, Li T, Ding H, Yuan D Community detection and attention-weighted federated learning based proactive edge caching for d2d-assisted wireless networks. *IEEE Trans Wireless Commun* (2023). 22:7287–303. doi:10.1109/TWC.2023.3249756

9. Li H, Sun M, Xia F, Xu X, Bilal M A survey of edge caching: Key issues and challenges. *Tsinghua Sci Technol* (2024) 29:818–42. doi:10.26599/TST.2023.9010051

10. Ma G, Wang Z, Zhang M, Ye J, Chen M, Zhu W Understanding performance of edge content caching for mobile video streaming. *IEEE J Selected Areas Commun* (2017). 35:1076–89. doi:10.1109/JSAC.2017.2680958

11. Wang X, Chen M, Taleb T, Ksentini A, Leung VC Cache in the air: exploiting content caching and delivery techniques for 5g systems. *IEEE Commun Mag* (2014). 52:131–9. doi:10.1109/MCOM.2014.6736753

12. Zhang X, Ren Y, Lv T, Hanzo L Caching scalable videos in the edge of wireless cellular networks. *IEEE Netw* (2023). 37:34–42. doi:10.1109/MNET.107.2100461

13. Feng H, Guo S, Yang L, Yang Y Collaborative data caching and computation offloading for multi-service mobile edge computing. *IEEE Trans Vehicular Technol* (2021). 70:9408–22. doi:10.1109/TVT.2021.3099303

14. Wu D, Li J, He P, Cui Y, Wang R Social-aware graph-based collaborative caching in edge-user networks. *IEEE Trans Vehicular Technol* (2023). 72:7926–41. doi:10.1109/TVT.2023.3241959

15. Sun H, Chen Y, Sha K, Huang S, Wang X, Shi W A proactive on-demand content placement strategy in edge intelligent gateways. *IEEE Trans Parallel Distributed Syst* (2023). 34:2072–90. doi:10.1109/tpds.2023.3249797

16. Zhu X, Jiang C, Kuang L, Zhao Z Cooperative multilayer edge caching in integrated satellite-terrestrial networks. *IEEE Trans Wireless Commun* (2022). 21:2924–37. doi:10.1109/TWC.2021.3117026

17. Wang R, Kan Z, Cui Y, Wu D, Zhen Y Cooperative caching strategy with content request prediction in internet of vehicles. *IEEE Internet Things J* (2021). 8:8964–75. doi:10.1109/JIOT.2021.3056084

18. Ayenew TM, Xenakis D, Alonso L, Passas N, Merakos L Demand-aware cooperative content caching in 5g/6g networks with mec-enabled edges. *IEEE Networking Lett* (2022). 4:118–22. doi:10.1109/LNET.2022.3192173

19. Tang J, Tang H, Zhang X, Cumanan K, Chen G, Wong K-K, et al. Energy minimization in d2d-assisted cache-enabled internet of things: a deep reinforcement learning approach. *IEEE Trans Ind Inform* (2020). 16:5412–23. doi:10.1109/TII.2019.2954127

20. Zhu J, Li R, Ding G, Wang C, Wu J, Zhao Z, et al. Aoi-based temporal attention graph neural network for popularity prediction and content caching.

IEEE Trans Cogn Commun Networking (2022). 9:345–58. doi:10.1109/TCCN.2022.3227920

21. Liu X, Derakhshani M, Lambotharan S Contextual learning for content caching with unknown time-varying popularity profiles via incremental clustering. *IEEE Trans Commun* 69 (2021):3011–24. doi:10.1109/tcomm.2021.3059305

22. Zhang W, Wu D, Yang W, Cai Y Caching on the move: a user interest-driven caching strategy for d2d content sharing. *IEEE Trans Vehicular Technol* (2019). 68:2958–71. doi:10.1109/TVT.2019.2895682

23. Li Z, Gao X, Li Q, Guo J, Yang B Edge caching enhancement for industrial internet: a recommendation-aided approach. *IEEE Internet Things J* (2022). 9:16941–52. doi:10.1109/JIOT.2022.3143506

24. Li C, Chen W Content pushing over idle timeslots: performance analysis and caching gains. *IEEE Trans Wireless Commun* (2021). 20:5586–98. doi:10.1109/TWC.2021.3068528

25. Zhang X, Qi Z, Min G, Miao W, Fan Q, Ma Z Cooperative edge caching based on temporal convolutional networks. *IEEE Trans Parallel Distributed Syst* (2022). 33:2093–105. doi:10.1109/TPDS.2021.3135257

26. Mehrizi S, Chatterjee S, Chatzinotas S, Ottersten B Online spatiotemporal popularity learning via variational bayes for cooperative caching. *IEEE Trans Commun* (2020). 68:7068–82. doi:10.1109/TCOMM.2020.3015478

27. Nguyen T-V, Dao N-N, Noh W, Cho S, et al. User-aware and flexible proactive caching using lstm and ensemble learning in iot-mec networks. *IEEE Internet Things J* (2022). 9:3251–69. doi:10.1109/JIOT.2021.3097768

28. Tao Y, Jiang Y, Zheng F-C, Wang Z, Zhu P, Tao M, et al. Content popularity prediction based on quantized federated bayesian learning in fog radio access networks. *IEEE Trans Commun* (2023). 71:893–907. doi:10.1109/TCOMM.2022.3229679

29. Li D, Zhang H, Yuan D, Zhang M Learning-based hierarchical edge caching for cloud-aided heterogeneous networks. *IEEE Trans Wireless Commun* (2023) 22:1648–63. doi:10.1109/TWC.2022.3206236

30. Jiang Y, Feng H, Zheng F-C, Niyato D, You X Deep learning-based edge caching in fog radio access networks. *IEEE Trans Wireless Commun* (2020). 19:8442–54. doi:10.1109/TWC.2020.3022907

31. Gao J, Zhang S, Zhao L, Shen X The design of dynamic probabilistic caching with time-varying content popularity. *IEEE Trans Mobile Comput* (2021). 20:1672–84. doi:10.1109/TMC.2020.2967038

32. Fan Q, Li X, Li J, He Q, Wang K, Wen J Pa-cache: evolving learning-based popularity-aware content caching in edge networks. *IEEE Trans Netw Serv Manage* (2021). 18:1746–57. doi:10.1109/tnsm.2021.3053645

33. Wang K, Deng N A privacy-protected popularity prediction scheme for content caching based on federated learning. *IEEE Trans Vehicular Technol* (2022). 71:10191–6. doi:10.1109/TVT.2022.3179413

34. Wang J, Cai S, Wang W, Zhou T Link cooperation effect of cooperative epidemics on complex networks. *Appl Maths Comput* (2023). 437:127537. doi:10.1016/j.amc.2022.127537

35. Zhang H, Cao L, Fu C, Cai S, Gao Y Epidemic spreading on multi-layer networks with active nodes. *Chaos: Interdiscip J Nonlinear Sci* (2023). 33:073128. doi:10.1063/5.0151777

36. Zhao J, He L, Zhang D, Gao X A tp-ddpg algorithm based on cache assistance for task offloading in urban rail transit. *IEEE Trans Vehicular Technol* (2023). 72:10671–81. doi:10.1109/TVT.2023.3253508

37. Lin P, Song Q, Jamalipour A Multidimensional cooperative caching in comp-integrated ultra-dense cellular networks. *IEEE Trans Wireless Commun* (2020). 19:1977–89. doi:10.1109/TWC.2019.2960329

38. Wang Y, Friderikos V Energy-efficient proactive caching with multipath routing. *Comput Netw* (2022). 216:109272. doi:10.1016/j.comnet.2022.109272

39. Feng H, Deng Y, Zhou Y, Min G Towards heat-recirculation-aware virtual machine placement in data centers. *IEEE Trans Netw Serv Manage* (2022). 19:256–70. doi:10.1109/TNSM.2021.3120295

40. Zhang L, Jin A, He Q, Chen M Two delayed seirs epidemic model in networks. In: 2012 International Symposium on Instrumentation and Measurement, Sensor Network and Automation (IMSNA); 25-28 August 2012; Sanya, China, 29 (2012). p. 592–5doi. doi:10.3760/cma.j.issn.1003-9406.2012.05.020

41. Jin W Research on material allocation method based on seir and multi-objective programming. In: 2023 IEEE International Conference on Image Processing and Computer Applications (ICIPCA); 11-13 August 2023; Changchun, China (2023). p. 1006–10. doi:10.1109/icipca59209.2023.10257749

42. Bernardini C, Silverston T, Festor O Mpc: popularity-based caching strategy for content centric networks. In: 2013 IEEE International Conference on Communications (ICC); 09-13 June 2013; Budapest, Hungary (2013). p. 3619–23. doi:10.1109/icc.2013.6655114

frontiers | Frontiers in Physics

TYPE Original Research
PUBLISHED 26 June 2024
DOI 10.3389/fphy.2024.1410089

OPEN ACCESS

EDITED BY
Xuzhen Zhu,
Beijing University of Posts and Telecommunications (BUPT), China

REVIEWED BY
Wenjie Dong,
Nanjing University of Aeronautics and Astronautics, China
Yunqiu Qiu,
Ocean University of China, China
Yaping Ge,
Hunan City University, China

*CORRESPONDENCE
Jianlin Jia,
jjl@imut.edu.cn

RECEIVED 31 March 2024
ACCEPTED 17 May 2024
PUBLISHED 26 June 2024

CITATION
Jia J, Huang Y, Zhang W and Chen Y (2024), Information propagation characteristic by individual hesitant-common trend on weighted network.
Front. Phys. 12:1410089.
doi: 10.3389/fphy.2024.1410089

Information propagation characteristic by individual hesitant-common trend on weighted network

Jianlin Jia[1]*, Yuwen Huang[1], Wanting Zhang[1] and Yanyan Chen[2]

[1]Key Laboratory of Civil Engineering Structure and Mechanics, Inner Mongolia University of Technology, Hohhot, China, [2]Beijing Key Laboratory of Traffic Engineering, Beijing University of Technology, Beijing, China

Within the context of contemporary society, the propagation of information is often subject to the influence of inter-individual connectivity, and individuals may exhibit divergent receptive attitudes towards identical information, a phenomenon denoted as the Hesitant-Common (HECO) trait. In light of this, the present study initially constructs a propagation network model devoid of correlation configurations to investigate the HECO characteristics within weighted social networks. Subsequently, the study employs a theoretical framework for edge partitioning, predicated on edge weights and HECO traits, to quantitatively analyze the mechanisms of individual information dissemination. Theoretical analyses and simulation outcomes consistently demonstrate that an augmentation in the proportion of common individuals facilitates both the diffusion and adoption of information. Concurrently, a phase transition crossover is observed, wherein the growth pattern of the ultimate adoption range, denoted as $R(\infty)$, transitions from a first-order discontinuous phase transition to a second-order continuous phase transition as the proportion of common individuals increases. An escalation in the weight distribution exponent is found to enhance information propagation. Furthermore, a reduction in the heterogeneity of degree distribution is conducive to the spread of information. Conversely, an increase in degree distribution heterogeneity and a diminution in the collective decision-making capacity can both exert inhibitory effects on the propagation of information.

KEYWORDS

complex networks, weighted network, information propagation, individual hesitant-common characteristics, heterogeneous information adoption model

1 Introduction

With the rapid development of social media platforms such as TikTok, WeChat, and Twitter, social networks have increasingly become integral to human life. These media facilitate the swift reception and dissemination of diverse information, greatly enhancing the convenience of people's work and daily activities. The communication pathways within social media constitute a vast network for information dissemination, with the world's largest social media platform, Facebook, boasting billions of active monthly users, and the monthly volume of information flow is incalculable [1]. However, this complexity of information interweaving also presents challenges: once harmful information spreads within the network, it can cause significant damage. Beyond the challenges of

information dissemination, social networks also play a crucial role in various fields such as healthcare [2, 3], cultural education [4, 5], and commercial marketing [6, 7]. They are utilized for analyzing information, signals, and financial communication patterns, demonstrating their multifunctionality in modern society. Therefore, an in-depth analysis of the information dissemination patterns within social networks is of significant importance for understanding their impact, optimizing information management, preventing risks, and promoting development in various sectors.

In recent years, numerous scholars have conducted research on information propagation models, including those based on the Internet of Things with layered structures [8], models grounded in game theory [9], and models inspired by heat transfer [10]. Among these, game theory-based models are capable of simulating decision-making processes of individuals aimed at maximizing their self-interest. However, these models are predicated on the assumption of rationality of the individuals, which may not be applicable to all social network contexts. Meanwhile, research on information propagation based on complex network theory and topological structures has emerged as a significant topic within the field of complex network studies [11–14]. There is an extensive body of research on the spread of epidemics across complex networks, and the modes of information propagation within social networks bear certain similarities to the spread of diseases in physically complex networks. Adopting and expanding the foundational models of epidemic propagation in complex networks can facilitate a better understanding of information dissemination in social networks. For instance, a modified Sub-Health-Healthy-Infection- Recovery (SHIR) model with time delays and nonlinear incidence rates has been established for two susceptible populations across different topological networks [15]. Guirui Liu and others developed the SIS-UAU model to describe the dynamics of epidemic and information propagation within overlay networks [16], by constructing a dual-layer network consisting of an epidemic dynamic evolution layer and an information propagation layer to study the dynamics of information and disease spread in superimposed networks. Furthermore, some scholars have described information propagation in complex networks using more refined models. Guan Gui and others formulated a SIR model with time delays, forced silence functions, and forgetting mechanisms in both homogeneous and heterogeneous networks to describe the dynamic mechanisms of rumor propagation [17]. To investigate the propagation trends of network rumors, the authors in [18] detailed the dynamic behavior of a delayed S2IS rumor propagation model with a saturation conversion function. Rumor propagation, as a hot topic in information propagation research [19–21], is also a category within social network dissemination, and such research aids various researchers in uncovering the underlying mechanisms of information propagation in social networks.

One of the primary mechanisms for information dissemination within social networks is through the interconnections among users [22]. Upon the inception of a piece of information, the originator initiates its propagation. It is possible that during the initial dissemination, multiple recipients receive the information simultaneously. Should a recipient successfully adopt the information, they then assume the role of a subsequent disseminator. Concurrently, this process may yield adopters who do not further propagate the information, as well as non-adopters. Ultimately, however, the information evolves into a shared resource among a majority of the network's participants.

Taking into account the various factors that influence information propagation, user behavior on social networks exhibits diversity and heterogeneity, thereby giving rise to distinct patterns of information dissemination. In real-world social networks, interactions are more likely to occur among individuals with similar interests or preferences, and generally, individuals prefer to receive and share information that aligns with their interests and preferences. Temporal thematic analysis of mobile communication systems has revealed homophily characteristics in social interactions, where communication between individuals with similar attributes (such as gender and age) tends to be more frequent [23]. Bakshy et al., based on Facebook data, observed ideological homophily within friendship networks, where both conservatives and liberals are more likely to associate with friends of similar political affiliations [24].

Numerous systems within contemporary society can be characterized as networks, where the constituent elements are represented as nodes. If the interactions between nodes are quantifiable, the interconnecting edges can be assigned weights, thus forming a weighted network. Consequently, the edge weights within a weighted network typically serve to denote the individual relationships between nodes. For instance, in transaction networks, these weights can signify the proportion of transactions between financial institutions [25], while in transportation networks, they may represent the percentage of tourists utilizing different travel routes [26]. Social networks exhibit complex topological structures with significant heterogeneity in connection strength and capacity. Constructing the inter-individual connections as edges with heterogeneous weight distributions is conducive to uncovering the impact of edge weight heterogeneity on information propagation.

Existing research has demonstrated that individual heterogeneity in adoption manifests as varying receptive attitudes towards the same information, and individuals' attitudes may change as they acquire different amounts of information [27, 28]. In their research presented in Ref. [29], Iyengar R. examined the propagation of obesity through social networking platforms, emphasizing the significance of group heterogeneity in the dissemination of health-related information. Golub B. investigated the learning processes predicated on individual heterogeneity within these networks and the subsequent influence on the collective intelligence of the group [30]. Furthermore, Lerman K. conducted empirical analyses on the dissemination of news across social media platforms, including Digg and Twitter, with a particular focus on the heterogeneity of user behaviors [31]. However, studies on information propagation in complex networks that consider group adoption heterogeneity are relatively scarce. Due to the distinct personalities of each individual in real-world social networks, the degree of information adoption varies. Based on the psychology of information adoption, this study categorizes the population within social networks into two types: common individuals and hesitant individuals, collectively referred to as the Hesitant-Common (HECO) model. Common individuals maintain a liberal attitude towards received information or behaviors and can adopt them at varying speeds, with an increased willingness to adopt as more information is received.

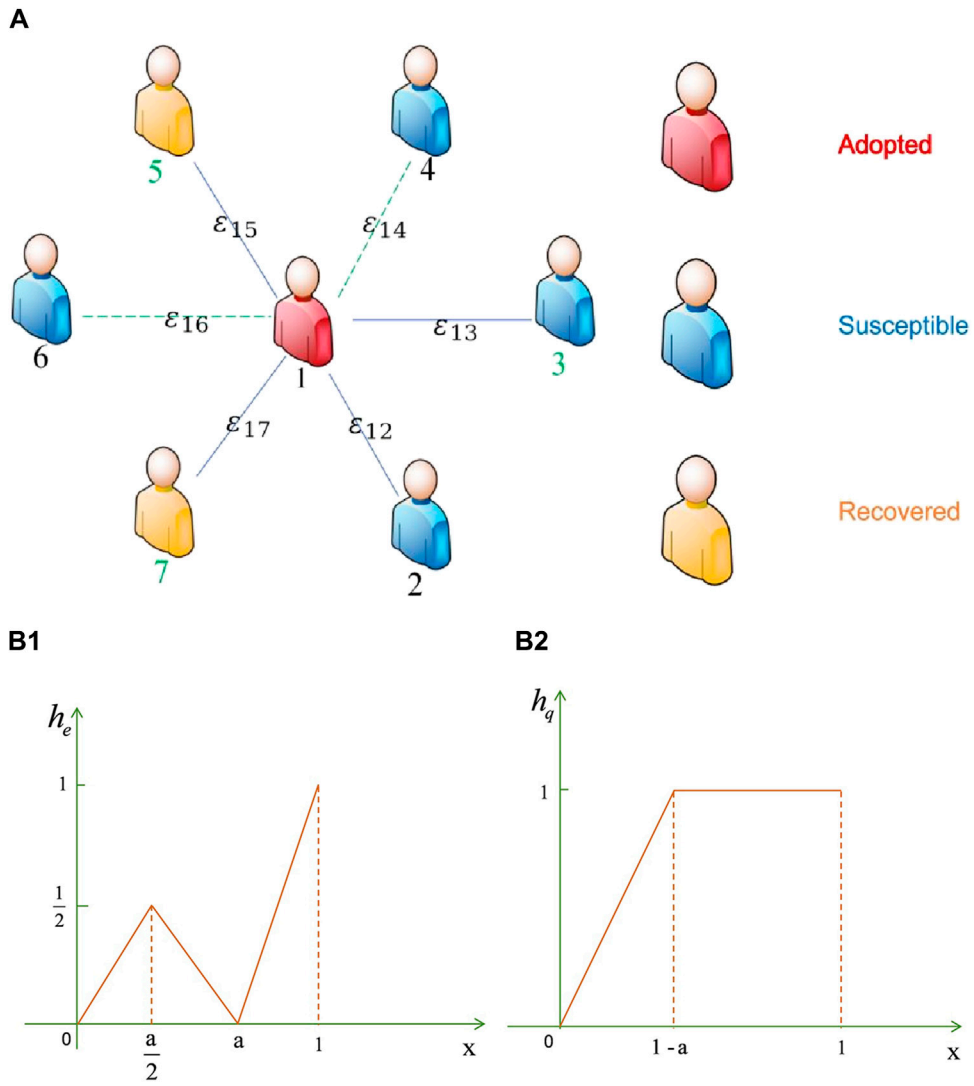

FIGURE 1
Subfigure **(A)** illustrates the schematic of the weighted social network propagation model. Different numerical labels with colors represent various types of populations, with black denoting the common population, such as 1, 2, 4, and 6. Green represents the hesitant population, such as 3, 5, and 7. The symbol ε represents the edge weight, which signifies the degree of interaction between two individuals. Blue solid lines indicate that information has not been disseminated through the connected edge, while green dashed lines signify that information has already been propagated through this edge and cannot be transmitted further via the same edge. Subfigures 1 **(B1,B2)** represent the information adoption functions for the hesitant and ordinary populations, respectively, where x is the ratio of the number of information units received by a node to its degree.

In contrast, hesitant individuals experience a period of deliberation regarding whether to adopt, repeatedly verifying the information before reaching a decision to adopt, facilitated by the acquisition of more information. For example, when a trending piece of information emerges on the internet, common individuals are more likely to discover and disseminate it. Among similar common individuals, the adoption rate is higher, leading to faster propagation of the trending information and a quicker approach to relative saturation in the adoption range. On the other hand, hesitant individuals often receive trending information through common individuals, adopt it after thorough verification, and thus propagate it more slowly, with the adoption range reaching relative saturation after a period of time. Therefore, categorizing the population in social networks based on adoption heterogeneity can contribute to a deeper understanding of the propagation mechanisms within social networks.

In consideration of the factors previously discussed, this study investigates the influence of group adoption heterogeneity on information dissemination within social networks on weighted networks and explores the HECO characteristics in the context of information propagation. A model of the information adoption function is proposed to explain the HECO characteristics. Subsequently, a set of partitioning principles based on edge weight and HECO characteristics is formulated to quantify and analyze the mechanisms of individual information propagation. The impact of information propagation on group heterogeneity is validated through simulation results, which are consistent with theoretical analysis. The structure of the remainder of this paper

is as follows: In the second section, an information propagation model based on group heterogeneity is established on weighted networks. The third section presents a theoretical analysis of edge partitioning based on edge weight and HECO characteristics. The fourth section examines the simulation results, confirming the propagation process of individual information in line with theoretical analysis. Finally, a summary is provided in the fifth section.

2 Information propagation model with hesitant-common trend

This section aims to construct a two-layer propagation network model based on an uncorrelated configuration model to investigate the impact of differences in HECO characteristics among populations on information dissemination within weighted social networks. In this model, the network consists of N nodes with a degree distribution P(k), and the propagation model follows the susceptible-adopted-recovered (SAR) paradigm. At any given moment, each node is in one of three states: susceptible state (S), adopted state (A), or recovered state (R). S-state nodes have not yet adopted the information and can receive information from neighboring nodes. A-state nodes have adopted the information and will pass it on to neighboring nodes. R-state nodes have lost interest in the information and no longer participate in the subsequent propagation process (i.e., they will neither adopt nor disseminate the information). The propagation mechanism is depicted in Figure 1A. In the weighted social network model presented in this study, an edge weight distribution is introduced to represent the degree of interaction between individuals, with different weight distributions reflecting the heterogeneity in information reception and dissemination among node connections. The edge weight between adjacent nodes i and j is denoted as ε_{ij}, and the weight distribution function is denoted as $f(\varepsilon)$. When a node i in state A sends information to a node j in state S, the probability of node j receiving the information is given by Eq. 1:

$$\beta_\varepsilon = \beta\left(\varepsilon_{ij}\right) = 1 - (1-\lambda)^{\varepsilon_{ij}} \tag{1}$$

Where λ is the propagation probability of information unit, and β_ε gradually monotonically increases with the increase of ε_{ij}. When $\beta_\varepsilon = 1$, $\beta_\varepsilon = \lambda$, that is, the weight value has no effect on information transmission.

Let m denote the total number of successfully received information units by a node in state S. Initially, in the weighted social network, there is no information propagation, meaning that for a node j in state S, $m_j = 0$. Subsequently, at each propagation time step, if node j successfully receives information transmitted via an edge from a neighboring node i in state A, then the count of adopted information units by node j increases by 1, such that m becomes $m_j \rightarrow m_j + 1$.

To characterize the decision-making capacity of a population, this study introduces a hesitancy parameter, denoted as a. A larger value of a indicates a stronger hesitancy, which corresponds to a weaker decision-making ability, and conversely, a smaller a signifies a stronger decision-making ability. Furthermore, to represent the impact of group adoption heterogeneity on information propagation, two functions are introduced to illustrate individual information adoption decision-making capabilities, as depicted in Figure 1B. The hesitant population, initially exhibit a phase of active adoption during the early stages of information dissemination. The propensity for active adoption increases with the acquisition of more information. However, due to their hesitancy, they subsequently enter a phase of passive adoption. When the number of acquired information units reaches the optimal decision-making capacity for adoption, they revert to an active mindset and remain unchanged thereafter. Eq. 2 represents the information adoption function for the hesitant population:

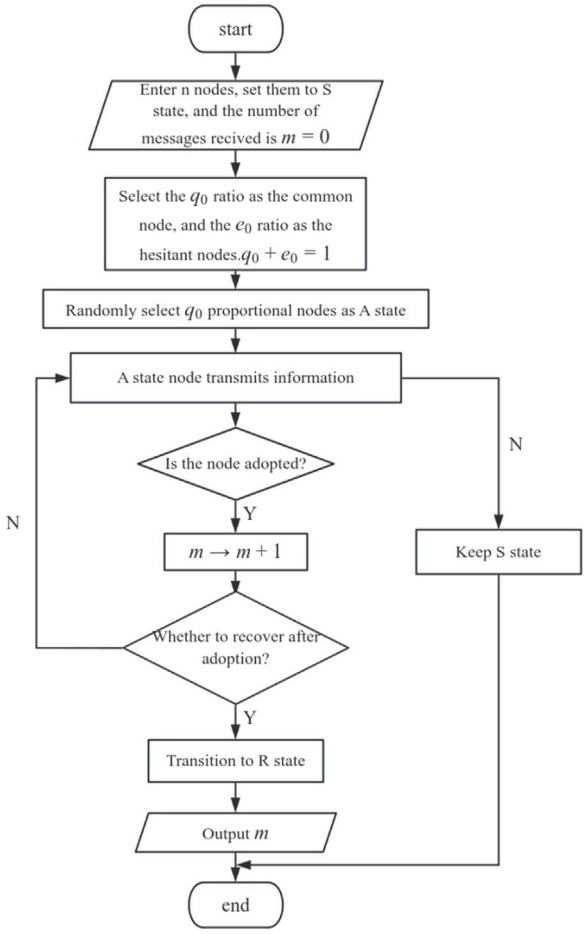

FIGURE 2
Simulated information dissemination process under weighted social network.

$$h_e(x,a) = \begin{cases} \dfrac{x}{a}, 0 < x \le \dfrac{a}{2} \\ \dfrac{-x+a}{a}, \dfrac{a}{2} \le x \le a \\ \dfrac{x-a}{1-a}, a \le x \le 1 \end{cases} \tag{2}$$

For the general population, there exists a normative reception and assimilation of information, wherein an increase in the quantity

of information acquired further enhances the adoption of information by this demographic. Eq. 3 delineates the information adoption function of the general population:

$$h_q(x,a) = \begin{cases} \dfrac{x}{1-a}, 0 < x \le 1-a \\ 1, x \ge 1-a \end{cases} \tag{3}$$

In the aforementioned equations, e and q represent the hesitant and common populations, respectively. The variable x represents the ratio of the total number m of successfully received messages to the degree for nodes in state S, which is used to characterize the collective information reception degree within a network. A higher value of x indicates a greater quantity of information successfully accepted by the network. When $x = 1$, the total number of successfully received messages is equal to the degree, implying that all nodes in state S have successfully received the information.

The simulation of information propagation in a weighted social network is depicted in Figure 2: A complex network with N nodes is constructed, where the edges between nodes are randomly generated according to the predefined network model, and all nodes are initially set to the S-state. A proportion q_0 of the nodes in the network is randomly selected to be common nodes, while the remaining proportion e_0 of nodes are designated as hesitant nodes (from which it follows that $e_0 + q_0 = 1$). Subsequently, a fraction ρ_0 of the total nodes is randomly chosen to be in the A-state, with the remaining nodes defaulting to the S-state. During information propagation, a node i in state A transmits information to an adjacent node j in state S via the corresponding edge with weight ε_{ij}. The probability that node j successfully receives the information is $\beta(\varepsilon_{ij})$, and upon successful reception, the count of adopted information units for node j becomes $m_j \to m_j + 1$. Due to the non-redundancy of information propagation, the information will not be disseminated through this edge again. For the group heterogeneity of node j, the probabilities of adopting information while in the hesitant and common states are $h_e(x,a)$ and $h_q(x,a)$, respectively, where $x = m_j/k_j$. A node j that successfully adopts the information transitions to state A; if unsuccessful, it remains in state S. A node i that has completed the propagation process may lose interest in the information with a recovery probability γ and transition to the R-state. The aforementioned propagation process is repeated until no nodes remain in state A, at which point the information propagation concludes.

3 Theory analysis

Building upon the literature [14, 32], this study examines the propagation of non-redundant information with group adoption heterogeneity on weighted networks. On this foundation, the paper proposes a theory of edge partitioning based on edge weight and HECO characteristics, thereby analyzing the information propagation mechanisms of the model. The study introduces nodes in a cavity state [33], which are capable of receiving information from neighbors but are unable to transmit information to other nodes. Assuming that edge weights are randomly distributed, the probability that a node has not received information from its neighbors by time t is characterized by Eq. 4:

$$\theta(t) = \sum_{\varepsilon} f(\varepsilon)\theta_{\varepsilon}(t) \tag{4}$$

Where $\theta_{\varepsilon}(t)$ is the probability that the A-state node does not propagate information to the neighboring nodes in S-state through the edge with the weight of ε by time t.

By time t, a node i in state S with degree k_i has received m pieces of information from its neighbors, an occurrence that can be represented as in Eq. 5:

$$\varphi(k_i,m,t) = \binom{k_i}{m}\theta(t)^{k_i-m}[1-\theta(t)]^m \tag{5}$$

Based on group heterogeneity, differences in HECO characteristics, and the information adoption function, if node i is a hesitant node in state S, and after time t, it has received $m(m > ak_i)$ pieces of information cumulatively but has not adopted the information and remains in state S, the probability is articulated by Eq. 6:

$$\begin{aligned}\phi_e(k_i,m,t,a) &= \sum_{r=0}^{m}\varphi(k_i,r,t)\prod_{l=0}^{r}\left[1-h_e\left(\frac{l}{k_i},a\right)\right] \\ &= \sum_{r=0}^{\frac{ak_i}{2}}\varphi(k_i,r,t)\prod_{l=0}^{r}\left(1-\frac{l}{\frac{ak_i}{2}}\right) \\ &\quad + \sum_{r=\frac{ak_i}{2}}^{ak_i}\varphi(k_i,n,t)\prod_{l=0}^{\frac{ak_i}{2}}\left(1-\frac{l}{\frac{ak_i}{2}}\right)\prod_{l=\frac{ak_i}{2}}^{r}\left(1-\frac{a-\frac{l}{k_i}}{a}\right) \\ &\quad + \sum_{n=ak_i}^{m}\varphi(k_i,n,t)\prod_{l=0}^{\frac{ak_i}{2}}\left(1-\frac{l}{\frac{ak_i}{2}}\right)\prod_{l=\frac{ak_i}{2}}^{ak_i}\left(1-\frac{a-\frac{l}{k_i}}{a}\right)\prod_{l=ak_i}^{n}\left(1-\frac{\frac{l}{k_i}-a}{1-a}\right)\end{aligned} \tag{6}$$

Similarly, when the received information m satisfies the conditions $m < \frac{ak_i}{2}$ and $\frac{ak_i}{2} < m < ak_i$, the probability of not having adopted the information and still being in state S is expressed by Eqs 7, 8:

$$\begin{aligned}\phi_e(k_i,m,t,a) &= \sum_{r=0}^{m}\varphi(k_i,r,t)\prod_{l=0}^{r}\left[1-h_e\left(\frac{l}{k_i},a\right)\right] \\ &= \sum_{r=0}^{m}\varphi(k_i,r,t)\prod_{l=0}^{r}\left(1-\frac{l}{\frac{ak_i}{2}}\right)\end{aligned} \tag{7}$$

$$\begin{aligned}\phi_e(k_i,m,t,a) &= \sum_{r=0}^{m}\varphi(k_i,r,t)\prod_{l=0}^{n}\left[1-h_e\left(\frac{l}{k_i},a\right)\right] \\ &= \sum_{r=0}^{\frac{ak_i}{2}}\varphi(k_i,r,t)\prod_{l=0}^{r}\left(1-\frac{l}{\frac{ak_i}{2}}\right) \\ &\quad + \sum_{r=\frac{ak_i}{2}}^{m}\varphi(k_i,r,t)\prod_{l=0}^{\frac{ak_i}{2}}\left(1-\frac{l}{\frac{ak_i}{2}}\right)\prod_{l=\frac{ak_i}{2}}^{r}\left(1-\frac{a-\frac{l}{k_i}}{a}\right)\end{aligned} \tag{8}$$

Then, for any hesitant node in state S, Eq. 9 can represent the probability that such nodes have not yet adopted the information by time t is:

$$\tau_e = \sum_{k_i} P(k_i)\phi_e(k_i,m,t,a) \tag{9}$$

Similarly, if node i is an common node in state S, and after time t, it has received m pieces of information cumulatively but has not

adopted the information and remains in state S, the probability is articulated by Eqs 10, 11:

$$\phi_q(k_i,m,t,a)=\sum_{r=0}^{m}\varphi(k_i,n,t)\prod_{l=0}^{r}\left[1-h_q\left(\frac{l}{k_i},a\right)\right]=\sum_{r=0}^{(1-a)k_i}\varphi(k_i,n,t)\prod_{l=0}^{r}\left[1-\frac{\frac{l}{(1-a)k_i}-a}{1-a}\right],(m>(1-a)k_i) \tag{10}$$

$$\phi_q(k_i,m,t,a)=\sum_{r=0}^{m}\varphi(k_i,r,t)\prod_{l=0}^{r}\left[1-h_q\left(\frac{l}{k_i},a\right)\right]=\sum_{r=0}^{m}\varphi(k_i,r,t)\prod_{l=0}^{r}\left[1-\frac{\frac{l}{(1-a)k_i}-a}{1-a}\right],(m<(1-a)k_i) \tag{11}$$

For any common node in state S, the probability of not adopting the information at the cut-off time t is:

$$\tau_q=\sum_{k_i}P(k_i)\phi(k_i,m,t,a) \tag{12}$$

Consequently, the probability that node i in state S, after time t, remains in state S after having cumulatively received m pieces of information is given by Eq. 13:

$$\phi(k_i,m,t,a)=(1-\rho_0)\left[e_0\phi_e(k_i,m,t,a)+q_0\phi_q(k_i,m,t,a)\right] \tag{13}$$

Then, in this weighted network, the proportion of S-state nodes at time t is delineated by Eq. 14:

$$\Phi(m,t,a)=\sum_{k}P(k)\phi(k,m,t,a)=(1-\rho_0)\left[e_0\tau_e+q_0\tau_q\right] \tag{14}$$

Due to the three states in the SAR model, this study introduces the term $\theta_\varepsilon(t)$ for calculation purposes. Initially, $\theta_\varepsilon(t)$ can be denoted using Eq. 15 as follows:

$$\theta_\varepsilon(t)=\eta_{S,\varepsilon}(t)+\eta_{A,\varepsilon}(t)+\eta_{R,\varepsilon}(t) \tag{15}$$

Where $\eta_{A,\varepsilon}(t)$ represents the probability that a node i in state S, by time t, has interacted with an adjacent node j in state A via an edge with weight ε but has not successfully adopted the information. $\eta_{S,\varepsilon}(t)$ and $\eta_{R,\varepsilon}(t)$ are the probabilities that a node i in state S interacts with an adjacent node j in state S (or R) via an edge with weight ε.

Initially, the cavity node theory is introduced to calculate $\eta_{S,\varepsilon}(t)$. A node i in the cavity state is unable to transmit information to other nodes. Thus, a node j in state S with degree k_j can receive information from the other k_j-1 adjacent nodes. Hence, the probability that node j has cumulatively received n pieces of information from its neighboring nodes by time t is articulated by Eq. 16:

$$\varphi(k_j-1,n,t)=\binom{k_j-1}{n}\theta(t)^{k_j-2-n}[1-\theta(t)]^n \tag{16}$$

Based on the differences in HECO characteristics and the information adoption function of the population, if node j is a hesitant node in state S, and after time t, it has received $n(n>a(k_j-1))$ pieces of information cumulatively but has not adopted the information and remains in state S, the probability is represented as:

$$\begin{aligned}\psi(k_j,n,t,a)&=\sum_{r=0}^{n}\varphi(k_j-1,r,t)\prod_{l=0}^{r}\left[1-h_e\left(\frac{l}{k_j},a\right)\right]\\&=\sum_{r=0}^{\frac{a(k_j-1)}{2}}\varphi(k_j-1,r,t)\prod_{l=0}^{r}\left(1-\frac{l}{\frac{a(k_j-1)}{2}}\right)\\&+\sum_{r=\frac{a(k_j-1)}{2}}^{a(k_j-1)}\varphi(k_j-1,r,t)\prod_{l=0}^{\frac{a(k_j-1)}{2}}\left(1-\frac{l}{\frac{a(k_j-1)}{2}}\right)\prod_{l=\frac{a(k_j-1)}{2}}^{r}\left(1-\frac{a-\frac{l}{k_j-1}}{a}\right)\\&+\sum_{r=a(k_j-1)}^{n}\varphi(k_j-1,n,t)\prod_{l=0}^{\frac{a(k_j-1)}{2}}\left(1-\frac{l}{\frac{a(k_j-1)}{2}}\right)\\&\times\prod_{l=\frac{a(k_j-1)}{2}}^{a(k_j-1)}\left(1-\frac{a-\frac{l}{k_j-1}}{a}\right)\prod_{l=a(k_j-1)}^{r}\left(1-\frac{\frac{l}{k_j-1}-a}{1-a}\right)\end{aligned} \tag{17}$$

Similarly, when the received information m satisfies the conditions $n<\frac{a(k_j-1)}{2}$ and $\frac{a(k_j-1)}{2}<n<a(k_j-1)$, the probability of not having adopted the information and still being in state S is represented as:

$$\begin{aligned}\psi(k_j,n,t,a)&=\sum_{r=0}^{n}\varphi(k_j-1,r,t)\prod_{l=0}^{r}\left[1-h_e\left(\frac{l}{k_j},a\right)\right]\\&=\sum_{r=0}^{\frac{a(k_j-1)}{2}}\varphi(k_j-1,r,t)\prod_{l=0}^{r}\left(1-\frac{l}{\frac{a(k_j-1)}{2}}\right)\\&+\sum_{r=\frac{a(k_j-1)}{2}}^{n}\varphi(k_j-1,r,t)\prod_{l=0}^{\frac{a(k_j-1)}{2}}\left(1-\frac{l}{\frac{a(k_j-1)}{2}}\right)\prod_{l=\frac{a(k_j-1)}{2}}^{r}\left(1-\frac{a-\frac{l}{k_j-1}}{a}\right)\end{aligned} \tag{18}$$

$$\psi(k_j,n,t,a)=\sum_{r=0}^{n}\varphi(k_j-1,r,t)\prod_{l=0}^{r}\left[1-h_e\left(\frac{l}{k_j},a\right)\right]=\sum_{r=0}^{n}\varphi(k_j-1,r,t)\prod_{l=0}^{r}\left(1-\frac{l}{\frac{a(k_j-1)}{2}}\right) \tag{19}$$

When node j is a common node in state S, and after time t, it has received n pieces of information cumulatively but has not adopted the information and remains in state S, the probability is represented as:

$$\psi(k_j,n,t,a)=\sum_{r=0}^{n}\varphi(k_j-1,r,t)\prod_{l=0}^{r}\left[1-h_q\left(\frac{l}{k_j-1},a\right)\right]=\sum_{r=0}^{(1-a)(k_j-1)}\varphi(k_j,r,t)\prod_{l=0}^{r}\left[1-\frac{\frac{l}{(1-a)(k_j-1)}-a}{1-a}\right],n>(1-a)(k_j-1) \tag{20}$$

$$\psi(k_j,n,t,a)=\sum_{r=0}^{n}\varphi(k_j-1,r,t)\prod_{l=0}^{n}\left[1-h_q\left(\frac{l}{k_j-1},a\right)\right]=\sum_{r=0}^{n}\varphi(k_j,r,t)\prod_{l=0}^{r}\left[1-\frac{\frac{l}{(1-a)(k_j-1)}-a}{1-a}\right],n\le(1-a)(k_j-1) \tag{21}$$

Consequently, the probability that a node j in state S remains in state S after cumulatively receiving n pieces of information by time t is given by Eq. 22:

$$\psi\left(k_j,n,t,a\right)=\left(1-\rho_0\right)\left[e_0\psi_e\left(k_j,n,t,a\right)+q_0\psi_q\left(k_j,n,t,a\right)\right] \quad (22)$$

The probability that a node i in state S can interact with a node j in state S via an edge with weight ε is:

$$\eta_{S,\varepsilon}(t)=\frac{\sum_{k_j}k_jP\left(k_j\right)\psi\left(k_j,n,t,a\right)}{\langle k\rangle} \quad (23)$$

Where $\frac{k_jP(k_j)}{\langle k\rangle}$ represents the probability of contact between node i and node j whose degree is k_j, and $\langle k\rangle$ is the network average degree.

Subsequently, analyze $\eta_{A,\varepsilon}(t)$ and $\eta_{R,\varepsilon}(t)$. Given that the probability of a node i in state S successfully adopting information from an adjacent node j in state A via an edge with weight ε is β_ε, then the probability $\theta_\varepsilon(t)$ can be further evolved as:

$$\frac{d\theta_\varepsilon(t)}{dt}=-\beta_\varepsilon\eta_{A,\varepsilon}(t) \quad (24)$$

In addition, a node in state A may lose interest in information transmission with probability γ and change to the state R, and $\eta_{R,\varepsilon}(t)$ can evolve into:

$$\frac{d\eta_{R,\varepsilon}(t)}{dt}=\gamma\eta_{A,\varepsilon}(t)\left(1-\beta_\varepsilon\right) \quad (25)$$

By combining the initial conditions $\theta_\varepsilon(0)=1$ and $\eta_{R,\varepsilon}(0)=0$, Eqs 18, 19 allows for the derivation of Eq. 26:

$$\eta_{R,\varepsilon}(t)=\gamma[1-\theta_\varepsilon(t)]\left(\frac{1}{\beta_\varepsilon}-1\right) \quad (26)$$

By substituting Eqs 17, 20 into Eq. 12, one arrives at Eq. 27:

$$\begin{aligned}\eta_{A,\varepsilon}(t)&=\theta_\varepsilon(t)-\eta_{S,\varepsilon}(t)-\eta_{R,\varepsilon}(t)\\&=\theta_\varepsilon(t)-\frac{\sum_{k_j}k_jP\left(k_j\right)\psi\left(k_j,n,t,a\right)}{\langle k\rangle}-\gamma[1-\theta_\varepsilon(t)]\left(\frac{1}{\beta_\varepsilon}-1\right)\end{aligned} \quad (27)$$

Substituting Eq. 21 into Eq. 18, $\theta_\varepsilon(t)$ evolves accordingly, as detailed in Eq. 28:

$$\begin{aligned}\frac{d\theta_\varepsilon(t)}{dt}&=\left\{\theta_\varepsilon(t)-\frac{\sum_{k_j}k_jP\left(k_j\right)\psi\left(k_j,n,t,a\right)}{\langle k\rangle}-\gamma[1-\theta_\varepsilon(t)]\left(\frac{1}{\beta_\varepsilon}-1\right)\right\}\\&=\beta_\varepsilon\frac{\sum_{k_j}k_jP\left(k_j\right)\psi\left(k_j,n,t,a\right)}{\langle k\rangle}+\gamma\left(1-\beta_\varepsilon\right)-\left[\gamma+\beta_\varepsilon\left(1-\gamma\right)\right]\theta_\varepsilon(t)\end{aligned} \quad (28)$$

In the whole network, the density changes of each state can be represented by Eqs 29, 30:

$$\frac{dR(t)}{dt}=\gamma A(t) \quad (29)$$

$$\frac{dA(t)}{dt}=-\frac{dS(t)}{dt}-\gamma A(t) \quad (30)$$

Therefore, the formula 11, 23, 24 can be iterated together to obtain each state density $S(t)$, $A(t)$ and $R(t)$ at any time step.

When $t\to\infty$, the status of nodes in the network does not change, and there are only S-state nodes and R-state nodes in the network. That is, when $\frac{d\theta_\varepsilon(t)}{dt}|_{t=\infty}\to 0$, $R(\infty)$ is the final information adoption size. At this time, the probability that the edge with the weight of ε does not propagate information is articulated by Eq. 31:

$$\theta_\varepsilon(\infty)=\frac{\beta_\varepsilon\sum_{k_j}k_jP\left(k_j\right)\psi\left(k_j,n,\infty,a\right)+\langle k\rangle\gamma\left(1-\beta_\varepsilon\right)}{\langle k\rangle\gamma+\left(1-\gamma\right)\beta_\varepsilon\langle k\rangle} \quad (31)$$

By combining the formula 11 and 25, the combinatorial iteration results in $S(\infty)$ and $R(\infty)$.

Next, focus on the analysis of critical propagation probability, leading to the introduction of Eq. 32:

$$\begin{aligned}\Theta[\beta_\varepsilon,\rho_0,a,\gamma,\lambda]=&\frac{\beta_\varepsilon\sum_{k_j}k_jP\left(k_j\right)\psi\left(k_j,n,\infty,a\right)+\langle k\rangle\gamma\left(1-\beta_\varepsilon\right)}{\langle k\rangle\gamma+\left(1-\gamma\right)\beta_\varepsilon\langle k\rangle}\\&+\frac{\gamma\left(1-\beta_\varepsilon\right)}{\gamma+\left(1-\gamma\right)\beta_\varepsilon}-\beta_\varepsilon(\infty)\end{aligned} \quad (32)$$

$\theta_\varepsilon^c(\infty)$ is used to represent the critical probability point of $\theta_\varepsilon(t)$. Under the unit critical propagation probability, when $t\to\infty$, information cannot propagate to node j through the corresponding edge. At the critical value of $\theta_\varepsilon^c(\infty)$, $\Theta[\beta_\varepsilon(\infty),\rho_0,a,\gamma,\lambda]$ is tangent to the horizontal axis. Thus, the critical condition can be delineated as shown in Eq. 33:

$$\frac{d\Theta}{d\theta_\varepsilon(\infty)}|_{\theta_\varepsilon^c(\infty)}=0 \quad (33)$$

4 Simulation and discussion

To validate the theoretical analysis mentioned above, we conducted numerical simulations and theoretical analysis based on weighted Erdos-Renyi (ER) networks [34] and weighted Scale-Free (SF) networks [35].

Firstly, a more comprehensive introduction to the Erdos-Renyi (ER) network and the Scale-Free (SF) network is provided. The ER network model is one of the most fundamental models in the study of complex network theory and holds significant importance for understanding randomness in networks and stochastic phenomena within networks. The construction rules are as follows: (1) There is a fixed number of nodes within the network; (2) Each pair of nodes is randomly connected with the same probability p, meaning that the existence of an edge (link) between any two nodes is independent, and this probability is identical for all node pairs; (3) The ER network model typically refers to an undirected graph, where edges have no direction; (4) The network contains no self-loops (nodes connecting to themselves) and multiple edges (more than one edge between the same pair of nodes) [36]. The ER network has practical applications, including: the ER model can be used to simulate random friendship formation in social networks [37], in bioinformatics, it is utilized to model the randomness of gene

regulatory networks or protein interaction networks [38], and it can also be applied in transportation networks to simulate random route selection in urban traffic networks [39].

The SF network is a network model characterized by a power-law distribution in the connectivity degree of its nodes. The basic steps for constructing an SF network are as follows: (1) Initial Network: Start with a small network, typically consisting of a few nodes and the connections between them; (2) Growth: Over time, the network grows by adding new nodes. Each new node comes with several edges that connect to certain nodes in the existing network; (3) Preferential Attachment: The probability that a new node connects to an existing node is proportional to its degree (i.e., the number of connections of the existing node). This means that the more connections a node has, the higher the likelihood it will attract new connections; (4) Network Topology: In this manner, the network's topology evolves over time, developing a special degree distribution known as a power-law distribution, which is one of the characteristics of SF networks; (5) No Self-Loops and Multiple Edges: Self-loops (nodes connecting to themselves) and multiple edges (more than one edge between two nodes) are generally not allowed during the construction process; (6) Network Size: Nodes and edges can continue to be added until the network reaches the desired scale [40]. Related instances of SF networks include: Protein interaction networks and metabolic networks in biological systems are often modeled as SF networks [41]. Certain parts of power transmission networks can be modeled as SF networks to study their robustness and vulnerability [42]. In financial markets, the network of transaction relationships between companies also exhibits characteristics of SF networks [43].

In the weighted ER network and SF network, 10,000 independent nodes are set in the network, the average degree of the network $\langle k\rangle = 10$, the weight distribution is $f_X(\varepsilon) \sim \varepsilon^{-\alpha_\varepsilon}$, $\varepsilon^{\max} \sim 1/(\alpha_\varepsilon - 1)$, and the average weight $\langle\varepsilon\rangle = 8$. In addition, the probability of the A-state node returning to the R-state is $\gamma = 1.0$.

In this paper, the relative variance X is used to illustrate the critical unit propagation probability and critical conditions in the simulation, and is articulated by Eq. 34 as follows:

$$\kappa = N\frac{\langle R(\infty)^2\rangle - \langle R(\infty)\rangle^2}{\langle R(\infty)\rangle} \tag{34}$$

Where $\langle ...\rangle$ is the set mean, and the maximum value of κ is the critical point of the final adoption scale.

The analysis of information dissemination models within this study relies on the thermodynamic classification of phase transitions. Phase transitions are categorized based on the mathematical characteristics—continuous or discontinuous—of the partial derivatives of free energy with respect to temperature and pressure at the transition point. This categorization includes first-order, second-order, and higher-order phase transitions, with the focus of this study being on the first two types. In the context of thermodynamics, a first-order phase transition is characterized by equal chemical potentials between the new and old phases, yet differing first-order partial derivatives. This type of transition is associated with a discontinuous change in both entropy and volume. A second-order phase transition is distinguished by equal chemical potentials and first-order partial derivatives between phases, but with second-order partial derivatives that are not equal, resulting in no change in entropy or volume. The phase transition model is employed to describe the growth rate of the dissemination range during the process of information dissemination. A rapid growth in the dissemination range with the unit dissemination probability, marked by a discontinuous change, is classified as a first-order discontinuous phase transition. In contrast, a slow growth exhibiting a continuous change is classified as a second-order continuous phase transition.

In this section, to conduct a more nuanced examination of the influence of the HECO characteristic on the propagation of information within social networks, we focus on two parameters that are most representative of the HECO trait: the proportion of the common population q_0 and the hesitation parameter a. Consequently, this section predominantly employs these two parameters, q_0 and a, in our simulation analysis to explore the distinct dissemination patterns of information across various proportions of hesitant and common populations within the network, as well as under different levels of individual decisiveness.

4.1 The propagation process of weighted ER network

In this paper, the propagation of information on weighted ER network is discussed first. The nodes in ER network obey Poisson distribution, that is, $P(k) = e^{-\langle k\rangle}\langle k\rangle^k/k!$.

Figure 3 describes the impact of the unitary propagation probability λ on the ultimate propagation range $R(\infty)$ in a weighted ER network when the decision-making ability of the hesitant population is relatively strong (hesitancy parameter $a = 0.2$), under different proportions of the hesitant population. The initial proportion of nodes in state A, $\rho_0 = 0.001$. Subfigures 3(a1) and 3(b1) indicate that as λ increases, the ultimate adoption range $R(\infty)$ gradually enlarges. It can also be observed that at higher values of λ ($\lambda > 0.5$), where the change in the ultimate propagation range with λ is minimal, the larger the proportion of the common population, the greater the ultimate adoption range $R(\infty)$ at equilibrium. When the proportion of the common population q_0 is large ($q_0 = 0.8$), the information propagation exhibits a first-order discontinuous phase transition, whereas for smaller or half proportions of the common population ($q_0 = 0.2$ and $q_0 = 0.5$), it exhibits a second-order continuous phase transition. Subfigures 3(a2) and 3(b2) present the statistical calculations of the relative standard deviation for both theoretical analysis and simulation values, as well as the critical points derived from subfigures 3(a1) and 3(b1). As the proportion of the common population increases, the growth in information adoption and the onset of the adoption explosion threshold are delayed. However, this delay results in a more rapid attainment of a global adoption state. This suggests that when the hesitant population possesses a strong decision-making ability, a smaller proportion of the common population results in faster propagation and an earlier onset, although the rate of propagation range growth with unitary propagation probability remains relatively slow. Conversely, when the proportion of the common population is large, the onset of information propagation is further delayed. Yet, the rate of propagation range growth with unitary propagation probability is more rapid, potentially leading to a discontinuous phase transition and a swifter achievement of a global adoption state. Moreover, in comparison to Figures 3A, B, an increase in the weighted distribution exponent is shown to advance

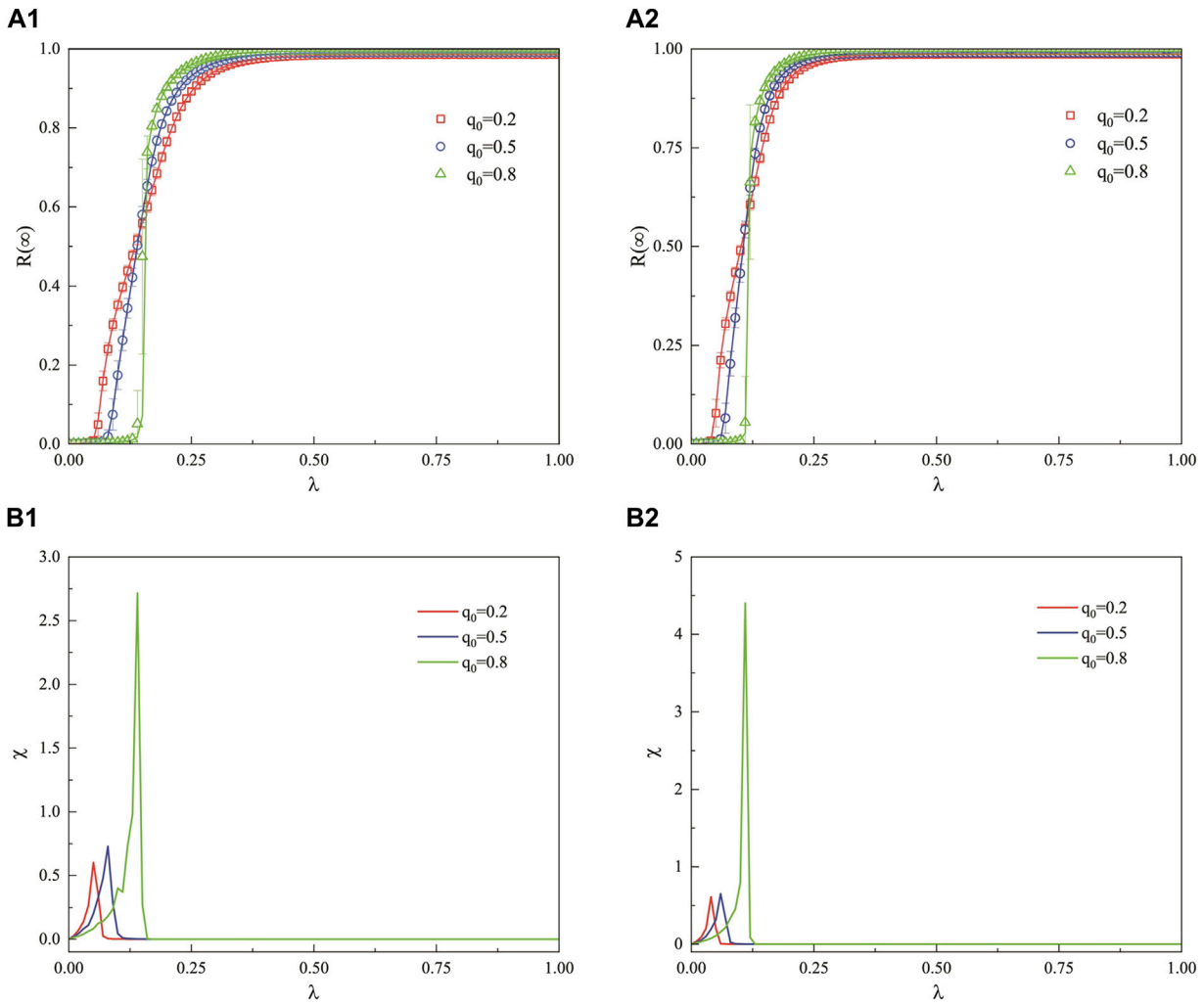

FIGURE 3
In the weighted ER network, when the decision-making ability of the hesitant population is relatively strong, the variation of the final propagation range for both adopting populations under different proportions q_0 as a function of the propagation probability λ is depicted. Subfigures **(A1,B1)** illustrate the impact of different edge weights ($\varepsilon = 25$ and $\varepsilon = 35$) on the propagation patterns, respectively. Subfigures 3 **(A2,B2)** represent the distribution of the relative standard deviation of the simulation results and the critical points of the propagation threshold in subfigures 3(a1) and 3(b1), respectively. Other parameters are set to $\rho_0 = 0.001$ and $a = 0.2$.

the adoption explosion point. However, variations in the weight distribution do not impact the phase transition mode.

Figure 4 illustrates the impact of the unit propagation probability λ on the ultimate propagation range in a weighted ER network when the decision-making ability of the hesitant population is moderate ($a = 0.5$), across various proportions of the hesitant population q_0. Subfigures 4(a1) and 4(b1) indicate that under different weight distributions, the proportion of the ordinary population q_0 does not significantly affect the propagation pattern of information; that is, the adoption outbreak points are essentially consistent, and both exhibit a first-order discontinuous phase transition. However, when the information propagation outbreak occurs, it is observed that a larger proportion of the ordinary population q_0 results in a larger ultimate adoption range $R(\infty)$ at equilibrium. Subfigures 4(a2) and 4(b2) present the relative standard deviation calculated from the statistical simulation values and the critical threshold for the propagation outbreak as shown in subfigures 4(a1) and 4(b1), respectively. As the proportion of the common population increases, information propagation can reach equilibrium at a relatively lower unit propagation probability λ in the early stages. These observations suggest that under moderate decision-making ability, regardless of the proportion of the common population, the outbreak threshold for information propagation remains the same, but a larger proportion of the common population leads to a greater jump in the adoption range during the outbreak and a more rapid achievement of the global adoption state. Similarly, when the proportion of the common population q_0 is small, the jump in the adoption range during the outbreak and the ultimate adoption range at equilibrium are also relatively smaller, failing to reach global propagation. Additionally, compared to Figure 4A, with Figure 4B, an increase in the weighted distribution index advances the adoption outbreak point, but changes in the weight distribution do not affect the phase transition pattern of propagation.

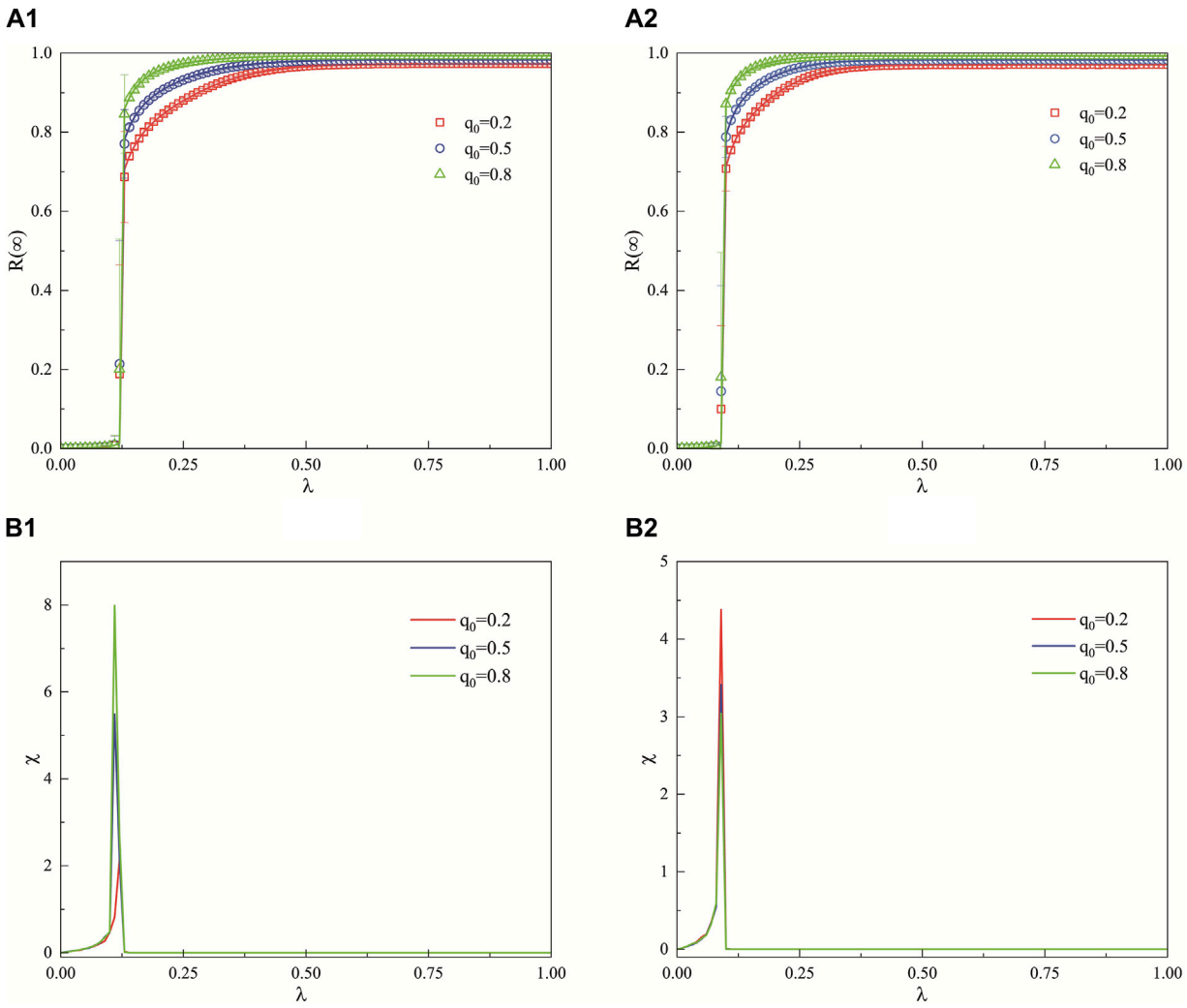

FIGURE 4
In the context of a weighted ER network, where the decision-making capacity of the hesitant population is moderate, this figure examines the effect of the unit propagation probability λ on the ultimate propagation range across various proportions of the common population q_0. Subfigures 4 **(A1,B1)** depict the influence of weight distribution variations ($\varepsilon = 25$ and $\varepsilon = 35$) on the propagation patterns. Subfigures 4 **(A2,B2)** present the statistical computation of the relative standard deviation of the simulated values and the critical threshold for propagation outbreak as indicated in subfigures 4(a1) and 4(b1), respectively. Additional parameters are fixed at $\rho_0 = 0.001$ and $a = 0.5$.

From Figures 5A1, B1, it can be observed that as the unit propagation probability λ increases, the ultimate adoption range $R(\infty)$ gradually enlarges, and the larger the proportion q_0 of the common population, the greater the ultimate adoption range $R(\infty)$ at equilibrium. At $q_0 = 0.8$ and $q_0 = 0.5$, the propagation pattern of the ultimate adoption range exhibits a second-order continuous phase transition, while at $q_0 = 0.2$, it shows a first-order discontinuous phase transition. Figures 5A2, B2 indicate that the larger the proportion q_0 of the common population, the smaller the unit propagation probability threshold at the time of adoption outbreak. Figures 5A, B demonstrate that when the decision-making ability of the hesitant population is low, a larger proportion of the common population can reach the information adoption outbreak point at a smaller unit propagation probability λ, and the ultimate adoption range at equilibrium is larger. Conversely, when there is a smaller proportion of the ordinary population, the outbreak threshold for information propagation is higher, and the ultimate adoption range at equilibrium is relatively smaller. Additionally, compared to Figure 5A, with Figure 5B, the adoption outbreak point advances with an increase in the weighted distribution index, but changes in the weight distribution do not alter the phase transition pattern of propagation.

Figure 6 describes the joint effect of the unit propagation probability λ and the hesitancy parameter a on the ultimate adoption range $R(\infty)$ in a weighted ER network when the proportions of the hesitant and common populations are equal ($q_0 = 0.5$), under different weight distributions (subfigure 6(a) with $\varepsilon = 25$ and subfigure 6(b) with $\varepsilon = 35$). The initial proportion of nodes in state A, $\rho_0 = 0.001$. The joint effect plane is divided into four regions based on different propagation patterns of information, Region I: With the increase in the unit propagation probability λ and the hesitation parameter a, the color temperature remains unchanged and is at its lowest, indicating that no information propagation phenomenon has occurred. Regions II and IV: With

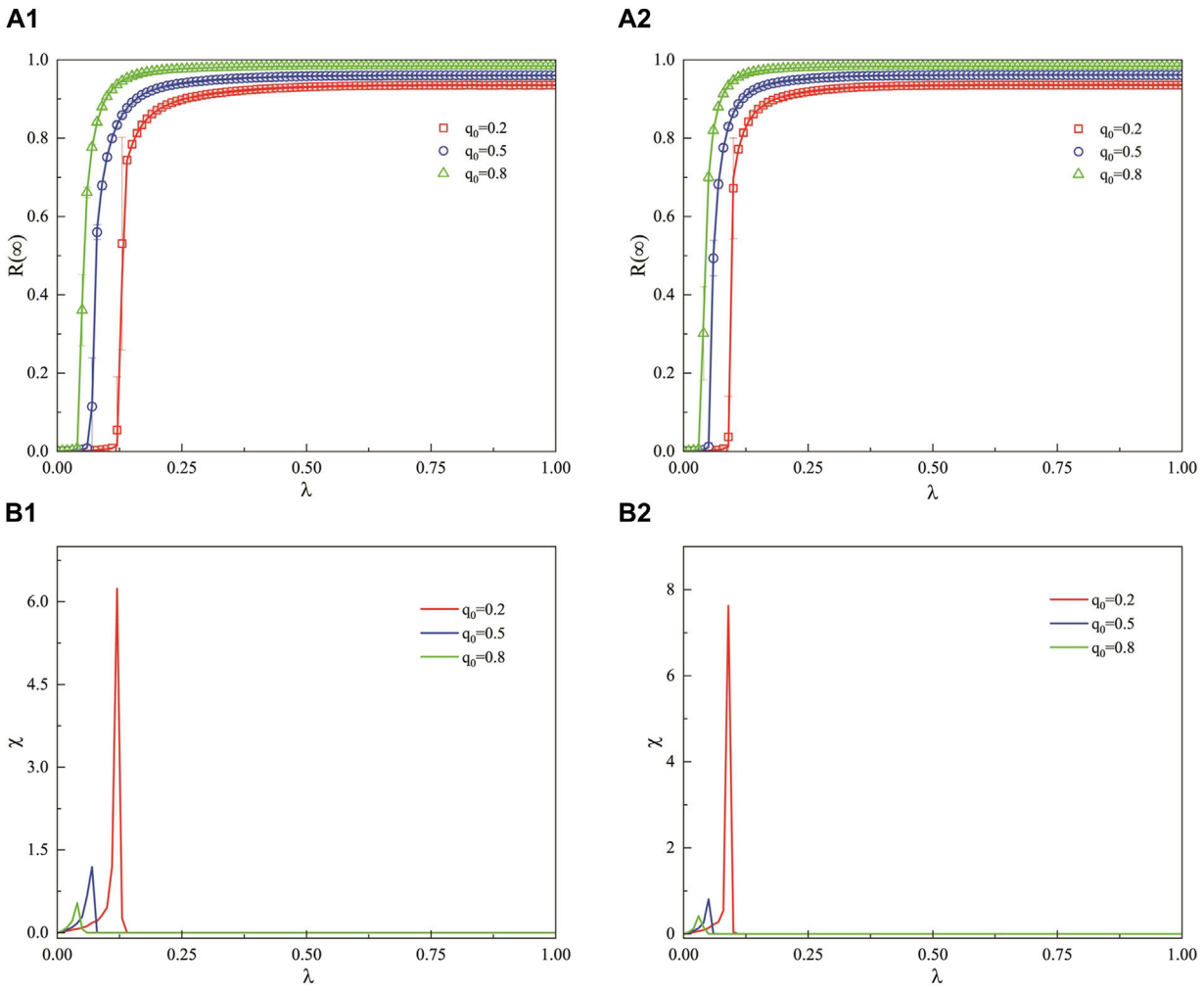

FIGURE 5
Under the weighted ER network, this figure presents the influence of the unit propagation probability λ on the ultimate adoption range across different proportions of the common population q_0 when the decision-making ability of the hesitant population is relatively weak. Subfigures **(A1,B1)** demonstrate the effects of changes in weight distribution (ε = 25 and ε = 35) on the propagation patterns. Subfigures 5 **(A2,B2)** represent the statistical computation of the relative standard deviation of the simulated values and the critical threshold for the information outbreak as indicated in subfigures 5(a1) and 5(b1). Other parameters are set to ρ_0 = 0.001 and a = 0.8.

the increase in the unit propagation probability λ and the hesitation parameter a, there is a distinct stage of continuous color temperature change in the color temperature map, signifying that a second-order continuous phase transition has occurred in these areas. Region III: Upon With the increase in the unit propagation probability λ and the hesitation parameter a, there is a distinct moment of abrupt color temperature change in the color temperature map, indicating that a first-order discontinuous phase transition has occurred in this area. In Region I, where the hesitancy parameter is very small, indicating a very strong decision-making ability of the hesitant population, no information propagation outbreak occurs. This is because the hesitant population, with strong decision-making ability, inhibits the spread of information. In Region II, as the hesitancy parameter increases (indicating a weakening decision-making ability), the growth of the ultimate adoption range $R(\infty)$ exhibits a second-order continuous phase transition. This is due to the hesitant population dominating in the early stages of information propagation when the decision-making ability is relatively strong, leading to an outbreak. Subsequently, as λ increases, the common population continues the propagation on the basis of the hesitant population. In Region III, with a further increase in the hesitancy parameter and a continued weakening of decision-making ability, the growth of the ultimate adoption range $R(\infty)$ exhibits a first-order discontinuous phase transition. In this region, the decision-making ability of the hesitant population is moderate, and the adoption capabilities of the hesitant and common populations are similar, with no dominant side. Both sides have similar outbreak thresholds and outbreak simultaneously during the propagation process, leading to a first-order discontinuous phase transition. In Region IV, where the hesitancy parameter is large and the decision-making ability of the population is very low, the growth of the ultimate adoption range $R(\infty)$ exhibits a second-order continuous phase transition. This is the result of the common population dominating the propagation when the decision-making ability of the hesitant population is low, hence the outbreak threshold for this second-order continuous propagation

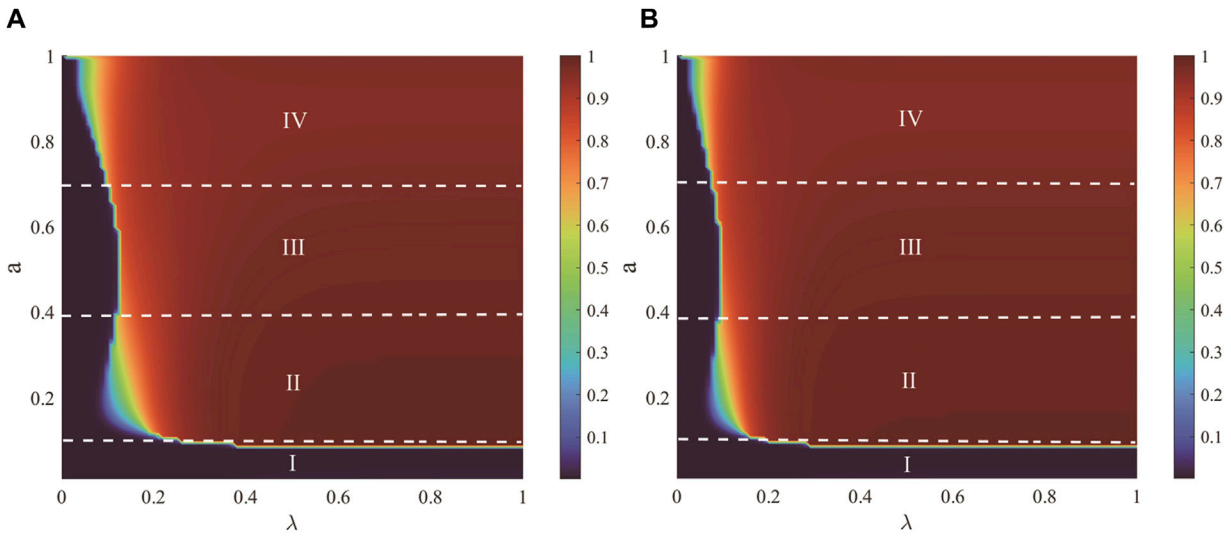

FIGURE 6
The joint effect of the unit propagation probability λ and the hesitancy parameter a on the ultimate adoption range $R(\infty)$ in a weighted ER network. Under different weight distributions, subfigure 6 **(A)** ($\varepsilon = 25$) and subfigure **(B)** ($\varepsilon = 35$) illustrate the occurrence of information stagnation propagation, first-order continuous phase transition, second-order continuous phase transition, and first-order discontinuous phase transition phenomena in regions I, II, III, and IV, respectively. All other parameters are set to $\rho_0 = 0.001$ and $q_0 = 0.5$.

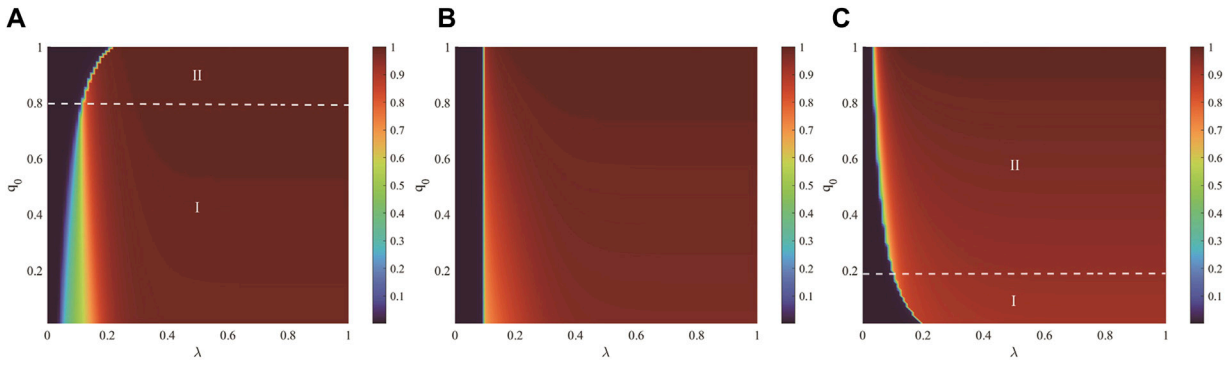

FIGURE 7
The joint effect of the unit propagation probability λ and the proportion of the common population q_0 on the ultimate adoption range $R(\infty)$ in a weighted ER network is depicted. Subfigures 7 **(A)** ($a = 0.2$), **(B)** ($a = 0.5$), and **(C)** ($a = 0.8$) represent the influence of λ and q_0 on the ultimate adoption range under different decision-making abilities of the hesitant population. In subfigure 7 **(A)**, Region I exhibits a second-order continuous phase transition, and Region II exhibits a first-order discontinuous phase transition; in subfigure 7 **(B)**, the entire region shows a first-order discontinuous phase transition; in subfigure 7 **(C)**, Region I exhibits a first-order discontinuous phase transition, and Region II exhibits a second-order continuous phase transition. All other parameters are set to $\rho_0 = 0.001$ and $a = 0.5$.

is smaller than that in Region II. This also illustrates that the common population has a stronger promoting effect on the outbreak of information propagation than the hesitant population. Furthermore, compared to Figures 6A, B indicates that an increase in the weighted distribution index can promote the adoption of information.

Figure 7 illustrates the joint effect of the unit propagation probability λ and the proportion of the common population q_0 on the ultimate adoption range $R(\infty)$ in a weighted ER network, under different decision-making abilities of the hesitant population with a constant weight distribution index. The initial proportion of nodes in state A, $\rho_0 = 0.001$, with hesitancy parameters a being 0.2 for subfigure 7(a), 0.5 for subfigure 7(b), and 0.8 for subfigure 7(c). In subfigure 7(a), where the hesitant population has a strong decision-making ability ($a = 0.2$), the figure can be divided into two regions based on the phase transition patterns. As the proportion of the common population q_0 increases, there is a transition from a second-order continuous phase transition in Region I to a first-order discontinuous phase transition in Region II. Region I: With the increase in the unit propagation probability λ and the proportion of the common population q_0, there is a distinct stage of continuous color temperature change in the color temperature map, signifying that a second-order continuous phase transition has occurred in these areas. Regions II: With the increase in the unit propagation

probability λ and the proportion of the common population q_0, there is a distinct moment of abrupt color temperature change in the color temperature map, indicating that a first-order discontinuous phase transition has occurred in this area. In Region I ($q_0 < 0.8$), the proportion of the hesitant population gradually decreases with increasing q_0, causing a delay in the outbreak of information propagation. However, the phase transition mode of propagation shifts from continuous to discontinuous. This is because the hesitant population, which is dominant at this stage, determines the outbreak of information propagation. Therefore, the more the hesitant population, the easier the outbreak, but due to their slower propagation speed, the growth of propagation is initially slow until the threshold of the common population is reached, after which the propagation range grows rapidly. In Region II ($0.8 < q_0 \leq 1$), where the common population is in the majority, the proportion of the hesitant population decreases with increasing q_0, insufficient to support an outbreak of propagation. The outbreak of information propagation becomes more delayed and approaches an outbreak that would occur if only the common population were present, leading to a first-order discontinuous propagation pattern that reaches a global adoption state. Observing horizontally at lower unit propagation probabilities ($\lambda < 0.2$), Region I has already reached global adoption, while Region II has not yet begun to propagate, confirming the above conclusions. In subfigure 7(b), the growth pattern of $R(\infty)$ is a first-order discontinuous phase transition across all regions. Upon With the increase in the unit propagation probability λ and the proportion of the common population q_0, The color temperature map exhibits an abrupt change in color temperature at a fixed unit propagation probability 'a', indicating the occurrence of a first-order discontinuous phase transition in that region. When the decision-making ability of the hesitant population is moderate ($a = 0.5$), the common and hesitant populations have equal dominance. The proportion of the common population q_0 does not affect the outbreak of information propagation; all propagation outbreaks have consistent thresholds as shown in the figure. Despite the consistent thresholds across different proportions, the different adoption phenomena of the hesitant and common populations lead to an increase in the ultimate adoption range $R(\infty)$ at the time of propagation outbreak as the proportion of the common population q_0 increases. This is because the common population has a stronger promoting effect on the propagation process than the hesitant population. Therefore, when there is a larger common population, the adoption rate during the propagation outbreak is faster, resulting in a larger adoption range. Subfigure 7(c) is divided into two regions based on the phase transition patterns, Region I: As the unit propagation probability λ and the proportion of the common population q_0 increase, the color temperature map exhibits a distinct moment of abrupt color temperature change, transitioning from the lowest to the highest color temperature, indicating that a first-order discontinuous phase transition has occurred in this region. Region II: With the increase in the unit propagation probability λ and the proportion of the common population q_0, the color temperature map displays a less pronounced continuous change in color temperature, showing a gradual transition from the lowest to the highest color temperature as compared to Region 1, signifying that a second-order continuous phase transition has taken place in this region. When the decision-making ability of the hesitant population is weak ($a = 0.8$), the adoption phenomenon of the common population dominates. In Region I ($q_0 < 0.2$), where the proportion of the common population is small, there is insufficient dominant population to guide the outbreak of propagation, making the propagation more closely aligned with the outbreak threshold of the hesitant population and exhibiting a discontinuous propagation pattern. As the proportion of the common population q_0 increases and enters Region II ($0.2 < q_o \leq 1$), the common population takes the lead in propagation, with the common population initiating the outbreak first, followed by the hesitant population, showing continuous characteristics. However, due to the promoting effect of the common population on information propagation, the continuous features are not as strong as those when the hesitant population is dominant in subfigure 7(a). Nevertheless, it can be observed from subfigure 7(c) that as the proportion of the common population increases, the ultimate propagation range at equilibrium also becomes larger.

4.2 The propagation process of weighted SF network

In the weighted SF network, the degree distribution heterogeneity of nodes is negatively correlated with the degree index ν, the degree of nodes follows the power distribution $P(k) = \xi k^{-\nu}$, $\xi = 1/\sum_k k^{-\nu}$, and the parameter ν represents the degree index of SF network.

Figure 8 demonstrates the impact of the unit propagation probability λ on the ultimate adoption range $R(\infty)$ for different proportions of the common population q_0 in a weighted SF network, when the decision-making ability of the hesitant population is strong (hesitancy parameter $a = 0.2$). Subfigures 8(a1) and 8(b1) show the effects of different degree indices $\nu = 2.1$ and $\nu = 4$ on the propagation patterns, respectively. The initial proportion of nodes in state A, $\rho_0 = 0.001$, and the edge weight is taken as $\varepsilon = 25$. It can be observed from subfigures 8(a1) and 8(b1) that as λ increases, $R(\infty)$ gradually enlarges. However, in subfigure 8(a1), an increase in the proportion of the common population enhances the ultimate adoption range at equilibrium, while in subfigure 8(b1), the ultimate propagation reaches global propagation at equilibrium. It is also noticeable that when the proportion q_0 is small ($q_0 = 0.2$), indicating a larger number of hesitant individuals, the propagation outbreak threshold occurs earlier compared to when the proportion is larger ($q_0 = 0.5$ and $q_0 = 0.8$). This is attributed to the stronger decision-making ability of the hesitant population, which takes the leading role. Therefore, when the dominant population is larger, it facilitates the outbreak of information propagation, aligning with the propagation phenomena and theories observed in weighted ER networks. Additionally, it is found that the propagation patterns during the outbreak differ; when $q_0 = 0.2$ and $q_0 = 0.5$, a second-order continuous propagation phenomenon is exhibited, but there is a change in the slope of the propagation trend line, due to the initial outbreak being dominated by the hesitant population followed by the inclusion of the common population, leading to a change in the propagation speed. Furthermore, as the degree index ν increases (indicating a decrease in degree distribution heterogeneity), making the

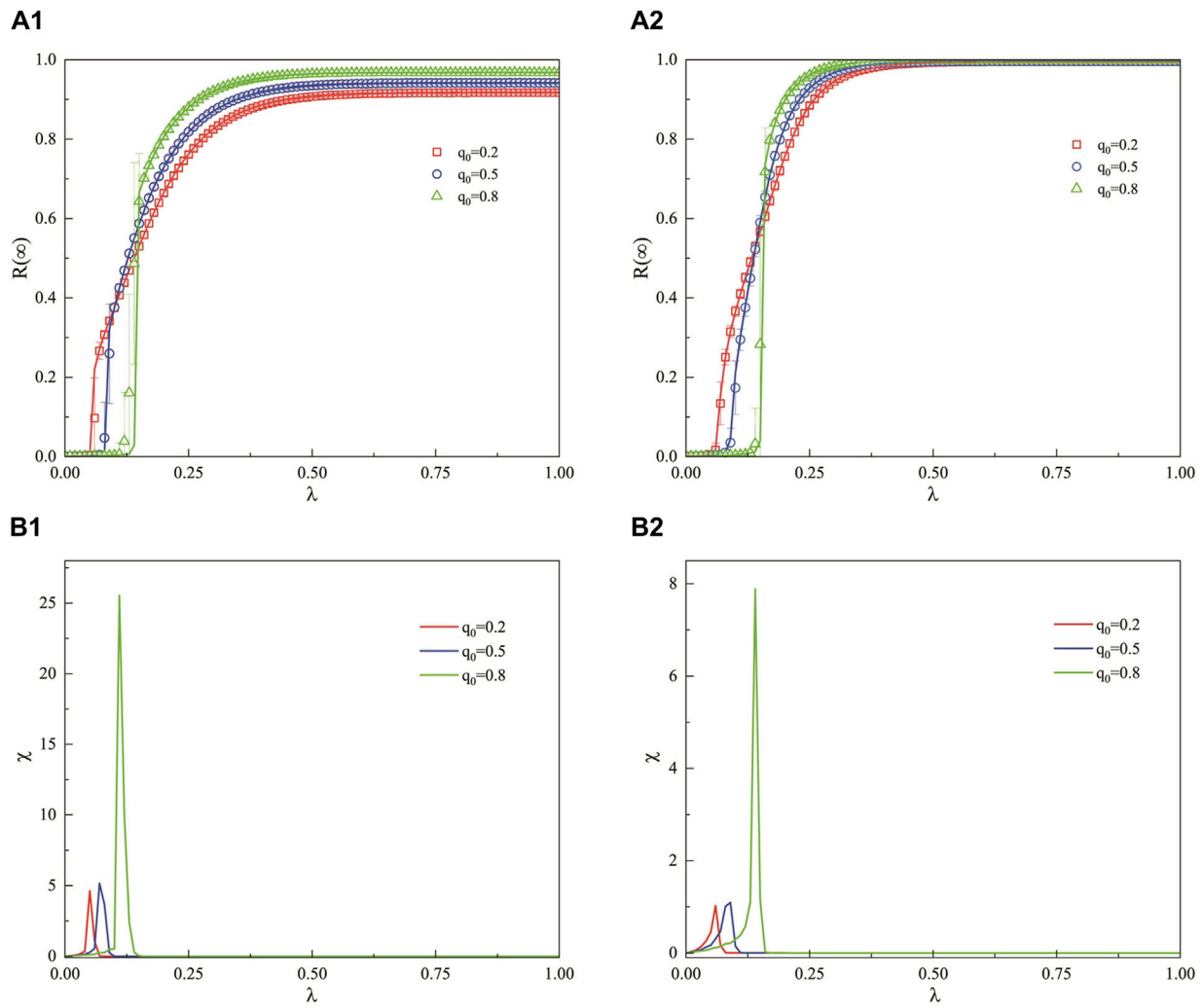

FIGURE 8
In a weighted SF network, when the decision-making ability of the hesitant population is relatively strong, this figure illustrates the impact of the unit propagation probability λ on the ultimate propagation range across different proportions of the common population q_0. Subfigures 8 **(A1)** (ν = 2.1) and 8 **(B1)** (ν = 4) describe the influence of different degree indices on the propagation patterns. Subfigures 8 **(A2,B2)** represent the statistical computation of the relative standard deviation of the simulated values and the critical threshold for propagation outbreak as indicated in subfigures 8(a1) and 8(b1), respectively. The remaining parameters are fixed at ρ_0 = 0.001, a = 0.2, and ε = 25.

degrees of individuals in the network more similar, the propagation outbreak threshold does not change significantly. However, the ultimate adoption range at equilibrium increases, and the propagation rate becomes faster, eventually reaching global adoption. Thus, when the decision-making ability of the hesitant population is strong, reducing the degree distribution heterogeneity can promote a larger ultimate adoption range and even global propagation at equilibrium. Subfigures 8(a2) and 8(b2) represent the relative standard deviation computed from the statistical analysis of the simulation values and the critical threshold for the propagation outbreak as indicated in subfigures 8(a1) and 8(b1), respectively. Moreover, the theoretical analysis (curves) matches well with the simulation values (symbols), indicating a good fit.

Figure 9 depicts the influence of the unit propagation probability λ on the ultimate adoption range in a weighted SF network when the decision-making ability of the hesitant population is moderate, across different proportions q_0 of the common population. Subfigures 9(a1) and 9(b1) showcase the effects of different degree indices (ν = 2.1 and ν = 4) on the propagation patterns. The initial proportion of nodes in state A, ρ_0 = 0.001, with an edge weight value of ε = 25. As λ increases, $R(\infty)$ gradually enlarges, and the proportion q_0 of the common population has no significant effect on the outbreak point of propagation. This is because, at this time, the adoption thresholds of both hesitant and common individuals are essentially the same, consistent with the propagation phenomena observed in the aforementioned ER networks. However, the larger the proportion of the common population, the greater the ultimate adoption range $R(\infty)$ achieved during the propagation outbreak. Additionally, as the degree heterogeneity index ν increases (indicating a decrease in degree distribution heterogeneity), making the degrees of individuals in the network more similar, the outbreak threshold for information propagation does not change significantly. However, the ultimate adoption range at equilibrium increases,

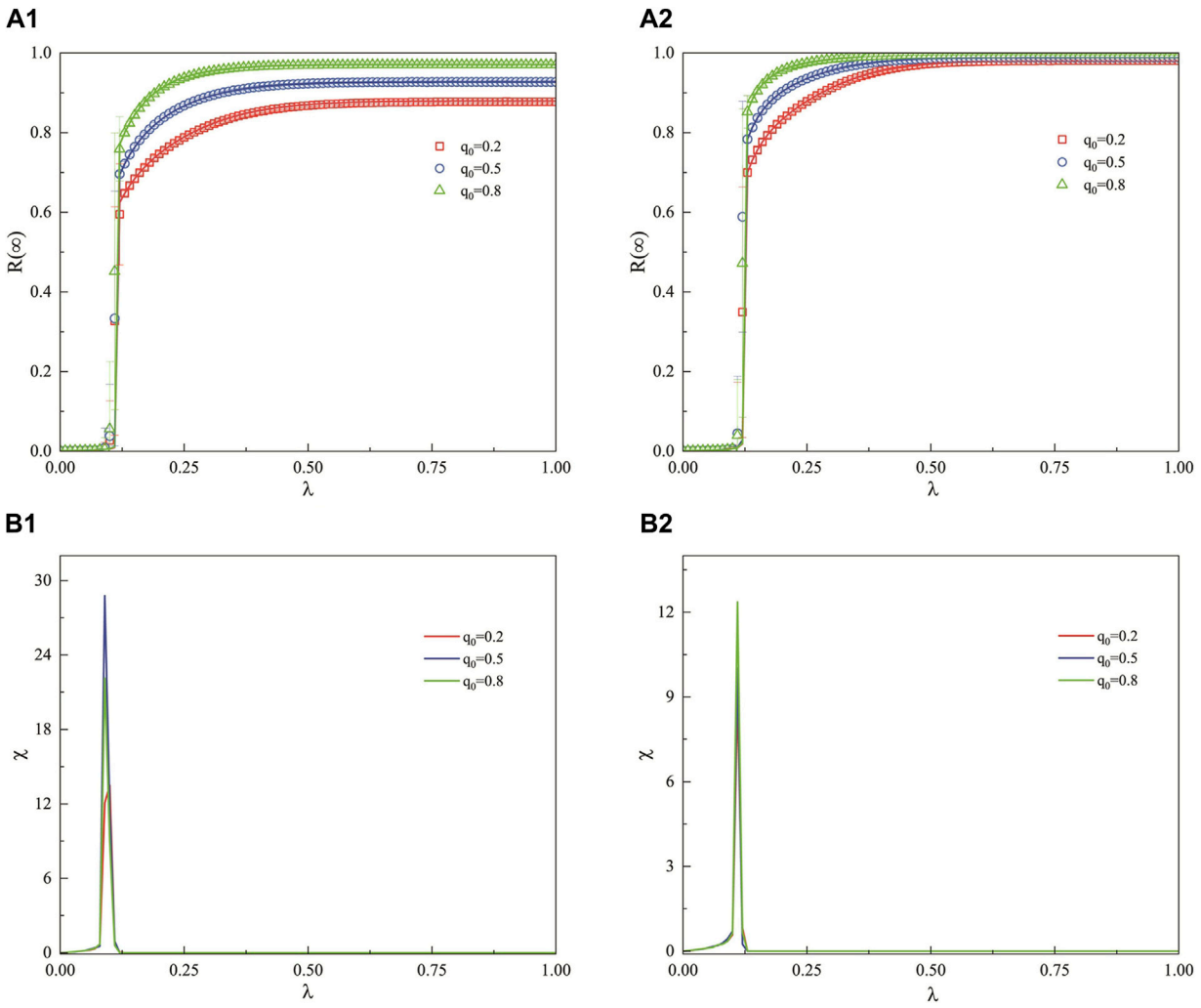

FIGURE 9
In a weighted SF network, this figure examines the influence of the unit propagation probability λ on the propagation range under different proportions of the common population q_0 when the decision-making ability of the hesitant population is moderate. Subfigures 9 **(A1)** with degree exponent $\nu = 2.1$ and 9 **(B1)** with $\nu = 4$ illustrate the effects of different degree indices on the propagation patterns. Subfigures 9 **(A2,B2)** depict the statistical computation of the relative standard deviation of the simulated values and the critical threshold for the propagation outbreak as indicated in subfigures 9(a1) and 9(b1), respectively. All other parameters are set to $\rho_0 = 0.001$, $a = 0.2$, and $\varepsilon = 25$.

and the propagation rate becomes faster, reaching global adoption at equilibrium. Subfigures 9(a2) and 9(b2) present the statistical computation of the relative standard deviation of the simulated values and the critical threshold for the propagation outbreak as indicated in subfigures 9(a1) and 9(b1), respectively. When the decision-making ability of the hesitant population is moderate, the growth pattern of the adoption range $R(\infty)$ is discontinuous for different proportions of the common population q_0 and different degree indices ν. Therefore, reducing the degree distribution heterogeneity can promote a larger ultimate adoption range in information propagation when the decision-making ability of the hesitant population is moderate. Moreover, the theoretical analysis (curves) matches well with the simulation values (symbols), indicating a good fit.

Figures 10A1, B1 present the influence of different degree indices ($\nu = 2.1$ and $\nu = 4$) on the propagation patterns, with an initial proportion of nodes in state A ($\rho_0 = 0.001$) and an edge weight value ($\varepsilon = 25$). As the unit propagation probability λ increases, the ultimate adoption range $R(\infty)$ gradually enlarges. From Figure 10A1, it can be observed that when $q_0 = 0.8$, indicating that the majority of the population is in the common state, the outbreak threshold for propagation occurs earlier compared to when $q_0 = 0.2$ and $q_0 = 0.5$. This is attributed to the weaker decision-making ability of the hesitant population, where the common population takes a dominant role in propagation. Furthermore, due to the promoting effect of the common population on propagation, a higher proportion of the common population leads to a larger ultimate propagation range at equilibrium. These conclusions and phenomena are consistent with the theories and observations derived from weighted ER networks. Comparing Figures 10A1, B1, it is noted that as the degree heterogeneity index ν increases (indicating a reduction in degree distribution heterogeneity) and the degrees of individuals in the network become more similar, the ultimate adoption range in Figure 10B1

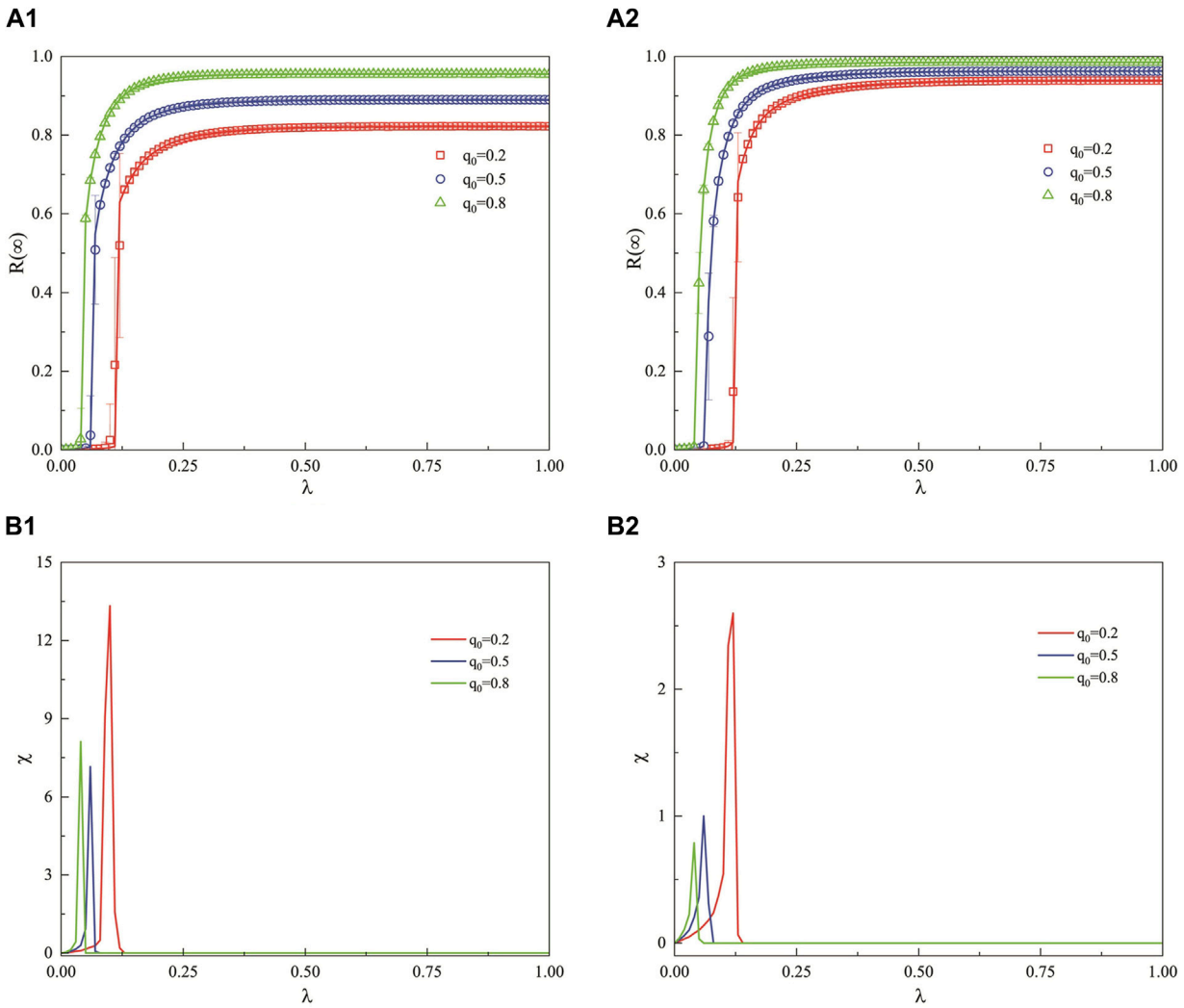

FIGURE 10
In a weighted SF network, this figure examines the impact of the unit propagation probability λ on the ultimate propagation range under different proportions q_0 of the common population when the decision-making ability of the hesitant population is relatively weak. Subfigures 10 **(A1)** with degree index $\nu = 2.1$ and 10 **(B1)** with $\nu = 4$ illustrate the effects of different degree indices on the propagation patterns. Subfigures 10 **(A2,B2)** provide the statistical computation of the relative standard deviation of the simulated values and the critical threshold for the propagation outbreak as indicated in subfigures 10(a1) and 10(b1), respectively. The remaining parameters are set to $\rho_0 = 0.001$, $a = 0.8$, and $\varepsilon = 25$.

is larger at equilibrium compared to that in Figure 10A1, although the outbreak threshold for propagation does not change. Figures 10A2, B2 provide the statistical computation of the relative standard deviation of the simulated values and the critical threshold for the propagation outbreak as indicated in Figures 10A1, B1, respectively. It can be seen from the figures that when the decision-making ability of the hesitant population is weak, reducing the degree distribution heterogeneity can increase the ultimate adoption range at equilibrium for information propagation. Moreover, the theoretical analysis values (curves) match well with the simulation values (symbols), indicating a good fit.

Figure 11 illustrates the combined effect of the unit propagation probability λ and the hesitancy parameter a on the ultimate adoption range $R(\infty)$ in a weighted SF network with a high degree of heterogeneity in the degree distribution. The initial proportion of nodes in state A, $\rho_0 = 0.001$, with an edge weight value of $\varepsilon = 25$ and a degree exponent $\nu = 2.1$. Figure 11A ($q_0 = 0.2$), 11(b) ($q_0 = 0.5$), and 11(c) ($q_0 = 0.8$) are each divided into three regions, the regional division of information propagation patterns is analogous to that in ER networks, where the delineation is based on the continuous and discontinuous changes in color temperature. Transitioning from Region I, representing the second-order continuous phase transition stage, to Region II, the first-order discontinuous phase transition stage, and finally to Region III, another second-order continuous phase transition stage. In Figure 11A, where the proportion of the common population is small ($q_0 = 0.2$), the outbreak threshold for information propagation initially increases and then decreases with the weakening of the population's decision-making ability, and the propagation rate follows a similar pattern. This suggests that in networks with high degree distribution heterogeneity and a larger hesitant population, the weakening of decision-making ability initially leads to a suppressive effect of the hesitant population on the outbreak of information propagation. Subsequently, as the

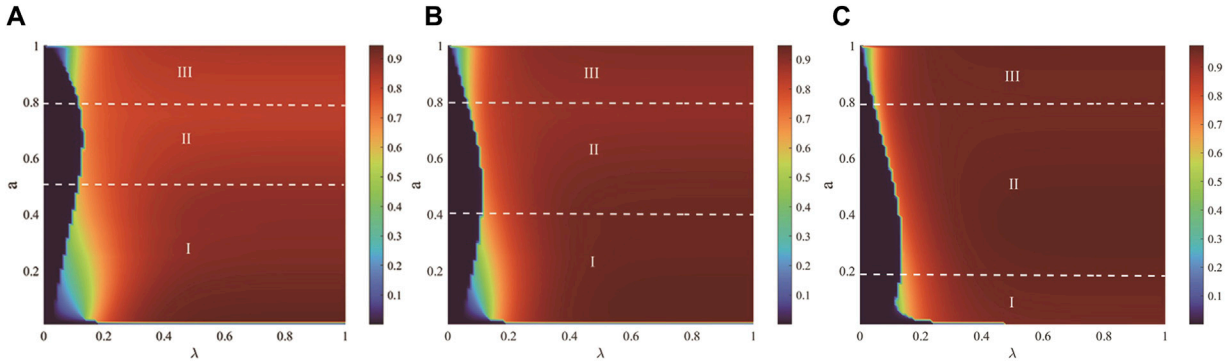

FIGURE 11
This figure illustrates the combined effect of the unit propagation probability λ and the hesitancy parameter a on the ultimate adoption range $R(\infty)$ in a weighted SF network. Subfigures 11 **(A–C)** correspond to different proportions of the coomon population, with **(A)** for $q_0 = 0.2$, **(B)** for $q_0 = 0.5$, and **(C)** for $q_0 = 0.8$. Each of these subfigures is divided into three distinct regions: Region I represents the second-order continuous phase transition stage, Region II the first-order discontinuous phase transition stage, and Region III the second-order continuous phase transition stage. The remaining parameters are set to $\rho_0 = 0.001$, $\varepsilon = 25$, and $\nu = 2.1$.

common population becomes dominant, the rate of information propagation accelerates. When the decision-making ability is very weak ($a \geq 0.8$), the suppressive effect of the hesitant population on information propagation is more pronounced, leading to a slower propagation rate. Figures 11B, C correspond to scenarios where the proportions of the common and hesitant populations are equal ($q_0 = 0.5$) and where the common population has a larger share ($q_0 = 0.8$), respectively. As the decision-making ability weakens, the propagation mechanism is similar to that when the proportion of the common population is small in Figure 11A, with the distinction that the dividing lines between Regions I and II in Figures 11B, C occur at $a = 0.4$ and $a = 0.2$, respectively. This indicates that when there is a smaller hesitant population with stronger decision-making ability, there is a promotional effect on information propagation.

Figure 12: This figure represents the combined effect of the unit propagation probability λ and the hesitancy parameter a on the ultimate adoption range $R(\infty)$ in a weighted SF network, where the degree distribution exhibits a relatively lower degree of heterogeneity. The initial proportion of nodes in state A, $\rho_0 = 0.001$, with an edge weight value of $\varepsilon = 25$ and a degree index $\nu = 4$. Figure 12A ($q_0 = 0.2$) and 12(b) ($q_0 = 0.5$) are each divided into four regions, the regional division of information propagation patterns is analogous to that in ER networks, where the delineation is based on the continuous and discontinuous changes in color temperature. Reflecting the transition of information propagation from non-propagation to discontinuous propagation, then to continuous propagation, back to discontinuous propagation, and finally to continuous propagation as the decision-making ability of the population weakens. When the network has a relatively low degree of heterogeneity and the population has a very strong decision-making ability ($a \leq 0.1$), but the proportion of the hesitant population is large or moderate, information propagation is challenging, transitioning from non-propagation to gradual propagation. As the decision-making ability decreases, the propagation mechanisms in regions II, III, and IV of Figures 12A, B are similar to those in Figures 11A, B. Figure 12C ($q_0 = 0.8$) is divided into two regions. When the common population constitutes a larger proportion of the network, the unit propagation probability at the outbreak threshold for information propagation decreases, and the propagation shifts from discontinuous to continuous as the decision-making ability of the population weakens. Due to the dominant role of the common population, which promotes propagation, the outbreak threshold decreases. However, when the decision-making ability of the hesitant population is very weak ($a \geq 0.8$), there is a suppressive effect on information propagation, but since the hesitant population is small, there is a brief phase of continuous propagation.

Figure 13 illustrates the combined effect of the unit propagation probability λ and the proportion of the common population q_0 on the ultimate adoption range $R(\infty)$ in a weighted SF network. Subfigures 13(a) and 13(b) depict the impact of λ and q_0 on the ultimate adoption range under different degree indices, with $\nu = 2.1$ and $\nu = 4$, respectively. The propagation patterns in Figures 13A, B are similar; when the population's decision-making ability is moderate, an increase in the proportion of the common population q_0 does not significantly affect the information propagation threshold. However, the larger the degree index ν, indicating less degree distribution heterogeneity, the greater the ultimate adoption range at equilibrium, and the faster the propagation rate, eventually leading to global adoption. Conversely, when the degree index is smaller ($\nu = 2.1$), it is only as q_0 increases, and the network is predominantly composed of common individuals, that information can achieve global adoption. Thus, a lower degree of distribution heterogeneity more effectively facilitates information propagation to reach a larger adoption range.

5 Conclusion

This study investigates the propagation of information in social networks within weighted networks, considering the heterogeneity in group adoption characteristics. The heterogeneity is characterized by distinct Hesitant-Common (HECO) traits in information adoption across different populations. The paper proposes two information adoption functions to elucidate the impact of group heterogeneity on information propagation. For common individuals, their adoption

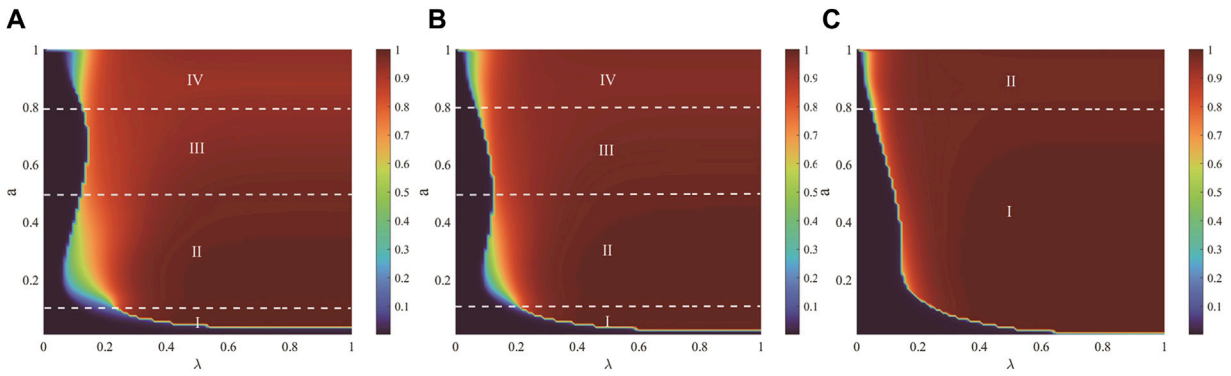

FIGURE 12
The joint effect of the unit propagation probability λ and the hesitancy parameter a on the ultimate adoption range $R(\infty)$ in a weighted SF network is depicted. Subfigures 12 **(A–C)** represent different proportions of the common population, with **(A)** for $q_0 = 0.2$ and **(B)** for $q_0 = 0.5$ each divided into four regions: Region I, the first-order discontinuous phase transition stage; Region II, the second-order continuous phase transition stage; Region III, another first-order discontinuous phase transition stage; and Region IV, the second-order continuous phase transition stage. **(C)** for $q_0 = 0.8$ is divided into two regions: Region I, the first-order discontinuous phase transition stage, and Region II, the second-order continuous phase transition stage. All other parameters are set to $\rho_0 = 0.001$, $\varepsilon = 25$, and $\nu = 4$.

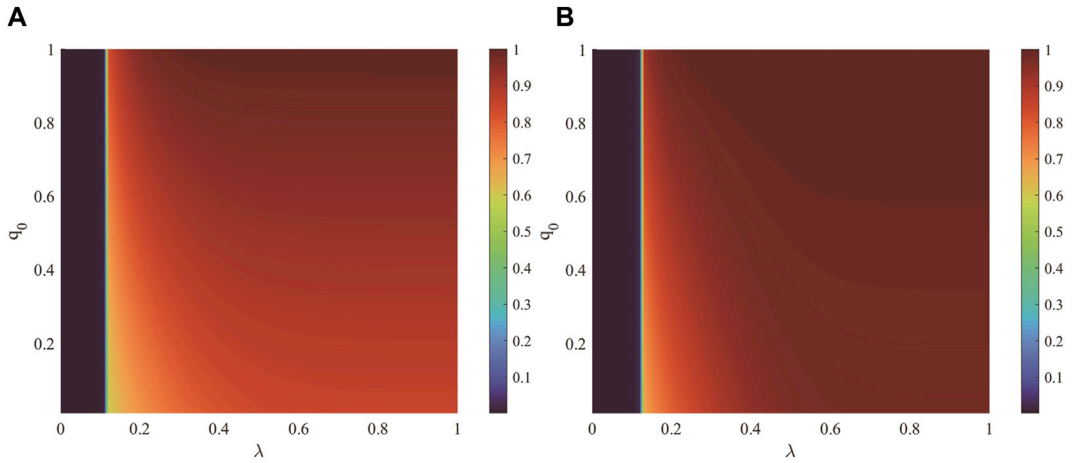

FIGURE 13
This figure delineates the joint impact of the unit propagation probability λ and the proportion of the common population q_0 on the ultimate adoption range $R(\infty)$ within a weighted SF network. Subfigures 13 **(A,B)** respectively illustrate the influence of λ and q_0 on the ultimate adoption range under different degree indices $\nu = 2.1$ and $\nu = 4$. All other parameters are held constant at $\rho_0 = 0.001$, $a = 0.5$, and $\varepsilon = 25$.

probability increases with the accumulation of received information. However, for hesitant individuals, the adoption probability initially increases similarly to that of common individuals but then declines as more information is received, eventually stabilizing and no longer changing once the optimal decision-making capacity is reached. The study randomly selects a proportion q_0 of the population as common individuals, with the remaining proportion e_0 designated as hesitant individuals. Interactions among individuals are modeled as edge weights in the social network, leading to the development of a social network information propagation model based on edge weights and HECO characteristics. This model is validated within both ER and SF networks.

Through simulation analysis, this study explores the information adoption behaviors of different types of individuals (hesitant and common), and investigates how these behaviors impact the speed and extent of information dissemination. It also observes phase transition phenomena during the information propagation process, particularly the correlation between the pattern of change in the ultimate adoption range and the proportion of common individuals. The study examines the impact of variations in the weight distribution index on the speed and efficiency of information propagation. It discusses how the heterogeneity in the degree distribution of nodes within the network affects information dissemination and how this heterogeneity interacts with the phase transition patterns of information propagation. The influence of decision-making ability on propagation is a focal point of consideration. Findings align with theoretical analysis, indicating that common individuals facilitate the spread and adoption of information. Furthermore, a phase transition crossover phenomenon is observed, where the

growth pattern of $R(\infty)$ shifts from a first-order discontinuous phase transition to a second-order continuous phase transition as the value of q_0 increases. An increase in the weight distribution exponent promotes information propagation. Furthermore, a decrease in degree distribution heterogeneity enhances the spread of information, while an increase in degree distribution heterogeneity, coupled with a weakening of the population's decision-making ability, inhibits information propagation.

The heterogeneity of groups within social networks plays a pivotal role in the propagation of information, yet there is a paucity of related research. This paper, through rigorous modeling and analysis, reveals the significant impact of the Hesitant-Common (HECO) attributes based on group heterogeneity on information dissemination. Furthermore, the HECO characteristics hold notable potential in practical applications, particularly in understanding and forecasting the dynamics of information propagation within social networks. Below are some potential applications of the HECO model across various domains: (1) Social Media Marketing: By understanding the extent to which users accept advertisements or trending information, the HECO model can assist marketers in designing more effective social media strategies to enhance the velocity and reach of information dissemination; (2) Public Health Campaigns: When promoting health information or awareness of vaccination initiatives, the model can predict the rate at which different demographic groups will accept health-related messages, thereby aiding health organizations in more accurately targeting their promotional resources; (3) Crisis Management: In emergency situations, comprehending the rapid spread of information is essential for an effective crisis response. The HECO model can forecast the speed and breadth of information propagation, assisting in the development of more robust emergency communication strategies; (4) Online Sentiment Analysis: Governments and corporations can utilize the HECO model to monitor and analyze the genesis and evolution of public opinion, thereby gaining a more profound understanding of the needs and reactions of the populace; (5) Product Promotion: Businesses can apply the HECO model to refine their strategies for new product promotion by identifying consumer groups most likely to rapidly accept and disseminate information, thus accelerating the market penetration of their products; (6) Information Security: Within the realm of cybersecurity, the HECO model can aid in the anticipation and prevention of the spread of misinformation or rumors by pinpointing key nodes in the propagation of information to bolster network defenses; (7) Traffic Planning: In the analysis of traffic networks, the conceptual framework of the HECO model can be employed to comprehend and optimize the flow of information, such as real-time traffic updates, to alleviate congestion and enhance traffic efficiency. By applying the HECO model in these domains, a deeper understanding and more effective utilization of the mechanisms of information propagation within social networks can be achieved, leading to improved quality and efficiency in decision-making processes. The research presented herein also offers a new direction for the study of information propagation in heterogeneous networks. However, this study only considers the propagation of group heterogeneity under basic scenarios and does not account for propagation within multi-layer networks. Additionally, the influence of parameters such as limited contact capacity is not considered. It is hoped that future research will have the opportunity to further explore this field.

Data availability statement

The original contributions presented in the study are included in the article/Supplementary Material, further inquiries can be directed to the corresponding author.

Author contributions

JJ: Methodology, Project administration, Supervision, Writing–review and editing. YH: Data curation, Formal Analysis, Methodology, Writing–original draft. WZ: Methodology, Writing–review and editing. YC: Validation, Writing–review and editing.

Funding

The author(s) declare that financial support was received for the research, authorship, and/or publication of this article. This work was supported by Education Department of Inner Mongolia Autonomous Region (NJZZ23074), Funds for basic scientific research of universities directly under the Autonomous region (ZTY2024065), Natural Science Foundation project of Inner Mongolia Autonomous Region (2024QN05046) and Research fund project of Inner Mongolia University of Technology.

Conflict of interest

The authors declare that the research was conducted in the absence of any commercial or financial relationships that could be construed as a potential conflict of interest.

Publisher's note

References

1. Houghton D, Pressey A, Istanbulluoglu D. Who needs social networking? An empirical enquiry into the capability of Facebook to meet human needs and satisfaction with life. *Comput Hum Behav* (2020) 104:106153. doi:10.1016/j.chb.2019.09.029

2. Khan S, Saravanan V, Lakshmi TJ, Deb N, Othman NA. Privacy protection of healthcare data over social networks using machine learning algorithms. *Comput Intelligence Neurosci* (2022) 2022:9985933–8. doi:10.1155/2022/9985933

3. Kolowitz B, Lauro GR, Venturella J, Georgiev Y, Barone M, Deible C, et al. Clinical social networking--a new revolution in provider communication and delivery of clinical information across providers of care? *J digital Imaging* (2014) 27(2):192–9. doi:10.1007/s10278-013-9653-0

4. Gil-Fernández R, Calderón-Garrido D, León-Gómez A, Martin-Piñol C. Comparativa del uso educativo de las redes sociales en los grados de Maestro: universidades presenciales y online. *Aloma* (2019) 37(2):75–81. doi:10.51698/aloma.2019.37.2.75-81

5. bt Yahya SMSA, Ahmad SB Preliminary study on educational user interface architecture for social network. *Int J Eng Technol* (2018) 7(4):457–62. doi:10.14419/ijet.v7i4.36.23916

6. Liu T, He X, Guo X, Zhao Y. The influence of the network evolutionary game model of user information behavior on enterprise innovation product promotion based on mobile social network marketing perspective. *Math Probl Eng* (2022) 2022.

7. Lee S, Park H. A study on the effect of social networking marketing on the purchase intention in the airline. *East Asian J Business Econ* (2021) 9(2):55–73.

8. Zhang Y, Pan D, Fan S. Analysis of layered information dissemination model and caching strategy in Social Internet of Things. *Nonlinear Dyn* (2023) 111(15):14379–94. doi:10.1007/s11071-023-08594-5

9. He J, Li Y, Zhu N. A game theory-based model for the dissemination of privacy information in online social networks. *Future Internet* (2023) 15(3):92–412. doi:10.3390/fi15030092

10. Chen J, Huang J, Xin C, Liu M. Research on information dissemination model based on heat transfer in online social network. *The J Supercomputing* (2022) 79(7):7717–35.

11. Zhu X, Wang W, Cai S, Stanley HE. Optimal imitation capacity and crossover phenomenon in the dynamics of social contagions. *J Stat Mech* (2018) 2018.

12. Pan D, Zhang Y. Analysis of information propagation and control of a layered SITR model in complex networks. *Front Phys* (2022) 10:985517. doi:10.3389/fphy.2022.985517

13. He L, Zhu L, Zhang Z. Turing instability induced by complex networks in a reaction–diffusion information propagation model. *Inf Sci* (2021) 578:762–94. doi:10.1016/j.ins.2021.08.037

14. Wang W, Tang M, Zhang H, Gao H, Do Y, Liu Z. Epidemic spreading on complex networks with general degree and weight distributions. *Phys Rev E, Stat nonlinear, soft matter Phys* (2014) 90(4):042803. doi:10.1103/physreve.90.042803

15. Guan G, Guo Z. Stability behavior of a two-susceptibility SHIR epidemic model with time delay in complex networks. *Nonlinear Dyn* (2021) 106(1):1083–110. doi:10.1007/s11071-021-06804-6

16. Liu G, Liu Z, Jin Z. Dynamics analysis of epidemic and information spreading in overlay networks. *J Theor Biol* (2018) 444:28–37. doi:10.1016/j.jtbi.2018.02.010

17. Cao B, Guan G, Shen S, Zhu L. Dynamical behaviors of a delayed SIR information propagation model with forced silence function and control measures in complex networks. *The Eur Phys J Plus* (2023) 138(5):402. doi:10.1140/epjp/s13360-023-04005-1

18. Ding N, Guan G, Shen S, Zhu L. Dynamical behaviors and optimal control of delayed S2IS rumor propagation model with saturated conversion function over complex networks. *Commun Nonlinear Sci Numer Simulation* (2024) 128:107603. doi:10.1016/j.cnsns.2023.107603

19. Zhu L, Yang F, Guan G, Zhang Z. Modeling the dynamics of rumor diffusion over complex networks. *Inf Sci* (2021) 562:240–58. doi:10.1016/j.ins.2020.12.071

20. Zhu L, Wang X, Zhang Z, Lei C. Spatial dynamics and optimization method for a rumor propagation model in both homogeneous and heterogeneous environment. *Nonlinear Dyn* (2021) 105(4):3791–817. doi:10.1007/s11071-021-06782-9

21. Zhu X, Ma J, Su X, Tian H, Wang W, Cai S. Information spreading on weighted multiplex social network. *Complexity* (2019) 2019:1–15. doi:10.1155/2019/5920187

22. Chen X, Zhang S. An SEIR model for information propagation with a hot search effect in complex networks. *Math biosciences Eng : MBE* (2023) 20(1):1251–73. doi:10.3934/mbe.2023057

23. Kovanen L, Kaski K, Kertész J, Saramäki J. Temporal motifs reveal homophily, gender-specific patterns, and group talk in call sequences. *Proc Natl Acad Sci USA* (2013) 110(45):18070–5. doi:10.1073/pnas.1307941110

24. Bakshy E, Messing S, Adamic LA. Political science. Exposure to ideologically diverse news and opinion on Facebook. *Science* (2015) 348(6289):1130–2. doi:10.1126/science.aaa1160

25. Gandy A, Veraart LAM. Adjustable network reconstruction with applications to CDS exposures. *J Multivariate Anal* (2019) 172:193–209. doi:10.1016/j.jmva.2018.08.011

26. Barrat A, Barthelemy M, Pastor-Satorras R, Vespignani A. The architecture of complex weighted networks. *Proc Natl Acad Sci USA* (2004) 101(11):3747–52. doi:10.1073/pnas.0400087101

27. Chen T, Li Q, Yang J, Cong G, Li G. Modeling of the public opinion polarization process with the considerations of individual heterogeneity and dynamic conformity. *Mathematics* (2019) 7(10):917. doi:10.3390/math7100917

28. Zhu X, Yang Q, Tian H, Ma J, Wang W. Contagion of information on two-layered weighted complex network. *IEEE Access* (2019) 7:155064–74. doi:10.1109/access.2019.2948941

29. Iyengar R, Van den Bulte C, Valente TW. Opinion leadership and social contagion in new product diffusion. *Marketing Sci* (2011) 30(2):195–212. doi:10.1287/mksc.1100.0566

30. Golub B, Jackson MO. Naive learning in social networks and the wisdom of crowds. *Am Econ J Microeconomics* (2010) 2(1):112–49. doi:10.1257/mic.2.1.112

31. Lerman K, Ghosh R. Information contagion: an empirical study of the spread of news on digg and twitter social networks. *Proc Int AAAI Conf Web Soc Media* (2010) 4(1):90–7. doi:10.1609/icwsm.v4i1.14021

32. Wang W, Tang M, Zhang H, Lai Y. Dynamics of social contagions with memory of nonredundant information. *Phys Rev E, Stat nonlinear, soft matter Phys* (2015) 92(1):012820. doi:10.1103/physreve.92.012820

33. Yuan X, Hu Y, Stanley HE, Havlin S. Eradicating catastrophic collapse in interdependent networks via reinforced nodes. *Proc Natl Acad Sci USA* (2017) 114(13):3311–5. doi:10.1073/pnas.1621369114

34. Arratia R, Gordon L, Waterman MS. The erdos-renyi law in distribution, for coin tossing and sequence matching. *Ann Stat* (1990) 18(2):539–70. doi:10.1214/aos/1176347615

35. Wang S, Cheng W. Novel method for spreading information with fewer resources in scale-free networks. *Physica A: Stat Mech its Appl* (2019) 524:15–29. doi:10.1016/j.physa.2019.03.018

36. Erdos P, Renyi A. On random graphs. *Publicationes Mathematicae (Debrecen)* (1959) 6.

37. McPherson M, Smith-Lovin L, Cook JM. Birds of a feather: homophily in social networks. *Annu Rev Sociol* (2001) 27(1):415–44. doi:10.1146/annurev.soc.27.1.415

38. Barabasi AL, Oltvai ZN. Network biology: understanding the cell's functional organization. *Nat Rev Genet* (2004) 5(2):101–13. doi:10.1038/nrg1272

39. Louf R, Barthélemy M. How congestion causes long waiting times: a statistical physics approach to traffic instability. *Phys Rev E* (2013) 88(6):062814.

40. Barabási AL, Albert R. Emergence of scaling in random networks. *science* (1999) 286(5439):509–12. doi:10.1126/science.286.5439.509

41. Jeong H, Tombor B, Albert R, Oltvai ZN, Barabási AL. The large-scale organization of metabolic networks. *Nature* (2000) 407(6804):651–4. doi:10.1038/35036627

42. Dobson I, Carreras BA, Lynch VE, Newman DE. Complex systems analysis of series of blackouts: cascading failure, critical points, and self-organization. *Chaos: Interdiscip J Nonlinear Sci* (2007) 17(2):026103. doi:10.1063/1.2737822

43. Boginski V, Butenko S, Pardalos PM. Statistical analysis of financial networks. *Comput Stat Data Anal* (2005) 48(2):431–43. doi:10.1016/j.csda.2004.02.004

frontiers | Frontiers in Physics

TYPE Original Research
PUBLISHED 02 August 2024
DOI 10.3389/fphy.2024.1437341

OPEN ACCESS

EDITED BY
Xuzhen Zhu,
Beijing University of Posts and Telecommunications (BUPT), China

REVIEWED BY
Ruiqi Li,
Beijing University of Chemical Technology, China
Peican Zhu,
Northwestern Polytechnical University, China

*CORRESPONDENCE
Jiajun Xian,
xianjiajun22@gmail.com

RECEIVED 23 May 2024
ACCEPTED 02 July 2024
PUBLISHED 02 August 2024

CITATION
Zhang W, Ye Y, Li Z, Xian J, Wang T, Liu D, Hu D and Liu M (2024), The coupled awareness-epidemic dynamics with individualized self-initiated awareness in multiplex networks. *Front. Phys.* 12:1437341. doi: 10.3389/fphy.2024.1437341

The coupled awareness-epidemic dynamics with individualized self-initiated awareness in multiplex networks

Wei Zhang[1], Yixuan Ye[1], Zongyi Li[1], Jiajun Xian[2,3]*, Teng Wang[1], Dandan Liu[4], Die Hu[5] and Ming Liu[2,3]

[1]Department of Computer Science, Shantou University, Shantou, China, [2]Yangtze Delta Region Institute (Quzhou), University of Electronic Science and Technology of China, Quzhou, Zhejiang, China, [3]Quzhou People's Hospital, Quzhou Affiliated Hospital of Wenzhou Medical University, Quzhou, Zhejiang, China, [4]Department of Automation, School of Electrical Engineering, Yancheng Institute of Technology, Yancheng, China, [5]Environment Design Department, Chengdu University, Chengdu, China

The outbreak of an epidemic often stimulates the generation of public awareness about epidemic prevention. This heightened awareness encourages individuals to take proactive protective measures, thereby curbing the transmission of the epidemic. Previous research commonly adopts an assumption that each individual has the same probability of awakening self-protection awareness after infection. However, in the real-world process, different individuals may generate varying awareness responses due to the differences in the amount of information received. Therefore, in this study, we first propose a coupled awareness-epidemic spreading model, where the self-initiated awareness of each individual can be influenced by the number of aware neighbors. Subsequently, we develop a Micro Markov Chain Approach to analyze the proposed model and explore the effects of different dynamic and structural parameters on the coupled dynamics. Findings indicate that individual awareness awakening can effectively promote awareness diffusion within the proposed coupled dynamics and inhibit epidemic transmission. Moreover, the influence of awareness diffusion on epidemic transmission exhibits a metacritical point, from which the epidemic threshold increases with the increase in the awareness diffusion probability. The research findings also suggest that the increase in the average degree of virtual-contact networks can reduce the value of the metacritical point, while the change in the average degree of the physical-contact networks does not affect the metacritical point. Finally, we conduct extensive experiments on four real networks and obtain results consistent with the above conclusions. The systematic research findings of this study provide new insights for exploring the interaction between individual awareness and epidemic transmission in the real world.

KEYWORDS

multiplex networks, coupled awareness-epidemic dynamics, self-initiated awareness, metacritical point, complex networks

1 Introduction

The spread of infectious diseases poses a significant threat to human health and can lead to substantial economic losses [1]. Throughout history, human society has repeatedly suffered devastating impacts from infectious diseases. For example, in the 16th and 17th centuries, the rampant smallpox virus led to a sharp decline in the population of indigenous peoples in the Americas. The outbreak of novel coronavirus pneumonia (COVID-19) in 2019 has caused nearly seven million deaths worldwide [2–4]. It is worth noting that the large-scale outbreak of an epidemic often effectively stimulates individuals to develop self-initiated awareness, which can effectively curb the spread of the epidemic [5–9]. For example, after the outbreak of the COVID-19 pandemic, information related to it started diffusing on social networks or community networks, thereby sparking the development of individual awareness about epidemic prevention [10, 11]. After developing self-initiated awareness, individuals will actively take a series of self-protective measures to reduce the risk of infection, such as wearing masks, frequent hand-washing, reducing outdoor activities, maintaining social distancing, and more [12]. These self-protective measures can effectively interrupt the transmission pathways of the virus, thereby suppressing further transmission of the disease [13–17]. Therefore, how to model and analyze the coupled awareness-epidemic dynamics has long been a subject of significant interest among scholars from various fields.

In real life, individuals can not only have physical contact with others, such as shaking hands and sharing meals, which promote the spread of diseases but also communicate with others to receive disease-related information and generate awareness of self-protection [18–22]. Therefore, in recent years, scholars typically adopt a two-layer multiplex network structure to establish the coupled awareness-epidemic dynamics in their research, aiming to explore the interaction between awareness diffusion and epidemic transmission in the real world [23–27]. In the two-layer multiplex network structure, the first layer is the physical-contact network, where nodes represent individuals in the real world, and edges represent physical contact relationships between individuals; the second layer (virtual contact) is the network with the same nodes as the physical-contact network, while edges represent information interaction between individuals [28–31]. In 2013, Granell et al. proposed a coupled awareness-epidemic dynamics model with the multiplex network structure to investigate the real-world coupled awareness-epidemic dynamics. They identified the presence of a metacritical point for awareness diffusion rate, and when the awareness diffusion rate is larger than this point, the epidemic threshold will increase with it [32]. Subsequently, scholars have proposed several improved models from different perspectives to consider the effects of various real-world factors on the coupled awareness-epidemic dynamics. For instance, Granell et al. further integrates mass media into the awareness diffusion process, elucidating that the metacritical point for epidemic outbreaks vanishes under the influence of mass media [33]. Chen et al. introduced a resource-epidemic coevolution model on a multiplex network and discovered an optimal heterogeneity of self-awareness at which the disease can be suppressed to the greatest extent [34]. Wu et al. introduce a two-layer network where the inter-layer coupling is induced by the movement of traveler individuals between layers, and they find that travelers' hopping preference for different layers can lead to non-monotonic changes in the epidemic threshold and spreading coverage [35]. Furthermore, many scholars have delved into the effects of the spatio-temporal characteristics of networks on epidemic spreading. Liu et al. proposed a spatio-temporal network model based on co-location interactions using massive cellphone data. They reveals that universal laws underlying spatio-temporal contact patterns among residents is essential for epidemic spreading [36]. Furthermore, Li et al. introduced a temporal multiplex network consisting of a static information spreading network and a temporal physical contact network with a layer-preference walk. They found that the epidemic threshold decreases with the decrease of the effective information spreading rate and the increase of the layer [37].

As mentioned above, scholars have made significant progress in the study of coupled awareness-epidemic dynamics. However, there is limited research that incorporates individualized self-initiated awareness into the coupled awareness-epidemic dynamics. In the real world coupled awareness-epidemic spreading, different individuals generate varying awareness responses due to the differences in the amount of information received from their neighbors. Hence, research on the coupled awareness-epidemic dynamics that takes into account individualized self-initiated awareness holds significant importance. In light of this, this study first proposes a coupled awareness-epidemic dynamics model that incorporates individualized self-initiated awareness, where the probability of infected individuals developing self-initiated awareness is influenced by the number of their aware neighbors. Subsequently, we develop the Microscopic Markov Chains Approach to theoretically analyze the aforementioned model and investigate the effects of crucial dynamics and structural parameters on the coupled awareness-epidemic dynamics.

The paper is structured as follows: Section 2 provides a detailed description of the coupled awareness-epidemic dynamics with individualized self-initiated awareness. In Section 3, we introduce the Micro Markov Chain Approach to analyze the previous model, and derive the stationary spread range and transmission threshold of the epidemic. In Section 4, we explore the effects of different dynamics and structural parameters on the coupled awareness-epidemic dynamics. Finally, Section 5 summarizes the entire work and outlines potential avenues for further study.

2 Model description

In the study, we consider the coupled awareness-epidemic dynamics on top of a two-layer multiplex networks as shown in Figure 1. The nodes of the two network layers are one-to-one correspondence, but the connectivity between them is different. Awareness of the epidemic diffuses on the second layer of the multiplex network (namely, the virtual-contact layer), and the epidemic takes place on the first layer (namely, the physical-contact network).

In the virtual-contact layer, an unaware-aware-unaware (UAU) model is adopted to depict the diffusion of epidemic awareness. Unaware (U) nodes have no epidemic awareness and will take no precautions against the epidemic, while aware (A) nodes know about the epidemic and will take certain preventive measures. The

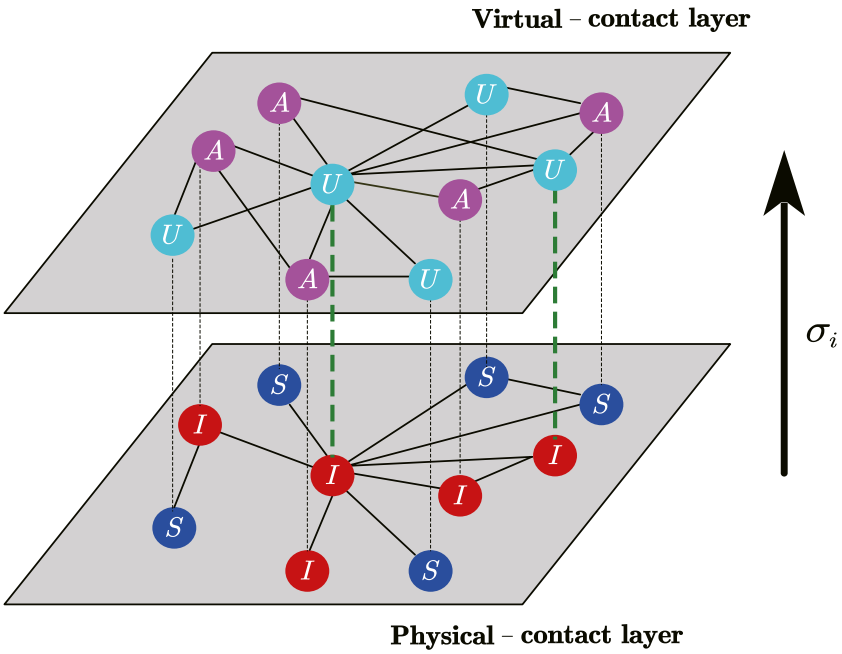

FIGURE 1
(Color online) A schematic illustration showcasing the coupled awareness-epidemic dynamics with individualized self-initiated awareness in multiplex networks. The first layer (physical-contact network) employs a susceptible-infected-susceptible (SIS) model to delineate the transmission of the epidemic. Within this layer, susceptible (S) nodes can be infected by their infected (I) neighbors. The second layer corresponds to the virtual-contact network, sharing identical nodes with the physical-contact network. In this layer, an unaware-aware-unaware (UAU) model captures the diffusion of epidemic awareness. Nodes in the unaware (U) state lack epidemic awareness and consequently take no preventive measures. Conversely, the aware (A) nodes possess knowledge about the epidemic and implement specific precautionary measures. Additionally, when a node in the unaware state becomes infected, it has a probability of σ_i to develop epidemic awareness autonomously.

diffusion of epidemic awareness occurs from the A-state node to the U-state node with a probability of λ, while the A-state node can revert to the U-state due to loss of awareness with a probability of δ. Besides, the moment when the U-state node is infected with the disease, it will develop a self-initiated awareness with the probability given by Eq. 1:

$$\sigma_i(t) = 1 - (1 - \sigma_0)^{\eta_A(t)+1} \tag{1}$$

where $\eta_A(t)$ is the count of neighbors in A-state of node i.

In physical-contact layer, a susceptible-infected-susceptible (SIS) model is adopted to describe the epidemic-transmitting process. The susceptible (S) node, both with and without epidemic awareness, can become infected by its infected (I) neighbor with the certain probability of β, and $\beta^A = \gamma\beta$, respectively, where $0 \le \gamma \le 1$ is an attenuation factor reflecting the influence of preventive measures taken by A-state nodes. Additionally, the likelihood of an infected node recovering spontaneously is represented by μ.

3 Theoretical analysis

3.1 Microscopic markov chain approach

We will provide an analytical derivation based on the Microscopic Markov Chain Approach (MMCA) for our model in this section. Denote $A = (a_{ij})_N$ and $B = (b_{ij})_N$ as the adjacency matrixes for the virtual-contact layer and physical-contact layer, respectively, where N represents the number of nodes. Taking both the virtual-contact layer and physical-contact layer into consideration, nodes within our model have four possible states, i.e., unaware-susceptible (US), aware-susceptible (AS), unaware-infected (UI), and aware-infected (AI). Let $P_i^{US}(t)$, $P_i^{AS}(t)$, $P_i^{UI}(t)$, $P_i^{AI}(t)$ denote the probability of node i being in US-state, AS-state, UI-state, AI-state at time t, respectively. The probability of node i being in A-state, U-state, I-state, and S-state can be calculated as $P_i^A = P_i^{AS}(t) + P_i^{AI}(t)$, $P_i^U = P_i^{US}(t) + P_i^{UI}(t)$, $P_i^I = P_i^{AI}(t) + P_i^{UI}(t)$, and $P_i^S = P_i^{US}(t) + P_i^{IS}(t)$, respectively. Besides, the probability of the U-state node i not being informed by any neighbor at time t can be given by Eq. 2.

$$\theta_i(t) = \prod_j \left[1 - a_{ij} P_j^A(t) \lambda\right] \tag{2}$$

The probabilities of node i being in the unaware-susceptible (US) state and the aware-susceptible (AS) state, and not being infected at time t, are given by Eqs 3 and 4, respectively.

$$q_i^U(t) = \prod_j \left[1 - b_{ij} P_j^I(t) \beta^U\right] \tag{3}$$

$$q_i^A(t) = \prod_j \left[1 - b_{ij} P_j^I(t) \beta^A\right] \tag{4}$$

Figure 2 shows the transition probability trees for the four possible states of nodes in our model. The dynamics governing $P_i^{UI}(t)$, $P_i^{US}(t)$, $P_i^{AS}(t)$, and $P_i^{AI}(t)$ are encapsulated in Eqs 5–8, respectively.

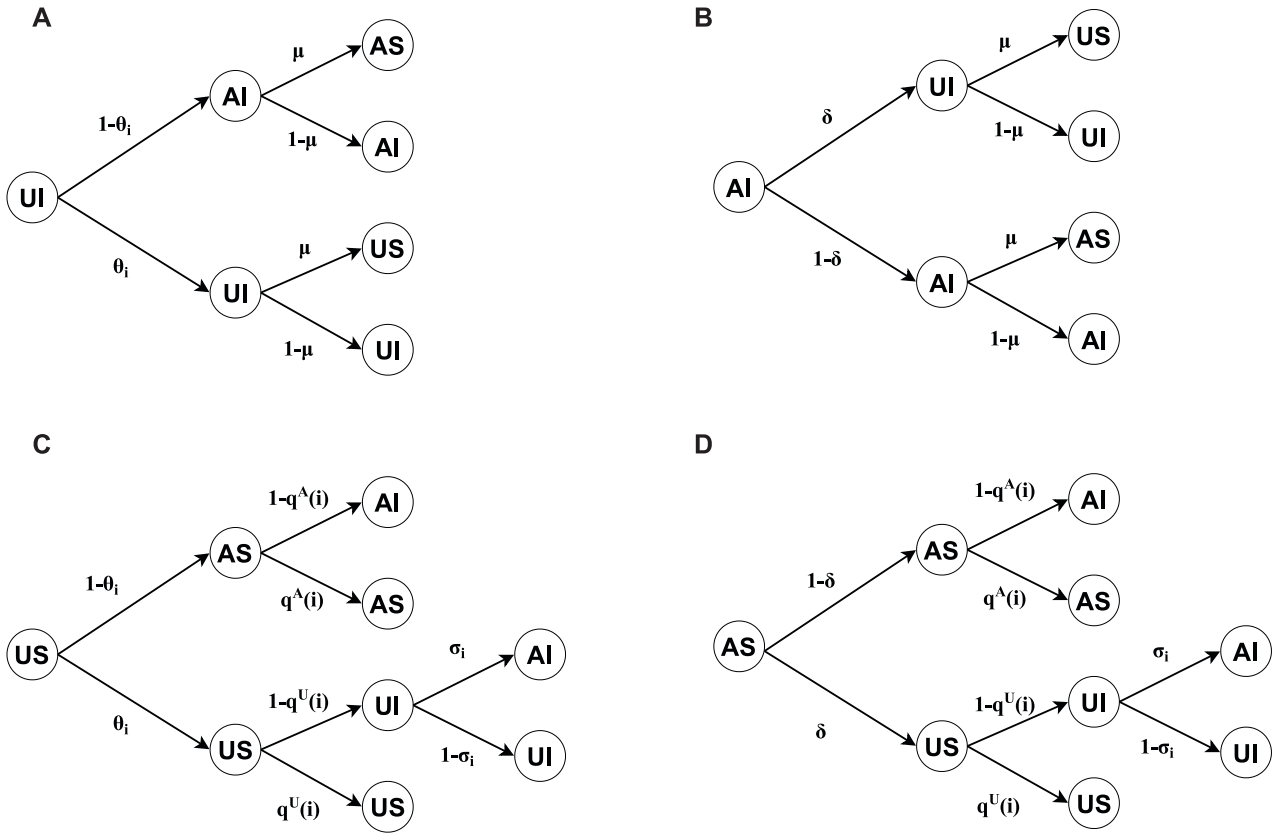

FIGURE 2
Transition probability trees are illustrated for four distinct node states: **(A)** unaware-infected (UI), **(B)** aware-infected (AI), **(C)** unaware-susceptible (US), and **(D)** aware-susceptible (AS). The tree roots denote the state of each node at time t, while their possible states at time $t+1$ are denoted by the leaves.

$$\begin{aligned} P_i^{\mathrm{UI}}(t+1) = {} & P_i^{\mathrm{UI}}(t)\theta_i(t)(1-\mu) + P_i^{\mathrm{AI}}(t)\delta(1-\mu) \\ & + P_i^{\mathrm{US}}(t)\theta_i(t)\left[1-q_i^{\mathrm{U}}(t)\right]\left[1-\sigma_i(t)\right] \\ & + P_i^{\mathrm{AS}}(t)\delta\left[1-q_i^{\mathrm{U}}(t)\right]\left[1-\sigma_i(t)\right] \end{aligned} \tag{5}$$

$$\begin{aligned} P_i^{\mathrm{US}}(t+1) = {} & P_i^{\mathrm{UI}}(t)\theta_i(t)\mu + P_i^{\mathrm{AI}}(t)\delta\mu \\ & + P_i^{\mathrm{US}}(t)\theta_i(t)q_i^{\mathrm{U}}(t) + P_i^{\mathrm{AS}}(t)\delta q_i^{\mathrm{U}}(t) \end{aligned} \tag{6}$$

$$\begin{aligned} P_i^{\mathrm{AS}}(t+1) = {} & P_i^{\mathrm{UI}}(t)\left[1-\theta_i(t)\right]\mu + P_i^{\mathrm{AI}}(t)(1-\delta)\mu \\ & + P_i^{\mathrm{US}}(t)\left[1-\theta_i(t)\right]q_i^{\mathrm{A}} + P_i^{\mathrm{AS}}(t)(1-\delta)q_i^{\mathrm{A}} \end{aligned} \tag{7}$$

$$\begin{aligned} P_i^{\mathrm{AI}}(t+1) = {} & P_i^{\mathrm{UI}}(t)\left[1-\theta_i(t)\right](1-\mu) + P_i^{\mathrm{AI}}(t)(1-\delta)(1-\mu) \\ & + P_i^{\mathrm{US}}(t)\{\left[1-\theta_i(t)\right]\left[1-q_i^{\mathrm{A}}(t)\right] + \theta_i(t)\left[1-q_i^{\mathrm{U}}(t)\right]\sigma_i(t)\} \\ & + P_i^{\mathrm{AS}}(t)\{\delta\left[1-q_i^{\mathrm{U}}(t)\right]\sigma_i(t) + (1-\delta)\left[1-q_i^{\mathrm{A}}(t)\right]\} \end{aligned} \tag{8}$$

3.2 Threshold analysis

The epidemic threshold is given by the parameter ρ^{I}, i.e., the fraction of I-state nodes in the system, and is calculated as shown in Eq. 9.

$$\rho^{\mathrm{I}} = \frac{1}{N}\sum_{i=1}^{N} P_i^{\mathrm{I}} = \frac{1}{N}\sum_{i=1}^{N}\left(P_i^{\mathrm{UI}} + P_i^{\mathrm{AI}}\right) \tag{9}$$

In the steady state, by summing Eqs 5, 8, we acquire

$$\begin{aligned} P_i^{\mathrm{I}} = {} & P_i^{\mathrm{I}}(1-\mu) + P_i^{\mathrm{US}}\left[\theta_i\left(1-q_i^{\mathrm{U}}\right) + (1-\theta_i)\left(1-q_i^{\mathrm{A}}\right)\right] \\ & + P_i^{\mathrm{AS}}\left[\delta\left(1-q_i^{\mathrm{U}}\right) + (1-\delta)\left(1-q_i^{\mathrm{A}}\right)\right]. \end{aligned} \tag{10}$$

Near the epidemic threshold, the fraction of I-state nodes is close to zero, i.e., $P_i^{\mathrm{I}} = \varepsilon_i \ll 1$. Accordingly, q_i^{U} and q_i^{A} can be approximately calculated as

$$q_i^{\mathrm{U}} \approx 1 - \beta^{\mathrm{U}}\sum_j b_{ji}\varepsilon_j = 1 - \omega_i, \tag{11}$$

and

$$q_i^{\mathrm{A}} \approx 1 - \gamma\beta^{\mathrm{U}}\sum_j b_{ji}\varepsilon_j = 1 - \gamma\omega_i, \tag{12}$$

respectively, where ω_i is given by Eq. 13:

$$\omega_i = \beta^{\mathrm{U}}\sum_j b_{ji}\varepsilon_j. \tag{13}$$

Substituting Eqs 11, 12 into Eq. 10 leads to

$$\begin{aligned} \varepsilon_i &= \varepsilon_i(1-\mu) + P_i^{\mathrm{US}}\left[\theta_i\omega_i + (1-\theta_i)\gamma\omega_i\right] \\ &\quad + P_i^{\mathrm{AS}}\left[\delta\omega_i + (1-\delta)\gamma\omega_i\right] \\ &= \varepsilon_i(1-\mu) + \left(P_i^{\mathrm{U}}\theta_i + P_i^{\mathrm{A}}\delta\right)\omega_i \\ &\quad + \left[P_i^{\mathrm{U}}(1-\theta_i) + P_i^{\mathrm{A}}(1-\delta)\right]\gamma\omega_i. \end{aligned} \tag{14}$$

Since $\varepsilon_i \ll 1$ in the stationary state, we should have $P_i^{\mathrm{US}} = P_i^{\mathrm{U}} - P_i^{\mathrm{UI}} \approx P_i^{\mathrm{U}}$ and $P_i^{\mathrm{AS}} = P_i^{\mathrm{A}} - P_i^{\mathrm{AI}} \approx P_i^{\mathrm{A}}$. Thus, removing $O(\varepsilon_i)$ terms in the stationary state of Eqs 6, 7 we get

$$P_i^{\mathrm{U}} = P_i^{\mathrm{U}}\theta_i + P_i^{\mathrm{A}}\delta \tag{15}$$

and

$$P_i^{\mathrm{A}} = P_i^{\mathrm{U}}(1-\theta_i) + P_i^{\mathrm{A}}(1-\delta). \tag{16}$$

Then, substituting Eqs 15, 16 into Eq. 14 leads to Eq. 17:

$$\begin{aligned}\varepsilon_i &= \varepsilon_i(1-\mu) + P_i^{\mathrm{U}}\omega_i + P_i^{\mathrm{A}}\gamma\omega_i \\ &= \varepsilon_i(1-\mu) + (P_i^{\mathrm{U}} + P_i^{\mathrm{A}}\gamma)\beta^{\mathrm{U}}\sum_j b_{ji}\varepsilon_j,\end{aligned} \tag{17}$$

which can be written as

$$\sum_j \left[\beta^{\mathrm{U}}\left[1 + (\gamma-1)P_i^{\mathrm{A}}\right]b_{ji} - \mu\delta_{ij}\right]\varepsilon_j = 0, \tag{18}$$

where δ_{ij} are the elements of the identity matrix. Defining matrix H with elements as given by Eq. 19:

$$h_{ji} = (P_i^{\mathrm{U}} + \gamma P_i^{\mathrm{A}})b_{ji} = \left[1 + (\gamma-1)P_i^{\mathrm{A}}\right]b_{ji}, \tag{19}$$

the nontrivial solutions of Eq. 18 are eigenvectors of H, whose largest real eigenvalues are equal to the epidemic threshold

$$\beta_c = \frac{\mu}{\Lambda_{max}(H)}. \tag{20}$$

Equation 20 provides a quantitative representation indicating that the epidemic threshold is dependent on the spreading dynamics on both network layers.

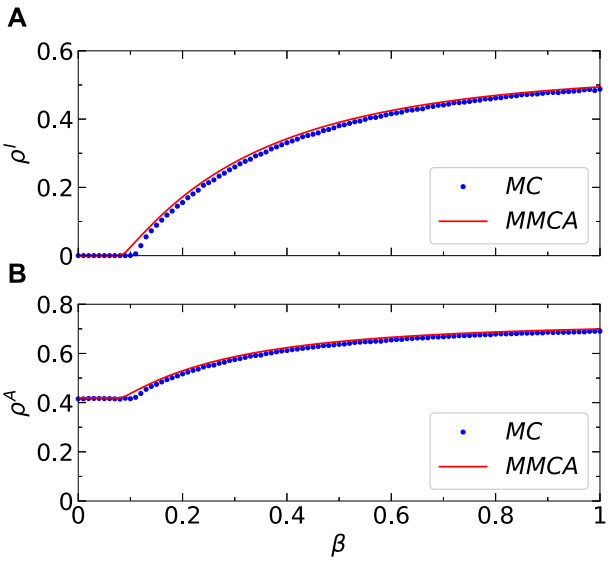

FIGURE 3
(Color online) Results comparisons between the Microscopic Markov Chains Approach (MMCA) and Monte Carlo (MC) simulations regarding the stationary fractions. **(A)** Comparisons between the stationary I-state individuals' fraction ρ^{I} obtained by MC simulations (dotted line) and the MMCA (solid line). **(B)** Comparisons between the stationary A-state individuals' fraction ρ^{A} obtained by Monte Carlo simulations (dotted line) and the MMCA (solid line). All the numerical simulations are performed on top of multiplex network G^0 and Additional parameters include $\mu = 0.5$ and $\gamma = 0$ in the physical-contact layer, $\lambda = 0.15$, $\sigma_0 = 0.5$, and $\delta = 0.6$ in the virtual-contact layer.

4 Simulation results

In this section, we explore the effects of various dynamics and structural parameters on the proposed coupled awareness-epidemic dynamics. In reality, the behavior of the same individual on the virtual-contact network and the physical-contact network may not be consistent. For example, individuals who appear active on the virtual-contact networks may have rare physical contact with others. To imitate the variability in individual behavior between the virtual-contact layer and the physical-contact layer, we employ three multiplex networks with varying inter-layer degree correlation r_s, namely, G^{-1}, G^0, and G^1, whose r_s are set to −1, 0, and 1, respectively. The physical-contact layers of the three multiplex networks are all sale-free networks with the number of nodes $N = 1000$, the average degree $K_{\mathrm{A}} = 5$, and the degree exponent $\varepsilon = 5$. In addition, the virtual-contact layers are scale-free networks, sharing identical node counts and degree exponents with the physical-contact layers, but with the average degree $K_{\mathrm{B}} = 10$. The setting of $K_{\mathrm{A}} > K_{\mathrm{B}}$ on the three multiplex networks is intended to imitate the real-world phenomenon where the density of virtual-contact networks is typically larger than that of physical-contact networks. We obtain the numerical simulation results presented in this section by averaging the outcomes of over 1,000 independent simulation experiments conducted on the aforementioned multiplex networks. Furthermore, we consistently set the initial infected nodes proportion in the epidemic transmission process at 0.2.

Firstly, we assess the efficacy of the MMCA method in describing the coupled awareness-epidemic dynamics proposed in this study on a group of multiplex networks. Figure 3 compares the dynamicsal results of the MMCA method and Monte Carlo (MC) simulation regarding ρ^{I} and ρ^{A} as a function of β on network G^0, which is a two-layer network with inter-layer degree correlation $r_s = 0$. In addition, Figure 4 shows the comparison results of ρ^{I} as a function of β and λ on three multiplex networks (that is, G^{-1}, G^0 and G^1) with distinct inter-layer degree correlations. It can be observed that the results obtained by the MMCA method have a good consistency with MC simulation in both Figures 3, 4, which verifies the accuracy and suitability of the MMCA method in solving the coupled awareness-epidemic spreading dynamics we proposed in this study. Hereinafter, we study the coupled dynamics proposed by the MMCA method.

Secondly, we conducted an analysis of how two significant dynamics parameters influence the stationary states of the proposedawareness-epidemic dynamics, namely, the basic self-initiated awareness probability σ_0 and infection attenuation factor γ, where σ_0 is the basic self-initiated awareness probability and the parameter γ governs the infection probability among aware individuals. Figures 5A–C illustrate the change of stationary I-state individuals fraction ρ^{I} with respect to the infection probability β on the multiplex networks G^{-1}, G^0, and G^1, respectively, when different values of σ_0 are considered. Observing the results, it can be concluded that when the value of σ_0 is non-zero, indicating that individuals on the networks

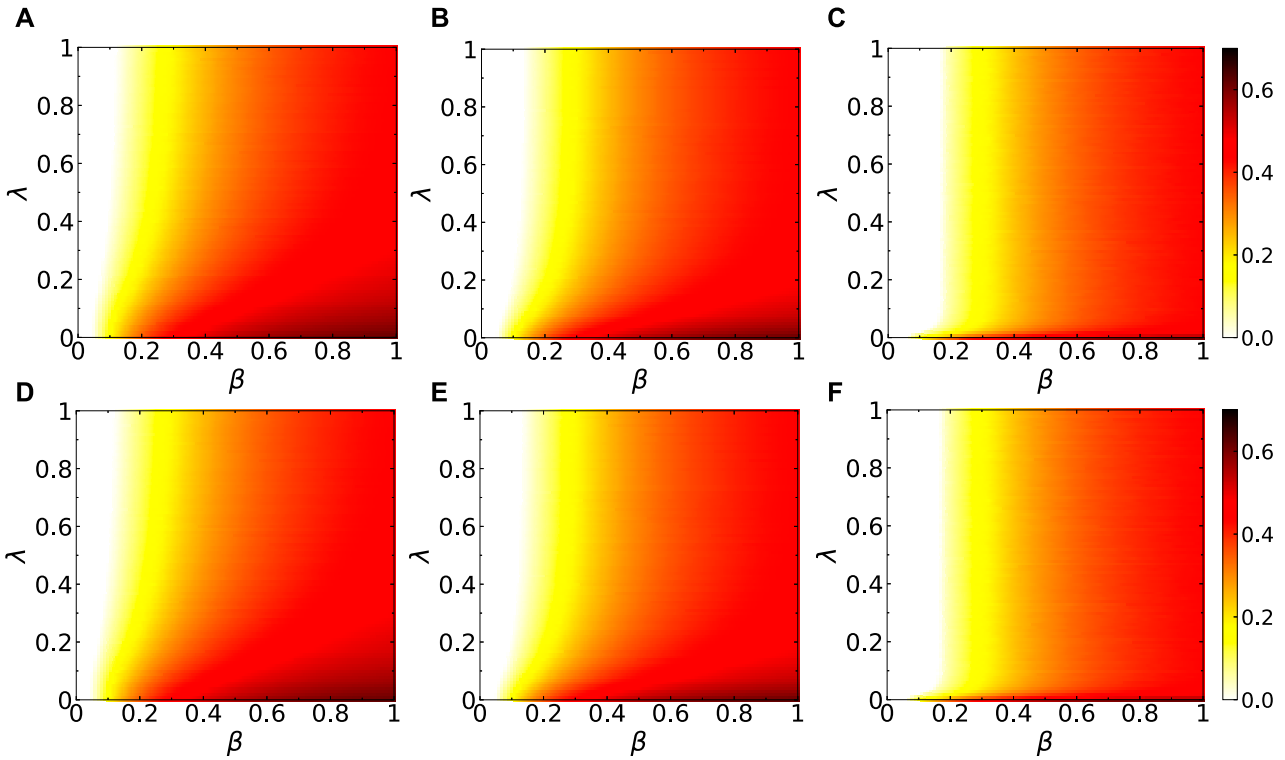

FIGURE 4
(Color online) Results comparisons of the full phase diagrams (λ-β) of ρ^{I} obtained by Microscopic Markov Chains Approach (MMCA) and Monte Carlo (MC) simulations. Top: the corresponding results of MMCA performed on top of multiplex network **(A)** G^{-1}, **(B)** G^{0}, and **(C)** G^{1}. Bottom: the corresponding results of MC simulations performed on top of multiplex network **(D)** G^{-1}, **(E)** G^{0}, and **(F)** G^{1}.The Additional parameters include $\mu = 0.5$ and $\gamma = 0$ in the physical-contact layer, $\lambda = 0.15$, $\sigma_0 = 0.5$, and $\delta = 0.6$ in the virtual-contact layer.

spontaneously generate self-initiated awareness, the stationary fraction of I-state individuals will be decreased on all the networks studied. It indicates that individual self-initiated awareness can suppress the process of epidemic transmission within the employed networks effectively. Figures 5D–F depict how the stationary A-state individuals fraction, denoted as ρ^{A}, varies in response to the infection probability β when considering different values of σ_0 on the multiplex networks G^{-1}, G^{0}, and G^{1}, respectively. Conclusions drawn from the results suggest that in the presence of a non-zero σ_0, ρ^{A} exhibits an increase across all the networks studied. Besides, with an increase in the σ_0 value, there is a corresponding rise in the value of ρ^{A}. Moreover, Figures 6A–C show the variation of ρ^{I} with respect to β on the multiplex networks G^{-1}, G^{0}, and G^{1}, respectively, when different values are set to γ. Upon scrutinizing the findings presented in the figures, it can be deduced that a decrease in the γ value results in a diminishment of ρ^{I} across all the networks studied. This is because in the proposed model, it is established that $\beta^{\mathrm{A}} = \gamma\beta^{\mathrm{U}}$. As the γ decreases, β^{A} also decreases, indicating a lower infection probability among aware individuals. Therefore, under the same dynamics conditions, the stationary fraction of ρ^{I} decreases with the decrease in γ.

Thirdly, we further analyzed the effects of three critical dynamics parameters on the epidemic threshold, namely, the infection attenuation factor γ, the diffusion probability of awareness λ, and the forgetting probability of aware individuals δ. Figure 7 portrays the variation of the epidemic threshold β_c concerning the infection attenuation factor γ on the multiplex networks with different inter-layer degree correlations. Analyzing the results from the figure, it can be inferred that a reduction in γ leads to an enhanced inhibitory impact of awareness on the epidemic, consequently yielding a larger value for β_c. Moreover, in network G^{1}, the β_c increases the fastest as γ decreases. This indicates that when there is a positive inter-layer degree correlation within the networks, the highly connected nodes in the awareness-spreading layer are more likely to become aware, which can enhance the epidemic threshold. Figures 8A–C depict how the epidemic threshold β_c varies concerning the awareness diffusion probability λ across the multiplex networks G^{-1}, G^{0}, and G^{1}, respectively, while considering distinct values for the awareness forgetting probability. As depicted in the figures, on all the networks studied, there is a metacritical point for the effects of awareness diffusion on epidemic transmission. Only when the awareness diffusion probability λ exceeds this metacritical point λ_c, does the epidemic threshold increase with the increasing awareness diffusion probability. Additionally, a decrease in the awareness of forgetting probability δ leads to an increase in β_c and a decrease in λ_c. This is because a smaller forgetting probability δ results in more persistent and widespread diffusion, which promotes the increase of epidemic threshold β_c and the decrease of the metacritical point λ_c that corresponds to it.

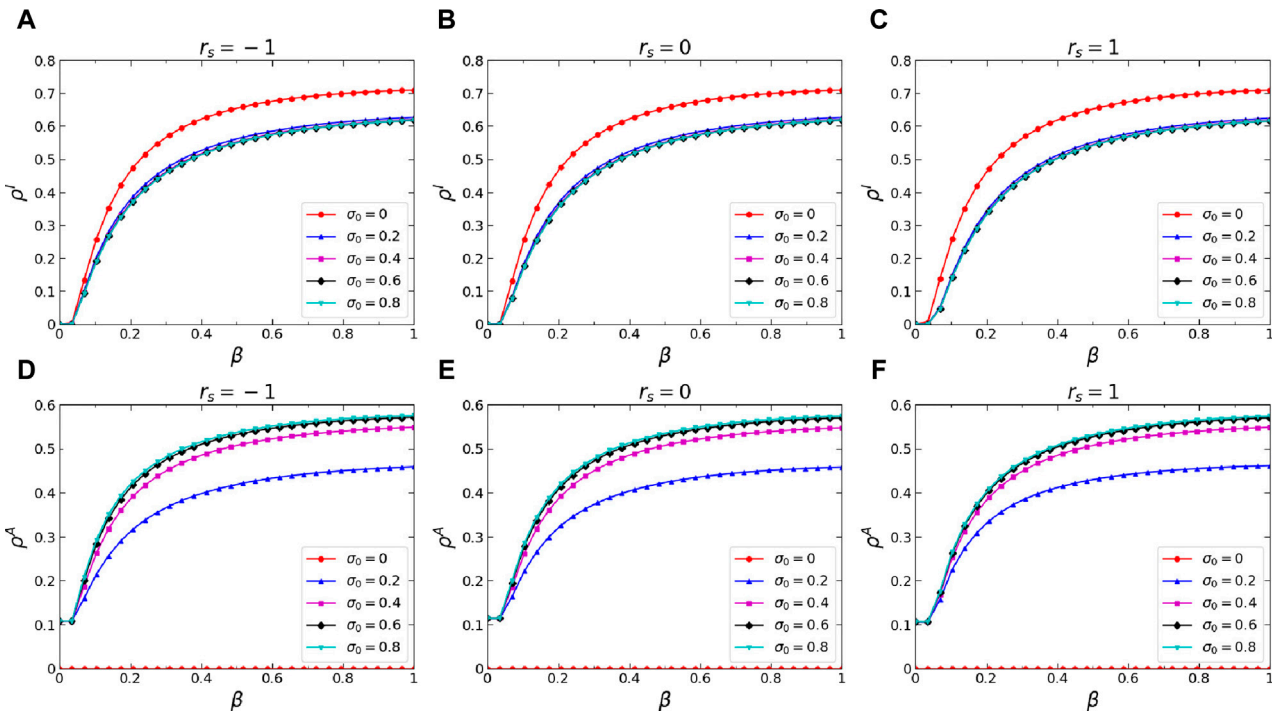

FIGURE 5
(Color online) Effects of the basic self-initiated awareness probability σ_0 on the stationary I-state individuals fraction ρ^I and stationary A-state individuals fraction ρ^A. Specifically, the stationary infeted individuals fraction ρ^I versus infection probability β when **(A)** $r_s = -1$, **(B)** $r_s = 0$, and **(C)** $r_s = 1$. The stationary aware individuals fraction ρ^A versus infection probability β when **(D)** $r_s = -1$, **(E)** $r_s = 0$, and **(F)** $r_s = 1$. The results when $\sigma_0 = 0$, $\sigma_0 = 0.2$, $\sigma_0 = 0.4$, $\sigma_0 = 0.6$, and $\sigma_0 = 0.8$ are denoted by red circle lines, blue trilateral lines, magenta square lines, black rhombus lines, and cyan inverted-triangle lines, respectively. Additional parameters include $\mu = 0.5$ and $\gamma = 0$ in the physical-contact layer, $\delta = 0.6$ and $\lambda = 0.15$ in the virtual-contact layer.

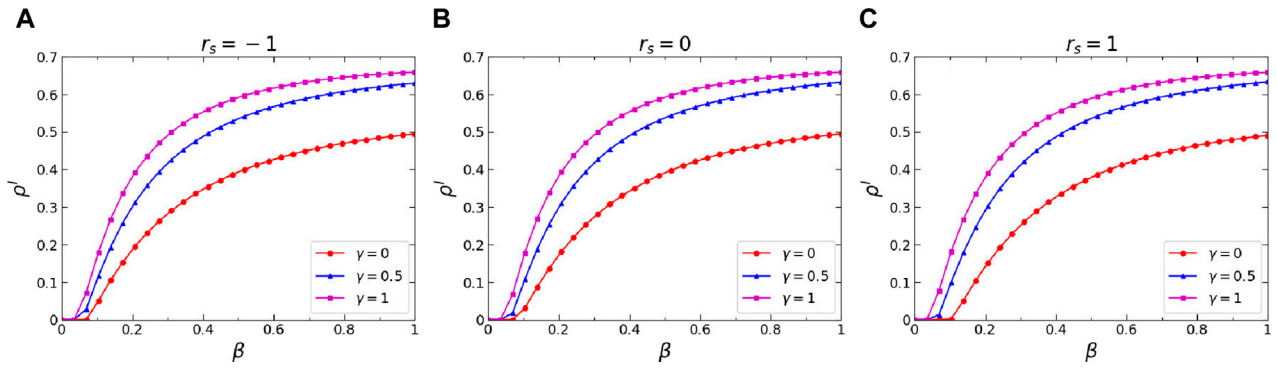

FIGURE 6
(Color online) Effects of the infection attenuation factor γ on the stationary I-state individuals fraction ρ^I. Specifically, the stationary I-state individuals fraction ρ^I versus infection probability β when **(A)** $r_s = -1$, **(B)** $r_s = 0$, and **(C)** $r_s = 1$. The outcomes corresponding to $\gamma = 0$, $\gamma = 0.5$, and $\gamma = 1$ are represented by red circular lines, blue triangular lines, and magenta square lines, respectively. Additional parameters include $\mu = 0.5$ in the physical-contact layer, $\lambda = 0.15$, $\sigma_0 = 0.5$, and $\delta = 0.6$ in the virtual-contact layer.

Finally, we investigate the effects of the average degree K_A and K_B of the virtual-contact layer and the physical-contact layer on the epidemic threshold β_c. In order to explore the role of K_A in the epidemic threshold, we construct three multiplex networks G^{K_A-5}, G^{K_A-10}, and G^{K_A-60} by randomly adding edges in virtual-contact network of G^1. The values of K_A in these networks are set to 5, 10, and 60, respectively, while keeping $K_B = 5$ constant. Figures 9A–C illustrate the changes of β_c concerning the awareness diffusion probability λ on three multiplex networks under different combinations of awareness forgetting probability δ and infected individual recovery probability μ. Comparing the results from the figures, it can be concluded that on all the networks studied, an increase in K_A not only leads to an increase in β_c but also causes a decrease in the metacritical point λ_c that corresponds to it. This

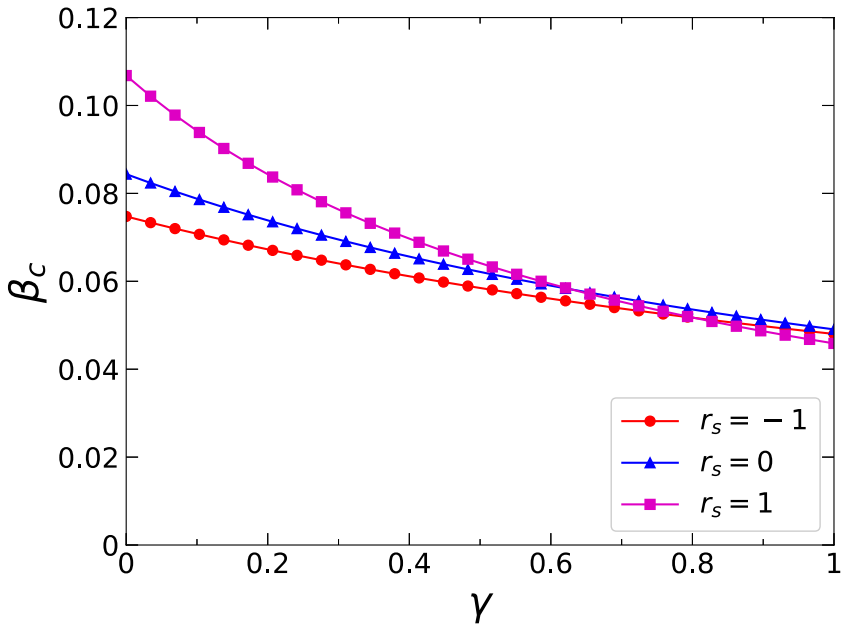

FIGURE 7
(Color online) Effects of the inter-layer degree correlations r_s on the epidemic threshold β_c. Specifically, the epidemic threshold β_c versus infection attenuation factor γ when $r_s = -1$, $r_s = 0$, and $r_s = 1$ are denoted by red circle lines, blue trilateral lines, and magenta square lines, respectively. The corresponding colored curves represent the theoretical predictions derived from Eq. 20. Additional parameters include $\beta = 0.5$ and $\mu = 0.5$ in the physical-contact layer, $\lambda = 0.15$, $\sigma_0 = 0.5$, and $\delta = 0.6$ in the virtual-contact layer.

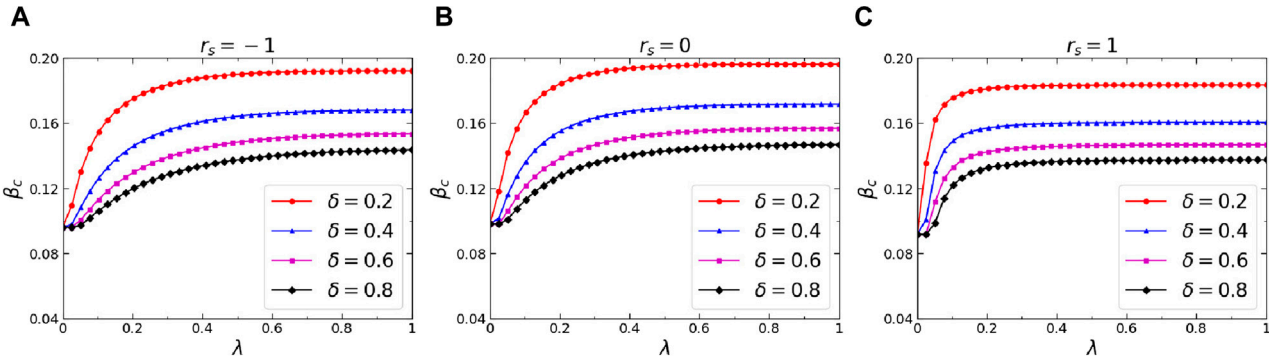

FIGURE 8
(Color online) Effects of the awareness forgetting probability δ on the epidemic threshold β_c. Specifically, the epidemic threshold β_c versus diffusion probability of awareness λ when **(A)** $r_s = -1$, **(B)** $r_s = 0$, and **(C)** $r_s = 1$. The results when $\delta = 0.2$, $\delta = 0.4$, $\delta = 0.6$, and $\delta = 0.8$ are denoted by red circle lines, blue trilateral lines, magenta square lines, and black rhombus lines, respectively. The corresponding colored curves represent the theoretical predictions derived from Eq. 20. Additional parameters include $\beta = 0.5$, $\gamma = 0$, and $\mu = 0.8$ in the physical-contact layer, $\sigma_0 = 0.5$ in the virtual-contact layer.

phenomenon can be explained by the fact that a higher average degree K_A in virtual-contact network facilitates the diffusion of awareness within the networks, resulting in a stronger inhibition on epidemic transmitting, thus β_c increases and λ_c decreases. To explore the influence of K_B on the epidemic threshold, we construct three multiplex networks G^{K_B-5}, G^{K_B-10}, and G^{K_B-30}, by randomly adding edges in the physical-contact layer of G^1. The values of K_B are configured as 5, 10, and 60, respectively, while maintaining a constant value of K_A at 10. Figures 9D–F show the changes of β_c concerning the diffusion probability of awareness λ on three multiplex networks under different combinations of awareness forgetting probability δ and infected individual recovery probability μ. Comparing the results from the figures, it can be concluded that on all the networks studied, an increase in K_B leads to a decrease in β_c when λ is constant. However, the change of K_B does not affect the metacritical point λ_c.

It should be noted that all the aforementioned results are based on the configured multiplex networks. To closely align with real-world scenarios, we conduct extensive experiments on a large number of real networks. The conclusions drawn from these experiments align with those from the configured multiplex networks. For a comprehensive overview of the detailed results, please refer to the Supplementary Material.

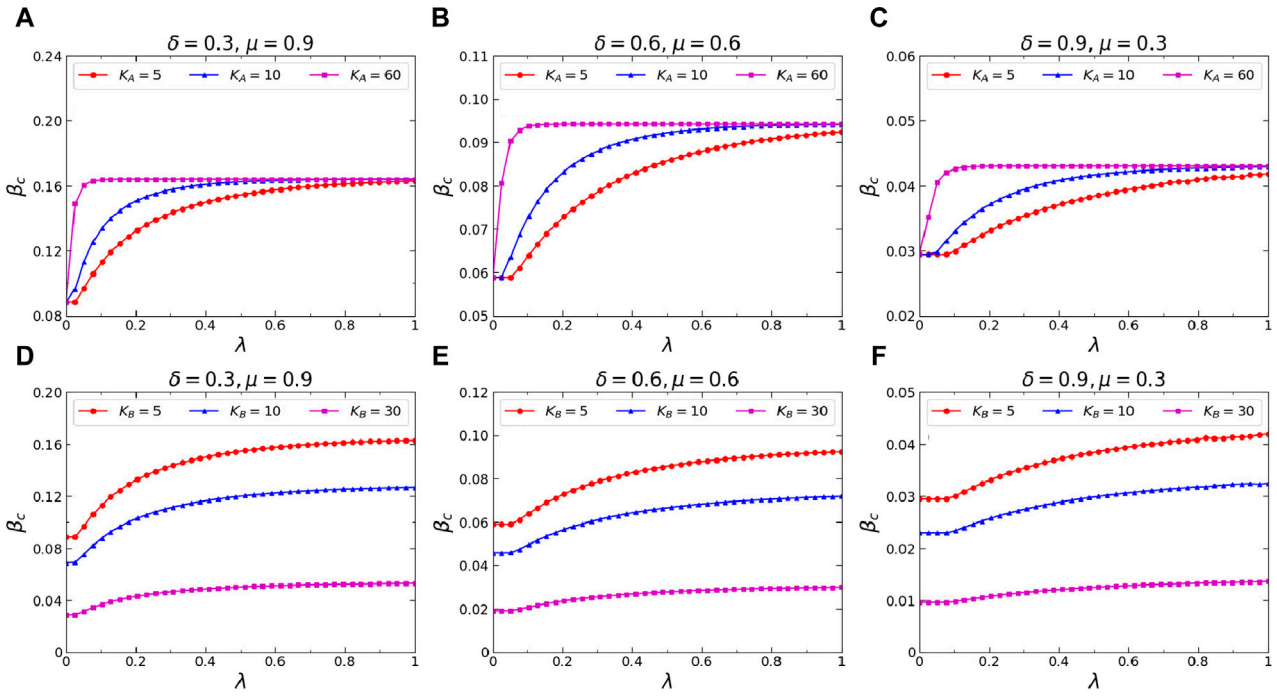

FIGURE 9
(Color online) Effects of the average degrees K_A and K_B of virtual-contact network and physical-contact network on the epidemic threshold β_c. Top: the epidemic threshold β_c versus awareness diffusion probability λ under different combinations of awareness forgetting probability δ and infected individual recovery probability, specifically, **(A)** $\delta = 0.3$, $\mu = 0.9$; **(B)** $\delta = 0.6$, $\mu = 0.6$; and **(C)** $\delta = 0.9$, $\mu = 0.3$. The results when $K_A = 5$, $K_A = 10$, and $K_A = 6$ are denoted by red circle lines, blue trilateral lines, and magenta square lines, respectively. Bottom: the epidemic threshold β_c versus diffusion probability of awareness λ when **(D)** $\delta = 0.3$, $\mu = 0.9$; **(E)** $\delta = 0.6$, $\mu = 0.6$; and **(F)** $\delta = 0.9$, $\mu = 0.3$. The results when $K_B = 5$, $K_B = 10$, and $K_B = 30$ are denoted by red circle lines, blue trilateral lines, and magenta square lines, respectively. The corresponding colored curves represent the theoretical predictions derived from Eq. 20. Additional parameters include $\beta = 0.5$ and $\gamma = 0.4$ in the physical-contact layer, $\sigma_0 = 0.5$, and $\lambda = 0.15$ in the virtual-contact layer.

5 Conclusion

The outbreak of an epidemic often stimulates the development of public awareness about disease prevention, which can effectively curb the process of epidemic transmission. Individuals generate different awareness responses due to varying amounts of information received from their neighbors. Therefore, considering the diversity in individual awareness responses is of significant research importance in the coupled awareness-epidemic dynamics. In this study, we first introduce a coupled awareness-epidemic dynamics model that incorporates the differences in individual awareness responses, where the self-initiated awareness probability of individuals is influenced by the number of their aware neighbors. Subsequently, we develop MMCA method for the analysis of the aforementioned model and validate the accuracy of the MMCA method in solving the coupled spreading model through MC numerical simulations. Next, we analyze the impact of crucial dynamics and structural parameters on the proposed coupled awareness-epidemic dynamics. Through abundant simulations and meticulous theoretical analyses, it has been demonstrated that individual awareness awakening can elevate the steady-state proportion of aware individuals on the networks, consequently mitigating epidemic transmission. Simultaneously, the impact of awareness diffusion on epidemic transmission exhibits a metacritical point λ_c. Specifically, when the awareness diffusion probability λ is larger than λ_c, the epidemic threshold β_c increases while the λ increases. Furthermore, the increase in the average degree K_A of the virtual-contact networks reduces the value of λ_c, while the change in the average degree K_B of the physical-contact networks do not affect λ_c. Finally, we conduct extensive experiments on a large number of real networks, yielding conclusions consistent with the configured multiplex networks. To sum up, this research comprehensively investigated the coupled awareness-epidemic dynamics with individualized self-initiated awareness. The research findings contribute to a deeper understanding of the interaction between awareness diffusion and epidemic transmission, providing essential theoretical insights for epidemic prevention and control.

Data availability statement

The datasets presented in this study are available upon request in the following online repository: https://github.com/20zyli3/zzz.

Author contributions

WZ: Methodology, Validation, Writing–original draft. YY: Methodology, Validation, Writing–original draft. ZL: Methodology, Validation, Writing–original draft. JX: Conceptualization, Funding acquisition, Methodology, Project administration, Software, Validation, Writing–original draft. TW: Methodology, Supervision, Validation, Writing–review and editing. DL: Supervision, Writing–review and editing. DH: Methodology,

Validation, Writing–original draft. ML: Methodology, Funding acquisition, Supervision, Writing–review and editing.

Funding

The author(s) declare that financial support was received for the research, authorship, and/or publication of this article. This work was supported by Shantou University under grants NTF20026 and NTF21041, the National Key Research and Development Program under Grant 2022YFB3104600, the China Postdoctoral Science Foundation Funded Project (2023M740519), Medico-Engineering Cooperation Funds from University of Electronic Science and Technology of China (Nos ZYGX2021YGLH213, ZYGX2022YGRH016), Interdisciplinary Crossing and Integration of Medicine and Engineering for Talent Training Fund, West China Hospital, Sichuan University under Grant No. HXDZ22010, the Municipal Government of Quzhou (Grant 2022D018, Grant 2022D029, Grant 2023D007, Grant 2023D015, Grant 2023D033, Grant 2023D034, Grant 2023D035), Zhejiang Provincial Natural Science Foundation of China under Grant No. LGF22G010009, and Guiding project of Quzhou Science and Technology Bureau (subject No 2022005, 2022K50, 2023K013, 2023K016).

Conflict of interest

The authors declare that the research was conducted in the absence of any commercial or financial relationships that could be construed as a potential conflict of interest.

Publisher's note

Supplementary material

The Supplementary Material for this article can be found online at: https://www.frontiersin.org/articles/10.3389/fphy.2024.1437341/full#supplementary-material

References

1. Morens DM, Folkers GK, Fauci AS. The challenge of emerging and re-merging infectious diseases. *Nature* (2004) 430:242–9. doi:10.1038/nature02759

2. Shereen MA, Khan S, Kazmi A, Bashir N, Siddique R. Covid-19 infection: emergence, transmission, and characteristics of human coronaviruses. *J Adv Res* (2020) 24:91–8. doi:10.1016/j.jare.2020.03.005

3. Tangcharoensathien V, Calleja N, Nguyen T, Purnat T, D'Agostino M, Garcia-Saiso S, et al. Framework for managing the covid-19 infodemic: methods and results of an online, crowdsourced who technical consultation. *J Med Internet Res* (2020) 22:e19659. doi:10.2196/19659

4. Cirrincione L, Plescia F, Ledda C, Rapisarda V, Martorana D, Lacca G, et al. Covid-19 pandemic: new prevention and protection measures. *Sustainability* (2022) 14:4766. doi:10.3390/su14084766

5. Wu J, Zuo R, He C, Xiong H, Zhao K, Hu Z. The effect of information literacy heterogeneity on epidemic spreading in information and epidemic coupled multiplex networks. *Physica A: Stat Mech its Appl* (2022) 596:127119. doi:10.1016/j.physa.2022.127119

6. W X, C Z. Epidemic spreading with an awareness-based adaptive mechanism in temporal multiplex networks. *Front Phys* (2023) 11:1285480. doi:10.3389/fphy.2023.1285480

7. Ma W, Zhang P, Zhao X, Xue L. The coupled dynamics of information dissemination and seir-based epidemic spreading in multiplex networks. *Physica A: Stat Mech its Appl* (2022) 588:126558. doi:10.1016/j.physa.2021.126558

8. Liang GCX, Cui X, Zhu P. An effective method for epidemic suppression by edge removing in complex network. *Front Phys* (2023) 11:1164847. doi:10.3389/fphy.2023.1164847

9. Wang JW, Zhang HF, Ma XJ, Wang J, Ma C, Zhu PC. Privacy-preserving identification of the influential nodes in networks. *Int J Mod Phys C* (2023) 34. doi:10.1142/S0129183123501280

10. Shi D, Shang F, Chen B, Expert P, Lü L, Stanley HE, et al. Local dominance unveils clusters in networks. *Commun Phys* (2024) 7:170. doi:10.1038/s42005-024-01635-4

11. Ji P, Ye J, Mu Y, Lin W, Tian Y, Hens C, et al. Signal propagation in complex networks. *Phys Rep* (2023) 1017:1–96. doi:10.1016/j.physrep.2023.03.005

12. Li R, Wang W, Di Z. Effects of human dynamics on epidemic spreading in côte d'ivoire. *Physica A: Stat Mech its Appl* (2017) 467:30–40. doi:10.1016/j.physa.2016.09.059

13. Xiong X, Zeng Z, Feng M, Szolnoki A. Coevolution of relationship and interaction in cooperative dynamical multiplex networks. *Chaos: An Interdiscip J Nonlinear Sci* (2024) 34:023118. doi:10.1063/5.0188168

14. Lima CMAO. Information about the new coronavirus disease (covid-19). *Radiologia Brasileira* (2020) 53(2). doi:10.1590/0100-3984.2020.53.2e1

15. Deng G, Peng Y, Tian Y, Zhu X. Analysis of influence of behavioral adoption threshold diversity on multi-layer network. *Entropy* (2023) 25:458. doi:10.3390/e25030458

16. Tian Y, Tian H, Cui Q, Zhu X. Phase transition phenomena in social propagation with dynamic fashion tendency and individual contact. *Chaos: Solitons Fractals* (2024) 178:114366. doi:10.1016/j.chaos.2023.114366

17. Chen J, Liu Y, Yue J, Duan X, Tang M. Coevolving spreading dynamics of negative information and epidemic on multiplex networks. *Nonlinear Dyn* (2022) 110:3881–91. doi:10.1007/s11071-022-07776-x

18. Zhu X, Zhang J, Liu S, Tian Y, Cui Y, Li Y, et al. Behavioral propagation influenced by fluctuating personality on single-layer limited-contact network. *Physica Scripta* (2024) 99:025252. doi:10.1088/1402-4896/ad1960

19. Wang J, Cai S, Wang W, Zhou T. Link cooperation effect of cooperative epidemics on complex networks. *Appl Mathematics Comput* (2023) 437:127537. doi:10.1016/j.amc.2022.127537

20. Chen J, Liu Y, Tang M, Yue J. Asymmetrically interacting dynamics with mutual confirmation from multi-source on multiplex networks. *Inf Sci* (2022) 619:478–90. doi:10.1016/j.ins.2022.11.033

21. Chen Y, Liu Y, Tang M, Lai YC. Epidemic dynamics with non-markovian travel in multilayer networks. *Commun Phys* (2023) 6:263. doi:10.1038/s42005-023-01369-9

22. Cai SM, Chen XH, Ye XJ, Tang M. Precisely identifying the epidemic thresholds in real networks via asynchronous updating. *Appl Mathematics Comput* (2019) 361:377–88. doi:10.1016/j.amc.2019.05.039

23. Liu Y, Zeng Q, Pan L, Tang M. Identify influential spreaders in asymmetrically interacting multiplex networks. *IEEE Trans Netw Sci Eng* (2023) 10:2201–11. doi:10.1109/TNSE.2023.3243560

24. Wang J, Yang C, Chen B. The interplay between disease spreading and awareness diffusion in multiplex networks with activity-driven structure. *Chaos: An Interdiscip J Nonlinear Sci* (2022) 32:073104. doi:10.1063/5.0087404

25. Tian Y, Tian H, Cui Y, Zhu X, Cui Q. Influence of behavioral adoption preference based on heterogeneous population on multiple weighted networks. *Appl Mathematics Comput* (2023) 446:127880. doi:10.1016/j.amc.2023.127880

26. Wang J, Xiong W, Wang R, Cai S, Wu D, Wang W, et al. Effects of the information-driven awareness on epidemic spreading on multiplex networks. *Chaos: An Interdiscip J Nonlinear Sci* (2022) 32:073123. doi:10.1063/5.0092031

27. Wang R, Zhang X, Wang M. A two-layer model with partial mapping: unveiling the interplay between information dissemination and disease diffusion. *Appl Mathematics Comput* (2024) 468:128507. doi:10.1016/j.amc.2023.128507

28. Zhu P, Zhi Q, Guo Y, Wang Z. Analysis of epidemic spreading process in adaptive networks. *IEEE Trans Circuits Syst Express Briefs* (2018): 1252–6. doi:10.1109/TCSII.2018.2877406

29. Cao LWX, Zhao H, X A, An X. Competitive information propagation considering local-global prevalence on multi-layer interconnected networks. *Front Phys* (2023) 11:1293177. doi:10.3389/fphy.2023.1293177

30. Zhu P, Wang X, Li S, Guo Y, Wang Z. Investigation of epidemic spreading process on multiplex networks by incorporating fatal properties. *Appl Mathematics Comput* (2019) 359:512–24. doi:10.1016/j.amc.2019.02.049

31. Wang Z, Guo Q, Sun S, Xia C. The impact of awareness diffusion on sir-like epidemics in multiplex networks. *Appl Mathematics Comput* (2019) 349:134–47. doi:10.1016/j.amc.2018.12.045

32. Granell C, Gómez S, Arenas A. Dynamical interplay between awareness and epidemic spreading in multiplex networks. *Phys Rev Lett* (2013) 111:128701. doi:10.1103/PhysRevLett.111.128701

33. Granell C, G´omez S, Arenas A. Competing spreading processes on multiplex networks: awareness and epidemics. *Phys Rev E* (2014) 90:012808. doi:10.1103/PhysRevE.90.012808

34. Chen X, Gong K, Wang R, Cai S, Wang W. Effects of heterogeneous self-protection awareness on resource-epidemic coevolution dynamics. *Appl Mathematics Comput* (2020) 385:125428. doi:10.1016/j.amc.2020.125428

35. Wu D, Liu Y, Tang M, Xu XK, Guan S. Impact of hopping characteristics of inter-layer commuters on epidemic spreading in multilayer networks. *Chaos: Solitons and Fractals* (2022) 159:112100. doi:10.1016/j.chaos.2022.112100

36. Liu C, Yang Y, Chen B, Cui T, Shang F, Fan J, et al. Revealing spatiotemporal interaction patterns behind complex cities. *Chaos: An Interdiscip J Nonlinear Sci* (2022) 32:081105. doi:10.1063/5.0098132

37. Li C, Yuan Z, Li X. Epidemic threshold in temporal multiplex networks with individual layer preference. *IEEE Trans Netw Sci Eng* (2021):1. doi:10.1109/TNSE.2021.3055352

frontiers | Frontiers in Physics

TYPE Original Research
PUBLISHED 09 September 2024
DOI 10.3389/fphy.2024.1462089

OPEN ACCESS

EDITED BY
Fei Xiong,
Beijing Jiaotong University, China

REVIEWED BY
Chengfang Ye,
Xiangtan University, China
Jiwei Xu,
Xi'an University of Posts and Telecommunications, China

*CORRESPONDENCE
Deping Xiong,
xiongdeping@126.com

RECEIVED 09 July 2024
ACCEPTED 23 August 2024
PUBLISHED 09 September 2024

CITATION
Ren L, Zhang J, Su Z, Lai F and Xiong D (2024) Evolution and governance of online public opinion during COVID-19: a hybrid approach using communication visualization, SIR modeling, and simulation validation.
Front. Phys. 12:1462089.
doi: 10.3389/fphy.2024.1462089

Evolution and governance of online public opinion during COVID-19: a hybrid approach using communication visualization, SIR modeling, and simulation validation

Lin Ren, Jiehua Zhang, Zhongyue Su, Fujun Lai and Deping Xiong*

School of Finance, Yunnan University of Finance and Economics, Kunming, China

Introduction: This study investigates the mechanisms of public opinion dissemination and governance strategies during public health events, using a two-stage SIR model informed by the Information Cascade Theory.

Methods: The research employs Gephi visual analysis to identify principal nodes of public opinion and combines model simulations with dynamic propagation analysis to verify the model's precision and applicability.

Results: The findings reveal that pivotal information nodes significantly accelerate the spread of public opinion, while ordinary nodes contribute to the natural attenuation of public discourse due to their strong spontaneous recovery capabilities. The simulation analysis further identifies the optimal timing for government intervention, particularly during the initial and peak phases of public opinion dissemination.

Discussion: Based on the results, the study recommends strategies to strengthen the management of key opinion nodes, enhance public information literacy, optimize policy implementation, and utilize simulation tools to assist in public opinion management. These recommendations offer valuable theoretical and practical insights for managing public opinion during public health events.

KEYWORDS

COVID-19, public opinion, visualization, two-stage SIR modeling, simulation

1 Introduction

As indicated in the 53rd Statistical Report on Internet Development in China, published by the China Internet Network Information Centre (CNNIC) on 22 March 2024, the number of Internet users in China had reached 1.092 billion by December 2023, representing a penetration rate of 77.5%[1]. The pervasive use of the Internet has facilitated the expression of ideas, but it has also precipitated significant social

1 The 53rd Statistical Report on Internet Development in China - Internet Development Research (cnnic.cn).

challenges associated with the proliferation of online public opinion. As indicated in the Global Risks Report 2021, the circulation of online public opinion on significant adverse occurrences not only results in economic losses but also endangers social stability and government credibility. In particular, in the context of COVID-19, the rapid dissemination of online public opinion has served to exacerbate social panic and the spread of rumours, thereby increasing the difficulty of public crisis management[2].

The COVID-19 in 2020 had an unprecedented impact on the public health system, economy and social order of various countries. In this context, the rapid dissemination of negative online public opinion may give rise to social panic, policy misunderstanding and the propagation of rumours, thereby further exacerbating the complexity and governance difficulty of public crises [1, 2]. It is becoming increasingly evident from research that the role of digital technology in public health responses is of paramount importance [3]. In particular, during the initial phase of an epidemic, the volume of information exchanged on social media platforms increases exponentially [4], accompanied by a proliferation of misinformation and fake news. The confluence of these factors in the context of information asymmetry had a profound impact on the public's trust in and compliance with anti-epidemic measures.

During the epidemic in China, several microblogging hotspots emerged, including reports of a woman leaving Hanzhou for Beijing, a patient who failed to report a suspected case in a Wuhan community who subsequently committed suicide, and the case of three members of a family of a retired departmental official in Hubei who were diagnosed with COVID-19 and refused to be quarantined. The rapid dissemination and fermentation of public opinion on the Internet has resulted in these incidents having a significant impact that extends well beyond their immediate consequences. In fact, they have triggered a greater and more persistent social panic. It is therefore of particular importance to monitor public opinion, comprehend the nuances of social opinion and proactively direct and regulate social opinion during a crisis.

The Chinese government places a significant emphasis on the management of public opinion on the Internet. At the Fifth Plenary Session of the 19th CPC Central Committee, the concept of "strengthening the construction of cybercivilisation" was first proposed in the "Recommendations of the Central Committee of the Communist Party of China on the Formulation of the 14th Five-Year Plan for the Development of the National Economy and Society and the Vision and Goals for the 23rd Five-Year Plan." This document placed considerable emphasis on the importance of the governance of public opinion on the Internet. In his remarks, General Secretary Xi Jinping highlighted the growing significance of the Internet as a key arena for public opinion struggles. He underscored the critical importance of China's ideological and regime security in the context of these ongoing battles in the digital domain. The implementation of the strategy of "Network Power" and the concept of "Community of Destiny in Cyberspace" has served to further highlight the urgency and importance of cyberspace governance. Consequently, the Chinese government has enacted a series of policies and regulations, including the Cybersecurity Law of the People's Republic of China, the Data Security Law of the People's Republic of China, and the Personal Information Protection Law of the People's Republic of China, with the objective of reinforcing the legal and institutional safeguards for the governance of cyber public opinion.

Online public opinion exerts significant influence on individual decision-making processes, particularly through the mechanisms of information asymmetry [5–7], herd behaviour [8], opinion leaders [9], and emotional contagion [10], among others. These factors, among others, exert an influence on individual decision-making processes. The completeness, vividness and relevance of the quality of opinion information can also exert a significant influence on user behaviour [11, 12]. During the COVID-19 outbreak, the lack of comprehensive and accurate information made internet users more vulnerable to misinformation, which led to irrational behaviors such as following rumors and disclosing personal information [13]. Therefore, beyond strengthening governance through institutional constraints, it is crucial for policymakers to understand evolving public opinion trends and the psychological state of the public. This understanding can help in making timely adjustments to publicity strategies and improving public policies, thereby guiding public opinion more effectively and mitigating adverse effects [14]. Research shows that timely dissemination of official information and active public involvement can significantly reduce the spread of rumors and alleviate panic [15, 16]. Effective governance of online public opinion requires a dual approach: crisis management, which addresses public opinion during a crisis, and prospective guidance, which prepares and manages public opinion before a crisis occurs [17].

The origins of online opinion research can be traced back to the 1990s, when researchers began to apply text analytics techniques from computer science to the prediction and analysis of opinion communication [18]. The advent of social media platforms has precipitated a phase of accelerated development in online opinion research, with researchers increasingly focusing on the far-reaching impact of social media on opinion communication [19, 20]. In terms of research content, studies have primarily focused on the concept and characteristics of online public opinion [21, 39], the governance subject and elemental structure of online public opinion [2, 22], the generation mechanism of online public opinion [23], and the evolutionary trend of online public opinion [42]; [24, 25]). Additionally, studies have explored the prediction and governance of online public opinion [26]. Notably, significant advancements have been made in the field of public opinion life cycle research. The information life cycle theory, proposed by Rogers et al. [27], provides a comprehensive framework for understanding the evolution of public opinion. Building on this theory, researchers have used quantitative analysis to break down the communication of public opinion into four distinct stages: latency, outbreak, spread, and dissipation. These studies not only offer empirical evidence for managing public opinion during emergencies but also provide a scientific foundation for policymakers to design effective intervention strategies [28, 29]. Notably, during the COVID-19, research highlighted the unique characteristics of information dissemination in crises and its significant impact on social stability [30].

2 Global Risks Report 2021 | World Economic Forum | World Economic Forum (weforum.org).

In terms of research methods, social network analysis methods [16, 17, 31–33] and improved neural network algorithms [34] have been employed. Furthermore, mathematical modelling methods for multi-subject simulation have been employed, including the SIR improvement models [27, 35], system dynamics models [36], and other methods which have gradually become popular for public opinion governance, and have shown a trend of diversification and disciplinary crossover.

While existing studies have made some progress in understanding the evolution and governance of online public opinion, there are still a number of deficiencies that require further investigation. Firstly, the research methodology employed is relatively homogeneous and lacks a comprehensive strategy that combines qualitative and quantitative analyses. This may result in an incomplete understanding and explanation of the phenomenon of public opinion. Secondly, there are limitations in the data and models used. For example, the data sources may be biased, while the existing algorithms and models may not be able to accurately capture the dynamics and diversity of public opinion. This limits the depth and breadth of the research. Moreover, the interdisciplinary integration is still inadequate, which constrains the capacity of researchers to delve into the intricacies of online public opinion from diverse vantages.

This study addresses the limitations of existing research through the following improvements: Firstly, the utilisation of Gephi software for the visual analysis of public opinion dissemination is presented, thereby offering a novel tool and methodology for the dynamic monitoring and intervention of the dissemination process. This improvement addresses the shortcomings of existing methodologies in identifying dissemination pathways. Secondly, within the context of the pandemic, this study employs a simulation of the public opinion dissemination mechanism on Weibo, extending and refining the two-stage SIR model based on infectious disease modelling. The model incorporates the actual characteristics of public opinion dissemination, thereby enhancing the accuracy and comprehensiveness of the analysis of microblogging network public opinion dissemination.

In conclusion, the contributions of this study can be summarized as follows: firstly, the study integrates information life cycle theory with visualisation tools such as Gephi [37] in order to meticulously characterise the dissemination characteristics of public opinion on Weibo from both temporal and structural perspectives. This approach allows for a more detailed understanding of public opinion propagation during COVID-19. Secondly, this paper builds upon and enhances the two-phase SIR model, which is based on the infectious disease model [35, 38]. It does so by integrating the actual characteristics of public opinion dissemination. This improves the accuracy and comprehensiveness of the analysis of microblogging network public opinion dissemination characteristics, and provides a more effective model for subsequent research.

The remainder of this study is structured as follows: the second part introduces the real-life characteristics of online public opinion communication and conducts visual analysis; the third part conducts theoretical analysis and modelling; the fourth part conducts case simulation and model reliability texting; and the fifth part summarises the findings and puts forward policy recommendations.

2 A visual analysis of online public opinion dissemination

In order to align the theoretical analysis with empirical evidence, this section employs visualisation techniques to illustrate the actual trajectory and attributes of public opinion dissemination on Weibo. Firstly, the dissemination of public opinion is mapped out over time by extracting data on the propagation of different negative events on Weibo within the same period. This allows the temporal characteristics of public opinion dissemination to be revealed. Secondly, the life cycle theory of public opinion propagation is employed to analyse the propagation characteristics of microblog public opinion. Ultimately, the Gephi software is employed to distinguish between core and ordinary nodes in the propagation of public opinion, thereby elucidating the structural characteristics of the microblog public opinion propagation path. The aforementioned analysis will furnish data that will inform the subsequent theoretical modelling and analysis.

2.1 Software introduction and application

Gephi is a network analysis software that enables data visualisation. It can visually display the nodes (individuals in the network) and edges (relationships between individuals) of the network. Its powerful graphical processing capabilities and diverse analysis algorithms can be employed to solve the problem of difficult to understand complex network relationships. It is widely used in the visual analysis of social network data [37]. In this paper, the dissemination visualisation analysis of microblog opinion dissemination data was carried out by Gephi. The specific steps included the importation of data in CSV format into Gephi, the calculation of the viewable concatenation within the circle of core nodes, and the multistep filtering, intersection and complementary processing of the degree values of the nodes. Additionally, the redundant nodes were deleted. Subsequently, the number of nodes, the number of edges and the type of graph of the network are analysed, the network parameters are adjusted and the layout is set.

2.2 Data preparation and event extraction

The data employed in this study were sourced from the Weibo platform (https://weibo.com). In order to obtain data pertaining to public opinion on typical negative events related to the COVID-19, we employed the use of crawler technology to collate relevant information from this platform. This encompassed user IDs, time nodes, retweets, comments, likes, comment texts, and location information. The extraction of events is divided into two stages.

In the initial phase of the investigation, the negative events that occurred during the early stages of the COVID-19 were identified through the "zhiweidata" platform (zhiweidata.co). The specific selection criterion is the Event Influence Index (EII), which identifies the six most influential negative events in the EII rankings between 1 December 2019 and 30 June 2020. The EII is calculated based on the cumulative impact of an event's dissemination on microblogs and is normalised to range from 0 to 100.

In the second step, data mining was conducted on the selected negative events. Initially, the crawler technique was employed to

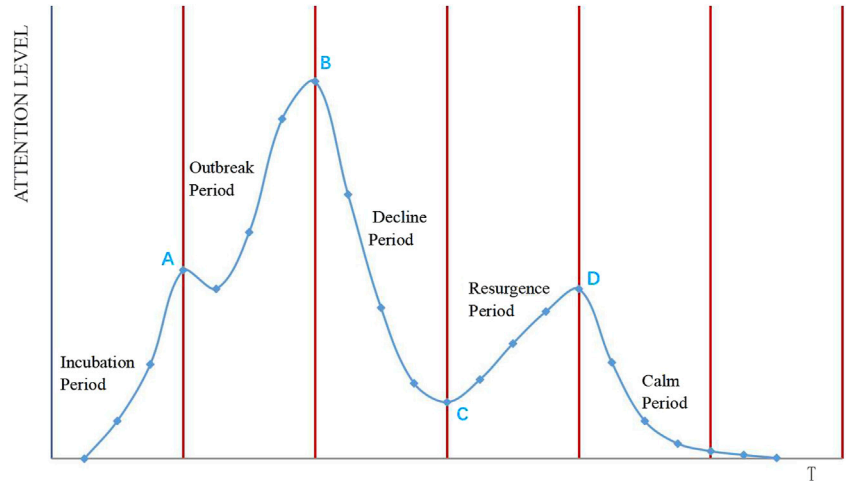

FIGURE 1
Weibo public opinion dissemination lifecycle diagram.

extract the opinion data pertaining to the negative events from the microblogging platform. Subsequently, the raw data were subjected to cleaning procedures, which entailed the removal of hyperlinks, numbering, and redundant symbols, with the objective of ensuring the neatness and coherence of the data set. In instances where data were absent, interpolation or deletion was employed to guarantee the integrity of the data set. In order to eliminate discrepancies between the magnitudes of the data, numerical data such as retweets, comments and likes were normalised.

2.3 A life cycle analysis of online public opinion dissemination

This paper builds upon the life cycle theory of public opinion [27] to develop a new typology for the life cycle of online public opinion communication during the Coronavirus Disease 2019 (COVID-19) pandemic. The proposed typology categorises the life cycle into five distinct phases: the incubation period, the outbreak period, the decline period, the resurgence period and the calm period. Furthermore, the typology identifies three critical peaks of public opinion intensity. The initial peak, designated "A," occurs during the incubation period, the subsequent peak, designated "B," occurs during the outbreak period, and the final peak, designated "D," occurs during the resurgence period. The aforementioned framework is illustrated in Figure 1.

As illustrated in the aforementioned figure, the incubation period is the interval preceding the level of concern reaching the incubation peak, designated as A. It is possible for there to be one or more incubation peaks during this phase. The outbreak period is the interval between the peak of the incubation period (A) and the peak of the outbreak period (B). It is during this period that public opinion undergoes a rapid intensification, attracting considerable attention. The decline period is the period between the peak of the outbreak period B and the commencement of the resurgence period C, during which there is a gradual decrease in public opinion attention. The resurgence period is the period between the conclusion of the decline period (C) and the peak of the resurgence period (D). During this period, public opinion may intensify once more, and this may occur again and again in the case of multiple resurgence periods. The period of calm is the interval between the peak of the resurgence period and the point at which public opinion reaches zero, indicating a gradual decline in public opinion.

In order to visually observe the evolution of microblog public opinion in the time dimension, the six microblog public opinion hotspot events extracted above were compared with the life cycle of online public opinion dissemination. This was done with a view to portraying their temporal public opinion dissemination evolution. The chart below depicts the evolution of public opinion over time, with the horizontal axis representing the number of days and the vertical axis indicating the degree of public opinion attention, quantified by the number of microblog retweets.

As illustrated in Figure 2, the incidents involving the Huanggang Health Commission's inadequate epidemic response and the Dali Municipal Government's expropriation of anti-epidemic materials from Chongqing and Huangshi exhibit a prototypical pattern of incubation, outbreak, decline, and calm periods. In contrast, the collapse of the Quanzhou isolation hospital follows a different pattern, characterised by an additional resurgence period with a distinct peak. A comparative analysis of six representative microblog public opinion events during the global COVID-19 pandemic demonstrates that the life cycle of online public opinion dissemination effectively captures the evolution patterns. The duration, intensity and impact of an event are key factors in determining the presence and prominence of the incubation and resurgence periods. It is noteworthy that these periods may not always manifest as a single peak. In instances where a resurgence period is absent, the decline and stabilisation of public opinion tend to occur concurrently.

2.4 Visualization and analysis of public opinion

In order to gain further insight into the communication structure of microblog public opinion events, this paper selects

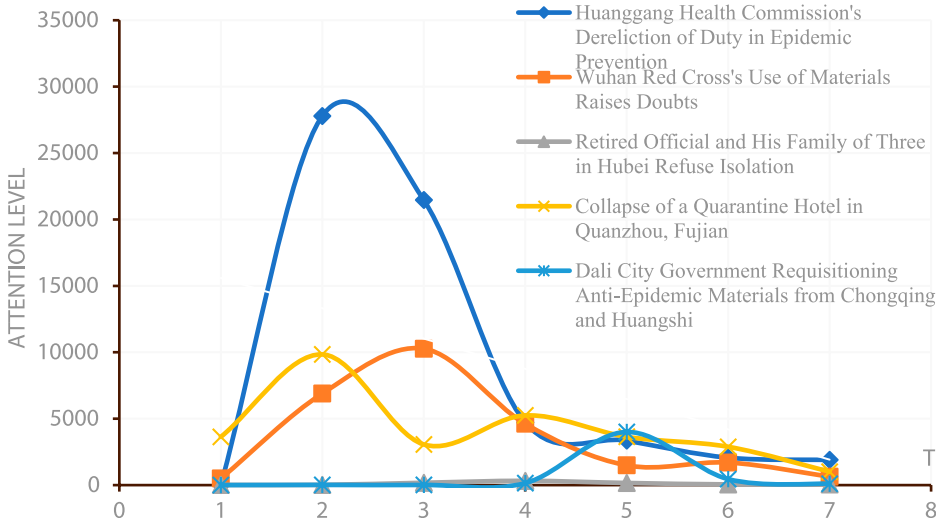

FIGURE 2
Comparative trend chart of online public opinion spread during public health emergencies.

the topic of "Unexplained Pneumonia in Wuhan" on the microblog platform as the research object. The data from this microblog was extracted using crawler technology between 31 December 2019 and 3 January 2020. This included information such as user IDs, comments, retweets and likes. The data regarding retweets, comments and likes were aggregated in order to ascertain the influence of different communication nodes. Accordingly, the following microblog opinion propagation map has been constructed with the assistance of the opinion visualisation tool Gephi, as depicted in Figure 3.

Figure 3 shows that, under the topic of "Unexplained Pneumonia in Wuhan," key nodes such as "CCTV News," "Tokyo Men's Illustrated Book," "Xiehe Hand and Foot Surgery," "Chen Jianghai," "Headline News," and "Qiao Kevin" have significantly higher influence compared to secondary nodes like "Between Coming and Going" and "Natsume's Little Brother." The number and area of nodes connected to key nodes are notably greater than those of secondary nodes. Key nodes attract substantial attention and drive the event's dissemination, while secondary nodes further spread the event. This cascading effect makes the "Unexplained Pneumonia in Wuhan" incident a highly influential public opinion event. Using Gephi, we can visualize the communication structure, showing that transmission is node-based, with key nodes triggering wider public opinion. Significant differences in communication impact highlight the crucial role of key nodes in shaping and influencing public sentiment.

2.5 Key features of online public opinion dissemination

The analyses reveal that the dissemination of public opinion during the early stages of the recent COVID-19 outbreak exhibited sudden and fractious characteristics. While Weibo discussions were initially low, information spread rapidly, reflecting the inherent instability of the communication landscape. Netizens often displayed intense negative emotions, with some users significantly influencing information spread through extensive retweets and engagement [30]. Integrating the microblog public opinion life cycle with Gephi's visualization analysis, we identify four key characteristics of public opinion dissemination during the COVID-19 pandemic:

- **Cyclicality:** Public opinion dissemination follows distinct phases—latency, outbreak, decline, warming-up, and calming-down—each with unique intensity and propagation patterns.
- **Opinion Leaders:** Key nodes (opinion leaders) play a crucial role by quickly attracting public attention and further spreading opinions through secondary nodes.
- **Context Dependence:** Dissemination is influenced by the event's context and external factors. Changes in anti-epidemic policies and epidemic data updates can rapidly alter dissemination direction and intensity.
- **Dynamics:** The dissemination process is dynamic, with significant variations in influence among nodes. The dissemination path and intensity of public opinion may fluctuate rapidly.

3 Theoretical analysis and modelling

On the basis of the preceding analysis of microblog opinion dissemination characteristics, this section introduces the Information Cascade Theory to further explore the generation mechanism of microblog online public opinion. The explanatory power of the model is enhanced by the construction of the social utility function of opinion dissemination among microblog users and the application of optimal control theory to optimise the analysis of the dissemination rate of opinions. In conclusion, this paper puts forward a more realistic two-stage SIR model with the aim of providing a comprehensive insight into the propagation mechanism of microblogging online public opinion.

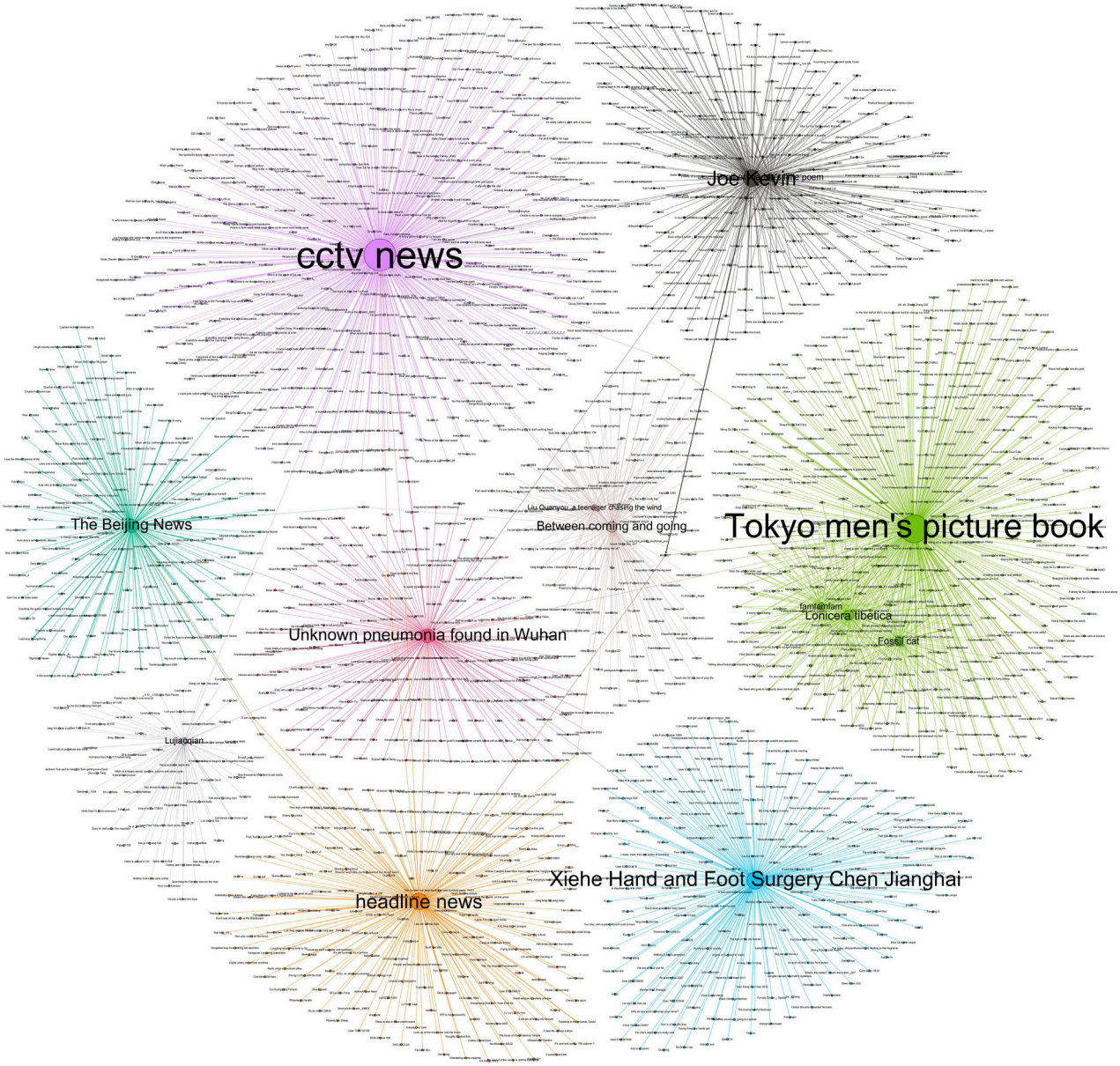

FIGURE 3
Visualization of online public opinion spread regarding the "Unknown Pneumonia Outbreak in Wuhan" incident.

3.1 Theoretical analysis

The Information Cascade model, proposed by Bikhchandani et al. [8], reveals that individuals operating in a decentralised manner exert influence and are themselves influenced. Individuals' behaviours may deviate from the principles of popular rationality, yet they are also susceptible to the influence of the majority group. This can result in a tendency to neglect one's own perceptions, a phenomenon known as the "illusion of group rationality," and a proclivity towards blind adherence to the prevailing opinion of the group. This phenomenon is also referred to as "animal spirits" in the context of Information Cascade Theory. Anderson and Holt [40] constructed a general model based on Bayes' law, which provides a theoretical framework for the Information Cascade Theory.

The phenomenon of the Information Cascade Theory is particularly evident in the context of microblog communication, where the decisions of netizens with regard to their communication are frequently shaped by a desire to align themselves with prevailing trends. In this context, microblog users' communication decisions are shaped by a combination of rational and irrational factors, resulting in a range of outcomes, including both positive and negative effects. The limited nature of microblogging cyberspace results in a reduction in the rate of public opinion dissemination, which in turn leads to a gradual weakening of the positive effect. As time progresses and the number of participants increases, the cost of dissemination rises, leading to an increase in the negative effect. Nonetheless, the typical lifespan of network memory is only 7 days [30], with the negative effect subsequently diminishing over time.

Accordingly, this paper presents a social utility function for microblogging users' opinion dissemination decisions, based on the trade-off between positive and negative effects, as described in Equations 1–3:

$$P = P(\beta) \quad (P' > 0, P'' < 0) \tag{1}$$

$$N = N(\beta) \quad (N' > 0, N'' > 0) \tag{2}$$

The social utility function for online public opinion dissemination, as proposed in this paper, is based on a trade-off between the two effects generated by public opinion dissemination. The function is constructed as follows:

$$U = U(P, N) \tag{3}$$

where P represents the positive effect, N represents the negative effect, and U denotes the total social utility.

3.2 Two-stage SIR modeling of microblog opinion dissemination

The classical SIR infectious disease model is an important mathematical model used in epidemiology to describe the process of infectious disease transmission. The model divides the population into three categories: susceptible (S), infected (I), and immune (R), and simulates the temporal changes in the number of individuals in these three categories through differential equations. The SIR model was first introduced into the analysis of public opinion dissemination by Daley and Kendall [41] who, with the help of the analogy of the spread of infectious diseases, revealed the mechanism of the spread of rumours in society. Building on the SIR model, this study categorises microblog users into three groups: Potential Opinion Spreaders (S), Opinion Spreaders (I), and Opinion Immune Users (R). The former denotes potential information disseminators who have not yet been exposed to public opinion information; the latter, trusting users who have already been exposed to and disseminated public opinion information; and the latter, immunisers, who have ceased disseminating public opinion information. In order to more accurately reflect the intricacies of opinion dissemination, we have enhanced the classical SIR model in two stages, integrating the aforementioned portrayal of dissemination characteristics.

The parameters used in this study are illustrated in Figure 4:

The symbols for the parameters are defined as follows:

S_1: Number of potential opinion spreaders among key nodes;

S_2: Number of potential opinion spreaders among ordinary nodes;

I_1: Number of opinion spreaders among key nodes;

I_2: Number of opinion spreaders among ordinary nodes;

R: Number of opinion immunizers;

N: Total number of Weibo users affected by the opinion;

a: Growth rate of new followers to the event;

b: Growth rate of followers who lose interest in the event;

β_1: Diffusion influence of ordinary nodes;

β_2: Diffusion influence of key nodes;

μ_1: Recovery rate of diffusion among ordinary nodes;

μ_2: Recovery rate of diffusion among key nodes;

λ: Resistance rate of recoverers to the opinion;

$1 - \lambda$: Probability of secondary infection.

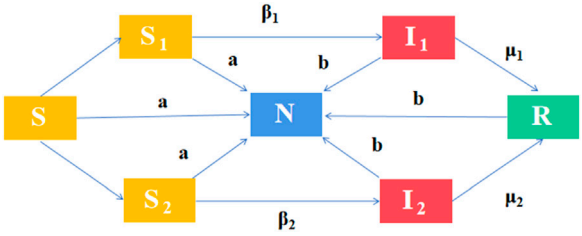

FIGURE 4
The parameter relationship diagram of the two-stage SIR segmented model.

Furthermore, we propose the following modeling approach for the two-stage SIR model:

The initial propagation phase is the first stage of the process. In this phase, the model introduces two key variables: the growth rate of new followers (a) and the growth rate of followers (b) who are no longer interested. Furthermore, the spreading influence (β_1 and β_2) and recovery rate (μ_1 and μ_2) of ordinary and key nodes are distinguished in order to more accurately model the spreading characteristics of information in a small initial area.

Stage 2: Diffusion spreading stage: As the information disseminates widely, the model also considers the impact of official information disclosure and government intervention. This stage demonstrates a decline in the rate of spread (β) over time, as well as an increase in the recovery rate (μ), through an analysis of the utility function in relation to the dissemination of public opinion. Furthermore, the model incorporates the resistance rate of recoverers to public opinion (λ) and the probability of secondary infection of public opinion ($1 - \lambda$) to provide a more comprehensive representation of the intricate propagation mechanisms underlying public opinion events on microblogs.

In light of the aforementioned enhancements, our proposed two-stage SIR model is capable of simulating the microblog opinion dissemination process in a more comprehensive manner, elucidating the dynamic alterations and attributes of information dissemination across distinct stages.

3.2.1 Research hypothesis

In fact, four factors merit particular attention: Firstly, the existence of information asymmetry gives rise to suspicion and speculation regarding the source of information, which in turn facilitates the dissemination of false information. Secondly, the tailored recommendations of information sources reinforce confirmation bias, thereby exacerbating the phenomenon of digital echo chambers. Thirdly, the influence of online opinion leaders, the reticence of elite users and the followers of ordinary users has challenged the theory of "The Spiral of Silence." Fourthly, the "rational" decision-making of dispersed individuals may result in unforeseen distortions of opinion, thereby giving rise to the formation of the "rabble" effect, which in turn serves to promote the development of social irrationality. Collectively, these factors render the phenomenon of the information waterfall susceptible to the formation of public opinion bias in online public opinion events, which in turn exerts an influence on public decision-making. In light of the aforementioned evidence, this paper puts forth the following four hypotheses:

Hypothesis 1. Network Users Have Complete Information Judgement.

Assuming that for an information set $S = \{s_1, s_2..., s_n\}$, where S is closed, convex, and $0 \in S$, for all s_i and s_j in S, either $s_i \succ s_j$ or $s_i \prec s_j$. This implies that Weibo users, as information receivers, possess the necessary information to evaluate different pieces of information, thereby having the capability to discern information. Consequently, information asymmetry is alleviated to some extent, leading to a reduction in the spread of false information. It's assumed that the network subject's judgement of information is complete.

Hypothesis 2. Information Dissemination Among Network Users Is Homogeneous.

Assuming that network users have equal dissemination and trust capabilities, the overall efficiency of information dissemination remains unchanged despite personalized recommendations. Homogeneous dissemination can mitigate the impact of confirmation bias on the overall public opinion and suppress the intensification of the "digital echo chamber" effect. However, due to the varying sizes of nodes, the probability of encountering and disseminating information through different nodes varies, leading to differences in dissemination effectiveness.

Hypothesis 3. Network Users Are Boundedly Rational, and Information Transmission Is Imperfect.

Due to the inability of network users to access fully symmetric information and their bounded rationality, they are more susceptible to the influence of opinion leaders. This bounded rationality leads ordinary users to follow opinion leaders, resulting in the "spiral of silence" phenomenon.

Hypothesis 4. The Total Number of Network Public Opinion Users, N, Dynamically Changes with External Factors such as Propagation and Exit Rates.

Network users are categorized into three types: S (potential disseminators), I (active disseminators), and R (immune individuals), with $S + I + R = N$ at any given time. The growth rate a and reduction rate b depend on the type and intensity of the external public opinion event and vary according to a fixed ratio throughout the "public opinion dissemination lifecycle." As the user population dynamically changes, the phenomenon of opinion distortion intensifies, contributing to the "mob effect" and potentially leading to societal irrationality.

3.2.2 First-stage modeling of microblog opinion dissemination

In the initial phase of the Weibo opinion dissemination model, the advantages of "following the trend" propagation are perceived to be positive, leading internet users to engage in "irrational" following behaviour by disregarding the information they receive. At this juncture, the number of disseminators increases exponentially, while the dissemination rate stabilises and propagates at a constant rate. To more accurately represent the actual processes occurring in opinion dissemination, this study employs the well-established SIR model for its initial modelling of online opinion diffusion on Weibo. In this model, S, I, and R represent the potential opinion spreaders, active opinion spreaders, and opinion receivers, or "immune" opinion recoverers, respectively. The definitions of the remaining parameter symbols utilized in the first stage are presented in Table 1, and the proof process is detailed in Equations 4–18.

$$\begin{cases} \dfrac{dS(t)}{dt} = aS(t) - \beta_1 S_1(t) I(t) - \beta_2 S_2(t) I(t) - bS(t) \\ \dfrac{dI(t)}{dt} = \beta_1 S_1(t) I(t) + \beta_2 S_2(t) I(t) - \mu_1 I_1(t) - \mu_2 I_2(t) - bI(t) \\ \dfrac{dR(t)}{dt} = \mu_1 I_1(t) + \mu_2 I_2(t) - bR(t) \\ S + I + R = N \\ S_1 + S_2 = S \\ I_1 + I_2 = I \end{cases} \tag{4}$$

Given that S, I,and R are continuous and differentiable functions of time t, and considering $a = b$, the model exhibits the following properties:

Property 1. The number of potential information disseminators S decreases over time t and approaches a lower bound, while the number of information trusters R increases over time t and approaches an upper bound.

Proof:

$$\frac{dS}{dt} = -\beta_1 S_1 I - \beta_2 S_2 I \le 0 \tag{5}$$

$$\frac{dR}{dt} = \mu_1 I_1 + \mu_2 I_2 \ge 0 \tag{6}$$

$$\lim_{t \to \infty} S(t) = \tilde{S} = M \tag{7}$$

$$\lim_{t \to \infty} R(t) = \tilde{R} = M - \tilde{S} = 0 \tag{8}$$

Property 2. When I reaches its maximum value, the intensity of public opinion also peaks.

Proof:

$$\because S(t) + I(t) + R(t) = N \tag{9}$$

Taking the total differential on both sides, we obtain:

$$\therefore S'(t) + I'(t) + R'(t) = 0 \tag{10}$$

According to Property 1 and using the Euler approximation method, we have:

$$S(t + \Delta t) \approx S(t) - \left(\beta_1 S_1(t) I(t) + \beta_2 S_2(t) I(t)\right)\Delta t \tag{11}$$

$$tI(t + \Delta t) \approx I(t) + \left(\beta_1 S_1(t) I(t) + \beta_2 S_2(t) I(t) - \mu_1 I_1 - \mu_2 I_2\right)\Delta t \tag{12}$$

$$R(t + \Delta t) \approx R(t) + \left(\mu_1 I_1 + \mu_2 I_2\right)\Delta t \tag{13}$$

$$\because \frac{dI}{dt} < 0 \tag{14}$$

$$\therefore \frac{\beta_1 S_1 + \beta_2 S_2}{\mu_1 + \mu_2} < 1 \tag{15}$$

Therefore, when $\frac{\beta_1 S_1 + \beta_2 S_2}{\mu_1 + \mu_2} < 1$, the number of disseminators begins to decrease, and the intensity of public opinion starts to decline. Conversely, when $\frac{\beta_1 S_1 + \beta_2 S_2}{\mu_1 + \mu_2} = 1$, I reaches its maximum value, and the intensity of public opinion peaks.

TABLE 1 Relevant parameters of the equations in the first stage.

Nodes	Potential spreaders	Trustors	Spread rate	Recovery rate	Growth rate	Reduction rate
Key nodes	S_1 (t)	I_1 (t)	β_1	μ_1	a	b
Secondary nodes	S_2 (t)	I_2 (t)	β_2	μ_2	a	b

Property 3. Given the initial value of S, parameters β and μ, and the proportion of each node, the influence of public opinion can be assessed.

Proof:

$$\frac{dI}{dS} = -1 + \frac{\mu_1 I + \mu_2 I}{\beta_1 S_1 I + \beta_2 S_2 I} \tag{16}$$

$$\frac{dI}{dS} = -1 + \frac{\mu_1 \kappa + \mu_2 \gamma}{\beta_1 S\kappa + \beta_2 S\gamma} \tag{17}$$

$$\frac{dI}{dS} = -1 + \frac{k}{S} \tag{18}$$

Where κ and γ represent the ratio of key information nodes to regular nodes, let $k = \frac{\mu_1 \kappa + \mu_2 \gamma}{\beta_1 \kappa + \beta_2 \gamma}$. When S is greater than k, I will decrease; when S is less than k, I will increase; and when $S = k$, I reaches its maximum. Let $K = \frac{S_n}{k}$ be the threshold to determine whether the public opinion has momentum. When K is greater than 1, the public opinion has a strong diffusion force, and when K is less than 1, the public opinion does not have significant influence.

3.2.3 Second-stage modeling of microblog opinion dissemination

In the second stage of Weibo public opinion dissemination, individual users face potential negative consequences (such as loss of personal reputation, account suspension, legal penalties, etc.) due to official information disclosures and government interventions. As a result, if users rationally analyze and assess the existing information before taking action, such rational behavior can lead to an increase in their overall welfare. The definitions of the parameter symbols employed in the second stage are set forth in Table 2.

Let $S(t)$ represent the number of potential spreaders at any time t, and $\frac{dS}{dt}$ represent the rate at which potential spreaders (S) decrease (i.e., convert to actual spreaders) at any time t, where $\frac{dS}{dt} = -\beta$.

Thus, to examine the optimal time path of β over the interval $[0, T]$, the spread decision of individual users can be described as a dynamic optimization problem of the social welfare function. Table 1, and the proof process is detailed in Equations 19–32:

$$Max \int_0^T U(P(\beta), N(\beta))dt \tag{19}$$

$$\text{s.t. } \frac{dS}{dt} = -\beta \tag{20}$$

$$S(0) = S_0, S_T \geq 0, S_0, T \text{ given} \tag{21}$$

To construct the Hamiltonian function, we have:

$$H = U(P(\beta), N(\beta)) - \lambda\beta \tag{22}$$

And assuming U, P, and N are nonlinear differential functions, the first-order conditions are:

$$\frac{\partial H}{\partial \beta} = U_P P'(\beta) + U_N N'(\beta) - \lambda = 0 \tag{23}$$

It is easily proven that the first-order conditions maximize the Hamiltonian function, leading to:

$$\frac{\partial^2 H}{\partial \lambda^2} = U_{PP} P'^2 + U_P P'' + U_{NN} N'^2 + U_N N'' < 0 \tag{24}$$

The differential equation for λ is given by: $\frac{d\lambda}{dt} = -\frac{\partial H}{\partial S} = 0$, where λ is a constant.

The transversality conditions are: $\lambda(T) \geq 0, S(T) \geq 0, \lambda(T)S(T) = 0$

When $\lambda(t) = 0$, the first-order condition becomes:

$$U_P P'(\beta) + U_N N'(\beta) = 0 \tag{25}$$

yields:

$$\beta^*(t) = \beta^* \tag{26}$$

The term $U_P P'(\beta)$ measures how changes in β affect the positive effect P, while $U_N N'(\beta)$ assesses how changes in β impact the negative effect N. Therefore, the equation $U_P P'(\beta) + U_N N'(\beta) = 0$ guides government agencies in choosing β^* based on the principle that the marginal utility and marginal negative utility of public opinion dissemination are equal.

Moreover, β^* satisfies $S(T) \geq 0$. Since β is a constant, integrating the motion equation with respect to t gives $S(t) = -\beta t + k$, where k is an arbitrary constant. Setting $t = 0$ yields $k = S_0$, thus:

$$S^*(t) = S_0 - \beta^* t \tag{27}$$

Thus, the number of potential disseminators at any given time depends on the size of β^*. Examining the impact of β^* on Weibo public opinion dissemination under three scenarios, where $\beta_1^* < \beta_2^* < \beta_3^*$:

(1) When the dissemination rate is low, β_1^*, the line is gently downward sloping, ensuring that $S(T)$ remains positive.
(2) When the dissemination rate is β_2^*, $S^*(t)$ at $t = T$ is zero. At this point, the government is still within the control limits for public opinion.
(3) When the dissemination rate is higher, β_3^* , $S(T)$ does not satisfy $S(T) = 0$. Therefore, β^* solutions are either β_1^* or β_2^*. For $\beta^* = \beta_3^*$, $S(T)$ must be zero, implying $\beta^* = \frac{S_0}{T}$.

In the model, the dissemination probability β^* does not change over time. Regardless of constraints, β^* remains constant. However, if a discount factor $e^{-\rho t}$ is introduced, and $\lambda^*(t) > 0$), then the path of $\beta^*(t)$ will be downward, meaning that the dissemination rate should decrease over time.

Thus, if the dissemination probability β^* varies with time, the Hamiltonian function becomes:

$$H = U(P(\beta), N(\beta))e^{-\rho t} - \lambda\beta \tag{28}$$

TABLE 2 Relevant parameters of the equations in the second stage.

Nodes	Potential spreaders	Trustors	Recovered	Spread rate	Recovery rate	Resistance rate of recovered	Probability of secondary infection
T time	$S(t)$	$I(t)$	$R(t)$	$\beta(t)$	$\mu(t)$	λ	$1-\lambda$

The first-order condition is:

$$\frac{\partial H}{\partial \beta} = U_P P'(\beta)e^{-\rho t} + U_N N'(\beta)e^{-\rho t} - \lambda = 0 \tag{29}$$

It can be proven that λ is a constant, and when $\lambda(T) = 0$, the solution still satisfies $\beta^*(t) = \beta^*$. However, when $\lambda(T) > 0$ and $S(T) = 0$, the first-order condition becomes:

$$U_P P'(\beta) + U_N N'(\beta) - ce^{-\rho t} = 0 \tag{30}$$

The path of $\beta^*(t)$ at this time is:

$$\frac{d\beta}{dt} = \frac{\rho c e^{\rho t}}{U_{PP}P'^2 + U_P P'' + U_{NN}N'^2 + U_N N''} < 0 \tag{31}$$

Therefore, in reality, the propagation rate of Weibo public opinion exhibits significant variability as the situation evolves. In the second stage, the multi-agent dynamics in Weibo public opinion lead to a continuous decrease in the propagation rate, eventually converging to zero.

Based on the characteristics of the second stage of propagation, the following model is established:

$$\begin{cases} \dfrac{dS(t)}{dt} = -\beta(t)S(t)I(t) + (1-\lambda)R(t) \\ \dfrac{dI(t)}{dt} = \beta(t)S(t)I(t) - \mu(t)I(t) \\ \dfrac{dR(t)}{dt} = \mu(t)I(t) - (1-\lambda)R(t) \\ S + I + R = N \end{cases} \tag{32}$$

where $\beta(t)$ is the propagation rate decreasing over time, $\mu(t)$ is the recovery rate increasing over time, λ represents the resistance rate of recoverers to public opinion, and $1-\lambda$ is the probability of secondary infection. This model is used to reveal the real-world situation where many public opinion events involve repeated interactions between real and false information.

4 Case simulation and model reliability testing

To verify the effectiveness of the proposed modified SIR model, this study selects the Weibo event "Questions Raised on the Wuhan Red Cross Material Usage" as a case. The modified SIR model is used for simulation to validate its effectiveness. Additionally, sensitivity analysis is conducted to ensure the reliability of the model.

4.1 Case description

On 30 January 2020, Wuhan Renai Hospital, which specializes in plastic surgery and reproductive health, received 16,000 N95 masks donated by the Hubei Red Cross. In contrast, Wuhan Union Hospital, a major facility for treating epidemic patients, only received 3,000 ordinary masks. This discrepancy attracted significant attention, with mainstream media outlets such as China Daily and CCTV reporting on the issue, causing the Weibo public opinion to reach its peak. On February 1, the Hubei Red Cross responded to the donation distribution concerns, Wuhan Red Cross adjusted the targeted donation process, and the Red Cross Society of China dispatched a work team to Wuhan, leading to a gradual calming of the public opinion.

4.2 Data collection and processing

For the case simulation, we selected the "Wuhan Red Cross material usage controversy" event, one of the six key public opinion incidents identified earlier. The study period spanned from 30 January 2020, to 14 February 2020. Data from the "zhiweidata" platform (zhiweidata.co) indicated that the event generated 48,759 original Weibo posts. The event lasted for 14 days and 16 h, peaking at a dissemination rate of 993 posts per hour and an average rate of 21 posts per hour. The peak volume reached 8,636 posts. Additional data, including likes, comments, retweets, and view counts, were also considered.

Data filtering and information fitting provided the following parameters: for key information nodes, $S_2 = 500$, connection points = 15, initial $I_0 = 5$, dissemination rate $\beta_1 = 2.5\%$, recovery rate $\mu_1 = 0.02\%$; for ordinary information nodes, $S_1 = 3000$, connection points = 5, initial $I_0 = 3$, dissemination rate $\beta_2 = 0.9\%$, recovery rate $\mu_2 = 0.08\%$. These parameters were used to fit the real development trend of the Weibo public opinion event using conformal interpolation, as illustrated in Figure 5.

4.3 Analysis of simulation results

Following the determination of the initial values and parameters of the model based on the aforementioned information, this paper employs Matlab for simulation and analysis. The simulation results derived from real data are illustrated in Figure 6.

According to the ratio trajectory of the number of key information nodes to the number of common information nodes in the initial stage, it can be observed that:

(1) The key nodes exert a strong driving effect on the ordinary nodes due to their high relevance, exhibiting a high propagation rate and low recovery rate. They possess the key "power" characteristics to promote the triggering of public opinion.
(2) In contrast, the propagation rate of the ordinary nodes is very slow compared with that of the key nodes, and the

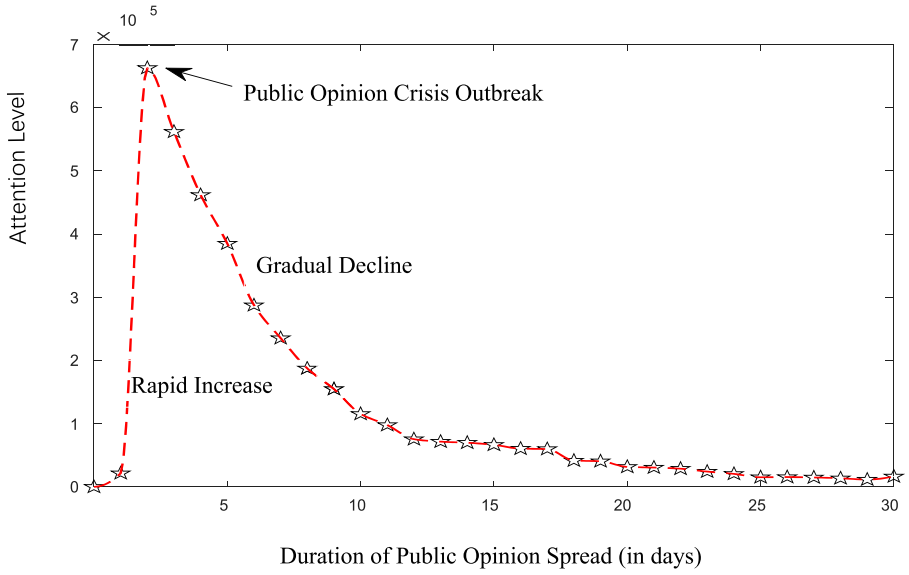

FIGURE 5
Trend chart of online public opinion spread regarding the "Wuhan Red Cross's Use of Materials Raises Doubts" incident.

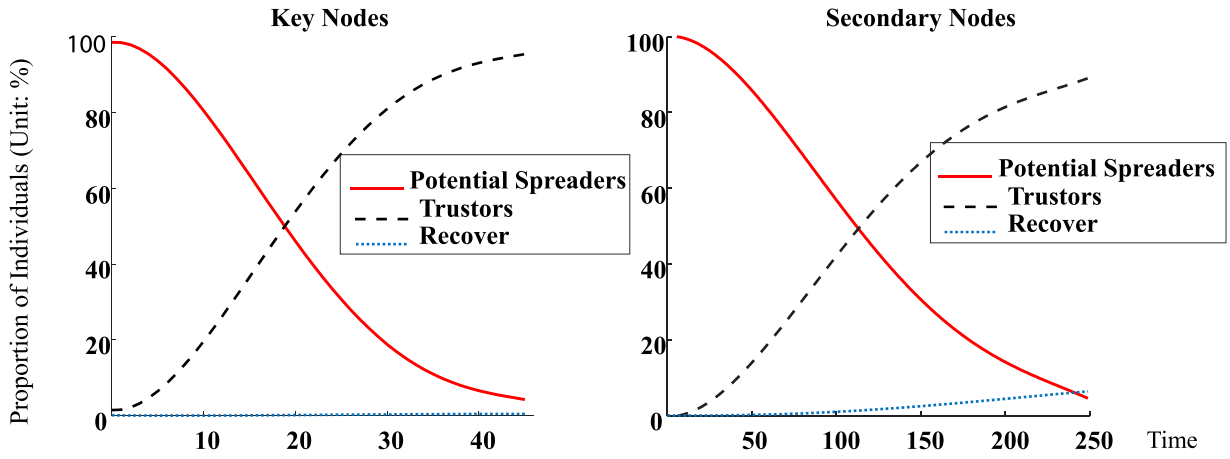

FIGURE 6
Simulation diagram of public opinion spread in the first stage.

spontaneous recovery rate of public opinion propagated by the ordinary nodes is high. The propagation process is equipped with an intrinsic immune system that suppresses public opinion.

(3) The propagation of different nodes ultimately reaches its peak, and the ratio of the three types of people can be stabilised.

In the second stage of public opinion dissemination, the dissemination rate β is exponentially decayed according to 3.4% of the initial value, with the decay function $y = exp(-ax)$, while the recovery rate $\mu = 0.1$ gradually increases with time. The probability of resistance after recovery by Internet users is set to 5%, based on the number of repeated alternations of true and false information in the event. The aforementioned configuration is employed to simulate the trend of public opinion dissemination in the second stage, as illustrated in Figure 7. The results demonstrate that as the intensity of public opinion diminishes and official media outlets intervene, the propagation of public opinion gradually decelerates, ultimately leading to a gradual return to a relatively calm state.

4.4 Sensitivity analysis

In order to enhance the reliability of the model, this paper conducts a sensitivity analysis by modifying the initial propagation

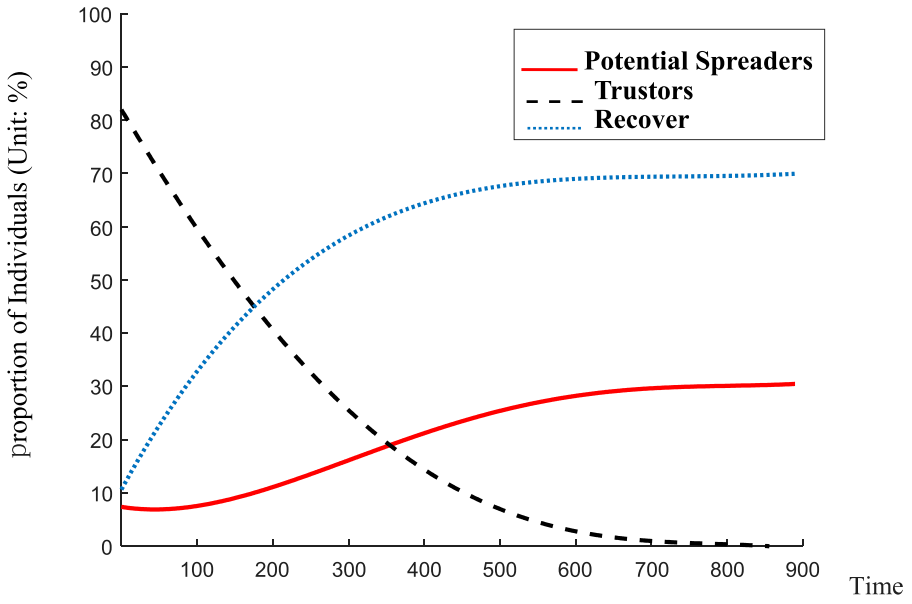

FIGURE 7
Simulation diagram of public opinion spread in the second stage.

rate, the recovery rate, the decay function and the resistance rate of public opinion information.

4.4.1 Effects of initial propagation rate and recovery rate on opinion spreading

When the initial propagation rate in the second stage is reduced to 2.5% while maintaining the initial value of the model and other parameters, it can be observed that the number of opinion information trusters converges to zero at a faster rate. Similarly, an increase in the initial recovery rate to 1.5% while maintaining the remaining parameters constant can facilitate a more rapid decline in the number of opinion information trusters. Furthermore, sensitivity tests with different initial values demonstrate that the speed of convergence of public opinion trustees increases in a sequential manner when the initial propagation rate of the second stage is set to 2%, 1.5%, and 1%, and the initial recovery rate is set to 2%, 2.5%, and 3.5%, respectively. Figure 8 illustrates that by reducing the number of pivotal nodes in the initial stages of public opinion formation and improving the overall quality of public opinion participants, it is possible to exert greater control over the direction of public opinion. This allows for adjustments to be made to the initial dissemination rate and recovery rate in subsequent stages.

4.4.2 Influence of decay rate on public opinion propagation

In order to investigate the impact of the decay rate on public opinion propagation, the initial value of the model and other parameters were maintained while the exponential decay function was adjusted to accelerate the decay rate in the second stage. The resulting propagation paths are illustrated in Figure 9, which depicts the effect of increasing the decay speed by a factor of 1 and a factor of 2, respectively. The findings indicate that the rate of convergence of the microblog opinion trustees towards zero is markedly accelerated with an increase in the decay speed of the propagation rate. Consequently, the public opinion management department may further expedite the cooling-off period for public opinion through policy measures such as enhanced supervision and the implementation of a punitive mechanism, thereby achieving more efficacious public opinion management.

4.4.3 Impact of information resistance on public opinion dissemination

In order to reduce the rate of secondary infection of public opinion by restorers, the second-stage public opinion information resistance is set at 10% while maintaining the initial value of the model and other parameters. A review of the collected data indicates an increase in the prevalence of popular comments such as “think with the available information” and “stay on the sidelines without direct evidence.” This indicates that microbloggers have become more circumspect in their engagement with public opinion, particularly in light of the repeated instances of factual manipulation. This is evidenced by the observed increase in the capacity to resist public opinion information. Figure 10 illustrates the communication path subsequent to the augmentation of information resistance.

As information resistance increases, the number of individuals who trust microblog opinion information decreases rapidly, and the speed at which public opinion stabilises significantly accelerates. It is therefore imperative that effective governance of the second stage of microblog opinion dissemination be established. The ability of microblog users to screen information and their level of resistance to public opinion are the key factors influencing the control and pacification speed of microblog public opinion in this stage.

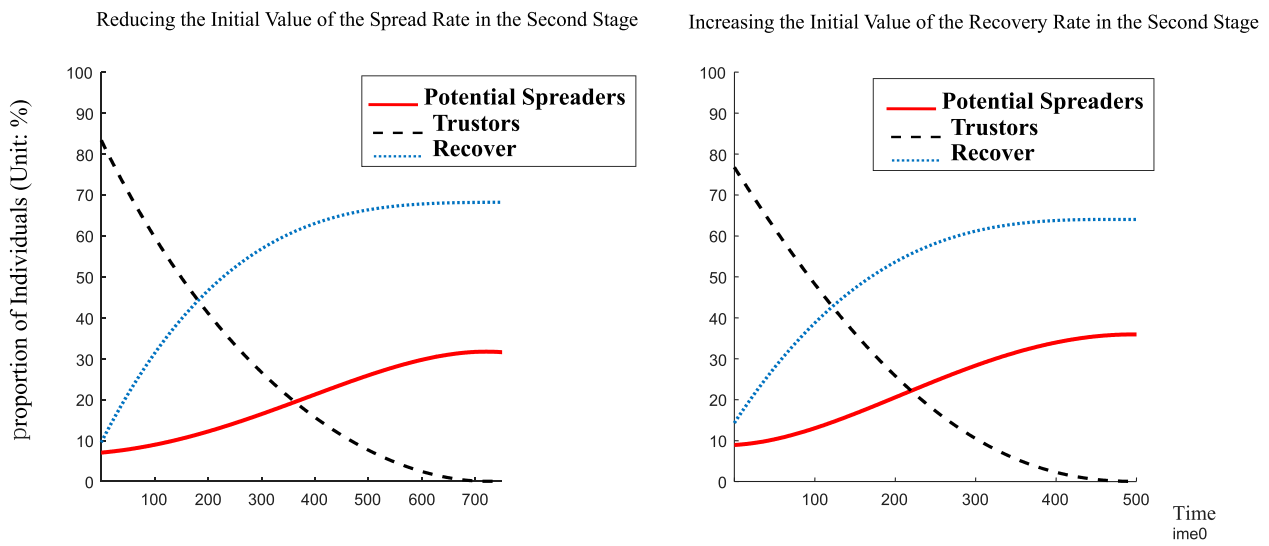

FIGURE 8
Comparison of the effects of initial spread rate and recovery rate on public opinion spread.

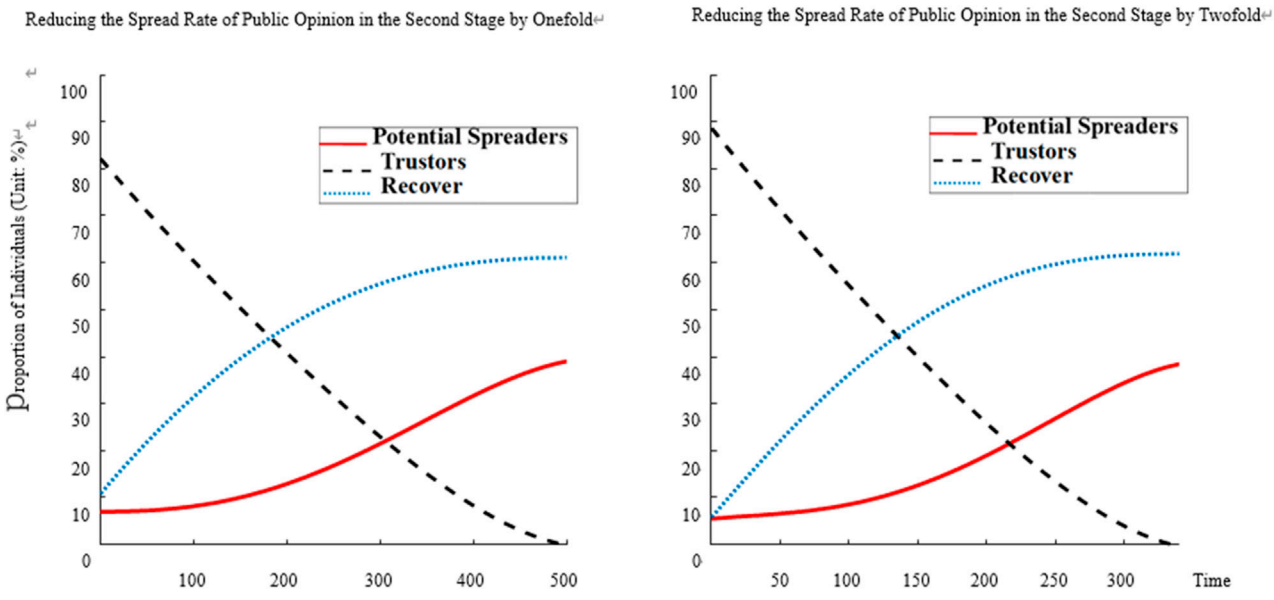

FIGURE 9
Comparison of the effects of decrease rate of spread rate on public opinion spread.

5 Conclusion and recommendations

5.1 Conclusion

This study identifies several key aspects of public opinion communication. Firstly, key information nodes exert a significant influence on the dissemination of public opinion, due to their high dissemination rate and low recovery rate. As a result, they are of critical importance in the rapid spread of public opinion. It is of the utmost importance to regulate these nodes in order to prevent the escalation of public opinion. Secondly, while ordinary information nodes propagate at a slower rate, they demonstrate robust spontaneous recovery, thereby playing a pivotal role in the natural suppression of public opinion. Furthermore, public opinion propagation is a dynamic process, with mechanisms that reduce dissemination and enhance recovery contributing to the gradual calming of public opinion, particularly following official intervention. This serves to validate the model's reliability and applicability. Ultimately, the simulation analysis indicates that the most effective government intervention occurs during the initial and peak stages of public opinion. It is imperative that prompt responses, information clarification and strengthened guidance are provided at these stages in order to effectively control the spread and impact of public opinion.

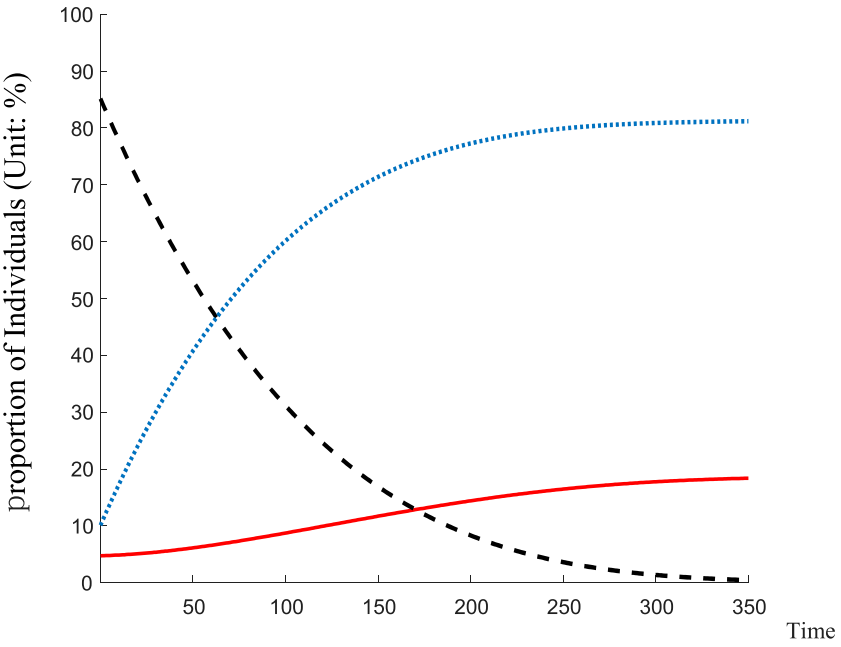

FIGURE 10
Increasing the resistance probability in the second stage.

5.2 Recommendations

Establish a dedicated public opinion monitoring system to track and analyze key information nodes in real time. This system should incorporate data mining and sentiment analysis to promptly identify content that may trigger widespread public opinion. Develop and refine an emergency response mechanism with contingency plans to assess and manage risks associated with these nodes. Rapidly deploy specialized teams to handle sudden public opinion events. Strengthen regulations and enforcement by introducing strict laws and penalties for the spread of false information related to these nodes and increase platform oversight to prevent the dissemination of malicious content.

Adopt adaptive policy measures to manage public opinion at different stages. In the initial phase, implement a comprehensive monitoring system to address and clarify false information swiftly to prevent escalation. Develop emergency response plans for timely risk assessment and management. During peak periods, enhance public opinion guidance with positive messaging to control discourse and reduce negative information spread. Monitor key nodes closely to prevent malicious content dissemination and enforce regulations on false information. In the decline phase, focus on stabilizing public sentiment and addressing residual issues through continuous updates and communication to restore social trust.

Optimize official information release strategies to ensure timely and transparent communication, thus preventing escalation due to delays. Establish a dedicated platform for regular updates and information dissemination to build public trust. Create channels for gathering public feedback on public opinion management to refine measures and encourage engagement. Collaborate with media outlets and social platforms to leverage their influence for positive guidance and to minimize negative information spread.

Integrate information literacy courses into educational curriculums to develop critical thinking and evaluation skills. Promote the development and dissemination of tools for verifying information authenticity in collaboration with technology companies. Increase public awareness through multi-channel campaigns, utilizing both social and traditional media, to educate the public on identifying and addressing false information.

Inhance research and data analysis to improve understanding and prediction of public opinion events. Support research institutions and universities in related studies and promote the development of public opinion analysis technologies. Integrate artificial intelligence and big data technologies to optimize monitoring and analysis processes, thereby improving the accuracy of trend predictions and supporting decision-making. Implementing these measures will help develop comprehensive and scientific strategies for effectively managing and controlling public opinion events.

Data availability statement

The original contributions presented in the study are included in the article/supplementary material, further inquiries can be directed to the corresponding author.

Author contributions

LR: Data curation, Funding acquisition, Writing–original draft, Writing–review and editing, Conceptualization. JZ: Formal

Analysis, Investigation, Project administration, Writing–original draft. ZS: Methodology, Software, Visualization, Writing–review and editing. FL: Resources, Validation, Writing–review and editing. DX: Conceptualization, Supervision, Writing–original draft, Writing–review and editing.

Funding

The author(s) declare that financial support was received for the research, authorship, and/or publication of this article. The authors acknowledge the financial support from the Humanities and Social Science Fund of Ministry of Education of China (Grant number 19YJC630136).

Conflict of interest

The authors declare that the research was conducted in the absence of any commercial or financial relationships that could be construed as a potential conflict of interest.

Publisher's note

References

1. Tsao S-F, Chen H, Tisseverasinghe T, Yang Y, Li L, Butt ZA. What social media told us in the time of COVID-19: a scoping review. *The Lancet Digital Health* (2021) 3(3): e175–94. doi:10.1016/s2589-7500(20)30315-0

2. Liu ZR. The exploration of government's management in public opinion crisis under the new media era. *Gansu Theor Res* (2009)(05) 32–5.

3. Budd J, Miller BS, Manning EM, Lampos V, Zhuang M, Edelstein M, et al. Digital technologies in the public-health response to COVID-19. *Nat Med* (2020) 26(8): 1183–92. doi:10.1038/s41591-020-1011-4

4. Cinelli M, Quattrociocchi W, Galeazzi A, Valensise CM, Brugnoli E, Schmidt AL, et al. The COVID-19 social media infodemic. *Scientific Rep* (2020) 10(1):16598–10. doi:10.1038/s41598-020-73510-5

5. Akerlof GA. The market for "lemons": quality uncertainty and the market mechanism. In: *Uncertainty in economics*. Elsevier (1978). p. 235–51.

6. Harris M, Raviv A. Control of corporate decisions: shareholders vs. management. *The Rev Financial Stud* (2010) 23(11):4115–47. doi:10.1093/rfs/hhq081

7. Spence M. Job market signaling. In: *Uncertainty in economics*. Amsterdam, Netherlands: Elsevier (1978). p. 281–306.

8. Bikhchandani S, Hirshleifer D, Welch I. A theory of fads, fashion, custom, and cultural change as informational cascades. *J Polit Economy* (1992) 100(5):992–1026. doi:10.1086/261849

9. Yin F, Xia X, Song N, Zhu L, Wu J. Quantify the role of superspreaders-opinion leaders-on COVID-19 information propagation in the Chinese Sina-microblog. *PloS one* (2020) 15(6):e0234023. doi:10.1371/journal.pone.0234023

10. Hatfield E, Cacioppo JT, Rapson RL. Emotional contagion. *Curr Dir Psychol Sci* (1993) 2(3):96–100. doi:10.1111/1467-8721.ep10770953

11. Böhme R, Moore T. The "iterated weakest link" model of adaptive security investment. *J Inf Security* (2016) 7(02):81–102. doi:10.4236/jis.2016.72006

12. Daradkeh M, Gawanmeh A, Mansoor W. Information adoption patterns and online knowledge payment behavior: the moderating role of product type. *Information* (2022) 13(9):414. doi:10.3390/info13090414

13. Citroen CL. The role of information in strategic decision-making. *Int J Inf Manag* (2011) 31(6):493–501. doi:10.1016/j.ijinfomgt.2011.02.005

14. Wang XQ, Wu QQ. Characteristics, influence and guiding strategies of online public opinion in major epidemics in the era of all-media. *Ideological and Theor Education* (2020)(03) 102–6. doi:10.13556/j.cnki.dncb.cn35-1274/j.2018.10.027

15. Kou Y, Gui X, Chen Y, Pine K. Conspiracy talk on social media: collective sensemaking during a public health crisis. *Proc ACM Human-Computer Interaction* (2017) 1(CSCW):1–21. doi:10.1145/3134696

16. Zhao Y, Zhu S, Wan Q, Li T, Zou C, Wang H, et al. Understanding how and by whom COVID-19 misinformation is spread on social media: coding and network analyses. *J Med Internet Res* (2022) 24(6):e37623. doi:10.2196/37623

17. Himelein-Wachowiak M, Giorgi S, Devoto A, Rahman M, Ungar L, Schwartz HA, et al. Bots and misinformation spread on social media: implications for COVID-19. *J Med Internet Res* (2021) 23(5):e26933. doi:10.2196/26933

18. Cowie J, Lehnert W. Information extraction. *Commun ACM* (1996) 39(1):80–91. doi:10.1145/234173.234209

19. Papacharissi Z, de Fatima Oliveira M. Affective news and networked publics: the rhythms of news storytelling on# Egypt. *J Commun* (2012) 62(2):266–82. doi:10.1111/j.1460-2466.2012.01630.x

20. Tufekci Z, Wilson C. Social media and the decision to participate in political protest: observations from Tahrir Square. *J Commun* (2012) 62(2):363–79. doi:10.1111/j.1460-2466.2012.01629.x

21. Thelwall M. Blog searching: the first general-purpose source of retrospective public opinion in the social sciences? *Online Inf Rev* (2007) 31(3):277–289. doi:10.1108/14684520710764069

22. Wang X, Xue XR. The online public opinion crisis and government governance in emergency public events: an analysis based on the online public opinion during the Wenchuan earthquake. *Inf and Comput (Theory Edition)* (2009)(16) 78+80. doi:10.16381/j.cnki.issn1003-207x.2020.03.006

23. Khan Y, Fazli G, Henry B, de Villa E, Tsamis C, Grant M, et al. The evidence base of primary research in public health emergency preparedness: a scoping review and stakeholder consultation. *BMC Public Health* (2015) 15:432–13. doi:10.1186/s12889-015-1750-1

24. Tian YL, Li X. An analysis of the evolution path of online public opinion on COVID-19 based on event-logic graph. *Inf Stud Theor and Appl* (2021) 44(03):76–83. doi:10.1016/j.pubrev.2019.101869

25. Zhang SL, Wang LC, Lou GZ (2021). Research on the public opinion analysis system based on knowledge graph. *J Mod Inf*, 41(04), 10–6. doi:10.2307/3319808

26. Xu Y, Huang T, Zuo Z, Wang X. Social media sentiment and COVID-19 transmission: results from a time-varying SIR model. PACIS (2021).

27. Rogers EM, Singhal A, Quinlan MM. Diffusion of innovations. In: *An integrated approach to communication theory and research*. Routledge (2014). p. 432–48.

28. Fink S, Association AM. *Crisis management: planning for the inevitable*. Amacom (1986).

29. Han SQ. The life cycle study of hot events in online public opinion. *Southeast Commun* (2018)(10) 88–90. doi:10.1016/S2589-7500(20)30315-0

30. Wang X, Oxholm G, Zhang D, Wang Y-F. Multimodal transfer: a hierarchical deep convolutional neural network for fast artistic style transfer. In: *Proceedings of the IEEE conference on computer vision and pattern recognition* (2017).

31. Anstead N, O'Loughlin B. Social media analysis and public opinion: the 2010 UK general election. *J computer-mediated Commun* (2015) 20(2):204–20. doi:10.1109/CVPR.2017.759

32. Rim H, Lee Y, Yoo S. Polarized public opinion responding to corporate social advocacy: social network analysis of boycotters and advocators. *Public relations Rev* (2020) 46(2):101869. doi:10.1016/j.pubrev.2019.101869

33. Wang Y-M, Guo T-Y, Li W-D, Chen B. Direct immune-SCIR public-opinion propagation model based on real-time online users. *Chin Phys B* (2020) 29(10):100204. doi:10.1088/1674-1056/aba9c0

34. Dahou A, Xiong S, Zhou J, Haddoud MH, Duan P. Word embeddings and convolutional neural network for Arabic sentiment classification. In: Proceedings of coling 2016, the 26th international conference on computational linguistics (2016) Technical papers.

35. Yuan J, Shi J, Wang J, Liu W. Modelling network public opinion polarization based on SIR model considering dynamic network structure. *Alexandria Eng J* (2022) 61(6):4557–71. doi:10.1016/j.aej.2021.10.014

36. Zhao JH, Wan KW. Research on the dynamics of public opinion dissemination in social networks based on the information propagation model - SIR infectious disease model. *Inf Sci* (2017) 35(12):34–8.

37. Jacomy M, Venturini T, Heymann S, Bastian M. ForceAtlas2, a continuous graph layout algorithm for handy network visualization designed for the Gephi software. *PloS one* (2014) 9(6):e98679. doi:10.1371/journal.pone.0098679

38. Ma N, Liu YJ. A staged modeling analysis of the communication influence of opinion leaders. *Chin J Manage Sci* (2020) 28(03):52–8. doi:10.1016/j.aej.2021.10.014

39. Wang XW, Xing YF, Zhang L, Li SM. Research on the development trends of online public opinion at home and abroad in the context of social media. *Inf and Comput* (2017) 38(04):6–14. doi:10.3969/j.issn.1008-0821.2021.04.002

40. Anderson LR, Holt CA. Information cascades in the laboratory. *The Am Econ Rev* (1997) 847–62. doi:10.2196/37623

41. Daley DJ, Kendall DG. Epidemics and rumours. *Nature* (1964) 204(4963):1118. doi:10.1038/2041118a0

42. Li M, Cao H (2020). Research on the mechanisms of online public opinion emergence in the context of information ecology: A qualitative comparative analysis based on 40 emergency events. *J. Infor. Sci.* 38(3):154–159. doi:10.13833/j.issn.1007-7634.2020.03.024

frontiers | Frontiers in Physics

TYPE Original Research
PUBLISHED 02 October 2024
DOI 10.3389/fphy.2024.1457287

OPEN ACCESS

EDITED BY
Shirui Pan,
Griffith University, Australia

REVIEWED BY
Fujun Lai,
Yunnan University of Finance and Economics, China
Manman Yuan,
Inner Mongolia University, China

*CORRESPONDENCE
Xiao Jian,
janxtian4@163.com

RECEIVED 30 June 2024
ACCEPTED 03 September 2024
PUBLISHED 02 October 2024

CITATION
Zhang L, Jian X and Ma Y (2024) Analysis of differences in fossil fuel consumption in the world based on the fractal time series and complex network.
Front. Phys. 12:1457287.
doi: 10.3389/fphy.2024.1457287

Analysis of differences in fossil fuel consumption in the world based on the fractal time series and complex network

Lin Zhang[1], Xiao Jian[2]* and Yuxuan Ma[3]

[1]School of Law, Shandong Normal University, Jinan, China, [2]School of Law, Zhongnan University of Economics and Law, Wuhan, China, [3]Department of Economics, Cornell University, Ithaca, NY, United States

Fossil fuels remain indispensable energy resources despite their non-renewable nature. Understanding the patterns of global fossil fuel consumption is essential for energy security and policy-making. This study employs complex network theory and fractal time series analysis to explore the underlying dynamics and patterns of fossil fuel consumption globally, with a focus on coal, oil, and gas consumption.The study applies the Hurst index to raw fossil fuel consumption data to identify fractal characteristics. Additionally, the visibility graph method is used to convert time series data into complex networks, allowing further analysis of consumption patterns. The study examines fossil fuel consumption in 38 countries to assess global trends and differences. The analysis reveals that global fossil fuel consumption follows a fractal time series pattern, with Hurst index values exceeding 0.9, indicating long-term memory characteristics. The application of the visibility graph method demonstrates variations in the Hurst index of degree distribution, enabling the differentiation of consumption patterns across regions. The method also uncovers distinct features of coal, oil, and gas consumption when viewed from a network perspective. The findings suggest that fossil fuel consumption has predictable long-term patterns, which are crucial for assessing future energy demands. The study highlights the importance of legislative measures to safeguard fossil fuel resources, especially for countries like China, where energy security and international competitiveness are paramount. Understanding these consumption patterns could guide future energy policies aimed at managing non-renewable resources more effectively.

KEYWORDS

fossil fuel, complex network, fractal time series, hurst index, legal protection, visibility graph

1 Introduction

Fossil fuel is a type of hydrocarbon or its derivatives, and it is a critical energy resource supporting the development of the global economy [1]. Especially, in modern society, fossil energy is still the most important part of energy consumption, which accounts for more than 80% of global disposable energy consumption. Many studies have focused on fossil fuels in recent decades. In the past half-century, the consumption of fossil fuels has increased substantially, about eight times since 1950. However, the type of fuel we rely on has also changed over time, from simple coal to a combination of oil and natural gas. Today, coal consumption is declining over the world, but oil and gas are still multiplying. Friedemann a J [2].

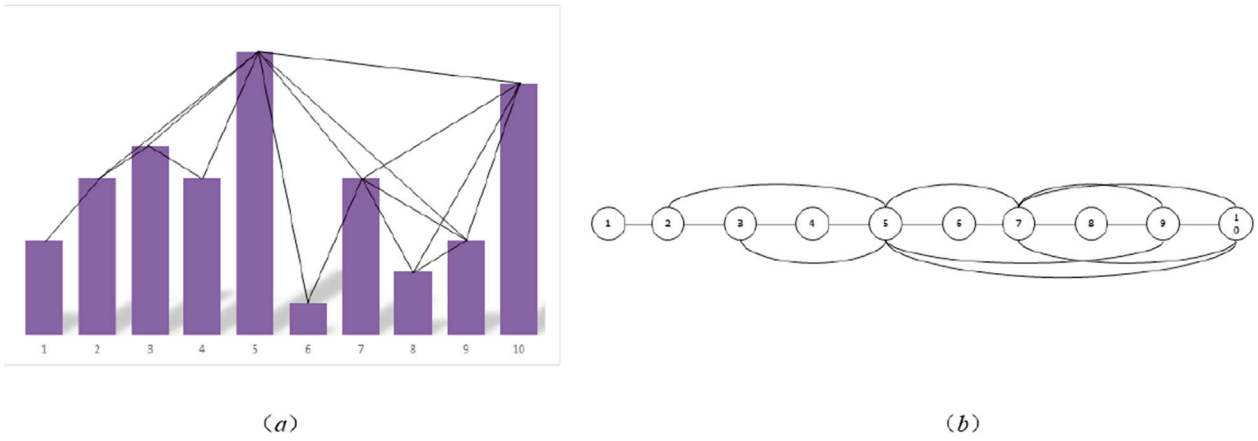

FIGURE 1
The visibility graph and its associated graph.

found that about 500 million tons of oil and its derivatives were used in the past year, indicating that fossil fuels have already become indispensable in human life.

A plethora of studies have been conducted on fossil fuels in recent decades. For example, the relationship between fossil fuel consumption and economic development has attracted much attention. Especially, COVID-19 has a significant impact on energy transportation [3], i.e., there is a strong relationship between freight and shipping routes and coronavirus cases, which affects the cost of oil transportation. By exploiting the data of fossil fuel consumption, equity price output, and exchange rates, S. L Vanessa [4] revealed the spatial relationship between COVID-19 and the national economy through the global vector autoregressive (GVAR) model. Some other studies [5–8] have also found that fossil fuel consumption directly affects economic development.

Fossil fuel consumption affects not only economic development but also environmental changes. For instance, F Martins [9] found that there is high dependence on fossil fuels in 29 European countries. SA Asongu [10] investigated fossil fuel energy consumption and other indicators of emissions from natural resources in Africa from 1980 to 2014. By applying LMDI and MRCI decomposition methods, it was found that global population growth is the most critical factor driving increased consumption of fossil products, and this varies from country to country [11]. Based on econometric models, Li [12] analyzed the relationship between carbon dioxide and China's emissions, real GDP, clean energy, fossil fuel consumption, and trade opening from 1992 to 2020.

Given that fossil fuels have a significant impact on economic development and environmental protection, it is of great significance to regulate and protect the rational extraction and utilization of fossil fuels from a legal perspective. C. Judith [13] believe that the natural gas power generation industry urgently needs legislation to promote and protect it. G. Fang [14] discussed the legal regulations on the safety of offshore oil and gas exploration and development operations in the European Union, and based on this, proposed legislative implications of the relevant legal regulation of the EU for the safety rules of offshore oil and gas operations in China. PA Valeryevna [15] advocated that in order to promote the construction of ecological civilization, it is necessary to provide legal guarantees for the rational use of resources. In addition, in combating fossil fuel crimes, practice has proven that the role of relevant special actions is phased. It is important to establish the legal relationship of fossil fuel mining rights and the mining order through law, and establish a sound long-term mechanism for security prevention.

Fractal time series is a type of time series of Brownian motion. Fractal Brownian motion is statistically self-similar and has long-term memory, i.e., a memory effect makes the changing trend in the future the same as that at present. The Hurst index can characterize this long-term correlation. N. Dimitrios [16] analyzed the time series of PM10 in Athens, and it was found that PM10 in Athens had chaotic and long-term memory. C. Oscar [17] introduced a hybrid intelligent method that combines fractal theory and fuzzy logic to predict the COVID-19 time series.

As the field of network science develops, its areas of application are becoming increasingly broad [18–23]. The visibility graph model has been used in many fields, including economy, finance, environment, climate, medicine, psychology, etc. Thomas [24] applied the visibility graph to analyze the time series of PM10. Based on the deep learning and the visibility graph, X. Zhang [25] analyzed the time series of sleep and obtained different classes of sleep states. Additionally, many studies exploited visibility models to analyze brain wave data [26–29]. Other studies also applied the visibility graph to the environment and economic field [30–33]. J. Hu [34] and X. fan [35] employed this model to analyze the U.S. electricity market and China's carbon trading market, respectively.

By leveraging the visibility graph, we provide a novel analytical framework that enhances the ability to detect, interpret, and predict complex dynamics in fossil fuel consumption. This has significant implications for network analysis, ultimately contributing to the advancement of knowledge and technology in this area. This paper mainly analyzes the internal characteristics of fossil fuel consumption, excavates much information on fossil fuel consumption, and provides a research basis for investigating the relationship between fossil fuel consumption and the economic environment in the future. Compared with previous research on fossil fuel consumption, this study has three obvious advantages: 1) Mapping time series to the complex network to find more hidden information of the series data, which helps to better understand the characteristics of this sequence; 2) the characteristics of the time series is represented by the fractal characteristics. However, when

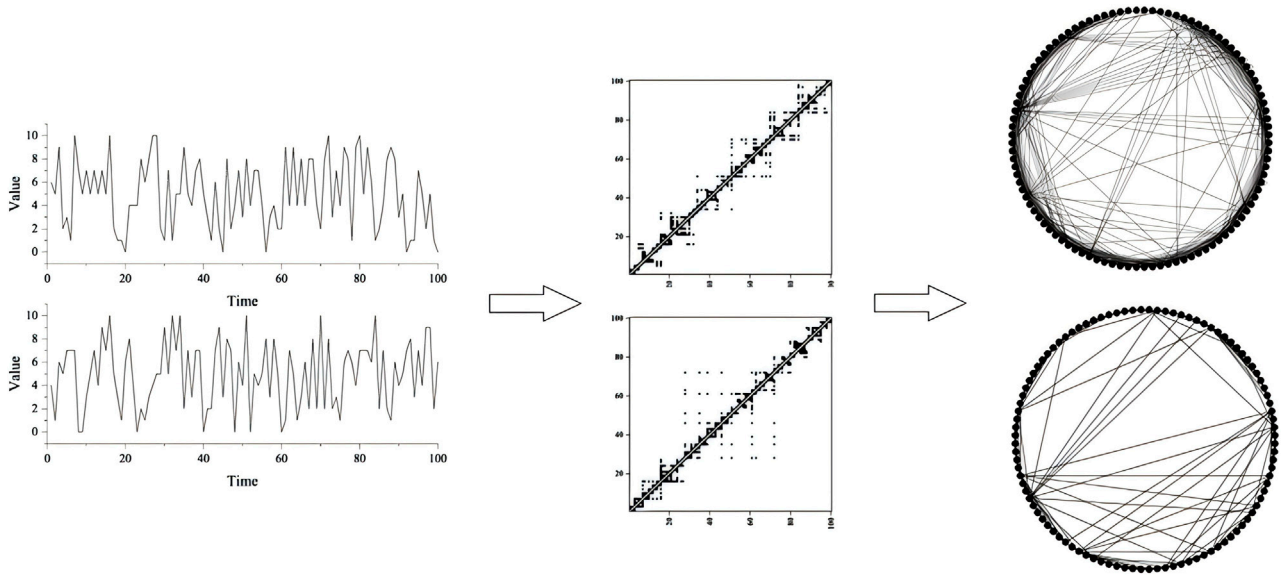

FIGURE 2
The flow chart of fossil fuel computation.

the time series are positively correlated, by mapping the time series data into a network and analyzing it through the Hurst index of the degree distribution of the network, it can be determined whether the impact of the time nodes on the future is random; 3) Complex network theory has high calculation efficiency and is suitable for big data applications. When applied to time series, complex networks can provide direct results compared with multi-fractal formalism.

The rest of this paper is organized as follows: Section 2 introduces the model that maps time series to a complex network, the complex network theory, and the data description of fossil fuel consumption based on the fractal time series theory. Then, in Section 3, the topography measles and the Hurst index of fossil fuel consumption are analyzed. Finally, the results and conclusion are presented in Section 4.

2 Model and data

2.1 Visibility graph

In this paper, the visibility graph method of time series proposed by Lacasa et al. [36] was utilized to construct the complex network for characterization. First, the discrete time series data $x(t)$ was mapped into one node in the network, and then the link between the nodes was built according to the visibility rule: any two points (t_a, x_a) and (t_c, x_c) within the series data will have the visibility if any other data (t_b, x_b) interpolating between them satisfies the following condition (Equation 1):

$$x_b < x_a + (x_c - x_a)\frac{t_b - t_a}{t_c - t_a} \tag{1}$$

That is, these two points (t_a, x_a) and (t_c, x_c) can be connected by a link in the resulting network. In Figure 1, the height of each vertical bar in the histogram of panel (a) denotes the data for each time series, and each bar represents one node in the corresponding graph in panel (b). Thus, two nodes in panel (b) will be connected, and a link should be added between them if the top indicated by the 2 bars can be seen in panel (a).

Figure 1 shows how to link the data. If one data bar (e.g., the fifth bar) is the highest, there are 3 bars between the fifth and the first bar, and these 2 bars are sheltering from the third bar. In this case, there is no edge linking nodes 1 and 5; Meanwhile, there are 4 bars between the fifth and 10th bars, but there is no bar to occlusion these 2 bars, so there is an edge to link them.

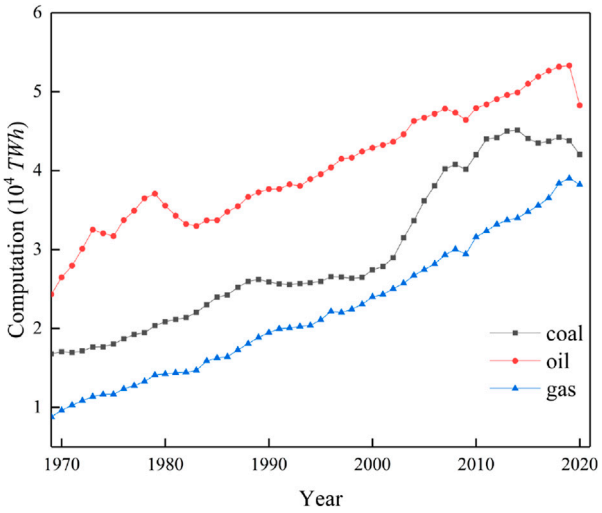

FIGURE 3
The line chart of global fossil fuel consumption.

2.2 The topological characteristics of visbility graph

2.2.1 Degree

In a graph structure, the number of edges connected to a node is the degree of the node, and the degree distribution of each node in the graph is the degree distribution [37].

2.2.2 Average path length

The average path length [38] of a visibility graph is to form one time node to time node will take an average of L time nodes. The definition of average short path length is given in Equation 2.

$$L = \frac{1}{N(N-1)} \sum_{i \in V} \sum_{i \neq j \in V} d_{ij}, \tag{2}$$

where N is the total number of nodes for this visibility graph, d_{ij} is the shortest path between the time nodes i and j.

2.2.3 Cluster coefficient

The cluster coefficient is given by Newman [39]. Intuitively, if we have two friends, they may be friends with each other. Similarly, for the visibility graph, if time nodes i and j have edges with time node k, time node i establishes a connection with j, thus the definition of cluster coefficient (Equation 3) is given below:

$$C_i = \frac{E_i}{C_{k_i}^2} \tag{3}$$

if E_i denotes the edges between the neighbors of time node i, and all the neighbors of time node i have edges, then the total number of edges is $C_{k_i}^2$.

For a visibility graph, the average cluster coefficient is the average of all time-node cluster coefficients. As shown in the Equation 4

$$C = \frac{1}{N} \sum_{i=1}^{N} C_i, \tag{4}$$

where N is the number of time nodes in this visibility graph.

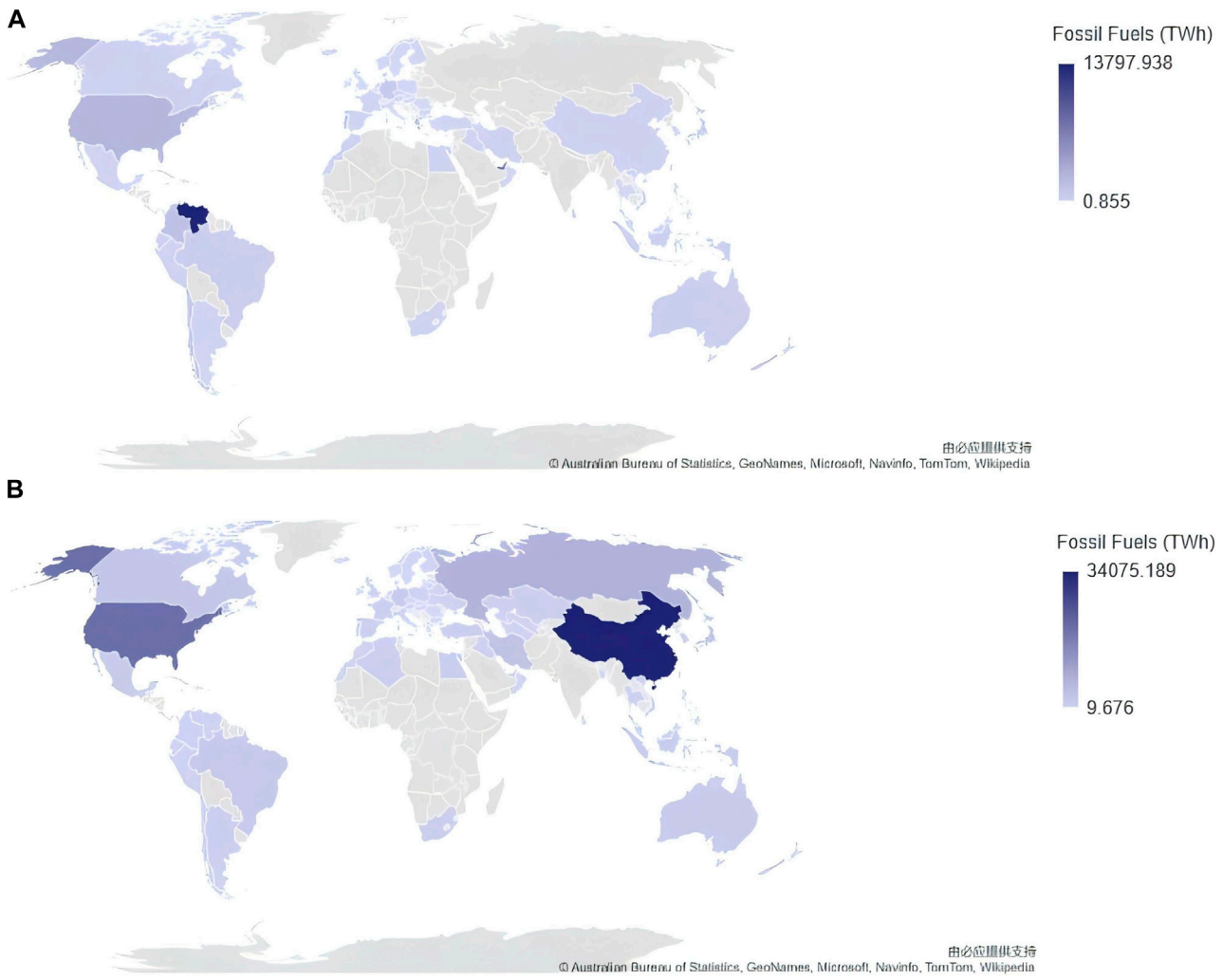

FIGURE 4
The map of global fossil fuel consumption in 1965 and 2020.

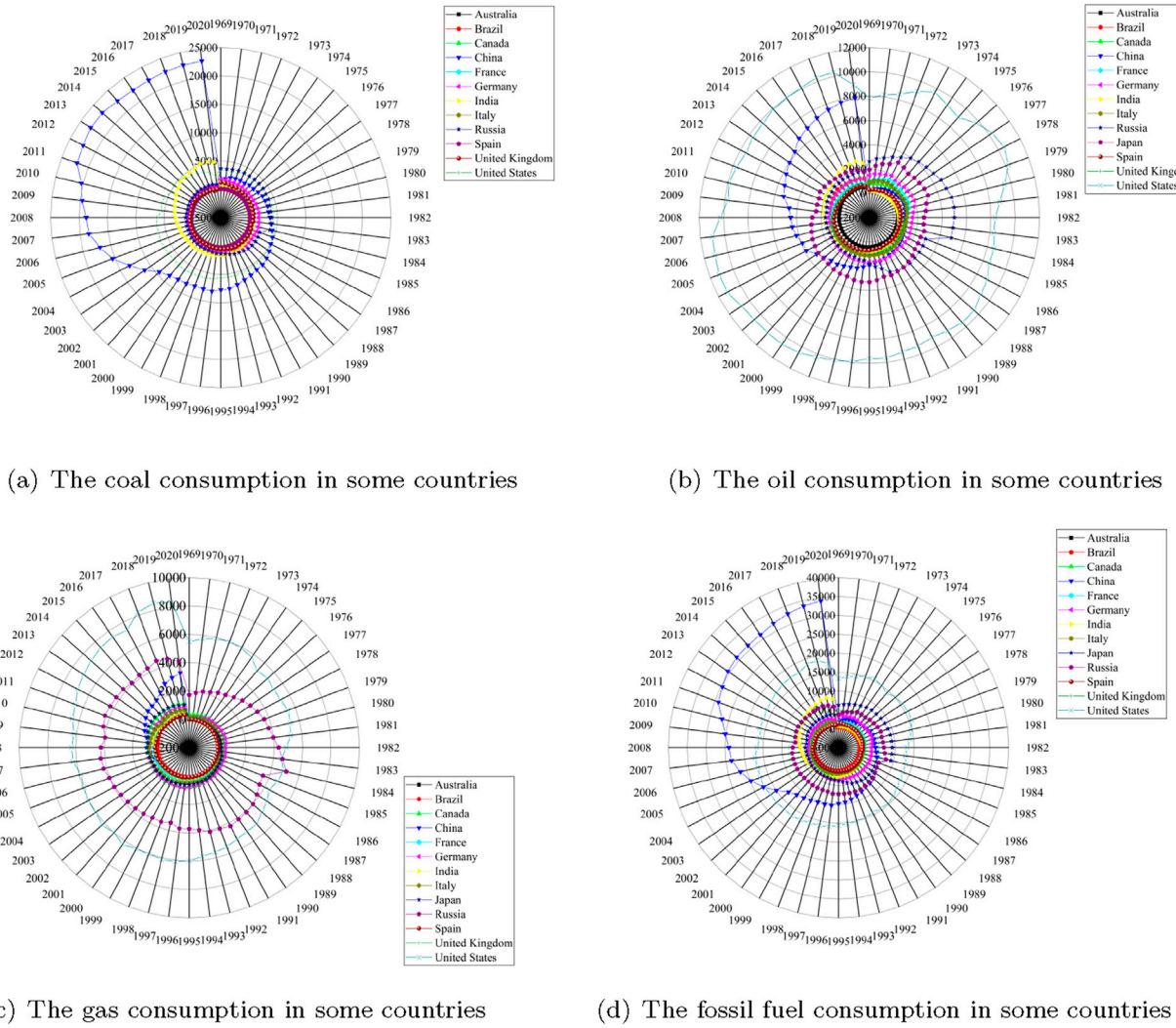

FIGURE 5
The coal, oil, gas, and fossil fuel consumption from 1965 to 2020 in some countries.

2.3 Fractal time series

For a time series $T = \{t_1, t_2, \ldots, t_n\}$, if T has fractal characteristics, then T has fractal characteristics of long correlation and self-similarity. The Hurst index can determine whether T is fractal time series.

The Hurst index can reflect the auto-correlation of time series, especially the hidden long-term trend, which is called the long-term memory in statistics. Many computational approaches can be adopted for the Hurst index, and this paper used R/S for calculation. For a time-node degree series $x = \{x_1, \ldots, x_i\}$:

(1) Let $e_n(m)$ be the average error of n time-node degrees. As shown in the Equation 5

$$e_n(m) = \sum_{i}^{n} (x_i - \bar{x}); \tag{5}$$

where, $\bar{x}$ is the average degree, $1 \le m \le M$, and M is the length of this series.

(2) $R(n)$ as shown in the Equation 6 can be obtained according to the difference between the maximum and minimum error of the time-node degree,

$$R_n(m) = \max_{1 \le n \le m} e_n(m) - \min_{1 \le n \le m} e_n(m); \tag{6}$$

(3) Based on the standard deviation $S(m)$, the ange analysis can be realized

$$\frac{R(m)}{S(n)} = \frac{\max_{1 \le n \le m} e_n(m) - \min_{1 \le n \le m} e_n(m)}{\sqrt{\frac{1}{m}\sum_{n=1}^{m} (x_n - \bar{x})^2}}; \tag{7}$$

(4) Through the exponential relationship between Equation 7 and the first m data nodes,

$$\frac{R(m)}{S(n)} = a \times m^H; \tag{8}$$

the following results can be obtained. As shown in the Equation 9:

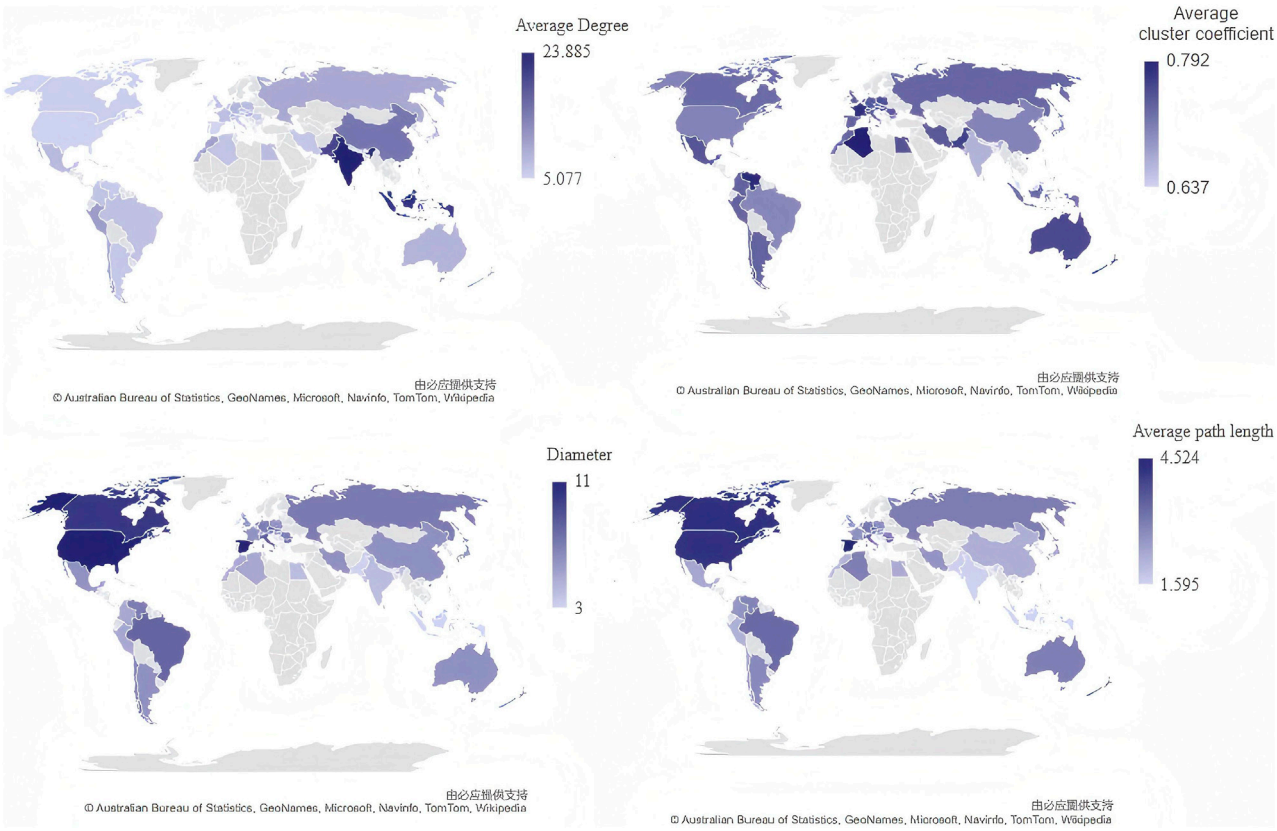

FIGURE 6
The characteristic of the visibility graph of coal consumption.

$$H(m) = \log_m \frac{R(m)}{aS(n)}, \quad m = 1, 2, \ldots, M. \tag{9}$$

where, H is the Hurst index, a is the coefficient, and the value of H is between 0 – 1.

When $H = 0.5$, the time nodes have random degree series, which indicates that the current trends will not affect future trends; when $0.5 < H \leq 1$, the time nodes have positively correlated degree series, which indicates that the current trends will affect future trends; when $0 \leq H < 0.5$, the time nodes have negatively correlated degree series, which indicates that the current trends will affect future trends;

As illustrated in Figure 2, the time series data is mapped to an adjacency matrix by the visibility graph, with the calculated degree, cluster coefficients, diameter, and average path length of the complex network.

2.3.1 Data

Since energy consumption keeps changes, it needs to be quantified. The quotient between the use of fossil fuels (oil, coal, and gas) and the inland energy consumption is referred to as fossil energy consumption [9] (FFC), as shown in Equation 10

$$FFC = \frac{E_{coal+E_{oil}+E_{gas}}}{inlandenergyconsumption}. \tag{10}$$

where E_{coal}, E_{oil}, and E_{Gas} are the energy consumption from solid fuels, oil, and gas, respectively.

The coal, oil, and gas consumption were obtained from the Our World in Data [40]. Due to the insufficient data in some countries, this study did not involve the countries with missing data and obtained the fossil fuel consumption data of 38 countries finally. From Figure 3, it can be seen that fossil fuel (coal, oil, and gas) consumption in the world has increased gradually in the given period. However, in 2020, all fossil fuel consumption decreased significantly. Meanwhile, as global awareness of environmental protection increases, more and more countries have begun using clean energy and replacing oil with natural gases. Besides, coal consumption is always between oil consumption and natural gas consumption.

3 Analysis

3.1 Fossil fuel consumption in different countries

By comparing the total fuel consumption of various countries in 1968 and 2020 in Figure 4, it can be found that Venezuela's total fuel consumption decreased from the first in the world to almost no fossil fuel consumption, while China's total fossil fuel consumption ranked from the last in 1968 to the top in 2020. These two maps show that the consumption of fossil fuels is closely related to economic development.

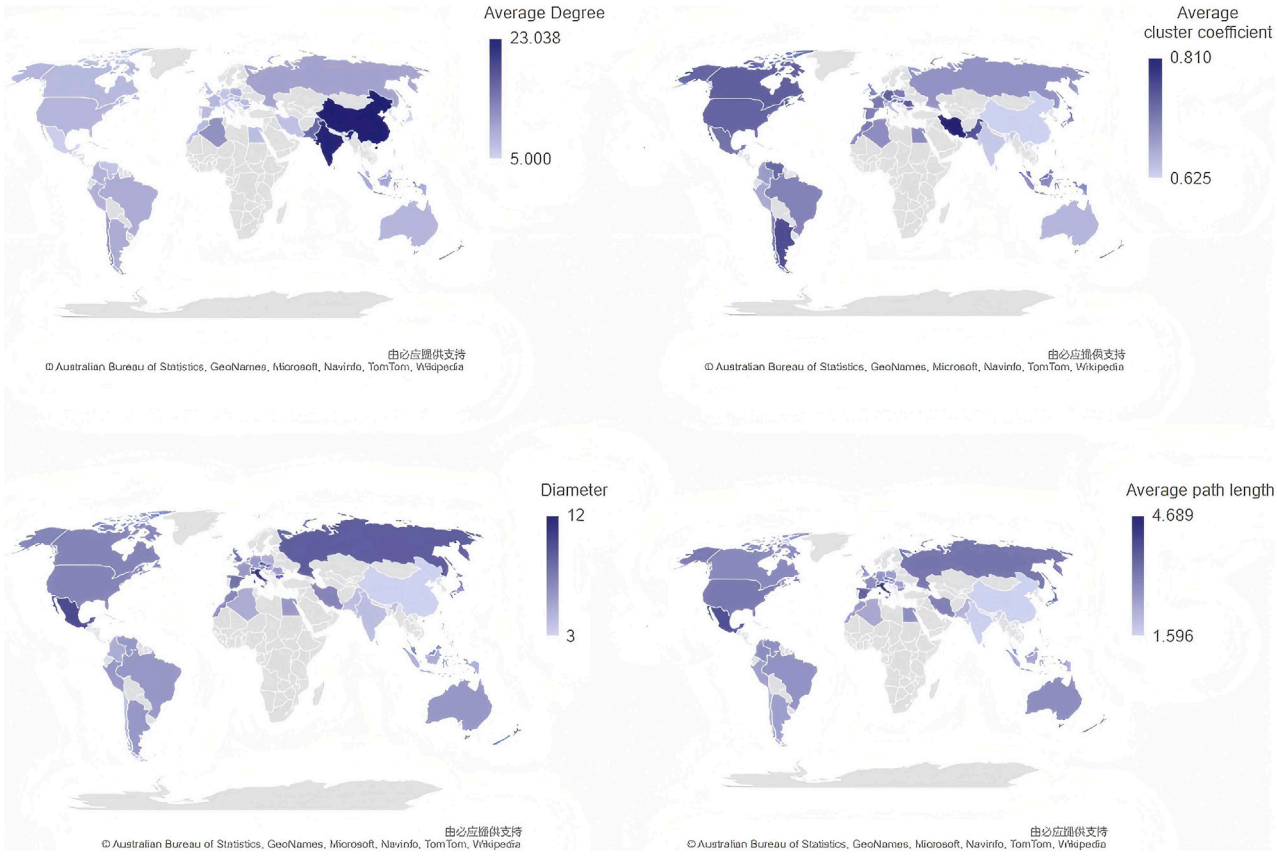

FIGURE 7
The characteristic of the visibility graph of oil consumption.

Figure 5 presents the time series of coal, oil, and gas consumption from 1986 to 2020 of 13 countries. The coal, oil, and gas consumption has increased in these 13 countries. Due to the differences in economy, policies, and resource reserves among these countries, there are significant variations in fuel consumption. Specifically, the growth of coal consumption in China is the most in the world. Since 2000, China's oil and coal consumption has increased substantially, becoming our country a major coal consumer. Meanwhile, the United States is the largest consumer of oil and gas. However, Figure 5D indicates that China has a high growth rate in energy consumption, and in 2004, China's total energy consumption exceeded the total energy consumption of the United States, which is highly related to the rapid development of China's economy.

3.2 Visibility graph of fossil fuel consumption

Network science provides a new tool for analyzing fossil fuel consumption data. The visibility network structure can be exploited to reveal the practical significance of fossil fuel consumption, and more hidden information about fossil fuel consumption can be obtained from the degree, degree distribution, cluster coefficient, average short length, and diameter of the network structure.

Through the definition of the visibility graph, it can be known that the degree is the number of other time nodes connected to one time node, and the average degree is the degree of all nodes on average. The more significant the average degree, the stronger the correlation between these data.

The average path length is the number of time nodes to pass between two time nodes to establish a connection. The average path length is the average number of time nodes to pass between two nodes to establish a connection. The diameter is the longest path among all the shortest paths, indicating the number of time nodes to pass to establish an edge connection with the weakest correlation between these two time nodes. A large average path length indicates a strong correlation between these data.

The clustering coefficient describes the relationship between two nodes with familiar neighbors, which reflects the relationship between two time nodes connected to the same time node. A larger clustering coefficient indicates a stronger attraction of one node to other nodes.

Figure 6 shows the visibility graph of coal consumption. These four maps present the average degree, average cluster coefficient, diameter, and average path length of coal consumption in the 38 countries, respectively. It can be found that India, Indonesia, Malaysia, and Pakistan are the top four countries in terms of average degree (all exceed 20). Meanwhile, the average path length in these four countries is less than 2, indicating that the correlation between

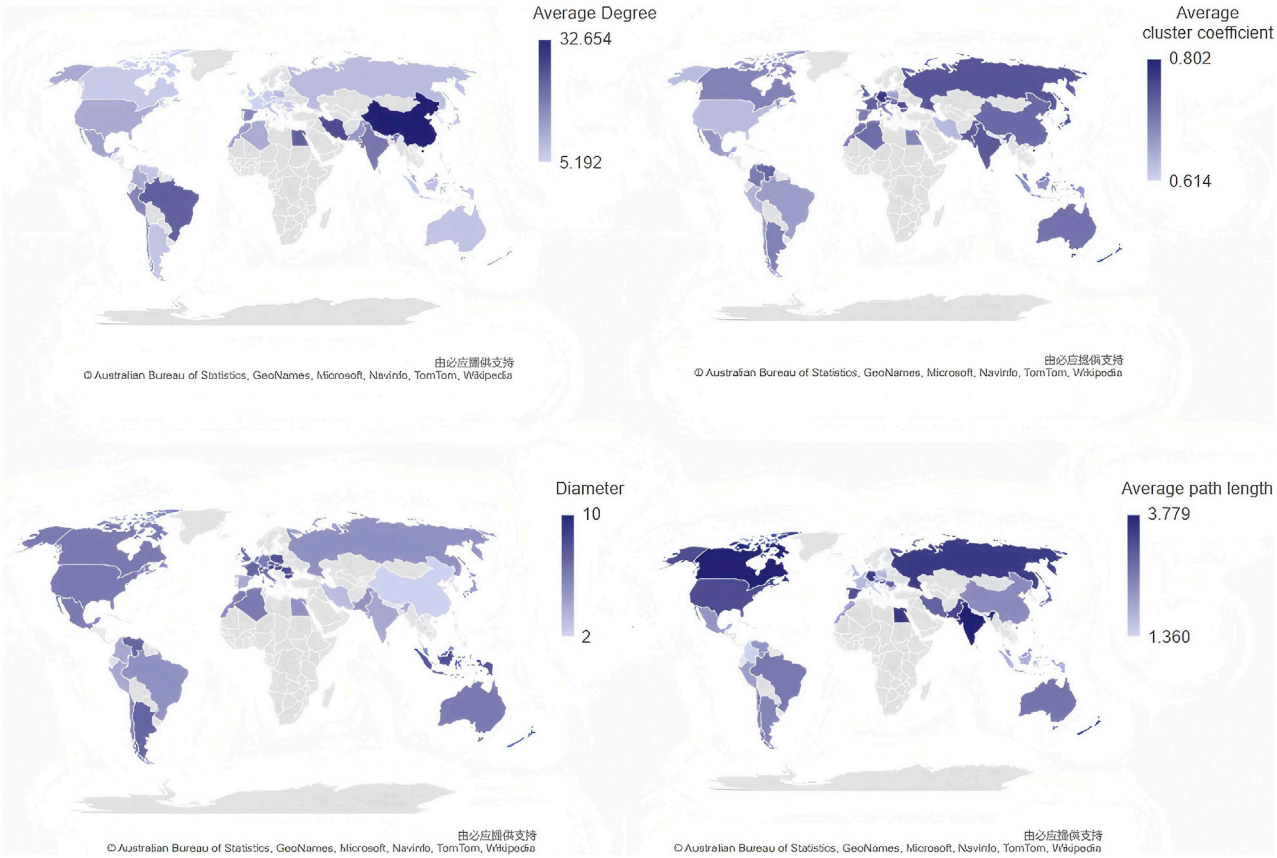

FIGURE 8
The characteristic of the visibility graph of gas consumption.

the coal consumption data of these four countries is the strongest. Besides, these five countries, including Algeria, Venezuela, France, Pakistan, and Australia, are the top five countries in terms of cluster coefficient, which indicates that these five countries are closely related to their neighboring nodes in coal consumption.

Figure 7 presents the visibility graph of oil consumption. Similar to Figure 6, this figure depicts the average degree, average cluster coefficient, diameter, and average path length of oil consumption in the 38 countries, respectively. It can be seen from these maps that the average degree of China and India is over 20. Italy, Czechia, Slovakia, and Mexico are the top four countries in terms of diameter (all exceed 10). Besides, Iran, Taiwan (China), Argentina, Romania, and Pakistan are the top four countries in terms of average cluster coefficient (all exceeds 0.75), and the average cluster coefficient of Iran is over 0.8, indicating that Iran is more strongly correlated with its neighbors in oil consumption. Moreover, Italy, Mexico, Spain, and Czechia are the top four countries in terms of the average path length of oil consumption (all exceed 3.5).

Figure 8 depicts the visibility graph of natural gas consumption in terms of average degree, average cluster coefficients, diameter, and average path length. It can be seen that China, Iran, Egypt, and Brazil are the top four countries in terms of average degree (all exceed 20). Meanwhile, these four countries have the smallest average path length, indicating that the correlation between the coal consumption data of these four countries is the strongest. Besides, the diameter of Austria, Hungary, Bulgaria, Netherlands, and Switzerland is over 9. Moreover, the average cluster coefficient of Slovakia, Germany, Hungary, Japan, Czechia, Romania, and Belgium is over 0.75.

3.3 Fractal analyze

Fractal is an essential feature of time series. In this section, the fractal characteristics of three fossil fuels are analyzed. Through Table 1, it can be found that the Hurst indices of coal, oil, and natural gas consumption data are all greater than 0.5. Meanwhile, the Hurst indices of most fossil fuel consumption exceed 0.9, indicating that the consumption of these three types of fossil fuels has long-term memory. When the Hurst index equals to 0.5, the sequence is the randomized time series. The closer the Hurst index is to 0.5, the stronger the stochasticity of the effect of the series on the future. In this paper, when the Hurst index is between 0.4 and 0.6, the series can be considered stochastic.

In Table 1, the Hurst index is marked in bold when it is between 0.4 and 0.5. The Hurst index of degree (HID) of 10 countries including Austria, Egypt, India, Indonesia, Iran, Mexico, Morocco, Poland, Switzerland, and the United States in coal consumption is in bold, indicating that in coal consumption, the current time nodes have a stochastic impact on future time nodes. The HID of the oil consumption of Argentina, Belgium, Egypt, Germany, Peru, Romania, Switzerland, and the United Kingdom are the same as that of the 10 countries in coal consumption; the same as

TABLE 1 The Hurst of fossil fuel consumption.

Country	Coal		Oil		Gas	
	Hurst	Degree Hurst	Hurst	Degree Hurst	Hurst	Degree Hurst
Algeria	0.975	0.110	0.981	0.753	0.940	**0.461**
Argentina	0.845	0.699	0.952	**0.550**	1.000	**0.476**
Australia	1.000	0.773	0.976	0.705	0.982	0.622
Austria	0.866	**0.513**	0.959	0.658	1.000	0.650
Belgium	0.975	0.379	0.962	**0.582**	0.999	0.661
Brazil	1.000	0.367	1.000	0.701	0.980	**0.494**
Bulgaria	0.867	0.047	1.000	0.681	1.000	0.627
Canada	0.972	0.239	0.976	0.744	0.987	0.613
Chile	0.942	0.170	1.000	0.731	0.985	0.739
China	0.989	0.657	0.945	0.804	0.826	0.896
Colombia	0.909	0.333	0.978	0.771	0.931	0.387
Czechia	1.000	0.737	0.897	0.730	1.000	0.774
Egypt	0.674	**0.508**	1.000	**0.560**	0.969	0.706
France	1.000	0.323	0.886	0.744	1.000	**0.422**
Germany	0.986	0.677	0.919	**0.577**	1.000	**0.515**
Hungary	1.000	0.687	0.978	0.609	1.000	**0.469**
India	0.948	**0.588**	0.955	0.653	0.987	0.664
Indonesia	0.911	**0.420**	1.000	0.656	1.000	0.625
Iran	0.897	**0.435**	1.000	0.281	0.940	**0.555**
Italy	0.890	0.621	0.917	0.761	1.000	0.689
Japan	1.000	0.712	0.845	0.692	1.000	0.180
Malaysia	0.903	0.699	1.000	0.796	1.000	0.692
Mexico	1.000	**0.494**	1.000	0.713	0.965	0.334
Morocco	0.922	**0.474**	0.995	0.386	0.966	**0.552**
Netherlands	0.995	0.732	0.969	0.624	0.902	**0.574**
New Zealand	0.963	0.619	0.985	0.630	1.000	**0.506**
Pakistan	0.698	0.825	1.000	0.938	0.980	0.745
Peru	1.006	0.657	0.912	**0.551**	0.940	0.685
Poland	0.988	**0.523**	0.942	0.632	0.937	0.683
Romania	0.940	0.660	0.995	**0.538**	1.000	**0.546**
Russia	1.000	0.702	1.000	0.717	0.987	**0.599**
Slovakia	0.990	0.614	1.000	0.719	1.000	**0.488**
Spain	0.917	0.650	1.000	0.720	1.000	0.843
Switzerland	0.927	**0.582**	0.736	**0.423**	1.000	**0.591**
Taiwan (China)	1.000	0.878	1.000	0.723	0.936	**0.535**
United Kingdom	0.946	0.347	0.944	**0.480**	1.000	0.772

(Continued on following page)

TABLE 1 (*Continued*) The Hurst of fossil fuel consumption.

Country	Coal		Oil		Gas	
	Hurst	Degree Hurst	Hurst	Degree Hurst	Hurst	Degree Hurst
United States	0.981	**0.546**	0.935	0.725	0.882	0.318
Venezuela	0.745	0.662	1.000	0.341	1.000	**0.524**

Bold value means the Hurst index is between 0.4 and 0.6, the series can be considered stochastic.

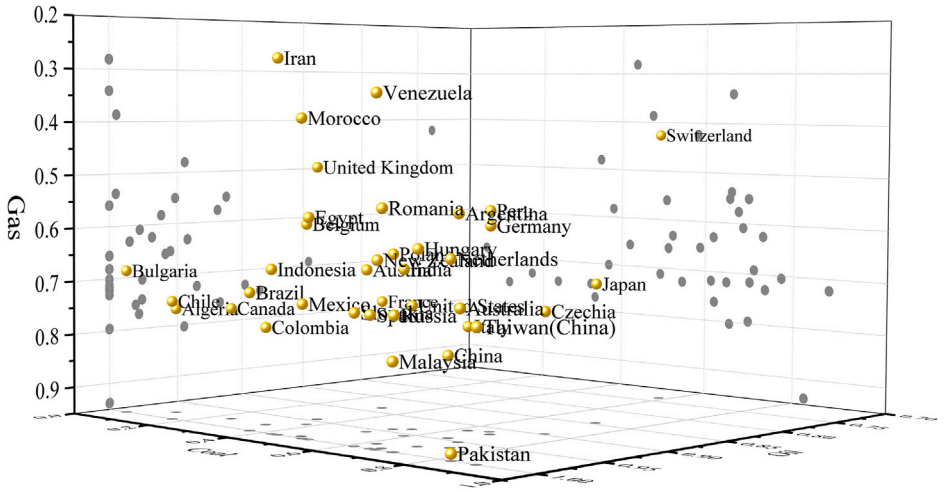

FIGURE 9
The Hurst of degree.

the previously mentioned, the countries in natural gas consumption are Algeria, Argentina, Brazil, France, Germany, Hungary, Iran, Morocco, Netherlands, New Zealand, Romania, Russia, Slovakia, Switzerland, Taiwan (China), and Venezuela, respectively.

Since the coal, oil, and gas consumption in these 38 countries are long-term memory time series, only analyzing the Hurst index of the primary data cannot discover new features in the original data. However, as shown in Figure 9, with the assistance of the Hurst of degree, new characteristics of fossil fuel consumption can be obtained. There are fuel consumption differences between different countries and in the same country.

4 Conclusion

This paper utilizes the Hurst index to analyze fossil fuel consumption time series data for 38 countries. The analysis reveals that all fossil fuel consumption data in these countries exhibit long-term memory characteristics, indicating a significant relationship between fossil fuel consumption and economic development.

The visibility graph method is employed to uncover hidden features (such as average degree, average clustering coefficient, and diameter) of the fossil fuel consumption data. These features help identify differences in fuel consumption between countries. Furthermore, fractal and complex network theory are applied to analyze fossil fuel consumption, revealing significant differences among the 38 countries. By using the Hurst index of the degree distribution, this study distinguishes global fossil fuel consumption patterns and determines whether current fuel consumption affects future consumption randomly. Additionally, the stable supply and economic security of national fossil fuel resources depend on the formulation and improvement of relevant resource protection laws. Without legal protection, the security of energy resources cannot be ensured, economic development needs cannot be met, and people's needs for survival and development cannot be satisfied.

Data availability statement

The original contributions presented in the study are included in the article/Supplementary Material, further inquiries can be directed to the corresponding author.

Author contributions

LZ: Conceptualization, Data curation, Methodology, Writing–original draft. XJ: Investigation, Methodology, Writing–review and editing. YM: Methodology, Software, Validation, Visualization, Writing–review and editing.

Funding

The author(s) declare that no financial support was received for the research, authorship, and/or publication of this article.

Acknowledgments

This work is supported by the 2024 Shandong Provincial Key Art and Science Youth Project "Research on Intellectual Property Protection of Traditional Crafts in the Yellow River National Cultural Park (Shandong Section)" (No. L2024Q05100112). Thanks to Chat GPT 3.5 for helping us polish the language.

Conflict of interest

The authors declare that the research was conducted in the absence of any commercial or financial relationships that could be construed as a potential conflict of interest.

Publisher's note

References

1. Diffenbaugh NS, Burke M. Global warming has increased global economic inequality. *Proc Natl Acad Sci* (2019) 116(20):9808–13. doi:10.1073/pnas.1816020116

2. Friedemann AJ. Half a million products are made out of fossil fuels. In: *Life after fossil fuels*. Springer (2021). p. 81–4.

3. Michail NA, Melas KD. Shipping markets in turmoil: an analysis of the covid-19 outbreak and its implications. *Transportation Res Interdiscip Perspect* (2020) 7:100178. doi:10.1016/j.trip.2020.100178

4. Smith LV, Tarui N, Yamagata T. Assessing the impact of covid-19 on global fossil fuel consumption and co2 emissions. *Energ Econ* (2021) 97:105170. doi:10.1016/j.eneco.2021.105170

5. Gokmenoglu KK, Sadeghieh M. Financial development, co2 emissions, fossil fuel consumption and economic growth: the case of Turkey. *Strateg Plann Energ Environ* (2019) 38(4):7–28. doi:10.1080/10485236.2019.12054409

6. Mensah IA, Sun M, Gao C, Omari-Sasu AY, Zhu D, Ampimah BC, et al. Analysis on the nexus of economic growth, fossil fuel energy consumption, co2 emissions and oil price in africa based on a pmg panel ardl approach. *J Clean Prod* (2019) 228:161–74. doi:10.1016/j.jclepro.2019.04.281

7. Kahia M, Ben Jebli M, Belloumi M. Analysis of the impact of renewable energy consumption and economic growth on carbon dioxide emissions in 12 mena countries. *Clean Tech Environ Pol* (2019) 21(4):871–85. doi:10.1007/s10098-019-01676-2

8. Gyimah J, Yao X, Tachega MA, Hayford IS, Opoku-Mensah E. Renewable energy consumption and economic growth: new evidence from Ghana. *Energy* (2022) 248:123559. doi:10.1016/j.energy.2022.123559

9. Martins F, Felgueiras C, Smitková M. Fossil fuel energy consumption in european countries. *Energ Proced* (2018) 153:107–11. doi:10.1016/j.egypro.2018.10.050

10. Asongu SA, Agboola MO, Alola AA, Bekun FV. The criticality of growth, urbanization, electricity and fossil fuel consumption to environment sustainability in africa. *Sci Total Environ* (2020) 712:136376. doi:10.1016/j.scitotenv.2019.136376

11. Chen J, Wu Y, Xu C, Song M, Liu X. Global non-fossil fuel consumption: driving factors, disparities, and trends. *Management Decis* (2018) 57:791–810. doi:10.1108/md-04-2018-0409

12. Li B, Haneklaus N. The role of clean energy, fossil fuel consumption and trade openness for carbon neutrality in China. *Energ Rep* (2022) 8:1090–8. doi:10.1016/j.egyr.2022.02.092

13. Cherni JA, Kentish J. Renewable energy policy and electricity market reforms in China. *Energy Policy* (2007) 35(7):3616–29. doi:10.1016/j.enpol.2006.12.024

14. Fang G, Tian L, Liu M, Fu M, Sun M. How to optimize the development of carbon trading in China—enlightenment from evolution rules of the eu carbon price. *Appl Energ* (2018) 211:1039–49. doi:10.1016/j.apenergy.2017.12.001

15. Valeryevna PA. Rational use of nature resources. *Eur Sci* (2017) 6(28)):54–8.

16. Nikolopoulos D, Moustris K, Petraki E, Koulougliotis D, Cantzos D. Fractal and long-memory traces in pm10 time series in athens, Greece. *Environments* (2019) 6(3):29. doi:10.3390/environments6030029

17. Castillo O, Melin P. Forecasting of covid-19 time series for countries in the world based on a hybrid approach combining the fractal dimension and fuzzy logic. *Chaos, Solitons and Fractals* (2020) 140:110242. doi:10.1016/j.chaos.2020.110242

18. Cheng L, Zhu P, Tang K, Gao C, Wang Z. Gin-sd: source detection in graphs with incomplete nodes via positional encoding and attentive fusion. *Proc AAAI Conf Artif Intelligence* (2024) 38:55–63. doi:10.1609/aaai.v38i1.27755

19. Zhong C, Xiong F, Pan S, Wang L, Xiong X. Hierarchical attention neural network for information cascade prediction. *Inf Sci* (2023) 622:1109–27. doi:10.1016/j.ins.2022.11.163

20. Zhu P, Pan Z, Tang K, Cui X, Wang J, Xuan Q. Node injection attack based on label propagation against graph neural network. *IEEE Trans Comput Soc Syst* (2024) 1–13. doi:10.1109/tcss.2024.3395794

21. Ni X, Xiong F, Pan S, Wu J, Wang L, Chen H. Community preserving social recommendation with cyclic transfer learning. *ACM Trans Inf Syst* (2023) 42(3):1–36. doi:10.1145/3631115

22. Zhu H, Xiong F, Chen H, Xiong X, Wang L. Incorporating a triple graph neural network with multiple implicit feedback for social recommendation. *ACM Trans Web* (2024) 18(2):1–26. doi:10.1145/3580517

23. Zhu P, Cheng L, Gao C, Wang Z, Li X. Locating multi-sources in social networks with a low infection rate. *IEEE Trans Netw Sci Eng* (2022) 9(3):1853–65. doi:10.1109/tnse.2022.3153968

24. Plocoste T, Carmona-Cabezas R, Jiménez-Hornero FJ, de Ravé EG, Calif R. Multifractal characterisation of particulate matter (pm10) time series in the caribbean basin using visibility graphs. *Atmos Pollut Res* (2021) 12(1):100–10. doi:10.1016/j.apr.2020.08.027

25. Zhang X, Landsness EC, Chen W, Miao H, Tang M, Brier LM, et al. Automated sleep state classification of wide-field calcium imaging data via multiplex visibility graphs and deep learning. *J Neurosci Methods* (2022) 366:109421. doi:10.1016/j.jneumeth.2021.109421

26. Zhu G, Li Y, Wen P. Analysis and classification of sleep stages based on difference visibility graphs from a single-channel eeg signal. *IEEE J Biomed Health Inform* (2014) 18(6):1813–21. doi:10.1109/jbhi.2014.2303991

27. Wang L, Long X, Arends JB, Aarts RM. Eeg analysis of seizure patterns using visibility graphs for detection of generalized seizures. *J Neurosci Methods* (2017) 290:85–94. doi:10.1016/j.jneumeth.2017.07.013

28. Gao Z-K, Guo W, Cai Q, Ma C, Zhang Y-B, Kurths J. Characterization of ssmvep-based eeg signals using multiplex limited penetrable horizontal visibility graph. *Chaos: Interdiscip J Nonlinear Sci* (2019) 29(7):073119. doi:10.1063/1.5108606

29. Supriya S, Siuly S, Wang H, Zhang Y. Eeg sleep stages analysis and classification based on weighed complex network features. *IEEE Trans Emerging Top Comput Intelligence* (2018) 5(2):236–46. doi:10.1109/tetci.2018.2876529

30. Hu J, Chen J, Zhu P, Hao S, Wang M, Li H, et al. Difference and cluster analysis on the carbon dioxide emissions in China during covid-19 lockdown via a complex network model. *Front Psychol* (2022) 12:795142. doi:10.3389/fpsyg.2021.795142

31. Cui X, Hu J, Ma Y, Wu P, Zhu P, Li H-J. Investigation of stock price network based on time series analysis and complex network. *Int J Mod Phys B* (2021) 35(13):2150171. doi:10.1142/s021797922150171x

32. He Z, Zhang S, Hu J, Dai F. An adaptive time series segmentation algorithm based on visibility graph and particle swarm optimization. *Physica A: Stat Mech its Appl* (2024) 636:129563. doi:10.1016/j.physa.2024.129563

33. Hu J, Chu C, Criado R, Chen J, Hao S, Wang M. Visibility graph and graph convolution networks-based segmentation of carbon emission in China. *Ann Operations Res* (2023) 1–22. doi:10.1007/s10479-023-05623-9

34. Hu J, Xia C, Li H, Zhu P, Xiong W. Properties and structural analyses of USA's regional electricity market: a visibility graph network approach. *Appl Mathematics Comput* (2020) 385:125434. doi:10.1016/j.amc.2020.125434

35. Fan X, Li X, Yin J, Tian L, Liang J. Similarity and heterogeneity of price dynamics across China's regional carbon markets: a visibility graph network approach. *Appl Energ* (2019) 235:739–46. doi:10.1016/j.apenergy.2018.11.007

36. Lacasa L, Luque B, Ballesteros F, Luque J, Nuno JC. From time series to complex networks: the visibility graph. *Proc Natl Acad Sci* (2008) 105(13):4972–5. doi:10.1073/pnas.0709247105

37. Watts DJ, Strogatz SH. Collective dynamics of 'small-world'networks. *nature* (1998) 393(6684):440–2. doi:10.1038/30918

38. Fronczak A, Fronczak P, Hołyst JA. Average path length in random networks. *Phys Rev E* (2004) 70(5):056110. doi:10.1103/physreve.70.056110

39. Newman ME. Properties of highly clustered networks. *Phys Rev E* (2003) 68(2):026121. doi:10.1103/physreve.68.026121

40. Hannah Ritchie MR, Rosado P. *Energy, our world in DataHttps://ourworldindata*. Oxford Martin School, University of Oxford.

frontiers | Frontiers in Physics

TYPE Original Research
PUBLISHED 16 October 2024
DOI 10.3389/fphy.2024.1490499

OPEN ACCESS

EDITED BY
Ningbo Zhang,
Beijing University of Posts and Telecommunications (BUPT), China

REVIEWED BY
Yasuko Kawahata,
Rikkyo University, Japan
Xiao Han,
Beijing Jiaotong University, China

*CORRESPONDENCE
Hua Li,
lh1@ustl.edu.cn

RECEIVED 03 September 2024
ACCEPTED 01 October 2024
PUBLISHED 16 October 2024

CITATION
Yan H, Li H, Sun Q and Jiang Y (2024) Communication dynamics of congestion warning information considering the attitudes of travelers.
Front. Phys. 12:1490499.
doi: 10.3389/fphy.2024.1490499

Communication dynamics of congestion warning information considering the attitudes of travelers

Huining Yan[1], Hua Li[2]*, Qiubai Sun[3] and Yuxi Jiang[4]

[1]School of Electronic and Information Engineering, University of Science and Technology Liaoning, Anshan, Liaoning, China, [2]School of Business Administration, University of Science and Technology Liaoning, Anshan, Liaoning, China, [3]Asset Company, University of Science and Technology Liaoning, Anshan, Liaoning, China, [4]School of Economics and Management, Dalian Jiaotong University, Dalian, Liaoning, China

Traffic congestion is a serious problem faced by many cities worldwide today. Congestion warning information is one of the important influencing factors of urban road congestion; To this end, based on the dynamics of infectious diseases, a congestion warning information dissemination model considering the attitudes of travelers and the network structure was constructed. The existence and stability of the equilibrium points of non congestion warning information and congestion warning information in the model were analyzed, and the optimal control strategy of the model was proposed. Numerical simulation was conducted to verify the results of theoretical analysis, simulate and analyze the impact of changes in various parameters in the model on the dissemination of congestion warning information, and perform sensitivity analysis on several parameters. The results indicate that travelers are more inclined towards "fast" modes of transportation and have a stronger willingness to share congestion warning information. The dissemination range of warning information is wider, which can play a positive role in reducing traffic congestion pressure.

KEYWORDS

congestion warning information, social networks, communication dynamics, traveler attitude, optimum control

1 Introduction

With the rapid development of the urban economy, urban traffic congestion has brought many inconveniences to people's travel, and alleviating the pressure of urban traffic congestion has become an important task that urgently needs to be solved in the development of many cities around the world. The dissemination of road congestion warning information is an important way to prevent and control urban congestion [1]. The attitude of travelers toward congestion warning information can affect the dissemination process of warning information to some extent, thereby affecting the degree of urban traffic congestion. Therefore, It is necessary to explore the dissemination mechanism of congestion warning information considering the attitude of travelers and propose corresponding optimization strategies.

In recent years, urban road congestion warning information has been disseminated among users through social networks and navigation apps, providing travel plans for

travelers and alleviating the pressure of urban traffic congestion. Scholars from different fields have conducted numerous studies on congestion warning information. Ahmad et al. proposed a novel detection scheme (IVCD) to support the propagation of congestion information that is about to occur on all roads in its coverage area [2]. Many scholars began discussing the application of space supply chain in transportation many years ago [3–9]. Yilmaz et al. proposed an urban traffic monitoring system that utilizes participatory sensing and cloud messaging capabilities and can issue warnings or suggestions to drivers near congested roads or on the route [10]. Online sharing of congestion warning information is an effective way to quickly spread congestion information. Travelers can make timely choices and change routes, which is beneficial for controlling vehicle diversion. Yang et al. proposed the concept of an event consistency proof suitable for vehicle networks and introduced two-stage transactions on the blockchain to send warning messages in appropriate regions and time periods [11]. Shi et al. proposed a framework for a physically informed spatiotemporal graph convolutional neural network (PSTGCN) based on the theory of physically informed deep learning to estimate congestion warning information [12]. Ning et al. proposed the traffic warning message dissemination system (TWMDS) framework, which allows travelers to quickly rebuild their travel paths to alleviate traffic congestion [13]. Humayun et al. promotes dissemination by using roadside message proxies to provide real-time traffic information about traffic congestion and unexpected traffic events [14]. Jiang et al. proposed an innovative early traffic congestion warning system to monitor and plan traffic conditions [15]. The above discussion describes the research conducted by scholars on how to develop and send a complete set of congestion warning information, indicating the importance of congestion warning information for urban traffic management.

There are lots of studies in transportation areas to discuss the value of information, Zhang et al. developed a day-to-day route-choice learning model with friends' travel information [16]. Chen et al. presented a model of a social network-based attitude diffusion system in the context of activity and travel choice behavior [17]. Yu et al. investigated the welfare effects of inaccurate pre-trip information on commuters' departure time choice under stochastic bottleneck capacity in the morning commute [18]. Han et al. experimentally investigated how routing advice influenced strategic uncertainty and analyzed compliance behavior and decision time that might affect strategic uncertainty [19].

The dissemination of congestion warning information is strongly influenced by travelers' psychological perceptions of congestion status. Many scholars have studied the attitudes of travelers toward road congestion. Khoo et al. believes that the choice of travel route is directly related to drivers' sensitivity to congestion and that changing the travel route is positively correlated with the degree of road congestion [20]. Huang et al. quantified drivers' response to congestion warning information and the traffic congestion mitigation effect based on congestion warning information [21]. Zhou et al. proposed that traffic congestion can be spread among people or through public media, leading to the interactive dissemination of warning information in the network [22]. Huang et al. considered two states in the warning information network, travelers receiving warning information and travelers not receiving warning information, and studied the impact of travelers' behavioral characteristics when facing warning information on the spread of congestion risk [23]. The warning information is divided into two types: "fast speed" and "short distance". These two types of warning information can lead travelers to make different travel decisions. The impact of various warning information, such as "fast speed" and "short distance", on traffic congestion pressure should be analyzed [24].

From the perspective of research methods, because the dissemination process of urban congestion warning information is similar to that of infectious diseases, infectious disease models can be widely applied to analyze various transmission mechanism problems. Saberi et al. (2020) described the dynamic process of urban traffic congestion transmission and dissipation based on the susceptibility infection recovery (SIR) model and monitored, predicted, and controlled the status of urban traffic congestion [25]. Jia et al. proposed an improved susceptible infected susceptible (SIS) congestion propagation model to estimate the probability of congestion risk (RPC) in subway networks [26]. Chen et al. established an urban traffic congestion propagation model based on the SIS propagation theory to study the mechanism and characteristics of urban traffic congestion propagation [27]. For example, Ma et al. established a new UAU-SEIR (Unaware Aware Unaware Susceptible Exposed Infected Recovered) model to study the impact of individual and mass media information dissemination on epidemic transmission [28]. She et al. constructed an SIS model to study the mutual influence between the spread of epidemics and the spread of opinions on the network [29]. Nian et al. explored the propagation patterns of public opinion in social networks based on the susceptible exposed infected recovered (SEIR) model and conducted empirical research on the relationships among rumor propagation, user characteristics, and differences in subject interests. The authors also analyzed the common effects of individual factors and the social environment [30]. Ojha et al. developed a model based on epidemiological methods for detecting and controlling false information propagation in OSNs [31].

In summary, most of the current research has focused on developing congestion warning information and controlling the spread of urban traffic congestion, with little research on the dissemination patterns of congestion warning information. Some studies have also considered the impact of congestion warning information on urban traffic congestion but have considered only two states: each traveler received or did not receive warning information. In addition, when network platforms push warning information, they directly push "fast" and "short distance" messages without considering that travelers' attitudes toward congestion directly affect the dissemination of congestion warning information. Therefore, to better predict and control the dissemination process of congestion warning information, it is necessary to consider the impact of network topology characteristics and complex user behavior characteristics on the dissemination process of congestion warning information in the social network. In view of this, this article divides travelers into ignorant, negative, positive, disseminator, and immune individuals based on the classic infectious disease SIR model and considers the structural characteristics of the congestion warning information dissemination network to construct a congestion warning information dissemination model to more accurately and

reasonably describe the dynamic laws of congestion warning information dissemination in social networks.

The remainder of this article is organized as follows: In the section on model construction, a congestion warning information dissemination model (SPEIR model) is constructed by considering the attitudes of travelers toward road congestion. In the section on model analysis, the basic regeneration number of the model is calculated, and the stability of no congestion warning information and the presence of congestion warning information are analyzed. In the section on the optimal control model, the optimal control model is constructed, and the optimal control strategy is proposed. In the numerical simulation section, the stability analysis in the previous section is simulated and verified, and the impact of parameter changes on the propagation process of congestion warning information is simulated. A sensitivity analysis of the parameters is conducted, and numerical simulations are conducted on the optimal control strategy. The conclusion section provides a summary of the entire article and highlights its limitations.

2 Materials and methods

The model constructed in this article is based on the classic SIR model, assuming that congestion warning information propagates in a mixed uniform network with nodes, each node represents a user in the social network, and the total number of nodes is variable. The information can be divided into 5 categories: (1) Ignorant, which refers to the group of people who have not been exposed to congestion warning information but are easily receptive to it, denoted as $S(t)$; (2) Negative individuals, who receive congestion warning messages but are not sensitive to congestion and hold a negative attitude, tend to choose the group with a "short distance", remember $P(t)$; (3) Positive individuals, who receive congestion warning information and are highly sensitive to road congestion, hold a positive attitude and are more inclined to choose the group with "fast speed", denoted as $E(t)$; (4) The disseminator, who receives congestion warning information and chooses to share it with other users, denoted as $I(t)$. (5) Immune individuals who are not interested in congestion warning information are referred to as $R(t)$.

In a social system, the number of users on social networks dynamically changes over time. Therefore, this article assumes that the number of people joining social networks per unit of time is B. Moreover, considering that ignorant, negative, positive, spreaders, and immune individuals may all exit social networks for certain reasons, this article assumes that each type of user has the same population migration rate μ.

When the ignorant individuals receive the congestion warning information, if they are willing to share congestion warning information with other users, they will transform into distributors with probability λ; if the ignorant person is not interested in congestion warning information, they will transition to an immune person based on probability η ; if the ignorant tends to have a shorter distance due to their sensitivity to traffic congestion, preference for congestion risk, or other reasons, then probability θ_1 becomes a negative factor; if there is a tendency toward "fast speed", then the probability θ_2 changes to a positive one.

Although passive individuals are not sensitive to traffic congestion, if they are willing to share congestion warning information with others, they will transform into distributors based on probability α; if a negative person gradually becomes uninterested in congestion warning information, they will transition to an immune person based on probability γ_1. If the active participants are willing to share congestion warning information, they will transform into disseminators based on probability γ_2 ; the disseminator will eventually transform into an immune recipient with a probability of ε. This article assumes that the immune state is the final absorption state in the network; that is, the immune recipient will not undergo a state change at any time.

In addition, the impact of network structure on the dissemination process of congestion warning information should be considered. If each social network user is viewed as a node in the network and the connections between users are viewed as edges between nodes, then the social network can be represented as a directed graph $= \langle V, E \rangle$. Among them, V represents the set of nodes, E represents the set of edges, and $(u, v) \in E$ represents the relationship edge to which node u points; that is, node u connects to node v. Obviously, the more edges a node has in a network, the closer the connections between nodes are. The more paths congestion warning information can propagate, the more conducive it is to the dissemination of congestion warning information. In graph theory, the degree k_i of node v_i is defined as the number of edges connected to that node. The average degree k_i of all nodes v_i in a network is called the average degree of the network, $\bar{k} = \frac{1}{N}\sum_{i=1}^{N} k_i$, where N represents the total number of nodes in the network. This article uses the average degree to describe the degree of closeness of the social network structure.

Based on the above assumptions, the state transition process of social network users during the dissemination of congestion warning information is obtained, as shown in Figure 1. Table 1 provides the meaning of each parameter in Figure 1, where all probabilities are positive constants.

(1) As shown in Figure 1, The changes in the states of the ignorant, negative, positive, spreader, and immune individuals per unit time are as follows: Within a unit of time, there are B users who have joined social networks and are all in an ignorant state; that is, they have not yet received congestion warning information. The population density of ignorant individuals who come into contact with distributors and receive congestion warning information is $\bar{k}(\theta_1 + \lambda + \theta_2 + \eta)S(t)I(t)$. Similarly, the density of people who quit social networks for some reason is $\mu S(t)$. Therefore, the density of the ignorant population changes by $B - \bar{k}(\theta_1 + \lambda + \theta_2 + \eta)S(t)I(t) - \mu S(t)$ per unit time.

(2) The density of people who transform from ignorant to negative within a unit of time is $\theta_1 S(t)I(t)\bar{k}$. The density of people who are willing to share congestion warning information with others and become spreaders is $\alpha P(t)$. The population density of passive individuals who forget or are not interested in congestion warning information, thus transforming into immune individuals. The density of negative individuals who withdraw from social networks for some reason is $\mu P(t)$. Therefore, the change in the density of

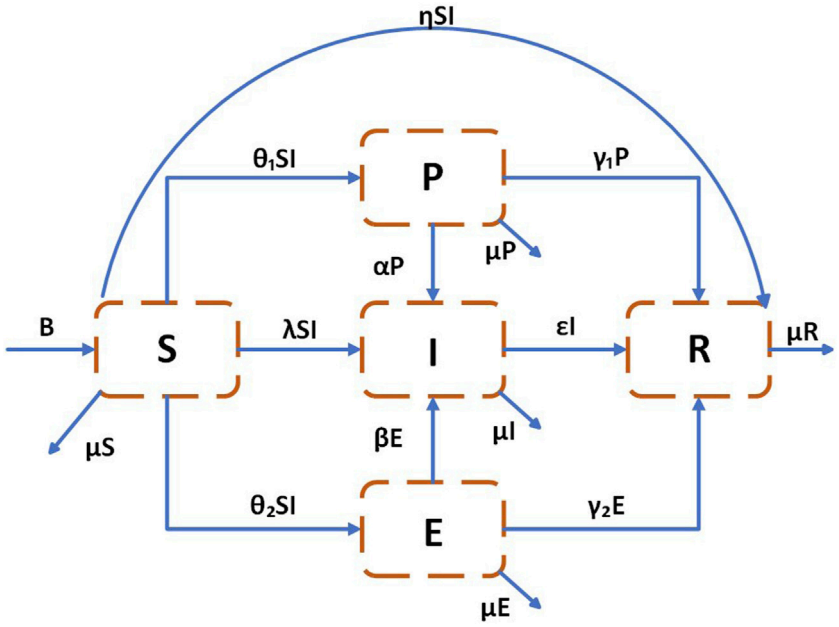

FIGURE 1
The flow diagram of the model.

TABLE 1 The parameters description of SPEIR model.

Parameter	Description
$S(t)$	The population density of ignorant individuals at time t
$P(t)$	The population density of negative individuals at time t
$E(t)$	The population density of positive individuals at time t
$I(t)$	The population density of disseminators at time t
$R(t)$	The population density of immunized individuals at time t
B	The number of immigrants in the social system per unit time
μ	Removal rate per unit time
λ	The probability of the ignorant transforming into the disseminator
θ_1	The probability of the ignorant transforming into the negative
θ_2	The probability of the ignorant transforming into positive
α	The probability of the negative transforming into the disseminator
β	The probability of the positive transforming into the disseminator
γ_1	The probability of the negative transforming into the immune
γ_2	The probability of the positive transforming into the immune
ε	The probability of the disseminator transforming into the immune
$\bar{k}$	Network average

negative individuals per unit of time is $\theta_1 S(t) I(t) \bar{k} - \alpha P(t) - \gamma_1 P(t) - \mu P(t)$.

(3) The density of people who transform from ignorant to active within a unit of time is $\theta_2 S(t) I(t) \bar{k}$. Similarly, the density of people who are willing to share congestion warning information with others and become distributors is $\beta E(t)$. Similarly, the population density of active participants who forget or are not interested in congestion warning information, thus transforming into immune recipients, is $\gamma_2 E(t)$. Similarly, the density of active users who withdraw from social networks for some reason is $\mu E(t)$. Therefore, the population density

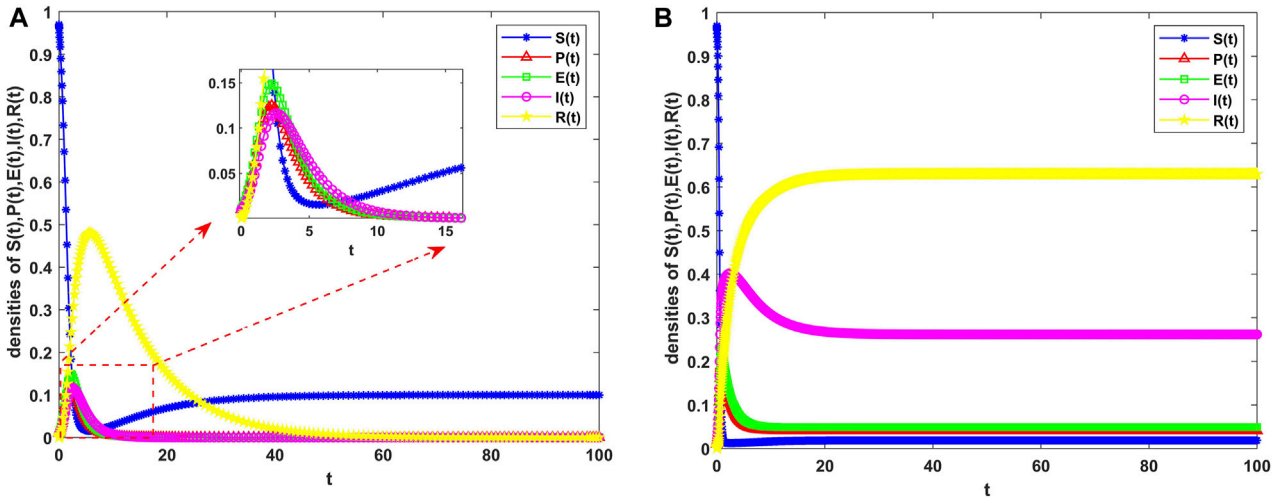

FIGURE 2
Stability of the equilibrium point of **(A)** $R_0 < 1$ and **(B)** $R_0 > 1$

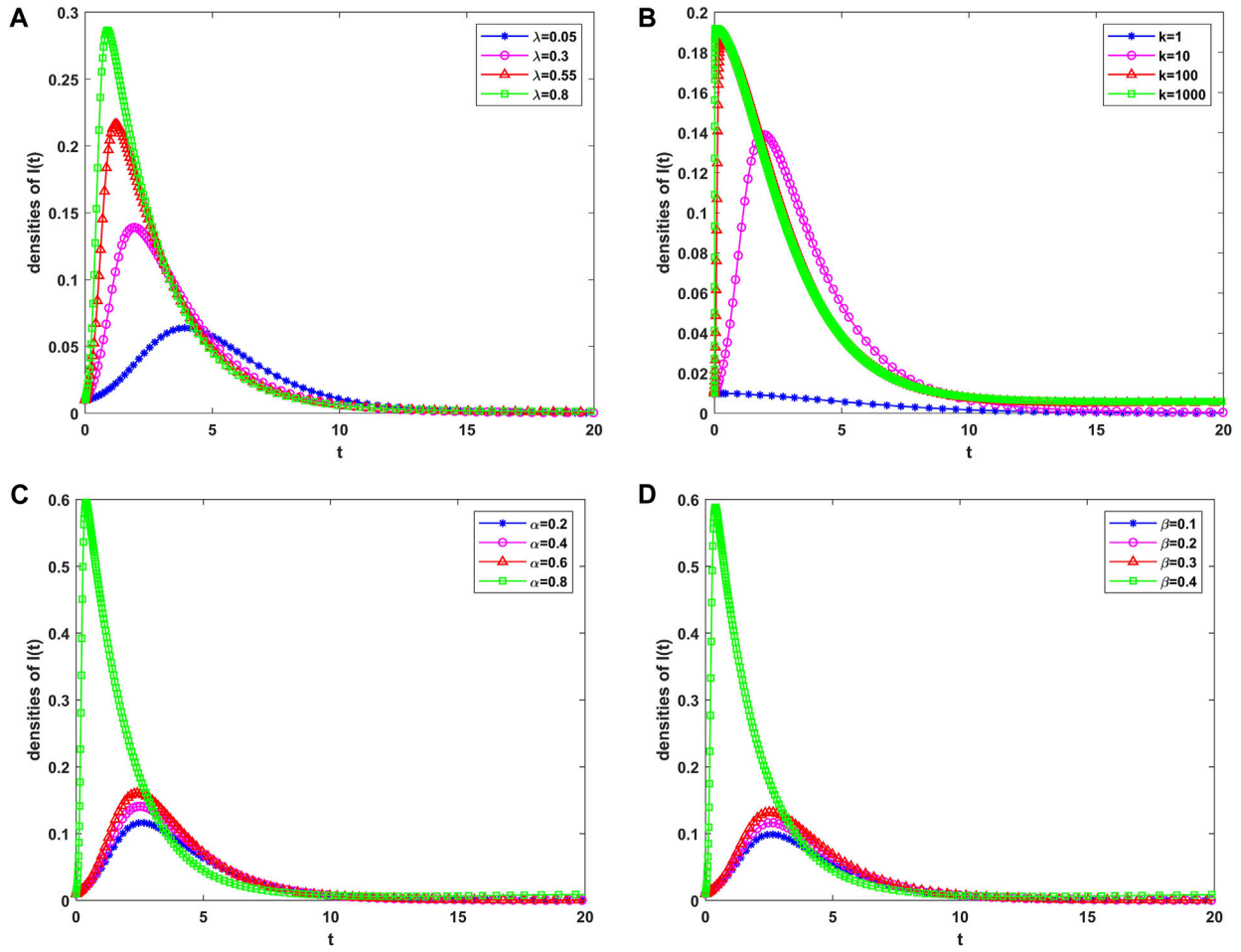

FIGURE 3
Trend of the density of disseminators over time under **(A)** different λ values, **(B)** different $\bar{k}$ values, **(C)** different α values and **(D)** different β values.

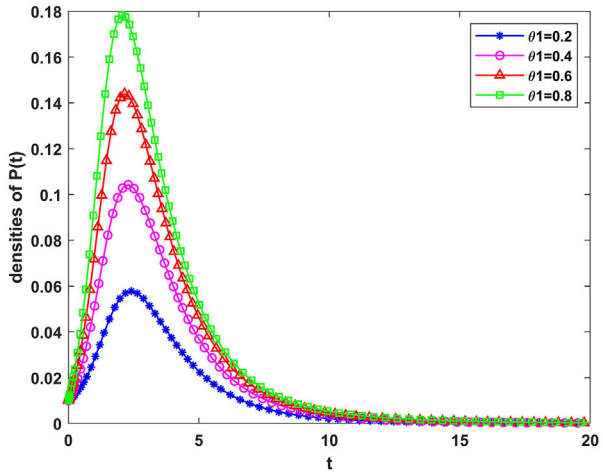

FIGURE 4
Trend of negative population density over time under different θ_1 values.

of positive individuals varies by $\theta_2 S(t)I(t)\bar{k} - \beta E(t) - \gamma_2 E(t) - \mu E(t)$ per unit time.

(4) The population density of ignorant individuals transforming into disseminators within a unit of time is $\lambda S(t)I(t)\bar{k}$; the density of the population where negatives transform into disseminators is $\alpha P(t)$; the population density of positive individuals transforming into disseminators is $\beta E(t)$; the population density of spreaders who forget or are not interested in congestion warning information and thus become immune recipients is $\varepsilon I(t)$; and the population density of disseminators who withdraw from social networks for some reason is $\mu I(t)$. Therefore, the population density of the spreader varies by $\lambda S(t)I(t)\bar{k} + \alpha P(t) + \beta E(t) - \varepsilon I(t) - \mu I(t)$ per unit time.

(5) The population density of uninformed, passive, active, and disseminators who become immune due to their neutrality or lack of interest in congestion warning information per unit of time is $\eta S(t)I(t)\bar{k} + \gamma_1 P(t) + \gamma_2 E(t) + \varepsilon I(t)$; the population density of immune individuals who withdraw from social networks for some reason is $\mu R(t)$. Therefore, the population density of immunized individuals varies by $\eta S(t)I(t)\bar{k} + \gamma_1 P(t) + \gamma_2 E(t) + \varepsilon I(t) - \mu R(t)$.

Based on the above analysis, this article considers the congestion warning information dissemination model for the sensitivity of travelers to traffic congestion as follows:

$$\begin{cases} \frac{dS(t)}{dt} = B - \theta_1 S(t)I(t)\bar{k} - \lambda S(t)I(t)\bar{k} - \theta_2 S(t)I(t)\bar{k} - \eta S(t)I(t)\bar{k} - \mu S(t), \\ \frac{dP(t)}{dt} = \theta_1 S(t)I(t)\bar{k} - \alpha P(t) - \gamma_1 P(t) - \mu P(t), \\ \frac{dE(t)}{dt} = \theta_2 S(t)I(t)\bar{k} - \beta E(t) - \gamma_2 E(t) - \mu E(t), \\ \frac{dI(t)}{dt} = \lambda S(t)I(t)\bar{k} + \alpha P(t) + \beta E(t) - \varepsilon I(t) - \mu I(t), \\ \frac{dR(t)}{dt} = \eta S(t)I(t)\bar{k} + \gamma_1 P(t) + \gamma_2 E(t) + \varepsilon I(t) - \mu R(t). \end{cases} \tag{1}$$

Satisfy $S(t) + P(t) + E(t) + I(t) + R(t) = 1$

3 Stability analysis of the model

It is not difficult to determine that the model has a balance point $E_0 = (\frac{B}{\mu}, 0, 0, 0, 0)$ without congestion warning information. The existence of this equilibrium point means that when the evolution of the congestion warning information dissemination system reaches a steady state, there will be no individual users infected by the congestion warning information, that is, the congestion warning information will no longer spread in the network. This article uses the next-generation matrix method to calculate the basic regeneration number R_0 [32] of Equation 1. The specific calculation process is shown in Equations 2–5.

Let $X = (I, R, P, E, S)^T$, then Equation 1 can be written as $\frac{dX}{dt} = F(X) - V(X)$

$$F(X) = \begin{pmatrix} \lambda S I \bar{k} \\ 0 \\ 0 \\ 0 \\ 0 \end{pmatrix}, V(X) = \begin{pmatrix} \varepsilon I + \mu I - \alpha P - \beta E \\ \mu R - \eta S I \bar{k} - \gamma_1 P - \gamma_2 E - \varepsilon I \\ \alpha P + \gamma_1 P + \mu P - \theta_1 S I \bar{k} \\ \beta E + \gamma_2 E + \mu E - \theta_2 S I \bar{k} \\ \theta_1 S I \bar{k} + \lambda S I \bar{k} + \theta_2 S I \bar{k} + \eta S I \bar{k} + \mu S - B \end{pmatrix}. \tag{2}$$

We can get:

$$F = \begin{pmatrix} \lambda S \bar{k} & 0 \\ 0 & 0 \end{pmatrix}, V = \begin{pmatrix} \varepsilon + \mu & 0 \\ -\varepsilon & \mu \end{pmatrix}. \tag{3}$$

Through calculation, it can be concluded that

$$FV^{-1} = \begin{pmatrix} \frac{\bar{k} S \lambda}{\mu + \varepsilon} & 0 \\ 0 & 0 \end{pmatrix}. \tag{4}$$

Therefore, the basic regeneration number of system Equation 1 is the spectral radius FV^{-1}, represented by R_0, and the calculated basic regeneration number of the system is:

$$R_0 = \frac{\bar{k} B \lambda}{\mu(\mu + \varepsilon)}. \tag{5}$$

Theorem 1. When $R_0 > 1$, there exists an equilibrium point $E^*(S^*, P^*, E^*, I^*, R^*)$ (Equation 6) for the propagation of congestion warning information in Equation 1, where (The proof process can be found in Supplementary Appendix A)

$$\begin{aligned} S^* &= \frac{(\mu+\varepsilon)(\mu+\alpha+\gamma_1)(\mu+\beta+\gamma_2)}{\bar{k}[\theta_1\alpha(\mu+\beta+\gamma_2) + \theta_2\beta(\mu+\alpha+\gamma_1) + \lambda(\mu+\alpha+\gamma_1)(\mu+\beta+\gamma_2)]}, \\ P^* &= \frac{I^*\bar{k}S^*\theta_1}{\mu+\alpha+\gamma_1}, E^* = \frac{I^*\bar{k}S^*\theta_2}{\mu+\beta+\gamma_2}, \\ I^* &= \frac{R_0\mu[\theta_1\alpha(\mu+\beta+\gamma_2) + \theta_2\beta(\mu+\alpha+\gamma_1)]}{\lambda(\theta_1+\theta_2+\lambda+\eta)\bar{k}(\mu+\alpha+\gamma_1)(\mu+\beta+\gamma_2)} + \frac{\mu\lambda(R_0-1)}{\lambda(\theta_1+\theta_2+\lambda+\eta)\bar{k}}, \\ R^* &= \frac{S^*\eta + P^*\gamma_1 + E^*\gamma_2 + \varepsilon I^*}{\mu}. \end{aligned} \tag{6}$$

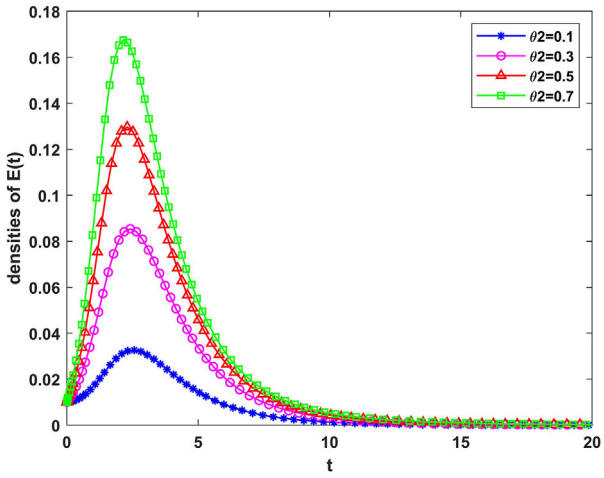

FIGURE 5
Trend of population density of active participants over time under different θ_2 values.

Theorem 2. When $R_0 < 1$, the equilibrium point E_0 of the congestion free warning information is locally asymptotically stable in the feasible domain. (The proof process can be found in Supplementary Appendix B)

Theorem 3. When $R_0 < 1$, the equilibrium point E_0 of the congestion-free warning information is globally asymptotically stable. (The proof process can be found in Supplementary Appendix C)

Theorem 4. When $R_0 > 1$ occurs, the congestion warning information at equilibrium point E^* is locally asymptotically stable. (The proof process can be found in Supplementary Appendix D)

Theorem 5. The congestion warning information has an equilibrium point $E^*(S^*, P^*, E^*, I^*, R^*)$ that is globally asymptotically stable. (The proof process can be found in Supplementary Appendix E)

4 Optimal control model

Convert the four proportional constants $\lambda, \theta_2, \alpha, \beta$ in the model into control variables $\lambda(t), \theta_2(t), \alpha(t), \beta(t)$

Therefore, it can be proposed that the objective function is Equation 7:

$$J(\lambda, \theta_2, \alpha, \beta) = \int_0^T \left[I(t) + E(t) - \frac{C_1}{2}\lambda^2(t) - \frac{C_2}{2}\theta_2^2(t) - \frac{C_3}{2}\alpha^2(t) - \frac{C_4}{2}\beta^2(t) \right] dt. \tag{7}$$

Satisfy the following state system:

$$\begin{cases} \frac{dS}{dt} = B - \theta_1 SI\bar{k} - \lambda(t)SI\bar{k} - \theta_2(t)SI\bar{k} - \eta SI\bar{k} - \mu S, \\ \frac{dP}{dt} = \theta_1 SI\bar{k} - \alpha(t)P - \gamma_1 P - \mu P, \\ \frac{dE}{dt} = \theta_2(t)SI\bar{k} - \beta(t)E - \gamma_2 E - \mu E, \\ \frac{dI}{dt} = \lambda(t)SI\bar{k} + \alpha(t)P + \beta(t)E - \varepsilon I - \mu I, \\ \frac{dR}{dt} = \eta SI\bar{k} + \gamma_1 P + \gamma_2 E + \varepsilon I - \mu R. \end{cases} \tag{8}$$

The initial conditions of system Equation 8 meet (Equation 9):

$$S(0) = S_0, P(0) = P_0, E(0) = E_0, I(0) = I_0, R(0) = R_0 \tag{9}$$

Where:

$$\lambda(t), \theta_2(t), \alpha(t), \beta(t) \in U \triangleq \left\{ (\lambda, \theta_2, \alpha, \beta) \,\middle|\, \begin{array}{l} (\lambda(t), \theta_2(t), \alpha(t), \beta(t)) \\ measurable, 0 \le \lambda(t), \theta_2(t), \alpha(t), \beta(t) \le 1, \forall t \in [0, T] \end{array} \right\}. \tag{10}$$

while U is the admissible control set (Equation 10). The time interval of control is between 0 and T, C_1, C_2, C_3, C_4 are positive weight coefficients shown the control strength and importance of four control measures.

Theorem 6. An optimal control pair $(\lambda^*, \theta_2{}^*, \alpha^*, \beta^*) \in U$ exists so that the function is established below (Equation 11) (The proof process can be found in Supplementary Appendix F):

$$J(\lambda^*, \theta_2{}^*, \alpha^*, \beta^*) = \max\{J(\lambda, \theta_2, \alpha, \beta): (\lambda, \theta_2, \alpha, \beta) \in U\}. \tag{11}$$

Theorem 7. For the optimal control pair $(\lambda^*, \theta_2{}^*, \alpha^*, \beta^*)$ of state System Equation 8, there exist adjoint variables $\xi_1, \xi_2, \xi_3, \xi_4, \xi_5$ that satisfy (Equation 12) (The proof process can be found in Supplementary Appendix G):

$$\begin{cases} \frac{d\xi_1}{dt} = \theta_1 I\bar{k}(\xi_1 - \xi_2) + \lambda(t)I\bar{k}(\xi_1 - \xi_4) + \theta_2(t)I\bar{k}(\xi_1 - \xi_3) \\ \qquad + \eta I\bar{k}(\xi_1 - \xi_5) + \xi_1\mu, \\ \frac{d\xi_2}{dt} = \alpha(t)(\xi_2 - \xi_4) + \gamma_1(\xi_2 - \xi_5) + \xi_2\mu, \\ \frac{d\xi_3}{dt} = 1 + \beta(t)(\xi_3 - \xi_4) + \gamma_2(\xi_3 - \xi_5) + \xi_3\mu, \\ \frac{d\xi_4}{dt} = 1 + \theta_1 S\bar{k}(\xi_1 - \xi_2) + \lambda(t)S\bar{k}(\xi_1 - \xi_4) + \theta_2(t)S\bar{k}(\xi_1 - \xi_3) \\ \qquad + \eta S\bar{k}(\xi_1 - \xi_5) + \varepsilon(\xi_4 - \xi_5) + \xi_4\mu. \\ \frac{d\xi_5}{dt} = \xi_5\mu \end{cases} \tag{12}$$

With boundary conditions (Equation 13):

$$\xi_1(T) = \xi_2(T) = \xi_3(T) = \xi_4(T) = \xi_5(T) = 0. \tag{13}$$

In addition, the optimal control pair $(\lambda^*, \theta_2{}^*, \alpha^*, \beta^*)$ of state System Equation 8 can be given by (Equation 14):

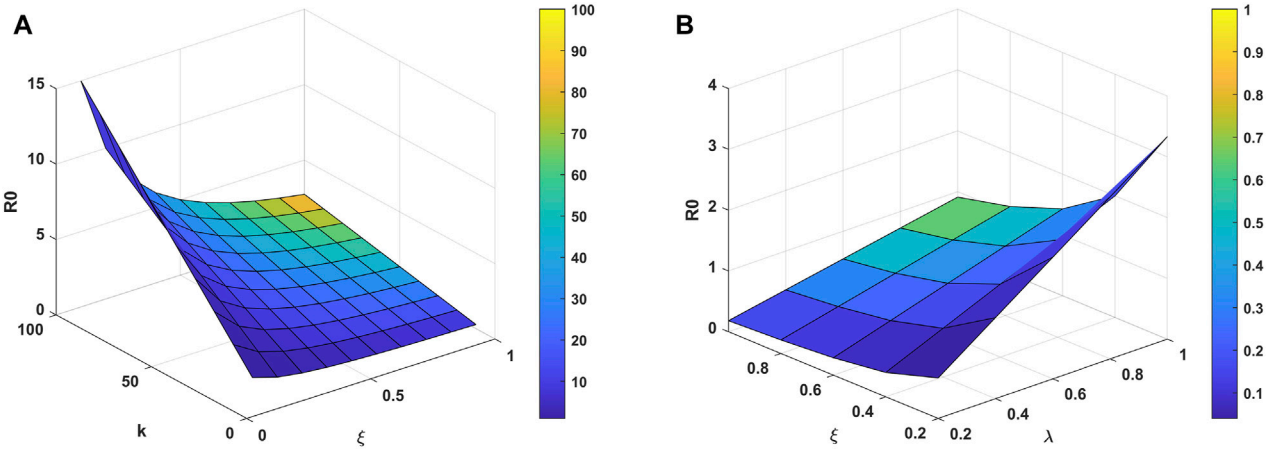

FIGURE 6
(A, B) The sensitivity analysis of the basic reproduction number.

$$\begin{aligned}
\lambda^*(t) &= \min\left\{\max\left\{\frac{SI\bar{k}(\xi_1-\xi_4)}{C_1},0\right\},1\right\},\\
\theta_2{}^*(t) &= \min\left\{\max\left\{\frac{SI\bar{k}(\xi_1-\xi_3)}{C_2},0\right\},1\right\},\\
\alpha^*(t) &= \min\left\{\max\left\{\frac{P(\xi_2-\xi_4)}{C_3},0\right\},1\right\},\\
\beta^*(t) &= \min\left\{\max\left\{\frac{E(\xi_3-\xi_4)}{C_4},0\right\},1\right\}.
\end{aligned} \tag{14}$$

5 Numerical simulations

In this section, MATLAB R2021a simulation software is used, and the *Runge – Kutta* method is used to numerically simulate the differential equation system given in Equation 1. To verify the theoretical analysis results, the impacts of different $\lambda, \theta_1, \theta_2, \alpha, \beta, \bar{k}$ parameters in the model on the propagation process of congestion warning information are analyzed, a sensitivity analysis is conducted on R_0, and the optimal control problem is numerically simulated. Assuming that congestion warning information is initially propagated in a mixed uniform network with N nodes, each node represents the users who can receive congestion warning information, $N(0) = 10000$. In the initial state, there are only 100 propagators, 100 positives, and 100 negatives, namely, $I(0) = P(0) = E(0) = \frac{100}{N} = 0.01, R(0) = 0, S(0) = 1 - I(0) - P(0) - E(0) - R(0) = 0.97$.

In $B = 0.01, \bar{k} = 7, \mu = 0.1, \lambda = 0.3, \theta_1 = 0.5, \theta_2 = 0.6, \eta = 0.2, \alpha = 0.2, \beta = 0.2, \gamma_1 = 0.3, \gamma_2 = 0.3, \xi = 0.6$, the population density changes of the uninformed, active, passive, spreading, and immune users who can receive congestion warning information in $R_0 = 0.3 < 1$ are shown in Figure 2A. In the process of disseminating congestion warning information, the population density values of positive, negative, disseminators, and immune individuals increase first, reaches their peak values, then begin to decrease, and finally become 0; the density of the ignorant population rapidly decreases until it reaches equilibrium. Theorems 2, 3 indicate that when $R_0 < 1$ occurs, congestion warning information will eventually disappear in the propagation network, indicating that the equilibrium point of no congestion warning information is stable. The simulation results shown in Figure 2A further confirm this conclusion.

When $B = 0.1, \bar{k} = 10, \mu = 0.1, \lambda = 0.7, \theta_1 = 0.5, \theta_2 = 0.6, \eta = 0.2, \alpha = 0.2, \beta = 0.2, \gamma_1 = 0.3, \gamma_2 = 0.3, \xi = 0.1$, the population density changes of the ignorant, active, passive, spreading, and immune users who can receive congestion warning information in $R_0 = 35 > 1$ are shown in Figure 2B. In the process of disseminating congestion warning information, as shown in Figure 2B, the population density values of positive, negative, spreading, and immune individuals in the congestion warning information first increase, reaches their peak values, and gradually stabilize. The population density of ignorant individuals gradually decreases until it reaches equilibrium. Theorems 1, 4, 5 indicate that the congestion warning information of the model established in this article has a stable equilibrium point at $R_0 > 1$; that is, it will continue to exist in the network at a certain amount. The simulation results shown in Figure 2B further verify the above conclusion.

Figures 3A–D depict the effects of different parameters in the model on the population density of congestion warning information disseminators. Figure 3A illustrates the trend of the population density of spreaders over time when $B = 0.01, \bar{k} = 10, \mu = 0.1, \theta_1 = 0.5, \theta_2 = 0.6, \eta = 0.2, \alpha = 0.2, \beta = 0.2, \gamma_1 = 0.3, \gamma_2 = 0.3, \xi = 0.6$ and λ take different values. Figure 3B illustrates the trend of the population density of spreaders over time when different values of $B = 0.01, \mu = 0.1, \lambda = 0.3, \theta_1 = 0.5, \theta_2 = 0.6, \eta = 0.2, \alpha = 0.2, \beta = 0.2, \gamma_1 = 0.3, \gamma_2 = 0.3, \xi = 0.6$ and $\bar{k}$ are taken. The results show that the larger λ is, the greater the probability of ignorant individuals spreading congestion warning information, the higher the peak density of the spreader population, and the shorter the time required to reach the peak. The network average λ represents the degree of closeness between users. As $\bar{k}$ increases, the disseminator of congestion warning information

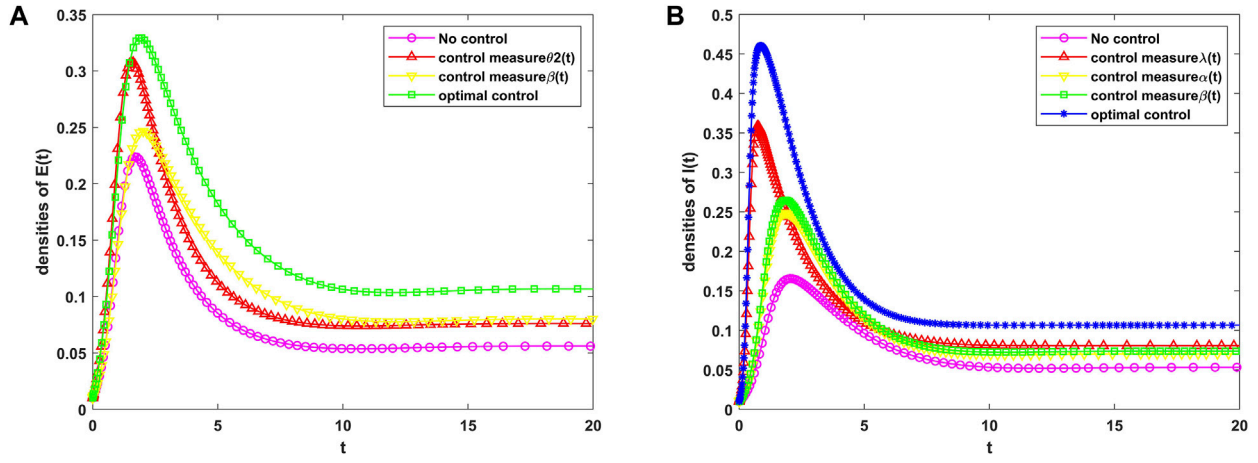

FIGURE 7
Trend of population density of **(A)** $E(t)$ and **(B)** $I(t)$ over time under the different control strategies.

will reach a higher peak in a shorter time. Figures 3A, B show that if ignorant individuals have a greater willingness to share congestion warning information with others or have closer contact with users after being exposed to it, this further promotes the dissemination of congestion warning information and alleviates traffic congestion pressure.

Figure 3C shows the trend of the population density of spreaders over time when $B=0.01,\mu=0.1,\lambda=0.3,\theta_1=0.5,\theta_2=0.6,\eta=0.2,\beta=0.2,\gamma_1=0.3,\gamma_2=0.3,\xi=0.6,\bar{k}=10$ and α take different values. The results show that the larger α is, the more willing people who are negative about congestion warning information are to make changes, realize the adverse effects of congestion on traffic, and share congestion information with others. The peak density of the spreader population is greater, and the time required to reach the peak is shorter. Figure 3D shows the trend of the population density of spreaders over time when $B=0.01,\mu=0.1,\lambda=0.3,\theta_1=0.5,\theta_2=0.6,\eta=0.2,\alpha=0.2,\gamma_1=0.3,\gamma_2=0.3,\xi=0.6,\bar{k}=10$ and β take different values. The results indicate that as the value of β increases, the willingness of congestion warning information enthusiasts to disseminate congestion warning information increases, resulting in a significant increase in the population density of disseminators.

Figure 4 shows the trend of the density of negative individuals over time when $B=0.01,\mu=0.1,\lambda=0.3,\theta_2=0.6,\eta=0.2,\alpha=0.2,\beta=0.2,\gamma_1=0.3,\gamma_2=0.3,\xi=0.6,\bar{k}=10$ and θ_1 take different values. Figure 5 shows the trend of the density of positive individuals over time when $B=0.01,\mu=0.1,\lambda=0.3,\theta_1=0.5,\eta=0.2,\alpha=0.2,\beta=0.2,\gamma_1=0.3,\gamma_2=0.3,\xi=0.6,\bar{k}=10$ and θ_2 take different values. The simulation results show that when an ignorant individual receives congestion warning information, if the ignorant individual tends to travel a shorter distance, the population density of the passive will increase with increasing congestion; if ignorant individuals tend to travel faster, then the population density of positive individuals will increase with increasing θ_2.

6 Discussion

To evaluate the influence of parameters $\bar{k},\lambda,\varepsilon$ on the basic regeneration number R_0, this article conducts a sensitivity analysis on R_0. Based on the previous calculation of $R_0=\frac{\bar{k}B\lambda}{\mu(\mu+\varepsilon)}$, it can be concluded that (Equation 15)

$$\frac{\partial R_0}{\partial \bar{k}}=\frac{B\lambda}{\mu(\mu+\varepsilon)}>0 \tag{15}$$

This means that as $\bar{k}$ increases, the basic regeneration number R_0 also increases, as shown in Figure 6A. This indicates that the greater the closeness between users is, the more conducive they are to the dissemination of congestion warning information; that is, the more people there are in contact with the disseminator, the more likely they are to be to spread congestion warning information.

For parameters λ and ε, it can be obtained that (Equations 16, 17)

$$\frac{\partial R_0}{\partial \lambda}=\frac{\bar{k}B}{\mu(\mu+\varepsilon)}>0 \tag{16}$$

$$\frac{\partial R_0}{\partial \bar{k}}=\frac{-\bar{k}B\lambda}{\mu(\mu+\varepsilon)^2}<0 \tag{17}$$

This means that the basic regeneration number R_0 increases with increasing λ and decreases with increasing ε. As shown in Figure 6B. From this, it can be seen that when ignorant individuals are exposed to congestion warning information, they are more willing to spontaneously spread congestion warning information, which promotes the dissemination of congestion warning information. In addition, if the disseminator is more likely to forget or shift his or her attention to congestion warning information, the dissemination of congestion warning information will be suppressed. In fact, the current speed of updating social information on the internet is extremely fast, and the attention given to irrelevant congestion warning information is very limited. Therefore, the forgetting mechanism has a significant

impact on the dissemination process of congestion warning information.

7 Optimal control simulation

To analyze the impact of the optimal control $(\lambda^*, \theta_2{}^*, \alpha^*, \beta^*)$ on the propagation process of congestion warning information when adopting the optimal control strategy, this section simulates the changes in the active participant $E(t)$ and the disseminator $I(t)$ during the period from $t = 0$ to $t = 20$. The simulation is divided into the following three situations: (1) no control, (2), control of only a single variable, and (3) optimal control strategy.

In the uncontrolled strategy, when $B = 0.1, \mu = 0.1, \lambda = 0.3, \theta_1 = 0.5, \theta_2 = 0.6, \eta = 0.2, \alpha = 0.2, \beta = 0.2, \quad \gamma_1 = 0.3, \gamma_2 = 0.3, \xi = 0.6, \bar{k} = 10$, let $B = 0.1, \mu = 0.1, \lambda = 0.3, \theta_1 = 0.5, \eta = 0.2, \alpha = 0.2, \beta = 0.2, \gamma_1 = 0.3, \gamma_2 = 0.3, \xi = 0.6, \bar{k} = 10$ to control $\theta_2{}^*$, let $B = 0.1, \mu = 0.1, \lambda = 0.3, \theta_1 = 0.5, \theta_2 = 0.6, \eta = 0.2, \alpha = 0.2, \gamma_1 = 0.3, \gamma_2 = 0.3, \xi = 0.6, \bar{k} = 10$ to control β^* and the trend of population density changes among active participants when adopting the optimal control strategy. As shown in Figure 7A, when the optimal control strategy is adopted for $\theta_2{}^*$ and β^*, the density of active participants reaches its maximum value, indicating that the more people tend to be "fast", the wider the dissemination range of congestion warning information, which is beneficial for alleviating traffic congestion pressure.

When $B = 0.1, \mu = 0.1, \lambda = 0.3, \theta_1 = 0.5, \theta_2 = 0.6, \eta = 0.2, \alpha = 0.2, \beta = 0.2, \gamma_1 = 0.3, \gamma_2 = 0.3, \xi = 0.6, \bar{k} = 10$, let $B = 0.1, \mu = 0.1, \lambda = 0.3, \theta_1 = 0.5, \theta_2 = 0.6, \eta = 0.2, \alpha = 0.2, \gamma_1 = 0.3, \gamma_2 = 0.3, \xi = 0.6, \bar{k} = 10$ control β^*, let $B = 0.1, \mu = 0.1, \theta_1 = 0.5, \theta_2 = 0.6, \eta = 0.2, \alpha = 0.2, \beta = 0.2, \gamma_1 = 0.3, \gamma_2 = 0.3, \xi = 0.6, \bar{k} = 10$ control λ^*, let $B = 0.1, \mu = 0.1, \lambda = 0.3, \theta_1 = 0.5, \theta_2 = 0.6, \eta = 0.2, \beta = 0.2, \gamma_1 = 0.3, \gamma_2 = 0.3, \xi = 0.6, \bar{k} = 10$ control α^* and change the density of the spreader population when adopting the optimal control strategy. As shown in Figure 7B, when λ^*, α^* and β^* adopt the optimal control strategy, the density of the spreader population reaches its maximum value. This indicates that the greater the willingness of the ignorant $S(t)$, the passive $P(t)$, and the active $E(t)$ to share congestion warning information is, the more conducive it is to the rapid dissemination of congestion warning information, which is conducive to the quick response of travelers and thus alleviates traffic congestion pressure.

8 Conclusion

In this paper, a congestion warning information dissemination model is constructed by considering the influence of travelers' attitudes on the dissemination of congestion warning information. The basic reproduction number is calculated, and the existence and stability of the equilibrium points of no congestion warning information and congestion warning information in the model are analyzed. The existence of the optimal control of the model is verified, and the optimal control strategy of the model is proposed. In addition, the basic theorem of the model and the impact of changes in various parameters in the simulation model on the propagation process of congestion warning information are verified through numerical simulation, and sensitivity analysis and optimization control simulation are carried out. The research conclusions of this article are as follows:

(1) Based on the combination of two attitudes (positive and negative) of travelers toward road congestion, the SPEIR model for both negative and positive individuals is introduced on the basis of the classic infectious disease model. Moreover, the dissemination of congestion warning information is influenced by the topology of social networks. Therefore, the network average is introduced to characterize the tightness of the social network structure, increasing the realism and reasonableness of the model.

(2) Based on the next-generation matrix method, the basic regeneration number is determined, and the existence and stability of the equilibrium points of congestion free warning information and congestion warning information in the model are evaluated. When the basic regeneration number $R_0 < 1$ is reached, the congestion warning information eventually disappears from the system and reaches stability. When $R_0 > 1$ occurs, congestion warning information will continue to exist in the system and gradually stabilize.

(3) By utilizing optimal control theory, establishing and discussing optimal control problems, and formulating optimal control strategies that simultaneously increase the population density of both positive and disseminator, important reference opinions are provided for controlling or mitigating traffic congestion.

(4) The sensitivity of travelers to road congestion directly affects the dissemination process of congestion warning information. A negative or more inclined attitude toward road congestion after receiving congestion warning information is not conducive to alleviating traffic congestion pressure; if travelers are more sensitive to road congestion, they are more inclined to choose "fast" modes of transportation and have a stronger willingness to share congestion warning information, which is beneficial for preventing and controlling traffic congestion outbreaks. Therefore, relevant departments have taken timely measures to achieve vehicle diversion and real-time push congestion warning information to improve the sensitivity of traveler information, providing a reference for using congestion warning information dissemination models to suppress practical problems of road congestion.

There are some limitations in this paper. First, the average field method is used to construct a congestion warning information dissemination model, without considering the impact of social network heterogeneity on the process of congestion warning information dissemination. Therefore, in the future, congestion warning information dissemination models for different network structures should be investigated. Second, Only MATLAB was used for numerical simulation of the model, but the real process of congestion warning information dissemination is often more complex.

Therefore, in the future, the effectiveness of the model can be further verified in a real network environment, taking into account various individual psychological and behavioral factors, as well as

the dynamic laws of congestion warning information dissemination evolution in a dual-layer coupled online and offline social network.

Data availability statement

The original contributions presented in the study are included in the article/Supplementary Material, further inquiries can be directed to the corresponding author.

Author contributions

HY: Conceptualization, Formal Analysis, Methodology, Writing–original draft, Writing–review and editing. HL: Methodology, Project administration, Supervision, Writing–review and editing. QS: Conceptualization, Formal Analysis, Investigation, Methodology, Supervision, Writing–review and editing. YJ: Formal Analysis, Methodology, Supervision, Writing–review and editing.

Funding

The author(s) declare that financial support was received for the research, authorship, and/or publication of this article. This work was supported by the 2023 Research Outcomes of Basic Scientific Research Projects of Liaoning Provincial Department of Education (JYTZD2023090) and the Liaoning Province Education Science Planning Project (JG20DB070).

Conflict of interest

Author QS was employed by Asset Company.

The remaining authors declare that the research was conducted in the absence of any commercial or financial relationships that could be construed as a potential conflict of interest.

Publisher's note

Supplementary Material

The Supplementary Material for this article can be found online at: https://www.frontiersin.org/articles/10.3389/fphy.2024.1490499/full#supplementary-material

References

1. He J, He Z, Fan B, Chen Y. Optimal location of lane-changing warning point in a two-lane road considering different traffic flows. *Physica a-Statistical Mech Its Appl* (2020) 540:123000. doi:10.1016/j.physa.2019.123000

2. Ahmad M, Chen QC, Khan Z, Ahmad M, Khurshid F. Infrastructure-based vehicular congestion detection scheme for V2i. *Int J Commun Syst* (2019) 32(3). doi:10.1002/dac.3877

3. Anderson JE, Dais JL, Garrard WL, Kornhauser AL. Personal rapid transit—a collection of papers on a new type of urban transportation. *Journal of Dynamic Systems Measurement* (1973) 95(4):440. doi:10.1115/1.3426748

4. Snickars F. Convexity and duality properties of a quadratic intraregional location model. *Reg Sci Urban Econ* (1978) 8(1):5–19. doi:10.1016/0166-0462(78)90009-1

5. Andersson ÅE, Marksjö B. General equilibrium models for allocation in space under interdependency and increasing returns to scale. *Reg Urban Econ* (1972) 2(2): 133–58. doi:10.1016/0034-3331(72)90020-6

6. Smith K, Krishnamoorthy M, Palaniswami M. Neural versus traditional approaches to the location of interacting hub facilities. *Location Sci* (1996) 4(3):155–71. doi:10.1016/s0966-8349(96)00017-4

7. O'kelly ME. A quadratic integer program for the location of interacting hub facilities. *Eur J Oper Res* (1987) 32(3):393–404. doi:10.1016/s0377-2217(87)80007-3

8. McDonald GT, Brown A. The land suitability approach to strategic land-use planning in urban fringe areas. *Landscape Plann* (1984) 11(2):125–50. doi:10.1016/0304-3924(84)90035-2

9. Heffley DR. Decomposition of the koopmans-beckmann problem. *Reg Sci Urban Econ* (1980) 10(4):571–80. doi:10.1016/0166-0462(80)90018-6

10. Yilmaz Ö, Görgu L, O'Grady MJ, O'Hare GMP. Cloud-assisted mobile crowd sensing for route and congestion monitoring. *Ieee Access* (2021) 9:157984–96. doi:10.1109/access.2021.3129932

11. Yang YT, Chou LD, Tseng CW, Tseng FH, Liu CC. Blockchain-based traffic event validation and trust verification for vanets. *Ieee Access* (2019) 7:30868–77. doi:10.1109/access.2019.2903202

12. Shi ZY, Chen YZ, Liu JC, Fan DC, Liang CQ. Physics-informed spatiotemporal learning framework for urban traffic state estimation. *J Transportation Eng A-Systems* (2023) 149(7). doi:10.1061/jtepbs.Teeng-7545

13. Ning HJ, An YS, Wei YX, Wu NQ, Mu C, Cheng HH, et al. Modeling and analysis of traffic warning message dissemination system in vanets. *Vehicular Commun* (2023) 39:100566. doi:10.1016/j.vehcom.2022.100566

14. Humayun M, Afsar S, Almufareh MF, Jhanjhi NZ, AlSuwailem M. Smart traffic management system for metropolitan cities of kingdom using cutting edge technologies. *J Adv Transportation* (2022) 2022:1–13. doi:10.1155/2022/4687319

15. Jiang P, Liu ZK, Zhang LF, Wang JZ. Advanced traffic congestion early warning system based on traffic flow forecasting and extenics evaluation. *Appl Soft Comput* (2022) 118:108544. doi:10.1016/j.asoc.2022.108544

16. Zhang C, Liu TL, Huang HJ, Chen J. A cumulative prospect theory approach to commuters' day-to-day route-choice modeling with friends' travel information. *Transportation Res C-Emerging Tech* (2018) 86:527–48. doi:10.1016/j.trc.2017.12.005

17. Chen Y, Frei A, Mahmassani HS. From personal attitudes to public opinion information diffusion in social networks toward sustainable transportation. *Transportation Res Rec* (2014) 2430(2430):28–37. doi:10.3141/2430-04

18. Yu Y, A XH, Jia B, Jiang R, Gao ZY, Zhang HM. Is providing inaccurate pre-trip information better than providing No information in the morning commute under stochastic bottleneck capacity? - sciencedirect. *Transportation Res C: Emerging Tech* (2021) 126:103085. doi:10.1016/j.trc.2021.103085

19. Han X, Sun Q, Xing Y, Gao Z-Y, Zhang HM. Reducing strategic uncertainty in transportation networks by personalized routing advice: a route-choice laboratory experiment. *Trav Behav Soc* (2024) 34:100701. doi:10.1016/j.tbs.2023.100701

20. Khoo HL, Asitha KS. An impact analysis of traffic image information system on driver travel choice. *Transportation Res A-Policy Pract* (2016) 88:175–94. doi:10.1016/j.tra.2016.03.014

21. Huang JH, Sun MG, Cheng Q. Congestion risk propagation model based on multi-layer time-varying network. *Int J Simulation Model* (2021) 20(4):730–41. doi:10.2507/ijsimm20-4-585

22. Zhou Y, Li Y, Jiang R, Geng E. Dynamic analysis of interactive transmission of warning information and traffic congestion. *J Geo-Information Sci* (2017) 19(10): 1279–86. doi:10.3724/SP.J.1047.2017.01279

23. Huang J, Sun M. Multi-network congestion risk propagation model considering driver behavior. *J Transporation Syst Eng and Inf Tech* (2021) 21(1):8–15. doi:10.2507/ijsimm20-4-585

24. Yang YR, Sun GX, Bin S. A two-tier network traffic congestion propagation model considering multiple warning messages complex systems and. *Complexity Sci* (2023) 1–9. doi:10.13306/j.1672-3813

25. Saberi M, Hamedmoghadam H, Ashfaq M, Hosseini SA, Gu Z, Shafiei S, et al. A simple contagion process describes spreading of traffic jams in urban networks. *Nat Commun* (2020) 11(1):1616. doi:10.1038/s41467-020-15353-2

26. Jia C, Zheng SY, Qian HQ, Cao BX, Zhang KT. Analysis of crowded propagation on the metro network. *Sustainability* (2022) 14(16):9829. doi:10.3390/su14169829

27. Chen YT, Yan QP, Mao JN, Huang H, Liu L. Urban traffic congestion propagation model based on SIS propagation theory. *J Chongqing Jiaotong University(Natural Science)* (2023) 42(06):103–10.

28. Ma WC, Zhang P, Zhao X, Xue LY. The coupled dynamics of information dissemination and seir-based epidemic spreading in multiplex networks. *Physica a-Statistical Mech Its Appl* (2022) 588:126558. doi:10.1016/j.physa.2021.126558

29. She BK, Liu J, Sundaram S, Paré PE. On a networked sis epidemic model with cooperative and antagonistic opinion dynamics. *Ieee Trans Control Netw Syst* (2022) 9(3):1154–65. doi:10.1109/tcns.2022.3145748

30. Nian FZ, Guo X, Li JZ. A new spreading model in the environment of epidemic-related online rumors. *Mod Phys Lett B* (2022) 36(04). doi:10.1142/s0217984921505692

31. Ojha RP, Srivastava PK, Awasthi S, Srivastava V, Pandey PS, Dwivedi RS, et al. Controlling of fake information dissemination in online social networks: an epidemiological approach. *Ieee Access* (2023) 11:32229–40. doi:10.1109/access.2023.3262737

32. van den Driessche P, Watmough J. Reproduction numbers and sub-threshold endemic equilibria for compartmental models of disease transmission. *Math biosciences* (2002) 180:29–48. doi:10.1016/s0025-5564(02)00108-6

frontiers | Frontiers in Physics

TYPE Original Research
PUBLISHED 17 October 2024
DOI 10.3389/fphy.2024.1491365

OPEN ACCESS

EDITED BY
Xuzhen Zhu,
Beijing University of Posts and Telecommunications (BUPT), China

REVIEWED BY
Shimin Cai,
University of Electronic Science and Technology of China, China
Wei Wang,
Chongqing Medical University, China
Run-Ran Liu,
Hangzhou Normal University, China

*CORRESPONDENCE
Huajian Xue,
xuehj@tlu.edu.cn
Tieliang Gao,
chrisgtl2012@163.com

RECEIVED 04 September 2024
ACCEPTED 02 October 2024
PUBLISHED 17 October 2024

CITATION
Li J, Xue H, Tang Q, Wang H and Gao T (2024) SABTR: semantic analysis-based tourism recommendation.
Front. Phys. 12:1491365.
doi: 10.3389/fphy.2024.1491365

SABTR: semantic analysis-based tourism recommendation

Jiao Li[1,2], Huajian Xue[3,4]*, Qigui Tang[1], Hailiang Wang[5] and Tieliang Gao[1,2]*

[1]Key Laboratory of Data Analysis and Financial Risk Prediction, Xinxiang University, Xinxiang, China, [2]Business School, Xinxiang University, Xinxiang, China, [3]College of Mathematics and Computer Science, Tongling University, Tongling, China, [4]Anhui Engineering Research Center Of Intelligent Manufacturing of Copper-based Materials, Tongling University, Tongling, China, [5]College of Electronic Information and Optical Engineering, Nankai University, Tianjin, China

Online tourism spot recommendations, as a key component of tourism services, aim to present travel options that align with users' personal preferences. However, current recommendation systems often underperform due to the sparsity of tourism data and the wide variance in user preferences. To address this challenge, we propose a Semantic Analysis-Based Tourism Recommendation framework, abbreviated as SABTR (Semantic Analysis-Based Tourism Recommendation). The framework comprises two stages: Firstly, Latent Dirichlet Allocation (LDA) models are utilized to deeply mine data between users and attractions, constructing two core matrices: the user similarity matrix and the attraction similarity matrix. Secondly, based on the user similarity matrix, similarity calculation methods are applied to predict ratings for tourism spots that users have not yet evaluated. Simultaneously, within the attraction similarity matrix, probability distributions for each attraction across various thematic interests are calculated. When the system identifies a user's interest in specific types of attractions, SABTR can select a series of related attractions from associated interest tags. Then, these candidate attractions are ranked according to both known and predicted user ratings, ultimately forming personalized attraction packages recommended to users. Extensive experiments have demonstrated that compared to existing tourism recommendation solutions, our method significantly improves the quality of attraction recommendations and enhances user satisfaction.

KEYWORDS

LDA, tourism recommendation, semantic analysis, similarity of users, rating prediction

1 Introduction

With the continuous development of tourism resources and the rapid advancement of information technology, a large amount of tourism resource information can be easily accessed by users through websites and travel applications. However, confronted with a vast array of options for tourist attractions, users often feel confused and hesitant when making choices. To improve the experience of tourists when selecting travel services, various tourism recommendation solutions have been introduced by both industry and academia. These aim to provide better travel experiences and intelligent services for tourists.

Hsieh et al. proposed a Bi-LSTM model in [1] to train on user travel time series data, predicting the migration of users' interest in tourist attractions through adaptively learned parameters. Ma et al. in [2] leveraged differential game theory and Bellman's continuous dynamic programming theory to generate more personalized low-carbon travel plans for

tourists, enhancing their environmental awareness and stimulating low-carbon, efficient, and sustainable development within the tourism supply chain. Yao et al. proposed a new Neural Network-enhanced Hidden Markov Structure Time Series Model in [3]. The model uses a neural network for trends and a hidden Markov model with four parts for seasonality: cyclical patterns, unexpected events, event intensity, and random errors. It was tested on US tourism data from 12 countries to suggest travel packages.

These tourism recommendation schemes have promoted the development of the tourism industry and enhanced the overall level of tourism public services. However, these methods do not delve deeply into the characteristics of tourism recommendations. Firstly, user-tourism data is quite sparse, making it difficult for traditional similarity algorithms to uncover the diverse interest distributions of users. Secondly, user ratings for tourism items are also sparse, making it hard to determine users' preferences for tourism items. Lastly, the temporal context of tourists choosing attractions is also a factor that needs to be considered in tourism recommendations. In response to these characteristics of tourism recommendations, we designed a probabilistic semantic analysis-based tourism recommendation algorithm called SABTR. This algorithm can extract user interests from sparse datasets, predict missing ratings for tourism items by tourists, and finally generate a list of tourism items that match tourists' preferences based on their behavior. The proposed SABTR approach can integrate tourists' hidden preferences (such as clicks and favorites) with their direct preferences (such as ratings and likes), ensuring the accuracy of tourists' interests while also ensuring the diversity of user interests. The specific work is as follows:

- We use a semantic analysis model to obtain the distribution of tourist interests by training history records of tourists. Based on this distribution, we design a user similarity algorithm. By aggregating ratings between similar users, we can infer missing tourism item evaluations for users.
- We design an online tourism recommendation scheme. When a tourist clicks on an interesting tourism item, we analyze the interest distribution associated with the item and its ratings to recommend high-rated tourism items that align with the tourist's interests.

The proposed scheme has been extensively tested on experimental datasets, and compared to other baseline algorithms, our method shows better accuracy and recall in tourism recommendations. Diverse interest-based attraction recommendations also provide a better service experience for users. The remaining sections of this paper are organized as follows: Initially, we will provide a review of the existing literature, clearly delineating the differences between the methodologies proposed in this study and those currently employed. Subsequently, we will present a detailed description of the framework of the proposed scheme, explaining how it effectively extracts user interests and predicts missing ratings for tourism projects. Furthermore, we will evaluate the effectiveness and efficiency of the proposed scheme through a series of experiments, summarizing the advantages and shortcomings of the algorithm in the conclusion section, and providing an outlook on future research work.

2 Related works

In this section, we review previous research achievements in tourism recommendation.

Yang et al. conducted an online survey collecting data from 496 users in the Ctrip dataset [4] and performed extensive experiments using Partial Least Squares Structural Equation Modeling (PLS-SEM) on the data. They concluded that perceived personalization, the visual appearance of tours, and the quality of provided travel information can meet users' personalized needs. Gasmi et al. [5] consider itinerary planning and travel recommendations as crucial tasks in tourism personalization. Since tourists are typically unfamiliar with points of interest (POIs) in new cities, They must choose and arrange points of interest (POIs) that suit their preferences, considering factors like starting point and travel time. Researchers suggest using Multi-Objective Evolutionary Algorithms (MOEAs) to find recommendations that balance two goals. Their experimental results on a dataset from Flicker demonstrate the efficiency of the proposed algorithm in generating personalized itinerary recommendation rules, which can help tourists plan their trips in unfamiliar towns. Ding et al., in reference [6], considered the travel itinerary planning problem under a total time constraint and uncertain travel times. This problem requires making a two-stage decision: first, selecting tourist attractions from a set of candidates to maximize the popularity utility for the tourist; second, planning the visiting sequence of these attractions under random travel times to maximize the activity utility for the tourist. Therefore, the paper constructs a two-stage stochastic optimization model with chance constraints for recommending tourist attractions. Compared to the benchmark model, the proposed model improves the recommendation accuracy by nearly 40%. Chen et al., in reference [7], suggest a model called Dynamic Trust Network-based Fuzzy Group Recommendation (DTN-FGR). It turns user ratings into Fuzzy Preference Relations to handle varying evaluation standards. It also uses a PageRank method to calculate user trust scores. This DTN-FGR model shows the best consistency compared to other group recommendation models. Liu et al. [8] suggest using historical check-ins from Location-Based Social Networks (LBSNs) to understand user preferences and boost tourism. A new privacy-focused POI recommendation model is proposed, combining a simplified Graph Convolutional Neural Network (GCN) with user privacy settings. This model offers efficient POI suggestions while safeguarding user privacy. Chen et al. [9] Show through research that metaverse tourism differs from physical travel. Experts say that tailor-made travel choices, socializing, immersive experiences, and getting visitor feedback can significantly improve the travel experience. Ding et al., in reference [10], sought to understand what motivates customers to leave positive or negative feedback. Analyzing over 10,000 Airbnb reviews, researchers used a structural topic model to uncover hidden themes linked to recommendation intentions. They found that positive feedback is mainly driven by the enjoyment of the experience, whereas negative feedback is linked to practical concerns and utilitarian value. Gamidullaeva et al., in reference [11], highlight the importance of combining diverse approaches to create a universal system for recommending travel information when customizing itineraries. The research goal is to introduce a

concept for a system that can suggest personalized travel routes. This concept includes processes for gathering and preparing data to create tourism offerings, techniques for tailoring these offerings to individual preferences, and the key steps to put these techniques into action. Chen et al., in reference [12], suggest a framework called GRM-RTrip, which uses graph networks to understand Points of Interest (POIs) from different angles, calculating the chances of moving from one POI to another. This information is then used to predict what users might like. The system treats trip planning like a game, using smart learning to create trips that give the best experience. Tests show it does better than other ways of suggesting trips. Nilashi, in reference [13], claims that Multi-Criteria Collaborative Filtering (MCCF), which considers various product features, offers more dependable and efficient recommendations on shopping sites. The study introduces a new recommendation agent using MCCF to enhance travel site recommendation systems. Extensive testing proves this method can accurately suggest relevant travel options to users, even with limited data.

Majid et al., in reference [14], examined sustainability and tourist involvement as key factors for sustainable development in tourism. They identified 23 AI innovations that could shape future research in this area. The study points out a current shortfall in AI solutions that fully address sustainability and tourist interaction. It also highlights blockchain's potential to revolutionize tourism and hospitality due to its transparency and efficiency. Jain et al. [15] analyzed 56 papers from 2012 to 2022 to uncover gaps in how technology is viewed in tourism. The research summarized key issues and proposed future study paths using a TCM framework. It also positioned tourism as a prime candidate for sustainable virtual investments in the metaverse. Kou et al., in reference [16], explore the application of the Balanced Scorecard for evaluating sustainable investment options in sectors like metaverse tourism. They suggest a hybrid approach combining quantum, spherical, and fuzzy decision-making to prioritize sustainable investment opportunities in the metaverse's tourism sector. Zheng et al. [17] concentrate on disabled tourists who are otherwise capable of traveling, recognizing that tourism could open up new patient-centered care options. The study discusses the challenges of conducting empirical research with tourists who have mental health issues. The paper recommends strategies like setting clear participant criteria, using randomized controlled trials, and adopting comprehensive health research methods. The research could guide tourism management and marketing efforts aimed at these groups. Abbasi-Moud et al. [18] suggested a tourism recommendation system based on user preferences. It starts by gathering user reviews from travel social networks to identify their likes. The reviews are then cleaned up, grouped by topic, and analyzed for sentiment to understand what tourists want. For each point of interest (POI), features are extracted from all the reviews about it. The system then suggests POIs that best match a user's preferences by comparing them semantically. This approach aims to improve on the inaccuracy of standard travel route recommendation algorithms. Esmaeili et al. [19] suggested a social commerce-based hybrid recommendation system to tailor tourist attraction lists to individual tourists, considering their preferences, trust, reputation, social ties, and communities. The method, which factors in multiple elements, was found to be superior to standard collaborative filtering, content-based, and hybrid recommendation techniques in experiments. Cheng et al., in reference [20], suggested an algorithm for recommending travel routes that considers users' interests and the distances between places. It begins by examining users' past travel patterns. The algorithm then determines users' preferences for certain themes and distances based on how long they spend at each attraction. It calculates the best route considering time limits, starting and ending locations. Tests using data from Flickr indicate that this algorithm is more accurate and has better recall than existing methods.

Previous methods identified similar tourism resources by calculating similarity, which could potentially lead to the echo chamber effect, limiting users' ability to discover potential points of interest. In contrast, our proposed algorithm, SABTR (Semantic Analysis Based on User's Behavioral Traces), aims to identify users' interests through semantic analysis. By analyzing users' behaviors such as clicks, favorites, and ratings on tourism resources, the algorithm determines users' preferences for specific types of tourism resources, rather than simply finding similar resources. This approach significantly broadens the scope of users' interests and enhances the accuracy of the tourism recommendation system by employing a rating-based sorting mechanism within similar interest resources, thereby better meeting users' personalized needs.

3 The proposed SABTR method

3.1 The overview of the SABTR

As shown in Figure 1, the proposed SABTR framework includes both an offline training component and an online analysis component. In the offline training phase, records of tourists' visits to tourist attractions are input into the SABTR framework for matrix factorization. The semantic analysis algorithm LDA (Latent Dirichlet Allocation) within SABTR can decompose the tourist-tourist attraction data into two matrices using the Gibbs sampling algorithm [21]: the tourist-interest topic matrix and the interest topic-tourist attraction matrix. In the tourist-interest topic matrix, the distribution of a tourist's interests is considered as the feature vector of the tourist, and then users with similar interests are clustered based on the similarity of these feature vectors. In the interest topic-tourist attraction matrix, for each tourist attraction, the topic distribution is counted and ranked according to the topic probability values.

For the online recommendation phase, when a user clicks on an interesting tourist attraction or rates one, based on the topic distribution of this attraction, several items from each topic are selected and added to the candidate recommendation list according to their topic probabilities. Then, the candidate items are sorted by their predicted ratings, and a suitable recommendation list is generated and sent to the user. The number of interest topics, the length of the recommendation list, and how many tourist attractions are returned for each interest topic will be determined through extensive experimentation in the experimental section.

3.2 Semantic analysis in the training phase

In real-life scenarios, tourists often select travel destinations based on their personal travel preferences. From the perspective of

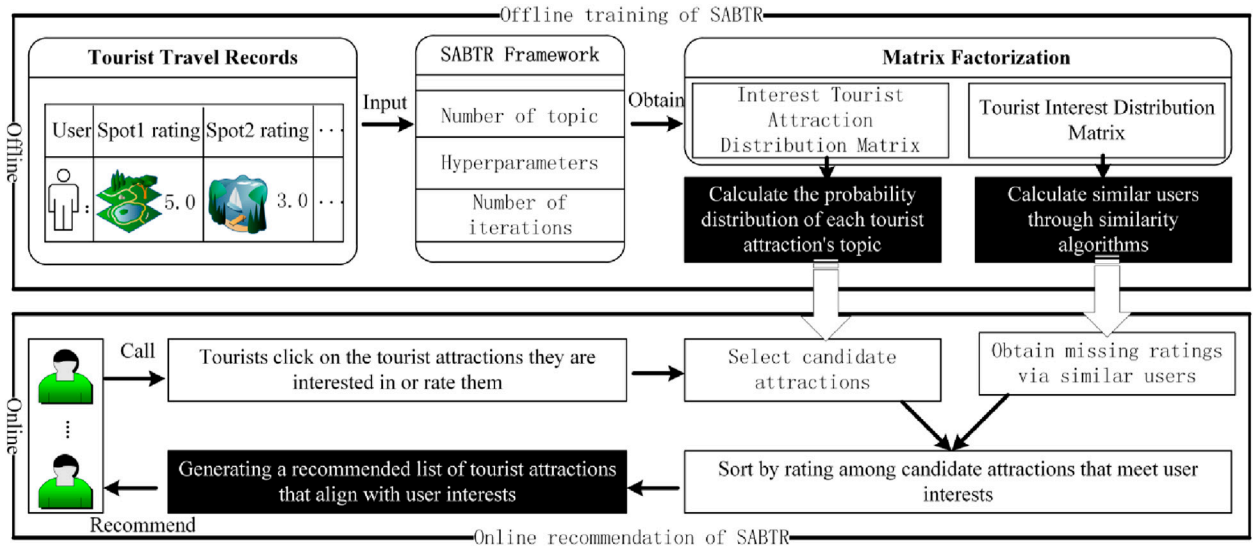

FIGURE 1
The Overview of SABTR Scheme. The SABTR scheme includes two stages: offline training and online recommendation. During the offline training phase of the model, a probability vector reflecting tourists' interest preferences was constructed by applying semantic analysis algorithms, and the distribution probability of attractions corresponding to each theme was analyzed. Based on these two vector matrices, the model is capable of predicting the missing ratings for attractions and determining the thematic affiliation of attractions. In the online recommendation phase, the model utilizes the thematic probability distribution of attractions and the predicted missing ratings to generate a list of recommended attractions with rating information for tourists.

probabilistic topic models, the process of tourists choosing attractions can be broken down into two steps: first, tourists pick out themes from a variety of travel topics that interest them; then, they select specific attractions to visit within those themes. The goal of a travel recommendation system is to analyze tourists' historical data, uncover their latent interests, and recommend attractions that align with their preferences.

Since tourists' interests are a latent variable, in our proposed Semantic Analysis-Based Tourist Recommendation system (SABTR), we employ the LDA (Latent Dirichlet Allocation) model to construct tourists' interest themes. LDA is a soft-clustering model that allows data points to be assigned to multiple categories with different probabilities, which means that attractions belonging to the same category share similar latent semantic features. Consequently, attractions with similar semantic features can be recommended to tourists who are interested in these features. Let the set of tourists be denoted as U, the set of themes as Z. In the context of travel recommendations, the themes associated with attractions can be considered as the interests of the users. Let the set of attractions be denoted as S. Let a user's attraction record be represented as a vector $\vec{s}$, and the thematic affiliation of each attraction as a vector $\vec{z}$. Then, the user semantic analysis in the proposed scheme is how to derive the thematic interests $\vec{z}$ of attractions based on the user's attraction record $\vec{s}$, i.e., solving for $p(\vec{z}\,|\,\vec{s})$. In the scheme, $(\vec{s},\vec{z})$ is considered as random variables, and the distribution of the variables is shown in the following formula:

$$p\left(\vec{s},\vec{z}\mid\alpha,\beta\right)=\prod_{k=1}^{K}\frac{\Delta\left(\vec{n}_k+\beta\right)}{\Delta\left(\beta\right)}.\prod_{m=1}^{M}\frac{\Delta\left(\vec{n}_m+\alpha\right)}{\Delta\left(\alpha\right)},\ \vec{n}_m=\left\{\vec{n}_m^{(k)}\right\}_{k=1}^{K}\quad(1)$$

where $\vec{\mathrm{n}}_m$ refers to the m-th tourist's topic distribution, and $\vec{\mathrm{n}}_k$ refers to the distribution of attractions for the k-th topic. $\vec{\mathrm{n}}_m^{(\mathrm{k})}$ represents the number of attractions in the k-th topic of the m-th tourist, and α and β are the hyperparameters of the Dirichlet distribution, while $\Delta(\alpha)$ and $\Delta(\beta)$ are the regularization factors in the Dirichlet distribution.

In the proposed SABTR algorithm, in order to cluster tourists and attractions, it is necessary to solve for $p(\mathrm{z_k}|\mathrm{u_m})$ and $p(\mathrm{s_t}|\mathrm{z_k})$ within the aforementioned probability distribution. $p(\mathrm{z_k}|\mathrm{u_m})$ refers to the probability of the m-th tourist's the k-th topic, which can be represented by θ_{mk}, and $p(\mathrm{s_t}|\mathrm{z_k})$ refers to the probability of the t-th attraction belonging to topic k, which can be represented by ϕ_{kt}. Since the topic interests are latent variables, it is difficult to directly estimate parameters $p(\mathrm{z_k}|\mathrm{u_m})$ and $p(\mathrm{s_t}|\mathrm{z_k})$ using maximum likelihood estimation. Therefore, this paper employs the Gibbs sampling algorithm to estimate these parameters.

In the initial step, each attraction is assigned a random topic, then during the sampling process, the topic transition probability of the target attraction is obtained using the interest distribution of other attractions (excluding the target attraction). Assuming an observed variable for an attraction $s_i = t$, where i = (m, n) is a subscript indicating the travel record of the n-th attraction for tourist $\mathrm{u_m}$. Using Bayes' theorem, we can obtain the sampling expression for the interest of attractions (i.e., the conditional probability of the attractions), as shown in the following formula:

$$\begin{aligned}p\left(\mathrm{z_i}\middle|\vec{\mathrm{z}}_{\neg\mathrm{i}},\vec{\mathrm{s}}\right)&=\frac{p\left(\vec{\mathrm{s}},\vec{\mathrm{z}}\right)}{p\left(\vec{\mathrm{s}},\vec{\mathrm{z}}_{\neg\mathrm{i}}\right)}=\frac{p\left(\vec{\mathrm{s}}\middle|\vec{\mathrm{z}}\right)}{p\left(\vec{\mathrm{s}}_{\neg\mathrm{i}}|\vec{\mathrm{z}}_{\neg\mathrm{i}}\right)}.\frac{p\left(\vec{\mathrm{z}}\right)}{p\left(\vec{\mathrm{z}}_{\neg\mathrm{i}}\right)}\propto\frac{\Delta\left(\vec{\mathrm{n}}_z+\beta\right)}{\Delta\left(\vec{\mathrm{n}}_{z,\neg\mathrm{i}}+\beta\right)}.\frac{\Delta\left(\vec{\mathrm{n}}_m+\alpha\right)}{\Delta\left(\vec{\mathrm{n}}_{m,\neg\mathrm{i}}+\alpha\right)}\\&=\frac{n_{k,\neg i}^{(\mathrm{t})}+\beta}{\sum_{t=1}^{V}\left(n_{k,\neg i}^{(\mathrm{t})}+\beta\right)}.\frac{n_{\mathrm{m},\neg i}^{(\mathrm{k})}+\alpha}{\left[\sum_{k=1}^{K}\left(n_{\mathrm{m},\neg i}^{(\mathrm{k})}+\alpha\right)\right]-1}\end{aligned}\quad(2)$$

where $\vec{z}_{\neg i}$ represents the current topic setting of all attractions except for attraction s_i, $n^{(t)}_{k,\neg i}$ indicates the number of other attractions (excluding attraction s_i) that have been assigned interest k, and $n^{(k)}_{m,\neg i}$ indicates the number of times attractions other than s_i, which belong to interest k, have been selected by tourists.

The conditional probability of an attraction's interest can be obtained from Equation 2, where in each iteration, every attraction is assigned a new interest through a roulette wheel algorithm. After the model converges, each attraction in every tourist's historical record will be assigned a theme. $\vec{\theta}_m$ refers to the topic distribution of the m-th tourist, and $\vec{\phi}_k$ refers to the attraction distribution of the k-th topic. The distributions of $\vec{\theta}_m$ and $\vec{\phi}_k$ follow the Multinomial distribution, and the prior of these two distribution belong to the Dirichlet distribution. By leveraging the conjugate property of the Dirichlet-Multinomial, it can be deduced that the posterior distributions of $\vec{\theta}_m$ and $\vec{\phi}_k$ follow the Dirichlet distribution. We can obtain the interest distribution of tourists θ_{mk} and the attraction distribution of interests ϕ_{kt} via the expectations of $Dir(\vec{\theta}_m|\vec{n}_{m,\neg i} + \alpha)$ and $Dir(\vec{\theta}_m|\vec{n}_{m,\neg i} + \alpha)$. The expressions are as follows:

$$\begin{aligned}\theta_{mk} &= p(z_k|u_m) = \frac{n^{(k)}_{m,\neg i} + \alpha_k}{\sum_{k=1}^{K}\left(n^{(k)}_{m,\neg i} + \alpha_k\right)} \\ \phi_{kt} &= p(s_t|z_k) = \frac{n^{(t)}_{k,\neg i} + \beta_t}{\sum_{t=1}^{V}\left(n^{(t)}_{k,\neg i} + \beta_t\right)}\end{aligned} \tag{3}$$

3.3 The creation of the tourism recommendation list

When parameters $p(z_k|u_m)$ and $p(s_t|z_k)$ are obtained, candidate attraction selection and similar user selection can be performed. Based on the obtained $p(z_k|u_m)$ the tourist's interest characteristics are transformed into an interest distribution vector. Let the interest distribution vector for the m-th user be denoted as $\bar{u}_m$, then the interest distribution vector for $\bar{u}_m$ is shown in the following formula:

$$\bar{u}_m = [p(z_1|u_m), p(z_2|u_m), \ldots p(z_k|u_m)] \tag{4}$$

Based on the cosine similarity formula for vectors, the similarity between users can be obtained, as shown in the following formula:

$$Sim\_val(u_o, u_i) = \mathrm{Cos}(\bar{u}_0, \bar{u}_i) = \frac{\bar{u}_0 \cdot \bar{u}_i}{\|\bar{u}_0\| \times \|\bar{u}_i\|} \tag{5}$$

where $Sim\_val(u_o, u_i)$ represents the numerical similarity between the target tourist u_o and other tourists u_i. $\|\bar{u}_0\|$ and $\|\bar{u}_i\|$ represent the magnitudes of the interest vectors for the target tourist and similar tourists, respectively. Tourists are considered valid similar tourists only after their similarity reaches a certain threshold. The condition for the similarity between tourists is shown in the following formula:

$$Sim(u_o) = \{u_i \mid Sim\_val(u_o, u_i) \geq \mu, u_o \neq u_i\} \tag{6}$$

where μ is the threshold for similarity, and $Sim(u_o)$ represents the similarity that meet the threshold. The ratings of these similar tourists for attractions can be used to predict missing ratings. After selecting similar users for each visitor, based on the attraction ratings from these similar users, the missing rating for the attraction by the tourist can be obtained. Considering the different rating styles of tourists, the prediction formula for the attraction rating is as follows:

$$\hat{r}_{u_o,s_t} = \tilde{u}_o + \frac{\sum_{u_i \in Sim(u_o)} Sim\_val(u_o, u_i) \cdot \left(r_{u_i,s_t} - \tilde{u}_i\right)}{\sum_{u_i \in Sim(u_o)} Sim\_val(u_o, u_i)} \tag{7}$$

where $\hat{r}_{u_o,s_t}$ indicates the predicted rating for the unrated attraction s_t by the tourist u_o, $\tilde{u}_o$ and $\tilde{u}_i$ represent the average ratings of the attractions by the tourist u_o and the similar tourists u_i,respectively. r_{u_i,s_t} denotes the rating of the attraction s_t by the tourist u_i.

After obtaining the ratings of attractions by tourists through the aforementioned strategy, these ratings can be used to rank the recommended attractions for tourists. When a tourist clicks on an attraction, the SABTR scheme calculates the probability of the theme classification for this attraction based on $p(s_t|z_k)$. Generally, an attraction may belong to multiple themes. Attractions under these themes could all be of interest to the tourist. We select multiple attractions from each theme and sort them according to their predicted ratings. The top-r attractions from the sorted list are then added to the recommendation list. The recommendation list for attractions is shown in the following formula:

$$\mathrm{Re}(s_i) = \left\{ s^r_{z_k} \middle| N\left(\sum_{r=1}^{R}\sum_{k=1}^{K} s^r_{z_k}\right) = L, \left(s_i, s^r_{z_k}\right) \in \bar{z}_k, \widehat{r}\left(s^1_{z_k}\right) \geq \widehat{r}\left(s^r_{z_k}\right) \right\} \tag{8}$$

where $\mathrm{Re}(s_i)$ is the recommendation list for the attraction s_i, and $\widehat{r}(s^1_{z_k})$ represents the attractions that belong to the topic z_k and have the highest ratings or predicted ratings. The variable r signifies the number of attractions selected from each theme. After an attraction is bookmarked, clicked, or rated by a tourist, semantic analysis is conducted on the attraction to determine the probability of its belonging to certain topics, and then the top r attractions are selected from each theme based on their ratings to be included in the recommendation list. The specific values and value ranges for the aforementioned parameters will be discussed in detail during the experimental phase.

4 Experiments

This section introduces the experimental dataset, evaluation criteria, baseline algorithms, algorithm performance comparison.

4.1 Dataset description

In the experimental phase, the required data includes the IDs of tourists, the tourist attractions they visit, and the ratings given by tourists to these attractions. Previous tourism datasets, such as dataset-tourist-attractions.csv and KG-Rec-Sys-Tourism-SG-main, either only contain information about attractions or have insufficient records of user visits to these attractions. To more effectively validate the proposed solution, this paper adapts the MovieLens (1M) dataset to the tourism recommendation scenario.

The rating.csv file can be used to simulate the rating data of attractions, while the movie.csv file can simulate the record of tourist attraction visits.

4.2 Experimental evaluation criteria

This paper uses Precision, Recall, and F1-measure to evaluate the performance of tourist attraction recommendations, uses RMSE (Root Mean Square Error) to measure the error between predicted and actual attraction ratings, and uses perplexity to assess the performance of semantic analysis models. The evaluation criteria are as follows:

$$
\begin{aligned}
&Perplexity = exp \wedge \left\{ -\left(\sum_{t=1}^{V} log\ (p(s_t)) \right) / (V) \right\} \\
&where \left[p(s_t) = \sum_{k=1}^{K} \sum_{m=1}^{M} p(s_t|z_k).p(z_k|u_m) \right] \\
&Precision(s) = \frac{N\left(Re(s) \cap U_{re,\neg s}\right)}{L} \\
&Recall(s) = \frac{N\left(Re(s) \cap U_{re,\neg s}\right)}{N\left(U_{re,\neg s}\right)} \\
&F1 - measure(s) = \frac{2.Precison.Recall}{Precison + Recall} \\
&RMSE = \sqrt{\frac{\sum_{u_i,s_j \in record(u_i(s))} \left(r_{u_i,s_j} - \hat{r}_{u_i,s_j}\right)^2}{N[record(u_i(s))]}}
\end{aligned}
\tag{9}
$$

Where V represents the total number of attractions, and the lower the perplexity value, the better the model's performance. Precision measures the accuracy of the attraction recommendations, Recall indicates the coverage rate of the attraction recommendations, and the F1-measure is a comprehensive evaluation metric of both precision and recall. $Re(s)$ represents the recommended list generated by the system after the user selects the attraction s. $U_{re,\neg s}$ represents the record of attractions visited by tourists (excluding the currently selected attraction s). r_{u_i,s_j} represents the actual rating of attraction s_j by the tourist u_i, and r_{u_i,s_j} represents the actual rating of attraction s_j by the tourist u_i.

4.3 The baseline algorithms

In this paper, we utilized high-performance experimental equipment, including an Intel Xeon 3206R CPU, 32 GB DDR4 memory, a 2x2 TB RAID hard drive configuration, and an NVIDIA RTX 3090 GPU, to ensure the accuracy and efficiency of the algorithm comparison. We conducted a comparative analysis of the recommendation system performance of the SABTR algorithm proposed in the paper with PLSA [22], LSI [23], and Skip-gram [24] algorithms.

PLSA and LSI, as fundamental topic models, can infer the distribution of users' interests by analyzing their historical records. The Skip-gram algorithm, on the other hand, is a word vector model that can convert attractions into distributed vector representations, and then recommend similar attractions to users by calculating the similarity between vectors.

To comprehensively evaluate the performance of these algorithms, we designed a series of experiments to measure from multiple dimensions, including precision, recall, and F1-score. Through these experiments, we aim to verify the advantages and limitations of the SABTR algorithm compared to existing algorithms in terms of recommendation system performance.

4.4 Parameter settings and performance comparison of the SABTR scheme

When comparing the proposed scheme with the aforementioned baseline algorithms, we first need to determine the optimal parameters for our scheme. For the semantic analysis model in the SABTR scheme (i.e., the LDA model), there are three key parameters: k (representing the number of attraction topics), α and β. In the experiment, we first set the number of attraction topics k to 50 (i.e., k = 50), and set the model's hyperparameters α and β to their default values. Next, we vary the number of model iterations from 500 to 1,350 and calculate the perplexity value after each iteration. By comparing the perplexity values at different numbers of iterations, we can find the optimal number of iterations for model convergence. Finally, we optimize the hyperparameters using the fixed iteration method (i.e., finding the optimal values of α and β while keeping other hyperparameters unchanged and fixing the number of tourist topics). The values of parameters are shown in Figure 2:

Figure 2A shows that when the number of iterations is 1,250, the value of perplexity is 3,957.26, which is the lowest during the iterative training process, indicating that the model has reached a state of convergence. Figure 2B illustrates the change in the model's perplexity value as the number of topic interests increases. It can be observed from the figure that the optimal number of interest categories for the model is 90 when the perplexity value is at its minimum (at this point, the perplexity value is 3,484.1). To find the optimal value of the hyperparameter α for tourist-interest distribution, we fix the number of interest categories (i.e., K = 90) and the value of the hyperparameter for interest-attraction distribution (i.e., β = 1/90), and increase the value of α from 0.010 to 0.024. From the series of perplexity values in Figure 2C, it can be seen that the optimal value of α is 0.022. Finally, increasing the value of β from 0.004 to 0.015, the optimal value of β can be seen in Figure 2D as 0.008. From the values of the hyperparameters, it can be inferred that the distribution of tourists' interests is relatively concentrated, while the topics to which attractions belong are more diverse.

When a tourist shows interest in an attraction, the recommendation system needs to determine the interests associated with the attraction and recommend attractions that match the tourist's interests. In terms of recommendation strategies, we need to focus on the following issues: when an attraction is associated with many themes, how many themes need to be considered to accurately meet the user's needs; among the selected themes, how many attractions should be chosen for each theme to improve the system's recommendation precision, recall

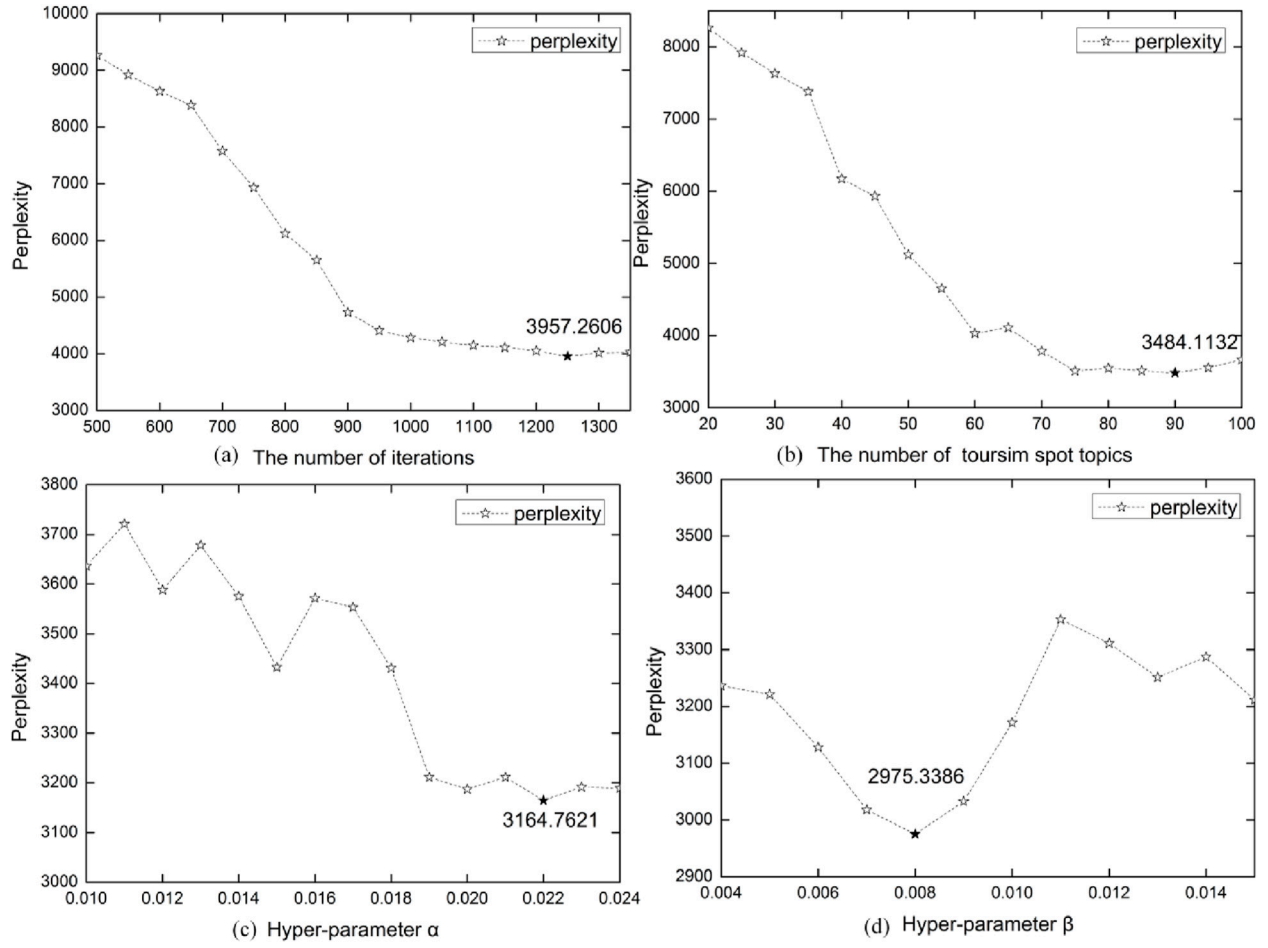

FIGURE 2
Parameters of the Semantic Analysis Mode. Figure 2A illustrates the trend of model performance as the number of iterations increases, with the core objective being to determine the optimal number of iterations for model convergence. Figure 2B presents the variation of model performance with the increase in the number of topics, aiming to find the topic count that yields the optimal model performance. Figures 2C, D respectively explore the impact of changes in model hyperparameters α and β on model performance, with the goal of identifying the optimal values for hyperparameters α and β that maximize model performance. **(A)** The number of iterations. **(B)** The number of tourism spot topics. **(C)** Hyper-parameter α. **(D)** Hyper-parameter β.

rate, and F1-measure. In order to determine the parameters of these recommendation strategies, experiments were conducted by increasing the number of topics and the number of attraction selections to compare the different results of the semantic analysis algorithm, as shown in Figure 3.

Figure 3A primarily analyzes the number of themes to which an attraction belongs. The experiment sets the range of themes from 1 to 10, and when making recommendations, five attractions are selected from each theme to be added to the recommendation list. The number of themes is continuously increased to compare the algorithm's precision, recall, and F1-measure. The results from Figure (a) show that as the number of themes to which an attraction belongs increases, the precision of the recommendations also increases. However, when the number of themes reaches 4, the accuracy of the recommendations begins to decline, and the recall does not improve, indicating that when a user is interested in an attraction, knowing the four main interests to which the attraction belongs can meet the user's needs. After determining the number of interest categories to which an attraction belongs, a series of experiments analyze how many attractions should be selected from each theme to improve the algorithm's performance. We set the number of attractions selected per theme to 5, 10, and 15 to compare the algorithm's performance, and the performance under different parameters is shown in Figures 3B–D. From the three sub-figures, it can be seen that when 10 attractions are selected from a theme, the algorithm has the best precision value, which is 0.2098, and at this time, The appropriate number for the recommendation list is 40.

The method for predicting attraction ratings is to aggregate the ratings of similar users for prediction. We need to determine two parameters: one is the similarity between similar users, and the other is the number of similar users to be selected for rating prediction. The paper first calculates the average similarity between tourists, and then identifies the optimal similarity and the optimal number of similar users based on the calculated Root Mean Square Error (RMSE) values. Next, we rank the candidate attractions based on the predicted ratings to form a recommendation list for tourists to refer to. In addition, we also compared the performance of the recommendation list obtained from the SABTR scheme with the recommendation list without ratings. As shown in Figure 4:

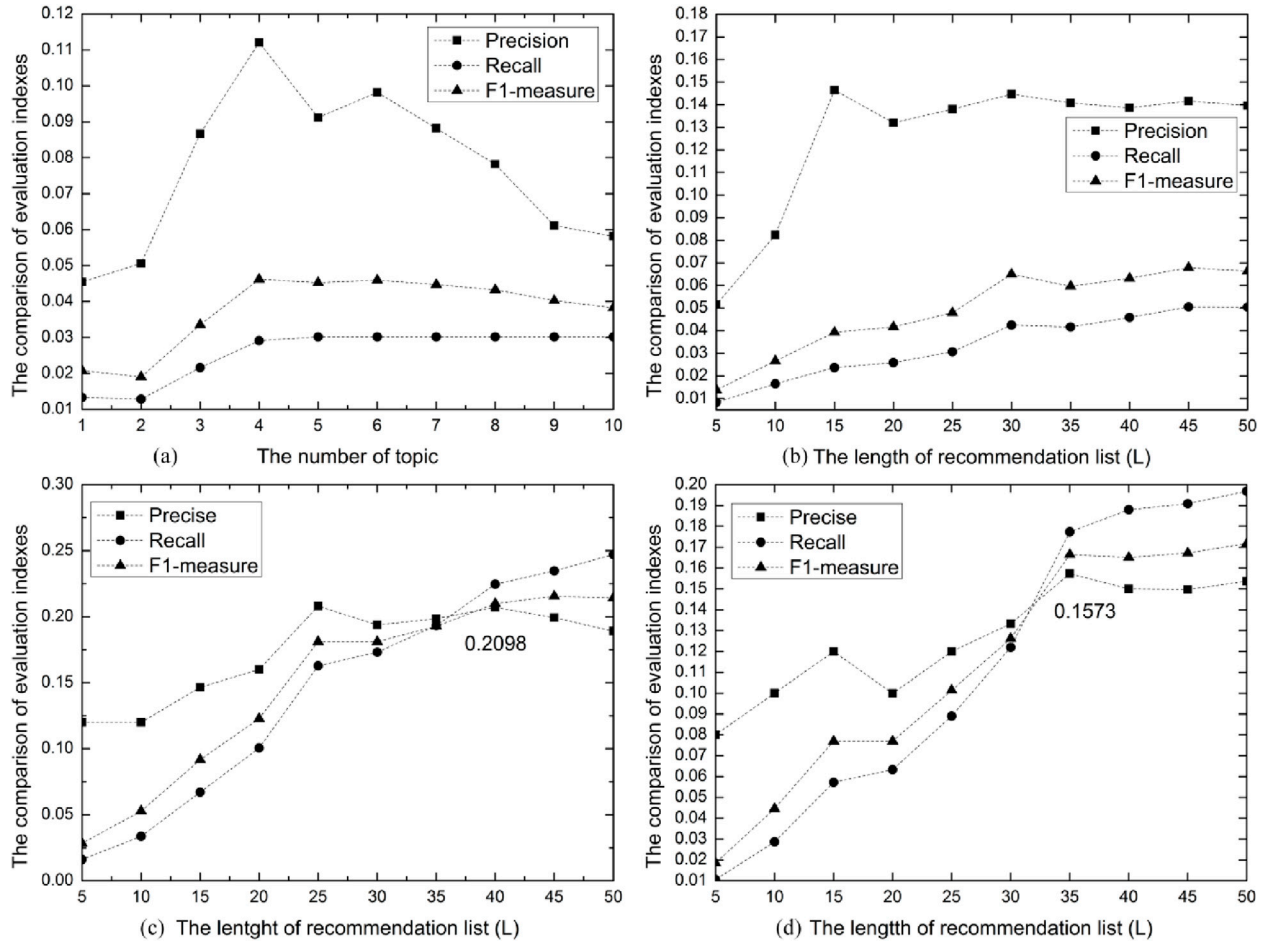

FIGURE 3
Recommendation Strategy of SABTR Approach. Figure 3A illustrates the trend of algorithm performance metrics as the number of themes to which attractions are categorized varies, with the aim of determining the optimal number of themes for achieving the best algorithm performance. Figures 3B–D further explore how algorithm performance fluctuates with the increase or decrease in the number of selected attractions within each specific theme, with the goal of identifying the optimal number of attractions per theme to maximize the overall performance of the algorithm. **(A)** The number of topic. **(B)** The length of recommendation list (L). **(C)** The lentght of recommendation list (L). **(D)** The lengtth of recommendation list (L).

Figure 4A illustrates the relationship between the number of similar users and their similarity for tourists. It can be observed that when the number of similar users is 8, the average similarity of these users exceeds 0.9; however, when the number of similar users increases to 24, the average similarity drops below 0.5. Therefore, the appropriate upper limit for the number of similar users is set to 24. Figures 4B, C use the model's RMSE to determine the optimal number of similar users and the similarity value. The results show that when the number of similar users is set to 12, the model's RMSE value is the lowest at 0.892; simultaneously, setting the similarity to 0.7 yields the best performance in rating prediction, further reducing the RMSE value to 0.861. Figure 4D compares the performance differences of the SABTR approach with and without rating sorting. When the recommendation list length is 10, the precision (precision) of the SABTR approach with rating sorting is 0.21469, while the precision of the SABTR approach without rating sorting is 0.19576, which is 9.6% higher for the former. However, as the recommendation list length increases, the system's precision decreases while the recall rate rises. When the recommendation list length reaches 45, the precision of the SABTR approach without rating sorting is 0.14675, slightly higher than the precision of the SABTR approach with rating sorting (0.14923). This indicates that including attractions with lower ratings in the recommendation list may reduce recommendation effectiveness.

After determining the optimal parameters for the SABTR approach, we compared its performance with other baseline algorithms. In this approach, 90 topics were selected, and the hyperparameters were set to 0.022 and 0.008, respectively. The length of the recommendation list was set to 40, with 4 topics chosen and 10 attractions selected within each topic. We divided the dataset into a training set and a testing set, where the proportion of the training set gradually increased from 30% to 90%, and correspondingly, the testing set proportion decreased from 70% to 10%. The performance comparison results of these algorithms are described in Table 1.

The data in Table 1 show that when the data density does not exceed 50%, the proposed SABTR method outperforms PLSA, Skip-Gram, and LSA. Especially when the data density is low (such as 30%), the precision of the SABTR algorithm is 22% higher than that of Skip-Gram. As the data density increases, the performance of

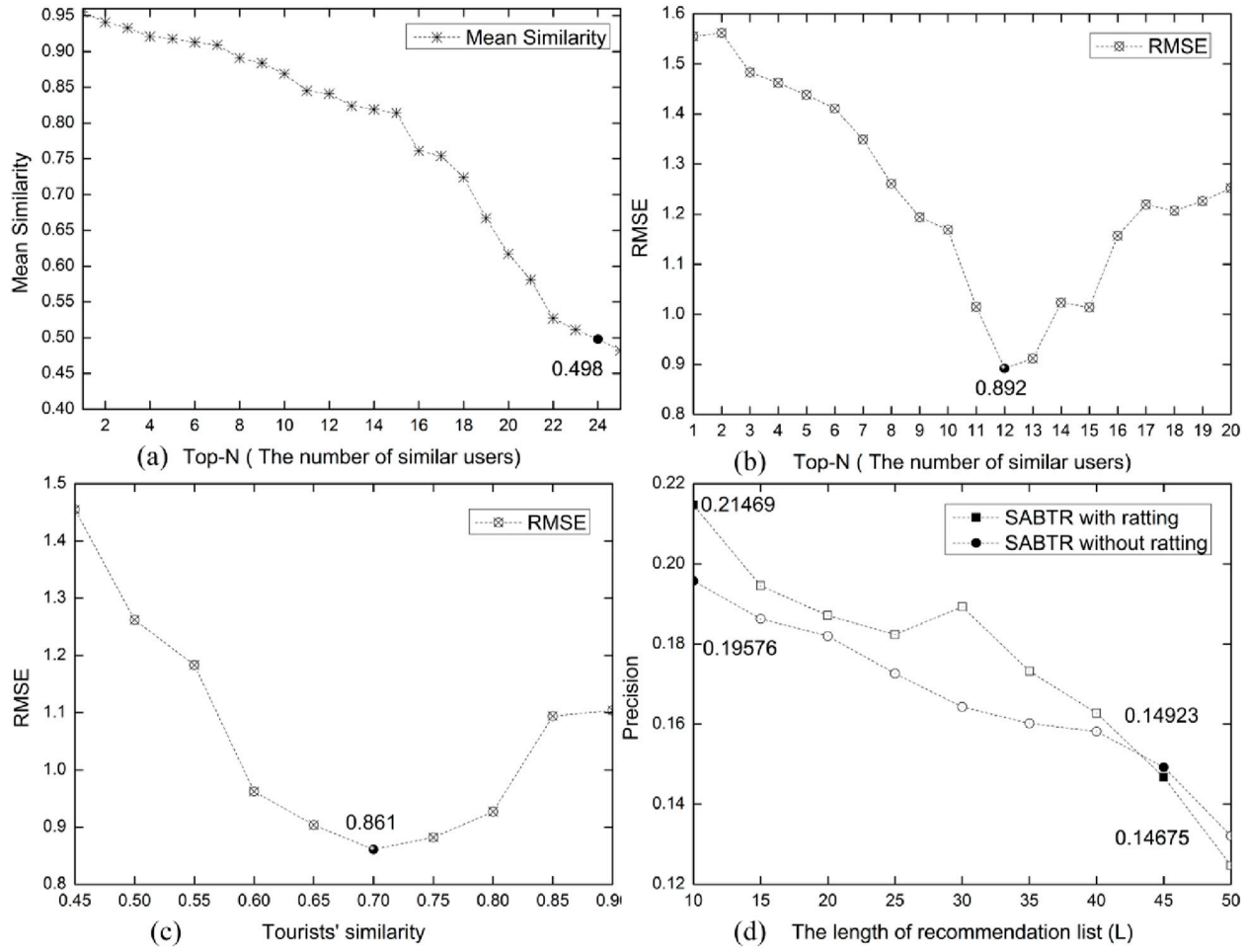

FIGURE 4
Parameters of the attraction rating prediction scheme and the ordering of attraction ratings in recommendations. Figure 4A describes the distribution of average similarity among similar users. Figure 4B explores the impact of the number of similar users on the Root Mean Square Error (RMSE). Figure 4C analyzes the effect of the similarity between tourists on the Root Mean Square Error (RMSE). Figure 4D compares the performance of the interest recommendation list generated by the SABTR method with that of a recommendation list without rating information.

both SABTR and the baseline algorithms improves; however, when the data density exceeds 50%, the precision of Skip-Gram surpasses that of SABTR, particularly when the data density reaches 90%, at which point the precision of Skip-Gram reaches 0.2502, an 18% increase compared to SABTR.

While Skip-Gram, as a word vector model, can find similar attractions by converting them into distributed vectors and using vector similarity, this does not necessarily mean it provides a better service experience for tourists. This is because it tends to find the most similar attractions, potentially leading tourists into an information echo chamber and causing interest fatigue. In contrast, SABTR analyzes the interest topic distribution of attractions through a topic model, helping to expand tourists' interests and meet their diverse needs. Especially in cases of insufficient data (e.g., when data density is 30%), SABTR performs best, effectively alleviating the cold start problem in recommendation systems, whereas other algorithms (Skip-Gram, PLSA, and LSA) exhibit overfitting in recommendations.

When the data density is 90%, the recommendation precision of the PLSA algorithm is 0.2050, close to that of SABTR (which has a recommendation precision of 0.2107), indicating that PLSA can also provide good recommendation performance when there is sufficient data. In contrast, LSA, due to the negative values in the interest factors it extracts, cannot effectively cluster attractions and tourists, performing the worst across four different data densities.

5 Conclusion and future work

In this paper, we propose a tourism recommendation scheme based on semantic analysis, aimed at recommending suitable attractions to tourists. The scheme primarily leverages semantic topic modeling for user clustering and attraction clustering. When a user expresses a preference for a particular attraction on a travel service website, other attractions similar to it enter the recommendation candidate list. Subsequently, the ratings for these candidate attractions are calculated based on the ratings given by other users who share similarities with this user. After ranking the candidate attractions according to their scores, a list of attractions tailored to the user's interests is generated and sent to the

TABLE 1 Performance comparison between SABTR and baseline algorithms.

Evaluation Metrics	Methods	Matrix Density = 30%	Matrix Density = 50%	Matrix Density = 70%	Matrix Density = 90%
Precision	SABTR	**0.1137**	**0.1412**	0.1871	0.2107
	Skip-Gram	0.0927	0.1238	**0.2325**	**0.2502**
	PLSA	0.0943	0.1134	0.1612	0.2050
	LSI	0.0794	0.0986	0.1211	0.1413
Recall	SABTR	**0.1211**	**0.1537**	0.2045	0.2247
	Skip-Gram	0.0836	0.1325	**0.2258**	**0.2487**
	PLSA	0.1132	0.1224	0.1724	0.2106
	LSI	0.0886	0.0971	0.1518	0.1753
F1-measure	SABTR	**0.1173**	**0.1471**	0.1954	0.2175
	Skip-Gram	0.0879	0.1280	**0.2291**	**0.2494**
	PLSA	0.1028	0.1177	0.1666	0.2078
	LSI	0.0984	0.0978	0.1347	0.1565

The bolded values in the table denote the most outstanding results in the performance comparison of different algorithms.

user. Experimental results demonstrate that the proposed scheme not only improves the accuracy and recall of recommendations but also saves tourists time in selecting travel resources, thereby enhancing the user's service experience.

The method we employ requires the use of tourists' travel records and rating data. Given the increasing emphasis on privacy concerns, future recommendation systems will also place greater importance on protecting user information. Therefore, in future work, we plan to adopt a federated learning framework, where instead of directly using individual user records, gradients provided by users will be utilized to analyze their interests. This approach allows us to recommend appropriate attractions while safeguarding user privacy.

Data availability statement

Publicly available datasets were analyzed in this study. This data can be found here: https://grouplens.org/datasets/movielens/.

Author contributions

JL: Supervision, Writing–review and editing. HX: Software, Writing–original draft, Writing–review and editing. QT: Investigation, Writing–review and editing. HW: Writing–review and editing. TG: Formal Analysis, Writing–review and editing.

Funding

The author(s) declare that financial support was received for the research, authorship, and/or publication of this article. 1. "Research on the Teaching Model of Deep Integration of Industry and Education in E-commerce Major Based on the OBE Concept", Henan Province Undergraduate Colleges and Universities' 2023 Annual Industry-Education Integration Project. 2. "Research on the Teaching Reform of "Software Development and Practice" Course Based on OBE Education Concept under the Ecology of Open Source Software (2023xj022)". 3. The project of enterprise temporary job of Science and engineering teachers from colleges and universities of Anhui Province (2024jsqygz104). 4. The Project of Artificial intelligence serving the characteristics of ten emerging industries of Anhui province (2023sdxx078).

Acknowledgments

In this article, we employed an AI large model to scrutinize the grammar of the text. We extend our gratitude to Moonshot AI for providing the "Kimi" artificial intelligence technology, version 1.0, 2024. For more information about this technology, you can visit the website: https://kimi.moonshot.cn.

Conflict of interest

The authors declare that the research was conducted in the absence of any commercial or financial relationships that could be construed as a potential conflict of interest.

Publisher's note

References

1. Hsieh SC. Tourism demand forecasting based on an LSTM network and its variants. *Algorithms* (2021) 14(8):243. doi:10.3390/a14080243

2. Ma D, Hu J, Yao F. Big data empowering low-carbon smart tourism study on low-carbon tourism O2Osupply chain considering consumer behaviors and corporate altruistic preferences. *Comput and Ind Eng* (2021) 153:107061. doi:10.1016/j.cie.2020.107061

3. Yao Y, Cao Y. A Neural network enhanced hidden Markov model for tourism demand forecasting. *Appl Soft Comput* (2020) 94:106465. doi:10.1016/j.asoc.2020.106465

4. Yang X, Zhang L, Feng Z. Personalized tourism recommendations and the E-tourism user experience. *J Trav Res* (2024) 63(5):1183–200. doi:10.1177/00472875231187332

5. Gasmi I, Soui M, Barhoumi K, Abed M. Recommendation rules to personalize itineraries for tourists in an unfamiliar city. *Appl Soft Comput* (2024) 150:111084. doi:10.1016/j.asoc.2023.111084

6. Ding Y, Zhang L, Huang C, Ge R. Two-stage travel itinerary recommendation optimization model considering stochastic traffic time. *Expert Syst Appl* (2024) 237:121536. doi:10.1016/j.eswa.2023.121536

7. Chen S, Tong J, Chen J. Collective tourist destination recommendation: a dynamic trust network-based fuzzy decision-making model. *Int J Fuzzy Syst* (2024) 1–17. doi:10.1007/s40815-024-01797-x

8. Liu Y, Zhou X, Kou H, Zhao Y, Xu X, Zhang X, et al. Privacy-preserving point-of-interest recommendation based on simplified graph convolutional network for geological traveling. *ACM Trans Intell Syst Technology* (2024) 15(4):1–17. doi:10.1145/3620677

9. Chen Z. Beyond boundaries: exploring the Metaverse in tourism. *Int J Contemp Hospitality Manage* (2024). doi:10.1108/ijchm-06-2023-0900

10. Ding K, Gong XY, Huang T, Choo WC. Recommend or not: a comparative analysis of customer reviews to uncover factors influencing explicit online recommendation behavior in peer-to-peer accommodation. *Eur Res Manage Business Econ* (2024) 30(1):100236. doi:10.1016/j.iedeen.2023.100236

11. Gamidullaeva L, Finogeev A, Kataev M, Bulysheva L. A design concept for a tourism recommender system for regional development. *Algorithms* (2023) 16(1):58. doi:10.3390/a16010058

12. Chen L, Cao J, Tao H, Wu J. Trip reinforcement recommendation with graph-based representation learning. *ACM Trans Knowledge Discov Data* (2023) 17(4):1–20. doi:10.1145/3564609

13. Nilashi M, Abumalloh RA, Samad S, Minaei-Bidgoli B, Thi HH, Alghamdi OA, et al. The impact of multi-criteria ratings in social networking sites on the performance of online recommendation agents. *Telematics Inform* (2023) 76:101919. doi:10.1016/j.tele.2022.101919

14. Majid GM, Tussyadiah I, Kim YR, Pal A. Intelligent automation for sustainable tourism: a systematic review. *J Sust Tourism* (2023) 31(11):2421–40. doi:10.1080/09669582.2023.2246681

15. Jain P, Singh RK, Mishra R, Rana NP. Emerging dimensions of blockchain application in tourism and hospitality sector: a systematic literature review. *J Hospitality Marketing and Manage* (2023) 32(4):454–76. doi:10.1080/19368623.2023.2184440

16. Kou G, Yüksel S, Dinçer H. A facial expression and expert recommendation fuzzy decision-making approach for sustainable business investments within the metaverse world. *Appl Soft Comput* (2023) 148:110849. doi:10.1016/j.asoc.2023.110849

17. Zheng D, Wen J, Kozak M, Phau I, Hou H, Wang W. Vulnerable populations with psychological disorders in tourism: methodological challenges and recommended solutions for empirical research. *Tourism Manage* (2023) 98(8):104760. doi:10.1016/j.tourman.2023.104760

18. Abbasi-Moud Z, Vahdat-Nejad H, Sadri J. Tourism recommendation system based on semantic clustering and sentiment analysis. *Expert Syst Appl* (2021) 167:114324. doi:10.1016/j.eswa.2020.114324

19. Esmaeili L, Mardani S, Golpayegani SAH, Madar ZZ. A novel tourism recommender system in the context of social commerce. *Expert Syst Appl* (2020) 149:113301. doi:10.1016/j.eswa.2020.113301

20. Cheng X. A travel route recommendation algorithm based on interest theme and distance matching. *EURASIP J Adv Signal Process* (2021) 2021(1):57. doi:10.1186/s13634-021-00759-x

21. Shim C, Vo BT, Vo BN, Ong J, Moratuwage D. Linear complexity Gibbs sampling for generalized labeled multi-Bernoulli filtering. *IEEE Trans Signal Process* (2023) 71:1981–94. doi:10.1109/tsp.2023.3277220

22. Duan L, Gao T, Ni W, Wang W. A hybrid intelligent service recommendation by latent semantics and explicit ratings. *Int J Intell Syst* (2021) 36(12):7867–94. doi:10.1002/int.22612

23. Gao T, Cheng B, Chen J, Chen M. Enhancing collaborative filtering via topic model integrated uniform euclidean distance. *China Commun* (2017) 14(11):48–58. doi:10.1109/cc.2017.8233650

24. Gao T, Duan L, Feng L, Ni W, Sheng QZ. A novel blockchain-based responsible recommendation system for service process creation and recommendation. *ACM Trans Intell Syst Technology* (2024) 15:1–24. doi:10.1145/3643858

frontiers | Frontiers in Physics

TYPE Original Research
PUBLISHED 01 November 2024
DOI 10.3389/fphy.2024.1493209

OPEN ACCESS

EDITED BY
Xuzhen Zhu,
Beijing University of Posts and Telecommunications (BUPT), China

REVIEWED BY
Zhidan Zhao,
Shantou University, China
Lei Gao,
Shandong Agricultural University, China
Chao Fan,
Chengdu University of Technology, China

*CORRESPONDENCE
Yali Wang,
ylwang@szcu.edu.cn

RECEIVED 08 September 2024
ACCEPTED 14 October 2024
PUBLISHED 01 November 2024

CITATION
Xue H, Wang Y and Tang Q (2024) Dynamic analysis of malicious behavior propagation based on feature selection in software network. *Front. Phys.* 12:1493209.
doi: 10.3389/fphy.2024.1493209

Dynamic analysis of malicious behavior propagation based on feature selection in software network

Huajian Xue[1,2], Yali Wang[3]* and Qiguang Tang[4]

[1]College of Mathematics and Computer Science, Tongling University, Tongling, China, [2]Anhui Engineering Research Center Of Intelligent Manufacturing Of Copper-based Materials, Tongling University, Tongling, China, [3]College of Computing Science and Artificial Intelligence, Suzhou City University, Suzhou, China, [4]Zhongyuan Oilfield Oil and Gas Engineering Service Center, Zhongyuan Oilfield Company of SINOPEC, Puyang, China

In the era of big data, the propagation of malicious software poses a significant threat to corporate data security. To safeguard data assets from the encroachment of malware, it is essential to conduct a dynamic analysis of various information propagation behaviors within software. This paper introduces a dynamic analysis detection method for malicious behavior based on feature extraction (MBDFE), designed to effectively identify and thwart the spread of malicious software. The method is divided into three stages: First, variable-length N-gram algorithms are utilized to extract subsequences of varying lengths from the sample API call sequences as continuous dynamic features. Second, feature selection techniques based on information gain are employed to identify suitable classification features. Lastly, recurrent neural networks (RNN) are applied for the classification training and prediction of diverse software behaviors. Experimental results and analysis demonstrate that this approach can accurately detect and promptly interrupt the information dissemination of malicious software when such behavior occurs, thereby enhancing the precision and timeliness of malware detection.

KEYWORDS

recurrent neural networks, information propagation, feature selection, dynamic analysis, software network

1 Introduction

In the information age, business data has become the lifeblood of enterprises, and one of the major risks in business operations is the destruction of commercial data by malicious software. Today, with the high integration of the Internet of Things, big data, and mobile Internet, malicious attacks pose an unprecedented threat to corporate data information. For instance, the "Panda Burning Incense" virus in 2006 infected millions of personal computer users and enterprise local area networks. The Aurora attack in 2010 led to the theft of information data from more than 20 companies worldwide. The ransomware virus attack in 2017 prevented the important servers of hundreds of companies from starting. These malicious software behaviors have stolen or destroyed corporate data assets, causing immeasurable losses to businesses. Whether enterprise information systems can be used normally and safely is an important issue that cannot be ignored. To combat the threat

posed by the explosive growth of malicious software to corporate data information systems, researchers have studied the detection of malicious behavior from different perspectives.

Social science researchers mainly conduct qualitative analysis in the detection of malicious behavior, analyzing various risk factors that enterprises face in the context of big data from a macro perspective [1–5]. Natural science researchers mainly study the behavior and characteristics of malicious software through methods such as N-gram, graph theory, and Bayesian classification [6–11], committing to finding a strategy that can quickly detect malicious software, thereby strengthening the risk prevention of corporate data assets. Although these schemes have improved the detection rate of malicious behavior, there are still shortcomings. Methods based on fixed-length N-grams struggle to fully describe the behavior of malicious software. On one hand, different behaviors of malicious software correspond to different sequences of API calls. Moreover, the number of API calls varies as the malicious software performs different operations. On the other hand, malicious software can evade traditional fixed-length API N-gram malware detection methods by inserting independent API calls during execution. Malware detection systems based on graph theory can detect variants of malicious software and have a high detection accuracy. However, these feature extraction methods have limitations. Typically, there are hundreds or thousands of vertices or edges in a program's behavioral call graph. Therefore, constructing a behavioral call graph is relatively difficult.

Based on an in-depth analysis of existing research results, in this paper, we proposes a malicious behavior detection method based on feature extraction(MBDFE), aimed at identifying whether the behavior of software programs contains malicious elements. The work of this paper mainly includes the following two aspects:

- This paper innovatively proposes a software feature selection technique that uses the N-gram algorithm to capture operation codes during the software execution process and employs an information gain calculation method to select the most representative software features. When new software behavior patterns are detected in the enterprise software information system, this feature selection technique can accurately extract the code that reflects its behavioral characteristics.
- This paper transforms the dynamic analysis of malicious behavior into a classification problem, inputs the extracted software feature codes into a recurrent neural network model for processing, and judges whether the software is malicious based on the classification results of the model's software behavior. This method can efficiently identify and warn of potential malicious behavior, providing timely security protection measures for enterprises.

The subsequent chapters of this paper are arranged as follows: Chapter 2 reviews the previous research work in the relevant field; Chapter 3 elaborates on the framework and specific implementation details of the proposed plan; Chapter 4 validates the performance of the proposed plan through extensive experiments; finally, Chapter 5 summarizes the proposed plan and provides a perspective on future research directions.

2 Related works

In this section, we review previous research achievements in malicious behavior detection. The identification of malicious software behavior is an interdisciplinary research direction, where both social science and natural science researchers have conducted in-depth studies on this topic. Social science researchers primarily employ qualitative analysis to examine the various risk factors of corporate risk in the context of big data [1–5], and subsequently propose strategies and countermeasures to address these risks.

Meng Fanfei in literature [1] reviews the development history of the COBIT framework, the concepts and theories related to IT governance and risk management, and applies the content of the COBIT framework to IT governance and enterprise risk management. The paper analyzes the advantages and feasibility of using the COBIT framework from multiple perspectives and proposes some techniques and methods in the application process to facilitate better integration of the COBIT framework into IT governance and risk management by enterprises. Peng Chaoran et al. [2] point out that the construction of domestic enterprise information platforms is lagging, and there are significant security risks in placing the data assets of large enterprises on platforms of foreign giants. They propose from a strategic height the construction of independent enterprise information resource platforms, accounting information standard firewalls, and enterprise information security regulations.

Liu Shangxi et al. in literature [3] use neural network technology to identify corporate tax risks. The paper uses the financial data of 578 enterprises as training samples, derives the characteristics of enterprise risks, and validates them with a sample of 386 enterprises, achieving a final accuracy of 99.8%. Yang Ling [4] constructs a corporate operation risk monitoring classification and grading index system based on a "big data platform". The system obtains real-time monitoring indicator data through a data asset collaborative application platform, realizes real-time risk early warning, emergency linkage, and closed-loop risk management according to preset thresholds, and regularly forms a business risk health index analysis report based on the statistical scores and weights of various indicators, serving as an important reference for leadership decision-making. Zhang Lizhe believes that corporate data asset management faces unprecedented risks in the era of big data. Establishing a comprehensive and reliable financial risk management system and strengthening the prevention of corporate financial risks should become a key research issue for enterprise development. In literature [5], the author analyzes the problems in the development of corporate financial risk management systems, discusses the significance of establishing a sound prevention system, and proposes suggestions for the construction of a financial risk management system model.

Natural science researchers primarily utilize statistical models or machine learning methods [6–11] to study the behaviors and characteristics of malicious software. They are committed to finding a strategy that can rapidly detect malicious software, thereby enhancing the risk prevention of corporate data assets. Wang Rui et al. in literature [6] combine dynamic taint propagation analysis and semantic analysis at the behavioral level to extract key system calls of malicious software, dependencies between calls, and related instruction information, constructing a

semantic-based malicious software behavior detection system to detect variants of malicious software.

Sathyanarayan et al. [7] use the static analysis method N-gram to extract the frequency of key API calls from programs, and by leveraging the correlation between malicious software semantics and API calls, construct behavioral signatures for entire families of malicious software through statistical comparison. Fang et al. [8] use dynamic analysis methods to extract API calls, return values, module names, and their frequencies as behavioral features from programs, and establish an integrated machine learning algorithm-based malicious software detection model to detect variants of malicious software. Park et al. [9] construct a Kernel Object Behavioral Graph (KOBG) for each piece of malicious software, and then detect new malicious software by clustering to mine the family's minimum weight common supergraph (Weighted Minimum Common Supergraph, WMinCS).

Ding et al. [10] use dynamic taint technology to construct a system call dependency graph based on the parameter dependency relationships between system calls, and then extract a common behavioral subgraph as a signature for each family of malicious software based on the maximum weight subgraph (maximum weight subgraph, MWS) algorithm to detect variants of malicious software.

Zhang et al. in [11] propose a deep detection method for malware based on behavior chains (MALDC). This method monitors behavior points based on API calls and then constructs behavior chains using the calling sequences of those behavior points at runtime. Finally, a deep detection method based on Long Short-Term Memory (LSTM) networks is used to detect malicious behavior from the behavior chains.

Li et al. in [12]propose a feature fusion, machine learning-based method to detect malicious mining code. Extracts multi-dim features via static and statistical analysis. Uses n-gram, TF-IDF for text feature vectors, selects best via classifier, and fuses with stats for model training.

Amer et al. in [13] attempted to create universal behavior models for malicious and benign processes, leveraging statistical, contextual, and graph mining features to capture API function relationships in call sequences. Generated models show behavior contrast, leading to relational perspective models that characterize process behaviors. Zhan et al. [14] propose an anomaly detection method for adversarial robustness, analyzing behavior units to tackle issues. Behavior units, extracted from related actions executing intentions, hold key semantic info for local behaviors, boosting analysis robustness. Using a multi-level DL model, it learns semantics and context of behavior units to counter local and broad-scale perturbation attacks. Wong et al. [15] use deep learning to pinpoint API calls linked to malware techniques in execution traces. APILI sets up multi-attention between API, resources, and techniques, using a neural net to incorporate MITRE ATT&CK, tactics, and procedures. It uses fine-tuned BERT for embedding and SVD for tech representation, with design tweaks like layering and noise to boost location accuracy. Chen et al. [16] propose a method for Windows malware detection uses deep learning on APIs with added parameters. It rates parameter sensitivity to malware via rules and clustering, then tags APIs by sensitivity. APIs are encoded by merging native and sensitivity embeddings to show security relations. These embeddings are used to train a deep neural network binary classifier for malware.

Pektaş et al. [17] employ the API call graph to depict the full spectrum of execution routes accessible to malware while it operates. This graph's embedding is converted into a compact numerical vector feature set for integration into a deep neural network. Following this, the detection of similarities within each binary function is efficiently trained and evaluated. Streamlining security analyst tasks, automating Android malware detection and family classification is crucial. Prior research leveraged machine learning to tackle these challenges. Yet, the growing app count poses a need for a scalable, accurate solution in cybersecurity. Here, Sun et al. in [18] introduce a method enhancing malware and family detection, also cutting analysis time.

Tharani et al. [19] introduces a range of feature categories and a streamlined feature extraction technique for Bitcoin and Ethereum transaction data, considering their interconnections. As per our awareness, no prior research has utilized feature engineering for malicious activity detection. These features' relevance was confirmed with eight classifiers: RF, XG, Silas, and neural networks.

Zou et al. [20] aim to merge the precision of graph-based detection with the scalability of social network analysis for Android malware. We analyze app function call graphs as social networks to find central nodes, then measure their intimacy with sensitive APIs. Our IntDroid tool was tested on a dataset with 3,988 benign and 4,265 malicious samples.

3 The proposed method

3.1 The Overview of MBDFE

The solution proposed in this paper is divided into three steps. The first step is to use variable-length N-gram to extract software behavior feature codes; the second step is to reduce the dimensionality of the feature codes through a feature selection method - information gain; the third step is to train the weights of the recurrent neural network with the features. The framework of the solution is shown in Figure 1:

As shown in Figure 1, the framework of the MBDFE method proposed in this study consists of three core components: feature extraction, feature selection, and software behavior recognition. During the feature extraction phase, the n-gram algorithm is used to extract the software's operation codes as feature codes. In the feature selection phase, the information gain algorithm is employed to select feature codes with higher information content as classification features. In the behavior recognition phase, after the classification features are processed through a recurrent neural network, the resulting software classification probability distribution is obtained, with the category having the highest probability being identified as the actual category of the software. In the proposed MBDFE algorithm, multiple variables are involved, the specific meanings of which are detailed in Table 1.

3.2 The extraction of variable-length N-gram features

The N-Gram model is a statistical probability language model based on the idea of dividing the content of a text into byte-sized

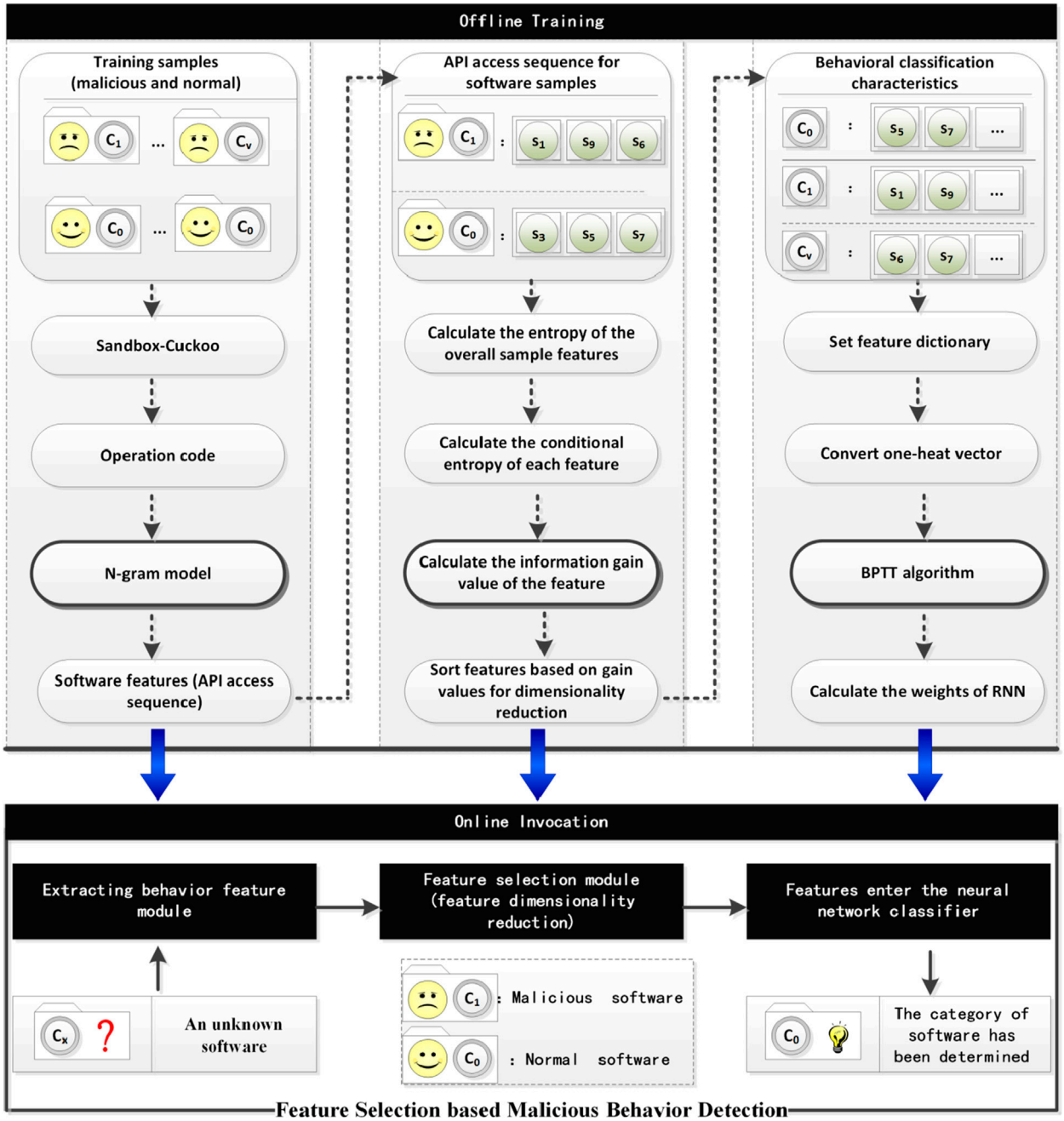

FIGURE 1
The overview of MBDFE scheme.

sliding windows of length N, forming a sequence of byte segments of length N. In the field of malicious behavior detection, the N-Gram algorithm extracts the operation codes from the disassembled files of software behavior and converts them into a set of bytes. Then, through a sliding window, a series of n-byte sequences are obtained. These sequences are the feature codes of the software behavior and are a feature extraction method based on the dynamic analysis of malicious software. The variable-length dynamic behavior feature extraction model breaks down the behavioral call sequence of malicious software into different N-grams, performs feature selection on each gram, and then combines them into hyper-grams of varying lengths as the behavioral features of malicious software. This approach aims to detect variants of obfuscated malicious software and improve the accuracy of malicious software detection. The N-Gram primarily utilizes the Markov assumption, and in the field of software malicious behavior detection, the model represents the co-occurrence probability of each byte code and its preceding feature codes. The model is shown in the following formula:

$$p(m_n|m_{n-1}...m_2m_1) = \frac{F(m_1m_2...m_n)}{F(m_1m_2...m_{n-1})} \quad (1)$$

TABLE 1 The variable symbols used in MBDFE scheme.

Variable symbol	Definition of symbols
T	It represents a certain characteristic behavior of the software
t	It represents the value of the characteristic behavior T
H(C)	It represents the entropy of the overall characteristic behavior of the software
H(C|T)	It represents the conditional entropy of feature T
$P(t)$	It represents the proportion of the presence of software behavior T in the entire sequence of software behaviors
$P(C_i \mid t)$	It represents the proportion of software sequences containing software behavior T and belonging to class c in the entire software system containing behavior T behavior sequences
U	It represents the weight between the input layer and the hidden layer in a recurrent neural network
V	It represents the weight between hidden layers
W	It represents the weight between the hidden layer and the output layer
ΔU	It represents the gradient of weight U
ΔV	It represents the gradient of weight V
ΔW	It represents the gradient of weight W
z_t^h	It represents the value of the hidden layer at time t
a_t^h	It represents the activation value of the hidden layer at time t
z_t^o	It represents the value of the output layer at time t
a_t^o	It represents the activation value of the output layer at time t
δ_t^o	It represents the gradient of the output layer at time t
δ_t^h	It represents the gradient of the hidden layer at time t
lr	It represents the learning rate in gradient descent algorithm

in the formula, $p(m_n|m_{n-1}...m_2m_1)$ represents the conditional probability of the operation code m_n given the preceding n−1 items, and $F(m_1m_2...m_n)$ and $F(m_1m_2...m_{n-1})$ represent the frequency of co-occurrence of the operation code sequence. By continuously changing the value of n, the most suitable feature code can be determined based on the derived probability values.

The variable-length N-gram algorithm extracts operation code slices from each software behavior invocation sequence and uses these slices to construct a set of feature codes for software behavior, with the following steps:

- Convert the sample program's invocation behavior into hexadecimal format and match the program's features against a computer virus database.
- Starting from the first position where a match occurs, use a sliding window method to continuously compare backward until no identical features are found. Ensure uniqueness while trying to keep the feature code as short as possible.
- Count the number, or frequency, of features in this byte stream that are included in the virus feature database.
- Set a threshold; when the count of a certain feature exceeds the threshold, add this byte stream to the virus database as a candidate feature code.

3.3 Feature selection by information gain

The feature set obtained through variable-length N-gram segmentation represents a collection of behavior sequences for each software. By training the software's behavior sequences, it is possible to determine the category to which the software sequence belongs (i.e., virus, trojan, ransomware, worm, or normal software access). In this paper, we use recurrent neural networks to classify the behavior sequences of software. However, the importance of features in the software behavior feature vector is not the same in the classification system. To select representative features and improve classification efficiency, it is necessary to quantify the importance of software behavior features. This paper uses Information Gain (IG) to measure the software behavior features. In Information Gain, the criterion is how much information the feature can bring to the classification system; the more information it brings, the more important the feature is.

In the classification system, when a software behavior feature T can be composed of multiple classes (for example, registry access behavior, which could be either normal or trojan behavior), the calculation of conditional entropy needs to consider all its possible values. In the software system, the specific value of the software feature behavior T is set as t. Generally, the values of t are t (indicating that t occurs) and not t (indicating that t does not

occur). At this point, the conditional entropy of the behavior feature T is as follows:

$$H(C|T) = P(t)H(C|t) + P(\bar{t})H(C|\bar{t}) \tag{2}$$

in the formula, $P(t)$ represents the proportion of the presence of software behavior T in the entire sequence of software behaviors, and indicates the proportion of software sequences that contain behavior T and belong to class C_i among all software behavior sequences in the software system that include behavior T. Similarly, $P(\bar{t})$ represents the proportion of sequences without behavior T in the entire sequence of software behaviors, and $P(C_i|\bar{t})$ denotes the proportion of software behavior sequences that do not contain behavior T and belong to class C_i among all software behavior sequences in the software system that do not include behavior T. The entropy of $H(C|t)$ and $H(C|t)$ shown in the following formula:

$$\begin{aligned} H(C|t) &= -\sum_{i=1}^{n} P(C_i|t)\log_2 P(C_i|t) \\ H(C|\bar{t}) &= -\sum_{i=1}^{n} P(C_i|\bar{t})\log_2 P(C_i|\bar{t}) \end{aligned} \tag{3}$$

The information gain of software behavior feature T is the difference between the entropy of the entire software behavior and the conditional entropy of software feature T. The formula is as follows:

$$\begin{aligned} IG(T) &= H(C) - H(C|T) \\ &= -\sum_{i=1}^{n} P(c_i).\log_2 P(c_i) \\ &\quad + \sum_{i=1}^{n} P(C_i|t)\log_2 P(C_i|t) + \sum_{i=1}^{n} P(C_i|\bar{t})\log_2 P(C_i|\bar{t}) \end{aligned} \tag{4}$$

3.4 Utilizing recurrent neural networks for malicious behavior detection

Before training a neural network, it is necessary to first randomly generate the three weights of the neural network: the weight U, the weight W and the weight V. When the behavioral feature vector is input into the network, the forward propagation is as shown in the following formula:

$$\begin{aligned} z_t^h &= x_t \cdot U + a_{t-1}^h \cdot W \\ a_t^h &= \tanh\left(x_t \cdot U + a_{t-1}^h \cdot W\right) \end{aligned} \tag{5}$$

where z_t^h refers to the value of the hidden layer at time t, a_t^h represents the activation value of the hidden layer at time t, x_t represents the one-hot vector of the API access list at time t, and $\tanh()$ is the activation function of the hidden layer. z_t^o represents the value of the output layer at time t, a_t^o represents the activation value of the output layer at time t, and $\mathrm{softmax}()$ is the activation function of the output layer. The forward propagation formula for the output layer is as follows:

$$\begin{aligned} z_t^o &= a_t^h \cdot V \\ a_t^o &= \mathrm{softmax}\left(a_t^h \cdot V\right) \end{aligned} \tag{6}$$

In this study, the input of RNN network [21] is the sequence of API accesses for each software, with the API access sequence length matching the training time series. After each time step's forward propagation calculates the output layer's activation, these values are collected into a list. Once the forward propagation for the entire sequence is complete, the cross-entropy is used to compute the error between the output layer's activations and the true output labels at each time step. This error is then backpropagated through time to each layer to compute the gradients, which are essential for updating the weights. The cross-entropy loss function is expressed as:

$$\mathrm{Loss} = -\sum_{i=1}^{L_1} y_t(i) * \ln a_t^o(i) \tag{7}$$

where L_1 is the length of the one-hot vector, y_t represents the category to which the input feature sequence belongs at time t, and the error of the output layer at each moment can be obtained through Formula 7. The output layer error can be used to calculate the gradient about the output layer through the chain rule. Define δ_t^o as the gradient of the output layer at time t, δ_t^h as the gradient of the hidden layer at time t, $\frac{\partial \mathrm{Loss}_t}{\partial a_t^o}$ as the gradient of the loss function at time t on the activation value of the output layer, and $\frac{\partial a_t^h}{\partial z_t^h}$ as the gradient of the activation value of the hidden layer at time t on the hidden layer. The gradients of U, V, and W are defined as ΔU , ΔV , and ΔW , and are solved as follows:

$$\begin{aligned} \Delta U &= \frac{\partial \mathrm{Loss}_t}{\partial a_t^o} \cdot \frac{\partial a_t^o}{\partial z_t^o} \cdot \frac{\partial z_t^o}{\partial a_t^h} \cdot \frac{\partial a_t^h}{\partial z_t^h} \cdot \frac{\partial z_t^h}{\partial U} + \frac{\partial \mathrm{Loss}_{t+1}}{\partial a_{t+1}^o} \cdot \frac{\partial a_{t+1}^o}{\partial z_{t+1}^o} \cdot \frac{\partial z_{t+1}^o}{\partial a_{t+1}^h} \cdot \frac{\partial a_{t+1}^h}{\partial z_{t+1}^h} \\ &\quad \cdot \frac{\partial z_{t+1}^h}{\partial a_t^h} \cdot \frac{\partial a_t^h}{\partial z_t^h} \cdot \frac{\partial z_t^h}{\partial U} \\ &= \delta_t^h \cdot \frac{\partial z_t^h}{\partial U} = \delta_t^h \cdot \frac{\partial\left(x_t \cdot U + a_{t-1}^h \cdot W\right)}{\partial U} = \delta_t^h \cdot x_t \\ \Delta V &= \frac{\partial \mathrm{Loss}_t}{\partial a_t^o} \cdot \frac{\partial a_t^o}{\partial z_t^o} \cdot \frac{\partial z_t^o}{\partial V} = \delta_t^o \cdot \frac{\partial z_t^o}{\partial V} = \delta_t^o \cdot \frac{\partial\left(a_t^h \cdot V\right)}{\partial V} = \delta_t^o \cdot a_t^h \\ \Delta U &= \frac{\partial \mathrm{Loss}_t}{\partial a_t^o} \cdot \frac{\partial a_t^o}{\partial z_t^o} \cdot \frac{\partial z_t^o}{\partial a_t^h} \cdot \frac{\partial a_t^h}{\partial z_t^h} \cdot \frac{\partial z_t^h}{\partial W} + \frac{\partial \mathrm{Loss}_{t+1}}{\partial a_{t+1}^o} \cdot \frac{\partial a_{t+1}^o}{\partial z_{t+1}^o} \cdot \frac{\partial z_{t+1}^o}{\partial a_{t+1}^h} \cdot \frac{\partial a_{t+1}^h}{\partial z_{t+1}^h} \\ &\quad \cdot \frac{\partial z_{t+1}^h}{\partial a_t^h} \cdot \frac{\partial a_t^h}{\partial z_t^h} \cdot \frac{\partial z_t^h}{\partial W} \\ &= \delta_t^h \cdot \frac{\partial z_t^h}{\partial U} = \delta_t^h \cdot \frac{\partial\left(x_t \cdot U + a_{t-1}^h \cdot W\right)}{\partial W} = \delta_t^h \cdot a_{t-1}^h \end{aligned} \tag{8}$$

The weight update of the network is the initial weight updated by the gradient descent method. Before updating, it is necessary to first calculate the cumulative update value of the weight gradient. The initial values of ΔU , ΔV , and ΔW are 0 matrices, and the matrix dimensions are consistent with the dimensions of U, V, and W. During each time step of the training feature sequence, ΔU , ΔV , and ΔW are accumulated and updated, and the cumulative update equation is as follows:

$$\begin{aligned} \Delta U &= \Delta U + \delta_t^h \cdot x_t \\ \Delta V &= \Delta V + \delta_t^o \cdot a_t^h \\ \Delta W &= \Delta W + \delta_t^h \cdot a_{t-1}^h \end{aligned} \tag{9}$$

When the feature sequence is not yet trained, the three weights are shared throughout the time sequence training process and will not be updated. Once the feature sequence of the entire software is trained, U, V, and W can be updated by the gradient descent method. The weight update equation is as follows:

$$\begin{aligned} U &= U - \mathrm{lr}*\Delta U \\ V &= V - \mathrm{lr}*\Delta V \\ W &= W - \mathrm{lr}*\Delta W \end{aligned} \tag{10}$$

When a software behavior is running, our proposed scheme can quickly determine the probability of this software belonging to various categories based on the sequence vector of software behavior and the weight vector, taking the category with the highest probability as the true category of this software, thereby quickly predicting whether the software has malicious behavior.

4 Experiments

4.1 Dataset

The experimental dataset includes 172 benign executable programs and 457 malicious software samples (across 4 types of malware: Trojans, worms, script viruses, and system viruses). All of these samples are Windows Portable Executable (PE) files, including formats such as EXE, DLL, OCX, SYS, and COM. The malicious samples were randomly selected from the malicious software sample set downloaded from the VX Heaven website, while the benign samples were collected from clean Windows systems and the school FTP website as good executable programs.

In order to obtain the behavioral characteristics of these programs, we selected the open-source dynamic analysis tool Cuckoo Sandbox [22]. The Cuckoo Sandbox mainly analyzes file types such as Windows executable files, DLL files, MS Office files, compressed files, etc. It can automatically analyze the dynamic behaviors of executable programs, including process behavior, network behavior, and file behavior. In our experiment, the architecture of the Cuckoo Sandbox primarily involves running the main Cuckoo program on the host machine (the host system is Ubuntu Server 16.10), with multiple guest machines (the environments required for the execution of malicious and benign programs are Windows series operating systems) connected to the host via a virtual network. Each guest machine has a Cuckoo Agent program that acts as a monitoring agent. For data storage security, we have connected a workstation to the Cuckoo host to back up the generated analysis reports and process data. Additionally, analysis can be conducted remotely via the internet by accessing the host. The structure of the Cuckoo Sandbox is shown in Figure 2:

4.2 Experimental evaluation criteria

The experiments in the paper evaluate the performance of the proposed scheme based on accuracy, recall, and F1-measure. For malicious software behavior prediction, accuracy refers to the proportion of predicted malicious samples that are truly malicious, while recall is the proportion of malicious samples in the dataset that we correctly identify as malicious through our scheme. We define TP as the number of positive samples in the dataset predicted as positive, FN as the number of positive samples in the dataset predicted as negative, FP as the number of negative samples predicted as positive, and TN as the number of negative samples predicted as negative. The evaluation criteria are shown in the following formulas:

$$\begin{aligned} Accuacy &= \frac{TP}{TP + FP} \\ \mathrm{Recall} &= \frac{TP}{TP + FN} \\ F1 - measure &= \frac{2Accuacy*\mathrm{Recall}}{Accuacy + \mathrm{Recall}} \end{aligned} \tag{11}$$

4.3 Experimental results and analysis

In this experiment, the hardware configuration utilized is as follows: the central processing unit (CPU) is an Intel Xeon Gold 6234, equipped with 32 GB of memory, a 2 TB hard disk drive, and an NVIDIA GeForce RTX 3080Ti graphics card. In the experiment, we divided the dataset into two parts, with 80% as the training set and 20% as the test set. Regarding the parameter settings for our scheme, we conducted the following experiments:

For the parameter n in the N-gram scheme, the range of values from 1 to 5 was tested, and the results are shown in the figure below:

From Figure 3, it can be observed that when the value of n is 4, the predictive performance is optimal, with the F1-measure of the scheme reaching 0.8627. However, with each increment of n in the n-gram scheme, the number of behavior features increases exponentially, and the time cost also rises. We can see in the chart that when n increases from 3 to 4, the time cost jumps from 386.24 s to 589.84 s. Considering that when n is taken as 3, the F1-measure of the proposed scheme for identifying malicious behavior reaches 0.8435, which is only about 2% less than the performance when n is 4, we opt for n to be 3 after a comprehensive assessment.

To validate the efficiency of the proposed solution, we first determined the parameters of the model, which consist of four elements: the number of iterations for the model, the learning rate of the model, the dimensionality of the hidden layer, and the number of features. By adjusting the aforementioned parameters, the model's mean loss and accuracy also continuously change, as shown in Figure 4.

From Figure 4A, it can be observed that when the number of iterations reaches 1800, the mean loss of the model is at its lowest, indicating that the model has converged at this point. Figures 4B, C show that when the learning rate is set to 0.04 and the dimensionality of the hidden layer is 220, the model performs the best, with a mean loss value of 0.23416. Regarding the selection of features, we defined the range of feature selection from 40 to 260, increasing by 20 each time, resulting in a series of accuracy values as depicted in Figure 4D. It can be seen from the figure that when the number of feature values is 200, the model's performance is optimal, with an accuracy value of 94.27%. When the number of feature values continues to increase, the model's performance remains essentially unchanged.

In terms of performance comparison, we compared our proposed scheme MBDFE with RNN and Naive Bayes. By varying the density of the dataset, the algorithm's running time and performance also change continuously, as shown in Figure 5:

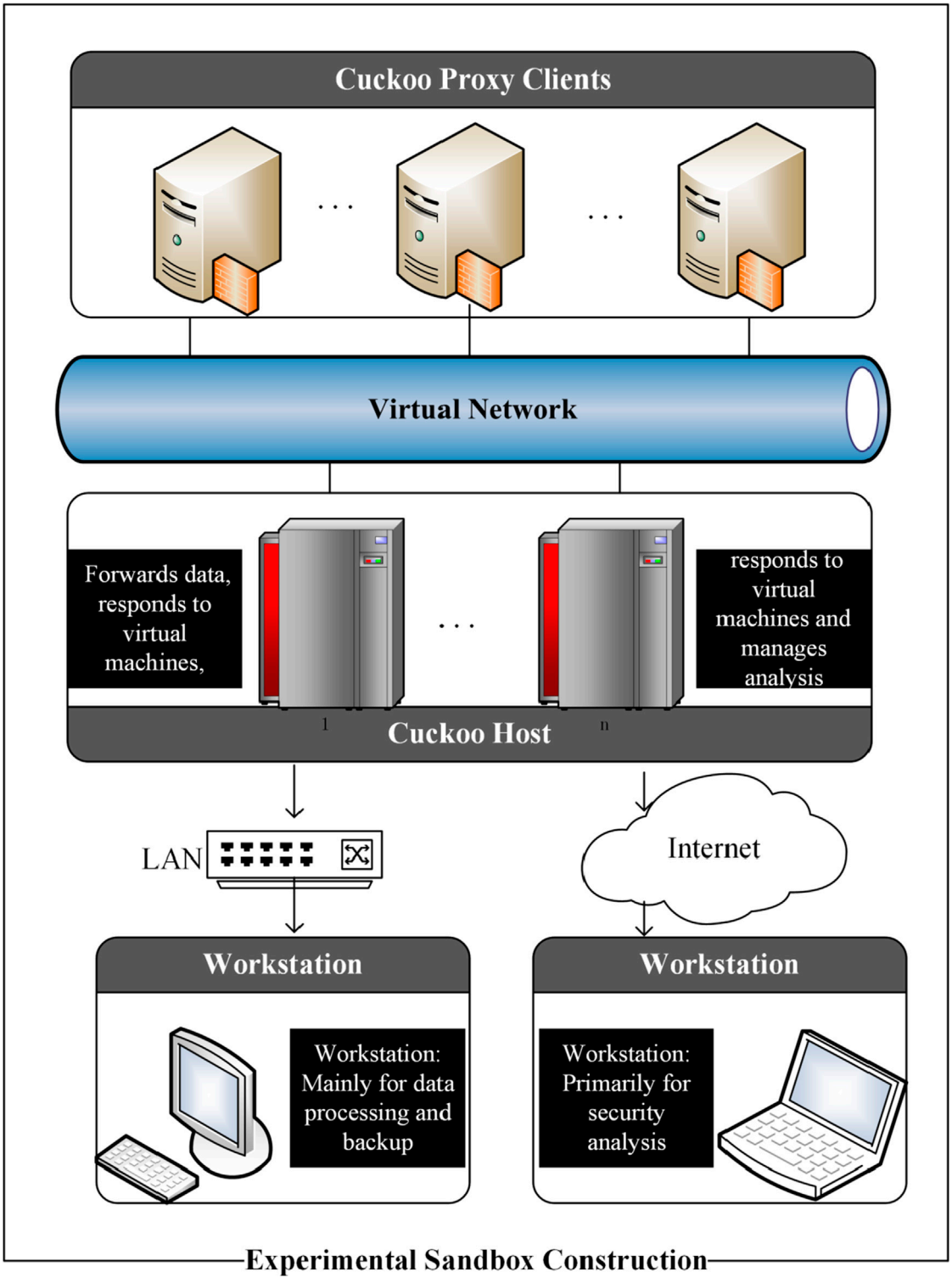

FIGURE 2
The structure of cuckoo sandbox.

From Figure 5B, it can be observed that the running times of the models vary. MBDFE and RNN require training the weights of the neural network, while the Bayesian method only needs to calculate the class probabilities for each feature, thus consuming relatively less time. MBDFE, as an RNN model based on feature selection, has an advantage in training time over traditional RNNs. As shown in the figure, when the data density reaches 80%, MBDFE's training time is 1813.15 s, compared to 2876.56 s for RNN, saving 36.97% in time.

Examining Figure 5A reveals that when the data density is less than 50%, MBDFE's performance is inferior to the Bayesian

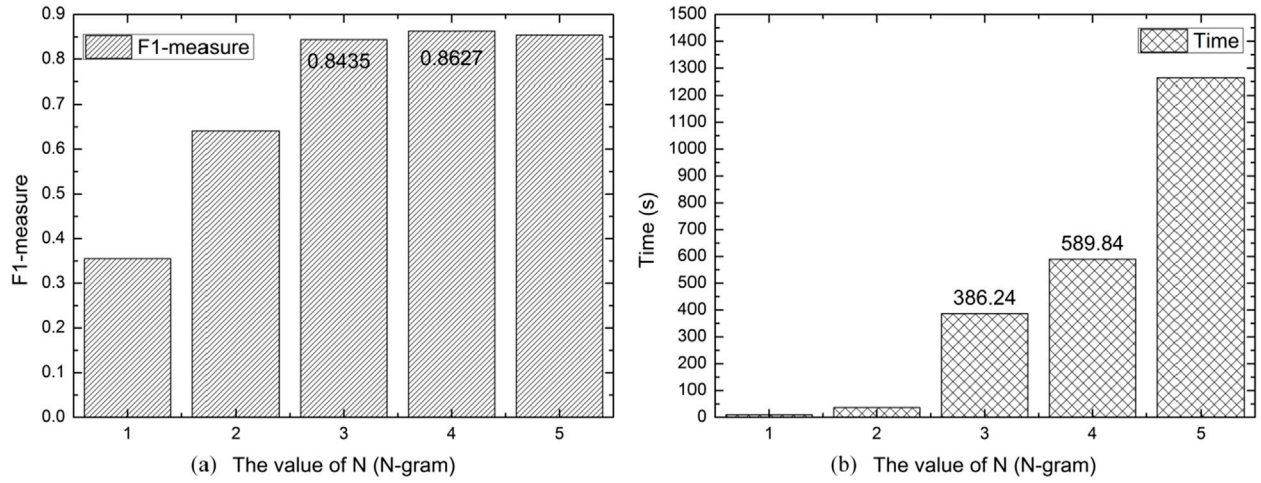

FIGURE 3
The Parameter of N-gram. **(A)** Illustrates the impact of the value of n in n-gram on the performance of the algorithm, and **(B)** shows the effect of the value of n in n-gram on the training time of the algorithm.

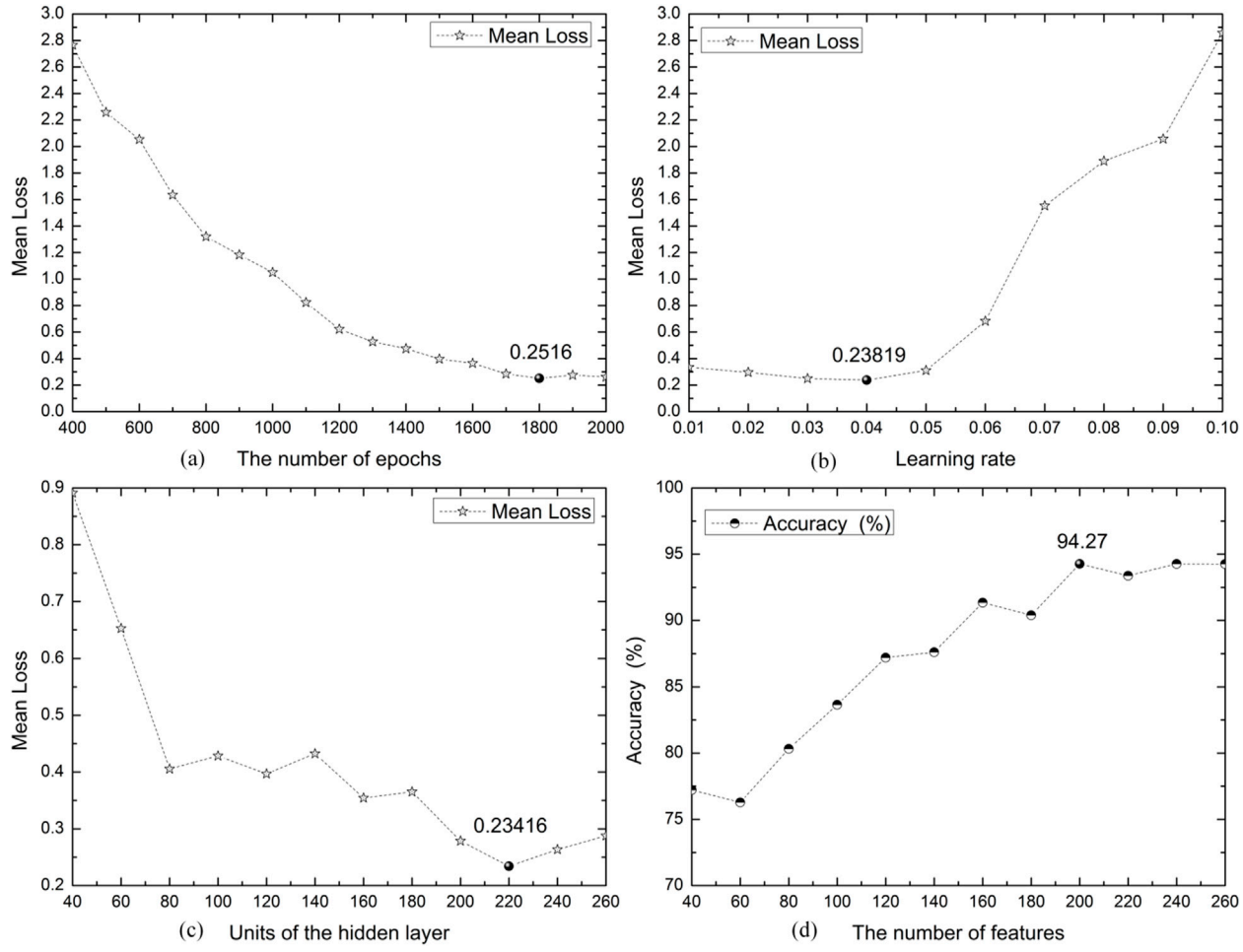

FIGURE 4
The Parameters of MBDFE. **(A)** Demonstrates the impact of the number of parameter iterations on algorithm performance, **(B)** shows the effect of the learning rate on algorithm performance, **(C)** illustrates the influence of the hidden layer dimensions on algorithm performance, and **(D)** presents the impact of the number of feature selections on algorithm performance.

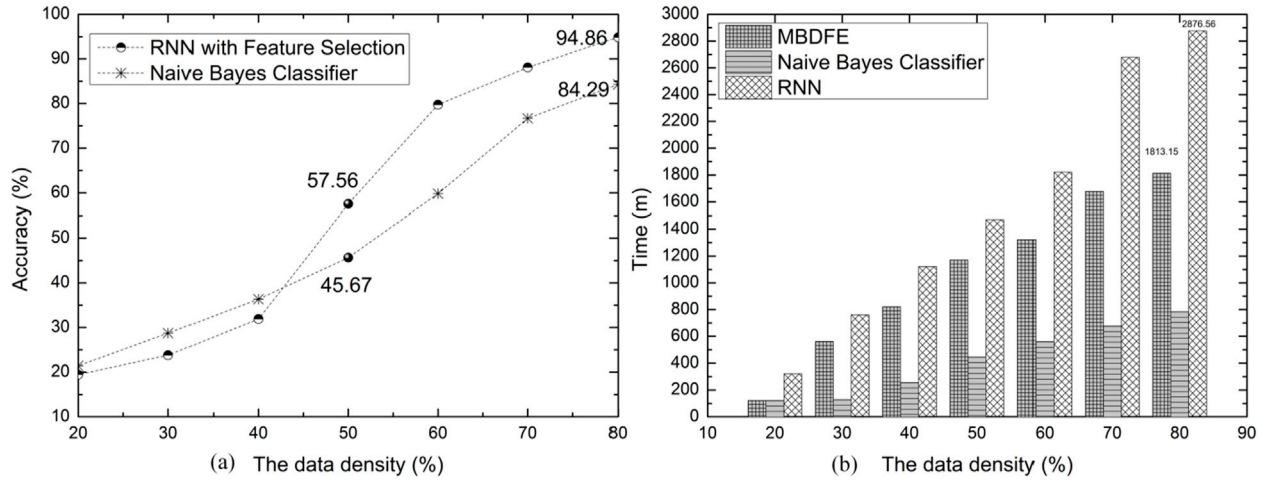

FIGURE 5
The Performance Comparison of Algorithms. **(A)** Presents a comparison of classification performance between the RNN with feature selection proposed in the MBDFE and the Naive Bayes algorithm. **(B)** Illustrates a comparison of algorithmic running times among the MBDFE, the RNN without feature selection, and the Naive Bayes algorithm.

classifier. This is because at lower data densities, the weights of the RNN model within MBDFE are not fully trained, leading to decreased classification performance. However, once the data density exceeds 50%, MBDFE's performance begins to surpass that of the Bayesian classifier. This is due to the Naive Bayes [23] model's assumption of feature independence, which is often not the case in practice, especially with malicious software behaviors that tend to be sequential, limiting the performance of the Bayesian model. In contrast, the RNN in MBDFE can handle sequential data, resulting in better classification performance after full training. Particularly at a data density of 80%, MBDFE achieves an accuracy rate of 94.86%, which is a 13% improvement over the Bayesian model's accuracy rate of 84.29%.

5 Conclusion and future work

This paper explores how to reduce the risk of corporate data assets being compromised by malicious activities and proposes a machine learning technique based on feature selection to identify malicious behaviors within software. The technique primarily uses feature selection algorithms to identify key features of software operation and applies them to a recurrent neural network classifier to determine whether the software's behavior is malicious. Experimental results show that compared to existing algorithms, this approach has improved accuracy in identification.

Although the proposed solution in this paper provides some reference value for malicious behavior detection, no technical solution can predict all malicious behaviors once and for all. Malware attackers will continuously change their attack methods, seeking vulnerabilities in defense systems. Future research should not only enhance the technology for identifying malicious behaviors but also formulate corresponding strategies at the management level based on the development trends of malicious behavior prediction methods. Our future research direction is to combine the engineering methods of natural sciences with the management methods of social sciences to propose an integrated solution for more effective detection and defense against malicious behaviors.

Data availability statement

The original contributions presented in the study are included in the article/supplementary material, further inquiries can be directed to the corresponding author.

Author contributions

HX: Methodology, Writing–original draft, Writing–review and editing. YW: Formal Analysis, Writing–review and editing. QT: Software, Writing–review and editing.

Funding

The author(s) declare that financial support was received for the research, authorship, and/or publication of this article. 1. The project of enterprise temporary job of Science and engineering teachers from colleges and universities of Anhui Province (2024jsqygz104). 2. The Project of Artificial intelligence serving the characteristics of ten emerging industries of Anhui province (2023sdxx078). 3. Research on the Teaching Reform of "Software Development and Practice" Course Based on OBE Education Concept under the Open Source Software Ecology of Tongling University (2023xj022).

Acknowledgments

In this study, we utilized the Kimi artificial intelligence technology, version 1.0, 2024, developed by Moonshot AI Co., Ltd., to meticulously check the grammar of our article. The

advanced algorithms and user-friendly interface of Kimi greatly facilitated our workflow, ensuring the accuracy and professionalism of the article's grammar. We are particularly grateful for the technical support and resources provided by Moonshot AI Co., Ltd., which enabled our research work to proceed smoothly. For more information about Kimi technology, you can visit the official website: https://kimi.moonshot.cn.

Conflict of interest

Author QT was employed by Zhongyuan Oilfield Company of SINOPEC.

The remaining authors declare that the research was conducted in the absence of any commercial or financial relationships that could be construed as a potential conflict of interest.

Publisher's note

All claims expressed in this article are solely those of the authors and do not necessarily represent those of their affiliated organizations, or those of the publisher, the editors and the reviewers. Any product that may be evaluated in this article, or claim that may be made by its manufacturer, is not guaranteed or endorsed by the publisher.

References

1. Fanfei M. Research on IT governance and risk management based on COBIT framework. *Shanghai Business* (2021) (1) 3.

2. Peng C. Risk factors and prevention measures of accounting informatization in the big data era. *Fiscal Res* (2014) 000(004):73–6. doi:10.19477/j.cnki.11-1077/f.2014.04.020

3. Liu S, Sun J. Big data thinking: application in tax risk management. *Econ Res Reference* (2016) (9) 19–26. doi:10.16110/j.cnki.issn2095-3151.2016.09.005

4. Yang L. Construction of enterprise operational risk control system based on "big data platform". *Econ Management (Digest Edition)* (2017) 38–9.

5. Zhang L. Construction of enterprise financial risk management system model based on big data. *China Management Informationization* (2017) (17) 2.

6. Rui W, Dengguo F, Yi Y, PuRui S. Semantic-based malicious code behavior feature extraction and detection method. *J Softw* (2012) 2:206–11. doi:10.3724/SP.J.1001.2012.03953

7. Sathyanarayan VS, Kohli P, Bruhadeshwar P. Signature generation and detection of malware families. In: *Proc. of the 13th Australia Conference on International Security and Privacy*, 5107. Berlin: Springer Press (2008). p. 336–349.

8. Ying F, Bo Y, Yong T, Liu L, Zexin L, Yi W, et al. A new malware classification approach based on malware dynamic analysis. In: *Proc. Of australasian conference on information security and privacy ACISP*. Berlin: Springer (2017). p. 173–89.

9. Park Y, Reeves DS, Stamp M. Deriving common malware behavior through graph clustering. *Comput and Security* (2013) 39:419–30. doi:10.1016/j.cose.2013.09.006

10. Ding Y, Xia X, Chen S, Li Y. A malware detection method based on family behavior graph. *Comput and Security* (2018) 73:73–86. doi:10.1016/j.cose.2017.10.007

11. Zhang H, Zhang W, Lv Z, Sangaiah AK, Huang T, Chilamkurti N. MALDC: a depth detection method for malware based on behavior chains. *World Wide Web* (2020) 23(2):991–1010. doi:10.1007/s11280-019-00675-z

12. Li S, Jiang L, Zhang Q, Wang Z, Tian Z, Guizani M. A malicious mining code detection method based on multi-features fusion. *IEEE Trans Netw Sci Eng* (2022) 10(5): 2731–9. doi:10.1109/tnse.2022.3155187

13. Amer E, Zelinka I, El-Sappagh S. A multi-perspective malware detection approach through behavioral fusion of api call sequence. *Comput and Security* (2021) 110:102449. doi:10.1016/j.cose.2021.102449

14. Zhan D, Tan K, Ye L, Yu X, Zhang H, He Z. An adversarial robust behavior sequence anomaly detection approach based on critical behavior unit learning. *IEEE Trans Comput* (2023) 72:3286–99. doi:10.1109/tc.2023.3292001

15. Wong GW, Huang YT, Guo YR, Sun Y, Chen MC. Attention-based API locating for malware techniques. *IEEE Trans Inf Forensics Security* (2023) 19:1199–212. doi:10.1109/tifs.2023.3330337

16. Chen X, Hao Z, Li L, Cui L, Zhu Y, Ding Z, et al. Cruparamer: learning on parameter-augmented api sequences for malware detection. *IEEE Trans Inf Forensics Security* (2022) 17:788–803. doi:10.1109/tifs.2022.3152360

17. Pektaş A, Acarman T. Deep learning for effective Android malware detection using API call graph embeddings. *Soft Comput* (2020) 24:1027–43. doi:10.1007/s00500-019-03940-5

18. Sun B, Takahashi T, Ban T, Inoue D. Detecting android malware and classifying its families in large-scale datasets. *ACM Trans Management Inf Syst (Tmis)* (2021) 13(2): 1–21. doi:10.1145/3464323

19. Tharani JS, Hóu Z, Charles EYA, Rathore P, Palaniswami M, Muthukkumarasamy V. Unified feature engineering for detection of malicious entities in blockchain networks. *IEEE Trans Inf Forensics Security* (2024) 19:8924–38. doi:10.1109/tifs.2024.3412421

20. Zou D, Wu Y, Yang S, Chauhan A, Yang W, Zhong J, et al. IntDroid: android malware detection based on API intimacy analysis. *ACM Trans Softw Eng Methodol (Tosem)* (2021) 30(3):1–32. doi:10.1145/3442588

21. Gao T, Duan L, Feng L, Ni W, Sheng QZ. A novel blockchain-based responsible recommendation system for service process creation and recommendation. *ACM Trans Intell Syst Technology* (2024) 15:1–24. doi:10.1145/3643858

22. Niveditha S, Rr P, Sathya K, Shreyanth S, Subramani N, Deivasigamani B, et al. Predicting malware classification and family using machine learning: a Cuckoo environment approach with automated feature selection. *Proced Computer Sci* (2024) 235:2434–51. doi:10.1016/j.procs.2024.04.230

23. Verma G, Sahu TP. A correlation-based feature weighting filter for multi-label Naive Bayes. *Int J Inf Technology* (2024) 16(1):611–9. doi:10.1007/s41870-023-01555-6

frontiers | Frontiers in Physics

TYPE Original Research
PUBLISHED 03 December 2024
DOI 10.3389/fphy.2024.1492423

OPEN ACCESS

EDITED BY
Xuzhen Zhu,
Beijing University of Posts and Telecommunications (BUPT), China

REVIEWED BY
Yang Tian,
Beijing Information Science and Technology University, China
Shuo He,
Zhengzhou University, China
Dandan Zhu,
Zhengzhou University of Light Industry, China

*CORRESPONDENCE
Feng Li,
cmulifeng455112@163.com

RECEIVED 06 September 2024
ACCEPTED 04 November 2024
PUBLISHED 03 December 2024

CITATION
Li F (2024) Dynamics analysis of epidemic spreading with individual heterogeneous infection thresholds.
Front. Phys. 12:1492423.
doi: 10.3389/fphy.2024.1492423

Dynamics analysis of epidemic spreading with individual heterogeneous infection thresholds

Feng Li[1,2]*

[1]Department of Rheumatology and Immunology, Shenzhen Children's Hospital, Shenzhen, China, [2]Department of Pediatrics, Anyang Maternal and Child Health Care Hospital, Anyang, China

In the real world, individuals may become infected with an epidemic after multiple exposures to the corresponding virus. This occurs because each individual possesses certain physical defenses and immune capabilities at the time of exposure to the virus. Repeated exposure to the virus can lead to a decline in immune competence, consequently resulting in epidemic infection. The susceptibility of individuals to an epidemic is heterogeneous. We model this characteristic as the individual heterogeneous infection threshold. Then, we propose an individual logarithmic-like infection threshold function on a single-layer complex network to reflect the heterogeneity of individual susceptibility on infecting the virus and the associated epidemic. Next, we introduce a partition theory based on the edge and logarithmic-like infection threshold function to qualitatively analyze the mechanisms of virus infection and epidemic spreading. Finally, simulation results on Erdő–Rényi (ER) and scale-free (SF) networks indicate that increasing both the epidemic infection initial threshold and outbreak threshold, as well as decreasing the virus and epidemic infection probability, can all effectively suppress epidemic spreading and epidemic infection outbreak. With an increase in the epidemic infection outbreak threshold, the increasing pattern of the final epidemic infection scale transitions from a second-order continuous phase transition to a first-order discontinuous phase transition. Additionally, degree distribution heterogeneity also significantly impacts the outbreak and spread of diseases. These findings provide valuable guidance for the formulation of immunization strategies.

KEYWORDS

epidemic spreading, individual heterogeneous infection threshold, transmission dynamic, complex network, partition theory

1 Introduction

As early as 1760, Bernoulli proposes the first model for the spread of smallpox, marking the birth of transmission dynamics [1]. In 2001, Pastor-Satorras and Vespignani were the first to utilize complex networks to describe transmission pathways and explore the impact of network topology on epidemic spread, subsequently investigating its implications on transmission dynamics [2]. This work garners widespread attention from scholars domestically and internationally, signaling the emergence of complex network transmission dynamics. Virus infection and epidemic spreading is one of the primary research subjects within this field. In most real-world networks, common

phenomena such as the spread of computer viruses and epidemics are interpreted through the lens of epidemic dynamics on complex networks [3–5]. The epidemic and infectious disease spreading not only affects public health but also leads to significant economic losses.

The study of epidemic spreading on complex networks primarily focuses on "simple" propagation, where the probability of epidemic infection remains constant across two consecutive contacts. Scholars have proposed several classic compartmental models tailored to different types of diseases, including the susceptible–infectious (SI) model, the susceptible–infectious–recovered (SIR) model, and the susceptible–infectious–susceptible (SIS) model [6]. [7] offered new perspectives for establishing a precise theoretical framework for spreading dynamics on complex networks by integrating the most commonly utilized theoretical methods which include mean-field [8], heterogeneous mean-field, quench mean-field [9], dynamical message-passing, link percolation, and pairwise approximation.

In the era of big data, we have more opportunities to access relevant data on human behavioral activities, including social activity data [10]. This authentic big data allow for a greater possibility of uncovering the true mechanisms behind epidemic and disease transmission [11]. Through the analysis of real-world data, researchers have discovered that human behavioral activities significantly influence epidemic and disease transmission [12]. Some scholars focus on accurately identifying the epidemic outbreak thresholds as these thresholds are crucial in many real-world scenarios. When the number of exposures an individual has to the virus reaches a certain threshold, the individual may become infected with the epidemic. The epidemic threshold represents the critical condition under which a system is in an active outbreak state [13]. A substantial amount of theoretical research has been conducted to predict the outbreak thresholds of SIR models [14–17].

In theoretical terms, accurately determining the epidemic infection outbreak thresholds can identify the critical conditions for the emergence of global large-scale epidemics [18]. It also significantly impacts the study of critical phenomena, including the determination of critical exponents [19]. In practical applications, epidemic infection outbreak thresholds can characterize the effectiveness of immunization strategies [20] and assist in identifying the optimal initial transmission source [21].

[22] utilized numerical computations based on the SIR epidemic model to relatively accurately predict the spread of COVID-19 and other pandemics. [23] employed time-varying networks to simulate the disease transmission process and proposed the most effective measures for controlling epidemic spread. [24] investigated the impact of vaccination on the dynamics of epidemic models, introducing a novel fractional-order discrete-time SIR epidemic model aimed at illustrating and quantifying the complex dynamics of the system. [25] considered the influence of individual and mass media information dissemination on epidemic spread, exploring the dynamic interactions between information transmission and susceptible-exposed-infectious-recovered (SEIR)-based epidemic spread. Additionally, unlike traditional information transmission, most current studies on epidemic spreading focus on "simple" propagation, i.e., a fixed infection threshold, overlooking the threshold heterogeneity [26–28].

From the factors discussed above, it is recognized that epidemic infection outbreak thresholds are critical in epidemic spreading, influencing not only the scale of outbreaks and their critical conditions but also providing effective guidance for the formulation of immunization strategies. Traditional studies on viral infection and epidemic transmission often assume that the probability of epidemic infection from two consecutive exposures is constant, suggesting that epidemic transmission lacks memory. Although this simplification facilitates the analysis of epidemic spread, it does not accurately reflect reality. In fact, human activities lead to a certain degree of memory and cumulative effects in the viruses and epidemic infections. As individuals are repeatedly exposed to the virus, the likelihood of epidemic infection outbreak increases.

Individuals possess certain physical defenses and immune capabilities. During initial exposure to the virus, factors such as the distance between individuals, the distribution of medical resources like masks, and variations in immune response may prevent the onset of disease. However, with an increasing number of viral exposures, individual immunity diminishes, significantly raising the probability of disease infection. Moreover, repeated epidemic infections can reduce sensitivity to the virus, leading to a diminishing marginal effect on the likelihood of developing the disease. Therefore, the individual susceptibility to infection epidemic is heterogeneous. Based on this understanding, we propose an individual heterogeneous infection threshold function, a logarithmic-like function, to explore the impact of individual characteristics on sensitivity to the virus and disease.

Based on the aforementioned motivations, we introduce a generalized SIR model on complex networks and propose an individual heterogeneous infection threshold function, a logarithmic-like function, to reflect the heterogeneity of individual susceptibility on infecting the virus and the associated disease. Furthermore, a partition theory based on the edge and individual heterogeneous infection threshold is proposed to theoretically analyze the dynamic processes of epidemic spreading. Finally, computer simulation results are presented to validate the findings of disease transmission, which align with the theoretical analysis. This study aims to leverage complex networks, computer simulations, and theoretical analyses to reveal the mechanisms and patterns of epidemic and disease transmission, thereby providing necessary theoretical support for early warning and control of epidemics and public sentiment. The rest of this paper is organized as follows: in Section 2, we build an epidemic spreading model with the individual heterogeneous infection threshold on complex networks. Section 3 exhibits an edge partition theory. In Section 4, the experimental results are discussed. Finally, Section 5 describes the conclusion.

2 Epidemic spreading model with individual heterogeneity

To investigate the impact of heterogeneity in individual susceptibility to infection epidemic on epidemic spreading mechanisms, we first construct two types of single-layer artificial complex network models, called the Erdő–Rényi (ER) networks [29] and the scale-free (SF) networks [30], for spreading dynamics. Each network has N nodes which represent individuals and degree distribution $P(k)$. The edges depict the interactions between individuals. We then apply a generalized SIR model, where each

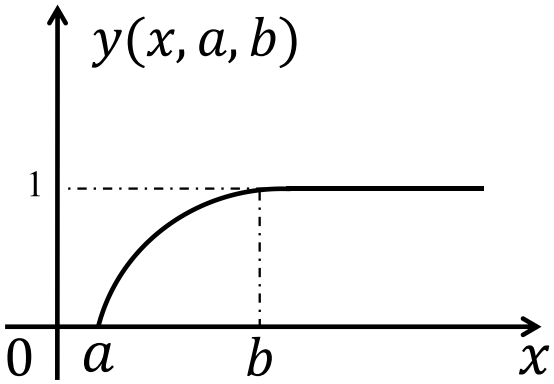

FIGURE 1
Illustration of the individual heterogeneous infection threshold model. The symbol x represents APIs of an S-state node, a represents the virus and epidemic infection initial threshold, and b denotes the epidemic infection outbreak threshold.

node can exist in one of three potential states: the susceptible state (S-state), where individuals are at risk of disease infection; the infected state (I-state), where individuals have contracted the disease and can spread the corresponding virus to their S-state neighbors; and the recovered state (R-state), where individuals have recovered from the infection and are no longer able to transition to any other state for a certain period of time.

Let the probability of one S-state node successfully being infected by the virus after coming into contact with its I-state neighbor node be λ. We introduce the concept of accumulated received infections (ARIs) to describe the infection accumulative total number of one S-state node by the virus from its I-state neighbors. Let n be the ARIs successfully received by the S-state node. Initially, $n_i = 0$ for the S-state node i, i.e., the virus has not yet spread within the population. At each time step, each I-state node transmits the virus to its S-state neighbors with a transmission probability of λ through the corresponding edge. If an S-state neighbor, denoted as node i, successfully receives the virus from an I-state node, the APIs of node i increases by 1, that is, $n_i \to n_i + 1$.

To investigate the impact of individual susceptibility heterogeneity to viruses and epidemic infection, an individual logarithmic-like infection threshold function, as shown in Figure 1, is proposed:

$$y(x,a,b) = \begin{cases} 0, & 0 \le x \le a, \\ \dfrac{\ln(x+1) - \ln(a+1)}{\ln(b+1) - \ln(a+1)}, & a < x < b, \\ 1, & x \ge b, \end{cases} \tag{1}$$

where a represents the virus and epidemic infection initial threshold, while b denotes the epidemic infection outbreak threshold. The difference $\delta = b - a$ indicates the interval between the disease infection threshold outbreak and the initial threshold.

Specifically, a indicates that the S-state node is infected with a certain number of viruses from its I-state neighbors, indicating the likelihood of converting to an I-state, i.e., the disease breaks out with a certain probability. δ denotes the interval length of the disease spreading probability for the S-state node. b indicates that the S-state node has received a sufficient quantity of viral infections from its I-state neighbors to make disease infection outbreak probability 1, that is, the probability that the S-state node infects epidemic and converts to I-state reaches 1. In other words, when the APIs of an S-state node are equal to or greater than b, the node will inevitably experience an epidemic infection outbreak and transition to the I-state.

The human body possesses immune capabilities and physical defenses. As individuals are exposed to the virus more frequently, the probability of epidemic infection outbreak increases. However, due to the increasing of APIs, individuals' sensitivity to the virus decreases, leading to a diminishing marginal effect of epidemic infection. Therefore, the logarithmic-like infection threshold function for individual heterogeneous infection is relevant and meaningful.

Next, we summarize the process of virus and epidemic spreading within complex networks. Initially, a proportion ρ_0 of nodes is randomly selected to be infected with the epidemic, while the remaining nodes are in the S-state. S-state nodes may come into contact with I-state nodes and have a probability of λ to contract the virus. As APIs of S-state nodes increase, the probability of an epidemic infection outbreak is $y(x,a,b)$. For I-state nodes, recovery occurs with a probability of γ due to factors such as physical isolation, medical treatment, and immune enhancement, after which they are not susceptible to reinfection for a certain period. Ultimately, the epidemic spreading ceases when there are no longer any infections or diseases present in the network. The proportion of individuals in the R-state at this point characterizes the final scale of the epidemic transmission process.

3 The analysis of partition theory based on edge and individual heterogeneity

To better investigate the epidemic spreading process, we develop a partition theory incorporating edge and the epidemic infection outbreak thresholds to analyze the effect of the individual heterogeneity on epidemic spreading. In this approach, we assume that nodes with identical degrees are statistically equivalent. The variables $S(t)$, $I(t)$, and $R(t)$ are employed to derive the evolution of epidemic spreading and depict the proportions of nodes in the S, I, and R states at time t, respectively. When $t \to \infty$, $R(\infty)$ is the final proportion of individuals in the complex network who have ever been infected by epidemic. Therefore, we can express the relationship as

$$S(t) + I(t) + R(t) = 1. \tag{2}$$

Let $\theta(t)$ be the probability that an S-state node has not been infected by the virus through a randomly chosen edge by time t. The probability that the S-state node i of degree k has q APIs from its I-state neighbors up to time t is

$$\phi(k_i, q, t) = C_{k_i}^{q} \theta(t)^{k_i - q} [1 - \theta(t)]^{q}. \tag{3}$$

By time t, the S-state node i has been infected q-times virus from its I-state neighbors. The node i does not experience an disease infection outbreak and remains in the S-state with the probability $\prod_{m=0}^{q} [1 - y(m,a,b)]$.

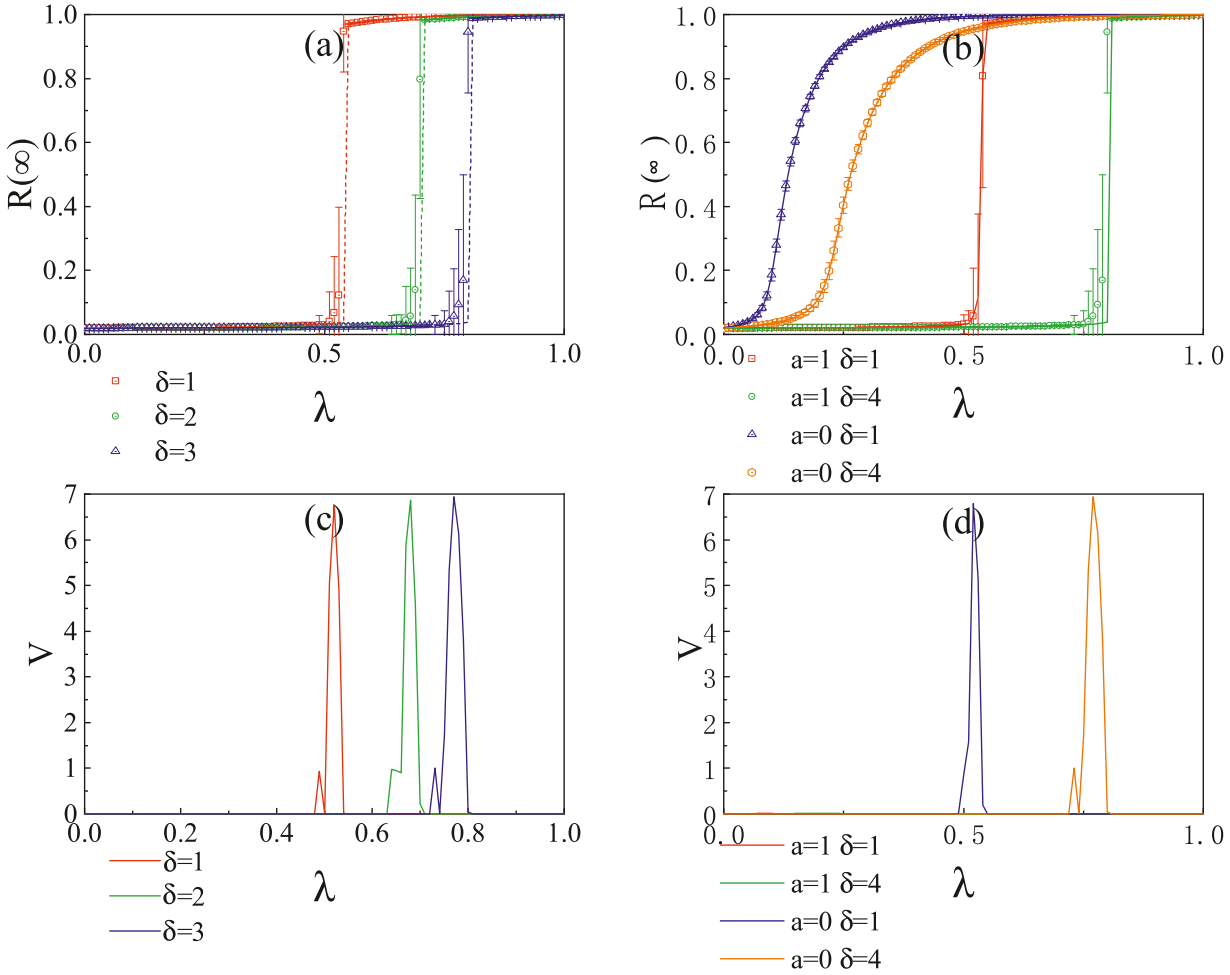

FIGURE 2
In the ER network, the impact of the infection probability λ on the final size $R(\infty)$ of the viral and epidemic outbreak with different a and δ. **(A)** illustrates the effect of δ on $R(\infty)$ when $a = 1$. **(B)** Combined effects of a and δ on $R(\infty)$. The number of seeds is set to 200. Symbols represent the simulation results, while the curves depict the theoretical results.

According to the logarithmic threshold function for epidemic spreading, the probability that an S-state node i has been infected by the virus q times without experiencing a disease infection outbreak by time t is

$$\begin{aligned} s(k_i,q,t) &= \sum_{q=0}^{\infty} \phi(k_i,q,t) \prod_{m=0}^{q} [1 - y(m,a,b)] \\ &= \sum_{q=0}^{a} \phi(k_i,q,t) + \sum_{q=a+1}^{b-1} \phi(k_i,q,t) \prod_{m=a+1}^{q} \left(1 - \frac{\ln(m+1) - \ln(a+1)}{\ln(b+1) - \ln(a+1)}\right) \\ &= \sum_{q=0}^{a} \phi(k_i,q,t) + \sum_{q=a}^{b-1} \phi(k_i,q,t) \prod_{m=a+1}^{q} \frac{\ln(b+1) - \ln(m+1)}{\ln(b+1) - \ln(a+1)}. \end{aligned} \tag{4}$$

The probability that the APIs of a randomly selected S-state nodes by time t are less than the corresponding epidemic infection outbreak threshold is

$$s(k,t) = \sum_{k_i} P(k_i) s(k_i,q,t). \tag{5}$$

Therefore, at time t, a randomly selected individual is in S-state, i.e., the proportion of S-state nodes in the network is

$$S(t) = (1 - \rho_0) s(k,t). \tag{6}$$

Our goal is to solve for the three terms in Equation 2, specifically to derive the values of $S(t)$, $I(t)$, and $R(t)$. As indicated from Equations 3–6, it is necessary to calculate $\theta(t)$ in order to obtain the expression for $S(t)$. Consider the neighbor node j of the I-state node i. The node j can only be in one of three states: S-state, I-state, or R-state. Let $\psi_S(t)$, $\psi_I(t)$ and $\psi_R(t)$ represent the probabilities of node j being in the S-state, I-state, and R-state, respectively. Additionally, $\theta(t)$ can be expressed as

$$\theta(t) = \psi_S(t) + \psi_I(t) + \psi_R(t). \tag{7}$$

Since node i is in the S-state, its neighbor j can only likely to be infected by the virus from the $k_j - 1$ neighbors except node i. Therefore, the probability of node j being infected by the virus u times at time t is denoted as

$$\phi(k_j - 1, u, t) = C_{k_j-1}^{u} \theta(t)^{k_j-1-u} [1 - \theta(t)]^{u}. \tag{8}$$

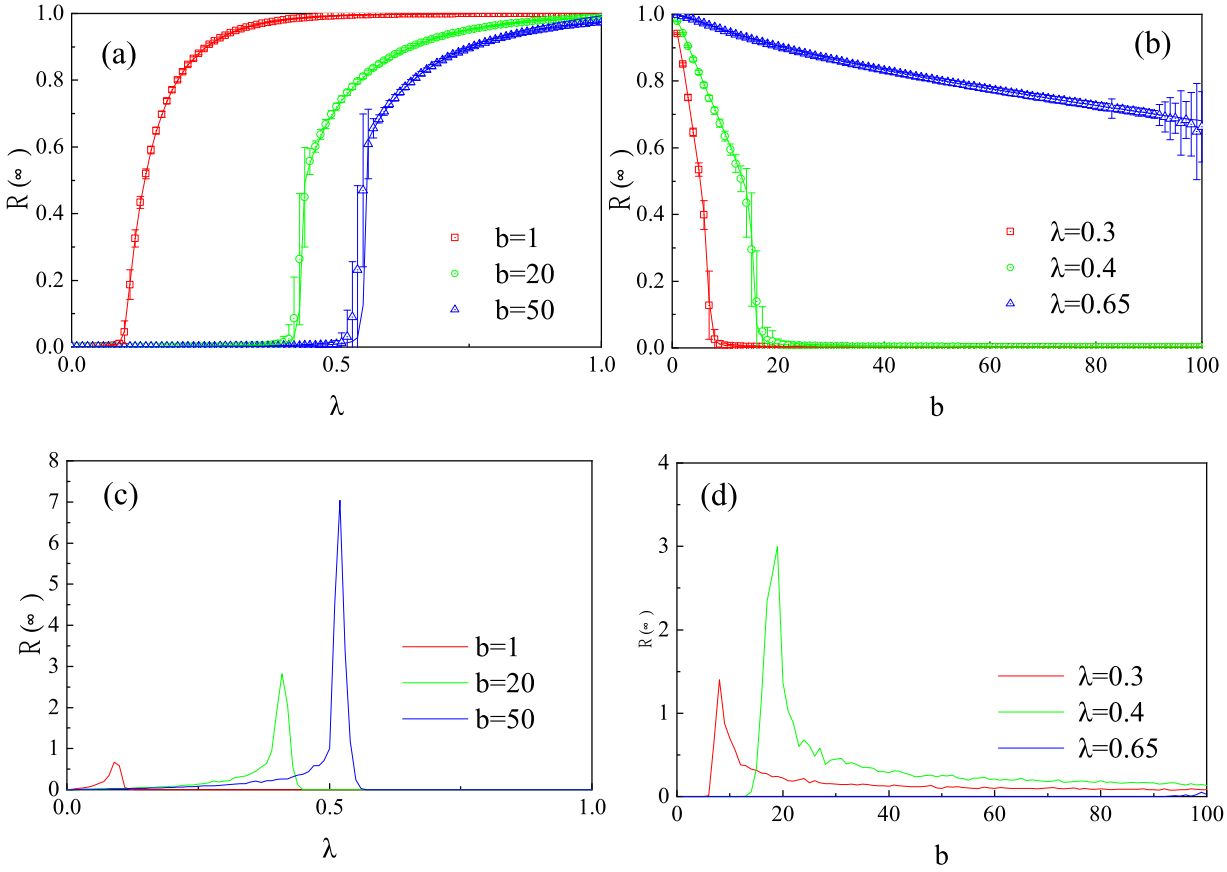

FIGURE 3
In the ER network, **(A)** illustrates the influence of the infection probability λ on the final epidemic outbreak size $R(\infty)$ when $a = 0$. **(B)** depicts the effect of the epidemic outbreak threshold parameter b on $R(\infty)$ under the same condition of $a = 0$. $\rho_0 = 0.0001$. Symbols represent simulation results, while curves denote theoretical predictions.

According to the logarithmic threshold function for disease spreading, the probability that an S-state node j has been infected by the virus u times without experiencing a disease infection outbreak by time t is

$$\begin{aligned}\varphi(k_j,t) &= \sum_{u=0}^{\infty}\phi(k_j-1,u,t)\prod_{m=0}^{u}[1-y(u,a,b)]\\ &= \sum_{u=0}^{a}\phi(k_i-1,u,t)+\sum_{u=a+1}^{b-1}\phi(k_i-1,u,t)\prod_{m=a+1}^{u}(1-y(u,a,b))\\ &= \sum_{u=0}^{a}\phi(k_i-1,u,t)+\sum_{u=a+1}^{b-1}\phi(k_i-1,u,t)\prod_{m=a+1}^{u}\frac{\ln(b+1)-\ln(m+1)}{\ln(b+1)-\ln(a+1)}.\end{aligned} \tag{9}$$

Let $\langle k\rangle$ be the average degree of the network, the probability that node i connects to node j with degree k_j is $k_jP(k_j)/\langle k\rangle$. Therefore, the probability that the node i connects to the S-state node j with degree k_j is

$$\psi_S(t) = (1-\rho_0)\frac{\sum_{k_j}k_jP(k_j)\varphi(k_j,t)}{\langle k\rangle}. \tag{10}$$

Due to variations in the distance between individuals, differences in individual immunity, and the protective measures taken by individuals, after the S-state node i comes into contact with the I-state node j, the node i has a probability of λ to become infected by the virus. Thus, the variation in $\theta(t)$ can be expressed as

$$\frac{d\theta(t)}{dt} = -\lambda\psi_I(t). \tag{11}$$

The I-state node has a probability of λ to infect its neighbors and a probability of γ to alter to the R-state. Therefore, the variation in $\psi_R(t)$ can be expressed as

$$\frac{d\psi_R(t)}{dt} = \gamma(1-\lambda)\psi_I(t). \tag{12}$$

Combining Equations 11, 12 and the initial conditions $\theta(0) = 1$ and $\psi_R(0) = 0$, we can obtain the evolution of $\psi_R(t)$:

$$\psi_R(t) = \gamma[1-\theta(t)]\left(\frac{1}{\lambda}-1\right). \tag{13}$$

Substituting Equation 10 and Equation 13 into Equation 7, we obtain

$$\begin{aligned}\psi_A(t) = \theta(t)-\psi_S(t)-\psi_R(t) = \theta(t)-(1-\rho_0)\frac{\sum_{k_j}k_jP(k_j)\varphi(k_j,t)}{\langle k\rangle}\\ -\gamma[1-\theta(t)]\left(\frac{1}{\lambda}-1\right).\end{aligned} \tag{14}$$

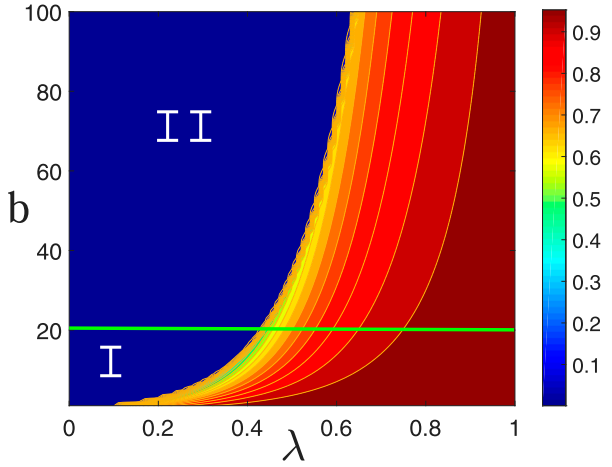

FIGURE 4
Joint effects of the infection probability λ and the epidemic outbreak threshold parameter b on the final outbreak size $R(\infty)$ in an ER network, with other parameters $a = 0$ and $\rho_0 = 0.0001$.

Substituting Equation 14 into Equation 11, the evolution of $\theta(t)$ can be rewritten as

$$\frac{d\theta(t)}{dt} = -\lambda\left\{\theta(t) - (1-\rho_0)\frac{\sum_{k_j} k_j P(k_j)\varphi(k_j,t)}{\langle k\rangle} - \gamma[1-\theta(t)]\left(\frac{1}{\lambda}-1\right)\right\}$$
$$= (1-\rho_0)\lambda\frac{\sum_{k_j} k_j P_X(k_j)\varphi(k_j,t)}{\langle k\rangle} + \gamma(1-\lambda) - [\lambda+(1-\lambda)\gamma]\theta(t). \tag{15}$$

Throughout the network, we have the density variation of each state

$$\frac{dA(t)}{dt} = -\frac{dS(t)}{dt} - \gamma A(t) \tag{16}$$

and

$$\frac{dR(t)}{dt} = \gamma A(t). \tag{17}$$

Equations 2–6; Equations 15–17 provide a comprehensive description of the transmission dynamics of viruses and diseases. By combining and iterating these equations, the density of each state at arbitrary time step, i.e., the values of $S(t)$, $A(t)$, and $R(t)$, can be calculated.

As $t \to \infty$, there are no I-state nodes, leaving only S-state nodes and R-state nodes in the network. $R(\infty)$ is the epidemic infection outbreak scale. Let $\frac{d\theta(t)}{dt}|_{t=\infty} \to 0$. The viruses and disease propagation of the network reaches a steady state. We obtain

$$\theta(\infty) = \frac{(1-\rho_0)\lambda\sum_{k_j} k_j P(k_j)\varphi(k_j,\infty) + \langle k\rangle\gamma(1-\lambda)}{\langle k\rangle\gamma + (1-\gamma)\lambda\langle k\rangle}. \tag{18}$$

In epidemic spreading, the maximum value of the steady-state fixed point of Equation 18 is of paramount importance and is denoted by the critical probability point $\theta_c(\infty)$. By determining when the critical probability point appears, the crucial conditions under which an epidemic infection outbreak occurs can be derived by

$$g[\theta(\infty),\rho_0,q,\gamma,\lambda] = \frac{(1-\rho_0)\lambda\sum_k kP(k)\varphi(k,\infty)}{\langle k\rangle\gamma + (1-\gamma)\lambda\langle k\rangle} + \frac{\gamma(1-\lambda)}{\gamma+(1-\gamma)\lambda} - \theta(\infty) \tag{19}$$

and

$$\frac{dg}{d\theta(\infty)}|_{\theta_c(\infty)} = 0. \tag{20}$$

From Equation 20, the critical infection probability can be calculated as

$$\lambda_c = \frac{\gamma}{\varepsilon+\gamma-1}, \tag{21}$$

where

$$\varepsilon = (1-\rho_0)\frac{\sum_k kP(k)\varphi\left(k_j,\infty\right)|_{\theta_c(\infty)}}{\langle k\rangle}. \tag{22}$$

Combining Equation 8 and Equation 9, we derive the expression of $\frac{d\varphi(k_j,\infty)}{d\theta(\infty)}$. Numerically solving Equation 18, Equation 21, and $\frac{d\varphi(k_j,\infty)}{d\theta(\infty)}$, we can obtain the critical value of the virus infection probability λ.

4 Results and discussions

Our paper focus on numerical experiments and theoretical analyses conducted on artificial ER networks and SF networks. The network size is $N = 10^4$, with an average network degree of $\langle k\rangle = 10$. For I-state nodes, measures such as physical isolation, physical defense, medication, and immune enhancement are implemented, so let the recovery probability be $\gamma = 1.0$. In ER networks, the degree distribution of nodes follows the Poisson distribution, i.e., $P(k) = e^{-\langle k\rangle}\frac{\langle k\rangle^k}{k!}$. In SF networks, the heterogeneity of node degree distribution is negatively correlated with the degree exponent v, with the heterogeneity decreasing as the degree exponent v increases. The degree distribution of nodes follows the power-law distribution $P(k) = \xi k^{-v}$, where $\xi = 1/\sum_k k^{-v}$. The minimum and maximum degree are $k_{min} = 4$ and $k_{max} \sim 100$, respectively. Our simulation results are the average value by running the simulation 1,000 times.

We use the relative variance $\mathcal{V}$ [31, 32] to illustrate the critical infection probability and critical conditions. The relative variance is

$$\mathcal{V} = N\frac{\langle R(\infty)^2\rangle - \langle R(\infty)\rangle^2}{\langle R(\infty)\rangle}, \tag{23}$$

where $\langle\cdots\rangle$ represents the ensemble average. The peak values of the relative variance represent the critical point of global epidemic spreading.

4.1 The epidemic spreading on the ER network

Figure 2A indicates that when $a = 1$, an increase in δ slows down the spread of the virus and the epidemic infection outbreak. The

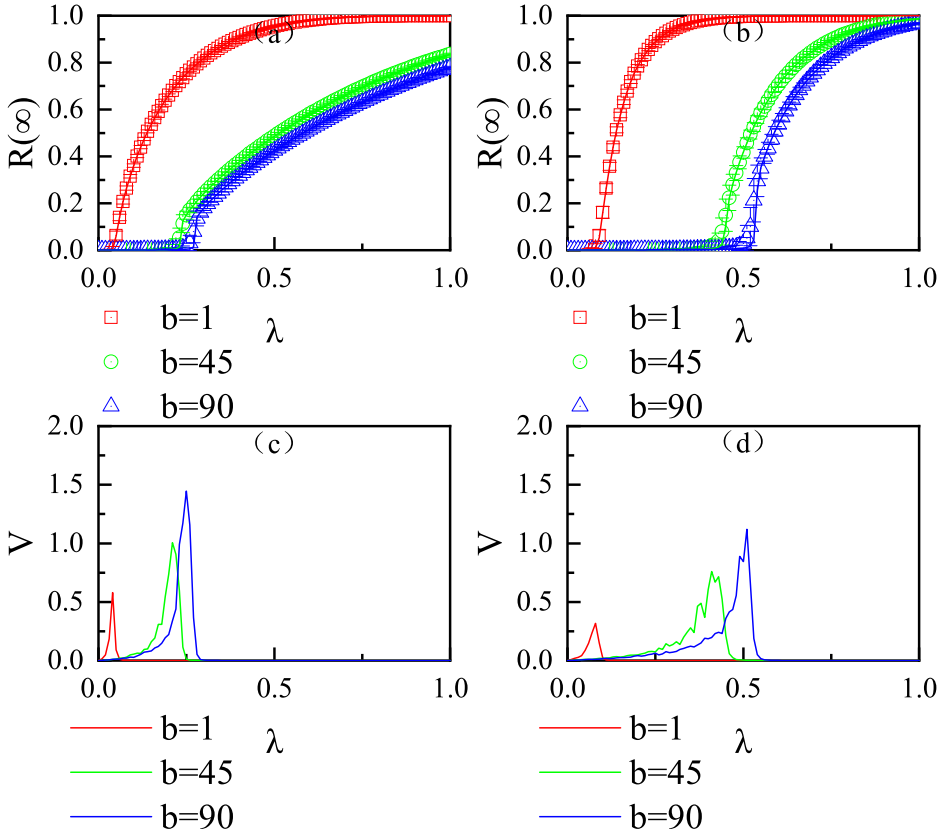

FIGURE 5
Influence of the virus infection probability λ on the final epidemic infection size $R(\infty)$ in SF networks with different degree distributions v. Specifically, **(A)** $v = 2.0$ and **(B)** $v = 4.0$, with $\rho_0 = 0.0001$ and $a = 0$.

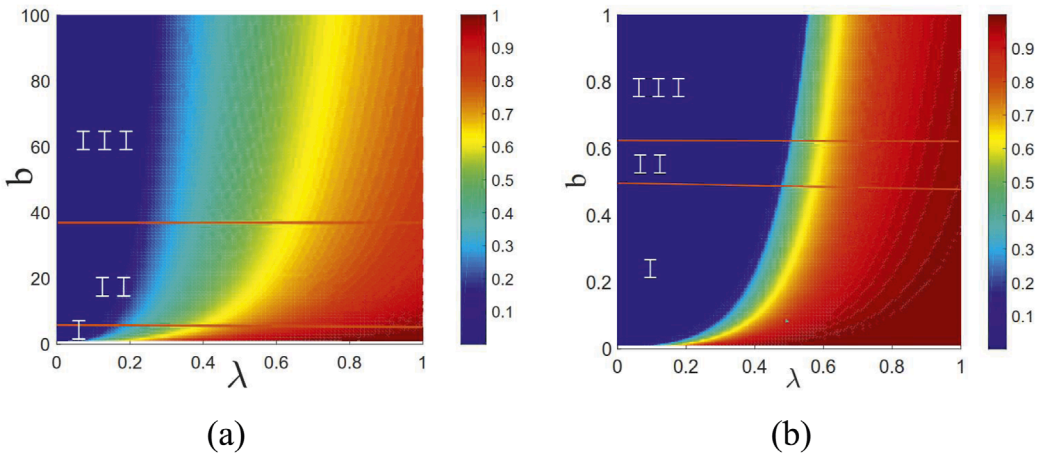

FIGURE 6
Joint effects of the virus infection probability λ and the epidemic outbreak threshold parameter b on the final epidemic size $R(\infty)$ in SF networks. Both scenarios of global epidemic infection outbreaks and localized epidemic infection outbreaks, as well as continuous and discontinuous phase transitions, are observed in **(A)** ($v = 2.0$) and **(B)** ($v = 4.0$). The other parameters are set to $a = 0$ and $\rho_0 = 0.0001$.

outbreak scale exhibits a first-order discontinuous phase transition. Figure 2B reveals that for the same δ, when $a = 0$, the epidemic outbreak scale corresponds to a second-order continuous phase transition. As a increases from 0 to 1, there is a significant suppression of virus transmission and epidemic infection outbreak, with the final epidemic infection outbreak scale transitioning

from a second-order continuous phase transition to a first-order discontinuous phase transition. Similarly, an increase in δ also mitigates the outbreak of the epidemic. Overall, increasing a and δ, as well as decreasing λ, can all effectively suppress the epidemic outbreak. Furthermore, Figures 2C, D display the relative variances of the theoretical analyses and the critical infection probabilities corresponding to (a) and (b), respectively. At the critical point, a phase transition occurs, leading to a global disease infection state. Our theoretical predictions (lines) align well with the simulation results (symbols).

Figure 3A shows the influence of the infection probability λ on the final epidemic outbreak size $R(\infty)$ when $a = 0$. As λ increases, the virus and disease spread more rapidly through the network, ultimately leading to a global epidemic infection outbreak. An increase in the epidemic infection outbreak threshold parameter b suppresses the occurrence of the disease. When b is small, the epidemic infection outbreak size exhibits second-order continuous phase transition. As b increases, the epidemic infection outbreak size transitions from a second-order continuous phase transition to a first-order discontinuous phase transition. Figure 3B illustrates the effect of b on the final epidemic infection outbreak size $R(\infty)$ when $a = 0$. With increasing b, the epidemic outbreak threshold becomes significantly higher, greatly reducing the likelihood of an epidemic outbreak. When λ is small, even a small b can effectively suppress the outbreak. However, when λ is large, variations in b become less effective in preventing the outbreak. Therefore, a combined approach of reducing λ and increasing b is necessary to effectively suppress the epidemic. Additionally, our theoretical predictions (lines) align well with the simulation results (symbols).

Figure 4 illustrates the joint effects of the infection probability λ and the epidemic infection outbreak threshold parameter b on the final scale of the epidemic outbreak $R(\infty)$. As shown in the figure, with an increase in λ, individuals become more susceptible to infection, leading to a gradual rise in the number of infected individuals, ultimately resulting in a global individual infection. Conversely, as b increases, the epidemic infection threshold probability decreases, resulting in a reduction in the number of individuals infected. Additionally, as b increases, a crossover phenomenon emerges in the trend of the graphical representation. The parameter space (b,λ) can be divided into two regions. In Region I, as λ increases, the increasing pattern of $R(\infty)$ exhibits characteristics of a second-order continuous phase transition. In Region II, as λ increases, the pattern of increase in $R(\infty)$ displays traits of a first-order discontinuous phase transition.

4.2 The epidemic spreading on the SF network

Figure 5 illustrates the effect of the epidemic infection probability λ on the final epidemic infection size $R(\infty)$ in scale-free networks characterized by heterogeneous degree distributions. The vertical subplots utilize the same degree distribution exponent, with the subplots in the first and second columns corresponding to $\nu = 2.1$ and $\nu = 4$, respectively. The initial seed density is set to $\rho_0 = 0.0001$. $a = 0$. When b is small, $R(\infty)$ gradually increases to global infection as λ increases, exhibiting a second-order continuous phase transition in the growth pattern of the final epidemic infection size. However, larger values of b suppress epidemic spreading. On one hand, epidemic spreading only occurs when λ is sufficiently high. On the other hand, higher values of b inhibit epidemic global epidemic infection and spreading. Furthermore, when b is large, the growth pattern of the final epidemic size displays a weak first-order discontinuous phase transition. Additionally, increasing the heterogeneity of the degree distribution (i.e., by using smaller values of the degree distribution exponent) facilitates disease infection.

Figure 6A, B explores the variation in the final epidemic infection size $R(\infty)$ in the epidemic spreading parameter space (λ, b) with $\nu = 2.0$ and $\nu = 4.0$, respectively. The initial seed fraction is set to $\rho_0 = 0.0001$. As the epidemic infection outbreak threshold parameter b increases, the growth pattern of $R(\infty)$ exhibits a crossover phase transition. The epidemic spreading parameter space (λ, b) is divided into three regions. In Region I, the epidemic spreads globally and the growth pattern of $R(\infty)$ displays second-order continuous phase transition characteristics. In Region II, the growth pattern of $R(\infty)$ remains a second-order continuous phase transition; however, the epidemic spreads locally due to the suppression by b on epidemic spreading. In Region III, the epidemic spreads locally and the growth pattern of $R(\infty)$ changes to a first-order discontinuous phase transition. Comparing (a) and (b), when ν is smaller, epidemic spreading begins with lower values of the virus infection probability λ and the epidemic outbreak threshold parameter b, but it is challenging for the epidemic to achieve global spread. However, when ν is larger, the epidemic spreads within the population only when λ and b exceed certain thresholds. However, under the same parameters, the weak degree distribution heterogeneity facilitates the occurrence of global epidemic spreading.

5 Conclusion

This paper considers the heterogeneity of individual susceptibility to infection epidemic and employs transmission dynamics to investigate the epidemic spreading process on single-layer complex networks. First, we propose a logarithmic-like threshold model and thoroughly examine its validity under the heterogeneity of individual infection epidemic susceptibility. Subsequently, we enhance the edge partition theory based on the individual logarithmic-like threshold function to analyze the epidemic spreading dynamic process. Through theoretical analysis and numerical simulations on ER and SF networks, we identify the factors influencing the scale of disease outbreaks and propose several strategies for mitigating epidemic spread.

Data availability statement

The raw data supporting the conclusions of this article will be made available by the authors, without undue reservation.

Author contributions

FL: conceptualization, data curation, formal analysis, investigation, methodology, project administration, resources,

software, supervision, validation, visualization, writing–original draft, and writing–review and editing.

Funding

The author(s) declare that no financial support was received for the research, authorship, and/or publication of this article.

Acknowledgments

The author would like to thank the reviewers for their insightful comments on the manuscript as their remarks led to an improvement of the work.

Conflict of interest

The author declares that the research was conducted in the absence of any commercial or financial relationships that could be construed as a potential conflict of interest.

Publisher's note

References

1. Bernoulli D. Essai d'une nouvelle analyse de la mortalite causée par la petite vérole et des avantages de l'inoculation pour la prévenir. *Histoire de l'Acad., Roy Sci.(Paris) avec Mém* (1760) 1–45. Available at: https://inria.hal.science/hal-04100467v1

2. Pastor-Satorras R, Vespignani A. Epidemic spreading in scale-free networks. *Phys Rev Lett* (2001) 86:3200–3. doi:10.1103/physrevlett.86.3200

3. Pastor-Satorras R, Castellano C, Van Mieghem P, Vespignani A. Epidemic processes in complex networks. *Rev Mod Phys* (2015) 87:925–79. doi:10.1103/revmodphys.87.925

4. Li Z, Zhu P, Zhao D, Deng Z, Wang Z. Suppression of epidemic spreading process on multiplex networks via active immunization. *Chaos: An Interdiscip J Nonlinear Sci* (2019) 29:073111. doi:10.1063/1.5093047

5. Yan G, Chen G, Eidenbenz S, Li N. Malware propagation in online social networks: nature, dynamics, and defense implications. In: *Proceedings of the 6th acm symposium on information, computer and communications security* (2011). p. 196–206.

6. Keeling MJ, Rohani P. *Modeling infectious diseases in humans and animals*. Princeton, NJ: Princeton university press (2011).

7. Wang W, Tang M, Stanley HE, Braunstein LA. Unification of theoretical approaches for epidemic spreading on complex networks. *Rep Prog Phys* (2017) 80:036603. doi:10.1088/1361-6633/aa5398

8. Li W, Xue X, Pan L, Lin T, Wang W. Competing spreading dynamics in simplicial complex. *Appl Mathematics Comput* (2022) 412:126595. doi:10.1016/j.amc.2021.126595

9. Feng L, Zhao Q, Zhou C. Epidemic spreading in heterogeneous networks with recurrent mobility patterns. *Phys Rev E* (2020) 102:022306. doi:10.1103/physreve.102.022306

10. Chun H, Kwak H, Eom YH, Ahn YY, Moon S, Jeong H. Comparison of online social relations in volume vs interaction: a case study of cyworld. In: *Proceedings of the 8th ACM SIGCOMM conference on Internet measurement* (2008). p. 57–70.

11. Zhang N, Yang Q, Zhu X. The impact of social resource allocation on epidemic transmission in complex networks. *Appl Mathematics Comput* (2022) 433:127405. doi:10.1016/j.amc.2022.127405

12. Gonzalez MC, Hidalgo CA, Barabasi AL. Understanding individual human mobility patterns. *nature* (2008) 453:779–82. doi:10.1038/nature06958

13. Moreno Y, Pastor-Satorras R, Vespignani A. Epidemic outbreaks in complex heterogeneous networks. *The Eur Phys J B-Condensed Matter Complex Syst* (2002) 26:521–9. doi:10.1140/epjb/e20020122

14. Zhu X, Wang Y, Zhang N, Yang H, Wang W. Influence of heterogeneity of infection thresholds on epidemic spreading with neighbor resource supporting. *Chaos: An Interdiscip J Nonlinear Sci* (2022) 32:083124. doi:10.1063/5.0098328

15. Basnarkov L, Tomovski I, Sandev T, Kocarev L. Non-markovian sir epidemic spreading model of covid-19. *Chaos, Solitons and Fractals* (2022) 160:112286. doi:10.1016/j.chaos.2022.112286

16. Kabir KA, Kuga K, Tanimoto J. Analysis of sir epidemic model with information spreading of awareness. *Chaos, Solitons and Fractals* (2019) 119:118–25. doi:10.1016/j.chaos.2018.12.017

17. Yavuz M, Özdemir N. Analysis of an epidemic spreading model with exponential decay law. *Math Sci Appl E-Notes* (2020) 8:142–54. doi:10.36753/mathenot.691638

18. Dorogovtsev SN, Goltsev AV, Mendes JF. Critical phenomena in complex networks. *Rev Mod Phys* (2008) 80:1275–335. doi:10.1103/revmodphys.80.1275

19. Mata AS, Boguñá M, Castellano C, Pastor-Satorras R. Lifespan method as a tool to study criticality in absorbing-state phase transitions. *Phys Rev E* (2015) 91:052117. doi:10.1103/physreve.91.052117

20. Cohen R, Havlin S, Ben-Avraham D. Efficient immunization strategies for computer networks and populations. *Phys Rev Lett* (2003) 91:247901. doi:10.1103/physrevlett.91.247901

21. Kitsak M, Gallos LK, Havlin S, Liljeros F, Muchnik L, Stanley HE, et al. Identification of influential spreaders in complex networks. *Nat Phys* (2010) 6:888–93. doi:10.1038/nphys1746

22. Marinov TT, Marinova RS. Dynamics of covid-19 using inverse problem for coefficient identification in sir epidemic models. *Chaos, Solitons and Fractals* (2020) 5:100041. doi:10.1016/j.csfx.2020.100041

23. Rizi AK, Faqeeh A, Badie-Modiri A, Kivelä M. Epidemic spreading and digital contact tracing: effects of heterogeneous mixing and quarantine failures. *Phys Rev E* (2022) 105:044313. doi:10.1103/physreve.105.044313

24. He ZY, Abbes A, Jahanshahi H, Alotaibi ND, Wang Y. Fractional-order discrete-time sir epidemic model with vaccination: chaos and complexity. *Mathematics* (2022) 10:165. doi:10.3390/math10020165

25. Ma W, Zhang P, Zhao X, Xue L. The coupled dynamics of information dissemination and seir-based epidemic spreading in multiplex networks. *Physica A: Stat Mech its Appl* (2022) 588:126558. doi:10.1016/j.physa.2021.126558

26. Li Z, Xiong F, Wang X, Chen H, Xiong X. Topological influence-aware recommendation on social networks. *Complexity* (2019) 2019:6325654. doi:10.1155/2019/6325654

27. Hu Y, Xiong F, Pan S, Xiong X, Wang L, Chen H. Bayesian personalized ranking based on multiple-layer neighborhoods. *Inf Sci* (2021) 542:156–76. doi:10.1016/j.ins.2020.06.067

28. Yang Q, Zhu X, Tian Y, Wang G, Zhang Y, Chen L. The influence of heterogeneity of adoption thresholds on limited information spreading. *Appl Mathematics Comput* (2021) 411:126448. doi:10.1016/j.amc.2021.126448

29. Erdos P, Rényi A, et al. On the evolution of random graphs. *Publ Math Inst Hung Acad Sci* (1960) 5:17–60. Available at: https://api.semanticscholar.org/CorpusID:18045682

30. Catanzaro M, Boguná M, Pastor-Satorras R. Generation of uncorrelated random scale-free networks. *Phys Rev E* (2005) 71:027103. doi:10.1103/physreve.71.027103

31. Shu P, Wei W, Ming T, Do Y. Numerical identification of epidemic thresholds for susceptible-infected-recovered model on finite-size networks. *Chaos* (2015) 25:063104. doi:10.1063/1.4922153

32. Chen X, Wang W, Cai S, Eugene SH, Braunstein LA. Optimal resource diffusion for suppressing disease spreading in multiplex networks. *J Stat Mech Theor Exp* (2018) 5:053501. doi:10.1088/1742-5468/aabfcc

frontiers | Frontiers in Physics

TYPE Original Research
PUBLISHED 03 January 2025
DOI 10.3389/fphy.2024.1492731

OPEN ACCESS

EDITED BY
Xuzhen Zhu,
Beijing University of Posts and Telecommunications (BUPT), China

REVIEWED BY
Aurelio Patelli,
Enrico Fermi Center for Study and Research, Italy
Siming Deng,
Dalian University of Technology, China
Zhongjin Li,
Hangzhou Dianzi University, China

*CORRESPONDENCE
Hongshu Chen,
hongshu.chen@bit.edu.cn

RECEIVED 07 September 2024
ACCEPTED 21 November 2024
PUBLISHED 03 January 2025

CITATION
Jia Y, Chen H, Liu J, Wang X, Guo R and Wang X (2025) Exploring network dynamics in scientific innovation: collaboration, knowledge combination, and innovative performance.
Front. Phys. 12:1492731.
doi: 10.3389/fphy.2024.1492731

Exploring network dynamics in scientific innovation: collaboration, knowledge combination, and innovative performance

Yangyang Jia[1], Hongshu Chen[1]*, Jingkang Liu[2], Xuefeng Wang[1], Rui Guo[3] and Ximeng Wang[4]

[1]School of Management, Beijing Institute of Technology, Beijing, China, [2]School of Economics, Beijing Institute of Technology, Beijing, China, [3]School of Public Policy and Management, University of Chinese Academy of Sciences, Beijing, China, [4]Cyber Finance Department, Postal Savings Bank of China, Beijing, China

The system of scientific innovation can be characterized as a complex, multi-layered network of actors, their products and knowledge elements. Despite the progress that has been made, a more comprehensive understanding of the interactions and dynamics of this multi-layered network remains a significant challenge. This paper constructs a multilayer longitudinal network to abstract institutions, products and ideas of the scientific system, then identifies patterns and elucidates the mechanism through which actor collaboration and their knowledge transmission influence the innovation performance and network dynamics. Aside from fostering a collaborative network of institutions via co-authorship, fine-grained knowledge elements are extracted using KeyBERT from academic papers to build knowledge network layer. Empirical studies demonstrate that actor collaboration and their unique and diverse ideas have a positive impact on the performance of the research products. This paper also presents empirical evidence that the embeddedness of the actors, their ideas and features of their research products influence the network dynamics. This study gains a deeper understanding of the driving factors that impact the interactions and dynamics of the multi-layered scientific networks.

KEYWORDS

scientific innovation, complex network, network dynamics, stochastic actor-oriented model, collaboration network, knowledge network

1 Introduction

The system of scientific development and innovation can be described as a complex, self-organizing, and constantly evolving multi-layered network [1]. The rapid accumulation of digital data on the process, as well as the results of scientific innovation, have made it possible to model the overall structure of this dynamic network system [2]. Scientists and institutions draw on knowledge resources from collaboration networks, feeding back into the new creation, recombination, and transmission of knowledge elements, giving rise to new theories, methodologies, and technologies, sparking widespread interest in exploring

network dynamics in this system that involves social, managerial and economic values [3–5].

Existing research on the patterns and dynamics of the scientific system modeling started with single-layer complex networks. As the scientific innovation landscape gradually shifts from individual to collaborative activities, research on the complex system began to attract extensive attention from the academic community to a series of topics such as the properties and structure of collaboration networks [6–8], collaboration patterns [9, 10] and the formation and evolution mechanism of collaboration network [11, 12]. These networks mainly built from the co-author articles, co-applicant patents or jointly undertaken research projects reflecting the formal or informal collaborations among individuals, organizations or even countries, are commonly used to reveal patterns of collaboration and research behaviors [13–15].

Further research then illustrated that the scientific innovation system may exist in a multiplex structure state, where its elements are simultaneously embedded in both collaboration networks and knowledge networks [16, 17]. The multi-layered network has been proved to be have an "internetwork effect", meaning that changes in one network may affect the utility of the other [18]. Knowledge networks in the existing studies are mainly created via co-occurrences in the substance or core elements of innovation products, including keywords of scientific papers [19], IPC codes of patents [20], topics [21], MeSH terms [22], hashtags [23] and so on, reflect the research theme, knowledge flow and combinatorial history in research collaboration.

Although multi-layered network frameworks have been proposed for describing scientific innovation, existing research has not yet developed a comprehensive model to measure the nodes and links within the multiplex structure, including actors, innovative products, and knowledge elements, nor has it fully understood the dynamics mechanisms. Research on complex networks of scientific innovation has been limited to either collaboration networks or knowledge networks, providing only partial views of the systematic structure, and inadequate understanding of the network dynamics. Some prior studies have explored the impact of the properties of knowledge owned by individuals or institutions on the collaboration dynamics [24, 25], which are generally discussed in a macro perspective that also includes economic, geographical, cultural and other factors. Despite the progress that has been made, a more comprehensive understanding of the interaction of the multi-layered networks of scientific innovation, and their network dynamics, remains a significant challenge.

In response to these challenges, we consider the interactions between actors, their innovative products and knowledge element exchanges to reveal how collaboration and knowledge transmission influence the innovation performance and the network dynamics of scientific innovation. This paper constructs multilayer longitudinal networks to abstract institutions, products and ideas of the scientific system, and then elucidate the interaction mechanism among different layers by answering two questions: what features from collaboration and knowledge network affect the innovation product layer and how the embeddedness of the actors, their ideas and research outcome influence the network dynamics. From empirical perspective, H1 Connect academic articles recommendation database is used to perform a case study in the field of protein structure research. We collected scientific papers published from year 2014 to year 2022, which have been recommended by researchers on H1 Connect with associated scores and opinion tags. To further enhance this dataset, we integrated information from the bibliographic database Web of Science. Fine-granular knowledge elements are then extracted using KeyBERT from scientific papers to build knowledge networks. These networks serve as the foundation for identifying patterns of knowledge combination. We finally employ the stochastic actor-oriented models to uncover the underlying mechanisms governing network evolution in the field of protein structure. This comprehensive study gains a deeper understanding of the driving factors that impact the interactions and dynamics of the multi-layered scientific networks.

2 Literature review

2.1 Multi-layered networks for scientific innovation system

The scientific innovation system can be abstracted as an evolving complex system of diverse basic units of science that are dynamically linked and coupled. The key research question is how to model and simulate the system. The large-scale scientific publication datasets have created new opportunities to model and explore this system. With the development of complex network theory and methodology, and also their application in the science of science, the modelling of scientific innovation system has gradually shifted from single layer to multi-layers networks. The collaboration and knowledge networks have always attracted the most attention from scholars, as collaboration reveals innovative behavior, and knowledge reflects results. For example, Guan and Liu [16] have constructed the collaboration networks based on joint assignees of patents and knowledge networks based on the co-application of IPC codes in each patent, and accordingly studied the impact of organizations' doubly network embeddedness on innovation. Graf and Kalthaus [26] have distinguished the research network into three levels: co-authorship at the researcher level, the collaboration between organizations, and international collaboration between countries. Luo and Zhang [27] have constituted a multi-network includes the collaboration network of R&D organizations, the collaboration network of R&D employees and the knowledge network. Ba, Mao [28] have investigated how city-level collaboration and knowledge networks influence innovation in the energy conservation field.

A rich body of literature concerning the multi-layered networks of the scientific innovation system has revolved around the impact of network embeddedness on innovation. Existing research have long recognized that the collaboration and knowledge recombination could affect innovation performance [29–31]. While network embeddedness, especially multi-network embeddedness offers a unique and valuable lens to gain deeper insights into innovation. Network embeddedness reflects the position of the actor and the connection to other actors in the network [32], which determines the ability to gather, integrate and allocate resources. Gonzalez-Brambila, Veloso [33] have examined how embeddedness in the collaboration network affects the research output and impact of scientists. Zhang and Luo [34] have explored the relationship between innovation and the knowledge network capital (i.e.,

knowledge combinatorial capacity, knowledge stocks, technological distance and network efficiency).

In summary, most existing literature focus on dual layers network to model and analyze the mechanism of the scientific innovation system. However, prior literature has demonstrated that the scientific innovation system is the evolving set of actors, artifacts, and activities (relations) [35]. Drawing on this, multi-layered networks cover innovation entities (a publication of actors), innovative products (artifacts), knowledge elements (content of artifacts) and the relations among them need to be constructed to better abstract the system. Exploration under this framework warrants further research as well.

2.2 Network dynamics on scientific collaboration

Scientific collaboration forms the fundamental nexus of sharing and connection among actors, which gradually evolves into a collaboration network as the number of entities and connections increase. The majority of existing studies focus on investigating static properties of collaboration networks, such as network structure [36–38] and tie configuration [39–41]. However, the nature of scientific collaboration is far from static, with innovative entities constantly establishing and discontinuing partnerships [42]. An increasing number of scholars start to adopt a dynamic perspective to investigate network generation and evolution. Many statistical methods have been applied to network dynamics analysis, such as stochastic actor-oriented models (SAOMs), exponential random graph models (ERGMs), multiple regression quadratic assignment programs (MRQAPs) and so on. Ma, Yang [11] have used the ERGMs to investigate the formation mechanism of big data technology collaboration networks. Fronzetti Colladon, Grippa [43] have applied SAOMs to investigate the dynamics of knowledge sharing in healthcare and explored factors that are likely to influence the evolution of idea sharing and advice seeking. Aalbers and Ma [44] have examined the influence of organizational relationships complexities to a firms' technological entry and exit through SAOMs. Empirical analysis on various scales have proved the feasibility and rationality of applying statistical methods like SAOMs to the analysis of the internal mechanism of network generation and evolution, through which the understanding of successful scientific collaborations can be further improved.

In the context of scientific innovation system, the dynamic coupling of units of the actors, innovative products and also knowledge elements affect the ongoing formation and breaking-up of ties in the collaboration network. Brennecke and Rank [45] have proved that different structural features of the firm's knowledge stock shape the transfer of advice among inventors. Parreira, Machado [24] have found that similar scientific structure could affect the international collaboration. Li, Zhang [46] have found that technological proximity is one of the key factors that promote international green technological collaboration. Meanwhile, the actors' performance is also closely associated with their scientific collaboration. Publishing high-quality papers could increase the academic reputation of the organization and attract more attention from academia and industry, which will lead to more academic opportunities and attract more partners [25, 47]. However, innovation performance is rarely included in the research framework of collaboration network dynamics, which may focus more on geographical, economic, social, cultural, cognitive and other macro factors.

2.3 Knowledge elements extraction and representations

The knowledge base of an innovative actor is widely regarded as an aggregation of its knowledge elements, while the article keywords or topics and predefined categorizations, such as IPC codes have been valid proxies for knowledge elements [28, 48, 49]. Although these identifiers are intuitive and clear, it is often difficult to grasp the rich context and semantic information of the text when deeply analyzing and understanding the micro-knowledge structure at the institutional or individual level [17]. Based on this, how to effectively extract knowledge elements from scientific texts becomes the key to further build knowledge networks.

Methods for extracting terms from unstructured text can be divided into four categories: statistical methods, clustering-based methods, graph-based methods, and deep learning methods. Statistical learning methods use determined mathematical functions to identify words with abnormal frequencies and generally do not require any information other than word frequency statistics from corpora. The aim of the clustering methods is to cluster the candidate terms, and then select the most representative terms from each cluster. The graph based methods represent the document into a graph, and use the graph ranking method to identify key terms [50]. Knowledge embedding methods based on deep learning have become a research focus in recent years for knowledge extraction from unstructured scientific texts [51]. This kind of method can make full use of the semantic and contextual information of words and phrases, and realize the accurate localization of knowledge elements in text. The unsupervised method KeyBERT uses BERT embedding to extract keywords that best represent the underlying text. Due to its focus on relevancy in sentences, contextual information in scientific texts can be taken into account when extracting knowledge elements, and the extraction results have been evidenced to be superior to traditional methods in terms of the similarity of keywords specified by the author [50].

3 Methodology

In this study, we abstract and model the complex scientific innovation system with innovative entities (actors), innovative products (artifacts) and knowledge elements, and the relations among these nodes. As illustrated in Figure 1, the multi-layered network consists of three layers of collaboration network, knowledge network and innovative products. The collaboration network is established through co-publication relationships among institutions. Here we select institutions, a population of individual authors, as the agent of actors, as this scale better captures the actors' ownership of knowledge. Scientific papers, as the main form of innovative products, constitute the innovative product layer. The knowledge network is constructed based on the co-occurrence of knowledge elements extracted from the

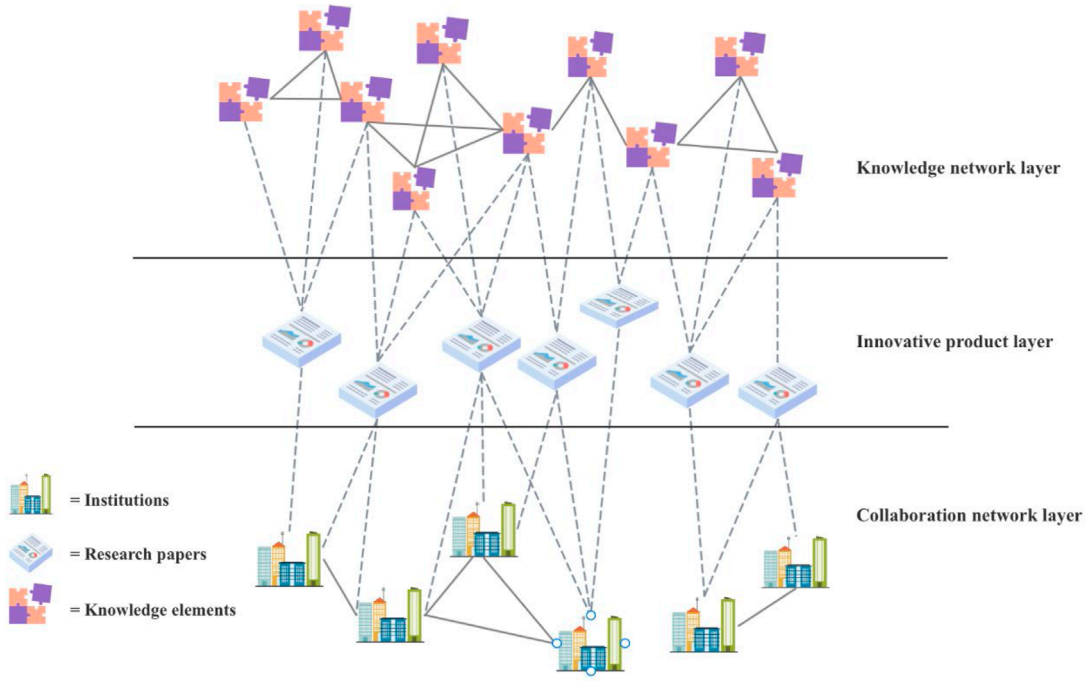

FIGURE 1
Framework of the multi-layered networks of modeling interactions of institutions, research papers and knowledge elements.

papers. As shown in Figure 1, each institution may produce a certain number of papers, and these research outcomes consist of knowledge elements that constitute institutions' knowledge base. The knowledge network and collaboration network are interconnected through the product layer.

Based on the abstract scientific innovation system, this study introduces a model of multi-layered network to explore the interaction and dynamics of scientific innovation. The methodology is comprised of four parts: (1) the multi-layered network construction, including the process of knowledge element extraction and construction of the knowledge network and collaboration network in which the institutions embedded; (2) the measurement of the actors' and their knowledge elements' embeddedness characteristics in the multi-layered network; (3) the investigation about how network embeddedness characteristics of institutions and their knowledge affect performance of innovation products; (4) the network dynamics analysis of the actors in the multi-layered network using SAOMs.

3.1 Multi-layered network construction

The knowledge elements of an institution, is the core competitive resources of innovation activities [52]. It has been proven that knowledge plays an important role in the dynamic changes of the cooperative relationship [25, 53]. In this study, we extract fine-granular knowledge elements using KeyBERT to build knowledge networks. These networks serve as the foundation for capturing patterns of knowledge combination, through which the deep structural and relational features can be intuitively represented and explored.

Knowledge elements refer to the facts, theories or methods of a certain topic in scientific or technical research, which are commonly used to represent the dimensions of knowledge areas [19, 54]. To capture rich information from scientific papers, we use KeyBERT, an unsupervised keyword extraction algorithm, to extract the set of terms that are most semantically representative to the content of the paper. KeyBERT algorithm relies on BERT pre-trained model to generate vectors of documents and candidate terms, and extracts terms by comparing the cosine similarity between them [55], which enables to select high-quality terms in scientific texts [50]. Since KeyBERT supports many embedding models, we choose SciBERT [56], which trained on scientific text, to obtain vector representation with state-of-the-art performance. Figure 2 shows the process of knowledge element extraction using KeyBERT, and the specific steps are as follows:

Step I: Creating the list of candidate terms: Extract N-grams ($n = 1, 2$) phrases form the document (abstract and title of papers), and then clean the term lists through exclusion of stop words.

Step II: Word embedding: Apply SciBERT model to generate embedded representations of the document and candidate words in the same vector space.

Step III: Selecting the most representative terms of a document: Calculate the cosine similarity between the word embedding vectors and document embedding vector to extract the top N terms with the highest similarity to best describe the document content. Considering that

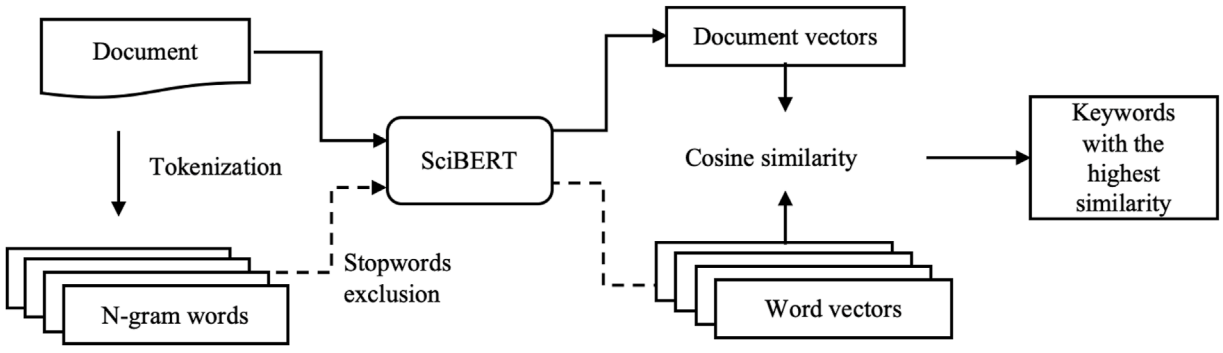

FIGURE 2
Process of knowledge elements extraction using KeyBERT.

documents of different lengths may contain different amounts of knowledge, the value of N is determined according to the length of the document. N is set as 5% of the document length.

This study constructs the knowledge network based on their co-occurrence relationships in scientific papers. Knowledge elements are linked through the combination process of scientific innovation [57], which forms the knowledge networks over time [19, 58]. Then following the prior studies [17, 27, 59], institutions are extracted from the datasets as the actors of generating innovation products, research papers; and ties are created based on their co-publication relations to form the collaboration network. Institutions and the knowledge elements they possess are linked through the jointly published papers, which form the innovation product layer.

3.2 Characteristics of the multi-layered network

The aim of our study is to investigate how the embeddedness of the actors and their knowledge transmission in the scientific system influence the innovation performance and network dynamics. This requires capturing the characteristics of institutions and their knowledge embedded in different layers of the multi-layered network. Indicators at the knowledge network, collaboration network and innovative product layer are described in Table 1 respectively.

This study measures the knowledge transmission and recombination features using four indicators, including diversity, uniqueness, combinatorial capability and knowledge proximity. The knowledge diversity and uniqueness stands for the variety and scarcity of the knowledge devoted to innovation activities [45]. The combinatorial capability relates to the position of an institution's knowledge elements relative to other elements [60], indicating the capability of accessing new information in the transmission [61]. In the calculation, the degree centrality of knowledge represents the feasibility and desirability of combination with other knowledge elements [27], while structural holes in the network implies non-redundant combination opportunities and further inventive capacity [16]. Knowledge proximity refers to the similarity of knowledge base between different institutions. Higher knowledge proximity reduces adverse selection risk caused by information asymmetry problems in the partner selection [53, 62]. In this study, we apply the doc2vec algorithm to generate vectors and then calculate cosine similarity between knowledge elements to measure knowledge proximity. In the collaboration network, being in a central position in the collaboration network allows institutions to access information and resources more effectively [54]. Due to the preferential attachment mechanism [3, 63], we apply the degree centrality to evaluate the direct partners of an institution.

The innovation performance of an institution is measured by the level of its innovative products. High-quality papers improve the academic reputation and visibility of the institutions, thus attracting more collaborators. In this study, we estimate the innovation performance of institutions using the H1 Connect innovation scores of their published papers. These scores are provided by senior researchers within the H1 Connect database who contribute their expertise by reading, reviewing, and recommending research papers on the platform.

3.3 Regression model

The recombination and transmission of existing knowledge are essential for institutions to achieve outstanding innovative output [64, 65]. From a network perspective, features from collaboration and knowledge network may affect the innovation product layer. Accordingly, we perform regression analysis of innovation performance and knowledge and collaboration characteristics.

As the innovation system is evolving, we model the evolution of collaboration networks and knowledge networks into different stages according to the publication year of the research papers. In regression analysis, these stages are seen as multiple time windows. The multi-layered network is constructed in each time window. All variables described in Section 3.2 have been calculated at the actor level and normalized respectively[1]. We then apply ordinary least

1 The knowledge proximity for regression model is calculated by $P_{it} = \sum_{j \in C_i} \cos\left(\vec{v_{it}}, \vec{v_{jt}}\right)/(n-1)$, where n is the number of institutions in collaboration network at period t.

TABLE 1 Indicators in the multi-layered networks.

Layer	Indictor and description	Measurement
Knowledge network	***knowledge_diversity***: the variety in knowledge elements possessed by the institution	$D_i = \lvert K_i \rvert$ K_i is the set of knowledge elements owned by the institution i
	knowledge_uniqueness: the scarcity of the knowledge possessed by the institution	$U_i = \frac{\sum_{s \in K_i} \frac{1}{N_s}}{\lvert K_i \rvert}$ N_s is the number of institutions that own knowledge element s.
	knowledge_combinatorial_capability: the combination of degree centrality and structural holes of the knowledge elements possessed by the institution	$CP_i = \frac{\sum_{s \in K_i}(d(s)+S_s)}{\lvert K_i \rvert}$ $S_s = 2 - \sum_q \left(p_{sq} + \sum_k p_{sk} p_{kq}\right)^2$ $d(s)$ is the degree centrality of knowledge element s in the knowledge network; $p_{sq} + \sum_k p_{sk} p_{kq}$ is the proportion of s's relations that are directly or indirectly invested in the connection with q.
	knowledge_proximity: the similarity of knowledge elements between different institutions	$P(i,j) = \cos\left(\vec{v_i}, \vec{v_j}\right)$ $\vec{v_i}$ and $\vec{v_j}$ represent the vector of knowledge elements owned by institution i and j respectively
Collaboration network	***degree_centrality***: the number of institution's partners in the collaboration network	$DC_i = \lvert W_i \rvert$ W_i is the set of institutions that collaborate with institution i
Innovative product layer	***innovation_performance***: the innovation level of papers published by the institution	$S_i = \frac{\sum_{j \in P_i} score_j}{\lvert P_i \rvert}$ $score_j$ is the innovation score of paper j, P_i is the set of papers published by institution i

squares (OLS) model with natural logarithm transformation of the explained variables for our estimation, the regression function is shown in Equation 1 [2].

$$\ln(S_{it}) = \beta_0 + \beta_1 D_{it} + \beta_2 U_{it} + \beta_3 CP_{it} + \beta_4 P_{it} + \beta_5 DC_{it} + \beta_6 X_{it} + u_i + e_{it} \quad (1)$$

Where i identifies institutions in t period, β_0 is the intercept and e_{it} is the error term, X_{it} is the control variabels. Individual fixed effects (u_i) ensure the individual heterogeneity can be controlled. In our sample, organizations show individual differences in other aspects besides the knowledge dimension and papers published by institutions may have other underlying qualities that have not been captured, so it is reasonable to adopt fixed effect regression, which is also statistically proved by Breusch-Pagan test and Hausman test. We also employ ordinary least squares (OLS) model with robust standard errors in the robustness check.

To isolate the effects of knowledge and collaboration features on innovation performance, additional control variables are considered in the analysis. One of such variables is the number of disciplines, computed by the number of unique WoS categories of papers published by the institution, which may affect the innovation performance. Besides, we measure the innovation input with the number of authors involved in papers published by the institution, which can serve as a proxy for the amount of human resources involved in the innovation activities [66]. For institution i that published paper j, the human resources involved from institution i in paper j is calculated as the total number of authors of paper j divided by the number of institutions involved.

Finally, we perform an additional analysis by using another indicator of innovation performance, the average number of citations, to provide a more comprehensive result. Citation are widely accepted as a measure of scientific impact and thus as a partial aspect of innovation performance. We calculate the additional indicator by dividing the total citations of papers published by institution i at time t by the number of papers. The citation data is from the Web of Science database. We log normalize the average number of citations of each institution to account for its skewed distribution.

3.4 Modeling network dynamics

We then model the network dynamics from an actor-oriented perspective, using stochastic actor-oriented model (SAOM). Actor layer of the multi-layered network, i.e. the collaboration network, is composed of a set of cooperation relations that are not independent of each other, and their relational changes (e.g., presence/absence of ties) may be the result of the network structure characteristics among actors or dyads, which is the endogenous effect difficult to measure in traditional regression models [67, 68]. SAOM is a statistical approach for modeling the process of network change with longitudinal network data using econometric discrete choice models and dynamic Markov models, which is able to capture endogenous effects related to the network and effectively deal with multicollinearity problems through built-in model [67, 69], thus enables us to understand which factors and dynamics could influence actors' collaboration from the network perspective.

2 Although many indicators are related to network density, the main dependent and independent variables in the regression are calculated from the institution' perspective, hence we have not included the network density, as it is a fixed value.

TABLE 2 Variables for SAOMs.

SAOM input	Effect	Variable
Network structure	Collaboration network	*degree_centrality*
Individual characteristics	Knowledge network	*knowledge_diversity*
		knowledge_uniqueness
		knowledge_combinatorial_capability
	Innovation performance	*innovation_performance*
	Control variable	*institution_classification*[3]
Proximity	Proximity	*knowledge_proximity*

SAOM is an actor-based simulation model where the change of network ties over time is driven by the actor's choices in accordance with a set of goals/preferences [68]. These preferences are modeled as an "evaluation function" (a linear combination of parameters and local graph statistics) that the actor seeks to maximize, which is shown in Equation 2. The model incorporate parameters embedded in network structure that endogenously influence the probabilities of tie changes and parameters related to characteristics of actors that exogenously influence the tie formation or termination [70]. Actors in the model are viewed as making choices one-at-a-time in mini-steps to maximize the evaluation function and possible changes can occur across different time points in sequence. The actor-oriented formulation also offers an explicit lens to gain a direct interpretation of parameters in SAOM [69].

$$f_i(\boldsymbol{\beta}, \boldsymbol{x}) = \sum_k \beta_k s_{ki}(\boldsymbol{x}) \tag{2}$$

where $f_i(\beta, x)$ is the value of the objective function for actor i depending on the state x of the network, $s_{ki}(x)$ represent the effects that affect the selection of the actor's connected edge, β_k are the statistical parameter estimation representing the effect.

The objective of using SAOM is to investigate which attributes characterize and affect the dynamic evolution of collaboration networks. These attributes include the knowledge dimension characteristics of institutions, their innovation performance and position in collaboration network. Table 2 summarizes and explains the indicators of different types required by the SAOM in this study. We estimate SAOM using the RSiena library, available in R statistical software [71].

4 Empirical study

4.1 Data

Our empirical analysis is performed on scientific paper data in the area of protein structure. With the implementation of the Human Proteome Project as well as the application of artificial intelligence in protein structure prediction [72], the field of protein structure research is characterized by rapid knowledge growth, diverse science linkages and widely existing collaborations. Our analysis mainly uses data from two primary sources, namely, (1) scientific papers and their peer-review information from H1 Connect research articles recommendation database[4]and (2) bibliographic data of the scientific papers from Web of Science (WoS) database[5]. Our final sample consists of papers published between 2014 and 2022 in the field of protein structure recommended in the H1 Connect.

Since innovation activities require sufficient time investment, and the scientific collaboration could last for three to 5 years [73], we choose a three-year time window to compare the network evolution in different periods. We divide the dataset into three periods: 2014–2016, 2017–2019, and 2020–2022, and select institutions that have co-published papers with other institutions within at least two periods. We then clean and consolidate the institutions in the dataset to ensure the standardization and consistency of their names[6] and then distinguish them into two categories—industrial organization and academic institution—the former is identified by the words "Ltd" (Limited),"Co" (Company) and so on contained in the name while the latter is identified by the words "University", "Institution", "School", "College", "Faculty" and so on [17]. Besides, since the keyword extraction in this study is based on abstract, papers missing abstract are deleted.

The innovation performance of institutions in this study is measured by the peer review scores in H1 Connect. The reviewers are experts who are global opinion leaders in the life sciences and medicine science. Peer experts give higher scores to papers that show outstanding innovation and importance, and existing research has proved that better recommendation scores are associated with higher performing papers [74].

4.2 Descriptive statistics

Figure 3 visualizes the collaboration networks in three periods, 2014–2016,2017–2019 and 2020–2022, respectively. Institutions are represented as nodes, whereas co-publishing relations are represented as ties. The descriptive network statistics are presented in Table 3[7]. The number of institutions participating in the protein structure research and their ties increase over three periods. The average number of collaborators for each institution also increased from 4.056 to 6.678, while the average path length of the network decreases from 3.220 to 2.929. This phenomenon indicates the connections between institutions and the efficiency of information transmission have been enhanced in the collaboration network layer. In addition, these networks do not show an obvious change in their density from the first to the third period, which means

3 1 for academic institutions or 2 for industrial organizations.

4 Last accessed on 15 January 2024.

5 The citation dataset downloaded on 1 October 2024.

6 Due to the limitations of the data itself, "University of California System" is listed as a single organization, and majority of records from both Web of Science and H1 Connect do not differentiate between the universities within the system.

7 The descriptive network statistics are calculated by Gephi.

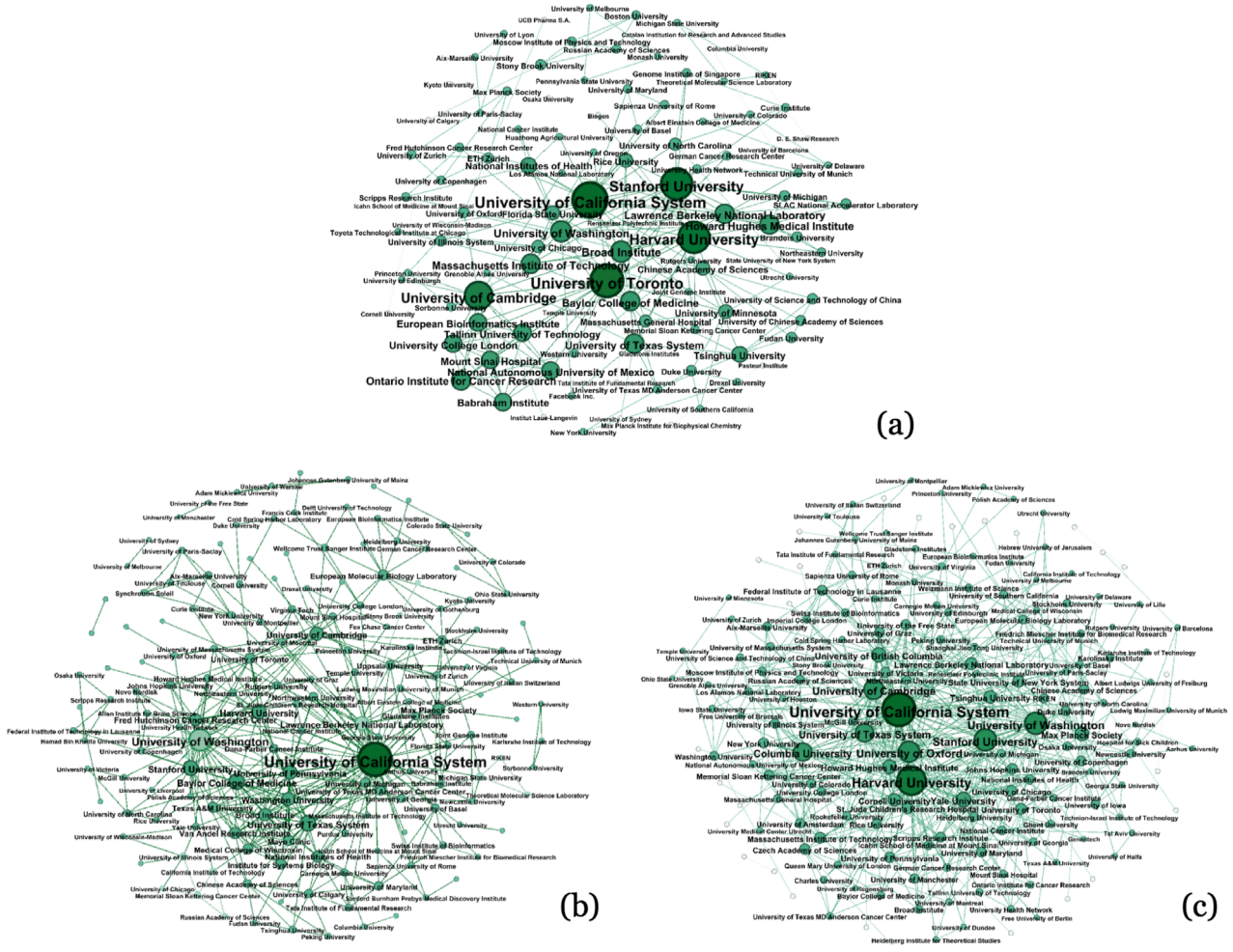

FIGURE 3
Collaboration networks for the periods of: **(A)** 2014–2016; **(B)** 2017–2019; **(C)** 2020–2022.

TABLE 3 Descriptive statistics in the collaboration network's evolution.

	2014–2016	2017–2019	2020–2022
Nodes	108	165	174
Edges	219	423	581
Components	12	9	4
Density	0.038	0.031	0.039
Average degree	4.056	5.127	6.678
Average path length	3.220	3.159	2.929
Average clustering coefficient	0.768	0.671	0.666

that the number of realized linkages grows at a similar rate as the number of actors.

We then select and create co-occurrence networks of knowledge elements, as illustrated in Figure 4, where the node size represents the frequency of the terms. Our visualization reveals several fundamental research topics in the field of protein structure, such as "protein structure", "structure prediction", "protein interaction" and so on. Moreover, we also recognize the emergence of some hot

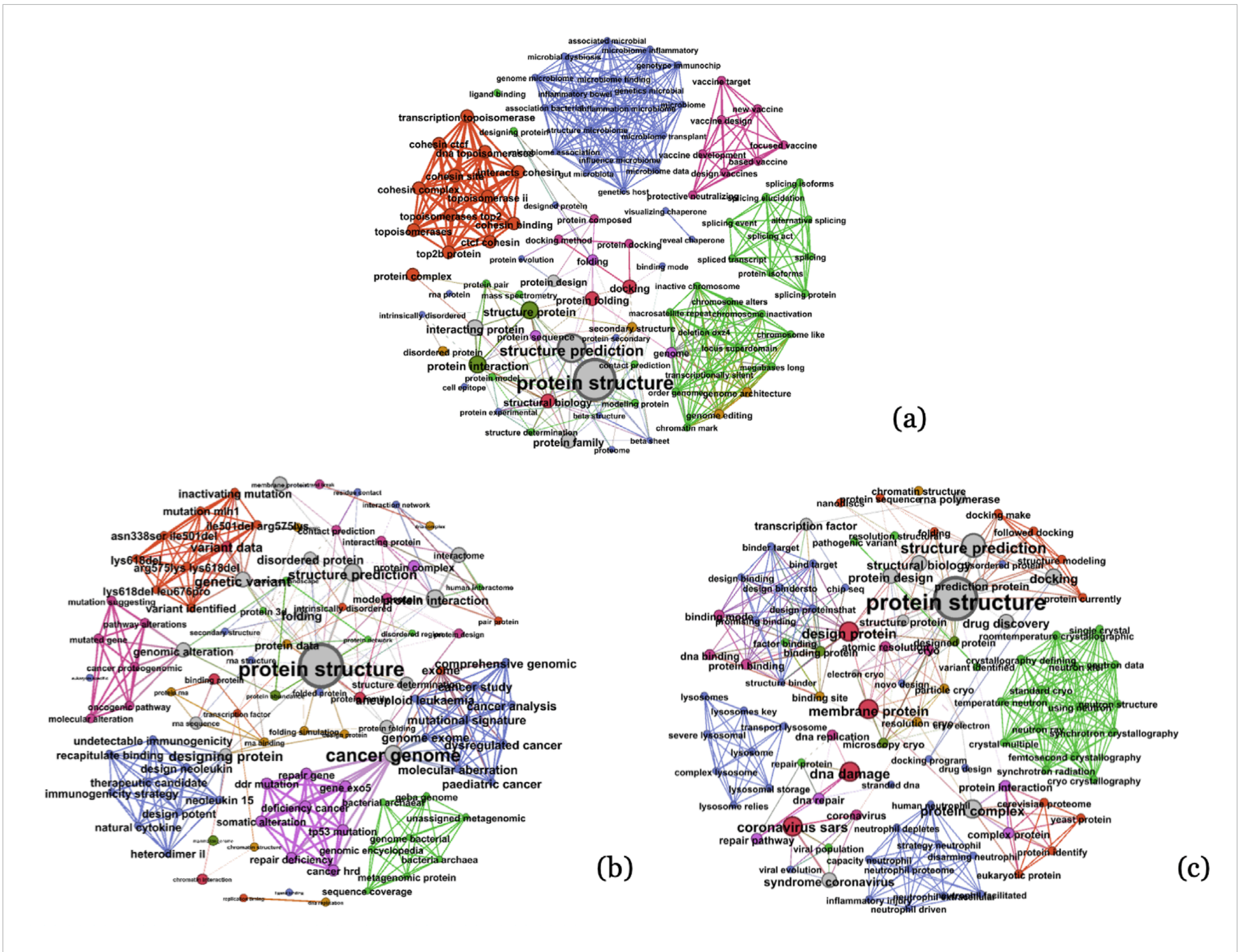

FIGURE 4
Co-occurrence network of the top 100 most frequently used keywords for the periods of: **(A)** 2014–2016; **(B)** 2017–2019; **(C)** 2020–2022.

topics, for example, in the third period, 2020–2022, "coronavirus sars" and "syndrome coronavirus" have received more attention and effort. Besides, these snapshots also show the tendency of increasing and strengthening knowledge linkages in the field of protein structure.

We compute the number of unique knowledge elements for each period and find an increasing trend, as shown in Table 4. It describes the descriptive statistical results of variables in knowledge layer and innovation performance in the product layer. The mean and median values of knowledge uniqueness and knowledge diversity have increased distinctly over three periods, which can be interpreted as a hint of vibrant innovation and knowledge production activities in the field of protein structure. Moreover, institutions' innovation performance, i.e. the average of innovation scores of papers published by institutions, also present an increasing trend in the mean and median values over the three periods, showing the vitality of high-quality research in the field of protein structure. However, the increase of standard deviation of innovation performance reveals that the difference of innovation capability between organizations expands over time.

4.3 Regression results

We present the results of estimating the regression models in Equation 1 in Table 5, testing what features from collaboration and knowledge network affect the innovation product performance. Model 1 reports the baseline OLS regression results, while Model 2 estimates the OLS regression with cluster-robust standard errors for robustness checks. In Model 1, the estimated coefficient for knowledge diversity is positive and significant ($\beta = 0.1240, p < 0.01$), indicating that institutions with more diverse knowledge could produce more outstanding innovation outputs. Meanwhile, knowledge uniqueness has a significant and positive effect on innovation performance with estimated coefficients of $\beta = 0.5269\,(p < 0.01)$. This result emphasizes the important role of unique knowledge resources in innovation. The influence of knowledge combinatorial capability and proximity on innovation performance is not significant in our estimation. In addition, the number of collaborators, i.e. degree centrality, proves instrumental in improving innovation performance ($\beta = 0.3413, p < 0.01$). The regression results of the control variables show that the number

TABLE 4 Descriptive statistics of variables in knowledge network and innovation performance.

	2014–2016			2017–2019			2020–2022		
	Mean	Median	S.D.	Mean	Median	S.D.	Mean	Median	S.D.
knowledge_uniqueness	0.0451	0.0357	0.0480	0.0575	0.0519	0.0389	0.0533	0.0476	0.0397
knowledge_diversity	6.7018	8.0000	5.8038	9.0000	9.0000	4.6608	9.4128	9.0000	4.6106
knowledge_combinatorial_capability	0.5149	0.4601	0.3613	0.7752	0.8068	0.3642	0.8774	0.9053	0.3941
knowledge_proximity	0.0143	0.0056	0.0143	0.0074	0.0062	0.0113	0.0079	0.0070	0.0125
innovation_performance	7.5577	5.0000	8.8986	12.9824	9.4000	11.5729	15.5881	10.3000	20.8938

TABLE 5 OLS results.

Variables	Model 1	Model 2
knowledge_diversity	0.1240*** (0.0326)	0.1240*** (0.0376)
knowledge_uniqueness	0.5269*** (0.0296)	0.5296*** (0.0302)
knowledge_combinatorial_capability	0.0411 (0.0363)	0.0411 (0.0384)
knowledge_proximity	0.0227 (0.0217)	0.0227 (0.0214)
degree_centrality	0.3413*** (0.0358)	0.3413*** (0.0428)
number_of_disciplines	-0.0897** (0.0353)	−0.0897*** (0.0323)
innovation_input	0.0581 (0.0417)	0.0581 (0.0485)
Constant	0.0220 (0.0168)	0.0220*** (0.0018)
N	642	642
Adjusted R^2	0.7385	0.8264

Notes: 1. Standard errors in parentheses. 2.*$p < 0.10$;**$p < 0.05$;***$p < 0.01$.

TABLE 6 OLS results using citation as measure of innovation performance.

Variables	Model 3	Model 4
knowledge_diversity	0.0910** (0.0433)	0.0910** (0.0427)
knowledge_uniqueness	0.3536*** (0.0394)	0.3536*** (0.0372)
knowledge_combinatorial_capability	0.1955*** (0.0483)	0.1955*** (0.0431)
knowledge_proximity	0.0933*** (0.0288)	0.0933*** (0.0330)
degree_centrality	0.3372*** (0.0477)	0.3372*** (0.0507)
number_of_disciplines	−0.0822* (0.0470)	−0.0822* (0.0434)
innovation_input	0.1293** (0.0555)	0.1293** (0.0619)
Constant	−0.0186 (0.0223)	−0.0186*** (0.0019)
N	642	642
Adjusted R^2	0.5641	0.7106

Notes: 1. Standard errors in parentheses. 2.*$p < 0.10$;**$p < 0.05$;***$p < 0.01$.

of disciplines may negatively affect the innovation performance of institutions ($\beta = -0.0897, p < 0.05$), which may be a signal that participating in too many research fields may lead to the dispersion of resources and the limitation of knowledge depth, thus detrimental to further innovation. The results of Model 2 are consistent with Model 1, confirming the validity of our conclusions.

For an additional analysis, we use average citation counts with natural logarithm transformation as an alternative measure of innovation performance, and report the regression results in Table 6. Model 3 presents the baseline OLS regression results, while Model 4 estimates the OLS regression with cluster-robust standard errors for robustness checks. Consist with regression results using peer-reviewed scores as measure of innovation performance, knowledge diversity, knowledge uniqueness and degree centrality in collaboration network have a significant and positive effect on citation performance in model 3 and model 4. Moreover, knowledge combinatorial capability shows a significant and positive influence on average citation counts, and knowledge proximity positively affects the citation counts. This suggests that the innovation output of institutions whose research is more closely aligned with others are more likely to gain citations and attentions. For the control variables, in Models 3 and 4, the number of disciplines has a negative impact on innovation performance in line with Model 1 and 2, but the coefficient for innovation input is positive and significant, indicating the number of scholars participating in innovative activities has expanded the visibility and impact of the research.

To summarize, it can be concluded that the knowledge diversity and uniqueness, the degree centrality in the collaboration network positively affect the institution's innovative performance measured by both the peer-reviewed scores and citations. Besides, the knowledge combinatorial capability and proximity have a positive impact on citations.

4.4 SAOM results

The SAOM estimation results are presented in Table 7. Convergence is good for the model, since the overall maximum convergence ratio is less than 0.25 and all convergence t-ratios are below 0.1. The estimation of the rate parameters shows that

TABLE 7 Results of SAOM analysis.

	Estimate	Standard error
Rate constant r rate (period 1)	8.461	0.897
Rate constant r rate (period 2)	17.552	2.242
Degree (density)	−2.046***	0.024
Knowledge proximity	−0.279*	0.134
Knowledge diversity	0.094***	0.015
Knowledge uniqueness	−0.994	1.278
Knowledge combinatorial capability	−0.383*	0.177
Institution classification	−0.859***	0.175
Innovation performance	0.093***	0.011

Notes: 1. † $p < 0.10$;*$p < 0.05$;**$p < 0.01$;***$p < 0.001$; all coverage t ratios <0.08.2. Overall maximum convergence ratio 0.09.

the tendency of institutions to change collaboration relations amplifies over time, from approximately 8.5 opportunities per organization in Period 1 to around 17.5 opportunities per institution in Period 2. The coefficient of degree (density) is negative and significant ($\beta = -2.046$), indicating that institutions with more collaborators are less inclined to form new ties with others. This model revels different effects of the knowledge characteristics on the propensity to collaborate, suggesting that there is a higher tendency for an institution with more knowledge diversity ($\beta = 0.094$) to link with more institutions, while a negative propensity is found for the institution with more knowledge proximity ($\beta = -0.279$). This phenomenon may be evidence that diverse and disparate knowledge is a source of collaboration and innovation in the field of protein structure. The negative parameter of the knowledge combinatorial capability ($\beta = -0.383$) reflects that institutions with higher knowledge combinatorial capability prefer independent research because the knowledge they own already has combinatorial experience and potential, in that case, they don't seem to have a strong incentive in seeking further collaborations. Besides, the institution classification negatively affects collaboration ($\beta = -0.859$), suggesting that academic institutions play a more important role in the evolution of collaboration networks than industrial organizations. The coefficient of knowledge uniqueness is not significant. As for innovation performance, it has a positive and significant effect on collaboration ($\beta = 0.093$), which shows that institutions that already have outstanding innovation outputs are still willing to establish new collaborative relationship.

We conduct robustness tests by altering the random seeds of the SAOM (Supplementary Table A1, A2). The random seed plays a crucial role in the iterations and parameter updates of the SAOM. If the model has converged to a stable state, different random seeds will produce similar results, indicating that the model outcomes are robust [71]. Changing random seeds in our model yields the same results as the initial findings in Table 7, reinforcing the robustness of our conclusions.

5 Discussion and conclusion

The scientific innovation is a system can be described as a multilayer network with complex structure, while more substantial efforts would be required to model the system and explore its dynamic mechanisms [2]. This paper constructs a multi-layered network to model scientific innovation system, in which the collaboration, innovation products and knowledge elements interact through the actors' innovation activities. Building on this, we analyze how social and knowledge network embeddedness of actors, and their ideas affects the innovation performance and the network dynamics.

Our empirical analysis is based on a dataset of research articles with review scores in the research area of protein structure. The key findings of our study highlight the positive effects of knowledge uniqueness, knowledge diversity and the number of partners of institutions influence the innovation performance of the research outputs. We also find that, in addition to these factors, knowledge combinatorial capability and proximity have a positive impact on citations. Second, this paper also presents empirical evidence that from a dynamic perspective, the institution's innovation performance positively affects the network dynamics, indicate that institutions with outstanding innovation products pursue establishing new collaboration and keep active in innovation activities. Besides, the knowledge diversity has a positive impact in the dynamics of the network, while the knowledge proximity plays a negative role, suggesting that actors tend to seek various diverse and distinct knowledge when choosing partners. These findings do not fully align with existing research [59, 75]. This may be related to datasets from different fields that were selected for empirical study. Emerging areas such as protein structure may have actors and links in the network are incentives to change, as reflected in our data. In this situation, institutions with more diverse and distinct knowledge are more inclined to collaborate with others to increase learning opportunities and thus achieve possible innovations. These reflect the heterogeneity of the underlying driving mechanisms of complex scientific systems and require further exploration and investigation.

Our results also indicate that some of the knowledge characteristics that promote innovation performance also serve as catalysts for network dynamics. Collaborations serves as the core driver of innovation [76, 77] and the organizations' performance is relevant to the positions they occupy in the collaboration network [78]. The knowledge fusion fostered in the multi-layer innovation network positively affects the actors' innovation output through collaboration, and the performance continue to influence the network dynamics, resulting in the creation of new ideas and findings. Our empirical results demonstrate that the position of an institution in the collaboration network fosters innovation, while their innovation performance reciprocally influences the evolution of scientific collaboration. This interplay elucidates the co-evolutionary process occurring between various layers within the scientific innovation system [4]. These results have direct implication for both innovation organizations and policymakers to encourage collaboration and incentivize innovation.

This study makes contributions as follows. It contributes to the existing literature on scientific innovation system by abstracting and modeling this system via a multi-layered complex network covering innovation entities (a population of actors), innovative

products (artifacts), knowledge elements (content of artifacts) and the relations among them. Besides, this study enriches the methods of measuring characteristics of the multi-layered network. Based on this, we investigate the underlying factors that impact innovation performance and investigate the mechanism through which the actor collaboration and their knowledge transmission in the scientific system influence network dynamics. We provide a framework for future research to study the patterns and evolutionary mechanism of scientific innovation systems.

This study also has several limitations. First, we explore the network dynamics of the scientific innovation system from an actor-oriented perspective. However, economic and social factors may also play an important role in it, which is hard to capture in our data. Second, the underlying mechanisms governing the scientific innovation system are rather complex and heterogeneous. This study takes the publication data in the field of protein structure as an example to shed light on it. This is an inspiring and meaningful attempt, but the complex scientific innovation system should be further explored in different contexts in future work.

Data availability statement

The data analyzed in this study is subject to the following licenses/restrictions: The publication data and the corresponding review data are extracted from two databases, H1 connect and Web of Science. Readers can seek out and examine related publications and review data on their own following the instruction in the manuscript. Requests to access these datasets should be directed to YJ, 18332273828@163.com.

Author contributions

YJ: Formal Analysis, Visualization, Writing–original draft. HC: Conceptualization, Funding acquisition, Validation, Writing–review and editing. JL: Data curation, Formal Analysis, Software, Writing–review and editing. XuW: Funding acquisition, Writing–review and editing. RG: Funding acquisition, Writing–review and editing. XiW: Writing–review and editing.

Funding

The author(s) declare that financial support was received for the research, authorship, and/or publication of this article. This work was supported by the National Natural Science Foundation of China under Grant Nos. 72004009, J2324014, 72074020, and 72204245.

Conflict of interest

Author XW was employed by company Postal Savings Bank of China.

The remaining authors declare that the research was conducted in the absence of any commercial or financial relationships that could be construed as a potential conflict of interest.

The author(s) declared that they were an editorial board member of Frontiers, at the time of submission. This had no impact on the peer review process and the final decision.

Publisher's note

All claims expressed in this article are solely those of the authors and do not necessarily represent those of their affiliated organizations, or those of the publisher, the editors and the reviewers. Any product that may be evaluated in this article, or claim that may be made by its manufacturer, is not guaranteed or endorsed by the publisher.

Supplementary material

The Supplementary Material for this article can be found online at: https://www.frontiersin.org/articles/10.3389/fphy.2024.1492731/full#supplementary-material.

References

1. Fortunato S, Bergstrom CT, Boerner K, Evans JA, Helbing D, Milojevic S, et al. Science of science. *Science* (2018) 359(6379). doi:10.1126/science.aao0185

2. Zeng A, Shen Z, Zhou J, Wu J, Fan Y, Wang Y, et al. The science of science: from the perspective of complex systems. *Phys Rep* (2017) 714-715:1–73. doi:10.1016/j.physrep.2017.10.001

3. Barabâsi A-L, Jeong H, Néda Z, Ravasz E, Schubert A, Vicsek T. Evolution of the social network of scientific collaborations. *Physica A: Stat Mech its Appl* (2002) 311(3-4):590–614. doi:10.1016/s0378-4371(02)00736-7

4. Zhang Y, Chen K. Network growth dynamics: the simultaneous interaction between network positions and research performance of collaborative organisations. *Technovation* (2022) 115:102538. doi:10.1016/j.technovation.2022.102538

5. Chen H, Jin Q, Wang X. How embeddedness affects the evolution of collaboration: the role of knowledge stock and social interactions. *arXiv* (2023). doi:10.48550/arXiv.2311.05909

6. Abbasi A, Hossain L, Leydesdorff L. Betweenness centrality as a driver of preferential attachment in the evolution of research collaboration networks. *J Informetrics* (2012) 6(3):403–12. doi:10.1016/j.joi.2012.01.002

7. Dworkin JD, Shinohara RT, Bassett DS. The emergent integrated network structure of scientific research. *PLOS ONE* (2019) 14(4):e0216146. doi:10.1371/journal.pone.0216146

8. Pinto PE, Vallone A, Honores G. The structure of collaboration networks: findings from three decades of co-invention patents in Chile. *J Informetrics* (2019) 13(4):100984. doi:10.1016/j.joi.2019.100984

9. Fan L, Guo L, Wang X, Xu L, Liu F. Does the author's collaboration mode lead to papers' different citation impacts? An empirical analysis based on propensity score matching. *J Informetrics* (2022) 16(4):101350. doi:10.1016/j.joi.2022.101350

10. Liu J, Guo X, Xu S, Song Y, Ding K. A new interpretation of scientific collaboration patterns from the perspective of symbiosis: an investigation for long-term collaboration in publications. *J Informetrics* (2023) 17(1):101372. doi:10.1016/j.joi.2022.101372

11. Ma Y, Yang X, Qu S, Kong L. Research on the formation mechanism of big data technology cooperation networks: empirical evidence from China. *Scientometrics* (2022) 127(3):1273–94. doi:10.1007/s11192-022-04270-4

12. Gao J, Liu S, Li Z. Cooperative evolution of China's excellent innovative research groups from the perspective of innovation ecosystem: taking an "environmental biogeochemistry" research innovation group as a case study. *Int J Environ Res Public Health* (2021) 18(23):12584. doi:10.3390/ijerph182312584

13. Kong X, Shi Y, Wang W, Ma K, Wan L, Xia F. The evolution of turing award collaboration network: bibliometric-level and network-level metrics. *IEEE Trans Comput Soc Syst* (2019) 6:1318–28. doi:10.1109/tcss.2019.2950445

14. Noben I, Brouwer J, Deinum JF, Hofman WHA. The development of university teachers' collaboration networks during a departmental professional development project. *Teach Teach Educ* (2022) 110:103579. doi:10.1016/j.tate.2021.103579

15. Grenno FE, dos Santos CZ, Schiavetti A, Profice CC. NGO scientific collaboration networks for marine conservation in the southern cone: a case study. *Environ Sci and Pol* (2023) 148:103554. doi:10.1016/j.envsci.2023.103554

16. Guan J, Liu N. Exploitative and exploratory innovations in knowledge network and collaboration network: a patent analysis in the technological field of nano-energy. *Res Pol* (2016) 45(1):97–112. doi:10.1016/j.respol.2015.08.002

17. Chen H, Jin Q, Wang X, Xiong F. Profiling academic-industrial collaborations in bibliometric-enhanced topic networks: a case study on digitalization research. *Technol Forecast Soc Change* (2022) 175:121402. doi:10.1016/j.techfore.2021.121402

18. Jiang H, Xia J, Cannella AA, Xiao T. Do ongoing networks block out new friends? Reconciling the embeddedness constraint dilemma on new alliance partner addition. *Strateg Manage J* (2018) 39(1):217–41. doi:10.1002/smj.2695

19. Guan J, Yan Y, Zhang JJ. The impact of collaboration and knowledge networks on citations. *J Informetrics* (2017) 11(2):407–22. doi:10.1016/j.joi.2017.02.007

20. Choi J, Yoon J. Measuring knowledge exploration distance at the patent level: application of network embedding and citation analysis. *J Informetrics* (2022) 16(2):101286. doi:10.1016/j.joi.2022.101286

21. Song B, Suh Y. Identifying convergence fields and technologies for industrial safety: LDA-based network analysis. *Technol Forecast Soc Change* (2019) 138:115–26. doi:10.1016/j.techfore.2018.08.013

22. Wang S, Ma Y, Mao J, Bai Y, Liang Z, Li G. Quantifying scientific breakthroughs by a novel disruption indicator based on knowledge entities. *J Assoc Inf Sci Technol* (2022) 74:150–67. doi:10.1002/asi.24719

23. Hellsten I, Leydesdorff L. Automated analysis of actor–topic networks on twitter: new approaches to the analysis of socio-semantic networks. *J Assoc Inf Sci Technol* (2020) 71(1):3–15. doi:10.1002/asi.24207

24. Parreira MR, Machado KB, Logares R, Diniz-Filho JAF, Nabout JC. The roles of geographic distance and socioeconomic factors on international collaboration among ecologists. *Scientometrics* (2017) 113(3):1539–50. doi:10.1007/s11192-017-2502-z

25. Wu L, Yi F, Bu Y, Lu W, Huang Y. Toward scientific collaboration: a cost-benefit perspective. *Res Pol* (2024) 53(2):104943. doi:10.1016/j.respol.2023.104943

26. Graf H, Kalthaus M. International research networks: determinants of country embeddedness. *Res Pol* (2018) 47(7):1198–214. doi:10.1016/j.respol.2018.04.001

27. Luo T, Zhang Z. Multi-network embeddedness and innovation performance of R&D employees. *Scientometrics* (2021) 126(9):8091–107. doi:10.1007/s11192-021-04106-7

28. Ba Z, Mao J, Ma Y, Liang Z. Exploring the effect of city-level collaboration and knowledge networks on innovation: evidence from energy conservation field. *J Informetrics* (2021) 15(3):101198. doi:10.1016/j.joi.2021.101198

29. Schumpeter J, Backhaus U. The theory of economic development. In: J Backhaus, editor. *Joseph alois schumpeter: entrepreneurship, style and vision*. Boston, MA: Springer US (2003) p. 61–116.

30. Uzzi B, Mukherjee S, Stringer M, Jones B. Atypical combinations and scientific impact. *Science* (2013) 342(6157):468–72. doi:10.1126/science.1240474

31. Adams J. Collaborations: the fourth age of research. *Nature* (2013) 497(7451):557–60. doi:10.1038/497557a

32. Granovetter M. Economic action and social structure: the problem of embeddedness. *Am J Sociol* (1985) 91(3):481–510. doi:10.1086/228311

33. Gonzalez-Brambila CN, Veloso FM, Krackhardt D. The impact of network embeddedness on research output. *Res Pol* (2013) 42(9):1555–67. doi:10.1016/j.respol.2013.07.008

34. Zhang Z, Luo T. Network capital, exploitative and exploratory innovations—from the perspective of network dynamics. *Technol Forecast Soc Change* (2020) 152:119910. doi:10.1016/j.techfore.2020.119910

35. Granstrand O, Holgersson M. Innovation ecosystems: a conceptual review and a new definition. *Technovation* (2020) 90-91:102098. doi:10.1016/j.technovation.2019.102098

36. Newman MEJ. Coauthorship networks and patterns of scientific collaboration. *Proc Natl Acad Sci* (2004) 101(Suppl. l_1):5200–5. doi:10.1073/pnas.0307545100

37. Badar K, Hite J, Ashraf N. Knowledge network centrality, formal rank and research performance: evidence for curvilinear and interaction effects. *Scientometrics* (2015) 105:1553–76. doi:10.1007/s11192-015-1652-0

38. Wang L, Li G, Ma Y, Yang L. Structure properties of collaboration network with tunable clustering. *Inf Sci* (2020) 506:37–50. doi:10.1016/j.ins.2019.08.002

39. Menger LM, Stallones L, Cross JE, Henry KL, Chen PY. Strengthening suicide prevention networks: interorganizational collaboration and tie strength. *Psychosocial Intervention* (2015) 24(3):155–65. doi:10.1016/j.psi.2015.07.005

40. Wang J. Knowledge creation in collaboration networks: effects of tie configuration. *Res Pol* (2016) 45(1):68–80. doi:10.1016/j.respol.2015.09.003

41. Moon H, Di Benedetto A, Kim SK. The effect of network tie position on a firm's innovation performance. *J Business Res* (2022) 144:821–9. doi:10.1016/j.jbusres.2022.02.035

42. Petersen AM. Quantifying the impact of weak, strong, and super ties in scientific careers. *Proc Natl Acad Sci* (2015) 112(34):E4671–E80. doi:10.1073/pnas.1501444112

43. Fronzetti Colladon A, Grippa F, Broccatelli C, Mauren C, McKinsey S, Kattan J, et al. Boosting advice and knowledge sharing among healthcare professionals. *J Knowledge Manage* (2023) 27(8):2017–33. doi:10.1108/jkm-06-2022-0499

44. Aalbers R, Ma R. The roles of supply networks and board interlocks in firms' technological entry and exit: evidence from the Chinese automotive industry. *Manage Organ Rev* (2023) 19(2):279–315. doi:10.1017/mor.2023.5

45. Brennecke J, Rank O. The firm's knowledge network and the transfer of advice among corporate inventors—a multilevel network study. *Res Pol* (2017) 46(4):768–83. doi:10.1016/j.respol.2017.02.002

46. Li Y, Zhang Y, Lee C-C, Li J. Structural characteristics and determinants of an international green technological collaboration network. *J Clean Prod* (2021) 324:129258. doi:10.1016/j.jclepro.2021.129258

47. Petersen AM, Fortunato S, Pan RK, Kaski K, Penner O, Rungi A, et al. Reputation and impact in academic careers. *Proc Natl Acad Sci* (2014) 111(43):15316–21. doi:10.1073/pnas.1323111111

48. Dibiaggio L, Nasiriyar M, Nesta L. Substitutability and complementarity of technological knowledge and the inventive performance of semiconductor companies. *Res Pol* (2014) 43(9):1582–93. doi:10.1016/j.respol.2014.04.001

49. Guan J, Liu N. Invention profiles and uneven growth in the field of emerging nano-energy. *Energy Policy* (2015) 76:146–57. doi:10.1016/j.enpol.2014.11.024

50. Khan MQ, Shahid A, Uddin MI, Roman M, Alharbi A, Alosaimi W, et al. Impact analysis of keyword extraction using contextual word embedding. *PeerJ Comput Sci* (2022) 8:e967. doi:10.7717/peerj-cs.967

51. Zhai Y, Ding Y, Zhang H. Innovation adoption: broadcasting versus virality. *J Assoc Inf Sci Technol* (2021) 72(4):403–16. doi:10.1002/asi.24420

52. Grant RM. Toward a knowledge-based theory of the firm. *Strateg Manage J* (1996) 17(S2):109–22. doi:10.1002/smj.4250171110

53. Yayavaram S, Srivastava MK, Sarkar M. Role of search for domain knowledge and architectural knowledge in alliance partner selection. *Strateg Manage J* (2018) 39(8):2277–302. doi:10.1002/smj.2791

54. Wang C, Rodan S, Fruin M, Xu X. Knowledge networks, collaboration networks, and exploratory innovation. *Acad Manage J* (2014) 57(2):484–514. doi:10.5465/amj.2011.0917

55. Sharma P, Li Y, editors. *Self-supervised contextual keyword and keyphrase retrieval with self-labelling* (2019).

56. Beltagy I, Cohan A, Lo K. *SciBERT: pretrained contextualized embeddings for scientific text*. ArXiv. 2019;abs/1903.10676.

57. Fleming L. Recombinant uncertainty in technological search. *Manage Sci* (2001) 47(1):117–32. doi:10.1287/mnsc.47.1.117.10671

58. Garud R, Kumaraswamy A. Vicious and virtuous circles in the management of knowledge: the case of infosys technologies. *MIS Q* (2005) 29(1):9–33. doi:10.2307/25148666

59. Jin Q, Chen H, Wang X, Xiong F. How do network embeddedness and knowledge stock influence collaboration dynamics? Evidence from patents. *J Informetrics* (2024) 18(4):101553. doi:10.1016/j.joi.2024.101553

60. Lian X, Guo Y, Su J. Technology stocks: a study on the characteristics that help transfer public research to industry. *Res Pol* (2021) 50(10):104361. doi:10.1016/j.respol.2021.104361

61. Burt RS. *Structural holes the social structure of competition*. Harvard University Press (1992).

62. Reuer JJ, Tong TW, Tyler BB, Ariño A. Executive preferences for governance modes and exchange partners: an information economics perspective. *Strateg Manage J* (2013) 34(9):1104–22. doi:10.1002/smj.2064

63. Reinholt M, Pedersen T, Foss NJ. Why a central network position isn't enough: the role of motivation and ability for knowledge sharing in employee networks. *Acad Manage J* (2011) 54(6):1277–97. doi:10.5465/amj.2009.0007

64. Carnabuci G, Operti E. Where do firms' recombinant capabilities come from? Intraorganizational networks, knowledge, and firms' ability to innovate through technological recombination. *Strateg Manage J* (2013) 34(13):1591–613. doi:10.1002/smj.2084

65. Schillebeeckx SJD, Lin Y, George G, Alnuaimi T. Knowledge recombination and inventor networks: the asymmetric effects of embeddedness on knowledge reuse and impact. *J Manage* (2021) 47(4):838–66. doi:10.1177/0149206320906865

66. Fronzetti Colladon A, Guardabascio B, Venturini F. A new mapping of technological interdependence. *Res Pol* (2025) 54(1):105126. doi:10.1016/j.respol.2024.105126

67. Snijders TAB, van de Bunt GG, Steglich CEG. Introduction to stochastic actor-based models for network dynamics. *Social Networks* (2010) 32(1):44–60. doi:10.1016/j.socnet.2009.02.004

68. Chen H, Mehra A, Tasselli S, Borgatti S. Network dynamics and organizations: a review and research agenda. *J Manage* (2022) 48:1602–60. doi:10.1177/01492063211063218

69. Block P, Stadtfeld C, Snijders TAB. Forms of dependence: comparing SAOMs and ERGMs from basic principles. *Sociological Methods and Res* (2019) 48(1):202–39. doi:10.1177/0049124116672680

70. Snijders TAB. Stochastic actor-oriented models for network dynamics. *Annu Rev Stat Its Appl* (2017) 4:343–63. doi:10.1146/annurev-statistics-060116-054035

71. Ripley RM, Preciado PB, editors. *Manual for RSiena* (2011).

72. Omenn GS, Lane L, Overall CM, Pineau C, Packer NH, Cristea IM, et al. The 2022 report on the human Proteome from the HUPO human Proteome project. *J Proteome Res* (2023) 22(4):1024–42. doi:10.1021/acs.jproteome.2c00498

73. Tong TW, Reuer JJ, Peng MW. International joint ventures and the value of growth options. *Acad Manage J* (2008) 51:1014–29. doi:10.5465/amj.2008.34789680

74. Bornmann L. Interrater reliability and convergent validity of F1000Prime peer review. *J Assoc Inf Sci Technol* (2015) 66(12):2415–26. doi:10.1002/asi.23334

75. Chen H, Song X, Jin Q, Wang X. Network dynamics in university-industry collaboration: a collaboration-knowledge dual-layer network perspective. *Scientometrics* (2022) 127(11):6637–60. doi:10.1007/s11192-022-04330-9

76. Taylor A, Greve HR. Superman or the fantastic four? Knowledge combination and experience in innovative teams. *Acad Manage J* (2006) 49:723–40. doi:10.5465/amj.2006.22083029

77. Melin G. Pragmatism and self-organization: research collaboration on the individual level. *Res Pol* (2000) 29(1):31–40. doi:10.1016/s0048-7333(99)00031-1

78. Mohnen M. Stars and brokers: knowledge spillovers among medical scientists. *Manage Sci* (2022) 68(4):2513–32. doi:10.1287/mnsc.2021.4032

Frontiers in Physics

Investigates complex questions in physics to understand the nature of the physical world

Addresses the biggest questions in physics, from macro to micro, and from theoretical to experimental and applied physics.

Discover the latest Research Topics

See more →

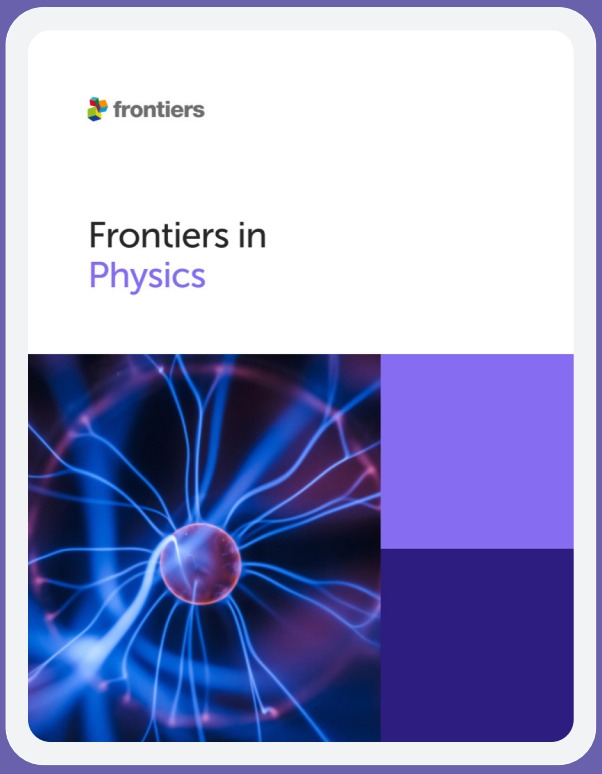

Frontiers

Avenue du Tribunal-Fédéral 34
1005 Lausanne, Switzerland
frontiersin.org

Contact us

+41 (0)21 510 17 00
frontiersin.org/about/contact